

University of Alberta

**Effectiveness of the Stress Relief Procedures and Their Effects on Local Buckling
Behaviour of Buried Pipes**

by

Bing Song



A thesis submitted to the Faculty of Graduate Studies and Research in partial
fulfillment of the requirements for the degree of Doctor of Philosophy

in

Structural Engineering

Department of Civil and Environmental Engineering

Edmonton, Alberta

Spring 2007



Library and
Archives Canada

Bibliothèque et
Archives Canada

Published Heritage
Branch

Direction du
Patrimoine de l'édition

395 Wellington Street
Ottawa ON K1A 0N4
Canada

395, rue Wellington
Ottawa ON K1A 0N4
Canada

Your file *Votre référence*
ISBN: 978-0-494-29751-3
Our file *Notre référence*
ISBN: 978-0-494-29751-3

NOTICE:

The author has granted a non-exclusive license allowing Library and Archives Canada to reproduce, publish, archive, preserve, conserve, communicate to the public by telecommunication or on the Internet, loan, distribute and sell theses worldwide, for commercial or non-commercial purposes, in microform, paper, electronic and/or any other formats.

The author retains copyright ownership and moral rights in this thesis. Neither the thesis nor substantial extracts from it may be printed or otherwise reproduced without the author's permission.

AVIS:

L'auteur a accordé une licence non exclusive permettant à la Bibliothèque et Archives Canada de reproduire, publier, archiver, sauvegarder, conserver, transmettre au public par télécommunication ou par l'Internet, prêter, distribuer et vendre des thèses partout dans le monde, à des fins commerciales ou autres, sur support microforme, papier, électronique et/ou autres formats.

L'auteur conserve la propriété du droit d'auteur et des droits moraux qui protègent cette thèse. Ni la thèse ni des extraits substantiels de celle-ci ne doivent être imprimés ou autrement reproduits sans son autorisation.

In compliance with the Canadian Privacy Act some supporting forms may have been removed from this thesis.

Conformément à la loi canadienne sur la protection de la vie privée, quelques formulaires secondaires ont été enlevés de cette thèse.

While these forms may be included in the document page count, their removal does not represent any loss of content from the thesis.

Bien que ces formulaires aient inclus dans la pagination, il n'y aura aucun contenu manquant.


Canada

University of Alberta

Library Release Form

Name of Author: **Bing Song**

Title of Thesis: **Effectiveness of the Stress Relief Procedures and Their Effects on Local Buckling Behaviour of Buried Pipes**

Degree: **Doctor of Philosophy**

Year this Degree Granted: **2007**

Permission is hereby granted to the University of Alberta Library to reproduce single copies of this thesis and to lend or sell such copies for private, scholarly or scientific research purposes only.

The author reserves all other publication and other rights in association with the copyright in the thesis, and except as herein before provided, neither the thesis nor any substantial portion thereof may be printed or otherwise reproduced in any material form whatever without the author's prior written permission.

Song, Bing

23 - 10910 - 53 Avenue
Edmonton, Alberta
T6H 0S3

Date: *Dec. 21 / 2006*

ABSTRACT

Buried pipelines are the prime mode used by energy industries in North America for transporting natural gas, crude oil, and other hydrocarbon products. At unstable slopes such pipelines in operation are often subjected to combination of large axial deformation and rotation because of geotechnical and environmental conditions. Large strain may be accumulated in the pipes under these loadings, and it may eventually result in the formation of local buckling or even fractures in the pipe wall. It is a common practice that a stress relief procedure is applied to a pipe by removing the soil around the pipe, allowing the pipe to spring back to a zero load state, the frequency of stress relief procedures is dependent on the severity of loading and soil conditions.

This research program was designed to investigate the effectiveness of stress relief procedures and evaluate the behaviour of buried pipes subjected to repetitive stress relief procedure, and assess the timely implementation of the procedure. In order to achieve the objectives, the research program was divided into three phases: Phase I: full-scale laboratory tests on pipeline segments under repetitive cyclic loading; Phase II: pipeline field monitoring program; Phase III: development of finite element model for buried pipelines under stress relief procedure.

A full-scale test program consisting of twelve pipe specimens was conducted. Six tests were loaded axially and other six were loaded under combined axial load and bending. Under each type of loading, the specimens were loaded either monotonically or cyclically. The pipes were under different levels of internal pressure. Results from full-scale tests and numerical analyses show that the load cycling has minimal effect on the global response of the pipes. However, there is more accumulated strain after peak response of pipe at buckling location in cyclic bending than in cyclic axial compression. The general behaviour of the pipe walls was very predictable by the numerical model.

Monitoring programs on two pipelines (Pembina River Crossing and Simonette River Crossing) constructed at active landslides in Alberta are used to obtain information

necessary for the analysis, assessment, and possible mitigation of geotechnical hazards. Slope movement and pipeline deformation data were collected for the calibration of the numerical model developed in the program. Data before and after the stress relief procedure were recorded for investigation of the effectiveness of the stress relief procedure.

A finite element model was developed to simulate the slope movement and the pipeline response at Pembina River Crossing situated at the active soil movement locations. Shell elements were used for pipe and 3D solid elements for soil. Soil-pipe interaction was simulated by setting a special layer of soil surrounding the pipeline. The model incorporates nonlinear material, soil creep and water table changes. The Modified Drucker-Prager Cap Model was used to model the soils based on parameters determined from the direct shear test results. The finite element model was calibrated by slope indicator data and strain gauge data obtained from the monitoring program with satisfactory agreement. The model was used to simulate the strain accumulation in the pipeline before and after the stress relief procedure. Reasonable agreement was achieved when compared to the field data. The model was also used to determine the critical section of the pipeline and to develop the optimum stress relief procedure and schedule for the pipeline at Pembina River Crossing. The guidelines for the stress relief schedule and procedures for the pipeline were given. The model was used in a parametric study to further understand the behaviour of buried pipelines under repeated soil movement and stress relief procedure.

ACKNOWLEDGEMENTS

This study was conducted with the financial assistance of the Geological Survey of Canada, Tokyo Gas and TransCanada Pipelines Ltd. I also acknowledge support, in the form of scholarships, provided by University of Alberta, and the ASME OMAE Calgary Chapter Graduate Scholarship in Engineering.

I first express heartfelt gratitude to my supervisor Dr. J.J. Roger Cheng, he has provided the precious opportunity, the ideal environment, and the best direction in style and content, by which I could sufficiently exploit my potential and complete this project to the best of my ability. More importantly, he led me into this promising field full of challenge and opportunity in which I believe that I am now better prepared to make my own contribution.

I am deeply grateful to my co-supervisors, Dr. Dave H. Chan and Dr. David W. Murray, for their invaluable guidance, assistance, and encouragement. Without their expertise, foresight, and advice, it would have been impossible for me to achieve present progress.

At the University of Alberta, Mr. Richard Helfrich and Larry Burden, technicians at the I.F. Morrison Structural Lab, helping with the testing program, are appreciated.

The cyclic compressive tests on 30'' diameter pipes were led by Dr. H-A Khoo, and 20'' diameter pipes by Dr. Sreekanda Das. Help from Dr. A. Dorey and fellow students Millan Sen and Xuejun Song with the test program is appreciated.

Many other people, including the administrative staff of Graduate Education Program in the Department of Civil and Environmental Engineering and my family members, have contributed to the completion of this project. I sincerely acknowledge the help provided by every one of them.

Table of Contents

CHAPTER 1 INTRODUCTION.....	1
1.1 General Background.....	1
1.2 Objective.....	2
1.3 Scope.....	2
1.4 Organization of the Thesis.....	4
CHAPTER 2 LITERATURE REVIEW.....	6
2.1 Slope Movement.....	6
2.2 Stress Relief Examples.....	7
2.3 Mechanism of Slope Instability.....	8
2.4 Analytical Methods of Pipe Soil Interaction.....	9
2.4.1 <i>Discrete Analysis.....</i>	9
2.4.2 <i>Continuum Analysis.....</i>	9
2.4.3 <i>Approximate Analytical Solutions.....</i>	10
2.5 Numerical Modeling of Pipe Soil Interaction.....	18
2.5.1 <i>Finite Difference Solution.....</i>	18
2.5.2 <i>Finite Element Method.....</i>	19
2.5.3 <i>Finite Element Analysis – Structural.....</i>	19
2.5.4 <i>Finite Element Analysis – Continuum Models.....</i>	22
CHAPTER 3 STRESS RELIEF TESTING PROGRAM WITH 20’ DIAMETER PIPES AND 30’ DIAMETER PIPES.....	23
3.1 Introduction	23
3.2 Compression Test Program	23
3.2.1 <i>Pretest Measurements.....</i>	24
3.2.2 <i>Test Setup.....</i>	25
3.2.3 <i>Instrumentation.....</i>	25
3.2.4 <i>Loading.....</i>	26
3.2.5 <i>Ancillary Test.....</i>	27

3.3	Compression Test Results.....	28
3.3.1	<i>General.....</i>	28
3.3.2	<i>Overall Results.....</i>	28
3.3.3	<i>30" Specimens Results.....</i>	29
3.3.4	<i>20" Specimens.....</i>	31
3.3.5	<i>Local Buckling Strain.....</i>	32
3.4	Bending Test Program	32
3.4.1	<i>Pretest Measurements</i>	33
3.4.2	<i>Test Setup.....</i>	34
3.4.3	<i>Instrumentation</i>	35
3.4.4	<i>Loading</i>	37
3.4.5	<i>Coupon Test.....</i>	40
3.5	Bending Test Results	41
3.5.1	<i>General</i>	41
3.5.2	<i>Overall Results</i>	42
3.5.3	<i>30" Inch Pipes Results.....</i>	43
3.5.4	<i>20" Pipes Results.....</i>	46
CHAPTER 4	FINITE ELEMENT ANALYSIS OF THE STRESS RELIEF	
	TEST RESULTS AND DISCUSSION	152
4.1	Introduction	152
4.2	Numerical Analysis of Compression Tests	152
4.2.1	<i>General</i>	152
4.2.2	<i>Discussion</i>	153
4.3	Numerical Analysis of Bending Tests	155
4.4	Summary and Conclusions.....	156
CHAPTER 5	PEMBINA RIVER CROSSING MONITORING PROGRAM	168
5.1	Description of the Pembina River Crossing	168
5.1.1	<i>Location</i>	168
5.1.2	<i>The Natural Ground.....</i>	168

5.1.3	<i>Site History</i>	169
5.2	Field Monitoring Program	169
5.3	Location of Instrumentation	170
5.4	Geologic Background	171
5.5	Hydrogeology	171
5.6	Available Field Data	172
5.6.1	<i>Slope Indicator</i>	172
5.6.2	<i>Strain Gauge</i>	173
 CHAPTER 6 SIMONETTE RIVER CROSSING MONITORING PROGRAM		220
6.1	Description of the Simonette River Crossing	220
6.1.1	<i>Location of the Site</i>	220
6.1.2	<i>History of the Pipeline</i>	220
6.2	Geology	220
6.2.1	<i>Regional Geology</i>	221
6.2.2	<i>Local Geology</i>	222
6.3	Hydrogeology	227
6.4	Available Field Data	228
6.4.1	<i>Slope Indicator</i>	228
6.4.2	<i>Strain Gauge</i>	228
6.5	Slope Stability	229
6.6	Summary	230
 CHAPTER 7 DEVELOPMENT OF NUMERICAL MODEL		249
7.1	Introduction	249
7.2	Preliminary Thoughts and Concerns	249
7.2.1	<i>What Is the Scope of the Model</i>	250
7.2.2	<i>Soil Properties</i>	251
7.2.3	<i>What Finite Element to Be Used</i>	251
7.2.4	<i>Stress Relief Procedures</i>	252
7.2.5	<i>Load History and Analysis Result Expectation</i>	252

7.3	Mechanism of Slope Movement.....	253
7.3.1	<i>Slope Indicator Data.....</i>	253
7.3.2	<i>Pipeline Monitoring Data.....</i>	259
7.4	Mechanical Behaviour and Conditions of Geotechnical Materials.....	260
7.4.1	<i>Soft Clay.....</i>	262
7.4.2	<i>Clay till.....</i>	262
7.4.3	<i>Slip Surface Layer.....</i>	263
7.4.4	<i>Sandstone.....</i>	263
7.5	Finite Element Modeling Procedures.....	263
7.5.1	<i>Introduction –Purpose of Finite Element Analysis.....</i>	264
7.5.2	<i>Geometry of the Model.....</i>	265
7.5.3	<i>Hydraulic Behaviour and Conditions.....</i>	266
7.5.4	<i>FE Mesh and Boundary Conditions.....</i>	267
7.5.5	<i>Numerical Approach and Hypothesis.....</i>	269
7.5.6	<i>Constitutive Model.....</i>	271
7.5.7	<i>Direct Shear Test.....</i>	276
7.5.8	<i>Load Sequence.....</i>	279
7.5.9	<i>Stress Relief Simulation.....</i>	281
7.6	Summary.....	282
 CHAPTER 8 FINITE ELEMENT RESULTS AND DISCUSSIONS.....		318
8.1	Validation of the Finite Element Model.....	318
8.1.1	<i>Slope Stress and Displacement.....</i>	318
8.1.2	<i>Comparisons of Soil Movement Data.....</i>	320
8.1.3	<i>Comparisons of Strain Gauge Data.....</i>	320
8.2	Simulation of Pipeline Response at Some Typical Years.....	322
8.3	Optimum Stress Relief Procedures.....	325
8.3.1	<i>Stress Relief Operating Schedule.....</i>	325
8.3.2	<i>Prediction of Next Stress Relief Procedure.....</i>	325
8.3.3	<i>Effective Scope of Stress Relief.....</i>	326

8.4	Discussion of FEA.....	328
CHAPTER 9	PARAMETRIC STUDY OF STRESS RELIEF PROGRAM..	381
9.1	Introduction.....	381
9.2	Parametric Studies.....	382
9.2.1	<i>Internal Pressure.....</i>	382
9.2.2	<i>D/t Ratio.....</i>	383
9.2.3	<i>Material Grade</i>	384
9.2.4	<i>Boundary Condition.....</i>	384
9.2.5	<i>Slip Surface.....</i>	385
9.2.6	<i>Pipe Soil Interaction.....</i>	385
9.2.7	<i>Soil Creep Parameters.....</i>	386
9.2.8	<i>Strain Accumulation Time.....</i>	387
9.2.9	<i>Soil Strength.....</i>	387
9.3	Summary of Parametric Study.....	388
CHAPTER 10	SUMMARY, CONCLUSIONS AND RECOMMENDATIONS	400
10.1	Summary.....	400
10.2	Conclusions.....	401
10.3	Recommendations.....	403
REFERENCES		405

List of Tables

Table 3.1	Test specimens and loading matrix.....	50
Table 3.2	Average pretest measurements.....	50
Table 3.3	Applied internal pressure.....	51
Table 3.4	General mechanical properties of the pipe 30 inch pipes.....	51
Table 3.5	Stress-strain relationship of the 30 inch pipe in the longitudinal direction ...	52
Table 3.6	Stress-strain relationship of the 20 inch pipe in the longitudinal direction....	53
Table 3.7	Location of buckling in the test.....	54
Table 3.8	Tested and predicted compressive D local buckling strain.....	54
Table 3.9	Test specimens and loading matrix.....	55
Table 3.10	Dimensions of specimens.....	55
Table 3.11	Expected loading on the specimens.....	56
Table 3.12	Summary of Mechanical Properties of Tension Coupons.....	56
Table 3.13	Location of buckling in the test.....	57
Table 3.14	Comparison of accumulated strain and critical strain for 30inch pipes	58
Table 4.1	Test and predicted compressive D local buckling strain.....	158
Table 5.1	Latitude and Longitude of Lodgepole and Edmonton.....	175
Table 5.2	The latest X and Y and Ratio of Y to X near ground at 12 SI locations.....	175
Table 6.1	Latitude and Longitude of Grande Prairie and Edmonton.....	233
Table 7.1	Locations of Climate Stations near LodgePole.....	283
Table 7.2	Soil Movement in X Direction near Ground Surface.....	283
Table 7.3	Soil Motion at SI5 in X direction (mm).....	284
Table 7.4	Total precipitation (mm) in 1987-1991 at Wildwood Newbery.....	284
Table 7.5	Total precipitation (mm) in 1992-1997.....	285
Table 7.6	Total precipitation (mm) in 1998-1999 at Entwistle.....	285
Table 7.7	Soil Motion at SI5A in X direction (mm).....	286
Table 7.8	Total precipitation (mm) in 2000-2001.....	286
Table 7.9	Soil Motion Increment in X direction.....	286
Table 7.10	Monthly Precipitation, mm, for 1986-2000.....	287
Table 7.11	Soil Motion at SI6 in X direction (mm).....	288

Table 7.12 Soil Motion at SI7 in X direction (mm).....	288
Table 7.13 Soil Motion at SI8 in X direction (mm).....	288
Table 7.14 Soil Motion at SI10A in X direction (mm).....	288
Table 7.15 Soil Motion at SI10B in X direction (mm).....	289
Table 7.16 Soil Motion at SI11A in X direction (mm).....	289
Table 7.17 Soil Motion at SI11B in X direction (mm).....	289
Table 7.18 Soil Motion at SI12 in X direction (mm).....	289
Table 7.19 Soil Motion at SI12A in X direction (mm).....	290
Table 7.20 Soil Motion at SI12B in X direction (mm).....	290
Table 7.21 SG1 SG2 SG3 SG4 at Station 1-4.....	290
Table 7.22 Soil Properties.....	291
Table 8.1 Comparison of Soil Movement U_2 , mm/yr near Ground Surface at 5SIs in 2000.....	329
Table 8.2 SG1 SG2 SG3 SG4 at Strain Gauge Stations 1-4.....	329
Table 8.3 Comparison of Average Axial Accumulated Strain in ϵ_a at Station 3 and Station 4 in the Year 2000.....	329
Table 8.4 Comparison of Average Axial Accumulated Stress σ_a at Station 3 and Station 4 in the Year 2000.....	329
Table 8.5 Comparison of Soil Movement U_2 , mm/yr near Ground Surface in 1995....	330
Table 8.6 Comparison of Soil Movement U_2 , mm/yr near Ground Surface in 1992....	330
Table 8.7 Comparison of Soil Movement U_2 , mm/yr near Ground Surface in 1989....	330
Table 8.8 Maximum Accumulated Compressive Stress/Strain and Theirs Locations in 1989, 1992, 1995, and 2000.....	330
Table 8.9 Estimation of Yearly Maximum Axial Stress/Strain Accumulation in 1986- 2005.....	331
Table 8.10 Soil Movement U_2 mm in three years near Ground Surface with normal precipitation.....	331
Table 9.1 Parametric Study Model Matrix.....	389
Table 9.2 Maximum Axial Stress Results Matrix.....	392

List of Figures

Figure 3.1	Plan view, angular coordinate system convention.....	59
Figure 3.2	Test setup.....	60
Figure 3.3	Test setup for 30 inch pipes.....	61
Figure 3.4	Test setup for 20 inch pipes.....	62
Figure 3.5	Locations of Demec points and their corresponding Demec gauge designation on the north face (45°) of 30 inch pipes.....	63
Figure 3.6	Locations of Demec points at 180° and 0° of 20 inch pipes.....	64
Figure 3.7	Locations and channel numbers for the strain gauges on the south face (225°) of 30 inch pipes.....	65
Figure 3.8	Locations and channel numbers for the strain gauges on the west, north and east faces (315°, 45° and 135°) of 30 inch pipes.....	66
Figure 3.9	Locations and channel numbers for the strain gauges on the 30 inch pipes.....	67
Figure 3.10	Engineering stress strain curves of tension coupons for 30 inch pipes.....	68
Figure 3.11	Engineering stress strain curves of tension coupons for 20 inch pipes.....	68
Figure 3.12	Comparison of the Engineering stress strain curves of 20 inch and 30 inch pipes.....	69
Figure 3.13	Comparison of the Engineering stress vs. jack stoke curves of 20 inch and 30 inch pipes	69
Figure 3.14	Buckled shape of D30P80AM-1, west elevation.....	70
Figure 3.15	Buckled shape of D30P80AC-2, south elevation.....	71
Figure 3.16	Buckled shape of D30P20AC-3, west elevation.....	72
Figure 3.17	Buckled shape of D20P80AM-4, west elevation.....	73
Figure 3.18	Buckled shape of D20P40AM-5, west elevation.....	74
Figure 3.19	Buckled shape of D20P40AC-6, west elevation.....	75
Figure 3.20	Global strain vs. average strain gauge reading for D30P80AM-1.....	76
Figure 3.21	Global strain vs. average strain gauge reading for D30P80AC-2.....	76
Figure 3.22	Global strain vs. average strain gauge reading for D30P20AC-3.....	77
Figure 3.23	Global strain vs. average strain gauge reading for D20P80AM-4.....	77
Figure 3.24	Global Strain vs. average strain gauge reading for D20P40AM-5.....	78

Figure 3.25	Global Strain vs. average strain gauge reading for D20P40AC-6.....	78
Figure 3.26	Selective Demec and average strain gauge readings for D30P80AM-1.....	79
Figure 3.27	Selective Demec and average strain gauge reading for D20P80AM-4.....	79
Figure 3.28	Load vs. net compressive global strain for the D30P80 specimens.....	80
Figure 3.29	Load vs. local D compressive strain for the D30P80 specimens.....	80
Figure 3.30	Load vs. net compressive global strain for D30P20AC-3 specimen.....	81
Figure 3.31	Load vs. local D compressive strain for D30P20AC-3 specimen.....	81
Figure 3.32	Load vs. net compressive global strain for D20P80AM-4 specimen.....	82
Figure 3.33	Load vs. D local compressive strain for D20P80AM-4.....	82
Figure 3.34	Global vs. D local compressive strain for D20P80AM-4 specimen.....	83
Figure 3.35	Load vs. net compressive global strain for D20P40 specimens.....	83
Figure 3.36	Load vs. D local compressive strain for the D20P40 specimens.....	84
Figure 3.37	Global vs. local D compressive strain for the D30P80 specimens.....	84
Figure 3.38	Global vs. local D compressive strain for D30P20AC-3 specimen.....	85
Figure 3.39	Global vs. D local compressive strain for D20P40 specimens.....	85
Figure 3.40	Plane View of Angular Coordinate System Convention.....	86
Figure 3.41	Initial Imperfection Measurement Apparatus.....	87
Figure 3.42	Schematic Test Setup.....	88
Figure 3.43	Front View of Test Setup for 30 inch Pipes.....	89
Figure 3.44	Back View of Test Setup for 30 inch Pipes.....	90
Figure 3.45	Test Setup for 20 inch Pipes.....	91
Figure 3.46	Locations of Demec Points and Strain Gauges and Their Corresponding Designation on the West Face (0°) for 20 inch Pipes (Unit: mm).....	92
Figure 3.47	Locations of Demec Points and Strain Gauges and Their Corresponding Designation on the East Face (180°) for 20 inch Pipes (Unit: mm).....	93
Figure 3.48	Locations of Demec Points and Strain Gauges and Their Corresponding Designation on the West Face (0°) for D30P80BC-8 and D30P20BC-9 (Demec Points for 7 th Specimen) (Unit: mm).....	94
Figure 3.49	Locations of Demec Points and Strain Gauges and Their Corresponding Designation on the East Face (180°) for D30P80BC-8 and D30P20BC-9 (Demec Points for 7 th Specimen) (Unit: mm).....	95

Figure 3.50	Locations of Demec Points and Strain Gauges and Their Corresponding Designation on the West Face (0°) for D30P0BC-7 (Unit: mm).....	96
Figure 3.51	Locations of Demec Points and Strain Gauges and Their Corresponding Designation on the East Face (180°) for D30P0BC-7 (Unit: mm).....	97
Figure 3.52	Locations of Strain Gauges and Their Corresponding Designation on the South Face (270°) and North Face (90°) for 20 inch Pipes (Unit: mm).....	98
Figure 3.53	Locations of Strain Gauges and Their Corresponding Designation on the South Face (270°) and North Face (90°) for 30 inch Pipes (Unit: mm).....	99
Figure 3.54	LVDTs on the West Face (0°) for 20 inch (30 inch) Pipes (Unit: mm)....	100
Figure 3.55	LVDTs on the East Face (180°) for 20 inch (30 inch) Pipes (Unit: mm)..	101
Figure 3.56	Setup of LVDTs	102
Figure 3.57	Cable Transducers Positions (Unit: mm).....	103
Figure 3.58	Photos of Cable Transducers.....	104
Figure 3.59	Typical Moment Curvature for a Monotonic Bending Test.....	105
Figure 3.60	Loading Sequence of Cyclic Tests.....	105
Figure 3.61	Position of Coupon in D20P40BM-11 (Unit: mm).....	106
Figure 3.62	Coupon in Longitudinal Direction for 20 inch Pipes (Unit: mm).....	107
Figure 3.63	Coupon in Hoop Direction for 20 inch Pipes (Unit: mm).....	108
Figure 3.64	Curve Coupon in Hoop Direction for 20 inch Pipes (Unit: mm).....	109
Figure 3.65	Stress vs. Strain Curve of Straightened Transverse Coupon #1.....	110
Figure 3.66	Stress vs. Strain Curve of Straightened Transverse Coupon #2.....	110
Figure 3.67	Stress vs. Strain Curve of Straightened Transverse Coupon #3	111
Figure 3.68	Stress vs. Strain Curve of Straightened Transverse Coupon #1-3.....	111
Figure 3.69	Stress vs. Strain Curve of Longitudinal Coupon #1.....	112
Figure 3.70	Stress vs. Strain Curve of Longitudinal Coupon #2.....	112
Figure 3.71	Stress vs. Strain Curve of Longitudinal Coupon #3.....	113
Figure 3.72	Stress vs. Strain Curve of Longitudinal Coupon #1-3.....	113
Figure 3.73	Stress vs. Strain for Curve Hoop Coupon #1-4.....	114
Figure 3.74	Buckle Position in D30P0BC-7.....	114
Figure 3.75	Buckle Shape of D30P0BC-7.....	116
Figure 3.76	Buckle Position in D30P80BC-8.....	117

Figure 3.77	Buckle Shape of D30P80BC-8.....	118
Figure 3.78	Second Bulge Position in D30P80BC-8.....	118
Figure 3.79	Buckle Position in D30P80BC-8 and D30P20BC-9.....	119
Figure 3.80	Buckle Shape of D30P20BC-9.....	119
Figure 3.81	The Family Picture of 30 inch Pipes After Tests.....	121
Figure 3.82	Buckle Position in D20P80BM-10.....	122
Figure 3.83	Buckle Shape of D20P80BM-10.....	123
Figure 3.84	Second Bulge Position in D20P80BM-10.....	123
Figure 3.85	Buckle Position in D20P40BM-11.....	124
Figure 3.86	Northern View of Buckle Shape in D20P40BM-11.....	125
Figure 3.87	Western View of Buckle Shape in D20P40BM-11.....	125
Figure 3.88	Buckle Position in D20P40BC-12.....	126
Figure 3.89	Buckle Position in D20P40BC-12.....	127
Figure 3.90	Buckle Shape of D20P40BC-12.....	128
Figure 3.91	Second Bulge Position in D20P40BC-12.....	128
Figure 3.92	The Family Picture of 20 inch Pipes after Tests.....	129
Figure 3.93	Global Moment vs. Global Curvature For D30P0BC-7.....	130
Figure 3.94	Global Moment vs. Global Curvature For D30P0BC-7.....	130
Figure 3.95	Global Moment vs. Local Strain at DC-9 For D30P0BC-7.....	131
Figure 3.96	Global Moment vs. Local Curvature at DC-9 For D30P0BC-7.....	131
Figure 3.97	Global Curvature vs. Local Curvature at DC-9 For D30P0BC-7.....	132
Figure 3.98	Global Curvature vs. Local Strain at DC-9 For D30P0BC-7.....	132
Figure 3.99	Global Moment vs. Global Curvature For D30P80BC-8.....	133
Figure 3.100	Global Moment vs. Global Curvature For D30P80BC-8.....	133
Figure 3.101	Global Moment vs. Local Strain At DC-1 For D30P80BC-8.....	134
Figure 3.102	Global Moment vs. Local Strain At DC-9 For D30P80BC-8.....	134
Figure 3.103	Global Moment vs. Local Curvature At DC-1 For D30P80BC-8.....	135
Figure 3.104	Global Curvature vs. Local Curvature At DC-1 For D30P80BC-8.....	135
Figure 3.105	Global Curvature vs. Local Strain At DC-1 For D30P80BC-8.....	136
Figure 3.106	Global Curvature vs. Local Strain At DC-9 For D30P80BC-8.....	136
Figure 3.107	Global Moment vs. Global Curvature For D30P20BC-9.....	137

Figure 3.108 Global Moment vs. Global Curvature For D30P20BC-9.....	137
Figure 3.109 Global Moment vs. Local Strain At DC-9 For D30P20BC-9.....	138
Figure 3.110 Global Moment vs. Local Curvature At DC-9 For D30P20BC-9.....	138
Figure 3.111 Global Curvature vs. Local Curvature At DC-9 For D30P20BC-9.....	139
Figure 3.112 Global Curvature vs. Local Strain At DC-9 For D30P20BC-9.....	139
Figure 3.113 Global Moment vs. Global Curvature For 30' Pipes.....	140
Figure 3.114 Global Moment vs. Global Curvature For D20P80BM-10.....	140
Figure 3.115 Global Moment vs. Local Strain At DC-3,4,5 For D20P80BM-10.....	141
Figure 3.116 Global Moment vs. Local Strain At DC-13,14,15 For D20P80BM-10....	141
Figure 3.117 Global Moment vs. Local Curvature At DC-3,4,5 For D20P80BM-10....	142
Figure 3.118 Global Curvature vs. Local Curvature At DC-3-5 For D20P80BM-10....	142
Figure 3.119 Global Curvature vs. Local Strain At DC-3-5 For D20P80BM-10.....	143
Figure 3.120 Global Curvature vs. Local Strain At DC-13-15 For D20P80BM-10.....	143
Figure 3.121 Global Moment vs. Global Curvature For D20P40BM-11.....	144
Figure 3.122 Global Moment vs. Local Strain At DC-10-13 For D20P40BM-11.....	144
Figure 3.123 Global Moment vs. Local Curvature At DC-10-13 For D20P40BM-11...	145
Figure 3.124 Global Curvature vs. Local Curvature At DC-10-13 For D20P40BM-11.	145
Figure 3.125 Global Curvature vs. Local Strain At DC-10-13 For D20P40BM-11.....	146
Figure 3.126 Global Moment vs. Global Curvature For D20P40BC-12.....	146
Figure 3.127 Global Moment vs. Global Curvature For D20P40BC-12.....	147
Figure 3.128 Global Moment vs. Local Strain At DC-3,4,5,6 For D20P40BC-12.....	147
Figure 3.129 Global Moment vs. Local strain At DC-14,15 For D20P40BC-12.....	148
Figure 3.130 Global Moment vs. Local Curvature At DC-3-6 For D20P40BC-12.....	148
Figure 3.131 Global Curvature vs. Local Curvature At DC-3-6 For D20P40BC-12.....	149
Figure 3.132 Global Curvature vs. Local Strain At DC-3-6 For D20P40BC-12.....	149
Figure 3.133 Global Curvature vs. Local Strain At DC-14,15 For D20P40BC-12.....	150
Figure 3.134 Global Moment vs. Global Curvature For D20P40BM-11, D20P40BC- 12	150
Figure 3.135 Global Moment vs. Global Curvature For D20P80BM-10, D20P40BM- 11	151

Figure 4.1	Test and predicted load vs. net compressive global strain for D30P80AM-1.....	159
Figure 4.2	Test and predicted load vs. D local compressive strain for D30P80AM-1.....	159
Figure 4.3	Test and predicted load vs. net compressive global strain for D30P80AC-2.....	160
Figure 4.4	Analytical load vs. net compressive global strain for P80 tests.....	160
Figure 4.5	Test and predicted load vs. net compressive global strain for D30P20AC-3.....	161
Figure 4.6	Test and predicted load vs. D local compressive strain for D30P20AC-3.....	161
Figure 4.7	Analytical load vs. net compressive global strain for P20 tests.....	162
Figure 4.8	Predicted deformed shape for P80 test.....	162
Figure 4.9	Predicted deformed shape for P20 test.....	163
Figure 4.10	Numerical analysis and test results of Net pipe load vs. End deformation for D20P80AM-4.....	163
Figure 4.11	Effect of hoop yield stress on the buckling behaviour of D20P80AM-4.....	164
Figure 4.12	Numerical analysis and test results of net pipe load vs. end deformation for AM-5.....	164
Figure 4.13	Test and Predicted Global Moment vs. Global Curvature for D30P0BC-7.....	165
Figure 4.14	Test and Predicted Global Moment vs. Global Curvature for D30P80BC-8.....	165
Figure 4.15	Test and Predicted Global Moment vs. Global Curvature for D30P20BC-9.....	166
Figure 4.16	Test and Predicted Global Moment vs. Global Curvature for D20P80BM-10.....	166
Figure 4.17	Test and Predicted Global Moment vs. Global Curvature for D20P40BM-11.....	167
Figure 4.18	Global Moment vs. Global Curvature for Specimens 10, 11, and 12.....	167
Figure 5.1	Geographic Location of Pembina River Crossing.....	176
Figure 5.2	Location Plan of Pembina River Crossing N.E. ¼ SEC.8 TWP.47 RGE.9 W5M.....	176

Figure 5.3	Plan of Pipeline with Strain Gauge Sections.....	177
Figure 5.4	Profile of Pipeline with Strain Gauge Sections.....	177
Figure 5.5	Pembina River Crossing Plan and Profile.....	178
Figure 5.6	Locations of Strain Gauges on Pipe Section.....	178
Figure 5.7	Profile of Pipeline and Slope at Pembina River Crossing with Instrumentation SIs and SGs.....	179
Figure 5.8	Soil Movement in X direction at SI5 at Different Period of Time.....	180
Figure 5.9	Soil Movement in X direction at SI5 at Different Depths.....	180
Figure 5.10	Soil Movement in Y direction at SI5 at Different Period of Time.....	181
Figure 5.11	Soil Movement in Y direction at SI5 at Different Depths.....	181
Figure 5.12	Soil Movement in X direction at SI5A at Different Period of Time.....	182
Figure 5.13	Soil Movement in X direction at SI5A at Different Depths.....	182
Figure 5.14	Soil Movement in Y direction at SI5A at Different Period of Time.....	183
Figure 5.15	Soil Movement in Y direction at SI5A at Different Depths.....	183
Figure 5.16	Soil Movement in X direction at SI6 at Different Period of Time.....	184
Figure 5.17	Soil Movement in X direction at SI6 at Different Depths.....	184
Figure 5.18	Soil Movement in Y direction at SI6 at Different Period of Time.....	185
Figure 5.19	Soil Movement in Y direction at SI6 at Different Depths.....	185
Figure 5.20	Soil Movement in X direction at SI7 at Different Period of Time.....	186
Figure 5.21	Soil Movement in X direction at SI7 at Different Depths.....	186
Figure 5.22	Soil Movement in Y direction at SI7 at Different Period of Time.....	187
Figure 5.23	Soil Movement in Y direction at SI7 at Different Depths.....	187
Figure 5.24	Soil Movement in X direction at SI8 at Different Period of Time.....	188
Figure 5.25	Soil Movement in X direction at SI8 at Different Depths.....	188
Figure 5.26	Soil Movement in Y direction at SI8 at Different Period of Time.....	189
Figure 5.27	Soil Movement in Y direction at SI8 at Different Depths.....	189
Figure 5.28	Soil Movement in X direction at SI10A at Different Period of Time.....	190
Figure 5.29	Soil Movement in X direction at SI10A at Different Depths.....	190
Figure 5.30	Soil Movement in Y direction at SI10A at Different Period of Time.....	191
Figure 5.31	Soil Movement in Y direction at SI10A at Different Depths.....	191
Figure 5.32	Soil Movement in X direction at SI10B at Different Period of Time.....	192

Figure 5.33	Soil Movement in X direction at SI10B at Different Depths.....	192
Figure 5.34	Soil Movement in Y direction at SI10B at Different Period of Time.....	193
Figure 5.35	Soil Movement in Y direction at SI10B at Different Depths.....	193
Figure 5.36	Soil Movement in X direction at SI11A at Different Period of Time.....	194
Figure 5.37	Soil Movement in X direction at SI11A at Different Depths.....	194
Figure 5.38	Soil Movement in Y direction at SI11A at Different Period of Time.....	195
Figure 5.39	Soil Movement in Y direction at SI11A at Different Depths.....	195
Figure 5.40	Soil Movement in X direction at SI11B at Different Period of Time.....	196
Figure 5.41	Soil Movement in X direction at SI11B at Different Depths.....	196
Figure 5.42	Soil Movement in Y direction at SI11B at Different Period of Time.....	197
Figure 5.43	Soil Movement in Y direction at SI11B at Different Depths.....	197
Figure 5.44	Soil Movement in X direction at SI12 at Different Period of Time.....	198
Figure 5.45	Soil Movement in X direction at SI12 at Different Depths.....	198
Figure 5.46	Soil Movement in Y direction at SI12 at Different Period of Time.....	199
Figure 5.47	Soil Movement in Y direction at SI12 at Different Depths.....	199
Figure 5.48	Soil Movement in X direction at SI12A at Different Period of Time.....	200
Figure 5.49	Soil Movement in X direction at SI12A at Different Depths.....	200
Figure 5.50	Soil Movement in Y direction at SI12A at Different Period of Time.....	201
Figure 5.51	Soil Movement in Y direction at SI12A at Different Depths.....	201
Figure 5.52	Soil Movement in X direction at SI12B at Different Period of Time.....	202
Figure 5.53	Soil Movement in X direction at SI12B at Different Depths.....	202
Figure 5.53	Soil Movement in Y direction at SI12B at Different Period of Time.....	203
Figure 5.54	Soil Movement in Y direction at SI12B at Different Depths.....	203
Figure 5.55	Strain Gauge 1 vs. time at Station 1.	204
Figure 5.56	Strain Gauge 2 vs. time at Station 1.....	204
Figure 5.57	Strain Gauge 3 vs. time at Station 1.....	205
Figure 5.58	Strain Gauge 4 vs. time at Station 1.....	205
Figure 5.59	Strain Gauge 1 vs. time at Station 2.....	206
Figure 5.60	Strain Gauge 2 vs. time at Station 2.....	206
Figure 5.61	Strain Gauge 3 vs. time at Station 2.....	207
Figure 5.62	Strain Gauge 4 vs. time at Station 2.....	207

Figure 5.63	Strain Gauge 1 vs. time at Station 3.....	208
Figure 5.64	Strain Gauge 2 vs. time at Station3.....	208
Figure 5.65	Strain Gauge 3 vs. time at Station 3.....	209
Figure 5.66	Strain Gauge 4 vs. time at Station 3.....	209
Figure 5.67	Strain Gauge 1 vs. time at Station 4.....	210
Figure 5.68	Strain Gauge 2 vs. time at Station 4.....	210
Figure 5.69	Strain Gauge 3 vs. time at Station 4.....	211
Figure 5.70	Strain Gauge 4 vs. time at Station 4..	211
Figure 5.71	Strain Gauge 1 vs. time at Station 1.....	212
Figure 5.72	Strain Gauge 2 vs. time at Station 1.....	212
Figure 5.73	Strain Gauge 3 vs. time at Station 1.....	213
Figure 5.74	Strain Gauge 4 vs. time at Station 1.....	213
Figure 5.75	Strain Gauge 1 vs. time at Station 2.....	214
Figure 5.76	Strain Gauge 2 vs. time at Station 2.....	214
Figure 5.77	Strain Gauge 3 vs. time at Station 2.....	215
Figure 5.78	Strain Gauge 4 vs. time at Station 2.....	215
Figure 5.79	Strain Gauge 1 vs. time at Station 3.	216
Figure 5.80	Strain Gauge 2 vs. time at Station 3.....	216
Figure 5.81	Strain Gauge 3 vs. time at Station 3.	217
Figure 5.82	Strain Gauge 4 vs. time at Station 3.	217
Figure 5.83	Strain Gauge 1 vs. time at Station 4.21.....	218
Figure 5.85	Strain Gauge 3 vs. time at Station 4	219
Figure 5.86	Strain Gauge 4 vs. time at Station 4.....	219
Figure 6.1	Geographic Location of Simonette River Crossing	234
Figure 6.2	Simonette River Crossing Pipeline Plan View and Strain Gauge Sections.234	
Figure 6.3	Simonette River Crossing Pipeline Profile and Strain Gauge Sections.....	234
Figure 6.4	Simonette River Crossing Plan View and Slope Indicator Locations.....	235
Figure 6.5	Locations of Strain Gauges on Pipe Station.....	235
Figure 6.6	Zeroed Strain vs. Time at Station 1.	236
Figure 6.7	Zeroed Strain vs. Time at Station 1.	236
Figure 6.8	Zeroed Strain vs. Time at Station 2.	237

Figure 6.9	Zeroed Strain vs. Time at Station 3.	237
Figure 6.10	Zeroed Strain vs. Time at Station 3..	238
Figure 6.11	Zeroed Strain vs. Time at Station 4..	238
Figure 6.12	Zeroed Strain vs. Time at Station 4.	239
Figure 6.13	Zeroed Strain vs. Time at Station 5.....	239
Figure 6.14	Zeroed Strain vs. Time at Station 5.	240
Figure 6.15	Zeroed Strain vs. Time at Station 6.....	240
Figure 6.16	Zeroed Strain vs. Time at Station 6.	241
Figure 6.17	Zeroed Strain vs. Time at Station 7..	241
Figure 6.18	Zeroed Strain vs. Time at Station 7.....	242
Figure 6.19	Zeroed Strain vs. Time at Station 8.....	242
Figure 6.20	Zeroed Strain vs. Time at Station 8.....	243
Figure 6.21	Zeroed Strain vs. Time at Station 9.	243
Figure 6.22	Zeroed Strain vs. Time at Station 10.....	244
Figure 6.23	Zeroed Strain vs. Time at Station 10.....	244
Figure 6.24	Zeroed Strain vs. Time at Station 11.....	245
Figure 6.25	Zeroed Strain vs. Time at Station 11.....	245
Figure 6.26	Zeroed Strain vs. Time at Station 12.....	246
Figure 6.27	Zeroed Strain vs. Time at Station 12.....	246
Figure 6.28	Zeroed Strain vs. Time at Station 13.	247
Figure 6.29	Zeroed Strain vs. Time at Station 14.....	247
Figure 6.30	Zeroed Strain vs. Time at Station 15.....	248
Figure 7.1	Soil Movement in X direction at Different Depths, U_2 , at SI5.....	293
Figure 7.2	Monthly Average Precipitation 1987-1999.....	293
Figure 7.3	Soil Movement in X direction at Different Depths, U_2 , at SI5A.....	294
Figure 7.4	Total Precipitation in 2000-2001.....	294
Figure 7.5	Soil Movement Increment in X direction at SI5A.....	295
Figure 7.6	Soil Movement in X direction at Different Depths, U_2 , at SI-6.....	295
Figure 7.7	Yearly and May-Sep Precipitation for Years 1986-2001.....	296
Figure 7.8	Monthly Soil Movement increment in X direction at SI6.....	296
Figure 7.9	Soil Movement in X direction at Different Depths, U_2 , at SI7.....	297

Figure 7.10	Monthly Soil Movement increment in X direction at SI7.....	297
Figure 7.11	Soil Movement in X direction at Different Depths, U_2 , at SI8.....	298
Figure 7.12	Soil Movement in X direction at Different Depths, U_2 , at SI10A.	298
Figure 7.13	Monthly Precipitation in 1997-1999 at Entwistle	299
Figure 7.14	Precipitation at Brazeau Lo 1997-1999	299
Figure 7.15	Soil Movement in X direction at Different Depths, U_2 , at SI10B..	300
Figure 7.16	Precipitation at Brazeau Lo, in 2000, 2001.....	300
Figure 7.17	Monthly increment of U_2 versus time at different depths for SI10B.....	301
Figure 7.18	Soil Movement in X direction at Different Depths, U_2 , at SI11A.	301
Figure 7.19	Soil Movement in X direction at Different Depths, U_2 , at SI11B..	302
Figure 7.20	Monthly increment of U_2 versus time at these same depths for SI11B.....	302
Figure 7.21	Soil Movement in X direction at Different Depths, U_2 , at SI12..	303
Figure 7.22	Precipitation at Brazeau Lo 1992-1997.....	303
Figure 7.23	Soil Movement in X direction at Different Depths, U_2 , at SI12A.	304
Figure 7.24	Monthly increment of U_2 versus time at these same depths for SI12A in 1999.....	304
Figure 7.25	Soil Movement in X direction at Different Depths, U_2 , at SI12B.....	305
Figure 7.26	Monthly increment of U_2 versus time at these same depths for SI12B.....	305
Figure 7.27	Pipe Cross Section and Slope Section.....	306
Figure 7.28	Soil Layers at Pembina River Crossing..	307
Figure 7.29	Boundary Conditions for FEA Model.	308
Figure 7.30	The Modified Drucker-Prager/Cap Model: Yield Surfaces in the $p-t$ Plane..	309
Figure 7.31	Typical Yield/Flow Surfaces in the Deviatoric Plane.....	309
Figure 7.32	Typical Cap Hardening..	310
Figure 7.33	Regions of Activity of Creep Mechanisms.....	310
Figure 7.34	Consolidation Creep Potentials in the $p-q$ Plane.	311
Figure 7.35	Direct Shear Box..	311
Figure 7.36	Soil Sample before Direct Shear Test.....	312
Figure 7.37	Soil Sample during Direct Shear Test.....	312
Figure 7.38	Soil Sample after Direct Shear Test.....	312

Figure 7.39	Profile of Soil Sample.....	313
Figure 7.40	Comparison of FEA with Direct Shear Test Results.....	315
Figure 7.41	Comparison of FEA with Direct Shear Test Results.....	315
Figure 7.42	Comparison of FEA with Direct Shear Test Results.....	316
Figure 7.43	Soil Removal Oder in Stress Relief Simulation.....	317
Figure 8.1	3D View of the Finite Element Model of the Pipeline and Slope.....	332
Figure 8.2	Soil Layer A.....	332
Figure 8.3	Contour of Stress S11 at Soil Layer A after Gravity Load.....	333
Figure 8.4	Slope Stress S22 Contour at Soil Layer A after Gravity Load	334
Figure 8.5	Slope Stress S33 Contour at Soil Layer A after Gravity Load	335
Figure 8.6	Contour of Soil Movement U_1 of Layer A after Gravity Load	336
Figure 8.7	Contour of Soil Movement U_2 of Layer A after Gravity Load.....	337
Figure 8.8	Contour of Soil Movement U_3 of Layer A after Gravity Load.....	338
Figure 8.9	Pore Pressure Contour at Soil Layer A at Water Table 14.....	339
Figure 8.10	Pore Pressure Contour at Soil Layer A at Water Table 16.....	340
Figure 8.11	Pore Pressure Contour at Soil Layer A at Water Table 20..	341
Figure 8.12	Pore Pressure Contour of Soil Layer A at Water Table 704..	342
Figure 8.13	Contour of Soil Movement U_2 of Layer A after Creep.....	343
Figure 8.14	Contour of Axial Stress S22 at the Critical Location of Pipeline Before Load	344
Figure 8.15	Contour of Axial Stress S22 at the Critical Location of Pipeline After Creep	345
Figure 8.16	Yearly and May-September Precipitation for Years 1986-2001.....	346
Figure 8.17	Comparison of Soil Movement U_2 at Different Depths for SI5 and SI8 in the Year 2000.	347
Figure 8.18	Comparison of Soil Movement U_2 at Different Depths for SI10B and SI11B in Year 2000.	348
Figure 8.19	Comparison of Soil Movement U_2 at Different Depths for SI12B in 2000 and SI5 in 1995.....	349
Figure 8.20	Comparison of Soil Movement U_2 at Different Depths for SI8 and SI12 in 1995.....	350

Figure 8.21	Comparison of Soil Movement U_2 at Different Depths for SI5 and SI8 in 1992	351
Figure 8.22	Comparison of Soil Movement U_2 at Different Depths for SI12 in 1992 and SI6 in 1989.....	352
Figure 8.23	Comparison of Soil Movement U_2 at Different Depths for SI7 in 1989....	353
Figure 8.24	Local Coordinate System of Shell Element.....	353
Figure 8.25	Top Axial Stress Accumulation of the Cross Section along the Pipeline in 2000.....	354
Figure 8.26	Top Axial Strain Accumulation of the Cross Section along the Pipeline in 2000.....	355
Figure 8.27	Bottom Axial Stress Accumulation of the Cross Section along the Pipeline in 2000.....	356
Figure 8.28	Bottom Axial Strain Accumulation of the Cross Section along the Pipeline in 2000.....	357
Figure 8.29	Top Axial Stress Accumulation of the Cross Section along the Pipeline in 1995.....	358
Figure 8.30	Top Axial Strain Accumulation of the Cross Section along the Pipeline in 1995.....	359
Figure 8.31	Bottom Axial Stress Accumulation of the Cross Section along the Pipeline in 1995.....	360
Figure 8.32	Bottom Axial Strain Accumulation of the Cross Section along the Pipeline in 1995.....	361
Figure 8.33	Top Axial Stress Accumulation of the Cross Section along the Pipeline in 1992.....	362
Figure 8.34	Top Axial Strain Accumulation of the Cross Section along the Pipeline in 1992.....	363
Figure 8.35	Bottom Axial Stress Accumulation of the Cross Section along the Pipeline in 1992.....	364
Figure 8.36	Bottom Axial Strain Accumulation of the Cross Section along the Pipeline in 1992.....	365

Figure 8.37	Top Axial Stress Accumulation of the Cross Section along the Pipeline in 1989.....	366
Figure 8.38	Top Axial Strain Accumulation of the Cross Section along the Pipeline in 1989.....	367
Figure 8.39	Bottom Axial Stress Accumulation of the Cross Section along the Pipeline in 1989.....	368
Figure 8.40	Bottom Axial Strain Accumulation of the Cross Section along the Pipeline in 1989.....	369
Figure 8.41	Yearly Max Axial Accumulated Stress vs. Precipitation for May-September at Brazeau Lo.....	370
Figure 8.42	Yearly Max Axial Accumulated Strain vs. Precipitation for May-September at Brazeau Lo.....	370
Figure 8.43	Yearly Max Axial Accumulated Stress vs. Precipitation for January-December at Other Climate Stations.....	371
Figure 8.44	Yearly Max Axial Accumulated Strain vs. Precipitation for January-December at Other Climate Stations.....	371
Figure 8.45	Relieved Stress at the Critical Location of Pipe vs. Distance from South Bank of Creek.....	372
Figure 8.46	Axial Stress Accumulation at the Top of Cross Section of Pipe Before and After Digging 60m Soil on South Slope.....	373
Figure 8.47	Axial Stress Accumulation at the Bottom of Cross Section of Pipe Before and After Digging 60m Soil on South Slope.....	374
Figure 8.48	Axial Stress Accumulation at the Top of Cross Section of Pipe Before and After Digging 89m Soil on South Slope Only and Also Digging North Slope	375
Figure 8.49	Axial Stress Accumulation at the Bottom of Cross Section of Pipe Before and After Digging 89m Soil on South Slope Only and Also Digging North Slope	376
Figure 8.50	Axial Stress Accumulation at the Top of Cross Section of Pipe Before and After Digging 115m Soil on South Slope Only and Also Digging North Slope	377

Figure 8.51	Axial Stress Accumulation at the Bottom of Cross Section of Pipe Before and After Digging 115m Soil on South Slope Only and Also Digging North Slope	378
Figure 8.52	Axial Stress Accumulation at the Top of Cross Section of Pipe Before and After Digging 178m Soil on South Slope Only and Also Digging North Slope	379
Figure 8.53	Axial Stress Accumulation at the Bottom of Cross Section of Pipe Before and After Digging 178m Soil on South Slope Only and Also Digging North Slope	380
Figure 9.1	Peak Axial Compressive Strain vs. Percentage of SMYS.....	394
Figure 9.2	Peak Axial Compressive Strain vs. D/t Ratio.....	394
Figure 9.3	Peak Axial Compressive Strain vs. Pipe Yield Strength.....	395
Figure 9.4	Peak Axial Compressive Strain vs. Boundary Condition.....	395
Figure 9.5	Peak Axial Compressive Strain vs. Slip Surface Condition.....	396
Figure 9.6	Pipe Soil Interaction Elements.....	396
Figure 9.7	Peak Axial Compressive Strain vs. Pipe-Soil Interaction Condition.....	397
Figure 9.8	Peak Axial Compressive Strain vs. Creep Parameter n.....	397
Figure 9.9	Peak Axial Compressive Strain vs. Creep Parameter m.....	398
Figure 9.10	Peak Axial Compressive Strain vs. Time Parameter m.....	398
Figure 9.11	Peak Axial Compressive Strain vs. Average Elastic Modulus.....	399

List of Symbols and Abbreviates

A	Cross sectional area of the pipeline; soil creep parameter
ASTM	American Society of Testing and Materials
CSA	Canadian Standard Association
C3D8R	8node 3D solid element with reduced integration from Abaqus library
C3D6	6node 3D solid element from Abaqus library
CGL	Committee on Gas and Liquid Fuel Lines
C	Applied axial force
C	Cohesion
°C	Degree Celsius
cos	Cosine function
C _y	Axial yield load under zero circumferential stress
d	Diameter of pipe
D _o	External pipeline diameter
DxxPnnXY-*	Test specimen designation described as the following
Dxx	The pipe diameter size;
Pnn	“nn” indicates the level of the hoop stress induced by the internal pressure as a percentage of the SMYS;
X	Type of loading; A is an axial compression test, and B is a bending test;
Y	The pattern of loading; M is monotonic loading, and C is cyclic loading;
*	Test specimen number
E	Modulus of elasticity of the pipeline material
E _h	Hardening modulus
FEA	Finite Element Analysis
F	Specified axial pipeline load
F _c	The cap yield surface
F _e	Limit elastic axial pipeline force
F _s	Drucker-Prager failure surface
F _t	Transition yield surface,
F _u	Ultimate strength

F_y	Yield strength
F_p	Limit plastic axial pipeline force
g	Gravity acceleration
G	Shear modulus
G_c^{cr}	Potential function
H	Depth from ground surface to centre of pipeline
I	Moment of Inertia, unit matrix
K	Effective length factor
K	Ratio of the yield stress in triaxial tension to that in triaxial compression
$K(\theta, f_i)$	Material parameter
κ	Relative pipeline/soil stiffness parameter
k_L	Longitudinal subgrade modulus
kL/r	Slenderness ratio
kN	Units of kilonewtons
K_0	Coefficient of lateral earth pressure at rest
K_1	Equivalent soil spring coefficient within the ground movement amplitude zone of influence
K_2	Equivalent soil spring coefficient outside the ground movement
(L_s)	Transverse fault movement
L_a	Distance from the fault plane to the effective anchor point for the initial
L_a	The Anchor length
L_{ae}	Elastic segment (and
L_{ap}	Plastic segment
L_c	Projected length of the pipeline deformation due to curvature effects
L	Length of specimen
L	Collar length of confinement collars at the ends of the specimens
L_1	Length of the elastic pipeline strain distribution
L_e	Effective length of the pipe specimen
L_2	Length of the plastic pipeline strain distribution
L_T	Transition length from the stable/unstable zone to the point of maximum transverse pipeline displacement

LVDT	Linear variable differential transducer
M	Creep material parameter
M	Maximum pipeline bending moment
Mm	Units of millimeters
Mp	Plastic moment capacity
M_y	Yield moment
MPa	Units of Megapascal, N/mm ²
M_{max}	Peak end moment
(\bar{M})	Nondimensional maximum pipeline bending moment
N	Creep material parameter
N	Units of newtons
NPS	Nominal pipe size
p	The equivalent pressure stress
P	Internal pressure
($p-t$)plan	The meridional plan
$p_a (\varepsilon_{vol}^{pl} + \varepsilon_{vol}^{cr})$	Evolution parameter
p_b	Hydrostatic compression yield stress
p_y	Internal pressure that causes yielding in the hoop direction
P_{cr}	Euler critical buckling load
P_J	Expected maximum jack load predicted by numerical analyses
P_{MTS}	Targeted maximum MTS 6000 Universal Testing Machine
P_N	Net axial force in pipe wall, $P_N = P_T + P_v$
P_p	Axial load due to the internal pressure
P_v	Axial load due to Poisson's effect
P_T	Axial load due to a temperature difference of 45°C
q	The Mises equivalent stress
r	Radius of gyration
r	The third stress invariant
ri	Inside radius of test specimen
r_c	Constant radius of curvature.

R	Outside radius of test specimen
$R(\theta, fi)$	Material parameter
Rads	Units of radians
S	The deviatoric stress
SI	Slope indicator
SG	Strain gauge
S_u	Undrained shear strength of soil
S11	Local hoop stress in pipe shell element. Soil stress in global coordinate system direction 1
S22	Local axial stress in pipe shell element. Soil stress in global coordinate system direction 2
S33	Local shell normal stress in pipe shell element. Soil stress in global coordinate system direction 3
S4R	4node doubly curved shell element from Abaqus library
Sin	Sine function
SMYS	Specified minimum yield strength
t	Time, deviatoric stress measure
t	Wall thickness
t_u	Ultimate axial soil load
U11	Soil displacement in global coordinate system direction 1
U22	Soil displacement in global coordinate system direction 2
U33	Soil displacement in global coordinate system direction 3
u_o	Axial ground movement at the stable/unstable slope interface
X80	SMYS = 80 ksi
X70	SMYS = 70 ksi
X60	SMYS = 60 ksi
y	Transverse ground movement
y	Pipeline transverse displacement
y_1	Transverse pipeline displacement
y_2	Transverse pipeline displacement
(\bar{y})	Nondimensional peak transverse pipeline displacement

$\alpha(\theta, fi)$	Material parameter
α	Adhesion factor
β	Intersection angle between the pipeline and fault plane
δ	Internal friction angle between pipeline and soil
$\varepsilon_{vol}^{in} 0$	Arbitrary origin of the volumetric inelastic strain
ε_{vol}^{cr}	Volumetric inelastic creep strain
ε_{vol}^{pl}	Volumetric inelastic plastic strain
$\varepsilon_{vol}^{cr} 0$	Initial volumetric creep strain
$\varepsilon_{vol}^{pl} 0$	Initial volumetric plastic strain
ε_n	Engineering strain
ε_p	Limit plastic pipeline strain;
ε_y	Pipeline yield strain
σ_n	Engineering stress
ε_p	True plastic strain
σ_p	True plastic stress
ε_G	Global strain
ε_e	Limit elastic pipeline strain;
ε_b	Maximum bending strain
ε_a	Aaverage axial strain
δ	Transverse ground movement amplitude.
δ_b	The Critical ground displacement due to bending)
δ_a	Critical ground displacement due to axial deformation
δ_f	Ground movement amplitude parallel to the fault line,
σ	Average axial pipeline stress
σ_y	Pipeline yield stress and
$\Delta\sigma_h$	Pipeline plastic stress increment
λ_L	Characteristic axial length,
η	Pipeline hardening parameter

ρ	Unit density of soil
Δ_G	End displacement of the specimen;
ϕ_y	Global curvature
ϕ_{\max}	Peak global curvature
ϕ_{INC}	Curvature increment
ψ	Global curvature
ϕ	Total rotation of the specimen, angle of internal friction
ϕ_1	Rotation of the top end of the pipe
ϕ_2	Rotation of the bottom end of the pipe
τ_f	Shear stress on the failure plane
σ'	Effective stress
ϵ_a	Average axial accumulated strain
$\dot{\epsilon}^{cr}$	Equivalent creep strain rate
σ_a	Average axial accumulated stress
$\beta(\theta, f_i)$	Angle of friction of the material
$d(\theta, f_i)$	Cohesion of the material
θ	Temperature
$f_i, i = 1, 2, 3..$	Predefined fields
Π -plane	Deviatoric principal stress plane
$\bar{\sigma}^{cr}$	Effective creep pressure

CHAPTER 1 INTRODUCTION

1.1 General Background

Buried pipeline is an effective method for transporting oil and natural gas to urban areas. Pipeline traverses long distance of diverse terrain and it often encounters many geologic hazards. The main risk to pipelines is from landslides. These geomorphic events that involve the descent of soil or rock in sloping terrains occur worldwide, often in conjunction with natural hazards like earthquakes, floods, or volcanic eruptions. Landslides can also be caused by excessive precipitation or human activities, such as deforestation or development, which disturb natural slope stability.

Pipeline constructed across ancient and currently geologically active landslides experiences significant deformation and subsidence, and is often subjected to severe loading conditions. Buried pipeline interacts closely with the surrounding soil and rock. Apart from hoop stress caused mainly by internal pressure and backfill, pipeline stresses are affected by displacements of the surrounding soil and rock. The soil and rock displacement come from soil movement such as landslide, slope creep and subsidence. Pipelines are sensitive to deformations that cause significant changes in the longitudinal stresses. As soil slides down, it imposes external loads on the pipe. If movements are sufficiently large, it may induce local buckling or fracture in the pipe. The relatively infrequent occurrence of landslide-induced pipelines failures may be costly and results in severe environmental damage and bears high financial, political, social and legal costs.

Pipeline owners and operators are frequently faced with difficult and expensive maintenance for pipelines located in areas with landslide potential. To maintain the pipeline within an active landslide, they implement comprehensive programs for identifying, evaluating, monitoring and mitigating the landslide hazards. A number of methods are available for the mitigation of the effects of landslide deformation on pipelines. These include stabilization of the landslide, relocation of the pipeline outside the landslide area, installation of the pipeline above the ground surface, installation below

the landslide using directional drilling or deep excavation, the use of deformable backfill such as polystyrene or other suitable material, and carrying out stress relief procedure.

The occasional remedial work—stress relief procedure has been carried out before the pipeline reaches a critical strain level, which involves removing the soil around the pipe, allowing the pipe to spring back to a zero-soil load state and reburying the pipe. The frequency of the remedial work is dependent on the severity and the rate of movement of the slope, and the maintenance policy of each individual company. This stress relief procedure is the focus of this research. This research is to explore the factors affecting the stress relief process and its effectiveness in relieving overstraining of a pipeline.

1.2. Objective

Stress relief procedure is applied to pipelines buried in active slopes. Pipeline is subjected to deformation as the surrounding soil moves. It is very important to prevent pipes from buckling. Stress relief procedure might be a good approach. A few questions commonly encountered are: before stress relief procedure, how much strain has accumulated in the pipe due to soil displacement? How long does it take to load up? Where is the critical location of the pipeline? Is the stress relief procedure effective? What is the sufficient scope of pipe for the stress relief? How often should the stress relief be performed?

The objective of this research project is to investigate the effectiveness of the stress relief procedure, deformation threshold of steel pipes for implementing this procedure, schedule or frequency of stress relief, and how stress relief procedure affects the local buckling behaviour of pipes. Results from this research should be able to help pipeline industries to operate their pipes more safely, efficiently and economically.

1.3 Scope

It has been identified in the above objective that the stress relief procedure is the core of this study. The research methodology is composed of three parts: laboratory testing program of full scale pipes under monotonic and repetitive loading, in-situ

pipeline and soil movement monitoring program and numerical simulation of a buried pipeline at Pembina River Crossing and Lodge Pole, Alberta, and stress relief procedures implemented for the pipeline.

Full-scale pipe tests are conducted in the program to study the effects of stress relief procedures on local buckling behaviour of the pipes. When soil slides along pipes, it imposes axial compression and bending moment. After the soil around the pipe has been excavated, the axial compression and bending moment in the pipe are relieved. Pipeline goes through a major cycle for every remedial work. Once the pipe is covered, a new loading cycle due to the soil movement begins. To study the effect of this pattern of loading, a test program with twelve pipe segments under cyclic axial compression and bending moment was carried out. Laboratory tests simulating the field conditions have been focused on the performance assessment and buckling mechanism of pipes.

The pipelines at Simonette and Pembina River Crossings in Alberta are situated in areas of active soil movement. Pipeline and slope monitoring program were designed and implemented at these two sites to examine the integrity of pipelines. An extensive instrumentation plan was carried out to monitor long term slope movement and pipe deformation. The current operating philosophy involves periodically excavating the lines to relieve stresses. This study provides useful information in the understanding of pipeline behaviour and pipe-soil interaction. Operating pipelines in these field conditions demonstrate complex performance under serviceability conditions.

To study buried pipeline in the slope at Pembina River Crossing, a finite element model is developed to simulate the slope movement and match the observed field response of the pipeline to investigate the stress relief procedure. The correlation between soil movement and precipitation is investigated. The model should be able to capture global and local behaviour of pipeline. Soil-pipe interaction is simulated by setting a weak layer of soil surrounding the pipeline. The model incorporates nonlinear material, pipe-soil interaction, soil creep and water table changes. The Modified Drucker-Prager Cap Model is used to model the soils based on parameters determined from the direct

shear test results. The finite element model is calibrated using field data from slope motion and pipe deformation. A comparison of the field data and FEA model results, including the magnitude of the accumulated strain in the pipe and soil movement is presented. Careful geotechnical study is performed. The model is used to simulate the strain accumulation and the stress relief in the pipeline, before and after the stress relief operation. Parametric study of the model is extended to different critical parameters such as soil conditions, pipeline internal pressure, pipe D/t ratio, water table, etc. to obtain characteristic behaviour of buried pipeline and effectiveness of the stress relief procedure.

Based on the results of laboratory test and numerical analysis, the critical locations of pipeline systems and optimum stress relief procedure can be determined.

1.4 Organization of the Thesis

The thesis consists of ten chapters. Apart from Chapter 1 introduction, Chapter 2 describes the literature review relevant to long term pipe-soil interaction and stress relief procedure, including slope instability mechanism, pipe/soil interaction, analytical modeling and finite element modeling of pipe/soil interaction.

Chapter 3 outlines the components of the laboratory testing program conducted to expand the experimental database on pipe responses. This includes details of the experimental parameters considered, the preparation of the test specimens, the test set-up, and the experimental testing procedure used in testing segments of the pipe as well as a complete description of the ancillary tests. A total of 12 tests were conducted, resulting in 12 sets of experimental results. A summary of the nominal target experimental loads for each of the test specimen is included in Chapter 3.

Chapter 4 presents the details of the finite element analysis model for the experimental test specimens. A brief introduction and review of the concepts of FEA is presented. The results of both the experimental testing program and the FEA numerical model, comparison of them, including moment-curvature response, stain accumulation

before and after bucking, are presented. Conclusion and discussion are summarized at the end of this chapter.

Chapter 5 summarizes the monitoring program of pipeline at Pembina River Crossing which includes description of the site, introduction of strain gauge data and slope indicator data, material behaviour, and field data reduction. Chapter 6 describes the monitoring program of the pipeline at Simonette River Crossing which includes description of the site, introduction of strain gauge data and slope indicator data, and field data reduction.

Chapter 7 outlines details of the numerical model developed for the pipeline and slope at Pembina River Crossing. An introduction of finite element analysis procedures and detailed discussion of the specific features employed in this research project are presented.

Chapter 8 presents the application of the finite element model (FEM) in studying the stress relief process. This chapter has four sections, including the validation of FEM, prediction of pipeline response for a given amount of soil movement, the optimum stress relief procedure, and discussions. It provides details of the comparisons of both the monitoring program and the results of the FEA numerical model. Conclusion and discussion are given at the end.

Chapter 9 presents the parametric study on the pipeline response with different variables. A total of 35 cases are examined using the validated FEA model and results are given in each case.

Chapter 10 is the final chapter of this thesis. In this chapter the information presented in the previous chapters is summarized. Conclusions are subsequently discussed from the results of this research. Finally, recommendations are presented for future research on the topic of stress relief procedures.

CHAPTER 2 LITERATURE REVIEW

Stress relief procedure is a common practice adopted by many pipeline companies. The key problem of the stress relief procedure is to determine the critical location and the magnitude of the accumulated strain in the pipeline. It is related with long-term pipe soil interaction (PSI). So far no established theoretical methodology is available to assess the effectiveness and the operation schedule of stress relief procedures. A literature review of the important subjects of PSI modeling is presented in this Chapter, including slope movement, stress relief examples, mechanism of slope instability, empirical and analytical studies on PSI, and numerical procedures.

2.1 Slope Movement

Buried pipelines in hilly or mountainous areas are subjected to slow movements of slopes in the order of 10^{-3} to 10^{-2} m per year. This results in the occurrence of unacceptable strain and may cause various failure modes in the pipelines (Bruschi et al. 1995). The slow movements of slopes have been explained as a result of rainfall precipitation (Scarpelli 1995; Grivas et al. 1996). Fracture of pipelines due to soil movements was reported by (EGIG 1993).

Slope instability is a critical issue for the management of the pipeline network. Typical types of slope failures are rotational slide, translational slide and flow (Winterkorn and Fang 1975). Data of case histories provide a foundation for developing understanding of mechanisms of slow ground movement through categorizing such effects as slope geometry, rainfall and movement characteristics.

Pipeline transmission systems in Western Canada are exposed to a significant ground movement hazard due to slope movements in much of the northern half of Alberta and British Columbia. As the nature of this hazard is a time-dependent one, its impact is expected to grow considerably in the future years. TransCanada-East's system also shows increasing evidence of the impact of this hazard over time.

2.2 Stress Relief Examples

In 1955, a natural gas pipeline was installed across Douglas Pass area in western Colorado (Bukovansky et al., 1985). The area has landslides. The pipeline designers had to accept the risk due to highway and access considerations. Landslides disrupted the pipeline and long sections of the pipeline were damaged in the 1960's and 70's. Mitigating measures in the area consisted of stress-relieving the pipeline through the excavation of a trench around and parallel to the pipelines. It is concluded that hazard mitigation through excavation is quick, relatively inexpensive and reliable.

Boivin and Cavanagh (1992) described two high-pressure gas pipelines of 273mm and 406mm in diameter, buried in unstable slopes in northwestern Alberta. The slope movement was from 1 to 17mm per month. When the pipelines were finally excavated for stress-relief purposes, over 300mm of rebound in each pipeline was observed.

Wong (1992) reported a pipeline in an area of unstable slope in western Alberta that ruptured and caused fire in 1986. The pipeline was located in a massive and deep seated landslide. The soils at the pipelines were essentially silty clays with an undrained shear strength ranging from 50 to 100kPa. The rupture was caused by bending and buckling of the pipeline due to excessive soil movement that was primarily parallel to the pipeline axis. Subsequent field measurements indicated that the average slope movement was 25 to 50mm per year, which could be accelerated due to unfavorable climatic conditions. It is estimated that stress-relieving operations (excavations) need to be carried out approximately every two years.

Cavanagh and Rizkalla (1992) reported a gas pipeline crossing the Simonette River in western Alberta that ruptured and caused an explosion and fire in 1978. The damage occurred after two years of operation of the pipeline and involved a pipeline length of less than 2m. Investigations indicate that slope instability and soil movement (both lateral and longitudinal to the pipeline) were at least partially responsible for the damage. In 1979, slope monitoring instrumentation was installed at the site and by September of 1980, the accumulated slope movement measured was approximately

40mm. In December of 1980, a section of the pipeline was excavated and permitted to rebound to an unstrained condition. Similar excavations were undertaken in 1982, 1983 and 1988. It is expected that periodic excavations will need to be undertaken in the future to strain relieve the pipeline.

Rizkalla et al. (1993) described landslide conditions in the northern Alberta area where sensitive river valley slopes pose risks to buried pipelines. The measured annual ground movements range from very slow creep to a rate of 60 mm per year. The width of a landslide that could interact with a pipeline in the area might range from 100 m to 2000 m. It is suggested that a rational approach to operating pipelines in such areas is to monitor pipeline displacement/strain and ground movements. When a critical build-up of pipeline strain is reached, the pipeline section undergoing soil movement is excavated and allowed to spring back to a reduced-strain state.

2.3 Mechanism of Slope Instability

Rizkalla and McIntyre (1991) investigated the mechanisms of slope instability which induce excessive stress and strain in a pipeline in northern Alberta. Erosion of river banks and down cutting of its channel bed is considered to be the basic causes of the slope instability.

Cruden and Varnes (1996) and (Wieczorek 1996) summarized the major factors affecting slope deformation and its stability, namely: creep, change in pore pressure in soil due to rainfalls, erosion at the toe of the slope, freeze-thaw cycles, weathering, change in groundwater level, tectonic uplift and glacial rebound, temperature variation. Some factors are more important than others for a specific site. For example, creep and change in pore pressure due to rainfalls were reported as major factors in creeping slopes influencing buried pipelines (Evgin 1997). Spring run-off due to snowmelt is another consideration.

Besides the factors listed above, cyclic load applied to soil in slope has to be carefully considered. This is because small cyclic loading may cause accumulated

irrecoverable deformation and excess pore pressure. Cyclic load may be due to the fluctuations of groundwater level, water content or temperature and variation of seepage forces.

2.4 Analytical Methods of Pipe Soil Interaction

There are a number of solution procedures which can be employed to investigate pipe soil interaction events and assess pipeline integrity including discrete analysis, continuum analysis, closed form solutions and approximate techniques. These methods rely on idealizations and simplifying assumptions on the structural configurations, stress distribution of the structure soil interface, mechanical behaviour and material response. In addition more comprehensive numerical procedures, such as the finite difference method and finite element method, are invaluable for investigating pipe soil interaction events and assessing pipeline integrity. Characteristics of these engineering tools are addressed with a discussion on the idealizations, limitations and mathematical formulations.

2.4.1 Discrete Analysis

The classical solution for idealization of the soil media as a linear, elastic foundation has been generally attributed to Winkler (Bowles, Joseph E., 1988). The model assumed that the surface soil displacement response could be approximated by a discrete series of independent elastic springs, defined by the characteristic spring stiffness and a function of the applied load. The inherent discontinuity of the Winkler model has been addressed by several studies including Hetnyi (1946) by the use of soil-soil shear springs between adjacent pipe-soil springs. A variation of the Winkler model has been used for the analysis of ice gouge/soil/pipeline interaction by Stepanov et al. (1998). The main advantage for this approach is that a complex three-dimensional problem is reduced to one-dimension. The model, however, is restricted to linear elastic behaviour and its appropriateness for large displacement or accumulated deformation response mechanisms is questionable.

2.4.2 Continuum Analysis

Continuum analysis of structure soil interaction problems has focused on

modeling the soil behaviour as an elastic half-space. For structure soil interaction, continuum analysis is generally represented by complex mathematical formulations that can account for isotropic, anisotropic, non-homogeneous and layered media. As discussed by Selvadurai (1979), two-parameter elastic, elastic-plastic and time dependent constitutive relationships can also be incorporated in the analysis. Some prominent references include Reissner (1958), and Vlazov and Leontiev (1966).

2.4.3 Approximate Analytical Solutions

Simplified analytical solutions for pipe soil interaction are generally based on a hybrid approach that incorporates simplifying assumptions and idealizations on the mechanisms in order to develop a viable computational procedure. The solutions consider limit equilibrium analysis, inference from experimental studies and numerical investigations, as well as theoretical treatment of parallel problems such as bearing capacity, anchor resistance, and pile capacity. The majority of the procedures simplifies the analysis to one-dimension, idealizes the pipeline and soil behaviour and incorporates empirical relationships to characterize pipe soil interaction. The solutions have been developed to characterize pipeline stress due to long-term slope instability.

Axial Pipe Soil Interaction

Simplified procedures for estimating pipeline stress due to relative axial displacement field is typically based on assuming full mobilization of the soil restraint and consideration of elastic or elastoplastic pipeline response.

For longitudinal landslide loading, the ultimate soil resistance per unit length, F_x , for a pipeline and the surrounding soils (clay or sand) can be expressed as (ASCE,1984)

$$(2.1) \quad \text{For clay } F_x = \pi d \alpha S_u$$

$$(2.2) \quad \text{For sand } F_x = 0.5 \pi d \rho g H (1 + K_0) \tan \delta$$

where α is adhesion factor, ρ is unit density of soil, g is gravity acceleration, d is diameter of pipe, S_u is undrained shear strength of soil, K_0 is coefficient of lateral earth

pressure at rest, δ is internal friction angle between pipeline and soil, H is depth from ground surface to centre of pipeline.

Rizkalla and McIntyre (1991) determined the critical slope movement for buried pipelines in clay assuming an elastic pipeline response and plastic soil behaviour.

$$(2.3) \quad u_o = \frac{F^2}{t_u E A}$$

where F is specified axial pipeline load, u_o is axial ground movement at the stable/unstable slope interface, t_u is the ultimate axial soil load, E is the pipeline elastic modulus and A is the pipeline cross-sectional area.

Rajani et al. (1995) and Trigg and Rizkalla (1994) extended the model of Rizkalla and McIntyre (1991). The pipeline response can be elastic or elastoplastic (or elastic-perfectly plastic, the inelastic region of the stress-strain diagram is idealized as a straight line). The soil of either clay or sand material can be elastic, bilinear (the stress-strain diagram consists of two straight lines in the elastic and inelastic regions, the material behaves linearly in the elastic range, and inelastic range with reduced slope) or elastoplastic. The axial edge displacement (\bar{u}_o) and non-dimensional axial force (\bar{F}):

$$(2.4) \quad \bar{u}_o = \frac{\pi D_o k_L u_o}{t_u}$$

$$(2.5) \quad \bar{F} = \frac{F \lambda_L}{t_u}$$

where D_o is the external pipeline diameter, k_L is the longitudinal subgrade modulus, and

$$\lambda_L \text{ is the characteristic axial length, } \lambda_L = \sqrt{\frac{\pi D_o k_L}{E A}}$$

A series of expressions were developed, for elastic pipe/soil interaction,

$$(2.6) \quad \bar{u}_o = \bar{F}$$

for elastic pipeline response and plastic soil behaviour, such that $F > \frac{t_u}{\lambda}$,

$$(2.7) \quad 2\bar{u}_o = \bar{F}^2$$

and for elastoplastic pipeline response and plastic soil behaviour

$$(2.8) \quad \bar{u}_o = -\frac{\kappa}{2}(1-\eta) + \frac{\eta}{2}\bar{F}^2 + \kappa\bar{F}(1-\eta) + \frac{1}{2}$$

where η is the pipeline hardening parameter $\left(\eta = \frac{E}{E_h}\right)$, which is defined as the ratio of the elastic modulus (E) to hardening modulus (E_h), κ is the relative pipeline/soil stiffness parameter $\left(\kappa = \frac{\pi D_o \varepsilon_y k_L}{\lambda t_u}\right)$, and ε_y is the pipeline yield strain.

Simmonds et al. (1996) present a simplified expression for estimating the critical slope displacement (δ_{cr}) to cause a specified pipeline strain distribution due to a longitudinal, block type ground movement.

$$(2.9) \quad \delta_{cr} = \frac{1}{2}[\varepsilon_e(L_1 + L'_1) + (\varepsilon_e + \varepsilon_p)(L_2 + L'_2)]$$

where ε_e is the limit elastic pipeline strain; ε_p is the limit plastic pipeline strain; L_1 is the length of the elastic pipeline strain distribution $\left(L_1 = \frac{F_e}{t_u}\right)$, F_e is the limit elastic axial pipeline force; L_2 is the length of the plastic pipeline strain distribution $\left(L_2 = \frac{F_p - F_e}{t_u}\right)$, and F_p is the limit plastic axial pipeline force. The terms (L'_1, L'_2) are the corresponding distribution lengths based on the assumed boundary condition.

Transverse Horizontal Pipe/Soil Interaction

Simplified procedures have also been developed for estimating pipeline distress due to relative transverse horizontal soil displacement field. The analyses are based on solutions to a beam on elastic foundation or assumptions with respect to the pipeline curvature response.

Based on a closed-form solution, Rajani et al. (1995) and Trigg and Rizkalla (1994) present a model to estimate the end load, displacement and maximum moment for a buried pipeline subject to a transverse, block type slide movement. The analysis assumes an initial straight pipeline section, symmetric double curvature pipeline response about the point of inflection and that the boundary restraint is fixed. The analysis parallels investigations on seismic ground fault movements with a relative pipe/fault angle of 90°. The pipeline response is assumed elastic and the soil behaviour is considered bilinear, elastoplastic. The equivalent nondimensional end load (\bar{F}) due to the transverse ground movement is

$$(2.10) \quad \bar{F} = \frac{F \lambda_L}{D_o S_u}$$

The nondimensional peak transverse pipeline displacement (\bar{y}) is

$$(2.11) \quad \bar{y} = \frac{k_s y}{S_u}$$

where y is the transverse ground movement. The nondimensional maximum pipeline bending moment (\bar{M}) is

$$(2.12) \quad \bar{M} = \frac{M \lambda_L}{F}$$

where M is the maximum pipeline bending moment due to the end load (F) with the maximum longitudinal stress defined by $\sigma = M/S$.

Although useful as a preliminary assessment tool, the inherent limitations should be addressed. In general terms, seismic design analysis of pipelines has shown that the global pipeline response can be approximated by flexure theory, for small amplitude fault movement or large crossing angles, and can be characterized as a tension cable, for large amplitude fault movement (O'Rourke and Liu 1999; Kennedy et al. 1977). For large axial strains, the analysis does not account for the coupling of axial forces and moment-curvature, nonlinear terms of the axial strain–displacement relationship or a reduction in bending stiffness.

Simmonds et al. (1996) presented a simple formulation to estimate the maximum elastic bending strain (ε_b) as,

$$(2.13) \quad \varepsilon_b = \frac{3 D_o y}{L_T^2}$$

where L_T is the transition length from the stable/unstable zone to the point of maximum transverse pipeline displacement and y is the pipeline transverse displacement. The expression assumes small deflection theory and a deflected pipeline mode shape.

Miyajima and Kitaura (1989) considered a spatially distributed transverse ground movement of a sine wave formulation, as shown. A system of equations defined the elastic flexural pipeline response, within the limits of small deflection theory, as a beam on an elastic foundation,

$$(2.14) \quad \begin{aligned} EI \frac{d^4 y_1}{dx^4} + K_1 y_1 &= K_1 \delta \left(1 - \sin \frac{\pi x}{L_\delta} \right) & 0 < x < \frac{L_\delta}{2} \\ EI \frac{d^4 y_2}{dx^4} + K_2 y_2 &= 0 & x \geq \frac{L_\delta}{2} \end{aligned}$$

where y_1 is the transverse pipeline displacement and K_1 is the equivalent soil spring coefficient within the ground movement amplitude zone of influence $\left(0 < x < \frac{L_\delta}{2} \right)$, y_2 is the transverse pipeline displacement and K_2 is the equivalent soil spring coefficient outside the ground movement amplitude zone of influence $\left(x \geq \frac{L_\delta}{2} \right)$, and δ is transverse ground movement amplitude. The soil spring coefficients are based on the recommendations of Japan Gas Association (1982).

Assuming a large zone of influence for the transverse fault movement (L_δ) or relatively flexible pipeline systems, O'Rourke (1989) considered the pipeline response to match the ground displacement field. For an elastic response, the maximum bending strain (ε_b) was,

$$(2.15) \quad \varepsilon_b = \frac{\pi^2 D_o \delta}{L_\delta^2}$$

Based on axial strain–displacement relationship, the average axial strain (ε_a) due to longitudinal elongation of the pipeline could be estimated

$$(2.16) \quad \varepsilon_a = \left(\frac{\pi \delta}{2 L_\delta} \right)^2$$

For small lengths of transverse displacement fields or rigid pipelines, O'Rourke (1989) defined the maximum pipeline strain considering bending only,

$$(2.17) \quad \varepsilon_b = \frac{P_u L_\delta}{3 \pi E D_o^2 t}$$

if considering fixed-end restraints,

$$(2.18) \quad \varepsilon_b = \frac{P_u L_\delta}{24 \pi E D_o^2 t}$$

Liu and O'Rourke (1997) developed a simplified expression for the two limiting cases of a pipeline acting in predominantly flexural response (i.e. small zone lengths of ground movement) and cable behaviour (i.e. large zone lengths of ground movement). The analysis considered elastic beam behaviour and assumed deformation modes.

The critical ground displacement due to bending (δ_b) was defined as,

$$(2.19) \quad \delta_b = \frac{5 P_u L_\delta^4}{384 E I} = \frac{5 P_u L_\delta^4}{384 \pi E D_o^3 t}$$

which represents pipeline behaviour as a simply supported beam.

In the limit of large distribution lengths of ground movement, the pipeline response was assumed to behave as a cable and the critical ground displacement due to axial deformation (δ_a) was obtained through the solution of simultaneous equations

$$(2.20) \quad \delta_a = \frac{p_u L_\delta^2}{16T}$$

$$\delta_a^2 = \frac{4L_\delta}{\pi^2} \left(\frac{\sigma L_\delta}{E} + \frac{\pi D_o^2 t \sigma^2}{2 E t_u} \right)$$

where σ is the average axial pipeline stress assumed constant in the displacement field. To obtain the combined response, flexure and axial deformation, superposition was assumed to define the critical ground movement,

$$(2.21) \quad \delta_{cr} = \frac{1}{\frac{1}{\delta_b} + \frac{1}{\delta_a}}$$

and the elastic pipeline strain was

$$(2.22) \quad \varepsilon = \begin{cases} \frac{\pi \delta}{2} \sqrt{\frac{t_u}{A E L_\delta}} \pm \frac{\pi^2 \delta D_o}{L_\delta^2} & \delta \leq \delta_{cr} \\ \frac{\pi \delta_{cr}}{2} \sqrt{\frac{t_u}{A E L_\delta}} \pm \frac{\pi^2 \delta_{cr} D_o}{L_\delta^2} & \delta > \delta_{cr} \end{cases}$$

Transverse vertical Pipe Soil Interaction

Vertical pipe/soil interaction is a problem commonly associated with arctic pipelines (e.g. frost heave, thaw settlement), buried offshore pipelines (e.g. upheaval buckling) and negative buoyancy effects (e.g. soil liquefaction).

The solutions are generally based on some formulation of the classical beam on elastic foundation problem and have been investigated for a number of boundary conditions and characteristic parameters. Some investigations include Ladanyi and Lemaire (1984), Kim et al. (1998) and Klever et al. (1990).

Oblique Pipe Soil Interaction

A number of simplified analytical solutions have been developed to examine the response of buried pipelines to seismic ground fault movement. Two of the major models will be presented with the respective idealizations and limitations addressed.

Studies conducted by O'Rourke and Liu (1999), Eslaamizaad and Robertson (1995), and ASCE (1984) provide a detailed discussion on these models.

Newmark and Hall (1975) developed one of the original procedures for estimating pipeline response subject to fault movement. The analysis considered only axial deformation (i.e. neglected beam curvature), employed small deflection theory and idealized the pipeline stress-strain response by linear segments. An average pipeline axial strain ($\bar{\varepsilon}_a$) response could be computed,

$$(2.23) \quad \bar{\varepsilon}_a = \frac{\delta_f}{2L_a} \left[\cos \beta + \frac{\delta_f}{4L_a} \sin^2 \beta \right]$$

where δ_f is the ground movement amplitude parallel to the fault line, L_a is the distance from the fault plane to the effective anchor point for the initial undeformed pipeline configuration, and β is the intersection angle between the pipeline and fault plane.

The anchor length (L_a) can be divided into an elastic segment (L_{ae}) and plastic segment (L_{ap}) based on,

$$(2.24) \quad L_{ae} = \frac{\sigma_y \pi D_o t}{t_u}$$

$$L_{ap} = \frac{\Delta\sigma_h \pi D_o t}{t_u}$$

where σ_y is the pipeline yield stress and $\Delta\sigma_h$ is the pipeline plastic stress increment (i.e. $\Delta\sigma_h = \sigma_p - \sigma_e$).

The Newmark-Hall procedure provides a lower bound estimate to the axial strain developed in the pipeline and thus over predicts the allowable ground movement. Furthermore, the results are not valid for a fully yielded section.

Conversely, Kennedy et al. (1977) presented an upper bound solution to pipeline strain through an extension of the Newmark-Hall procedure and considered lateral soil pressure, deformation profile, large deformations and associated bending strain. The

model assumes large amplitude ground movement and neglects the pipeline bending stiffness (i.e. pipeline acts as a tension cable). The total pipeline elongation can be estimated,

$$(2.25) \quad \Delta L = \delta_f \cos \beta + \frac{\delta_f^2 \sin^2 \beta}{3L_c}$$

where L_c is the projected length of the pipeline deformation due to curvature effects ($L_c = \sqrt{r_c \delta_f \sin \beta}$), where r_c is the constant radius of curvature.

2.5 Numerical Modeling of Pipe Soil Interaction

The analytical solutions are advantageous in terms of the simplicity, functionality and utility for conducting preliminary assessment of pipeline integrity and parametric analysis. The procedures, however, are limited by the underlying assumptions and idealizations considered. Furthermore, analytical difficulties are encountered for pipe soil interaction events that consider non-uniform boundary conditions, spatial variation in characteristics of the pipeline and soil media, large amplitude, accumulated or cyclic deformational loading mechanisms, and nonlinear material behaviour. For these issues, numerical methods provide a rational basis for conducting pipe soil interaction studies. Two commonly employed numerical procedures are the finite difference method and finite element method.

2.5.1 Finite Difference Solution

The finite difference method is one of several numerical procedures that exist for the analysis of higher-order differential equations. The method is based on employing finite difference calculus to approximate the differential equation at discrete points of a domain to obtain a solution for a system of algebraic equations. For pipe soil interaction the procedure can be based on the classical beam on elastic foundation expression but typically finite difference analysis has been limited to pile soil interaction studies. The solution is generally constrained by boundary conditions, degrees of freedom and discretization arrangements.

2.5.2 Finite Element Method

Analysis of complex pipe soil interaction events can be effectively and efficiently conducted using the finite element method. In general terms, the finite element method is based on the piecewise approximation to an exact solution by polynomial functions that define a region of space on a discretized domain interconnected at common points. The polynomial or shape functions represent the displacement field or stress state over the element through interpolation of nodal field quantities. For this process, conditions of compatibility and continuity are met. The finite element method can be based on a variational principle or weighted residual technique to obtain a set of equations for each element and assembled to define the response for the complete domain. Cook et al. (1989) and Bathe (1996) present a detailed discussion on finite element method and modeling procedures.

2.5.3 Finite Element Analysis – Structural Models

The current state of practice for analyzing pipe soil interaction events by the finite element method is based on a structural-type finite element model. The basic components of the numerical model are beam and spring elements, which are idealizations of the continuum pipe soil response. The structural model is a relatively simple tool that can be employed for the development of numerical models that can account for significant pipe soil interaction lengths in the order of kilometers. The procedure is significantly more efficient and requires substantially less computational resources than equivalent continuum analysis, which will be further addressed in the next section.

The pipeline response is typically modeled by specialized beam elements that can account for internal pressure and thermal strain due to temperature differential. Additional variables that consider ovalization, warping, pressure stiffening, and nonlinear curved beam effects are also available within some commercial software packages.

The soil continuum is discretized by spring elements that represent the load–displacement response per unit length of pipeline and are generally considered

mutually uncoupled. The numerical model may also account for nonlinear geometric (i.e. displacement, strain) and material (i.e. elasticity, plasticity) analysis.

The relative simplicity and elegance of the finite element method to model complex engineering problems has to be balanced with a fundamental knowledge of the theoretical basis, underlying assumptions and limitations of the element formulations.

Application of the finite element method employing structural-type models to analyze pipe/soil interaction events has encompassed a wide engineering field. Some of the issues have included thermal strains Svan et al. (1992). Klever et al. (1990), frost heave C-FER (1995, 1992) and ice gouge deformation events (Kenny et al., 2000). In these studies, the finite element method has been employed for a parametric investigation and specific case analyses for predicting pipeline/soil interaction.

Kim et al. (1998) investigated the computed buried pipeline response to ground subsidence, for three boundary conditions, in comparison with the classical solutions developed by Hetnyi (1946). The finite element analysis employed ABAQUS/Standard with the PIPE31H element. The study considered nominally elastic conditions with the maximum ground subsidence on the order of 0.150m and maximum axial stress approaching yield conditions. Although a three-dimensional pipe element was employed, the analysis appears to have only considered the vertical downward soil response within a two-dimensional framework. For long-term pipe/soil interaction, Bruschi et al. (1995) conducted a parametric analysis on pipeline response to relative axial and transverse soil movement. The soil behaviour was modeled as nonlinear elastoplastic springs and the pipeline response was considered linear elastic. The influence of soil motion displacement magnitude, relative orientation with respect to the pipeline and length of slippage was considered. The influence of excavation on pipeline strain relief and failure modes with respect to specified limit states was also investigated.

The analysis of Bruschi et al. (1995) was consistent with the investigations conducted at C-CORE (Kenny et al., 2000) for the response of buried pipelines subject to

ice gouge events. The longitudinal distribution of axial stress/strain and curvature response was dependent on factors defining the coupled nonlinear interaction. Specifically, these issues include the relative pipeline and soil stiffness, ultimate soil strength properties, soil displacement field (i.e. distribution and magnitude) and characteristics of the transition zone from the imposed geotechnical loads to the “anchored” pipeline section.

For small soil displacement magnitudes, of the order of 0.01m at a 10° incident angle, Bruschi et al. (1995) stated that the critical failure mechanism was axial deformation due to longitudinal soil movement. The moment-curvature relationship dominated for larger transverse amplitudes of 1.0m soil displacement at 70° incident angle. The intermediate case, 0.1m at 40° incident angle, was limited by the coupled axial–flexural pipeline response.

Bruschi et al. (1995) also highlighted the importance for considering pipeline route geometry with respect to the soil displacement field magnitude, distribution and direction. Pipeline forces developed by the slope instability may be transferred to “anchoring” sections that are not directly subjected to the relative soil motion. For pipeline sections associated with radial curves, sagbends or overbends this may significantly influence the stress–strain response and potentially trigger a failure mechanism.

Bruschi et al. (1996) applied the numerical procedure presented in Bruschi et al. (1995) for analyzing specific case studies for two pipeline routes located in Italy. Physical pipeline parameters such as route configuration, geometry, mechanical properties and operational characteristics were considered. Representative soil behaviour was defined by the undrained shear strength parameter and modeled by bilinear elastoplastic springs. The magnitude, distribution and direction of the displacement field were based on *in-situ* measurements acquired from slope inclinometers. In addition, as part of a pipeline monitoring program, the axial strain–time history response was also recorded by vibrating wire strain gauges located at discrete longitudinal stations.

Based on numerical calculations, the analysis demonstrated that the magnitude and distribution of pipeline strain was a function of the location, distribution and incident angle of the relative slope movement. Bruschi et al. (1996) noted the transition zone defining the relative soil displacement field may be one of the critical parameters that influences the pipeline response.

2.5.4 Finite Element Analysis – Continuum Models

Continuum finite element models are robust and comprehensive numerical tools that can address a number of limitations in the structural-type finite element analysis. Some of these issues include limitations in reproducing soil constitutive behaviour, soil deformation mechanisms (e.g. shear load transfer), soil/pipe interaction (e.g. variable circumferential or longitudinal pressure distribution) or complex pipeline response mechanisms (e.g. ovalization, or wrinkling).

The significant disadvantages of continuum finite element modeling are the demands on computational resources, limited availability of realistic soil constitutive models, and the requisite experience and knowledge of the analyst. A number of studies have been conducted to investigate pipe/soil interaction using continuum finite element modeling; such as Bruschi et al. (1995), or pipeline response; such as Yoosef-Ghodsii et al. (2000).

CHAPTER 3 STRESS RELIEF TESTING PROGRAM WITH 20" DIAMETER PIPES AND 30" DIAMETER PIPES

3.1 Introduction

The objective of this experimental program is to study the behaviour of pipes subjected to load cycles encountered in the field at an unstable slope site. As the soil slides down, it imposes axial, transverse, and vertical loads on the pipe. These external forces translate into additional axial compression and bending moment in the pipe. The axial compression and bending moment in the pipe are relieved when the soil is dug up during the stress relief procedure. As a result, the pipe goes through a major load cycle for every remedial work. To study the effect of this pattern of loading, a test program with cyclic axial compression and bending moment was designed and carried out.

There are twelve tests in the test program with six 762 mm (30 inch) and six 508 mm (20 inch) diameter pipes. The 762 mm pipe is grade X70 (Specified Minimum Yield Stress (SMYS) = 483 MPa or 70 ksi), and the 508 mm pipe is grade X80 (SMYS = 552 MPa or 80 ksi). Three pipes of each size undergo axial deformation, and another three undergo both axial and bending deformation. All tests are carried out with internal pressure.

3.2 Compression Test Program

The following two sections only deal with results of the compression test. The internal pressure and the loading pattern for the 762 mm and the 508 mm pipe compression test series are shown in Table 3.1. In Table 3.1 the following designation is used to identify the test specimen for all the twelve specimens in the test program:

Specimen **DxxPnnXY**-*

Dxx: indicates the pipe diameter size, e.g. D30 is a 30 inch (762 mm) diameter pipe and D20 is a 20 inch (508 mm) diameter pipe.

Pnn: "nn" indicates the level of the hoop stress induced by the internal pressure as a percentage of the SMYS, e.g. P40 is the 40% SMYS hoop stress.

X: indicates the type of loading. A is an axial compression test, and B is a bending test.

(A is used in this phase of test program.)

Y: indicates the pattern of loading. M is monotonic loading, and C is cyclic loading.

*: indicates the test specimen number.

For example, D30P80AM-1 represents a 30 inch pipe with an internal pressure that induces 80% SMYS hoop stress under a monotonic axial loading. It is the first specimen tested in the program.

3.2.1 Pretest Measurements

In order to facilitate the presentation of the test results, the angular coordinate system shown in Figure 3.1 was adopted. The first quadrant was taken between 0° and 90°, and the fourth quadrant was taken as 270° to 360° (0°). Various physical dimensions of the pipe specimen were measured before it was welded to the end plates. All measurements for the 270° location (seam weld) were taken at an offset of approximately 25 mm.

- 1) Thickness was measured at four points (45°, 135°, 225°, and 315°) per cross-section. At both ends of the pipe, the measurements were taken with a micrometer and an ultrasound thickness gauge. At the mid-length of the pipe, the thickness was measured with only an ultrasound thickness gauge.
- 2) The length of the pipe was measured at four points (45°, 135°, 225°, and 315°). The 30 inch pipes vary from 2409 to 2504 mm, which essentially can be considered to be 2500 mm, and the 20 inch pipes vary from 1844 to 1845 mm with an average length of 1845 mm.
- 3) The outside diameter of the pipe was measured at four locations (0°-180°, 90°-360°, 45°-135°, and 135°-315°) on both ends of the specimen.
- 4) The average measured dimensions are shown in Table 3.2. Note that the thickness value from the ultrasound device was consistently lower than the value by the micrometer. The total average thickness is the average of all the measurements taken regardless of the device used. The average thickness was 8.64 mm, and the outside

diameter was 762.46 mm for the 30 inch specimens and 11.61 mm and 509.50 mm for the thickness and diameter of the 20 inch pipes. These values were used in calculating the required internal pressure applied in the test.

Preliminary numerical analysis based on the pretest measurement data under-predicted the peak load for the 30 inch pipe tests. As a result, the thicknesses of the remaining unused pieces of the pipe were measured. It was found that the average thickness of the remaining pieces is 8.84 mm. The numerical simulation of the tests is discussed in the latter section.

3.2.2 Test Setup

Due to testing machine capability of 6MN at I.F. Morrison Structures Laboratory in University of Alberta, the compressive tests were carried out at C-FER Technologies facility using the 15 MN Universal Testing System. The test setup is shown in Figures 3.2, 3.3, and 3.4. Both ends of the pipe specimen were connected to the 76 mm end plates with a full penetration groove weld. A 150 mm wide collar was attached at each end to reduce the effect of the end connection in initiating buckling. These collars were made from segments of the pipe used in the test. A load transfer block was placed between the UTS piston and the top end plate for the purpose of aligning the load. Another use of the transfer block was to bring out the load from the UTS piston closer to the wall of the pipe. The block was 24 inches in diameter, the UTS piston was 18 inches in diameter, and the pipes were 30 inches and 20 inches.

3.2.3 Instrumentation

Various electronic and manual measurements were taken during the test.

- 1) For the strain measurement, a 10-inch (254 mm) Demec gauge was employed for the 762 mm pipes, and a 5-inch (127 mm) Demec gauge was used for the 508 mm pipes. The locations of the Demec points for the 30 inch pipes are shown in Figure 3.5, while Figure 3.6 shows the Demec arrangement for the 20 inch specimens. Punch holes were stamped beside Demec points. If a Demec point happened to fall off during the test, the distance between these punch holes was measured in place of the

distance between the Demec points. When the distance between the Demec points was out of the range of the Demec gauge, the distance between the points was then measured with a caliper. The caliper was also used to measure the distance between the punch holes.

- 2) A line of strain gauges was placed on the face of 225° locations. Two additional strain gauges each were placed on the other three faces (315°, 45° and 135°) at the top and the bottom of the specimen for load alignment. Hoop strain gauges were also placed at mid-height on the 45° and 225° faces. Locations of all gauges are shown in Figures 3.7 to 3.8 for the 30 inch pipes and Figures 3.9 for the 20 inch specimens.
- 3) Load history measurements including internal pressure, axial load, and axial deformation were recorded electronically during the test. The UTS load was measured with an internal load cell, the internal pressure with a pressure transducer, and the axial deformation through UTS stroke and also through a Lino Pot (linear potentiometer).

3.2.4 Loading

In general, the pipe was first pressurised to the target pressure. While pressurising the pipe, the UTS load was adjusted accordingly to offset the pressure force on the end plate so that there was zero net axial force on the pipe wall. However, there was an exception for the specimen D30P80AM-1. It was pressurised without the adjustment of the UTS load. The applied internal pressure for the test is shown in Table 3.3.

The subsequent loading phase of the specimen was carried out with stroke control. Loading was stopped when significant local buckling had occurred. In the monotonic test, the specimen was subjected to an increasing stroke. While in a cyclic test, cycling of the load was carried out at various increasing stroke levels. For every load cycle, the specimen was first unloaded to a zero pipe wall axial load. Then it was reloaded back to the approximate load (before yielding) or stroke level (after yielding) at the start of unloading. Three cycles of loading and unloading were carried out at each point where the load cycling was taking place. Load cycling was carried out at a few points before and after the peak load.

3.2.5 Ancillary Test

Three tension coupon tests were carried out for each of the 30 inch and 20 inch pipes to obtain the material properties of the pipes in the longitudinal direction. In the test, the cross-section area was also measured at various points of loading after the peak load was reached. The test results are shown in Figures 3.10 and 3.11 and Tables 3.4, 3.5, and 3.6. Note that the nominal strain is obtained from the extensometer reading. Figure 3.12 shows distinct differences in properties between X70 and X80 material used in the 30 inch and 20 inch pipes, respectively. To avoid damage to the extensometer, the extensometer was removed from the X80 tension coupons before the coupons broke. Therefore, stress vs. jack stroke curves of two materials were plotted in Figure 3.13 for better comparison. It can be seen from Figure 3.13 that X80 material exhibits a unique behaviour. The ultimate strength of the material was reached immediately following the yield strength.

The true plastic strain and true stress relationship shown in Tables 3.5 and 3.6 was calculated from the nominal strain and the engineering stress data up to the peak load point of the tension coupon test. Beyond the peak load point, the true plastic strain and true stress relationship was approximated by the change in the cross-section area and its corresponding load. Up to the peak load, the true stress can be calculated as

$$(3.1) \quad \sigma_p = (1 + \varepsilon_n) \sigma_n$$

where ε_n = engineering strain; σ_n = engineering stress.

The true plastic strain is given by

$$(3.2) \quad \varepsilon_p = \ln(1 + \varepsilon_n) - \frac{\sigma_p}{E}$$

where E = elastic modulus.

For points beyond the peak load, the true stress is approximated by

$$(3.3) \quad \sigma_p = \sigma_n \left(\frac{A_0}{A} \right)$$

where A_0 = original cross-section area; A = the current cross-section area.

The corresponding true plastic strain is given by

$$(3.4) \quad \varepsilon_p = \ln\left(\frac{A_0}{A}\right) - \frac{\sigma_p}{E}.$$

3.3 Compression Test Results

This section presents the compression test results from the six specimens.

3.3.1 General

The following definitions are adopted in the discussion of the test results.

- 1) Even though collars were attached to each end of the pipe, it was not expected to increase the overall stiffness of the specimen appreciably because they were only tightened snugly. Thus, the effective length of the specimen is taken as the overall length of the pipe. The global strain is defined as the average strain over the effective length of the pipe specimen.

$$(3.5) \quad \varepsilon_G = \frac{\Delta_G}{L_e}$$

where ε_G = global strain;

Δ_G = end displacement of the specimen;

L_e = effective length of the pipe specimen, taken as the overall length of the pipe.

- 2) The local D strain is taken as the average strain over the gauge length of the pipe of diameter D. It is calculated using the Demec gauge measurement.
- 3) The local buckling strain is defined as the D local strain at the peak axial force.
- 4) Net strain measures the change in the strain from point when the net axial force in the pipe is zero and the internal pressure is at the target level.

3.3.2 Overall Results

The final buckled shapes of the tests are shown in Figures 3.14 to 3.16 and Figures 3.17 to 3.19 for 30 inch and 20 inch specimens, respectively. There is only one buckle developed for D30P80AM-1 and D20P40AC-6, but there are two each for other specimens. The one buckle for D30P80AM-1 and D20P40AC-6 extends all the way around the pipe. However, the buckle for other four specimens developed only halfway

around the pipe. The two buckles occurred at the opposite face of the specimen and at a different elevation. Table 3.7 lists the location of the buckle for each specimen.

Preliminary inspection of the test data indicates that there is some discrepancy between the stroke reading and the actual specimen deformation. At the early stage of loading before buckling is initiated, the global strain and the strain gauge reading should be roughly equal. The slope of the global strain versus average strain gauge reading plot should be close to unity. But that was not the case, as can be seen in Figures 3.20 to 3.22 and 3.23 to 3.25. The slope of the linear least square fit line has a range of 0.645 to 0.6778 for 30 inch tests and 0.8914 to 0.9480 for 20 inch specimens. To ensure that the strain gauge readings were correct before any correction was carried out, they were checked against the Demec gauge data. In Figure 3.26 for D30P80AM-1 and Figure 3.27 for D20P80AM-4, the readings from the Demec gauge closely match those of the strain gauge. Consequently, global strain values are corrected by a factor of 0.6637 for 30 inch tests and 0.9253 for 20 inch specimens, which is the average slope of all the least squares fit lines. All global strain data in this report have been corrected with the correction factors except for those in Figures 3.20 to 3.25.

3.3.3 30" Specimens Results

Three specimens test results are presented here.

D30P80AM-1 and D30P80AC-2

The load-deformation curves for D30P80AM-1 and D30P80AC-2 are shown in Figures 3.28 and 3.29. The round dots indicate points where the load cycling took place. In Figure 3.29, only the upper envelope of the load-deformation is shown for D30P80AC-2. Up to the peak load, there is little difference in the pipe response between the monotonic and cyclic test, even though D30P80AC-2 had already gone through a few load cycles. However after the peak load, load-deformation plots for both tests start to deviate. The main reason for the difference is the shape and the location of buckling. D30P80AM-1 buckled at one elevation, while D30P80AC-2 buckled at two elevations.

In Figure 3.29, load versus local D strain based on the local strain at both buckling locations of D30P80AC-2 are shown together with the results for D30P80AM-1. Considering the difference in the buckled shape, the load – local D strain curves for both tests are not that far apart. It can be seen that the peak load occurred almost at the instance the load-deformation response became non-linear. For D30P80AM-1, the peak load is shown to occur at a significant higher local strain than the point where the nonlinearity starts. This is mainly due to the lack of sampling points around the peak load. As shown in Figure 3.29, there is hardly any inelastic deformation before the peak load. This is because in the material test shown in Figure 3.10, the pipe was found to have well-defined yield plateau (Dorey, et al.).

For the load-cycling range considered, there is no significant difference in the pipe response under monotonic or cyclic loading, as can be seen in Figure 3.29. The load-deformation curve during the load cycling stage is essentially linear and is parallel to the initial linear segment of D30P80AM-1. There is also very little hysteresis loop. This indicates that there is little inelastic deformation during the load cycling. Thus, for the load range applied in the test, the load cycling should have little effect on the pipe response.

D30P20AC-3

The results of D30P20AC-3 are shown in Figures 3.30 and 3.31. Similar to Figure 3.29, only the upper envelope of the load-deformation is plotted in Figure 3.31. The local D strain data are for the buckling location at the elevation 700 mm from the bottom. For D30P20AC-3, buckling occurred on the south face while the Demec gauge is on the north face. But the buckle did not extend all the way around the pipe. As a result, the D local strain decreases after the buckling starts.

Similar to D30P80AC-2, there is very little inelastic deformation before the peak load. The peak load occurred almost at the same time the load-deformation response becomes non-linear. The load-deformation curve during the load cycling stage is also essentially linear and is parallel to the initial linear segment of the overall load

deformation curve. There is also very little hysteresis loop. However, the loop does get slightly bigger during the later stage of loading.

3.3.4 20" Specimens

Three specimens test results are presented here.

D20P80AM-4

The load-deformation curve for D20P80AM-4 is shown in Figure 3.32 with peak load at 8173 kN and a corresponding global strain of 5844 $\mu\epsilon$. This P- ϵ Diagram has a gentle slope after peak load. There is much non-linear deformation before the peak load, which starts from global strain of 1504 $\mu\epsilon$ (corresponding load is 4496 kN) to 5844 $\mu\epsilon$. Figure 3.33 shows load vs. D local strain at Demec 9 of specimen D20P80AM-4. At the load level of 4496 kN, load vs. D local strain changes from linearity to non-linearity, and it has a gentle slope after peak load, the same trend as load vs. global strain. Figure 3.34 shows global strain vs. D local strain at Demec 9 of specimen D20P80AM-4. D local strain increases faster than global strain. At the load level of 4496 kN, D local strain over global strain changes from the rate of 1.23 to 3.24.

D20P40AM-5 and D20P40AC-6

The load-deformation curves for D20P40AM-5 and D20P40AC-6 are shown in Figures 3.35 and 3.36. The round dots indicate where the load cycling took place. In Figure 3.36, only the upper envelope of the load-deformation is shown for D20P40AC-6. Up to the peak load, there is little difference in the pipe response between the monotonic and cyclic tests, even though D20P40AC-6 had already gone through a few load cycles. After the peak load, load-deformation plots for both tests were parallel. The main reason for the similarity is that both specimens buckled at two different positions with half-wrinkles.

In Figure 3.36, load vs. D local strain based on the local strain at both buckling locations of D20P40AM-5 and D20P40AC-6 are shown together. Considering the difference in the buckled shape, the load vs. D local strain curves for both tests are not that far apart. It can be seen that the peak load occurred almost at the instance the load-

deformation response becomes non-linear. Even after the peak load, there is not much difference between these curves.

For the load-cycling range considered, there is no significant difference in the pipe response under monotonic or cyclic loading, as can be seen in Figure 3.36. The load-deformation curve during the load cycling stage is essentially linear and is parallel to the initial linear segment of D20P40AM-5. There is also very little hysteresis loop. This indicates that there is little inelastic deformation during the load cycling. Thus for the load range applied in the test, the load cycling should have little effect on the pipe response.

3.3.5 Local Buckling Strain

Global strain versus local D strain plots for the tests are shown in Figures 3.37, 3.25, 3.21, and 3.26. Since the material has a large yield plateau, the D local buckling strain is taken as the point on the curve where the line deviates from linearity. These points also correspond to the local strain value at the peak load. They can be clearly identified on the plots for D30P80AM-1 and D30P80AC-2. For D30P20AC-3, the D local buckling strain falls somewhere between 2760 and 3000 $\mu\epsilon$. For the purpose of the discussion, it is taken as 2760 $\mu\epsilon$. From Figures 3.34 and 3.39, local buckling strain of specimen D20P80AM-4, D20P40AM-5, and D20P40AC-6 are 4478 $\mu\epsilon$, 10500 $\mu\epsilon$, and 10500 $\mu\epsilon$, respectively.

Table 3.8 gives both the measured buckling strain and the predicted strain for 30 inch tests based on the von Misés yield criterion and the measured material properties. The predicted strain is calculated with the assumption that buckling occurs when the yield strength is reached. The predicted buckling strain matches well against the measured strain.

3.4 Bending Test Program

The following two sections covers the test results of 508 mm (20 inches) and 762 mm (30 inches) pipes under monotonic and cyclic bending moment combined with

constant axial load and different internal pressures. Three 508 mm pipes of grade X80 (SMYS = 552 MPa or 80 ksi) and three 762 mm pipes of grade X70 (SMYS = 483 MPa or 70 ksi) are tested in this phase. All six pipes undergo either monotonic or cyclic bending deformation, as indicated in Table 3.9. Each test involves subjecting the specimen to a constant axial load and internal pressure, while applying an increasing curvature (rotation) until buckling on the compressive side develops. Normally a noticeable drop in the bending moment is observed after buckling. The curvature continues to increase until the buckled shape develops fully and the bending moment drops at least 30% from the peak moment.

The internal pressure and loading pattern for each specimen are shown in the Table 3.9. Test specimen designation used to identify the specimens is **DxxPnnXY-***

Dxx: indicates the pipe diameter. D30 is a 30 inch diameter pipe; D20 is a 20 inch diameter pipe.

Pnn: “nn” indicates the level of the hoop stress induced by the internal pressure as a percentage of the SMYS (Specified Minimum Yield Strength).

X: indicates the type of loading. A is an axial compression test, and B is a bending test. (B is used in this phase of the test program.)

Y: indicates the pattern of loading. M is monotonic (bending) loading, and C is cyclic loading.

*: indicates the test specimen number.

For example, D30P80BC-8 stands for a 30 inch pipe with an internal pressure that induces 80% SMYS hoop stress and under cyclic bending. It is the 8th specimen in the program.

3.4.1 Pretest Measurements

In order to facilitate the presentation of the test results, the angular coordinate system shown in Figure 3.40 was adopted. The first quadrant was taken between 0° and 90°, and the fourth quadrant was taken from 270° to 360° (0°). Various physical dimensions of the pipe specimen were measured before it was welded to the end plates.

All measurements for the seam weld position were taken at an offset of approximately 25 mm.

- 1) Thickness was measured at 8 points (0° , 45° , 90° , 135° , 180° , 225° , 270° , and 315°) at 3 cross-sections. At both ends of the pipe, the measurements were taken with a micrometer and an ultrasound thickness gauge. At the mid-length of the pipe, the thickness was measured with only an ultrasound thickness gauge.
- 2) The outside diameter of the pipe was measured at four locations (0° - 180° , 45° - 225° , 90° - 270° , and 135° - 315°) with a 24 inches caliper for 20 inches pipes and a measuring tape for 30 inches pipes at both ends of the specimens. The average measured dimensions are shown in Table 3.10. Note that the thickness values from the ultrasound device were consistently lower than the values by the micrometer. The average thickness is the average of all the measurements taken regardless of the device used. The average thickness was 11.7 mm and 8.6 mm, and the outside diameter was 508.1 mm and 762.3 mm for the 20 inch pipes and 30 inch pipes, respectively. These values were used in calculating the required internal pressure applied in the test.
- 3) The length of the pipe was measured at four points (45° , 135° , 225° , and 315°) with a measuring tape. For the 30 inch pipes, they vary from 2798 mm to 2809 mm; the average length of the three pipes is 2805 mm. For the 20 inches pipes, they vary from 2345 mm to 2348 mm; the average length of the three pipes is 2347 mm.
- 4) Before welding the end plates, initial imperfection measurement were taken at an interval of 22.5° at ten equally spaced cross-sections 214.7 mm apart along the longitudinal length starting at 100 mm from the bottom end for 20 inch pipes. These measurements were taken at fourteen cross-sections spaced 180 mm apart starting at 140 mm from the bottom end for 30 inch pipes. The apparatus shown in Figure 3.41 was used to measure the distance from the center of the rotating arm to the inside face of the pipe wall.

3.4.2 Test Setup

The tests were carried out at the I.F. Morrison Structural Engineering Laboratory at the University of Alberta using the 6600 kN capacity MTS6000 Universal Testing

Machine. The schematic test setup is shown in Figure 3.42, Figures 3.43 and 3.44 are front and back views of the 30 inch pipe test setup, and Figure 3.45 is a 20 inches pipe test setup. Both ends of the pipe specimen were welded to a 76 mm end plate with full penetration groove welds. A 150 mm collar was attached at each end of the pipe to reduce the effect of the end connection in initiating buckling. These collars were made from segments of the same pipe used in the test. After the instrumentation was installed and the imperfection measurements taken, the test specimen was placed into the testing assembly.

3.4.3 Instrumentation

Various electronic and manual measurements were taken during the test.

- 1) Five inch (127 mm) Demec gauges for 20 inch pipes and 10 inch (254 mm) Demec gauges for 30 inch pipes were employed for measuring both the compression side and the tension side of the test specimens. The locations of the Demec points and their corresponding Demec gauge designations on the West and East faces (0° , 180°) for 20 inch pipes are shown in Figures 3.46 and 3.47, respectively; for 30 inches pipes they are shown in Figures 3.48 and 3.49. Indentations were also stamped adjacent to Demec points as back-up gauge points. If a Demec point fell off during the test, the distance between these punch holes was measured in place of the distance between the Demec points. When the distance between the Demec points was out of the range of the Demec gauge, the distance between the points was then measured with a caliper. The caliper was also used to measure the distance between the indentations when Demec points were not available. Demec readings were recorded over the pre-buckling range in order to verify the consistency between the electronic strain gauge measurements and the manually recorded Demec measurements, which in turn would provide confidence to the post-buckling manual readings for which there is no confirming electronic strain gauge data.
- 2) One line of strain gauges was placed on the extreme compression face (0°) at 127 mm intervals, starting at 285 mm from the both ends for 20 inch pipes; and at 254 mm intervals starting at 387 mm from the both ends for 30 inch specimens 8 and 9 (D30P80BC-8 and D30P20BC-9). For 30 inch specimen 7 (D30P0BC-7), the first

strain gauge on the top end starts at 336 mm from the end of the pipe; the rest of the strain gauges are the same as specimens 8 and 9. The reason for the different strain gauge arrangement for specimen 7 is due to the existence of a girth weld in the specimen 7. The girth weld is located at 387 mm from one end of the pipe, as shown in Figures 3.50 and 3.51. The locations of the strain gauges and their corresponding designation on the West face (0°) for 20 inch pipes are shown in Figure 3.46; for 30 inch specimens 8 and 9 they are shown in Figure 3.48. Specimen 7 is shown in Figure 2.50.

On the extreme tension face (180°) one line of strain gauges was placed at 254 mm intervals starting at 285 mm from the both ends for 20 inch pipes, and at 508 mm intervals starting at 387 mm from the both ends for 30 inch specimens 8 and 9. For 30 inch specimen 7, the first strain gauge on the top end starts at 336 mm from the end of the pipe, while the rest strain of the gauges are the same as 30 inch specimens 8 and 9. The locations of strain gauges and their corresponding designation on the East face (180°) for 20 inch pipes are shown in Figure 3.47; for 30 inch specimens 8 and 9, they are shown in Figure 3.49, and for 30 inches specimen 7 they are shown in Figure 3.51.

Additional two strain gauges were placed 25 mm away from the other two faces (90° and 270°), in the middle of the specimen, to detect any out-of-plane bending or mis-alignment. Four additional hoop strain gauges were also placed 25 mm away from the four faces (0° , 90° , 180° , and 270°), at the mid-height of the pipe for load alignment. Locations of all gauges are shown in Figures 3.46, 3.47, and 3.52 for 20 inch specimens and Figures 3.48 to 3.51 and 3.53 for 30 inch specimens.

- 3) Load history measurements including the internal pressure, eccentric jack load, axial deformation, and axial load were recorded electronically during the test. The MTS load was measured with an internal load cell, the internal pressure with a pressure transducer, the axial deformation through MTS stroke, and the eccentric jack load with a load cell.
- 4) LVDTs were installed on the compression and tension surfaces to measure the lateral movement of the pipe. They were spaced at 254 mm intervals starting 285 mm from

both ends for 20 inch pipes and 515 mm from both ends for 30 inch pipes, as shown in Figures 3.54 and 3.55. Photos of the LVDTs setup are shown in Figure 3.56.

- 5) Rotation meters were installed at the end plates to measure the end rotations. One rotation meter was used at each end plate.
- 6) Cable transducers were used to measure the relative movement of the end plates with respect to each other and with respect to the strong floor. An overall cable transducer hooked from the top of the overhead of the MTS to a distance of 200 mm away from the bottom of the jack, was used to measure the deformation from the bottom of the jack, through to the top of the jack, along the upper loading arm, and to the top of the MTS. Their locations are shown schematically in Figure 3.57 and photographically in Figure 3.58. This data can be used for the end rotation of the test specimen if the rotation meters happen to malfunction.
- 7) The amplitude of the buckle shape was measured with a carpenter contour gauge.
- 8) End shortening was measured through MTS stroke.

3.4.4 Loading

After the specimen was instrumented and aligned in the test frame, the pipe was first pressurized to the prescribed internal pressure level using the pneumatic pump. This was followed by increasing the MTS load to the desired net axial load for the pipe, given in Table 3.11, and at the same time maintaining the desired internal pressure. The end rotation was increased by means of the eccentric jack until failure occurred, while maintaining the desired net axial load by adjusting the MTS load accordingly to offset the jack load and the changing pressure force and to maintain internal pressure during the test. Failure was considered to have occurred when there was a noticeable drop in the applied bending moment with an increasing end rotation. Table 3.11 shows the internal pressure p , the corresponding percentage of the SMYS of the pressure, the axial force in pipe due to the Poisson effect (P_v), the axial force in pipe caused by a temperature difference of 45°C (P_T), the net axial force in the pipe wall (P_N), the reaction force due to internal pressure on the end plates (P_p), the expected maximum jack load (P_J) predicted by numerical analyses, and the targeted maximum MTS load (P_{MTS}). The net axial force in the pipe wall is the summation of temperature and Poisson effects, i.e. $P_N = P_T + P_v$.

The targeted maximum MTS load is the total load from the net axial force, the reaction on the end plate, and the jack load, i.e. $P_N + P_P + P_J$.

The axial load and pressure were applied in alternating steps. First, about two-thirds of the desired pressure was applied. It was followed by an increase in axial load. Then finally both the pressure and the axial load were brought up to their full test level. Once the specimen had deformed freely under the internal pressure and the desired net axial wall force, the ends were constrained by tightening the collar in preparation for the bending of the test specimen.

The subsequent loading phase of the specimen was carried out with load control first; when significant local buckling had occurred, stroke control was used. The force in the eccentric jack was applied in small steps to give the specimen global end moments and to increase the pipe's curvature.

In the monotonic test, the specimen was subjected to an increasing stroke. The load in the jack was increased by increments of approximately 100 kN at a time, which corresponded to increase in the global end moment of approximately 150 kN.m. After a prescribed increment in moment was achieved, both the internal pressure and the MTS loads were adjusted in order to re-establish the desired levels. Once the desired load levels had been reached and the loads had stabilized, a set of instrument readings was taken at each load interval. At intervals of approximately 450 kN.m, manual Demec readings were recorded. During the test a plot of the force in the jack versus the total stroke of the system was generated. The total stroke was calculated as the jack stroke plus the stroke of the MTS testing machine. This plot was then used to observe the point at which the load versus stroke behaviour started to become non-linear. When the plot became non-linear, instrument readings were taken with every 50 kN increase in jack force rather than at 100 kN intervals. This process was continued until the system began to become less stable. This occurred at a point near the peak moment resistance of the pipe. At this point it became difficult to maintain the jack force at a constant level. Beyond this point the load was no longer increased by 50 kN between instrument

readings, but rather the stroke of the jack was increased by small increments, which corresponded to varying decrements in the amount of global end moment depending on the location on the post-buckling curve. It should be noted that for the entire test duration, both the internal pressure and the axial load were maintained at constant values. The total jack stroke at the peak load is noted as “the stroke at peak load”, which is used later on in the test as a reference value.

In a cyclic test, cycling of the load was carried out at various stroke levels. For every load cycle, the specimen was first unloaded to the target net pipe wall axial load; Demec readings were taken. Then it was reloaded back to the approximate load or stroke level at the start of unloading. Three cycles of loading and unloading were carried out at each point where the load cycling was taking place. At the third reloading, Demec readings were taken again. Load cycling was carried out at a few points before and after the peak load. Load cycling points were decided as follows.

From the moment-curvature curve of the monotonically loaded pipe specimens, the global curvature ϕ_y corresponding to the yield moment M_y and the global curvature ϕ_{max} corresponding to the peak end moment M_{max} are identified. The yield moment is defined as the proportional limit in the moment-curvature curve. ϕ_y and ϕ_{max} are then used in determining the loading sequence of the cyclicly loaded specimens. The first point of cyclic bending moment is at the moment level of $0.5M_y$ and the second point is at the moment level M_y . All subsequent moment cycles are carried out at a curvature increment of ϕ_{INC} . The value of ϕ_{INC} is determined from ϕ_y and ϕ_{max} . It is selected such that at least one cycling sequence is carried out between M_y and M_{max} and is taken as

$$(3.6) \quad \phi_{INC} = \frac{(\phi_{max} - \phi_y)}{2}.$$

The last point of the load cycling is where the load is at least 95% below the M_{max} of the test. At each point, the loading is cycled three times. One cycle implies the unloading of the pipe to a zero end moment and reloading it to the initial moment level or until the initial curvature is reached. In the unloading phase, the jack force was first

unloaded, followed by the MTS load. The pipe was then depressurized. The loading phase was then repeated in a reverse order until the end rotation had exceeded the rotation at the end of the previous loading phase, and the cycle continued. Figures 3.59 and 3.60 show the loading processes of monotonic and cyclic tests, respectively. During the tests, the electronic data was recorded at a regular interval in all phases of loading and unloading.

3.4.5 Coupon Test

The 30 inch pipes used in this test phase are of the same pipe materials as the 30 inches pipes used in Phase I. Therefore no coupons were prepared and tested in this phase for the 30 inch specimens. However, the 20 inch pipes used in this phase were from a different heat than that of the 20 inch pipes used in Phase I. Therefore a new set of coupons were prepared for the 20 inch specimens. As the strength of pipes increases, the material properties in longitudinal and hoop directions might differ significantly. Therefore, seven transverse tension coupons in addition to three longitudinal coupons were prepared and tested to obtain the material properties of the 20 inch pipe. These coupons were cut from the bottom part of specimen D20P40BM-11, away from the buckled region, as shown in Figure 3.61, after the bending test was finished. Since the coupons were cut far from the buckled region, it is believed that the effect from the buckling on the material properties has been minimized.

Figures 3.62 and 3.63 show the geometry of the longitudinal and transverse tension coupons, respectively. A piece of steel of 250 mm wide x 400 mm arc length cut from specimen 11 was pressed to a flat plate before three transverse coupons, as shown in Figure 3.63, were made. Four other transverse coupons were machined from the same segment of specimen 11 without the flattening procedure. Figure 3.64 shows the shape of these four special coupons. These coupons were machined flat at the gauge length region while the gripping regions were left curved. This will avoid plastic deformation imposed in the gauge length region due to the flattening procedure. Cross-section area was measured at three locations within the gauge length before the test.

The stress vs. strain curves of three sets of tension coupons are shown in Figures 3.65 to 3.73 and the results of each set are summarized in Table 3.12.

From the Figure 3.65 to Figure 3.73, the yield strength of curve hoop coupons is higher than that in longitudinal direction. Data from straightened hoop coupons are inconsistent due to plastic deformation before tension tests. We regard data from curve hoop coupons as typical hoop direction results.

3.5 Bending Test Results

This section presents the bending test results from the six specimens.

3.5.1 General

The following definitions are adopted in the discussion of the test results.

- 1) Even though collars were attached to each end of the pipe, it was not expected to increase the overall stiffness of the specimen appreciably because they were only tightened snugly. Thus, the effective length of the specimen is taken as the overall length of the pipe. The global curvature is defined as the total rotation of the specimen over the effective length of the pipe.

$$(3.7) \quad \psi = \phi/L_e$$

$$(3.8) \quad \phi = \phi_1 + \phi_2$$

where ψ = the global curvature;

ϕ = total rotation of the specimen;

ϕ_1 = rotation of the top end of the pipe;

ϕ_2 = rotation of the bottom end of the pipe;

L_e = the effective length of the specimen, taken as the overall length of the pipe.

- 2) Local strain is the average strain over the buckle shape length of the pipe. It is calculated using the Demec gauge measurement.
- 3) The local buckling strain is defined as the local strain at the peak moment.
- 4) The critical local strain is defined as the relevant strain at the intersection between the initial trend straight line and the second trend straight line in the global curvature vs. local strain diagram.

3.5.2 Overall Results

The final buckled shapes of the tests are shown in Figures 3.74 to 3.92. There is only one buckle developed in specimens 7, 9 and 11. There are two buckles formed in specimens 8, 10 and 12 at the beginning, but only one is developed fully. These buckles occurred on the compressive side in different elevations and extended about halfway around the pipe from 0° - 90° and 270° - 360° . A diamond-shaped buckle happened to specimen 7 while bulge buckled shapes were observed for other tests. Table 3.13 lists locations of buckles for each specimen.

Data obtained from each test was reduced and presented in Figures 3.93 to 3.133. In each test, global moment vs. global curvature curves (both from rotational meters and cable transducers), global moment vs. local strain curves, global moment vs. local curvature curves, global curvature vs. local curvature curves, and global curvature vs. local strain curves are presented.

For cyclic loading specimens, the global moment vs. global curvature curves show that data obtained from rotational meters is more reliable than that obtained from the cable transducer. It can be attributed to the mechanical slip in the cable transducer when reverse traveling occurs in the device. Figures 3.93 and 3.94, 3.99 and 3.100, 3.107 and 3.108, and 3.126 and 3.127 show the global moment vs. global curvature curves from rotational meters and cable transducers, respectively. In Figure 3.94, in the first 4 to 6 cycles the slope of the cyclic loading line is negative, which is unreasonable. Curvature from the cable transducer shows smaller value than that from the rotational meter. Therefore the rotational meter reading is used to calculate the global curvature for other relevant curves.

In global moment vs. local strain diagrams, for example in Figure 3.95, for each load cycle, the first Demec reading was taken (labelled "1" in Figure 3.95) before the first unloading cycle. Then it was unloaded to the target net pipe wall axial load (applied moment was zero) and the second set of Demec readings were taken (labelled "2"). The pipe was reloaded back to the approximate same load or stroke level as at the start of

unloading, After three cycles of loading and unloading were carried out at each point where the load cycling was taking place, a third Demec reading was taken before further reloading (labeled “3”).

3.5.3 30” Inch Pipes Results

The results from each test are discussed in the following sections.

D30P0BC-7

The results for specimen D30P0BC-7 are shown in Figures 3.93 to Figure 3.98. The global moment vs. global curvature is shown in Figure 3.93; the round dots indicate points where the load cycling took place. There is very little inelastic deformation before the peak moment, which occurs almost as the same time as the moment-curvature response becomes non-linear. During the load cycling stage, the moment-curvature curve is also essentially linear, in the 6th cycle it is parallel to the initial segment of moment-curvature curve. Afterwards, the slope of the line segment at each cyclic point is gradually decreasing, reflecting the softening of the specimen. There is very little hysteresis loop. However, the loop gets slightly bigger at the later stage of loading.

Figure 3.95 shows global moment vs. local strain at the DC-9 location, the buckling location 350 mm from the top of the pipe (See Figure 3.75). At each cyclic point local strain accumulates after three repeated cycles. The maximum local strain accumulation of $21,654\mu\epsilon$ occurs right after the peak global moment at the 6th cycle. Then it reduces at the subsequent load cycles, which do not show much accumulation of local strain. The same trend as the local strain is observed from the local curvature, see Figure 3.96. Figure 3.97 shows global curvature vs. local curvature at position DC-9. Local curvature increases faster than global curvature with the rate of 1.33 before the peak moment. Between 5th and 6th cyclic points, local curvature increases while global curvature decreases. Then at the 6th cyclic range, local curvature grows 28.3×10^{-6} rad/mm, which is much bigger than that in later cycles. During the cyclic loading ranges, the rate of local curvature to global curvature gradually increases, outside the cyclic loading range; the rate keeps the same as 8.124 after the 6th load cycling. From Figure

3.98, the critical local strain at DC-9 is $2,754\mu\epsilon$, the corresponding global curvature is 3.98×10^{-6} rad/mm. Specimen D30P0BC-7, without internal pressure, is more sensitive to the slight increment right after the peak load. The cyclic loading pattern affects the local behaviour of pipe, and the effect progressively reduces.

D30P80BC-8

The results for specimen D30P80BC-8 are shown in Figure 3.99 to Figure 3.106. The global moment vs. global curvature is shown in Figures 3.99. By comparison with specimen D30P0BC-7, specimen D30P80BC-8 has a gentler slope after peak moment. There is much non-linear deformation before the peak moment. After the peak moment, the moment capacity does not drop much, reflecting a more stable behaviour. The moment-curvature curve during the load cycling stage is essentially linear, they are parallel to the initial segment of moment-curvature curve except that at the last two cycles the slope of the line segment is decreasing, which indicates the softening of the specimen. There is very little hysteresis loop. However, the loop gets slightly bigger at the last two load cycles.

The local strain data in Figure 3.101 is for the buckling location at the elevation 386 mm from the bottom between DC-1 (see Figure 3.77) and Figure 3.102 is for the second bulge at the elevation 380 mm from the top between DC-9 (see Figure 3.78). At 4th (before peak load), 5th (after peak load) and 6th cyclic range, local strain at DC-1 accumulates. The maximum local strain accumulation of $3,937\mu\epsilon$ occurs right after peak global moment at the 5th cycle. At the 4th and 6th cycle local strain accumulations are $1,969\mu\epsilon$ and $1,181\mu\epsilon$, respectively. Local curvature has the same trend as local strain at DC-1, as shown in Figure 3.103. From Figure 3.102 only at 3rd (before peak load) cyclic range, local strain at DC-9 accumulates $198\mu\epsilon$. Starting from the 4th cycle, it is decreasing at each load cyclic range. The maximum local strain reduction is $1,969\mu\epsilon$ at the 5th and 6th cyclic ranges. This happens because buckling at DC-1 developed fully and unloading took place at DC-9. Figure 3.104 shows global curvature vs. local curvature at position DC-1. Local curvature increases faster than global curvature with the rate of 1.924 before peak moment, and the rate keeps the same as 11.815 after the

peak moment. During the cyclic loading ranges, the rate of local curvature to global curvature gradually increases, the maximum local curvature growth occurs at the 5th cyclic range. In Figures 3.105 and 3.106, the critical local strains at DC-1 and DC-9 are $3,329\mu\epsilon$ and $2,073\mu\epsilon$. The corresponding global curvatures are 3.98×10^{-6} rad/mm and 3.19×10^{-6} rad/mm, respectively. Specimen D30P80BC-8, with high internal pressure, has little influence from the cyclic load pattern in that the influence locates near the peak load (accordingly about 2.0×10^{-6} rad/mm global curvature away from that at the peak load).

D30P20BC-9

The results for specimen D30P20BC-9 are shown in Figure 3.107 to Figure 3.112. The global moment vs. global curvature is shown in Figure 3.107. There is a little inelastic deformation before the peak moment, which occurs right after the moment-curvature response becomes non-linear. During the load cycling stage the moment-curvature curve is also essentially linear. There is very little hysteresis loop.

Figure 3.109 shows global moment vs. local strain at DC-9, the buckling location 370 mm from the top of the pipe (See Figure 3.80). After the 3rd cycle at each cyclic range, local strain accumulates. The maximum local strain accumulation of $3,937\mu\epsilon$, (which is exactly the same as specimen D30P80BC-8), occurs right after peak global moment at the 6th cycle. At the 5th (peak moment) and 7th cycle local strain accumulations are $1,181\mu\epsilon$ and $1,968\mu\epsilon$, respectively. Local curvature at DC-9 has the same trend as local strain, see Figure 3.110. Figure 3.111 shows global curvature vs. local curvature at position DC-9. Local curvature increases faster than global curvature with a rate of 1.266 before the peak moment and 7.06 after the peak moment. At the 6th cyclic range, local curvature grows the most, 5.12×10^{-6} rad/mm. During the cyclic loading ranges, the rate of local curvature to global curvature gradually increases. From Figure 3.112, the critical local strain at DC-9 is $3,102\mu\epsilon$; the corresponding global curvature is 5.2×10^{-6} rad/mm. Specimen D30P20BC-9, with relatively low internal pressure, has some influence from the cyclic load pattern, which starts before the peak load. However, it is not as significant as D30P0BC-7.

30" Pipes Comparison

From previous results, a conclusion can be drawn that the less internal pressure, the more effect the cyclic loading pattern imposes on the pipe. The accumulated local strain during the cycle right after the peak moment are $21,654\mu\epsilon$, $3,937\mu\epsilon$, and $3,937\mu\epsilon$ for zero pressure, 20% SMYS pressure, and 80% SMYS pressure pipes, respectively. Figure 3.113 shows the global moment vs. global curvature of three 30 inch pipes. The deformed shape is in Figure 3.81. Peak moment for the 7th, 9th and 8th (internal pressure is 0, 20%, 80%) specimens is 1914 kN.m, 1894 kN.m, and 1599 kN.m, respectively. With higher internal pressure, moment capacity is reduced as expected. As internal pressure increases, moment-curvature curve becomes gentler and cyclic loading affects less.

The critical compressive strains obtained from the tests are $2,754\mu\epsilon$, $3,102\mu\epsilon$, and $3,329\mu\epsilon$ for zero pressure, 20% SMYS pressure, and 80% SMYS pressure pipes, respectively.

3.5.4 20" Pipes Results

D20P80BM-10

The results for specimen D20P80BM-10 are shown in Figures 3.114 to 3.120. The global moment vs. global curvature curve is shown in Figure 3.114 with peak moment at 1309 kN.m and corresponding curvature 28.67×10^{-6} rad/mm. This M- ϕ diagram has a gentle slope after the peak moment. There is much non-linear deformation before the peak moment. Non-linear deformation starts from a curvature of 6.57×10^{-6} rad/mm to 28.67×10^{-6} rad/mm.

In Figures 3.115 and 3.119, local strain data are for the buckling location at the elevation 675 mm from the bottom at DC-3, 4 and 5 (see Figures 3.82 and 3.83) and the bulge at the elevation 260 mm from the top at DC-13, 14 and 15 (see Figure 3.82, 3.84). Figure 3.115 shows the moment-strain curve at DC-3, 4 and 5; after the peak moment,

local strain tends to increase linearly. Accordingly, the local curvature has the same trend as the local strain, see Figure 3.117.

Figure 3.116 shows the moment-strain curve at DC-13, 14 and 15; after peak moment (1299 kN.m) at 1263 kN.m, local strain decreases dramatically. This happens because buckling at DC-3, 4, and 5 developed fully which causes load drop at DC-13, 14 and 15. Figure 3.118 shows global curvature vs. local curvature at position DC-3, 4 and 5. Local curvature increases faster than global curvature with the rate of 1.178 before critical point (relevant to peak moment), and the rate keeps the same as 4.83 after critical point. It is noted that before the critical point (global curvature 27×10^{-6} rad/mm) there is a cusp in the curve around a global curvature of 18.8×10^{-6} rad/mm. This is due to precision changing from the Demec gauge to divider. In figures 3.119 and 3.120, the critical local strain at DC-3, 4 and 5, DC-13, 14 and 15 is $4,166 \mu\epsilon$ and $3,571 \mu\epsilon$. The corresponding global curvature is 22×10^{-6} rad/mm and 16×10^{-6} rad/mm, respectively.

D20P40BM-11

The results for specimen D20P40BM-11 are shown in Figures 3.121 to 3.125. The global moment vs. global curvature diagram is shown in Figure 3.121 with peak moment at 1614 kN.m and a corresponding curvature of 19.6×10^{-6} rad/mm. This M- ϕ diagram has a sharp dropping slope after the peak moment by comparison with specimen D20P80BM-10. There is little non-linear deformation before the peak moment.

In Figures 3.122 and 3.125, local strain data is for the buckling location at the elevation 720 mm from the top at DC-10~13 (see Figure 3.85 to 87). Figure 3.122 shows moment-strain curve at DC-10~13. After peak moment, local strain tends to increase linearly, accordingly, local curvature has the same trend as local strain, see Figure 3.123. Figure 3.124 shows global curvature vs. local curvature at position DC-10~13. Local curvature increases faster than global curvature with the rate of 1.178 before the critical point (relevant to peak moment), and the rate keeps the same as 3.25 after the critical point. In Figure 3.125, the critical local strain at DC-10~13 is $3,766 \mu\epsilon$ and the corresponding global curvature is 14.84×10^{-6} rad/mm.

D20P40BM-12

The results for the specimen D20P40BC-12 are shown in Figure 3.126 to Figure 3.133. The global moment vs. global curvature is shown in Figure 3.126. There is much non-linear deformation before the peak moment. After the peak moment, the moment capacity does not drop much. The moment-curvature curve shows increasing hysteresis loop as the global curvature increases.

In Figures 3.128, 3.129, 3.132 and 3.133, the local strain data is for the buckling location at the elevation 630 mm from the bottom between DC-3~6 (see Figure 3.88, 3.89, and 3.90) and the bulge at the elevation 410 mm from the top between DC-14, 15 (see Figure 3.88 and 3.91). In Figure 3.128, at the 6th (after peak load) and 7th cyclic range, local strains at DC-3~6 accumulate. The maximum local strain accumulation of $2,898\mu\epsilon$ occurs at the 7th cycle. At the 6th cycle local strain accumulation is $335\mu\epsilon$. Accordingly, local curvature has the same trend as local strain at DC-3~6, see Figure 3.130. From Figure 3.129, local strain at DC-14, 15 decreases. The maximum local strain reduction is $1,614\mu\epsilon$ and occurs at the 7th cyclic range. This happens because buckling at DC-3~6 developed fully which causes load drop at DC-14,15. Figure 3.131 shows global curvature vs. local curvature at position DC-3~6. Local curvature increases faster than global curvature with the rate of 2.5. During the cyclic loading ranges, the rate of local curvature to global curvature gradually decreases; the maximum rate occurs at the 5th load cycle range. From Figure 3.132 and 3.133, the critical local strain at DC-3~6 and DC-14, 15 is $2,958\mu\epsilon$ and $4,577\mu\epsilon$; the corresponding global curvature is 19×10^{-6} rad/mm and 14×10^{-6} rad/mm, respectively.

20 Inch Pipes Comparison

Figure 3.134 shows moment-curvature diagrams for D20P40BM-11, D20P40BC-12. Up to the peak load, there is little difference between the two curves, though D20P40BC-12 has already gone through a few load cycles before the peak moment. However after peak load, moment-curvature plots for both tests start to deviate. The main reason for the difference is the shape and the location of buckling. D20P40BM-11 buckles at one location, while D20P40BM-12 buckles at two locations. The buckled shapes of the three

20 inch pipes can be seen in Figure 3.92. Figure 3.135 shows moment-curvature diagrams for D20P80BM-10 and D20P40BM-11. Similar to 30 inch pipes, the less internal pressure, the higher moment capacity the pipe has. Peak moment for the 10th and 11th (internal pressure is 80%, 40%) specimens is 1309 kN.m and 1614 kN.m, respectively. As internal pressure increases, moment-curvature curve becomes gentler.

The maximum accumulated local strain of $2898\mu\epsilon$ for D20P40BC-12 occurs at the 7th cycle, which is much later after the peak moment is achieved. This is different from 30 inch specimens in which the maximum accumulated local strain normally occurs right after the peak moment. The critical compressive strains obtained from the 20 inches pipe tests are $3571\mu\epsilon$, $3,766\mu\epsilon$, and $2958\mu\epsilon$ for 80% SMYS pressure with monotonic loading, 40% SMYS pressure pipes with monotonic loading, and 40% SMYS pressure pipes with cyclic loading, respectively. Relative strain comparisons are shown in table 3.14.

Table 3.1 Test specimens and loading matrix

Test	Loading Type	Internal Pressure (x% SMYS)
D30P80AM-1	Monotonic	80%
D30P80AC-2	Cyclic	80%
D30P20AC-3	Cyclic	20%
D20P80AM-4	Monotonic	80%
D20P40AM-5	Monotonic	40%
D20P40AC-6	Cyclic	40%

Table 3.2 Average pretest measurements

Specimen	Average Thickness (mm)			Outside
	Ultrasound	Micrometer	Total Average	Diameter (mm)
D30P80AM-1	8.58	8.65	8.61	762.8
D30P80AC-2	8.63	8.71	8.66	762.3
D30P20AC-3	8.62	8.72	8.66	762.4
Average	8.61	8.69	8.64	762.5
D20P80AM-4	11.58	11.66	11.62	509.6
D20P40AM-5	11.51	11.63	11.57	509.3
D20P40AC-6	11.60	11.70	11.65	509.6
Average	11.56	11.66	11.61	509.5

Table 3.3 . Applied internal pressure

Specimen	Internal Pressure (MPa)	Internal Pressure (x% SMYS)
D30P80AM-1	9.0	80%
D30P80AC-2	9.0	80%
D30P20AC-3	2.2	20%
D20P80AM-4	20.2	80%
D20P40AM-5	10.1	40%
D20P40AC-6	10.1	40%

Table 3.4 General mechanical properties of the pipe

30 inch pipes

Specimen	1	2	3	Average
% Elongation	24.5	27.4	25.8	25.9
Ultimate strength, σ_{ult} (MPa)	598	598	601	599
0.5% yield strength, $\sigma_{y0.5\%}$ (MPa)	596	563	568	567
Elastic Modulus, E (MPa)	196000	199000	203000	199300

20 inch pipes

Specimen	1	2	3	Average
% Elongation	-	22.3	17.0	19.7
Ultimate strength, σ_{ult} (MPa)	710	-	723	717
0.5% yield strength, $\sigma_{y0.5\%}$ (MPa)	650	636	638	641
Elastic Modulus, E (MPa)	199100	198500	199600	199100

Table 3.5 Stress-strain relationship of the 30 inch pipe in the longitudinal direction

Nominal Strain	Engineering Stress (Mpa)	True plastic strain	True plastic stress (MPa)
0.00000	0.0	0.00000	0.0
0.00284	567.0	0.00000	568.6
0.01740	567.0	0.01437	576.9
0.03850	586.7	0.03474	609.3
0.05627	594.6	0.05161	628.0
0.07835	598.1	0.07221	644.9
0.09672	597.6	0.08904	655.4
0.10507	597.2	0.23136	742.4
0.13353	586.9	0.53490	925.7
		0.61707	970.7
		0.93508	1111.3
		1.25873	1254.4

Table 3.6 Stress-strain relationship of the 20 inch pipe in the longitudinal direction

Nominal strain	Engineering stress (MPa)	True plastic strain	True stress (MPa)
0.00000	0.0	0.00000	0.0
0.00131	261.3	0.00000	261.6
0.00154	303.2	0.00002	303.7
0.00167	325.0	0.00004	325.5
0.00191	366.7	0.00007	367.4
0.00204	386.9	0.00010	387.7
0.00219	410.3	0.00013	411.2
0.00227	423.0	0.00015	424.0
0.00240	441.8	0.00019	442.8
0.00258	464.3	0.00024	465.5
0.00266	476.3	0.00027	477.6
0.00288	502.4	0.00035	503.8
0.00331	551.6	0.00054	553.4
0.00465	624.5	0.00150	627.4
0.00577	660.1	0.00244	663.9
0.00748	689.6	0.00398	694.8
0.01144	699.5	0.00784	707.5
0.01187	700.2	0.00826	708.5
0.01330	707.1	0.00962	716.5
0.01583	708.5	0.01211	719.7
		0.11786	762.6
		0.20275	805.1
		0.32943	869.0
		0.38836	904.3
		0.46547	927.0
		0.58006	989.9
		0.68306	1039.8
		0.84319	1084.7

Table 3.7 Location of buckling in each specimen

Specimen	Buckle location
D30P80AM-1	Buckle occurred exactly in between Demec D2 and D3, and on strain gauge SG2 (700 mm from the bottom).
D30P80AC-2	The specimen buckled at two locations. Buckle was first noticed at the strain gauge SG14 (350 mm from the top) on the east face of the specimen. A second buckle subsequently developed on the west face close to the elevation of the centre of the Demec gauge D8 (800 mm from the top).
D30P20AC-3	The specimen buckled at two locations. Buckle was first noticed at the elevation in between SG2 and SG3 (700 mm from the bottom) on the south face of the specimen. A second buckle subsequently was also noticed to have developed on the north face within the collar (100 mm from the bottom). As a result, the collar was then tightened to prevent further development of the second buckle.
D20P80AM-4	Wrinkle is almost concentric and formed along Demec 9.
D20P40AM-5	Two half-wrinkles formed. One through Demec 6 on north-west side and the other one through Demecs 28 and 29 on south-east side.
D20P40AC-6	Two half-wrinkles formed. One through Demecs 8 and 9 on north-west side and the other one through Demecs 30 and 31 on south-east side. The half-wrinkle through Demecs 30 and 31 is skewed.

Table 3.8 Tested and predicted compressive D local buckling strain

Specimen	D local compressive buckling strain, microstrain	
	Test	Static yield strength, 567 MPa
D30P80AM-1	2000	1900
D30P80AC-2	2150	1900
D30P20AC-3	2760	2700

Table 3.9 Test specimens and loading matrix

Test specimens	Bending Moment Loading Pattern	Internal Pressure (x% SMYS)
D30P0BC-7	Cyclic	0
D30P80BC-8	Cyclic	80%
D30P20BC-9	Cyclic	20%
D20P80BM-10	Monotonic	80%
D20P40BM-11	Monotonic	40%
D20P40BC-12	Cyclic	40%

Table 3.10 Dimensions of specimens

Specimen	Ultrasound Gauge (mm)	Micrometer (mm)	Average Thickness (mm)	Outside Diameter (mm)	Length (mm)
D30P0BC-7	8.53	8.77	8.63	761.8	2809.3
D30P80BC-8	8.39	8.69	8.51	762.4	2807.8
D30P20BC-9	8.54	8.71	8.60	762.8	2798.5
Average	8.49	8.72	8.58	762.3	2805.2
D20P80BM-10	11.64	11.72	11.70	508.0	2347.2
D20P40BM-11	11.67	11.73	11.69	508.1	2344.8
D20P40BM-12	11.67	11.73	11.70	508.0	2347.8
Average	11.66	11.73	11.70	508.1	2346.6

Table 3.11 Expected loading on the specimens

Specimen	p (psi)	% SYMS	P _p (kN)	P _v (kN)	P _T (kN)	P _N (kN)	P _J (kN)	P _{MTS} (kN)
D30P0BC-7	0	0	0	0	-2119	-2119	-1305	-3424
D30P80BC-8	1278	80	-3843	2177	-2119	58	-1012	-4797
D30P20BC-9	320	20	-961	544	-2119	-1575	-1259	-3795
D20P40BM-11	1544	40	-1968	1210	-1922	-712	-1141	-3822
D20P80BM-10	3088	80	-3937	2419	-1922	497	-920	-4360
D20P40BC-12	1544	40	-1968	1210	-1922	-712	-1141	-3822

Table 3.12 Summary of Mechanical Properties of Tension Coupons

Specimens	0.5% Yield Strength (MPa)	Ultimate Strength (MPa)	Elastic Modulus (MPa)	Final Elongation (%)
Longitudinal #1	664	747	201600	18.3
Longitudinal #2	663	748	203200	19.1
Longitudinal #2	647	741	198600	18.8
Average	658	745	201133	18.7
Hoop #1	572	703	196700	17.8
Hoop #2	576	686	199900	17.6
Hoop #3	544	672	202200	NA
Average	564	687	199600	17.7
Hoop (curve) #1	697	722	202300	12.0*
Hoop (curve) #2	681	707	207600	11.7*
Hoop (curve) #3	698	721	211200	NA
Hoop (curve) #4	697	712	211400	11.4*
Average	693	715	208100	11.7*

* based on 60mm gauge

Table 3.13 Location of buckling in the test

Specimens	Buckle location
D30P0BC-7	The specimen buckled at Demec gauges DC-8 and DC-9 with a maximum width of 730 mm along the half circle of the specimen. The center elevation of the buckle located 350 mm away from the top of the pipe. See Figure 3.74 and Figure 3.75.
D30P80BC-8	The specimen buckled at two locations on the compressive side. A buckle was first noticed near strain gauge SG40 (386 mm from the bottom). The peak of the buckle located 310 mm away from the bottom of the pipe. See Figures 3.76, 3.77, and 3.79 The second buckle subsequently occurred but with less magnitude at Demec gauge DC-9 with a maximum width of 200 mm along the half circle of the specimen, the center elevation of which located 380 mm away from the top of the pipe. See Figures 3.76 and 3.78.
D30P20BC-9	The specimen buckled at Demec gauge DC-9 with a maximum width of 120 mm along the half circle of the specimen. The center elevation of the buckle located 370 mm away from the top of the pipe. See Figures 3.79 and 3.80. A family picture of the failed 30 inches pipes is shown in Figure 3.81.
D20P80BM-10	The specimen buckled at two locations on the compressive side. A buckle was first noticed between strain gauge SG44 (792 mm from the bottom) and strain gauge SG41 (411 mm from the bottom). The peak of the buckle located 675 mm away from the bottom of the pipe. See Figures 3.82 and 3.83. The second buckle subsequently occurred but with less magnitude at Demec gauges DC-14 and DC-15 with a maximum width of 200 mm along the half circle of the specimen, the center elevation of which located 260 mm away from the top of the pipe. See Figures 3.82 and 3.84.
D20P40BM-11	The specimen buckled between Demec gauges DC-10, DC-11 and DC-12 on the compressive side with a maximum width of 200 mm along the half circle of the specimen, the center elevation of which located 720 mm away from the top of the pipe. See Figures 3.85, 3.86 and 3.87.

D20P40BC-12	The specimen buckled at two locations on the compressive side. A buckle was first noticed at the elevation in between strain gauge SG44 (792 mm from the bottom) and strain gauge SG42 (538 mm from the bottom). The peak of the buckle located 630 mm away from the bottom of the pipe. See Figures 3.88, 3.89 and 3.90. The second buckle subsequently occurred but with less magnitude at Demec gauges DC-14 and DC-15 with a maximum width of 300 mm along the half circle of the specimen, the center elevation of which located 410 mm away from the top of the pipe. See Figures 3.88 and 3.91. A family picture of the failed 20 inches pipes is shown in Figure 3.92.
-------------	--

Table 3.14 Comparison of accumulated strain and critical strain for 30inch pipes

Specimen Number	Max strain accumulation, $\mu\epsilon$	Critical strain, $\mu\epsilon$
D30P0BC-7	21,654	2754
D30P20BC-9	3937	3102
D30P80BC-8	3937	3329
D20P80BM-10	NA	3571
D20P40BM-11	NA	3766
D20P40BC-12	2898	2958

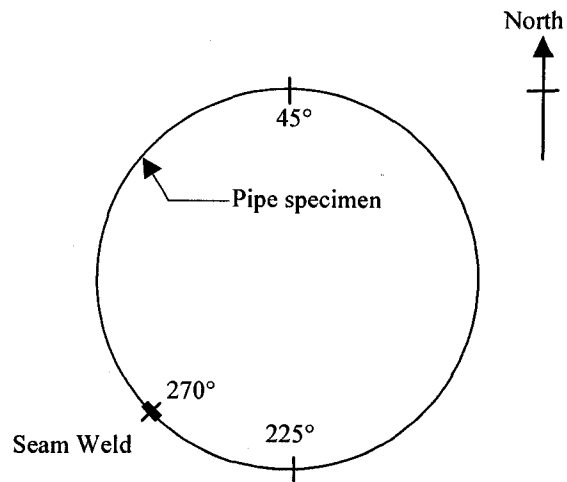


Figure 3.1 Plan view, angular coordinate system convention

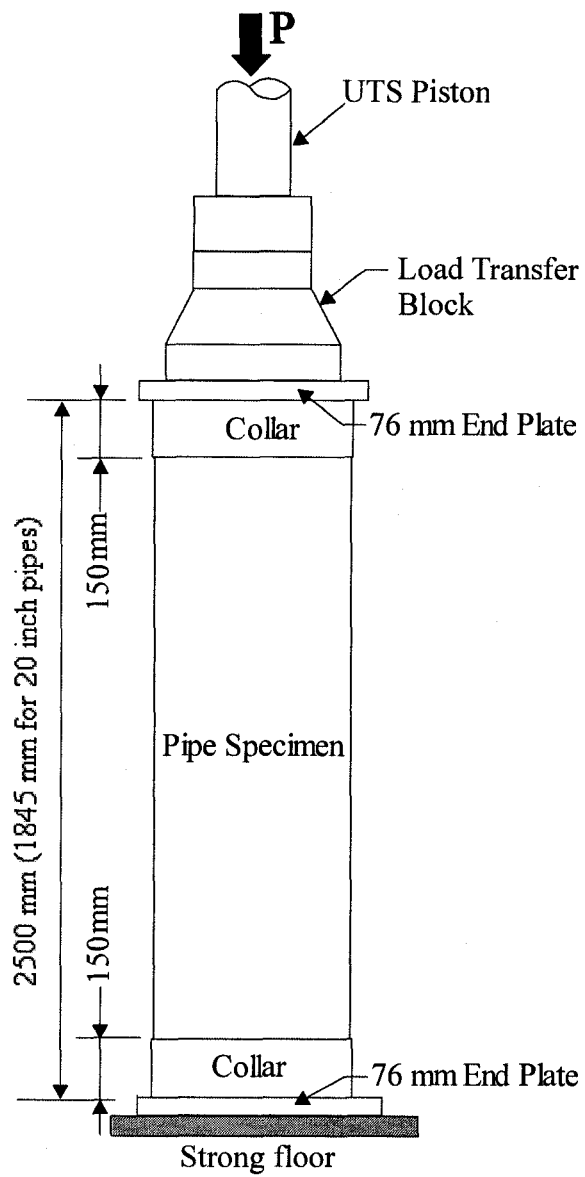


Figure 3.2 Test setup

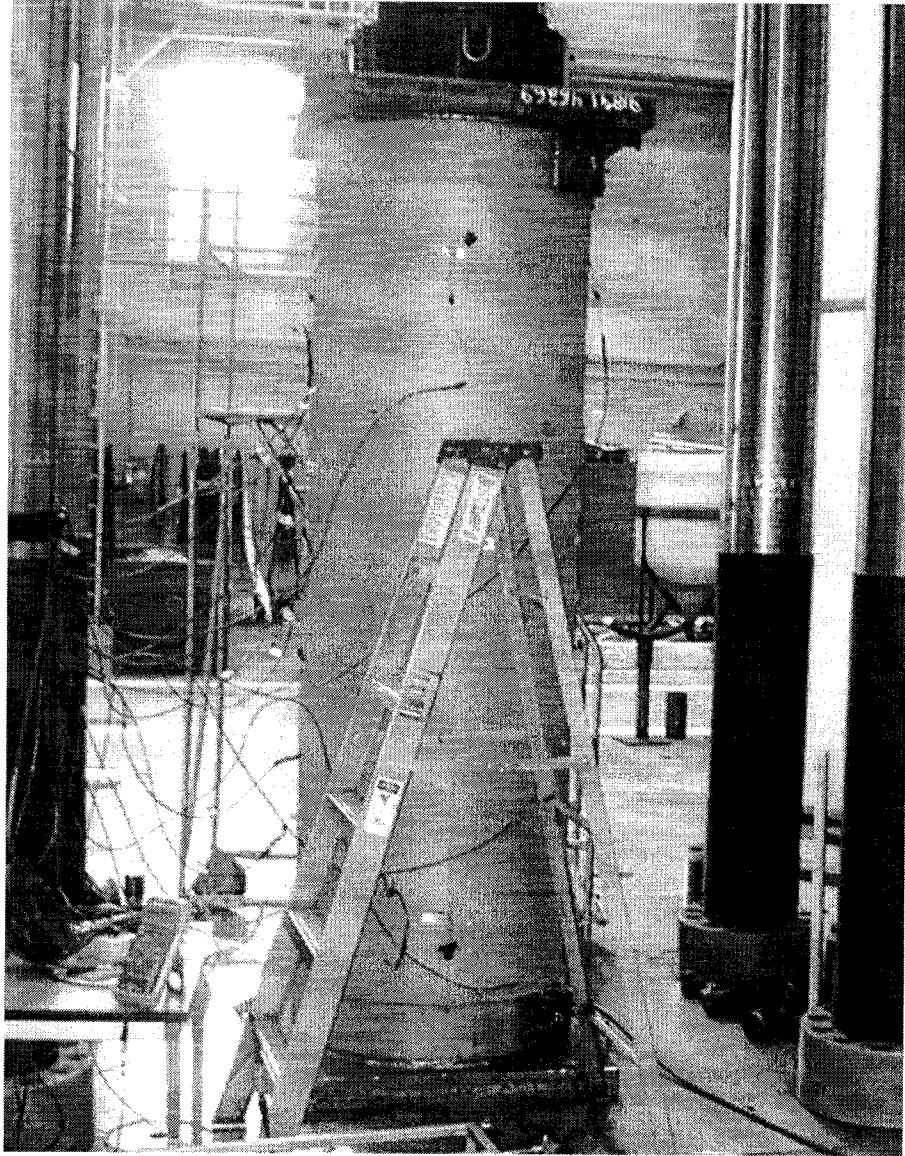


Figure 3.3 Test setup for 30 inch pipes

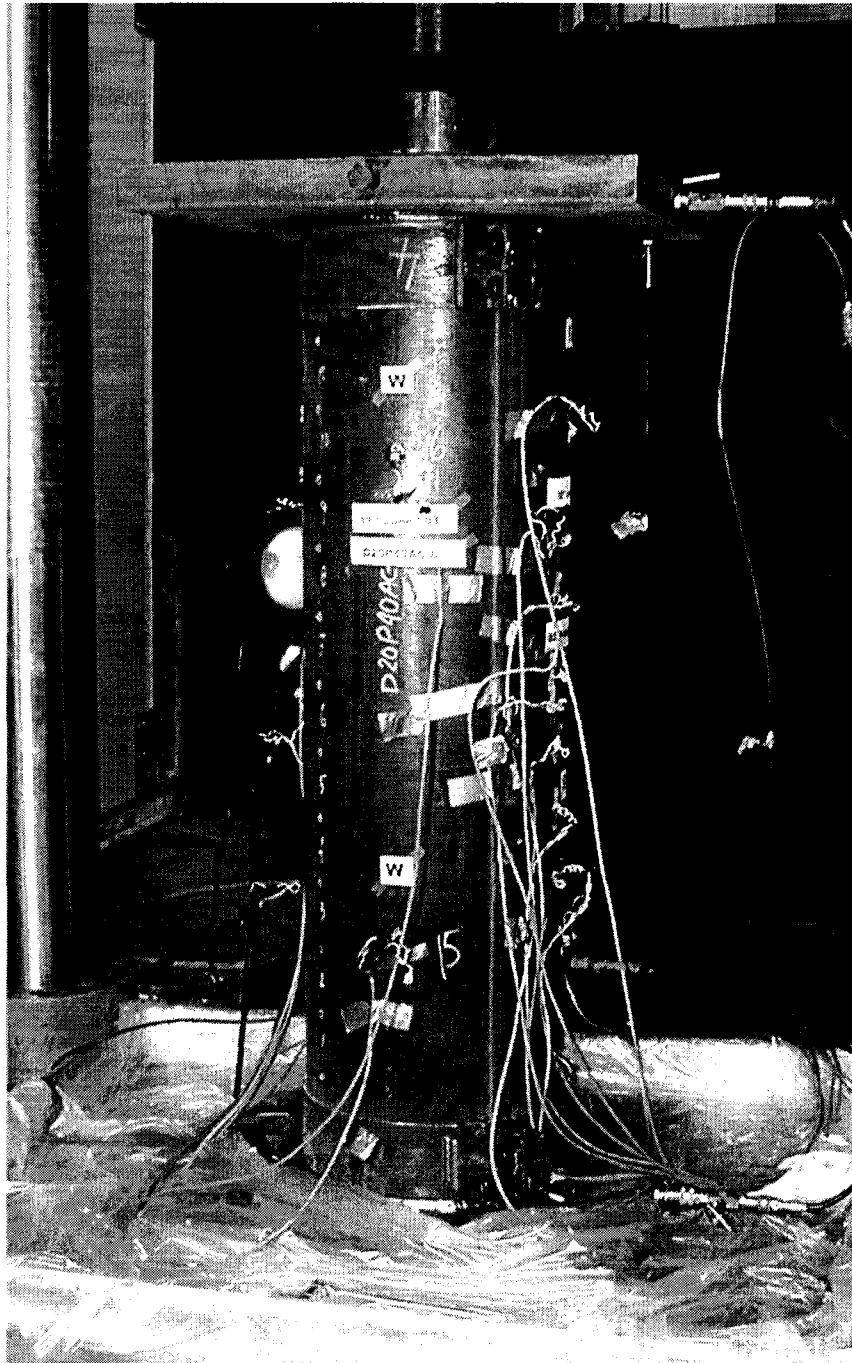


Figure 3.4 Test setup for 20 inch pipes

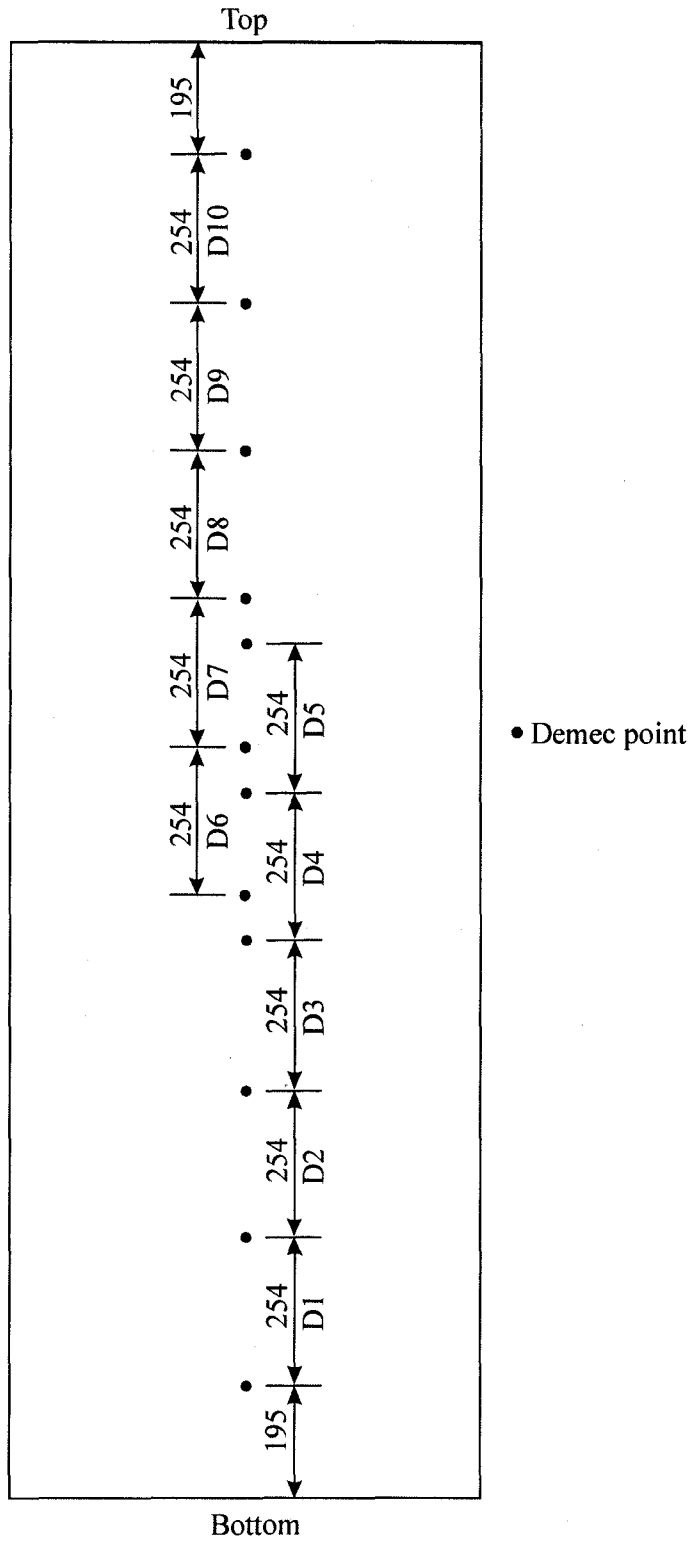


Figure 3.5 Locations of Demec points and their corresponding Demec gauge designation on the north face (45°) of 30 inch pipes

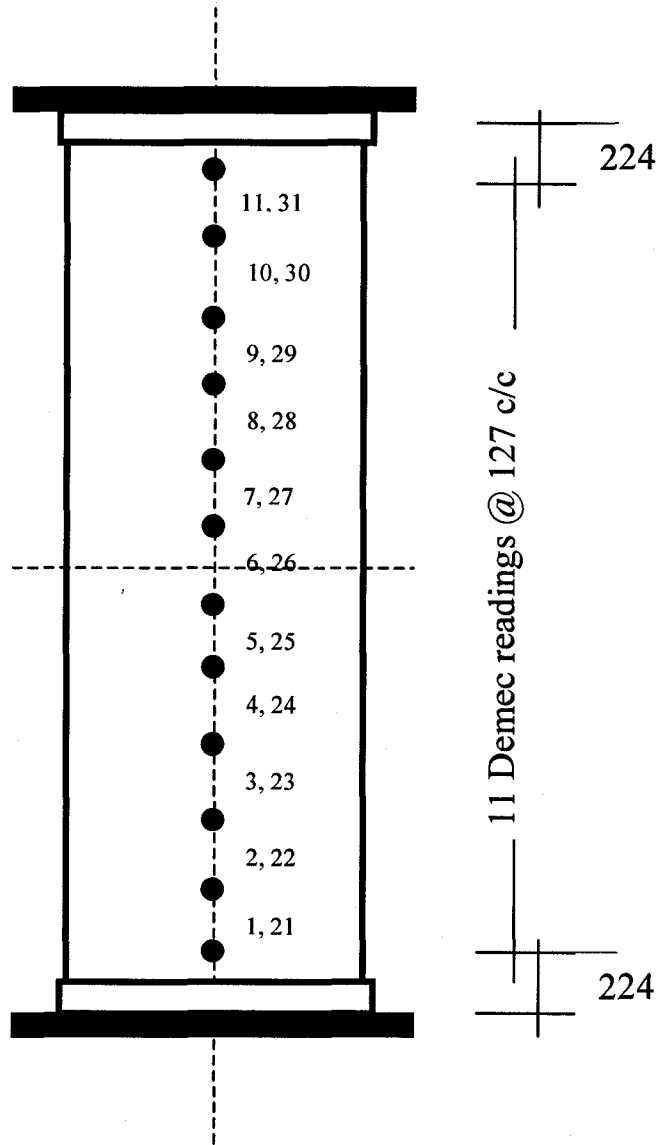


Figure 3.6 Locations of Demec points at 180° and 0° of 20 inch pipes

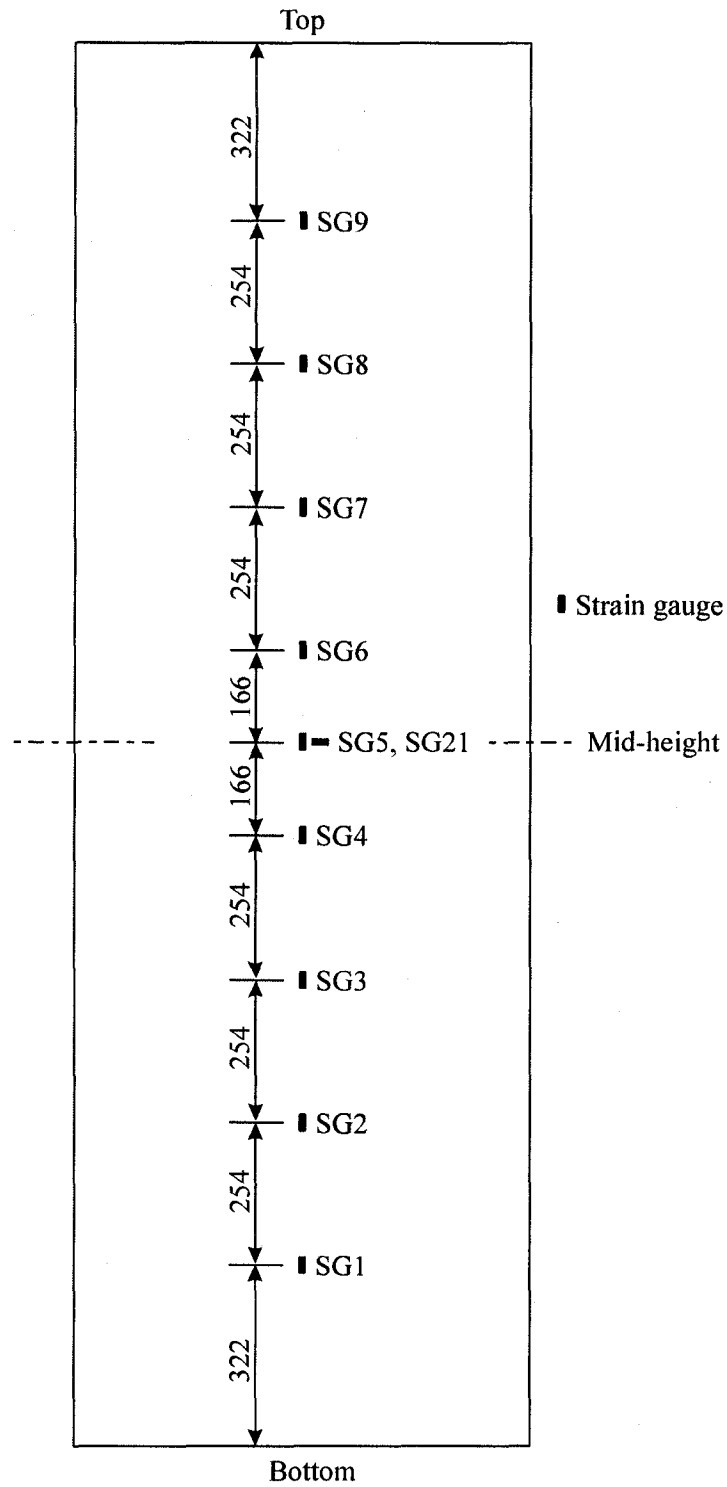


Figure 3.7 Locations and channel numbers for the strain gauges on the south face (225°) of 30 inch pipes

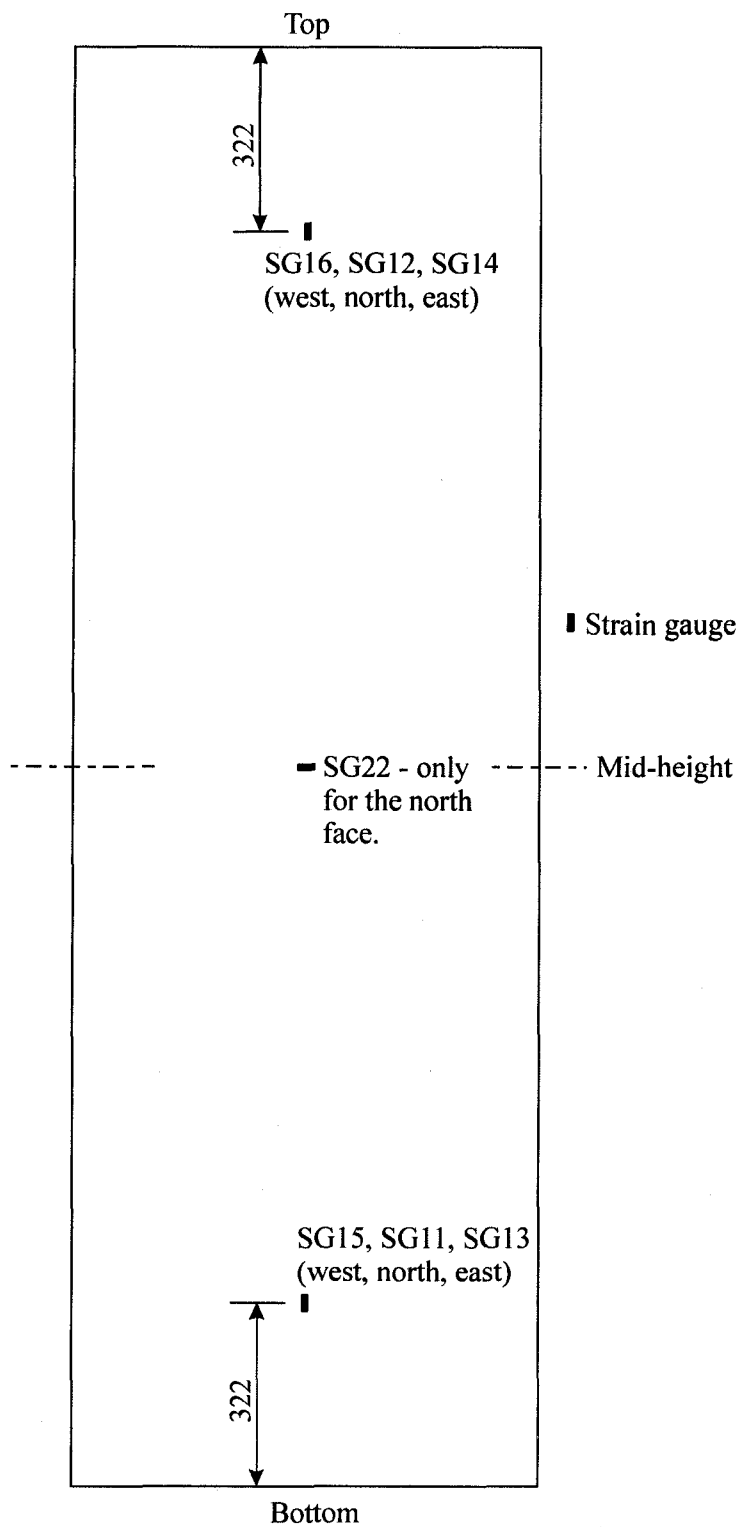


Figure 3.8 Locations and channel numbers for the strain gauges on the west, north and east faces (315° , 45° and 135°) of 30 inch pipes

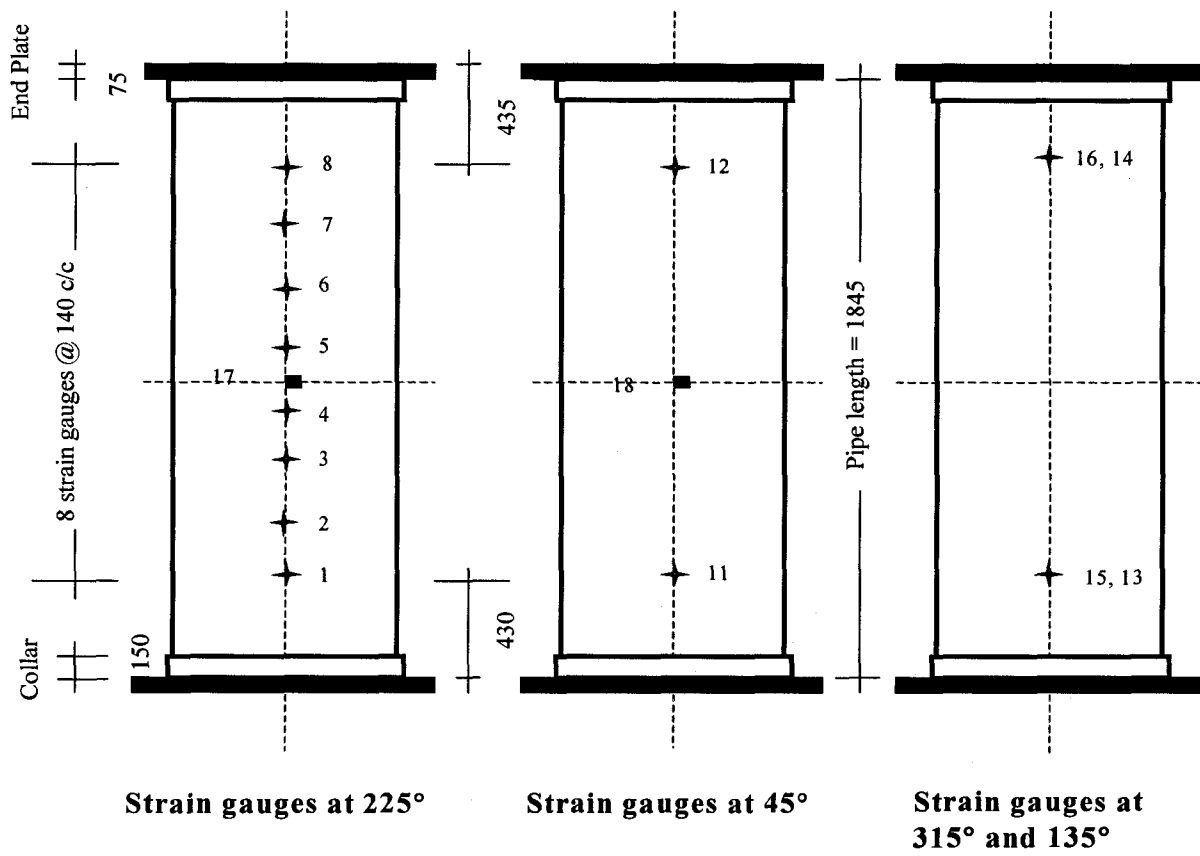


Figure 3.9 Locations and channel numbers for the strain gauges on the 30 inch pipes

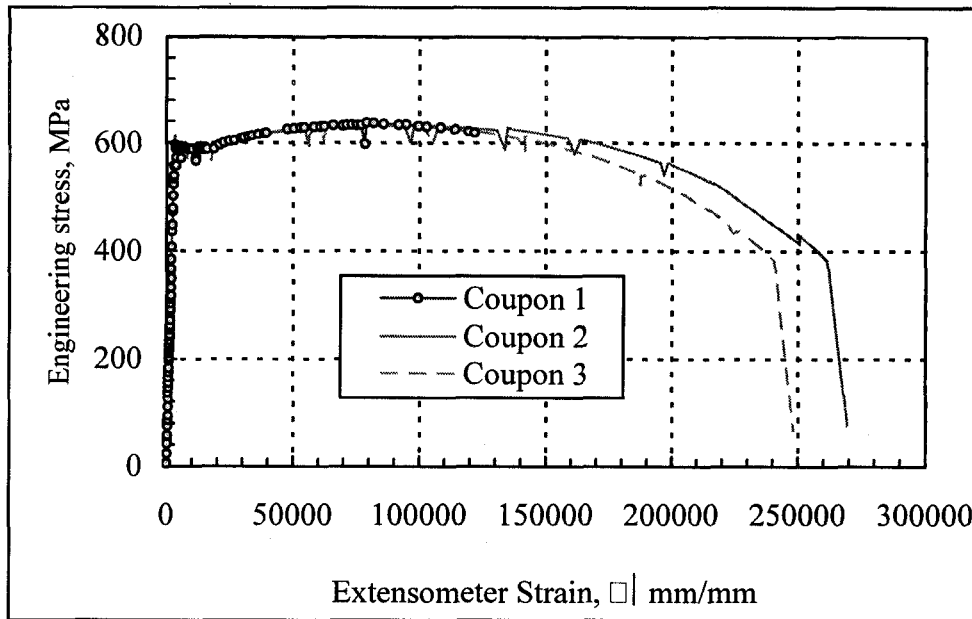


Figure 3.10 Engineering stress strain curves of tension coupons for 30 inch pipes

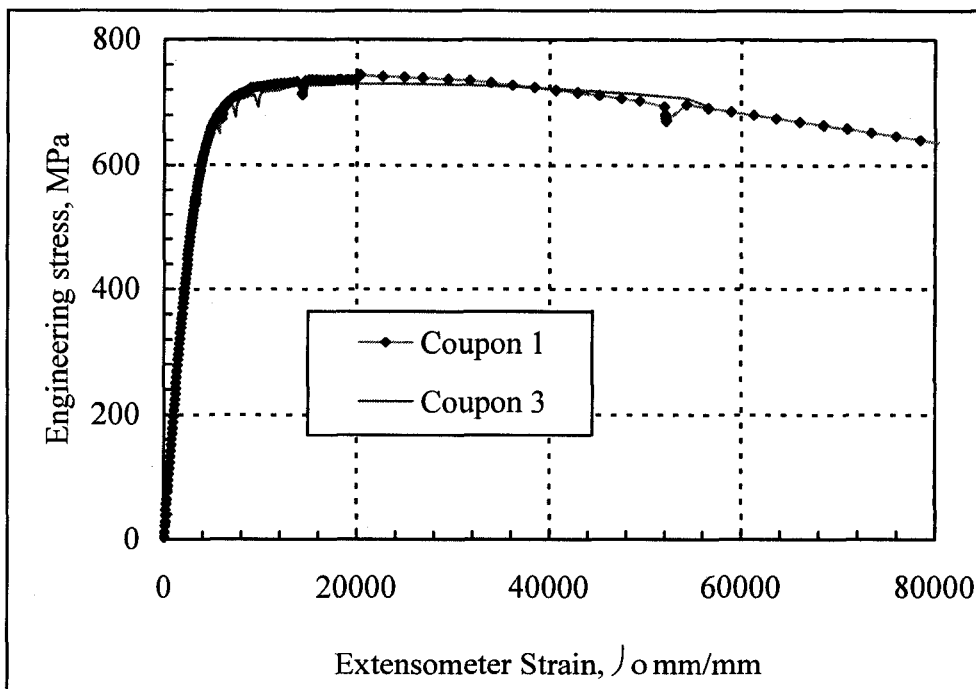


Figure 3.11 Engineering stress strain curves of tension coupons for 20 inch pipes

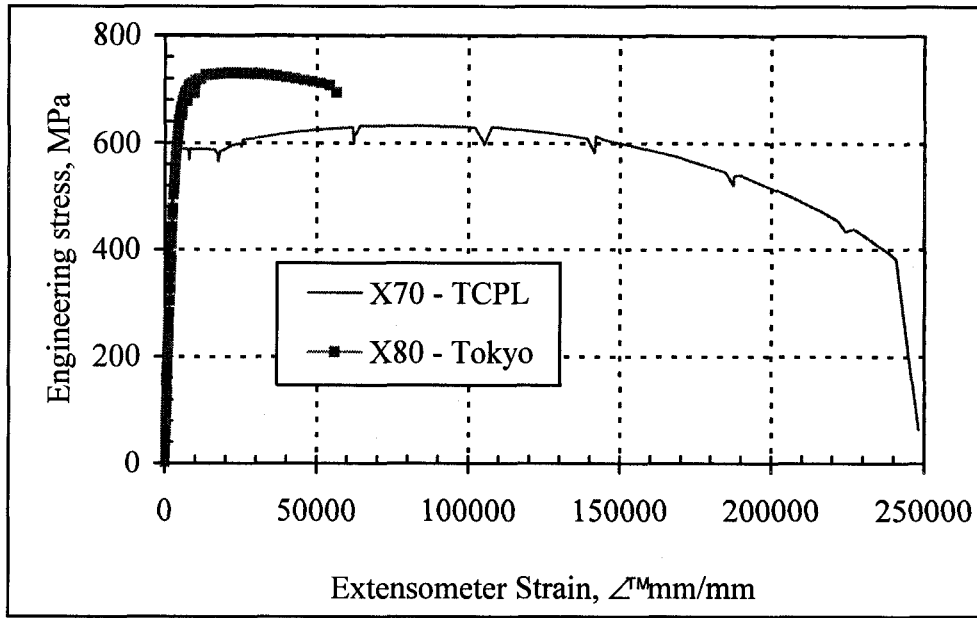


Figure 3.12 Comparison of the Engineering stress strain curves of 20 inch and 30 inch pipes

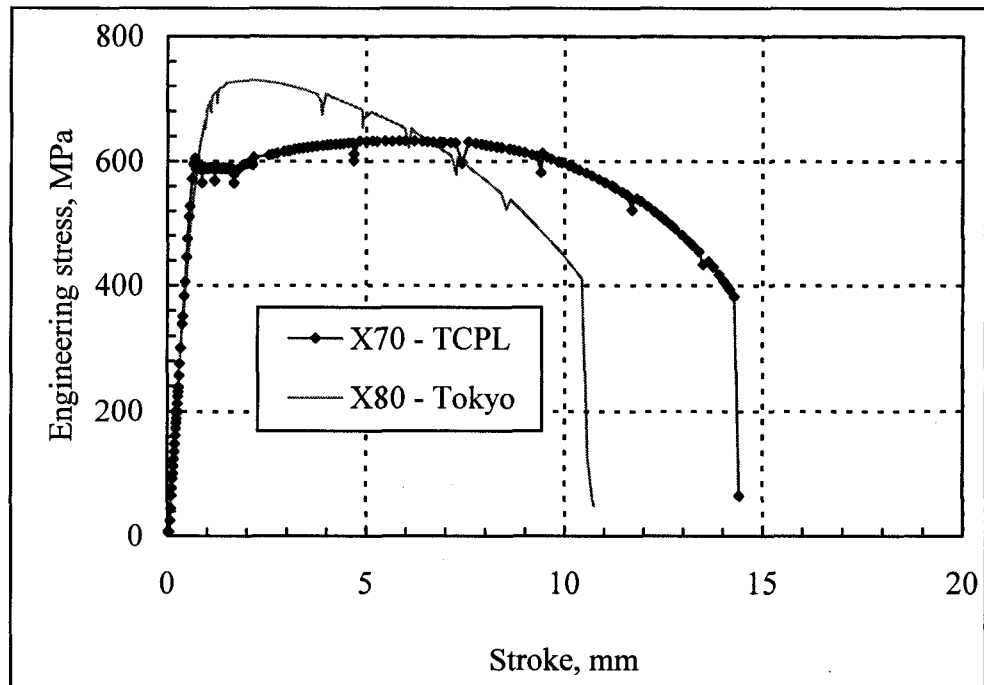


Figure 3.13 Comparison of the Engineering stress vs. jack stroke curves of 20 inch and 30 inch pipes

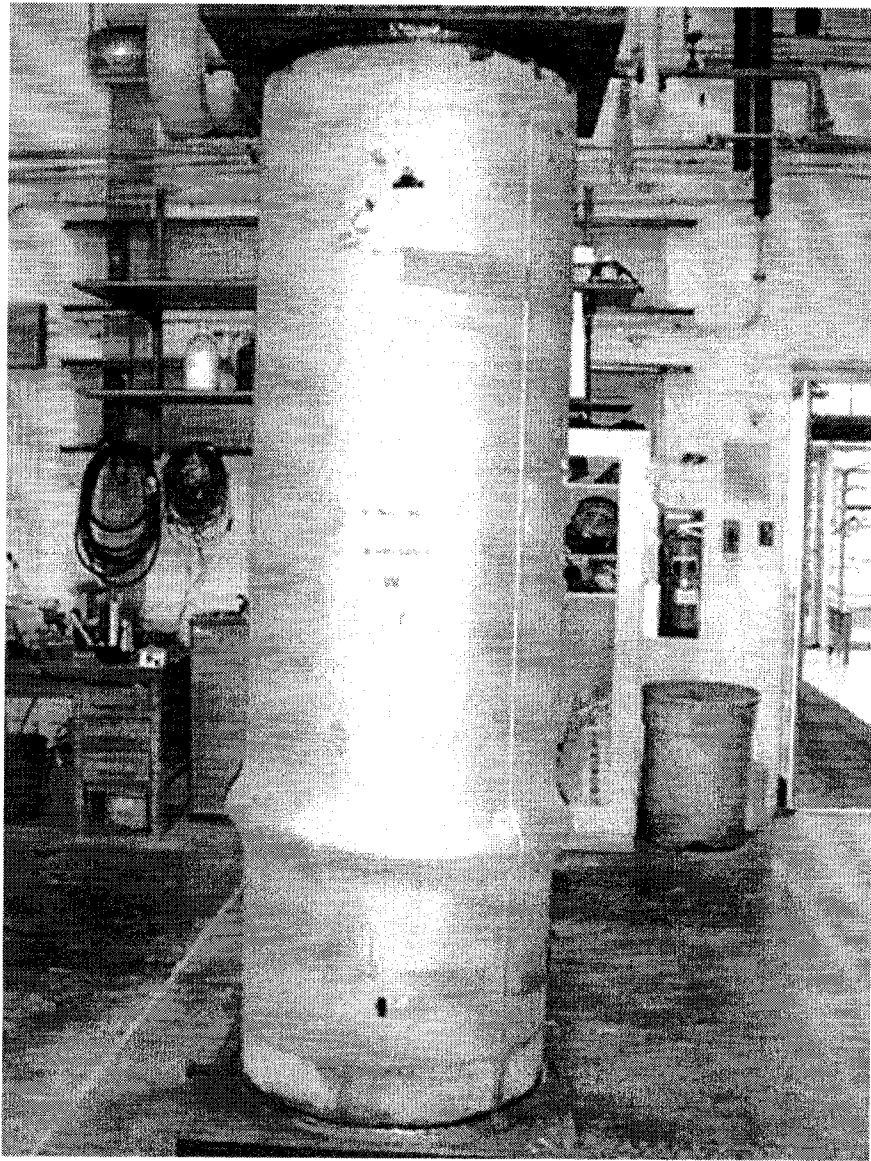


Figure 3.14 Buckled shape of D30P80AM-1, west elevation

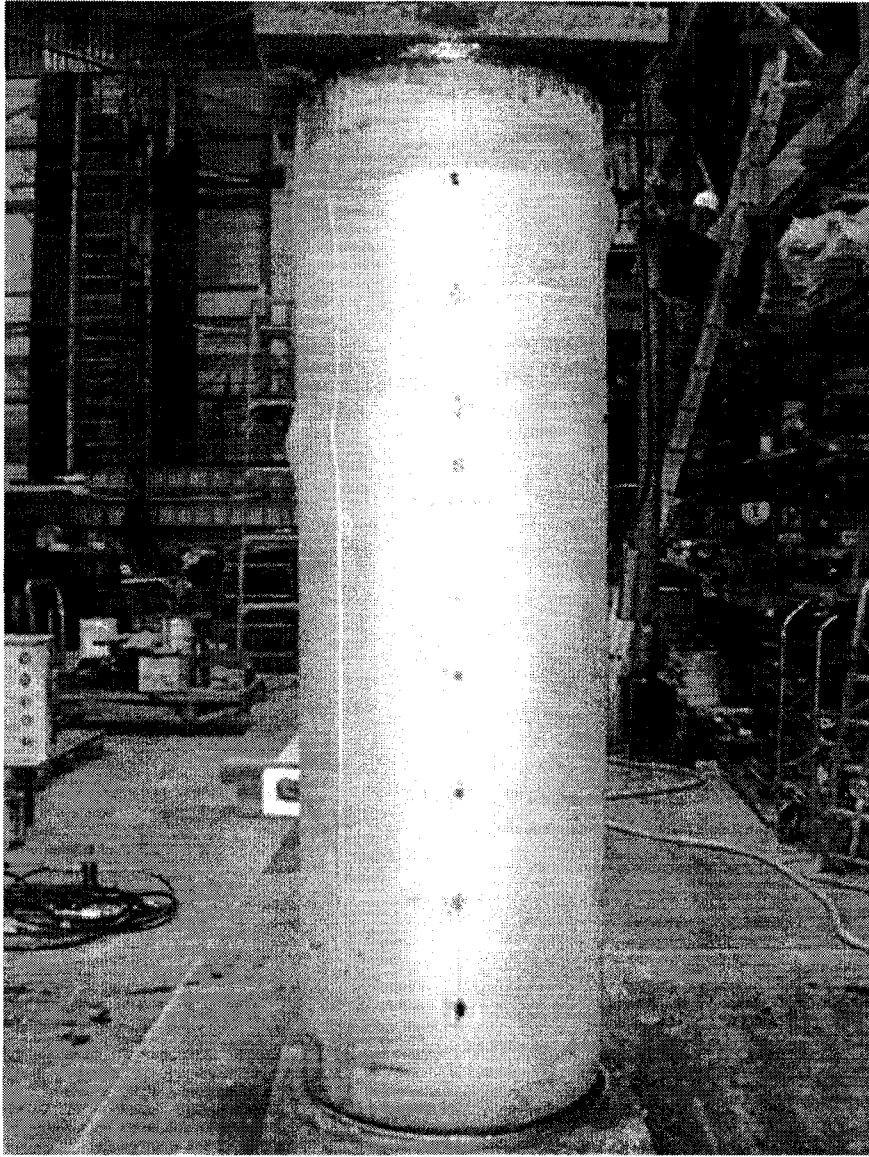


Figure 3.15 Buckled shape of D30P80AC-2, south elevation

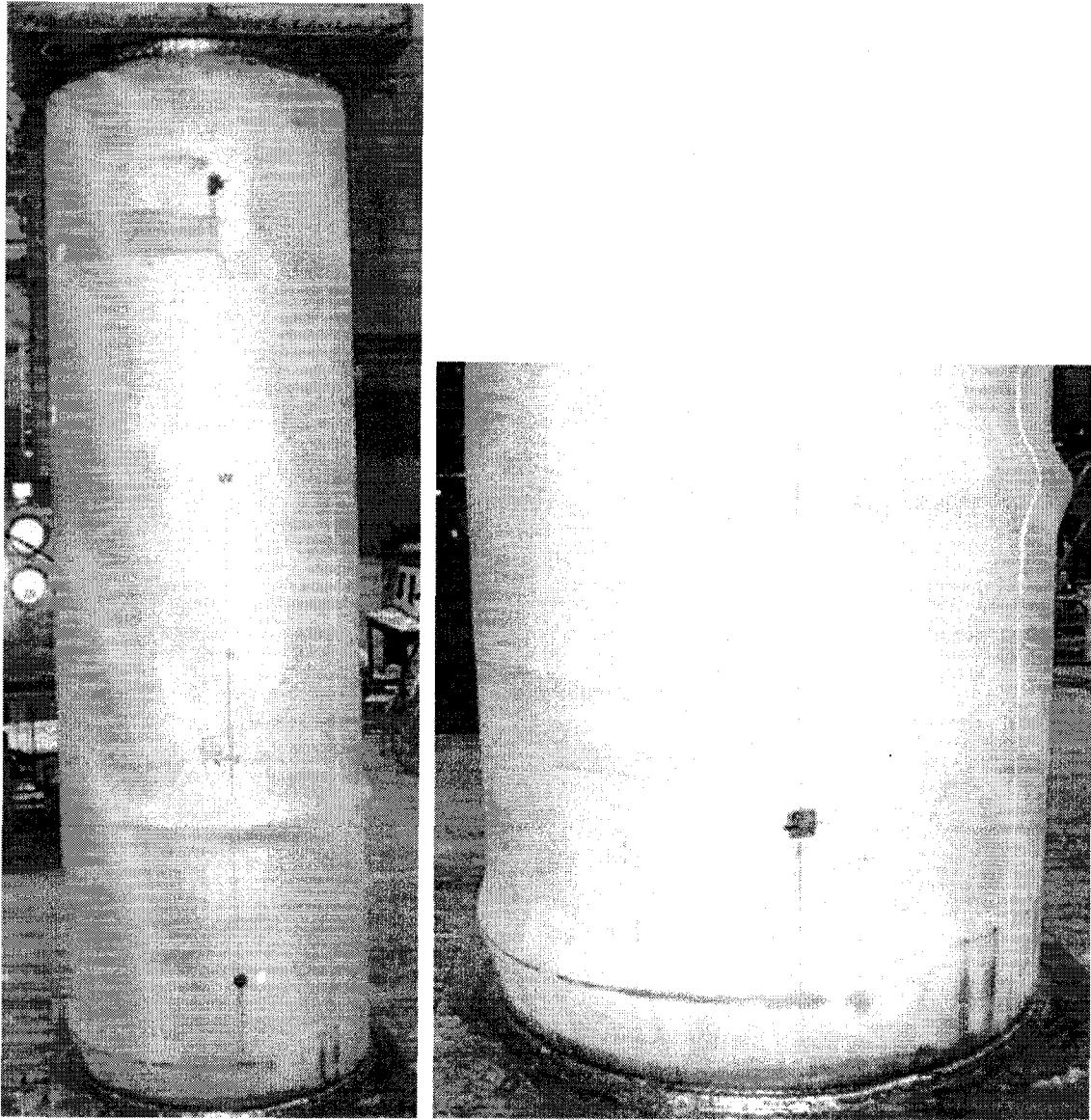


Figure 3.16 Buckled shape of D30P20AC-3, west elevation

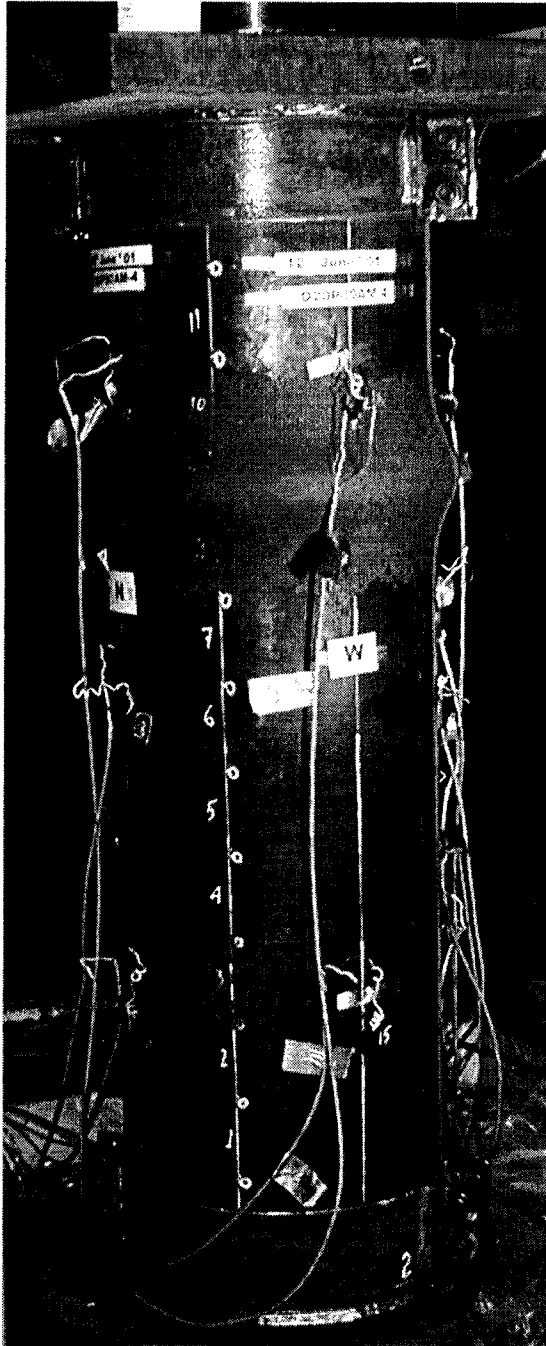


Figure 3.17 Buckled shape of D20P80AM-4, west elevation

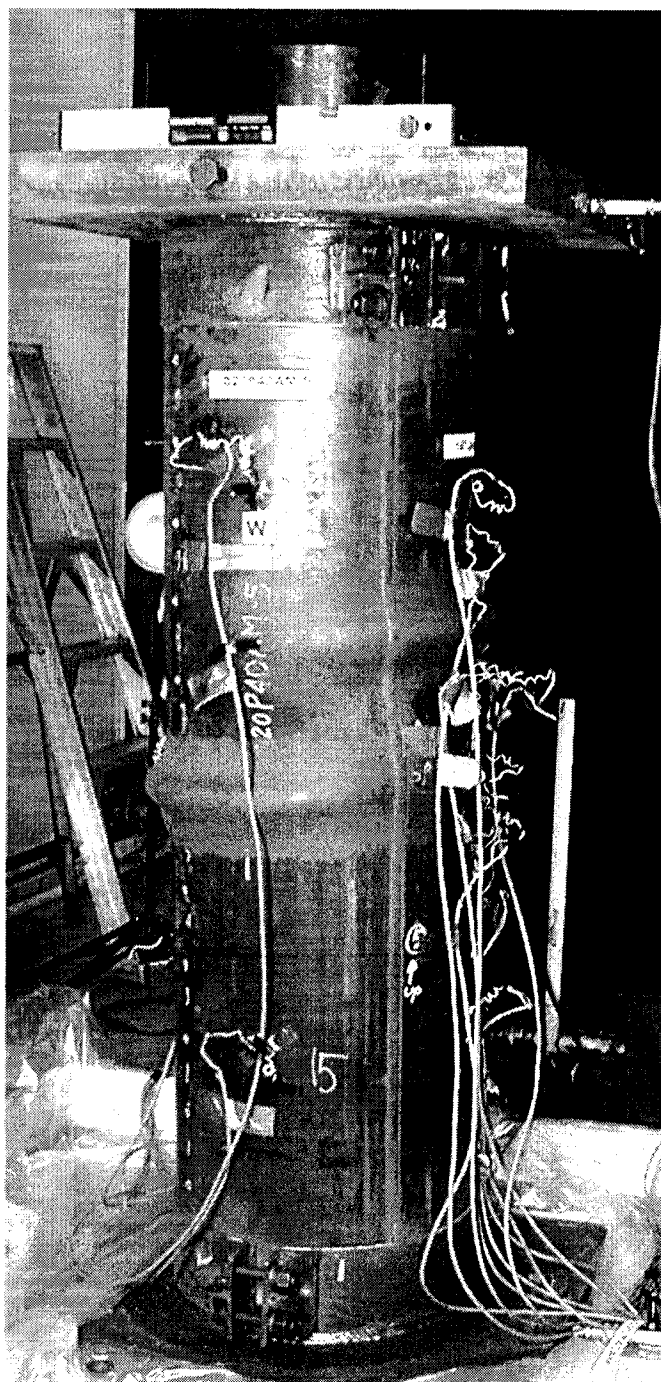


Figure 3.18 Buckled shape of D20P40AM-5, west elevation

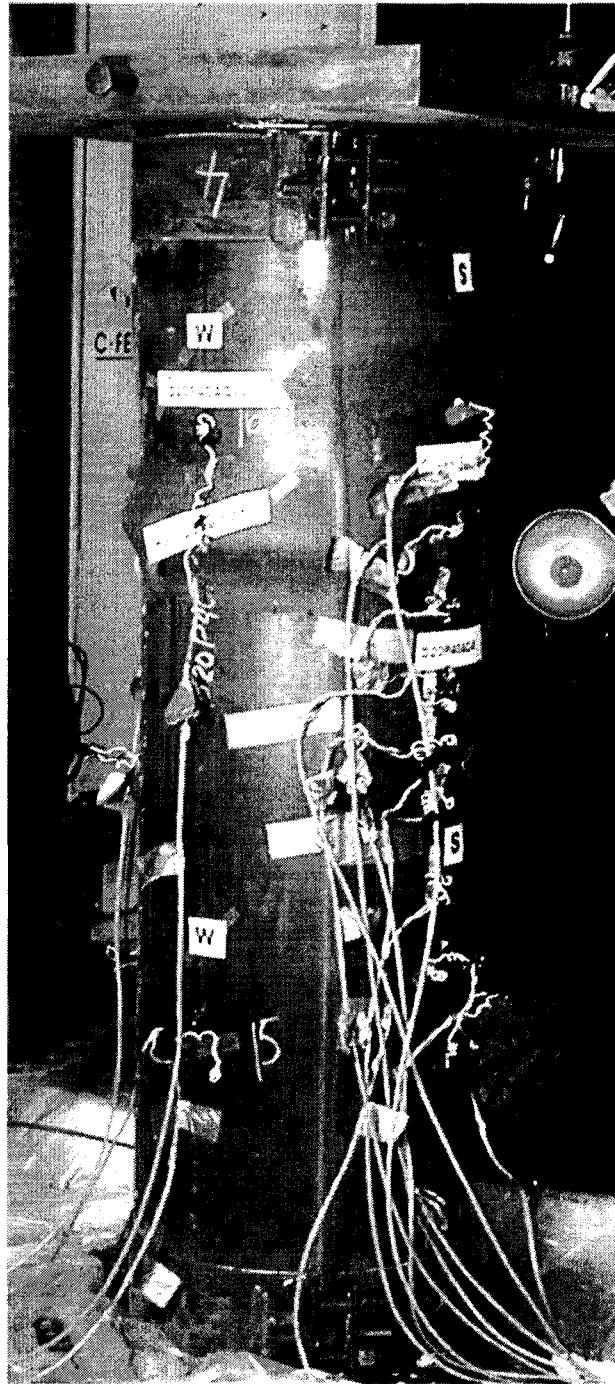


Figure 3.19 Buckled shape of D20P40AC-6, west elevation

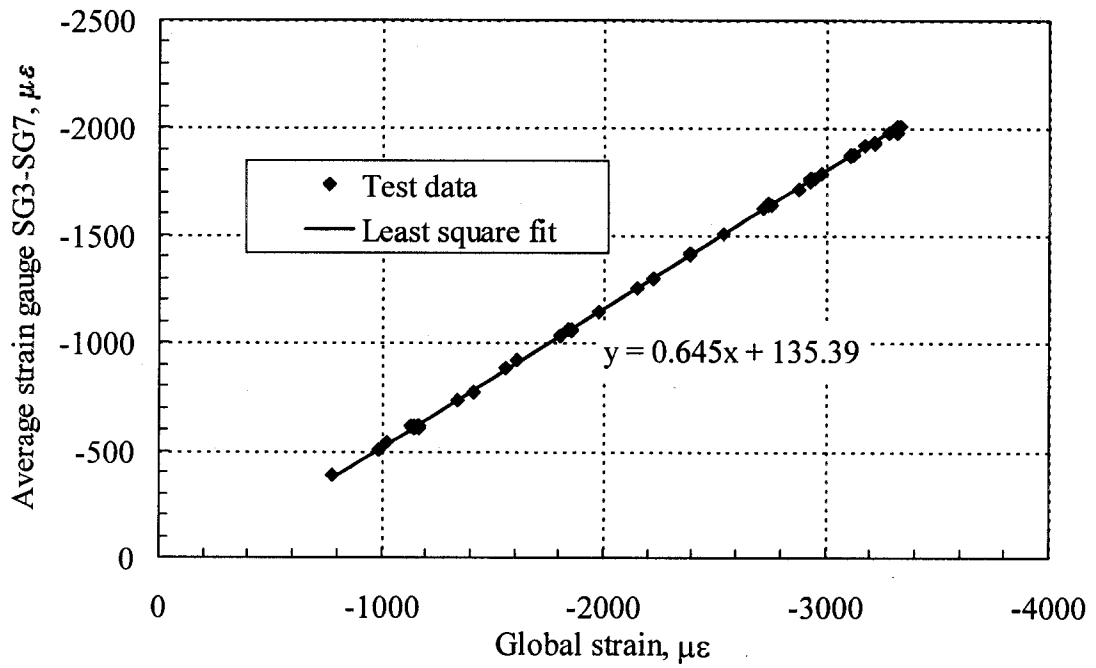


Figure 3.20 Global strain vs. average strain gauge reading for D30P80AM-1

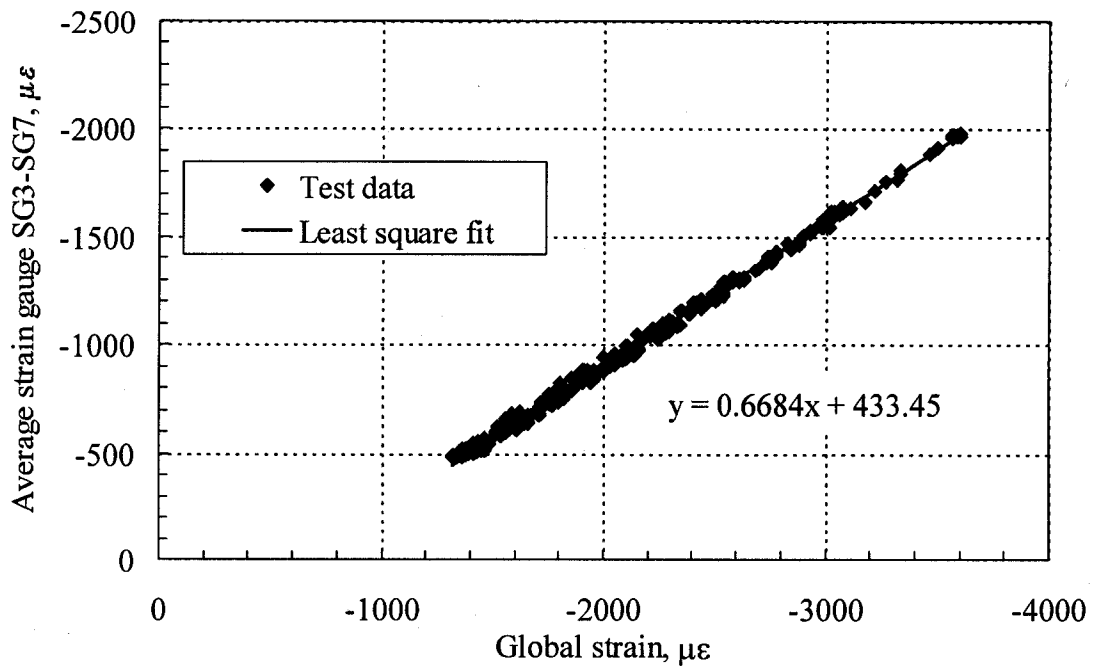


Figure 3.21 Global strain vs. average strain gauge reading for D30P80AC-2

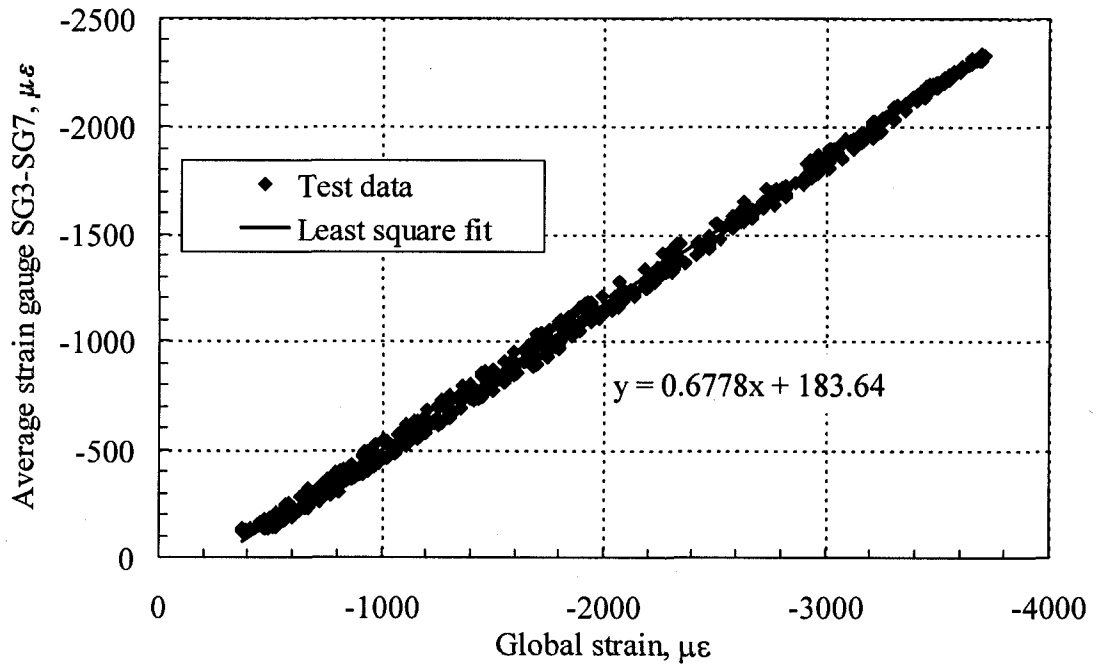


Figure 3.22 Global strain vs. average strain gauge reading for D30P20AC-3

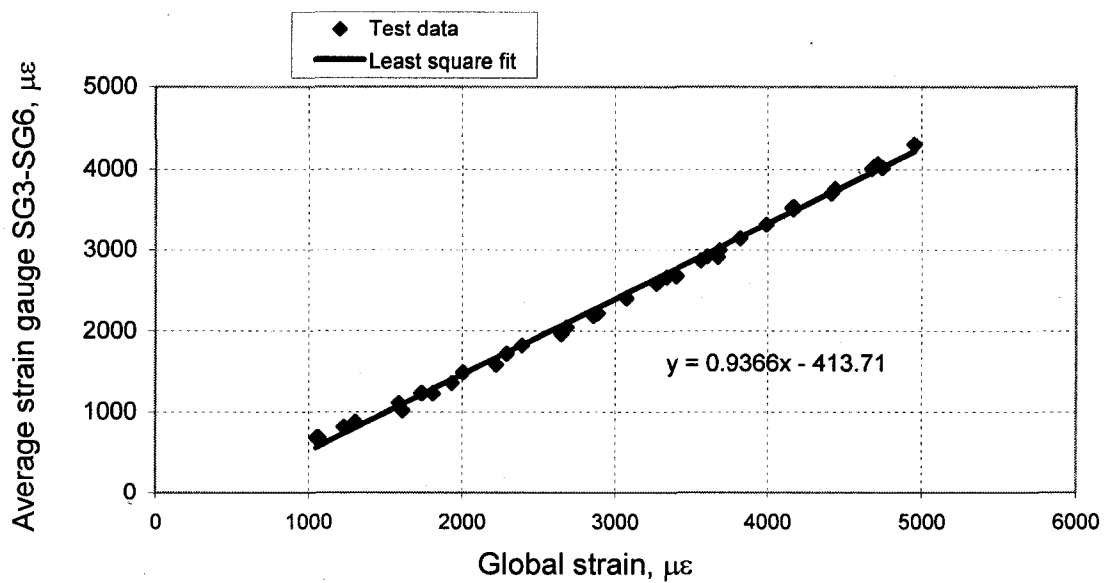


Figure 3.23 Global strain vs. average strain gauge reading for D20P80AM-4

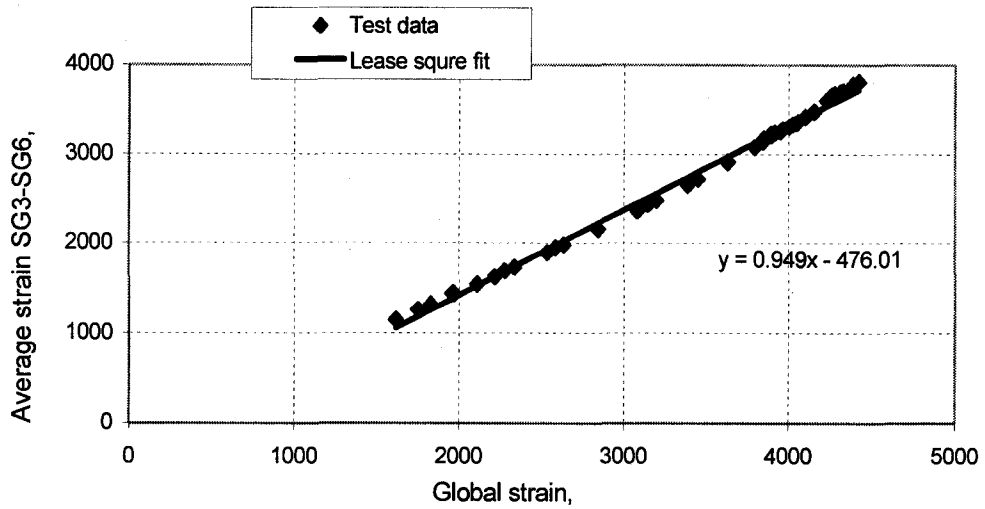


Figure 3.24 Global Strain vs. average strain gauge reading for D20P40AM-5

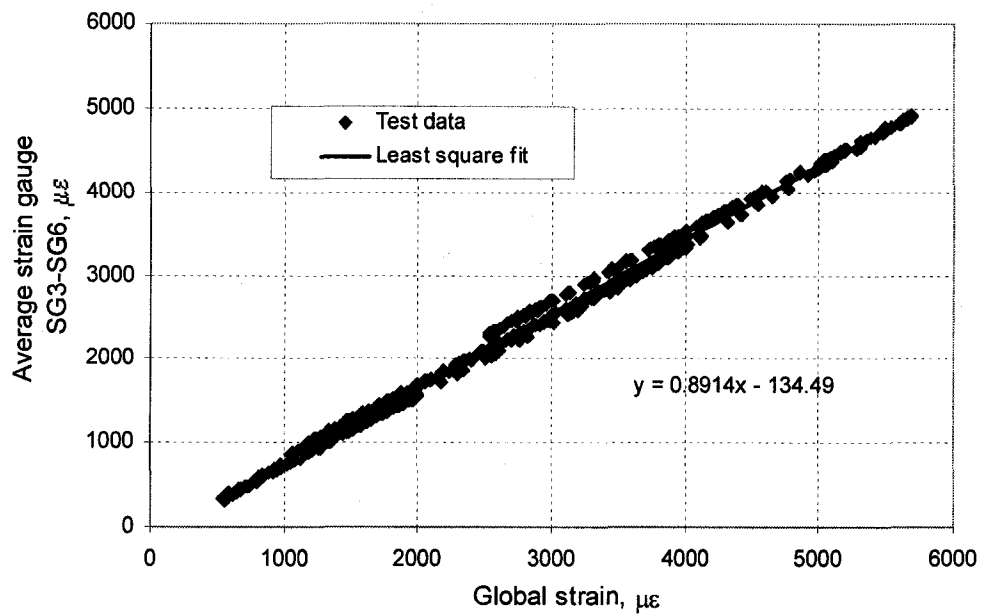


Figure 3.25 Global Strain vs. average strain gauge reading for D20P40AC-6

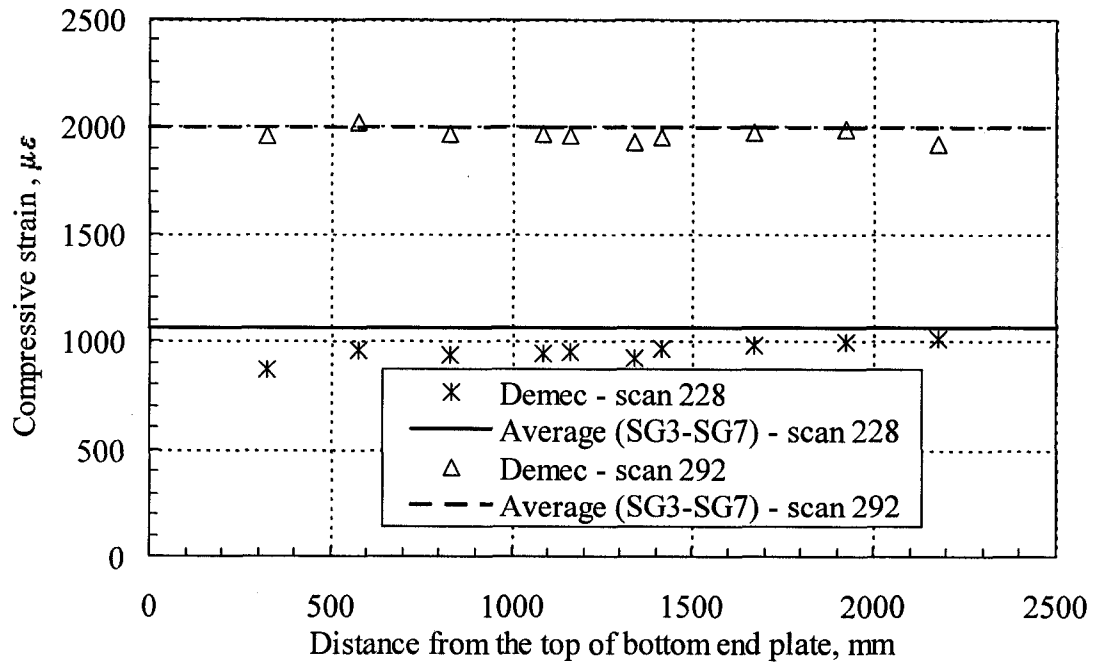


Figure 3.26 Selective Demec and average strain gauge readings for D30P80AM-1

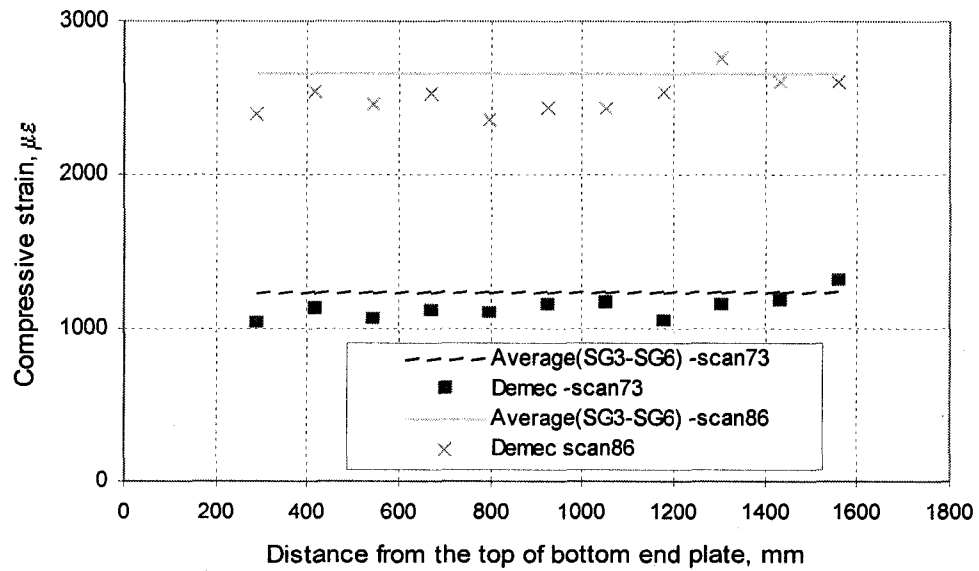


Figure 3.27 Selective Demec and average strain gauge reading for D20P80AM-4

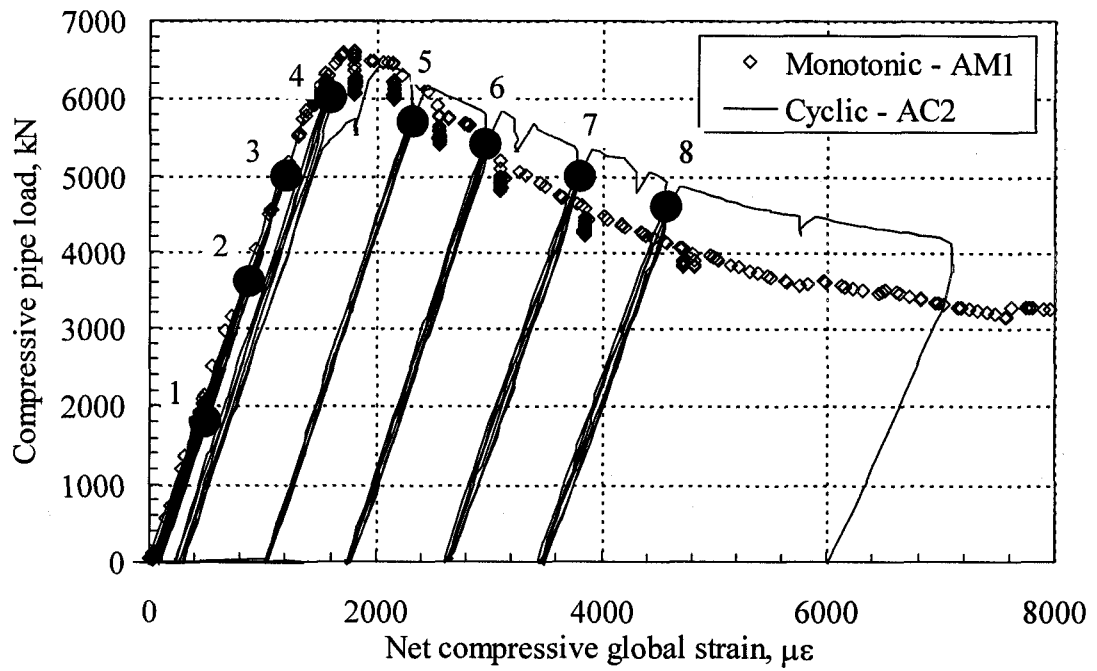


Figure 3.28 Load vs. net compressive global strain for the D30P80 specimens

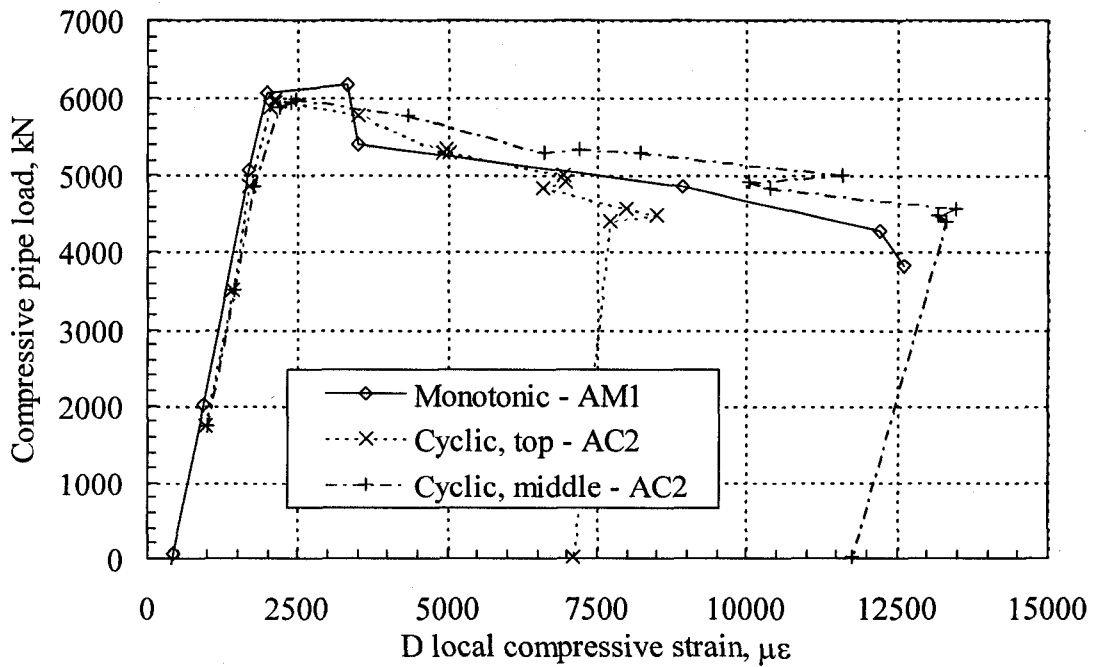


Figure 3.29 Load vs. local D compressive strain for the D30P80 specimens

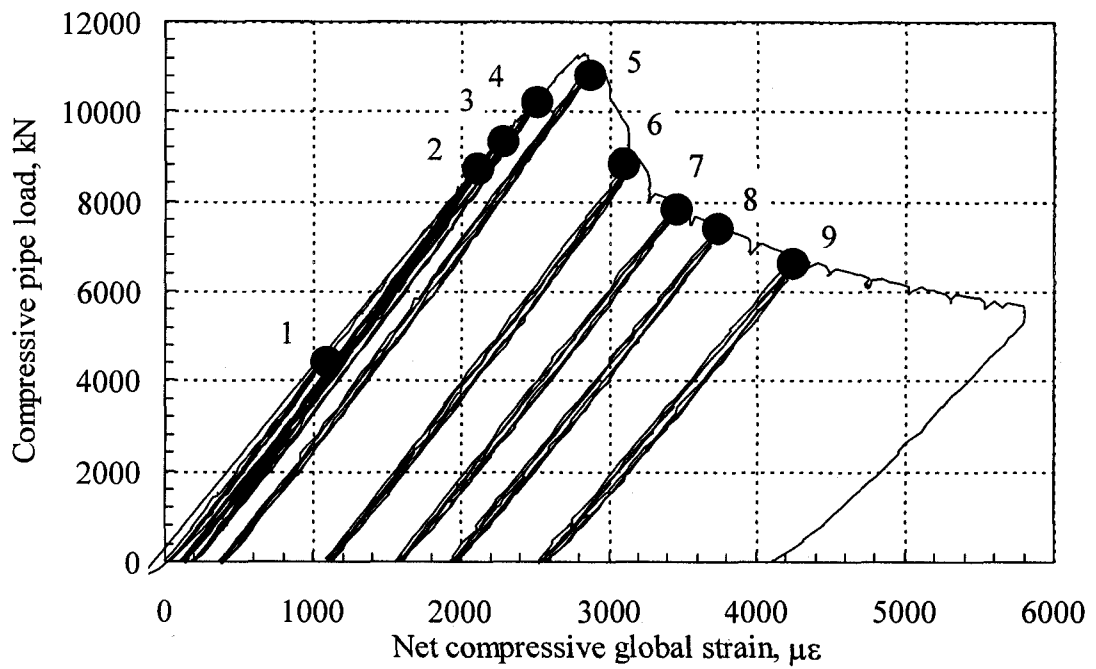


Figure 3.30 Load vs. net compressive global strain for D30P20AC-3 specimen.

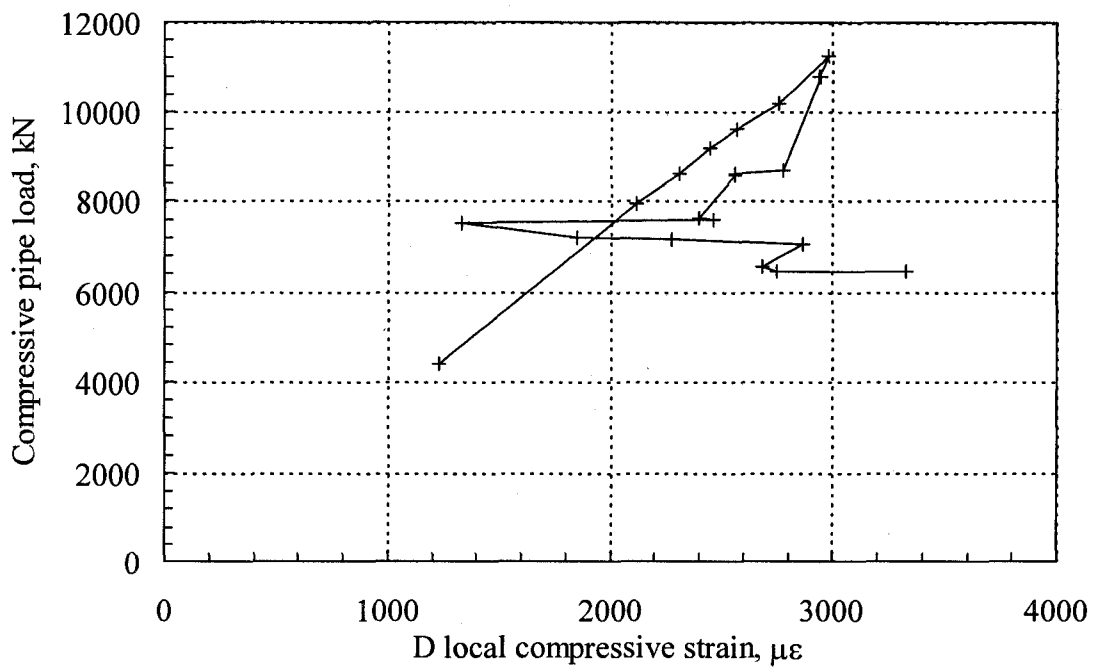


Figure 3.31 Load vs. local D compressive strain for D30P20AC-3 specimen

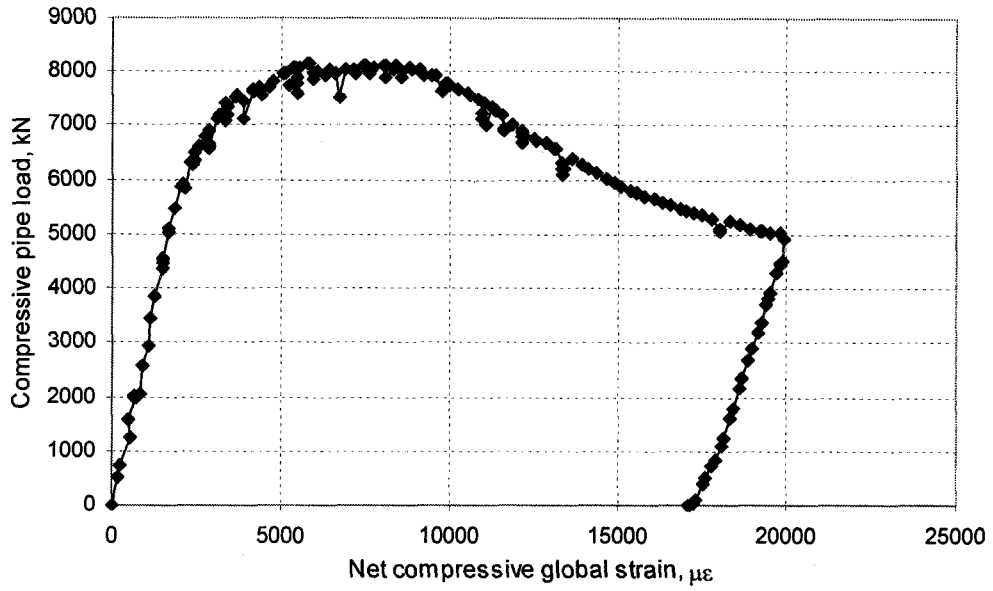


Figure 3.32 Load vs. net compressive global strain for D20P80AM-4 specimen

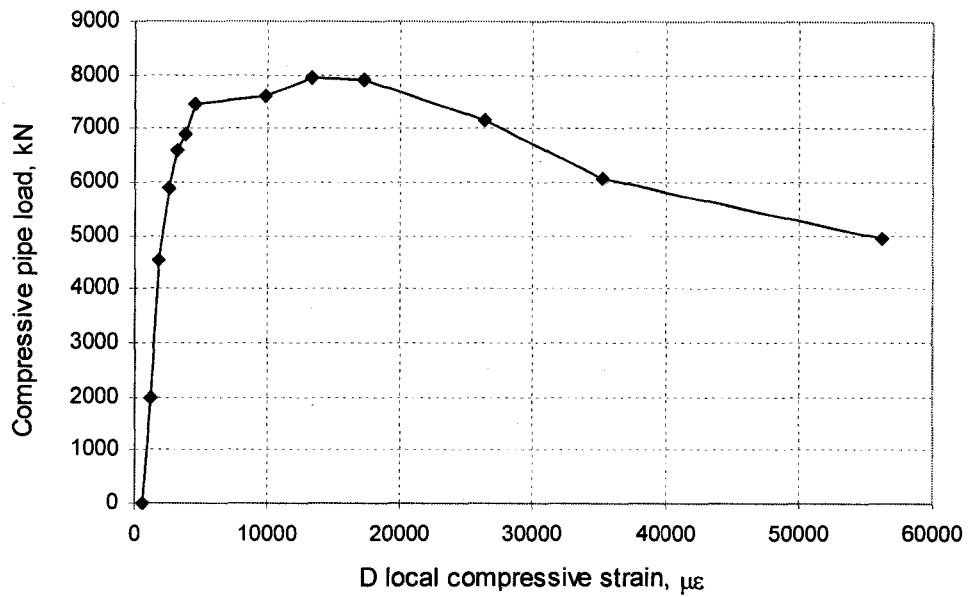


Figure 3.33 Load vs. D local compressive strain for D20P80AM-4

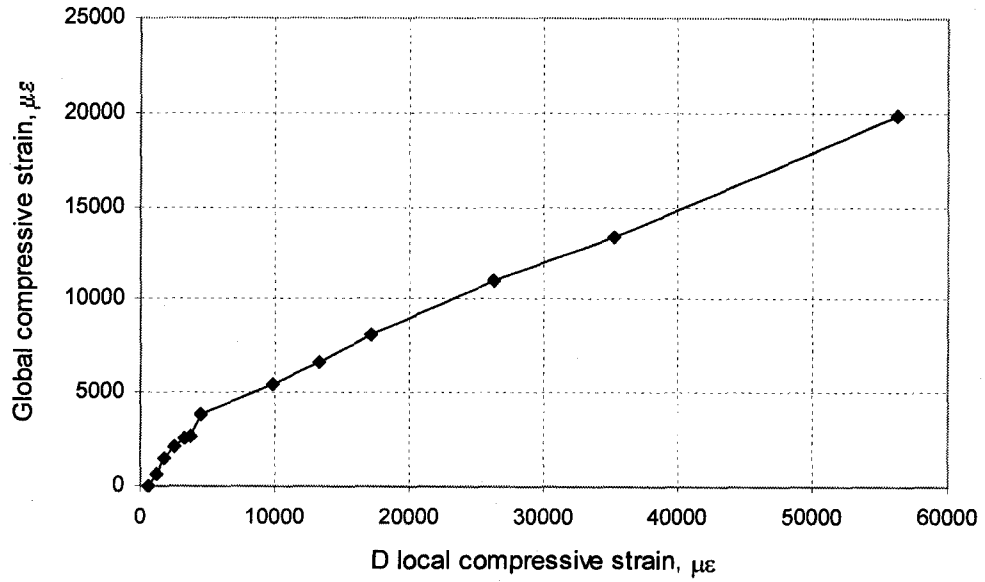


Figure 3.34 Global vs. D local compressive strain for D20P80AM-4 specimen

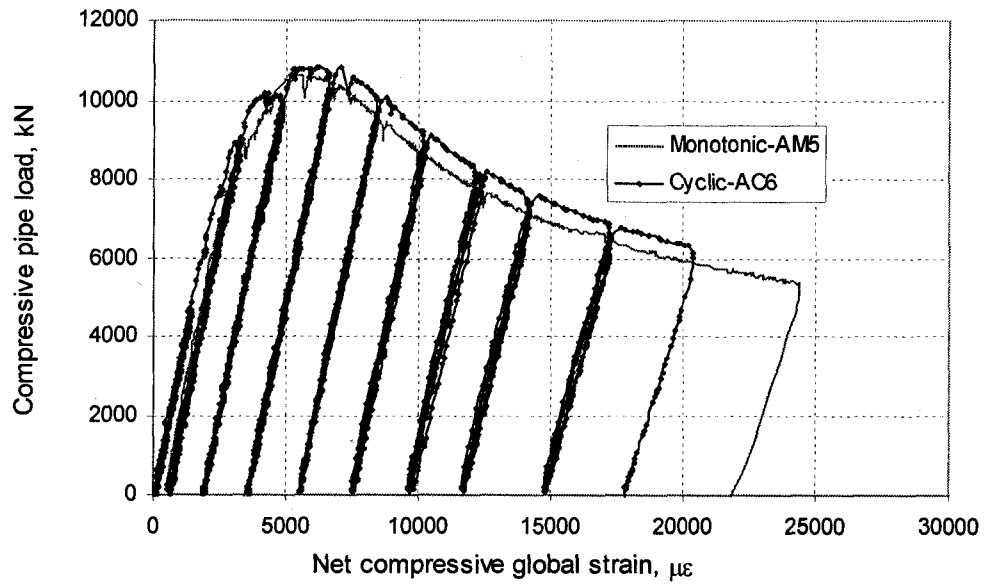


Figure 3.35 Load vs. net compressive global strain for D20P40 specimens

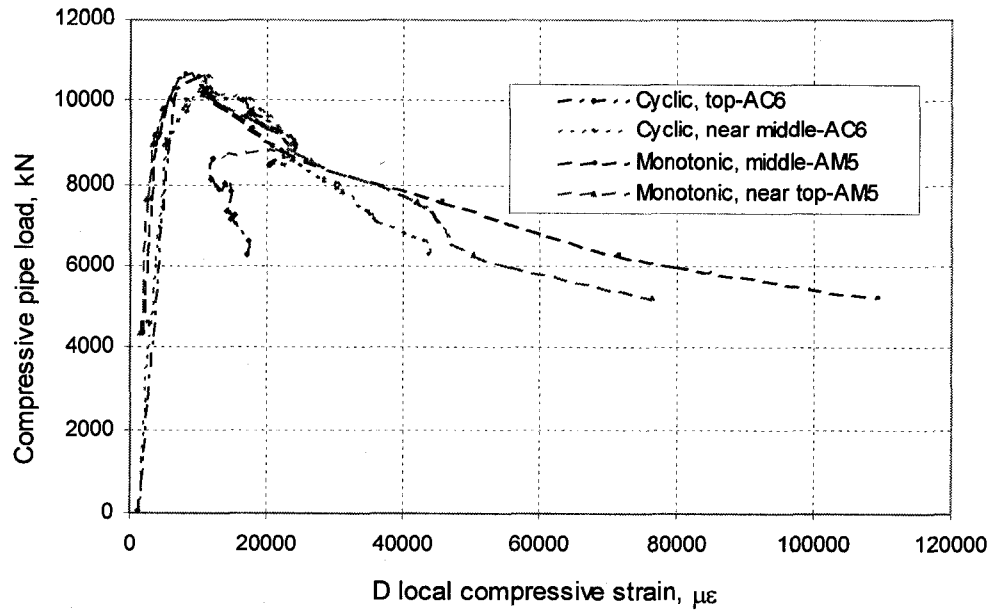


Figure 3.36 Load vs. D local compressive strain for the D20P40 specimens

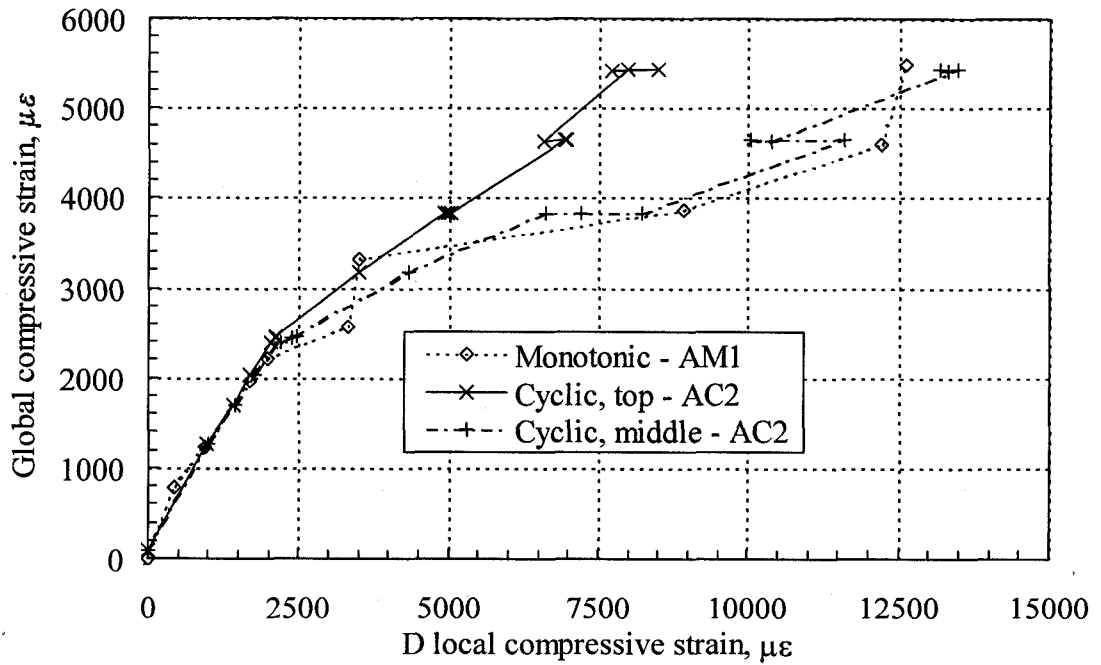


Figure 3.37 Global vs. local D compressive strain for the D30P80 specimens

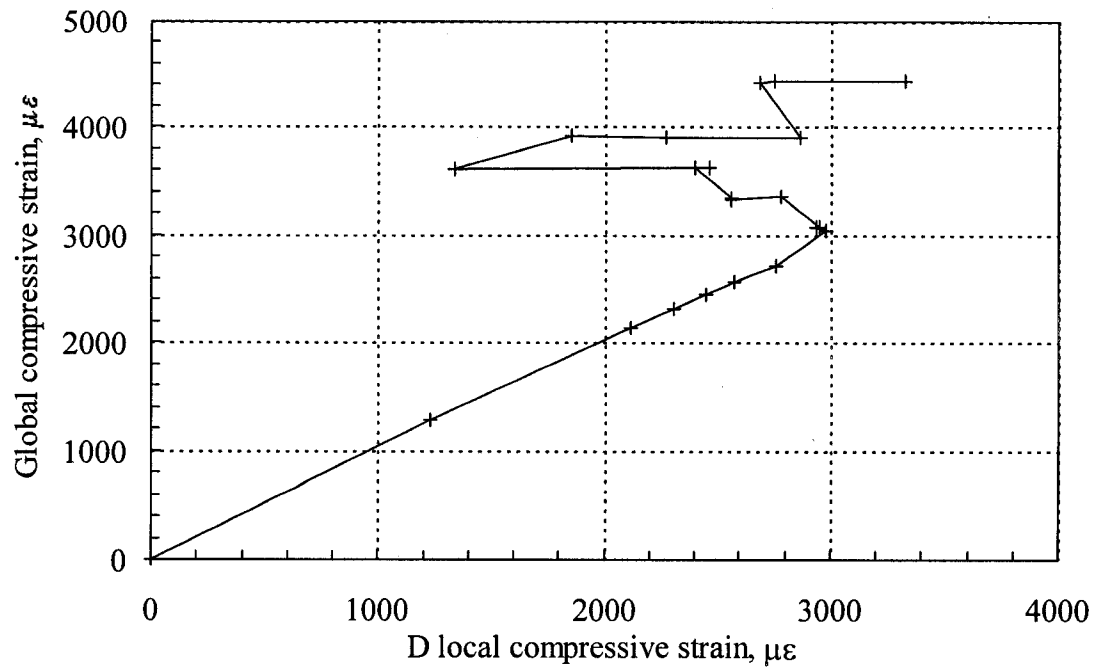


Figure 3.38 Global vs. local D compressive strain for D30P20AC-3 specimen

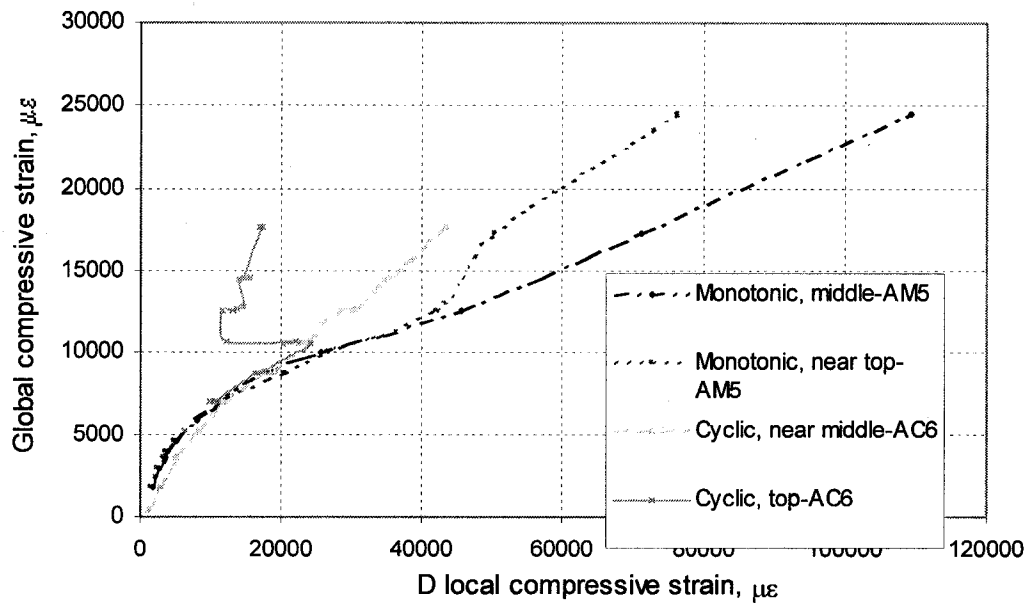
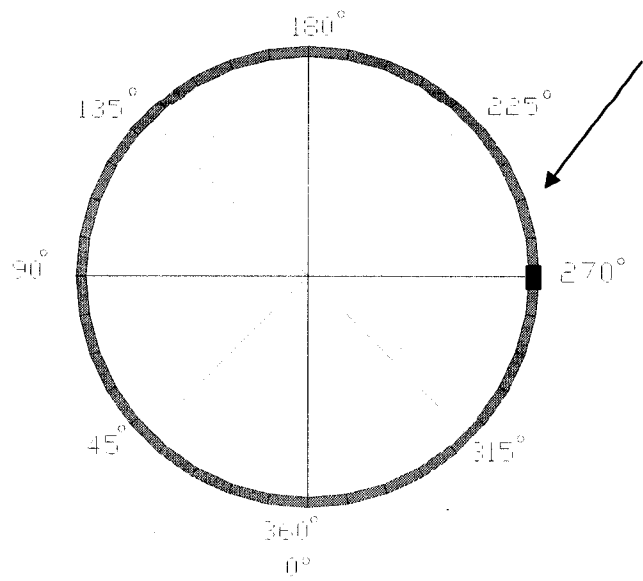
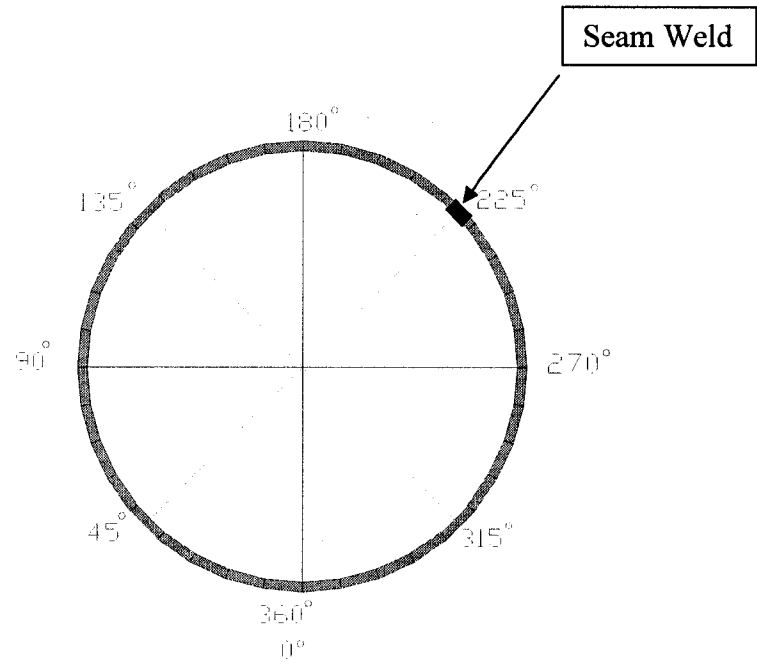


Figure 3.39 Global vs. D local compressive strain for D20P40 specimens



Top View Of 20 inch Pipe



Top View Of 30 inch Pipe

Figure 3.40 Plane View of Angular Coordinate System Convention

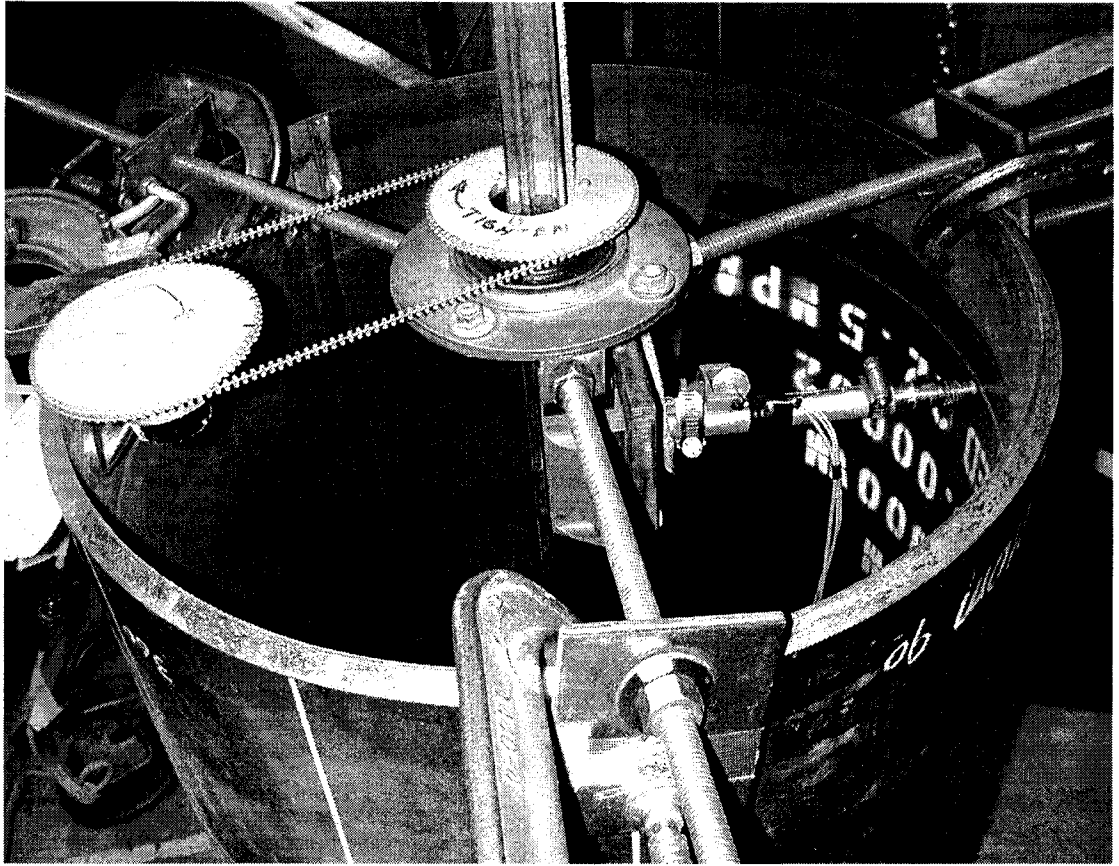


Figure 3.41 Initial Imperfection Measurement Apparatus

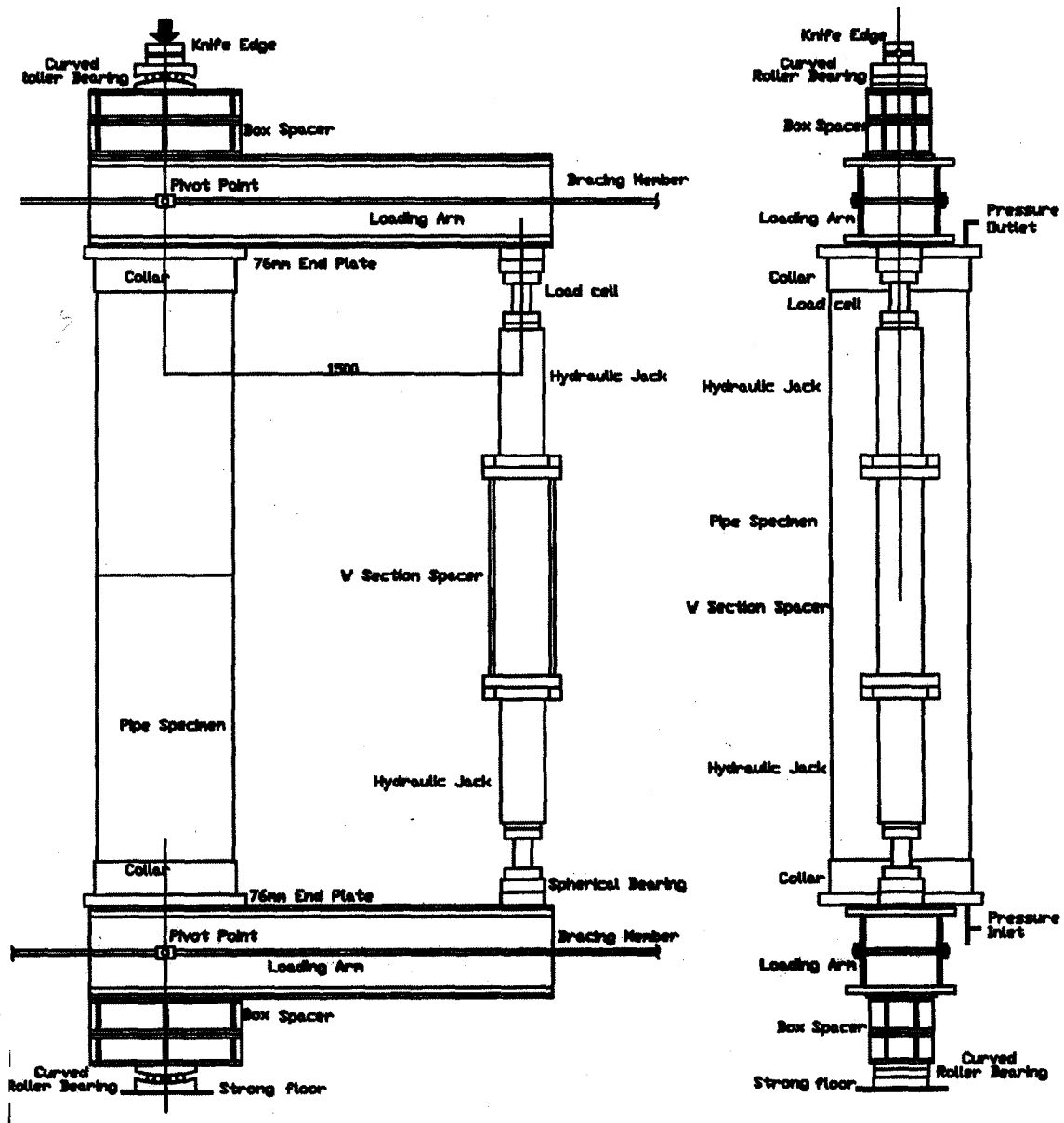


Figure 3.42 Schematic Test Setup

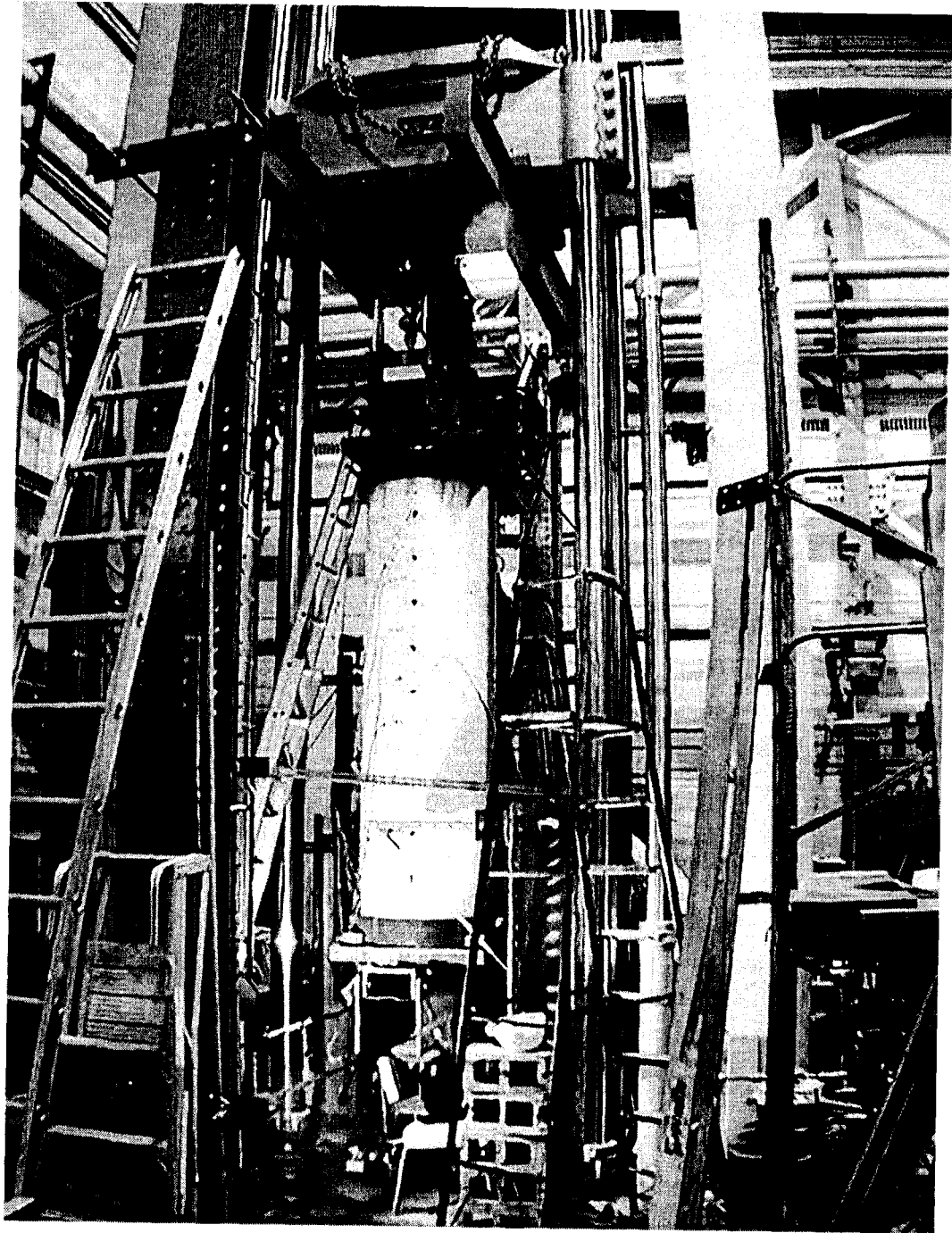


Figure 3.43 Front View of Test Setup for 30 inch Pipes

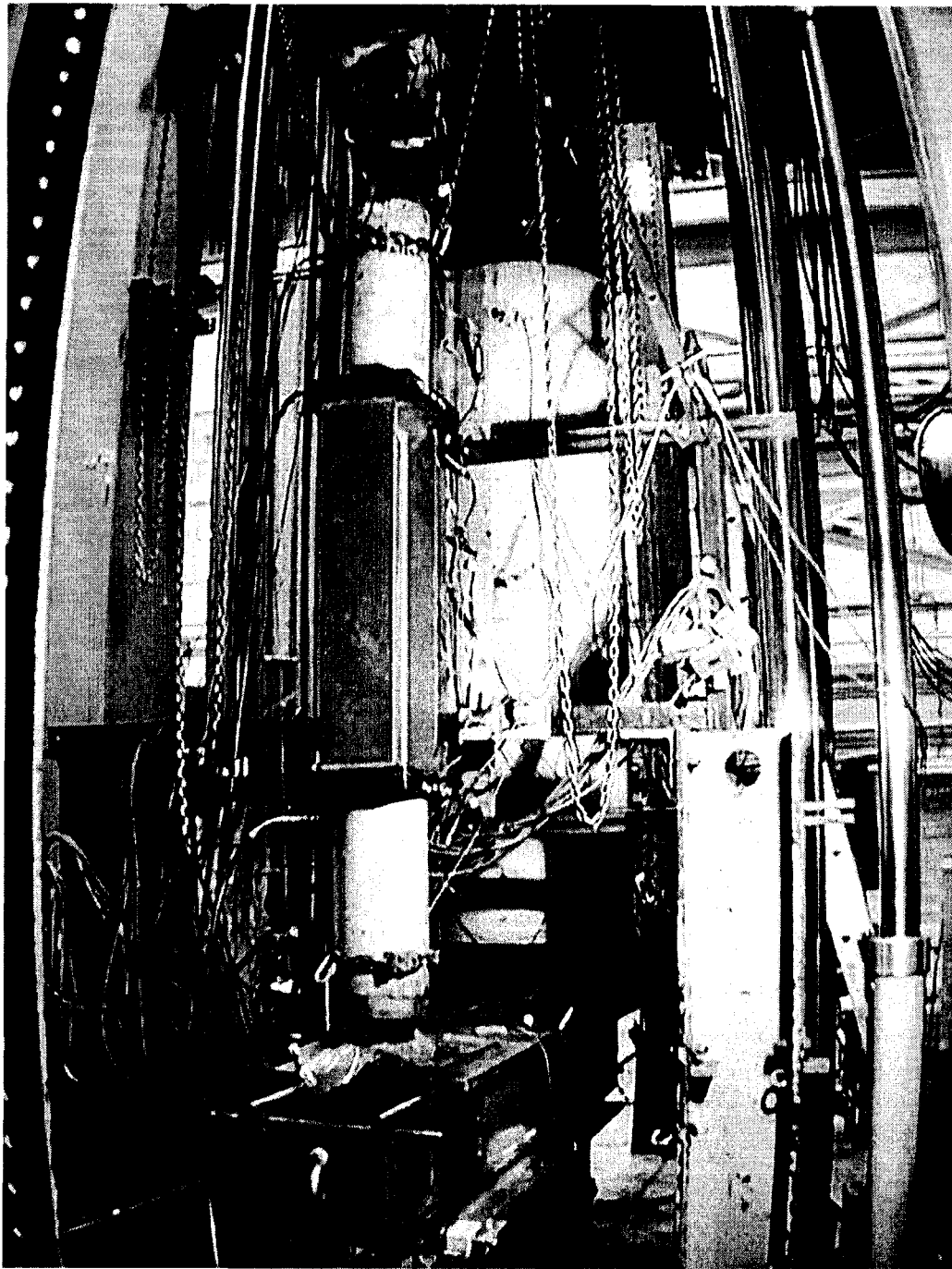


Figure 3.44 Back View of Test Setup for 30 inch Pipes

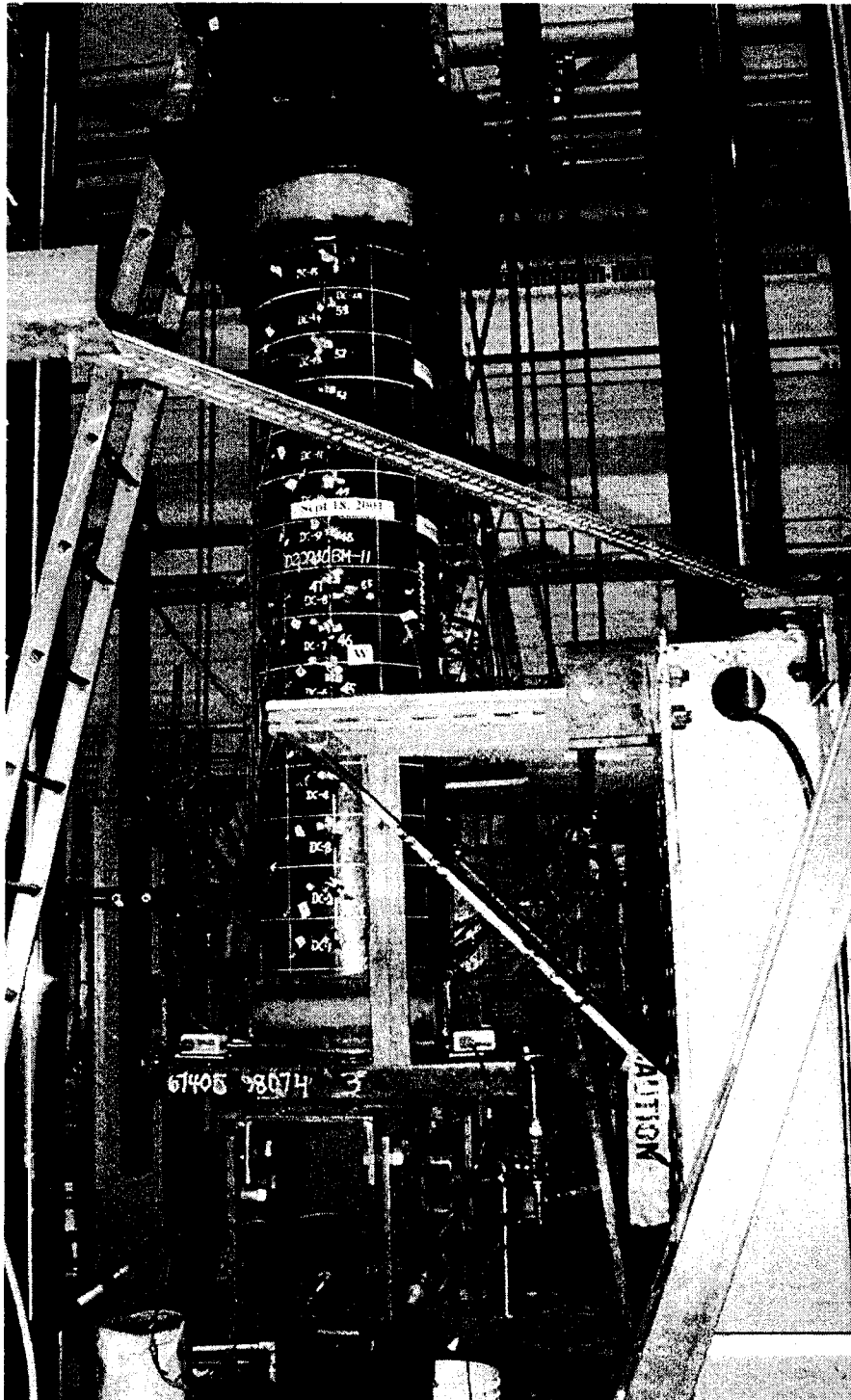


Figure 3.45 Test Setup for 20 inch Pipes

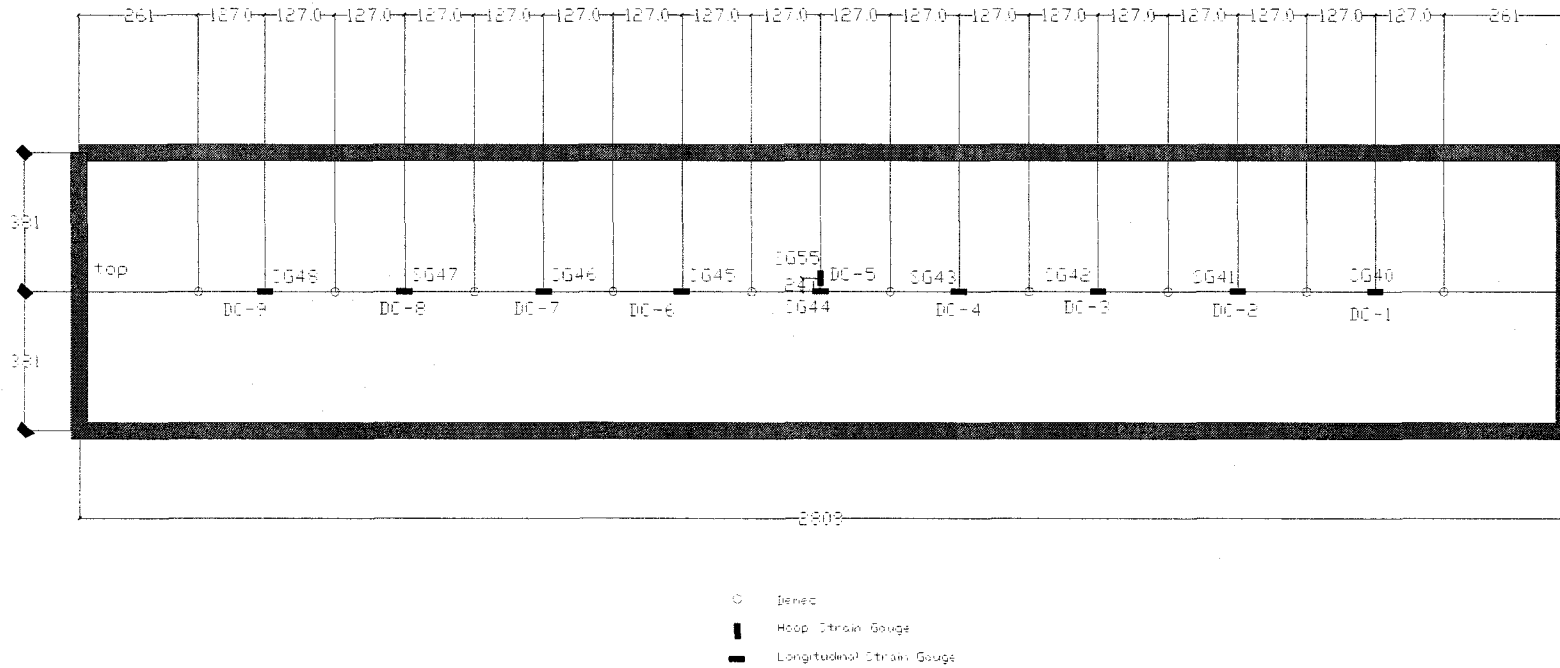


Figure 3.48 Locations of Demec Points and Strain Gauges and Their Corresponding Designation on the West Face (0°) for D30P80BC-8 and D30P20BC-9 (Demec Points for 7th Specimen) (Unit: mm)

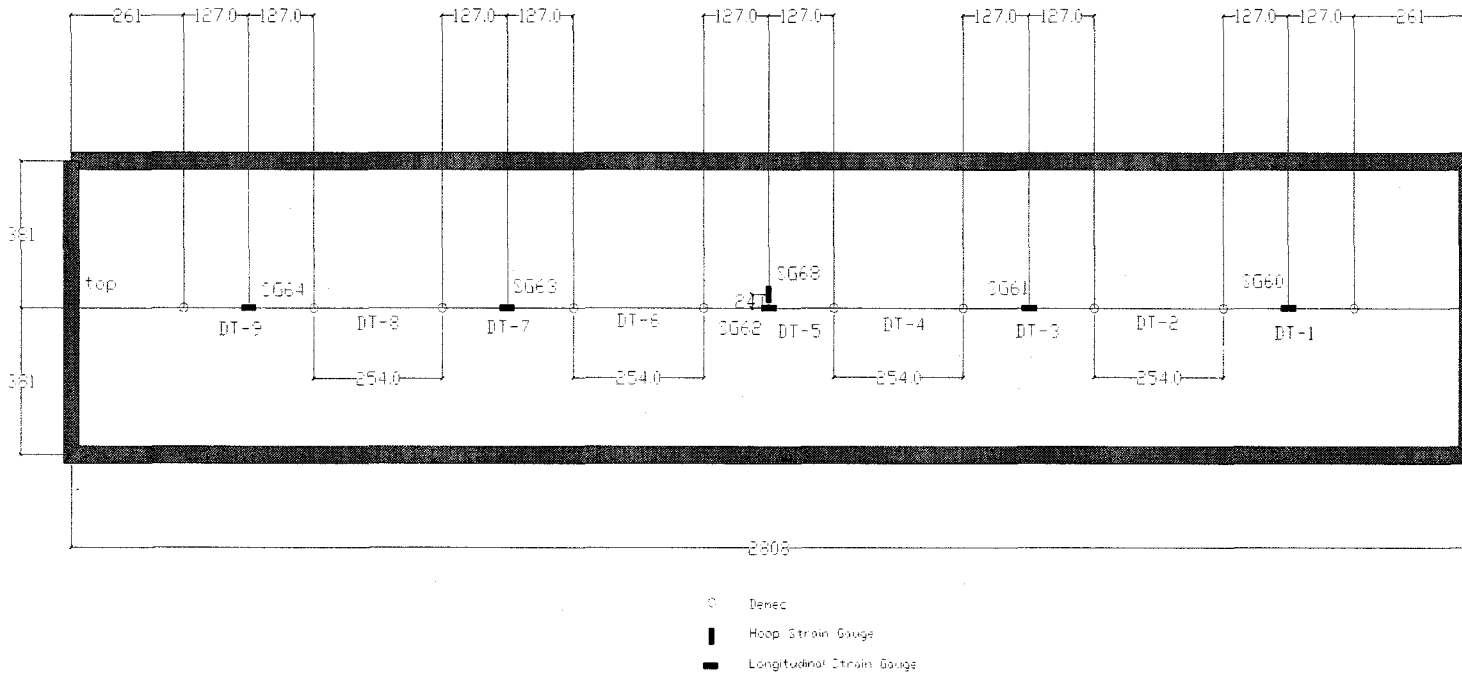


Figure 3.49 Locations of Demec Points and Strain Gauges and Their Corresponding Designation on the East Face (180°) for D30P80BC-8 and D30P20BC-9 (Demec Points for 7th Specimen) (Unit: mm)

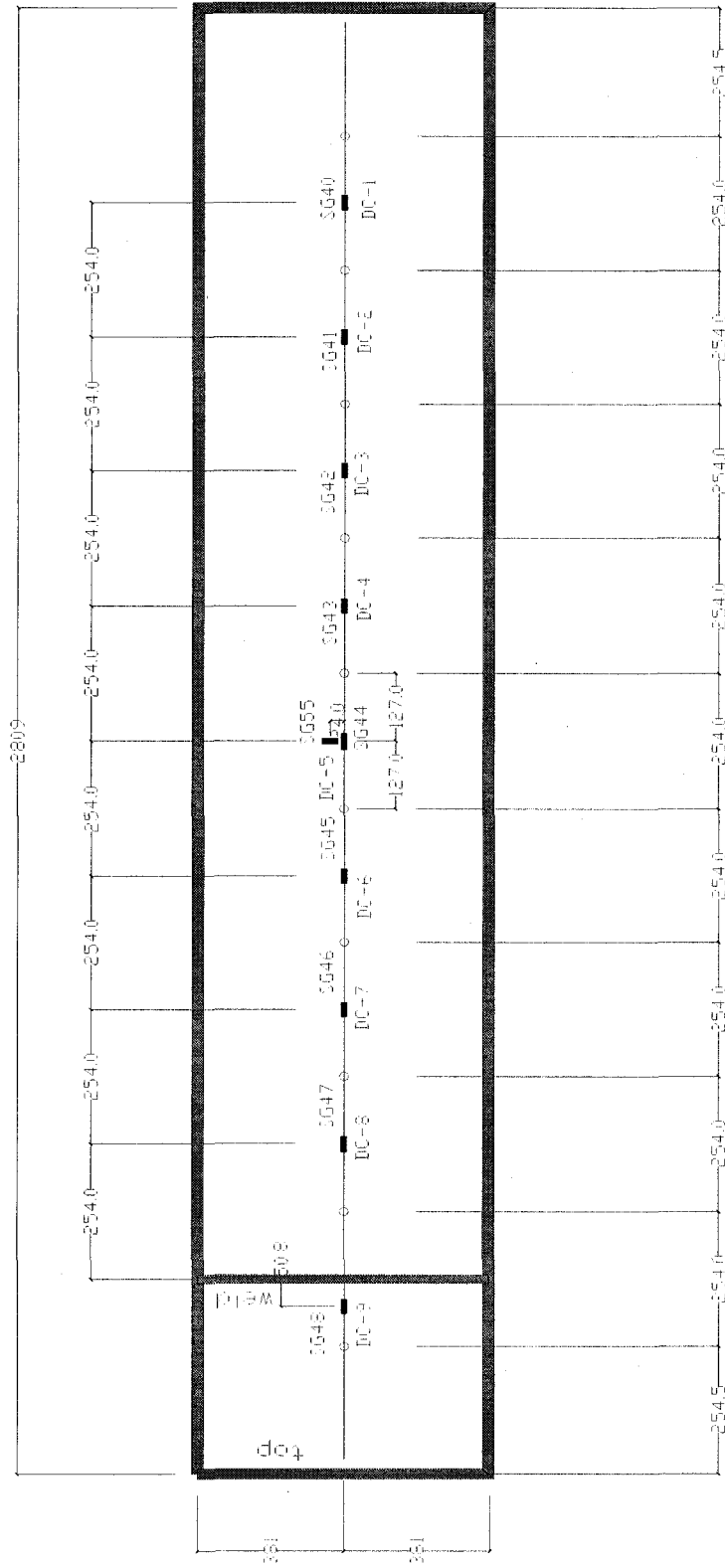


Figure 3.50 Locations of Demec Points and Strain Gauges and Their Corresponding Designation on the West Face (0°) for D30P0BC-7 (Unit: mm)

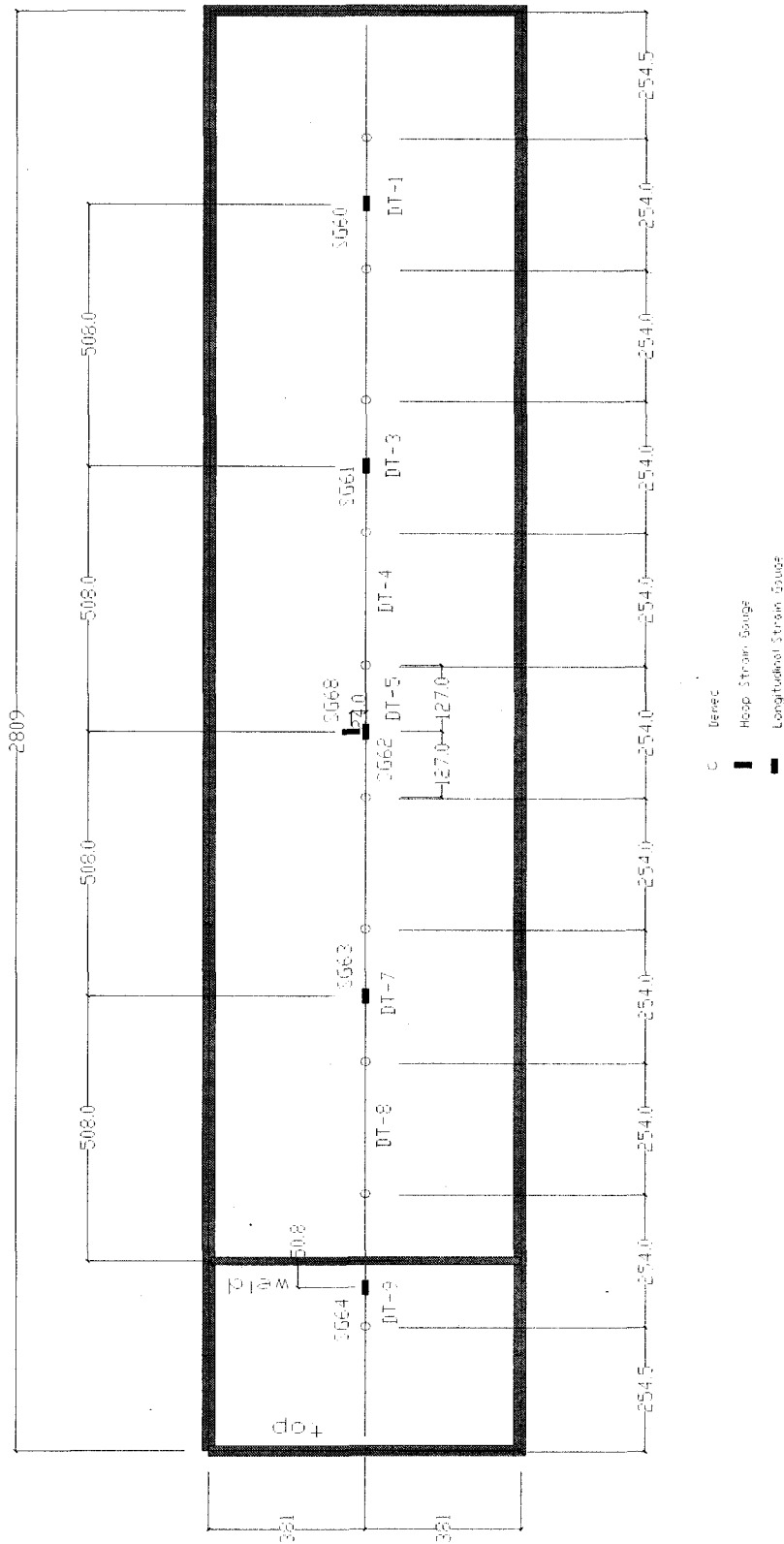


Figure 3.51 Locations of Demec Points and Strain Gauges and Their Corresponding Designation on the East Face (180°) for D30P0BC-7 (Unit: mm)

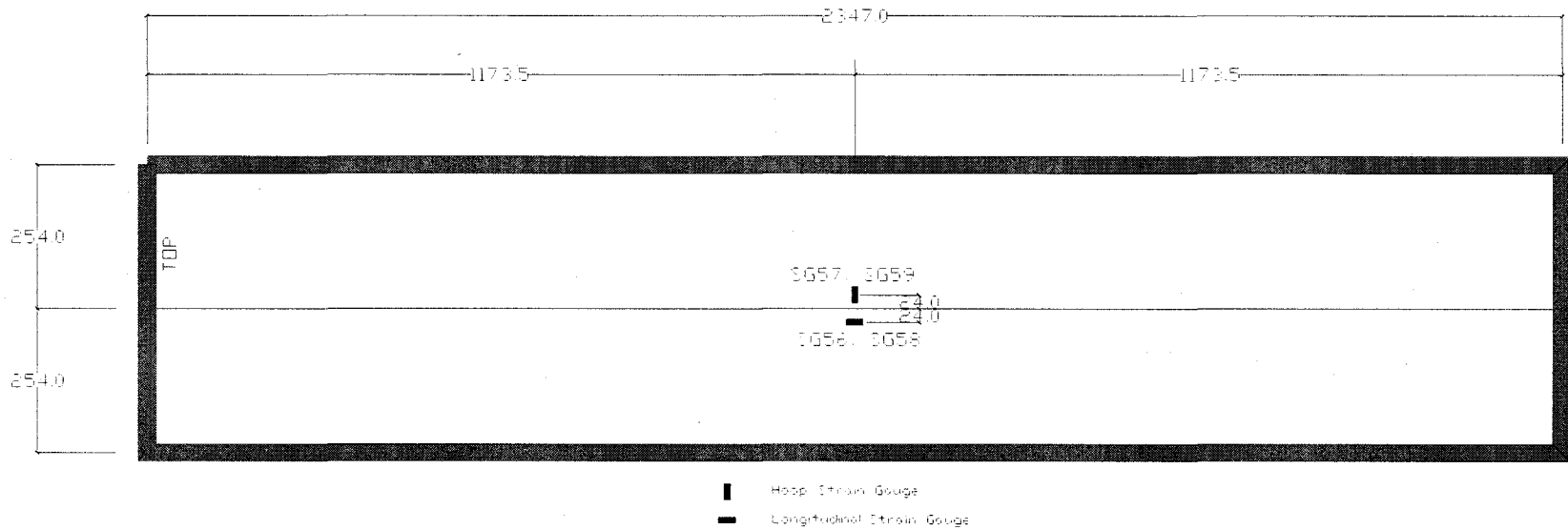


Figure 3.52 Locations of Strain Gauges and Their Corresponding Designation on the South Face (270°) and North Face (90°) for 20 inch Pipes (Unit: mm)

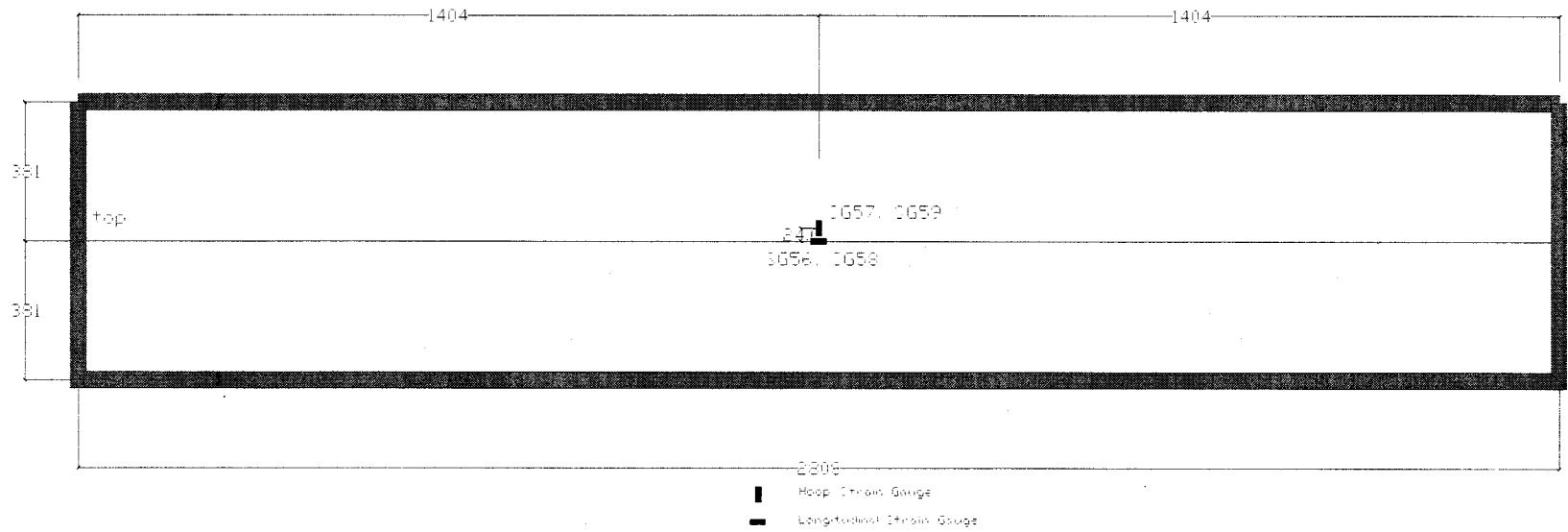


Figure 3.53 Locations of Strain Gauges and Their Corresponding Designation on the South Face (270°) and North Face (90°) for 30 inch Pipes (Unit: mm)

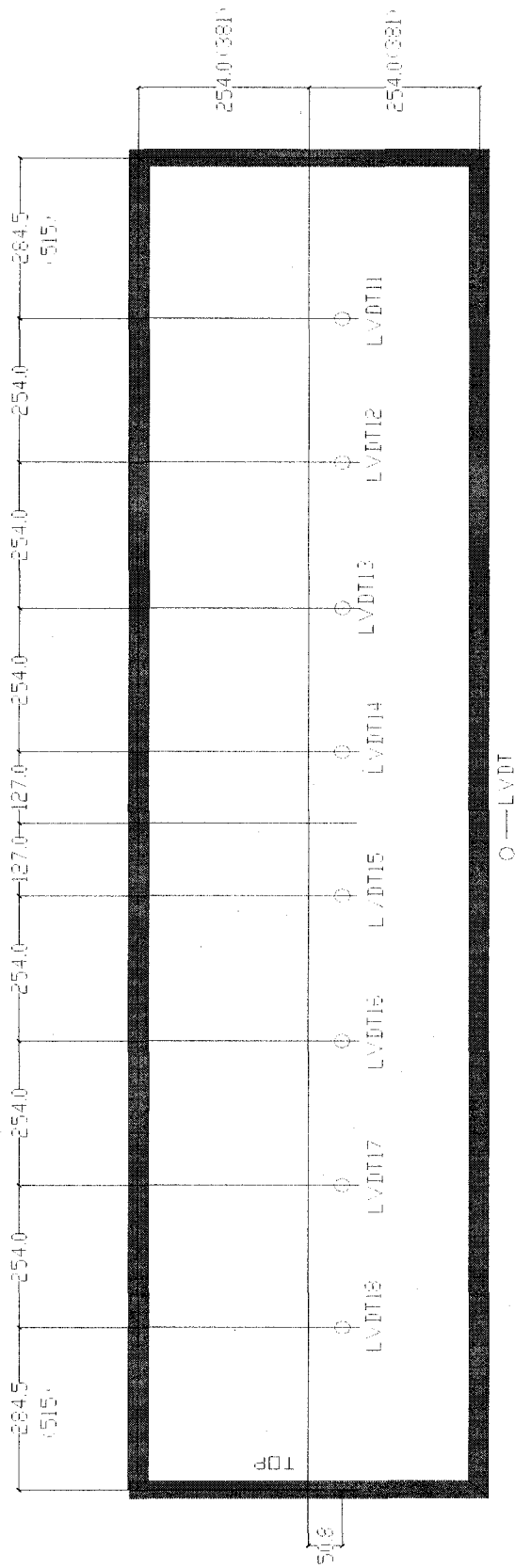


Figure 3.54 LVDTs on the West Face (0°) for 20 inch (30 inch) Pipes (Unit: mm)

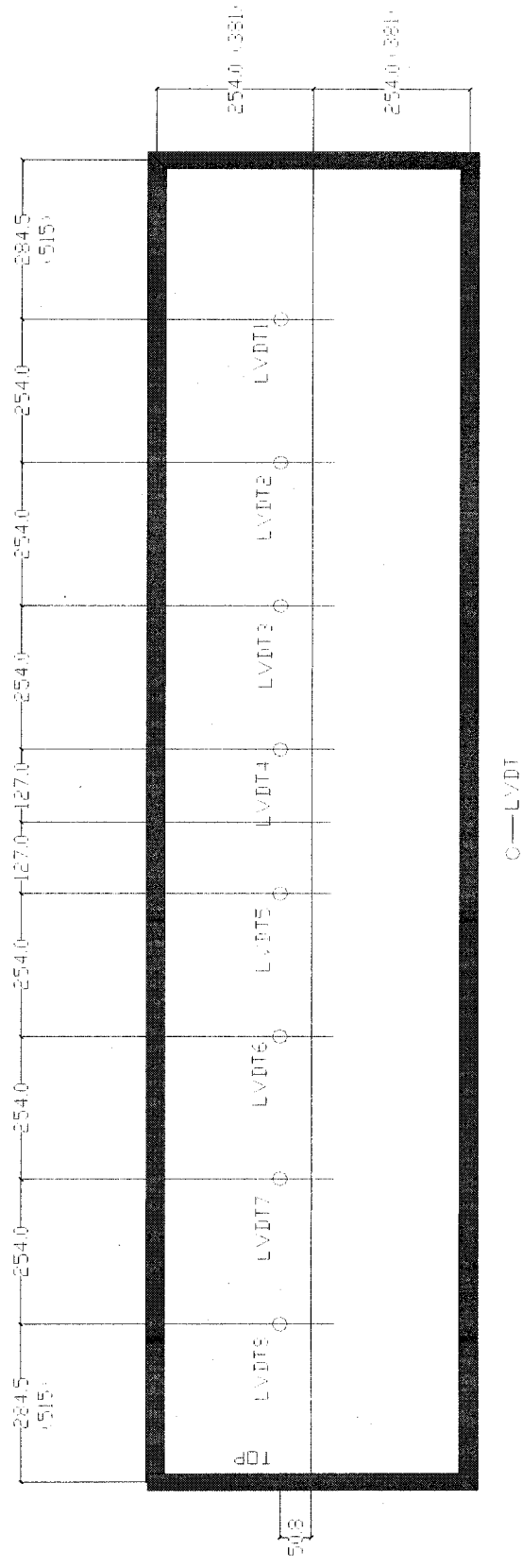


Figure 3.55 LVDTs on the East Face (180°) for 20 inch (30 inch) Pipes (Unit: mm)

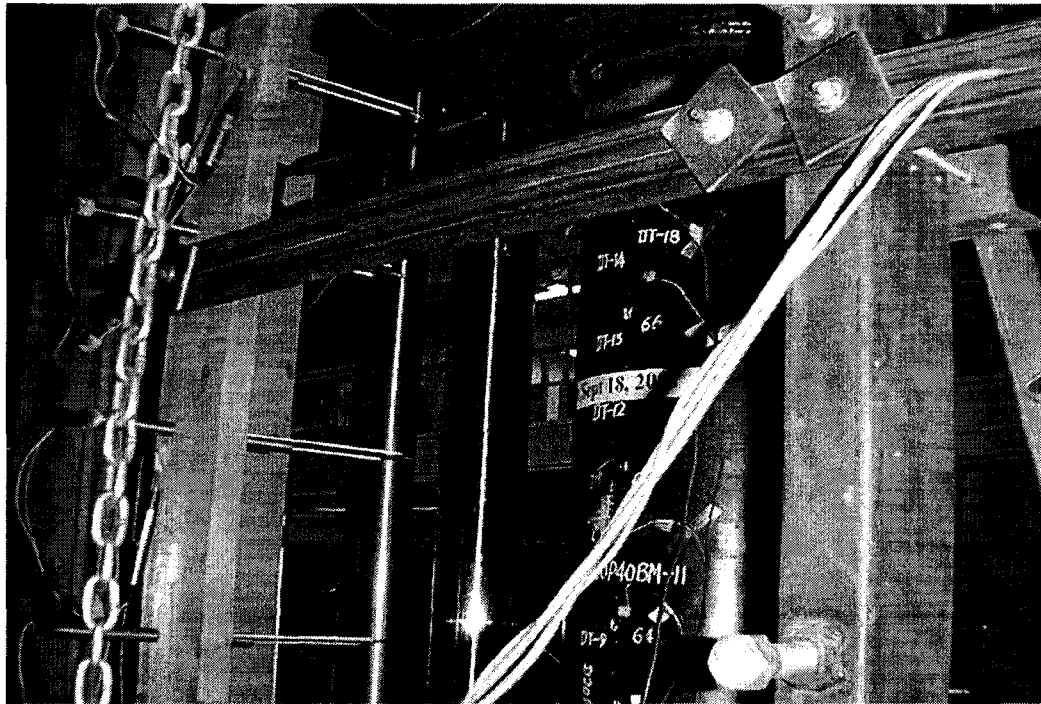
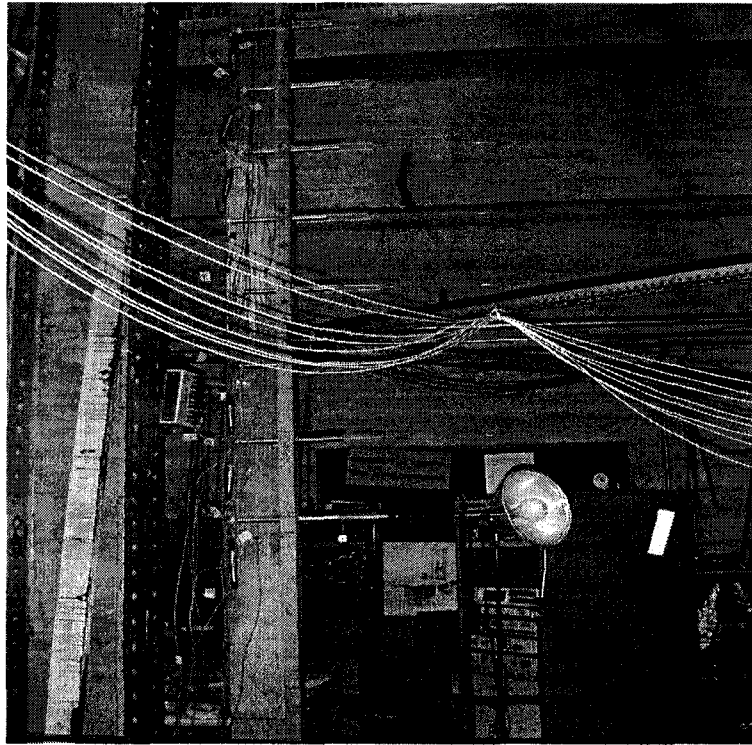


Figure 3.56 Setup of LVDTs

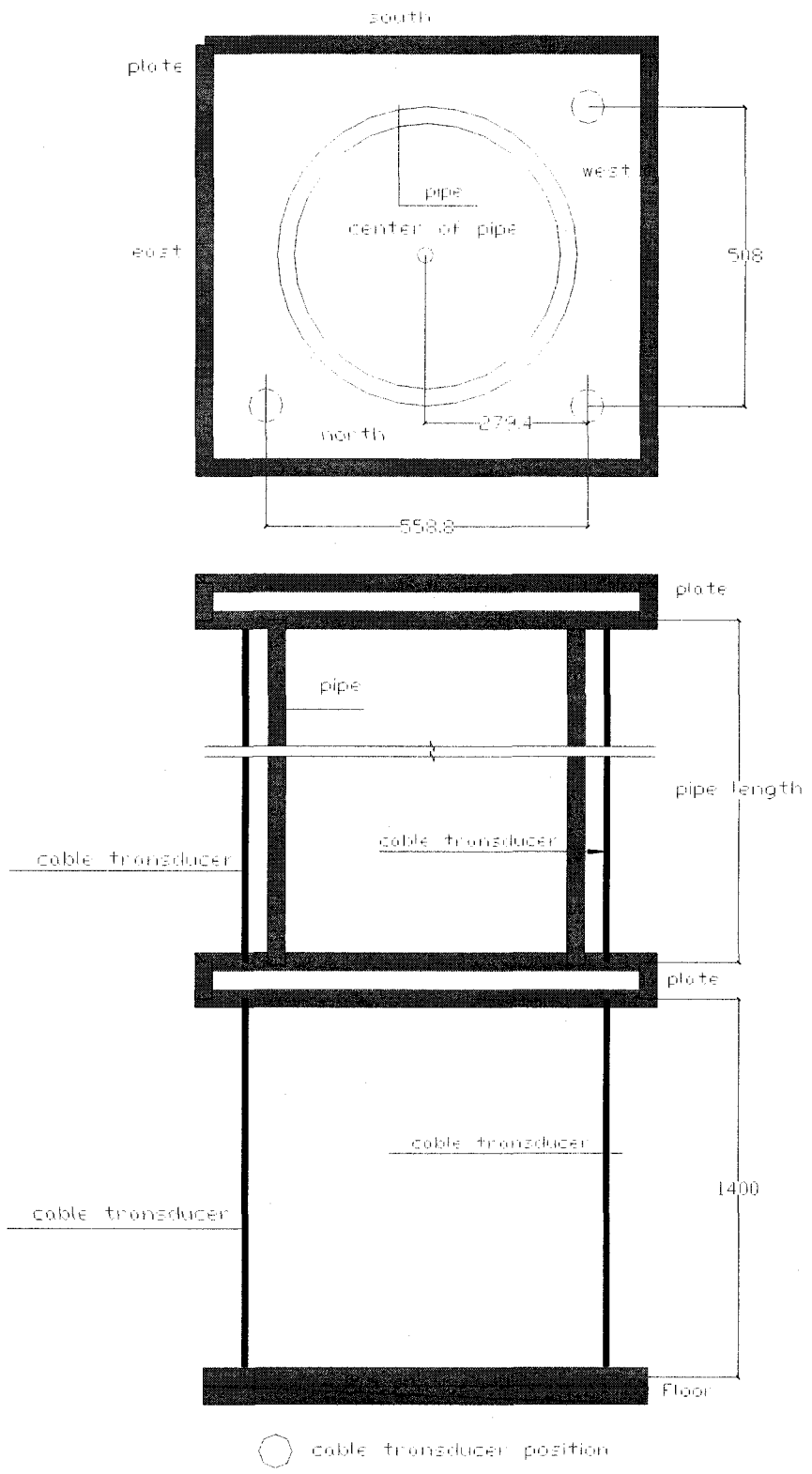


Figure 3.57 Cable Transducers Positions (Unit: mm)

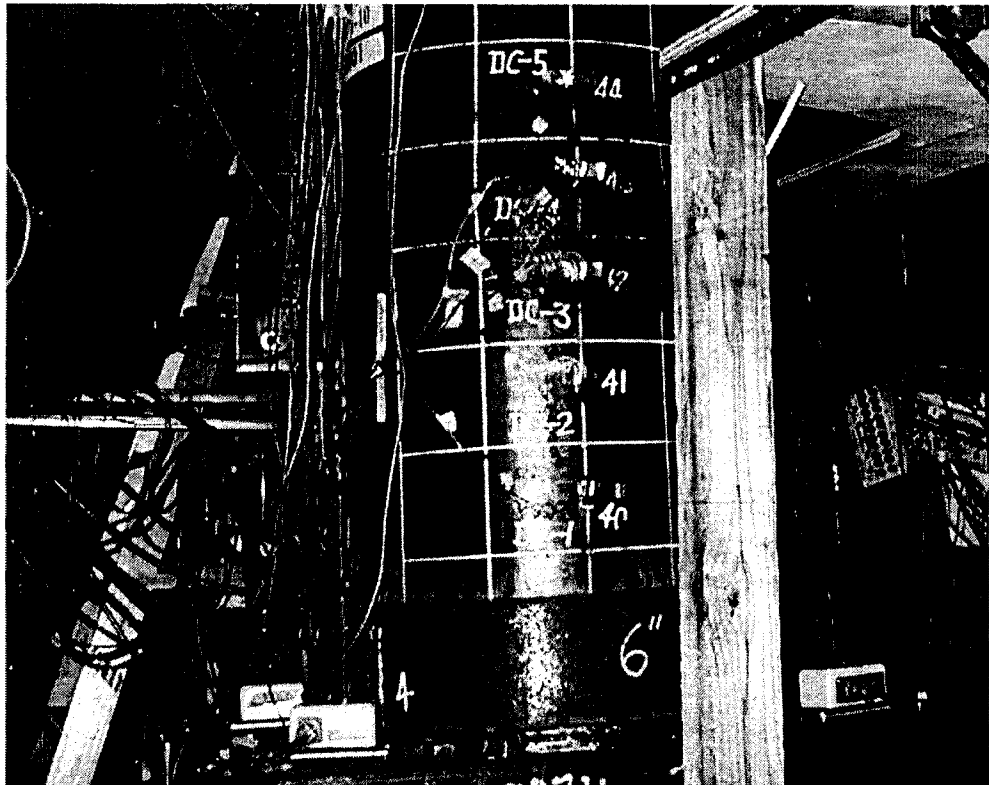
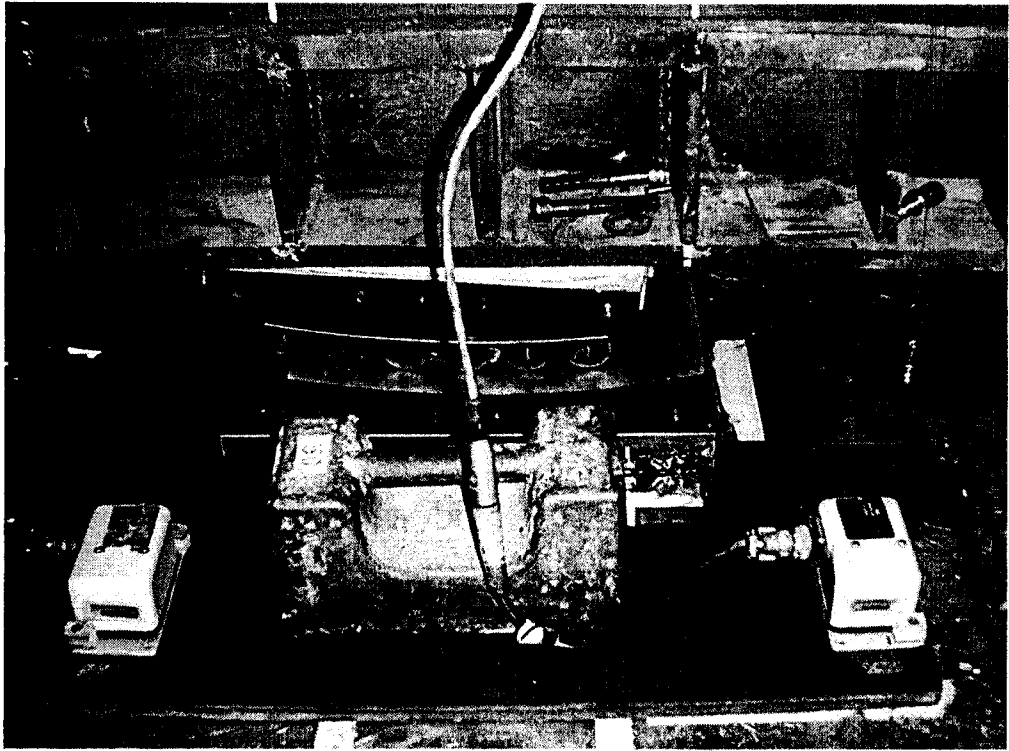


Figure 3.58 Photos of Cable Transducers

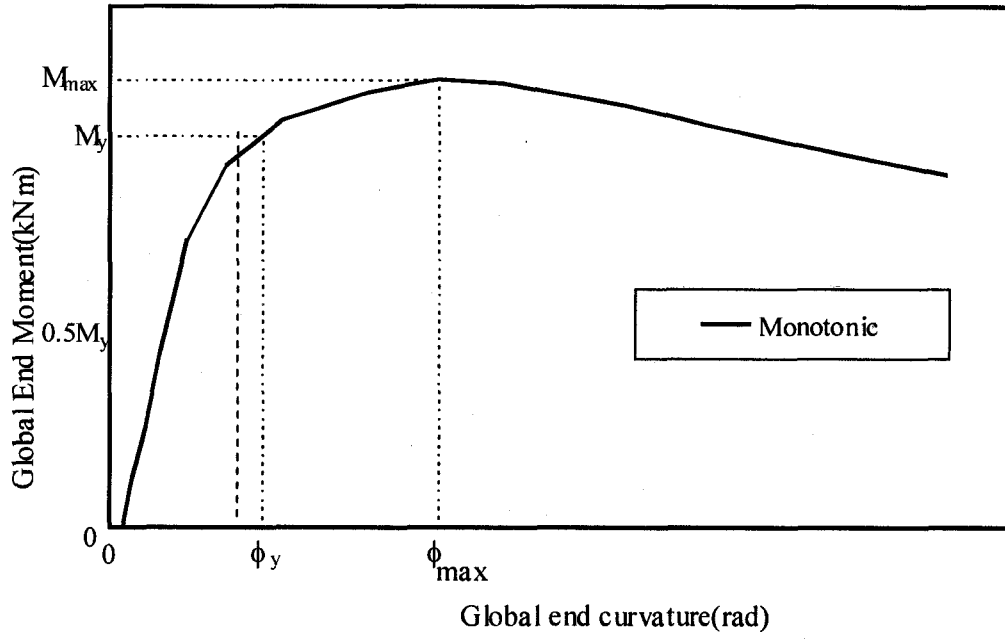


Figure 3.59 Typical Moment Curvature for a Monotonic Bending Test

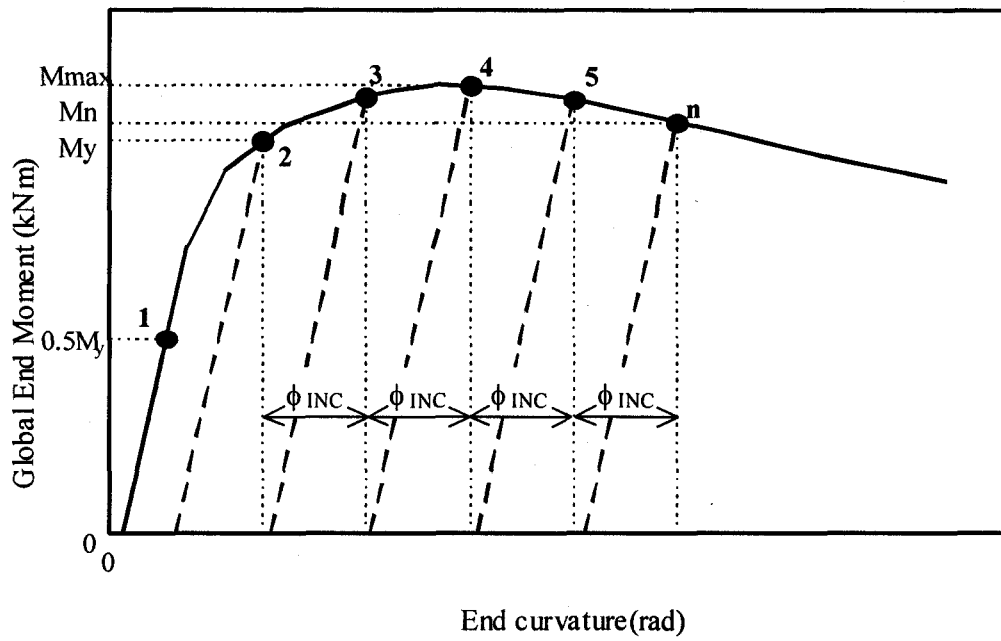


Figure 3.60 Loading Sequence of Cyclic Tests

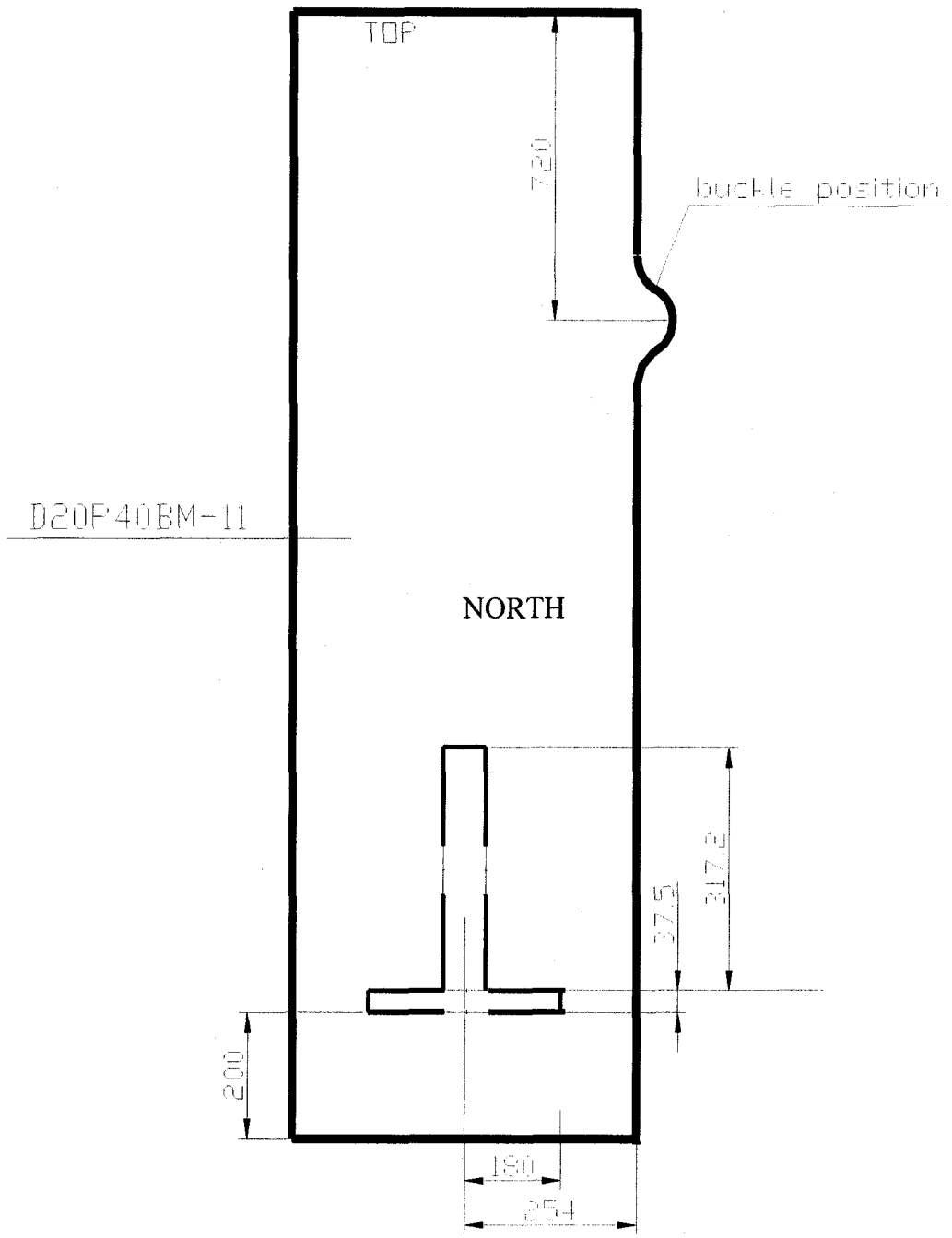


Figure 3.61 Position of Coupon in D20P40BM-11 (Unit: mm)

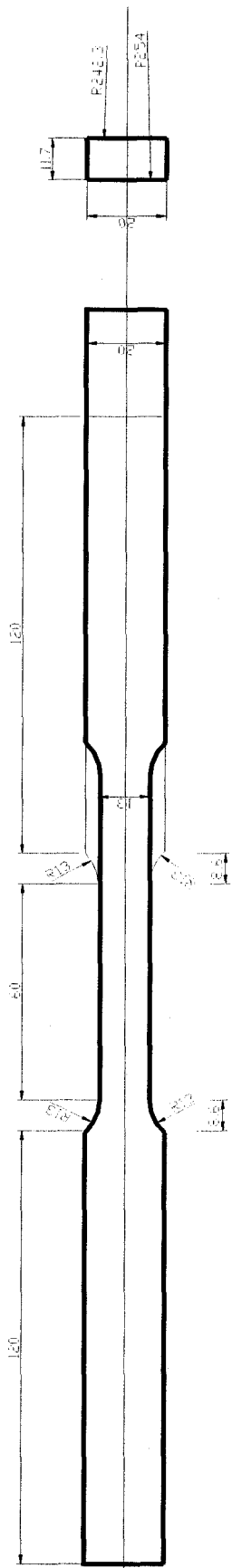


Figure 3.62 Coupon in Longitudinal Direction for 20 inch Pipes (Unit: mm)

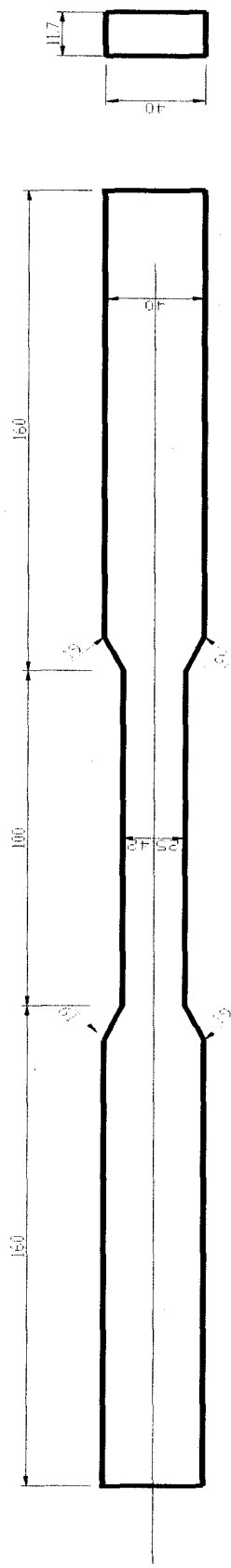


Figure 3.63 Coupon in Hoop Direction for 20 inch Pipes (Unit: mm)

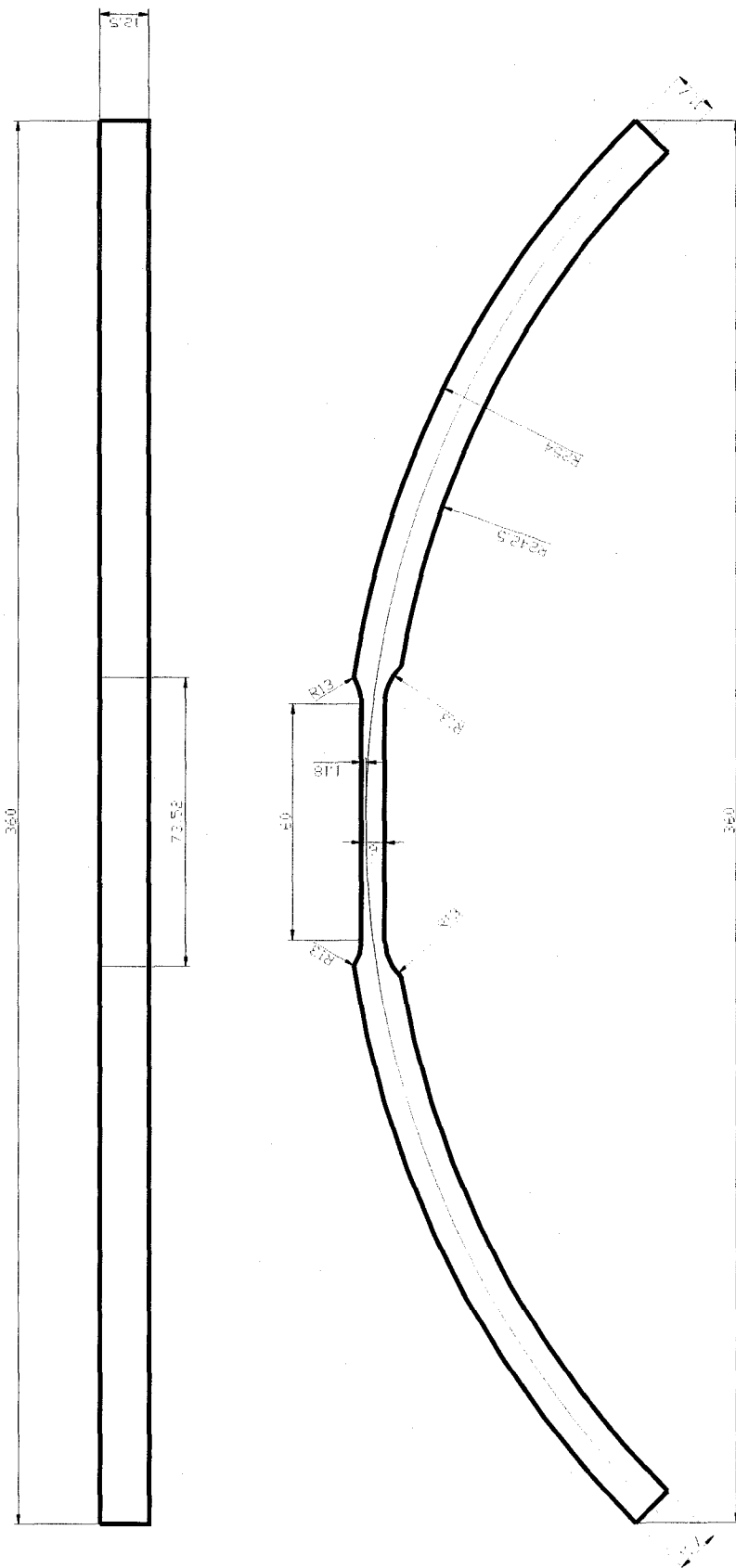


Figure 3.64 Curve Coupon in Hoop Direction for 20 inch Pipes (Unit: mm)

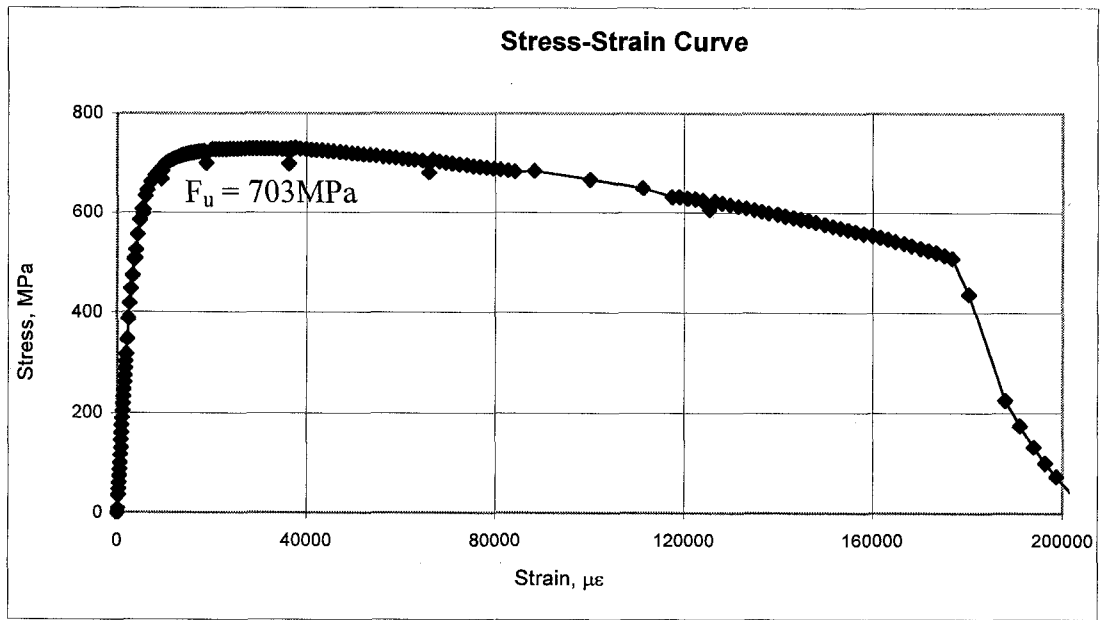


Figure 3.65 Stress vs. Strain Curve of Straightened Transverse Coupon #1

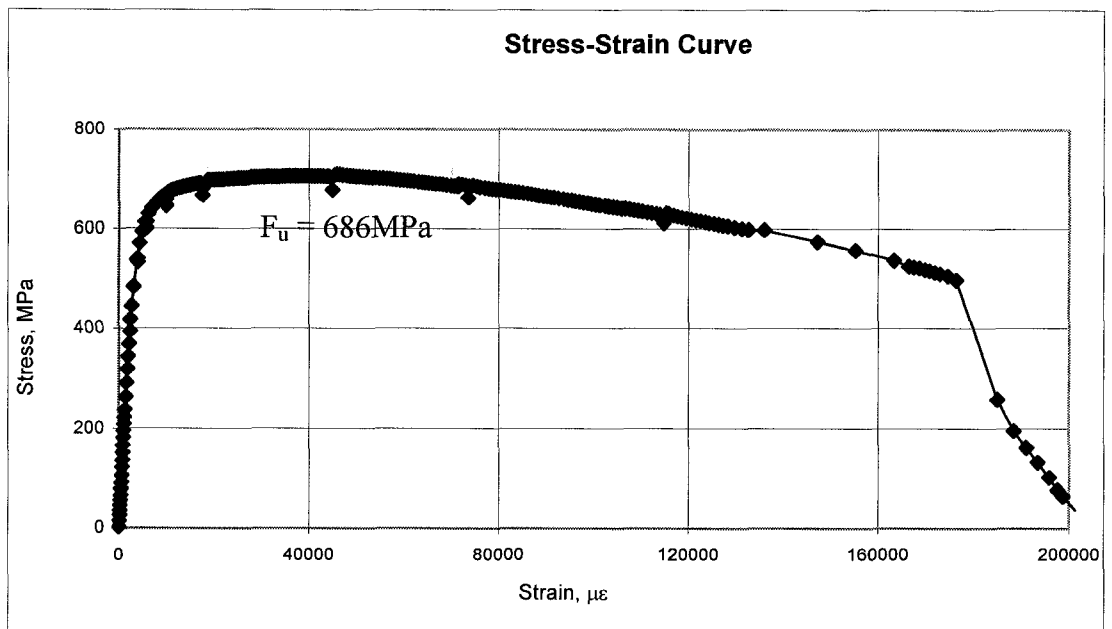


Figure 3.66 Stress vs. Strain Curve of Straightened Transverse Coupon #2

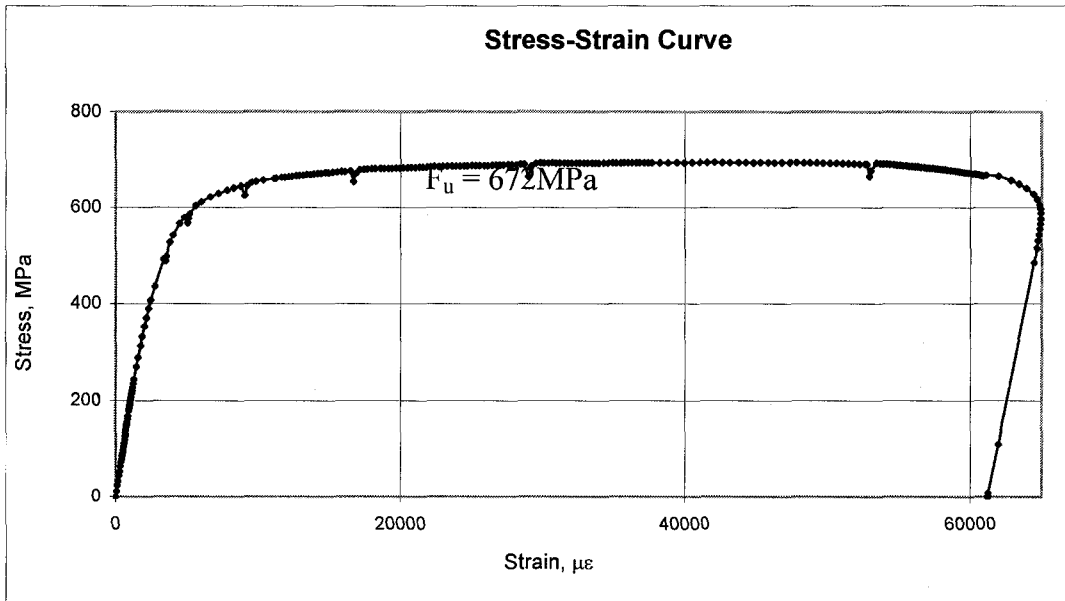


Figure 3.67 Stress vs. Strain Curve of Straightened Transverse Coupon #3

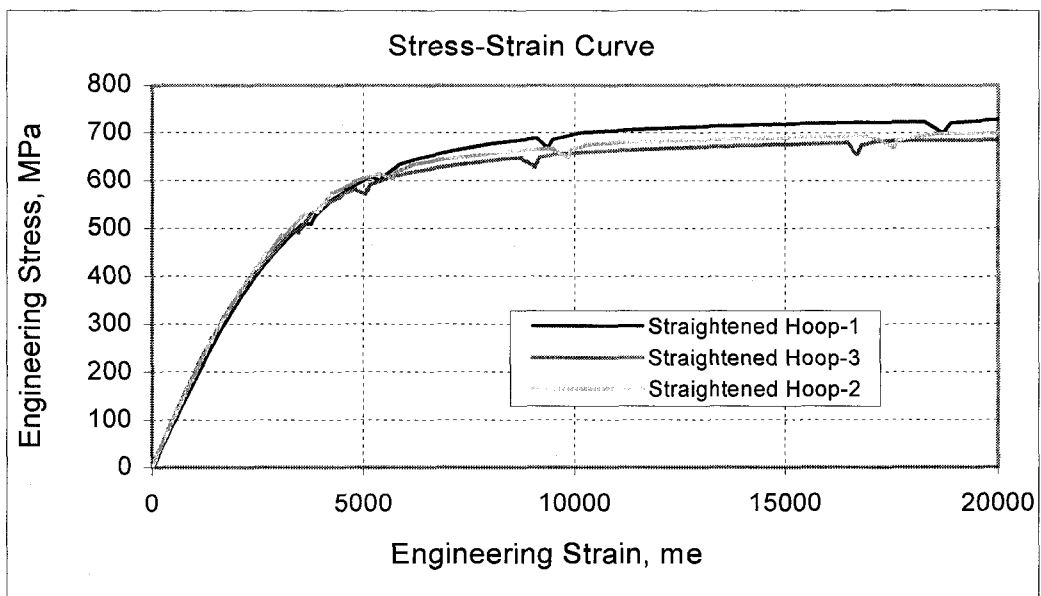


Figure 3.68 Stress vs. Strain Curve of Straightened Transverse Coupon #1-3

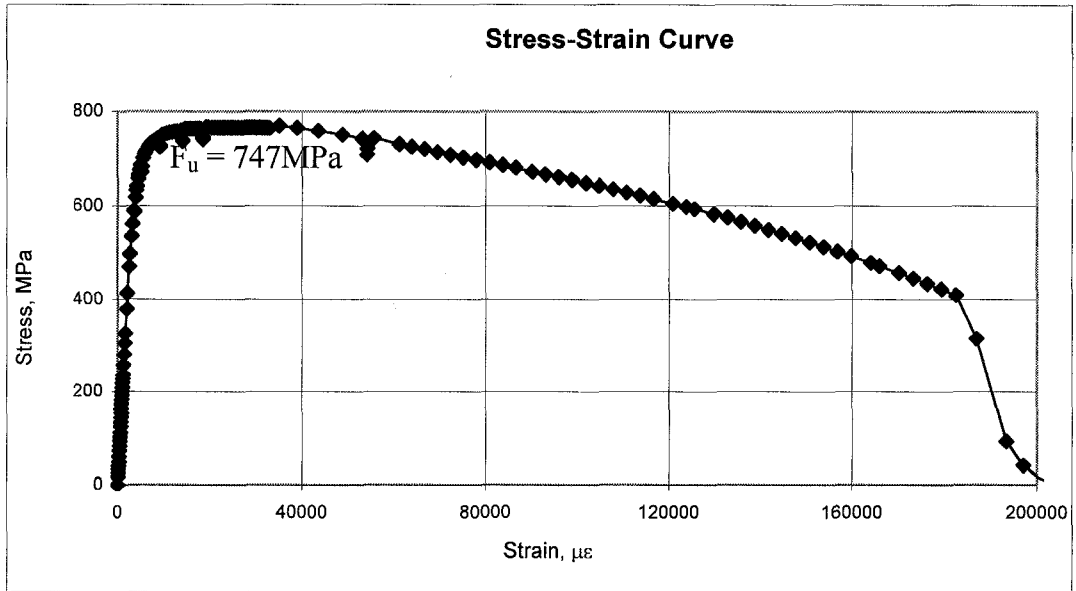


Figure 3.69 Stress vs. Strain Curve of Longitudinal Coupon #1

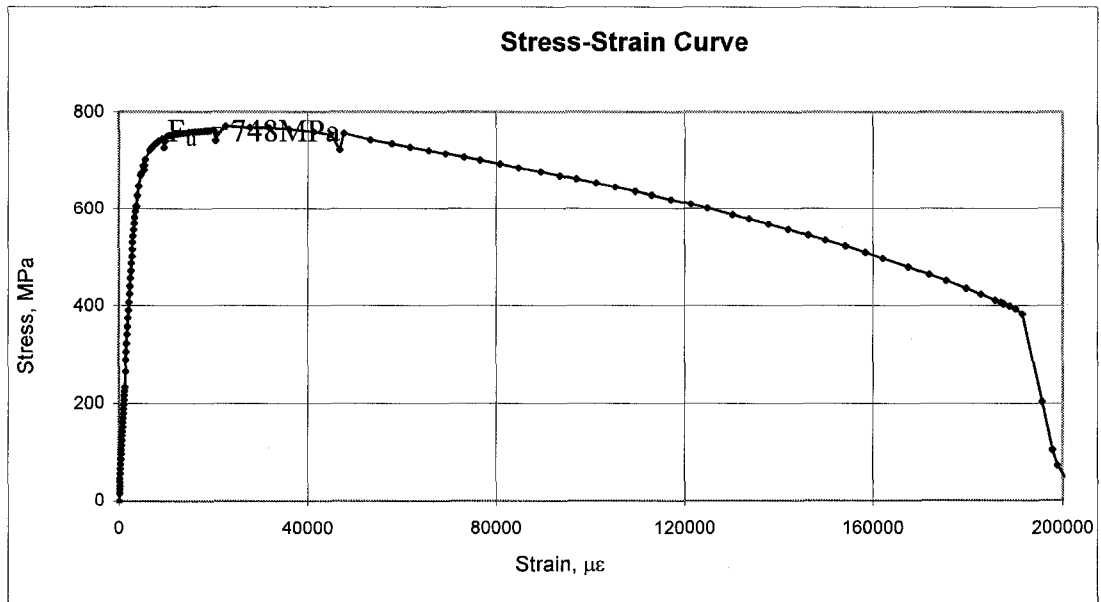


Figure 3.70 Stress vs. Strain Curve of Longitudinal Coupon #2

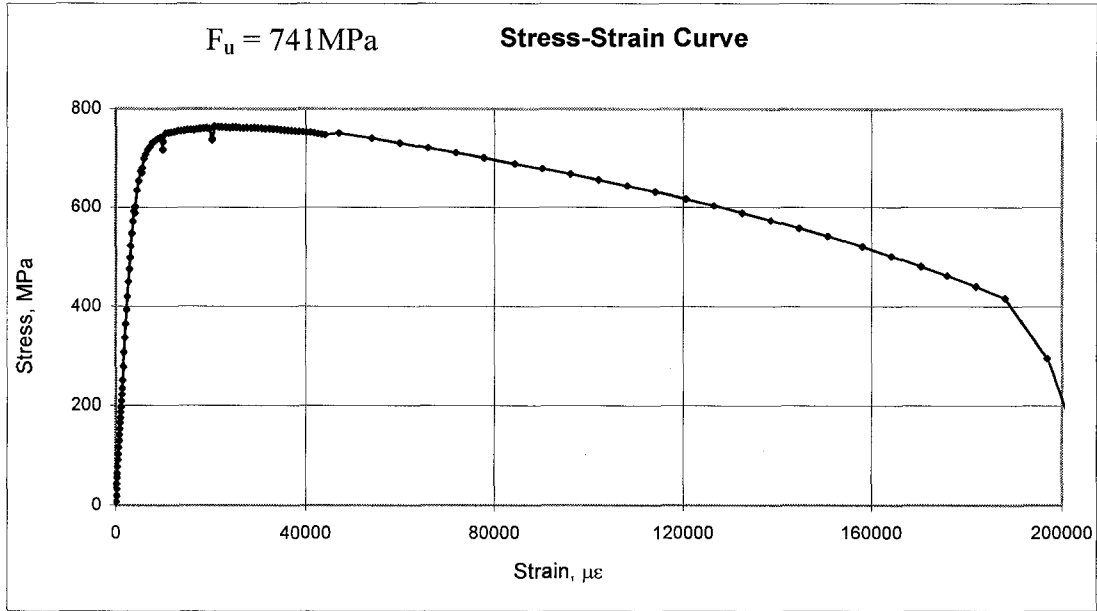


Figure 3.71 Stress vs. Strain Curve of Longitudinal Coupon #3

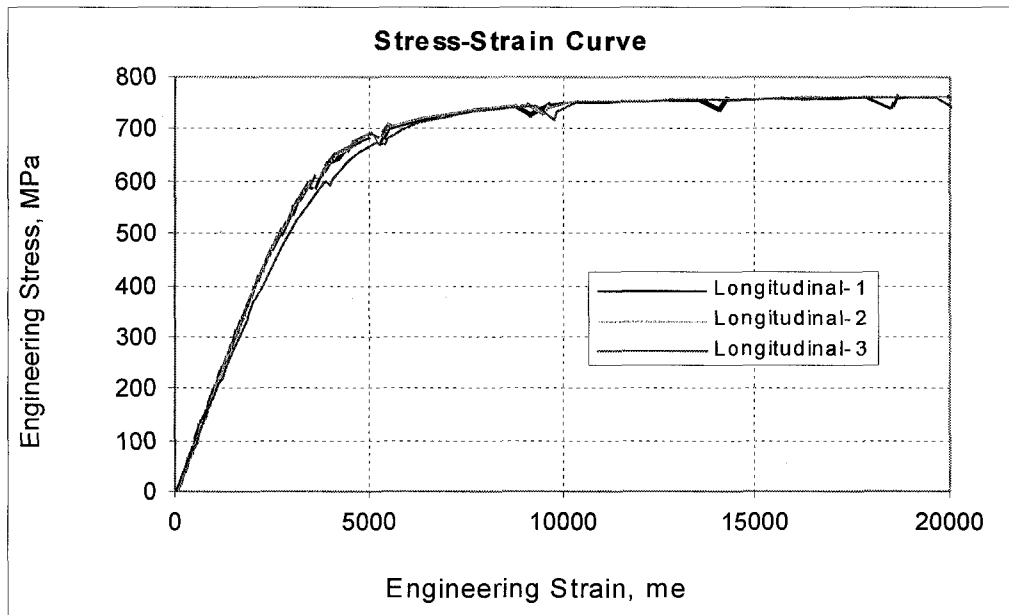


Figure 3.72 Stress vs. Strain Curve of Longitudinal Coupon #1-3

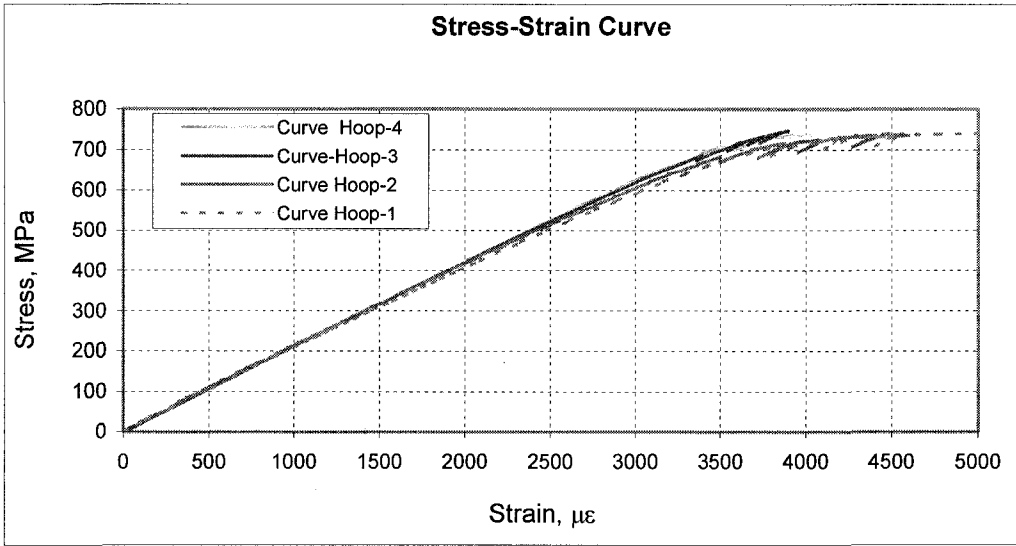
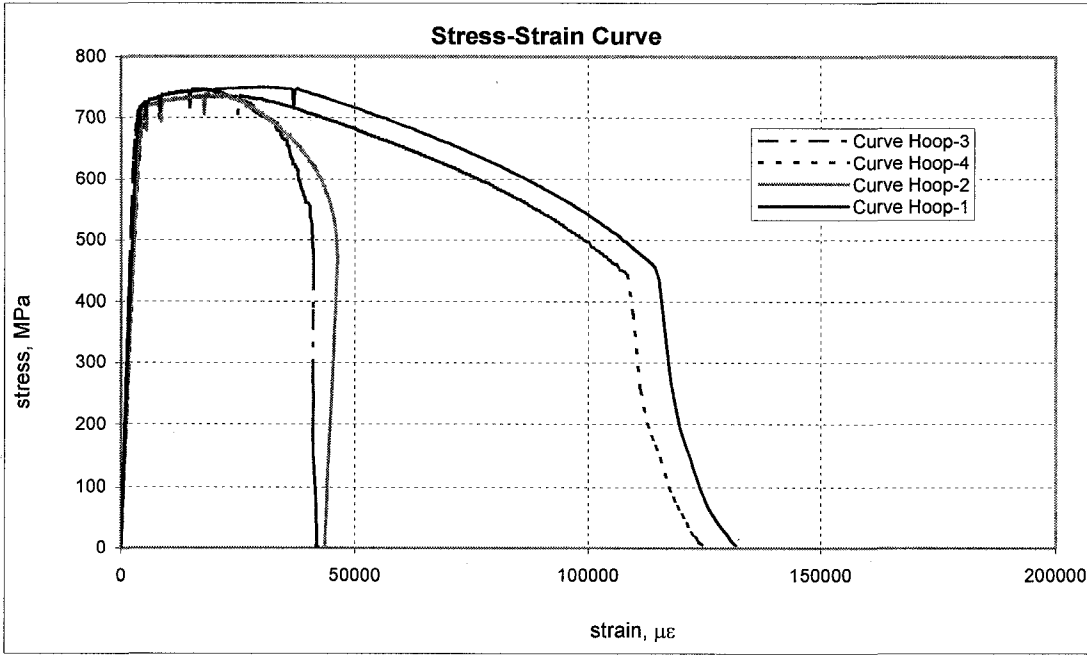


Figure 3.73 Stress vs. Strain for Curve Hoop Coupon #1-4

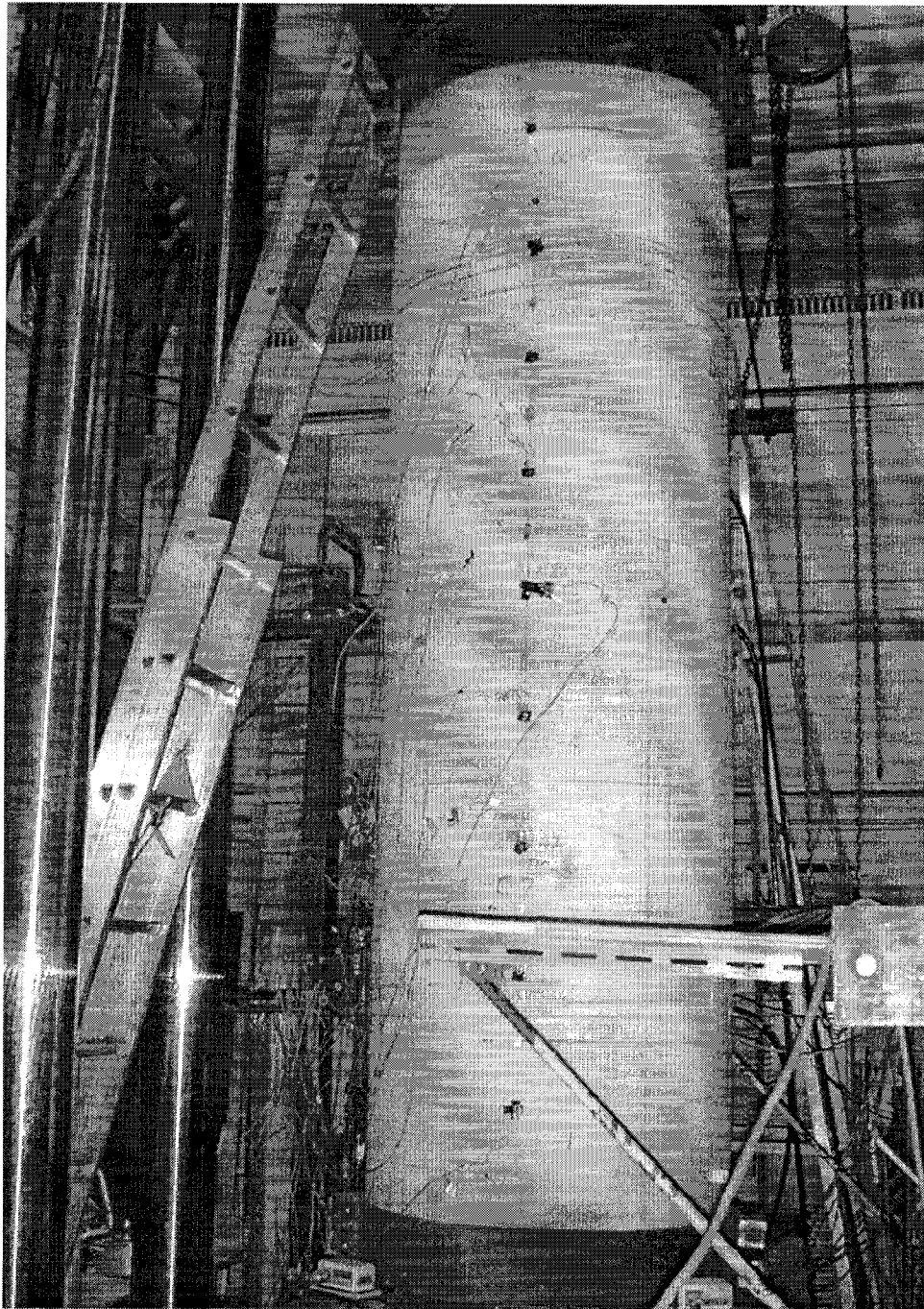


Figure 3.74 Buckle Position in D30P0BC-7

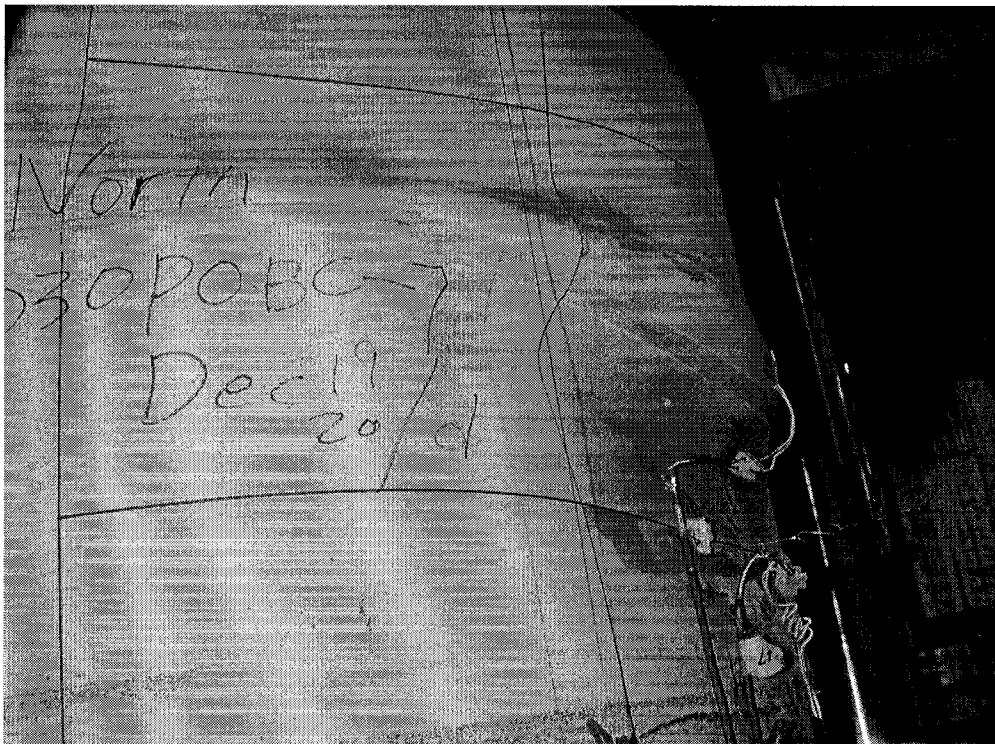
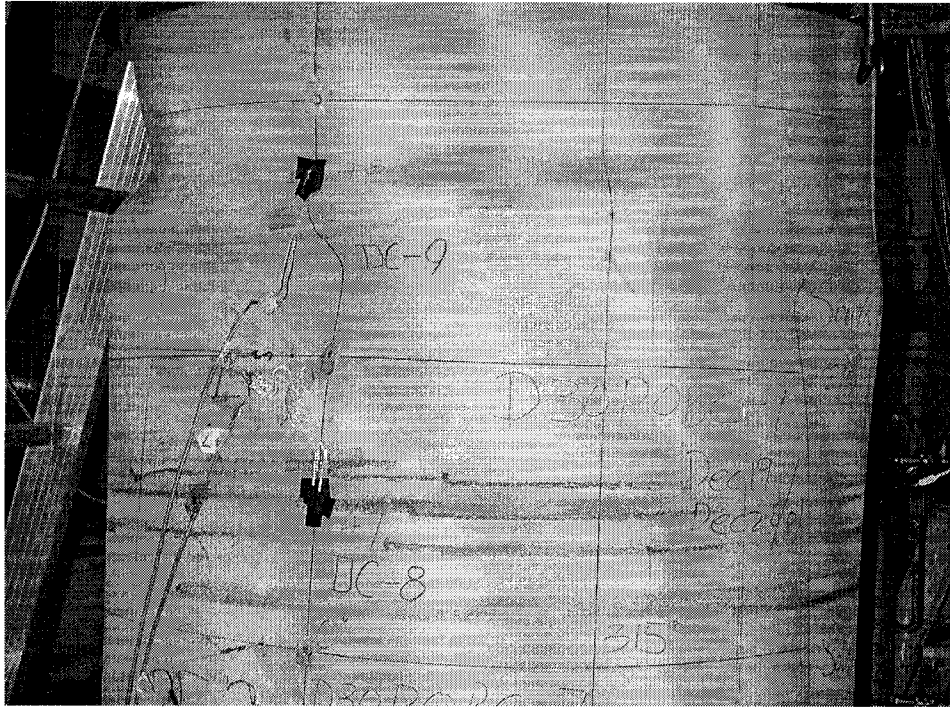


Figure 3.75 Buckle Shape of D30P0BC-7

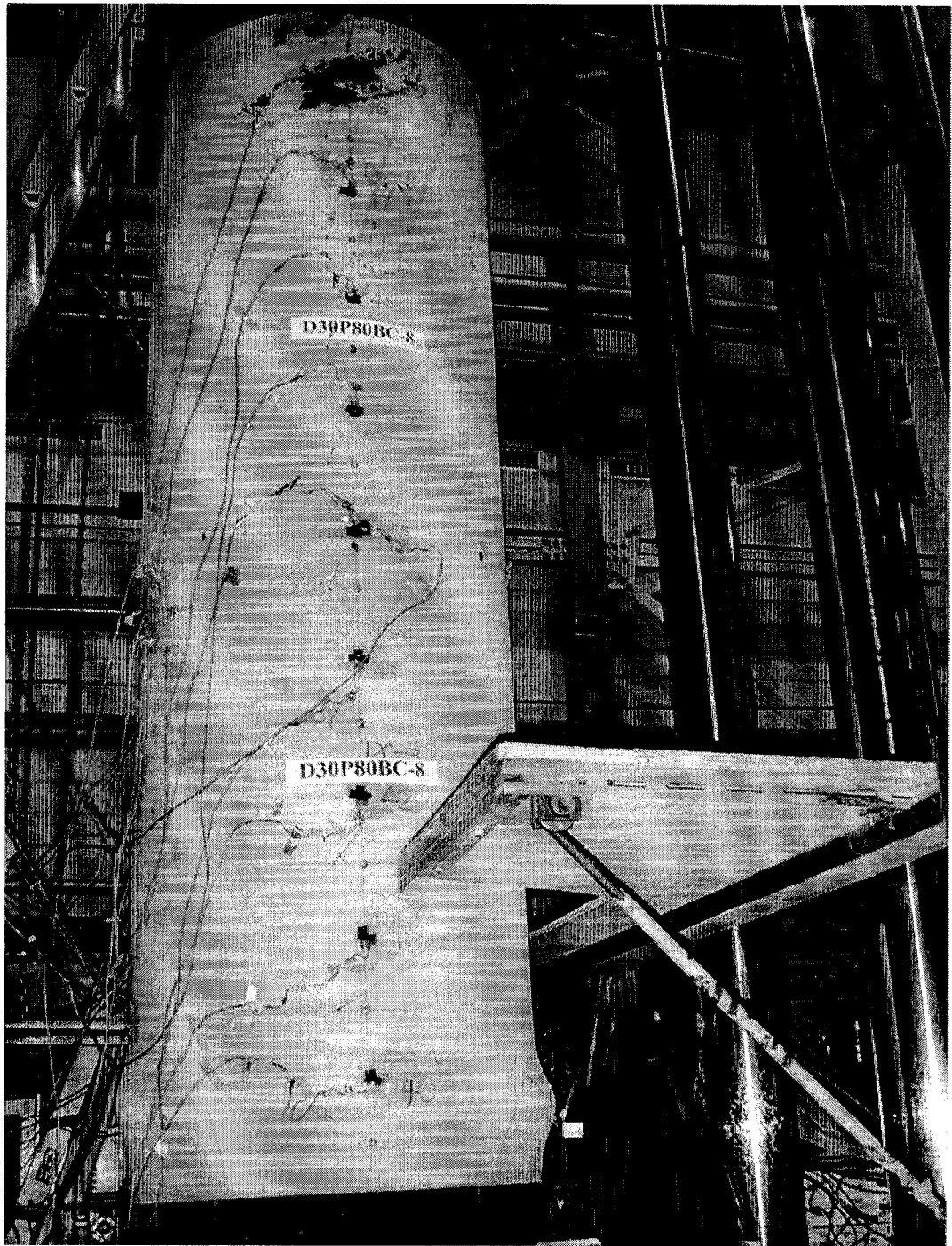


Figure 3.76 Buckle Position in D30P80BC-8

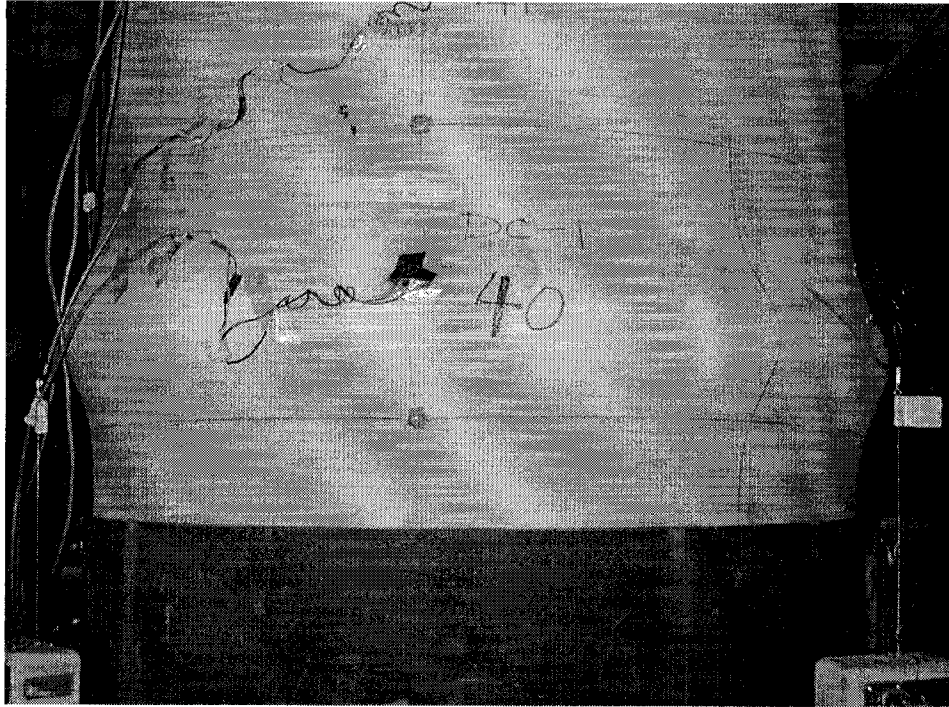


Figure 3.77 Buckle Shape of D30P80BC-8

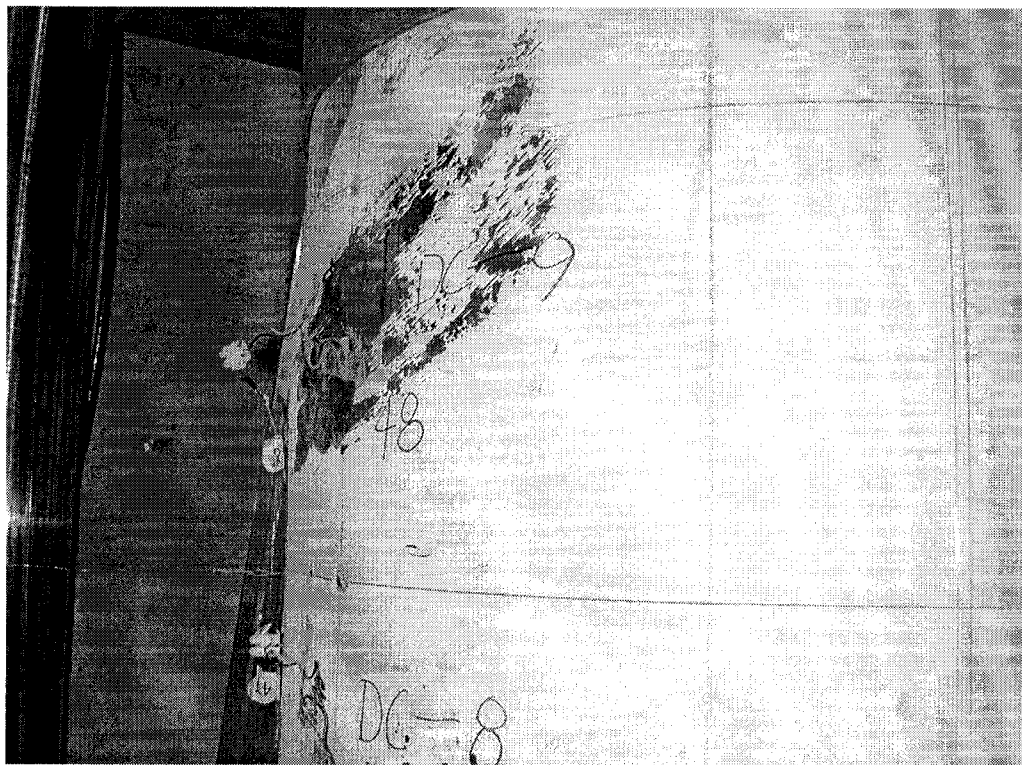


Figure 3.78 Second Bulge Position in D30P80BC-8

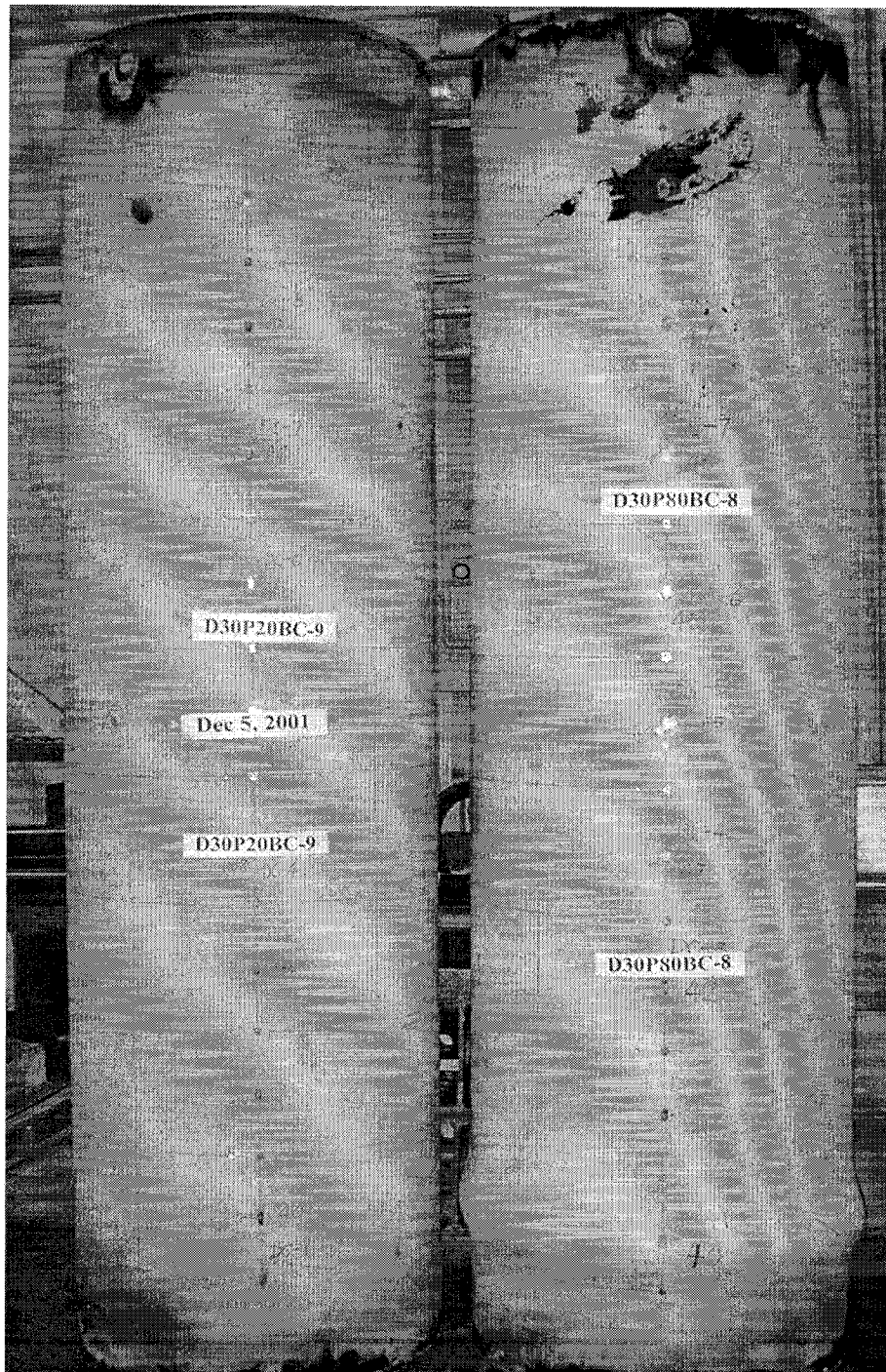


Figure 3.79 Buckle Position in D30P80BC-8 and D30P20BC-9

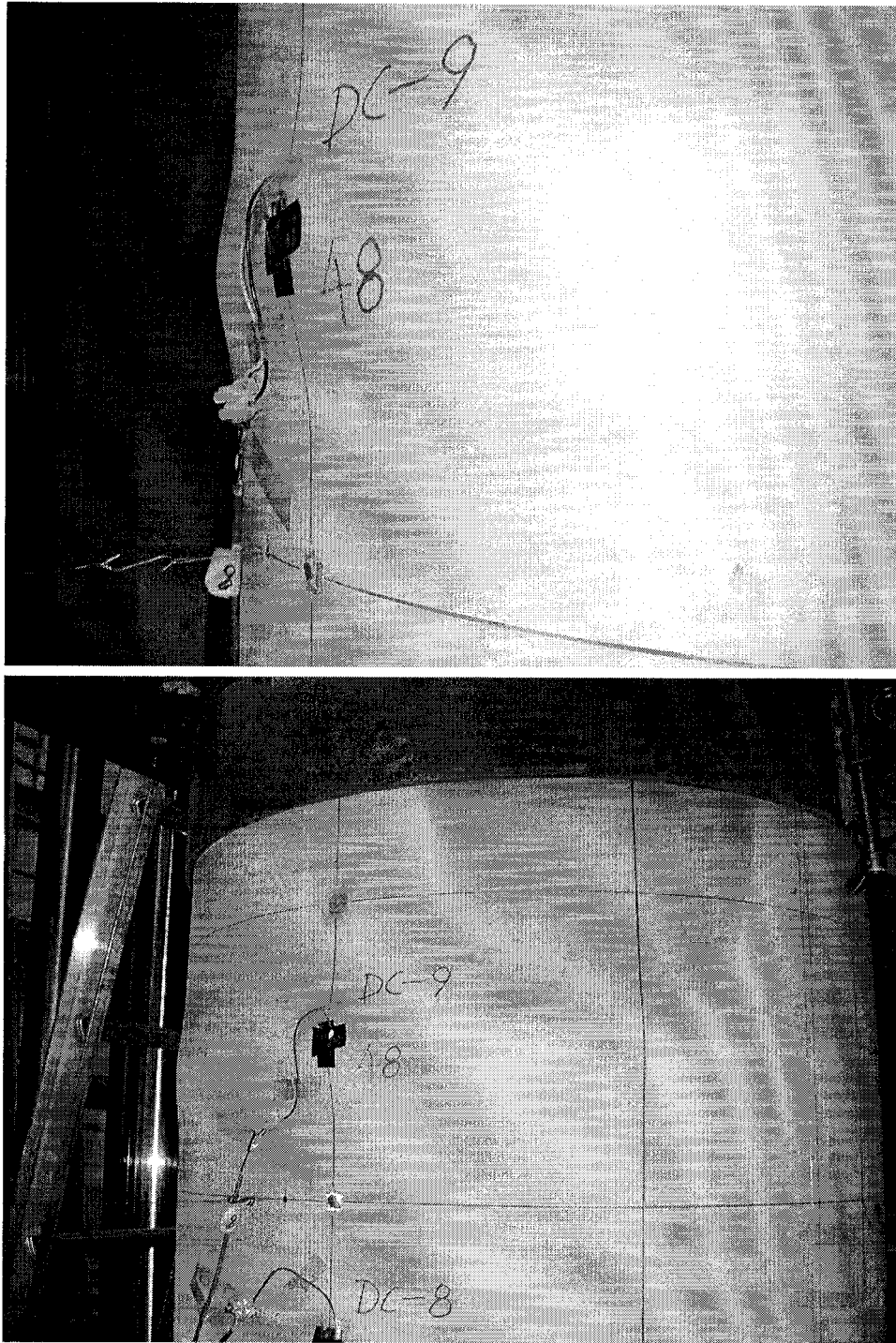


Figure 3.80 Buckle Shape of D30P20BC-9

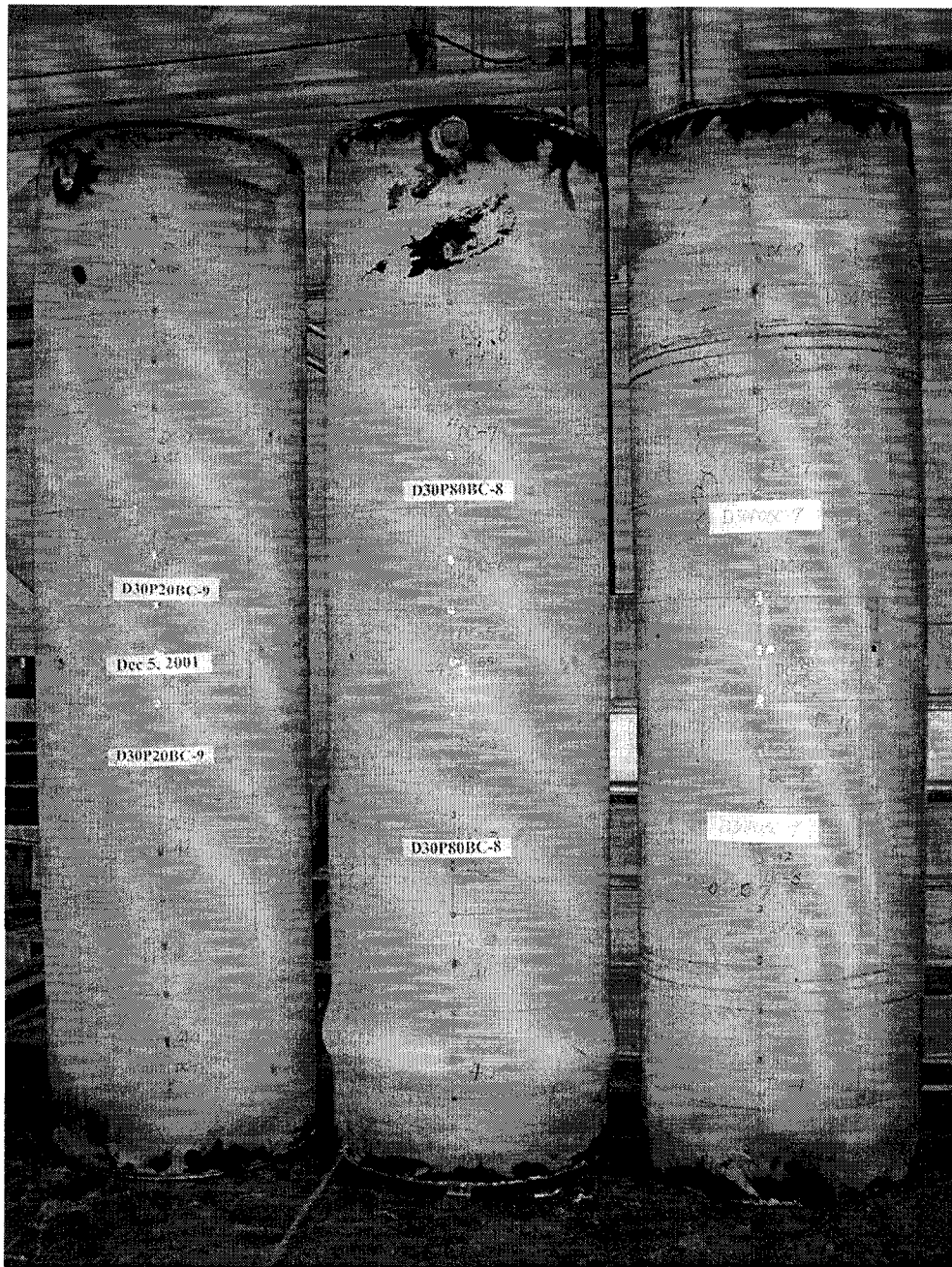


Figure 3.81 The Family Picture of 30 inch Pipes After Tests

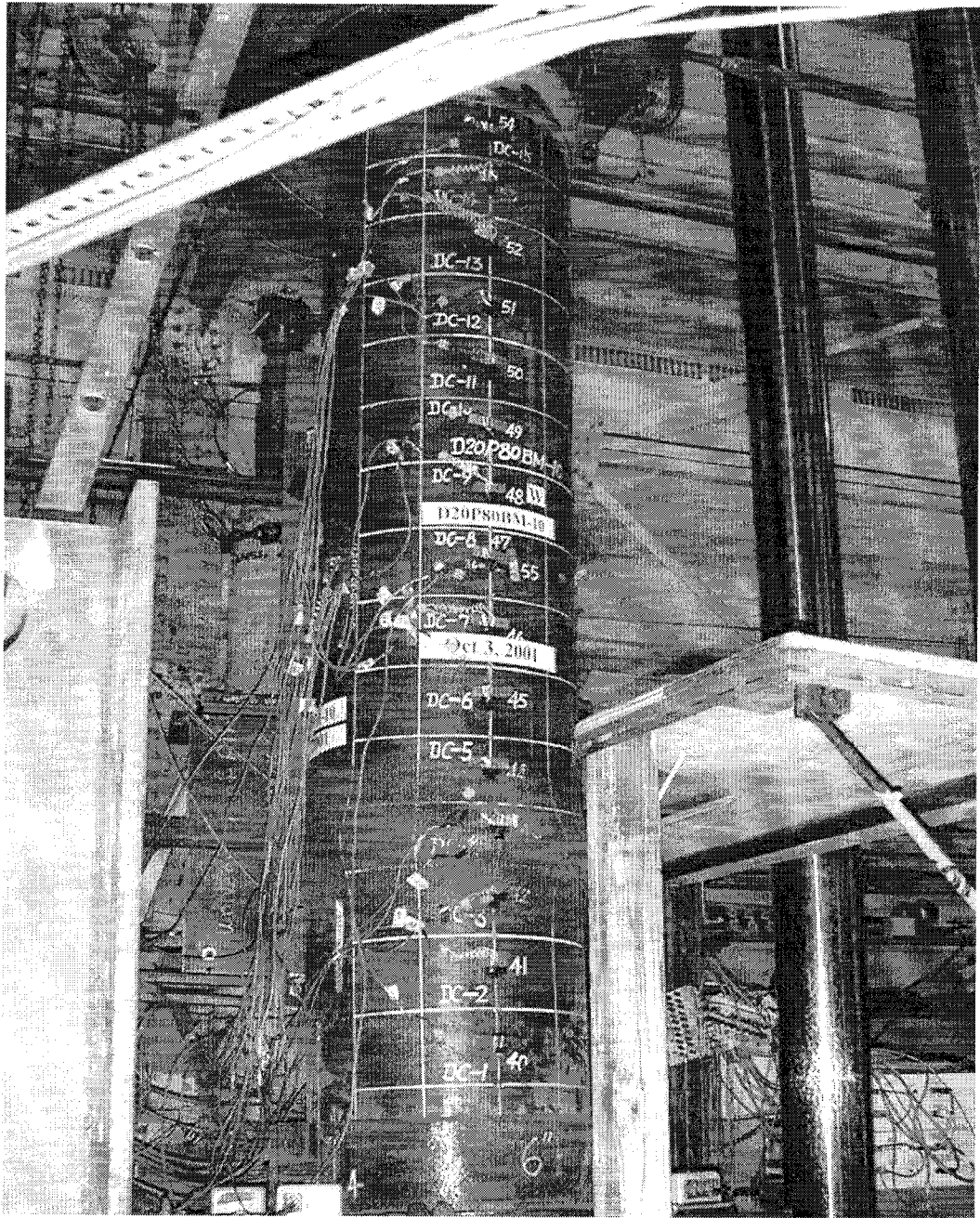


Figure 3.82 Buckle Position in D20P80BM-10

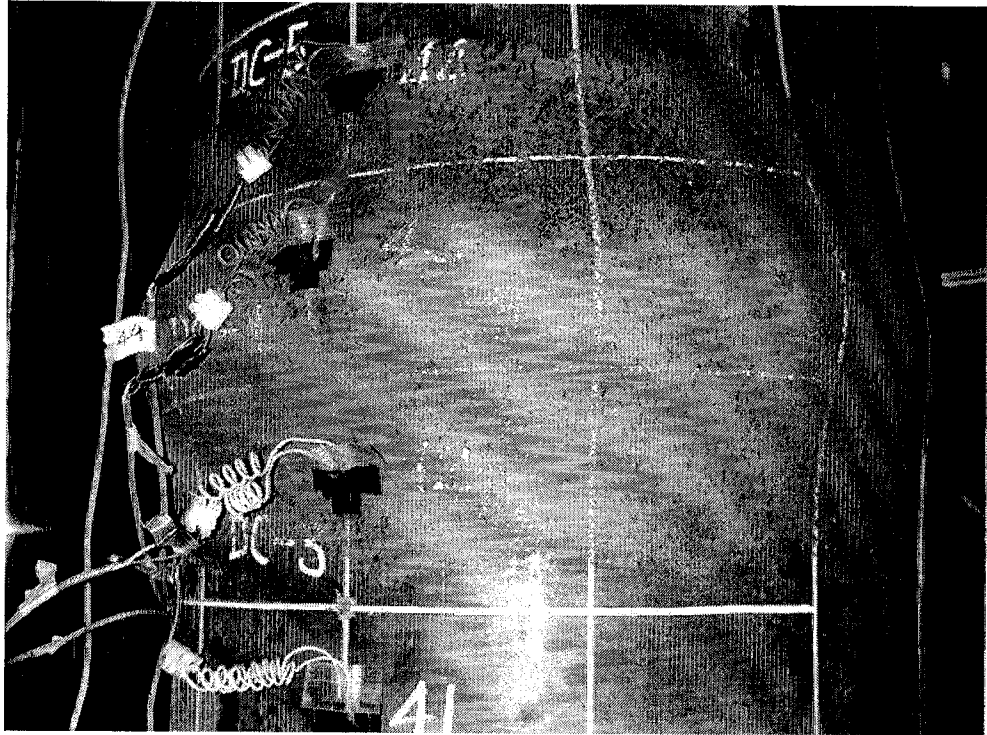


Figure 3.83 Buckle Shape of D20P80BM-10

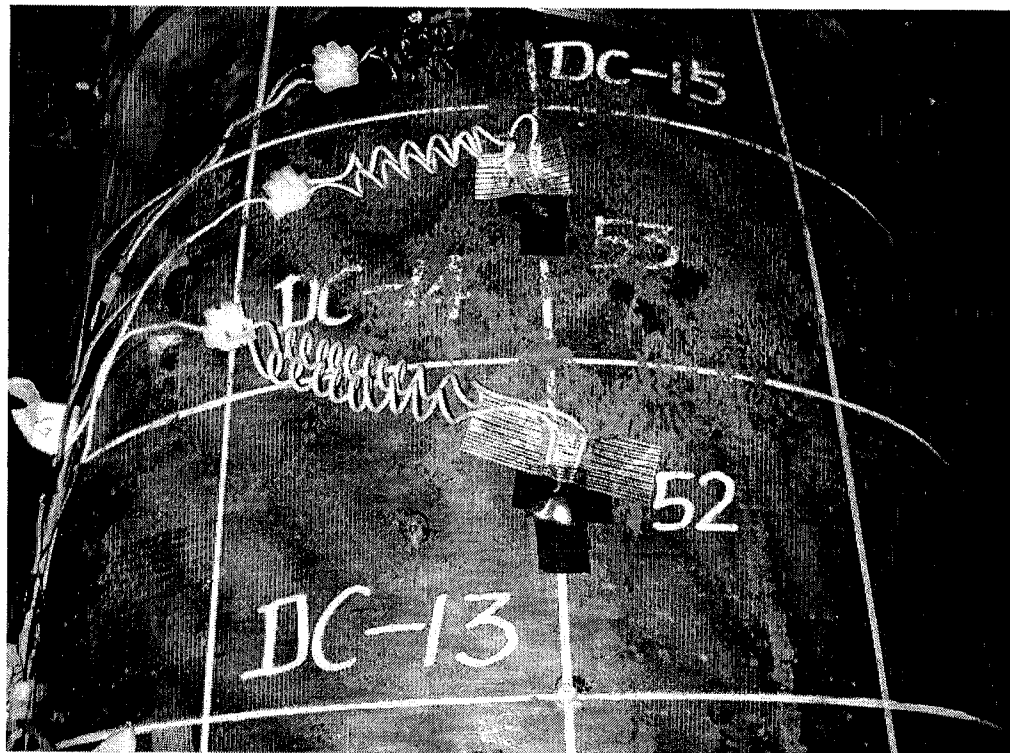


Figure 3.84 Second Bulge Position in D20P80BM-10

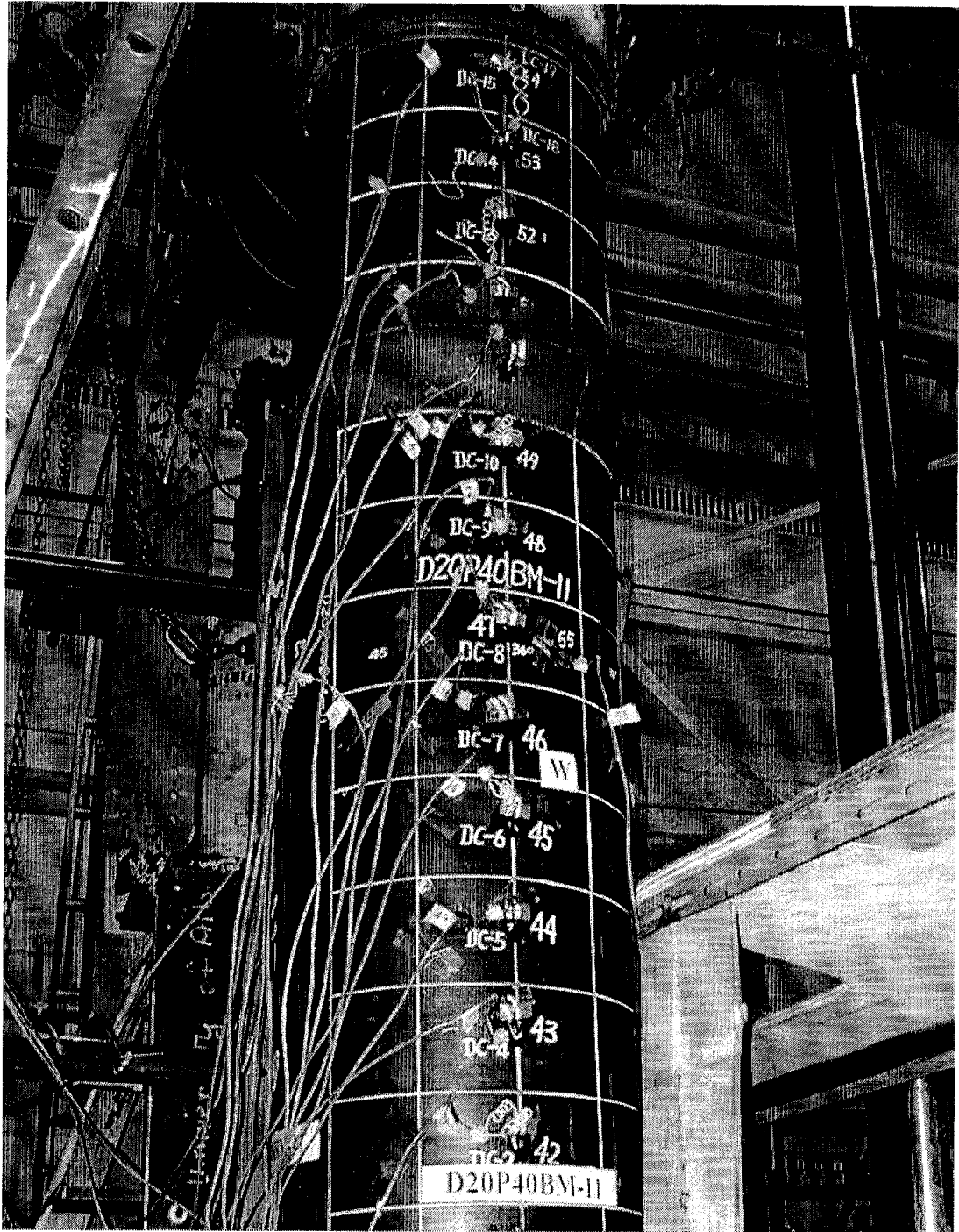


Figure 3.85 Buckle Position in D20P40BM-11

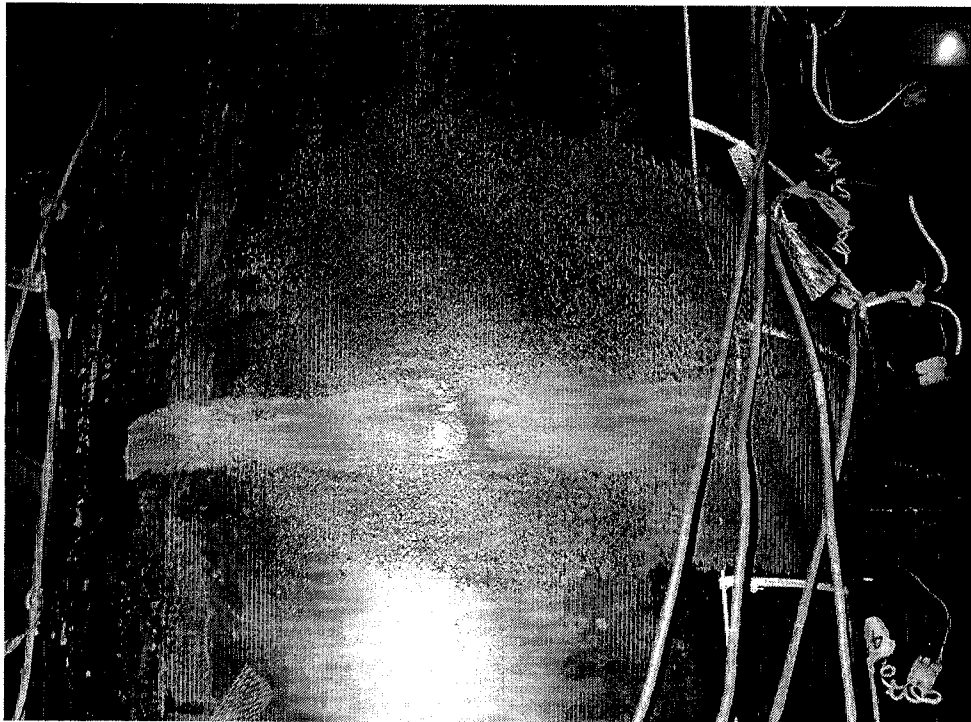


Figure 3.86 Northern View of Buckle Shape in D20P40BM-11

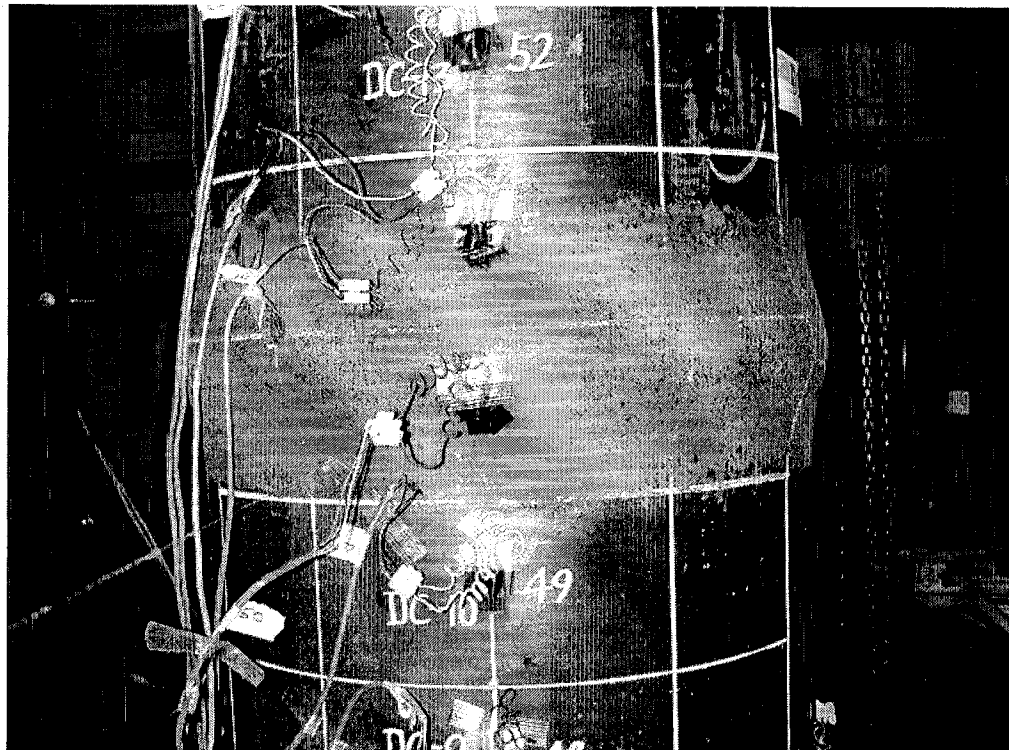


Figure 3.87 Western View of Buckle Shape in D20P40BM-11

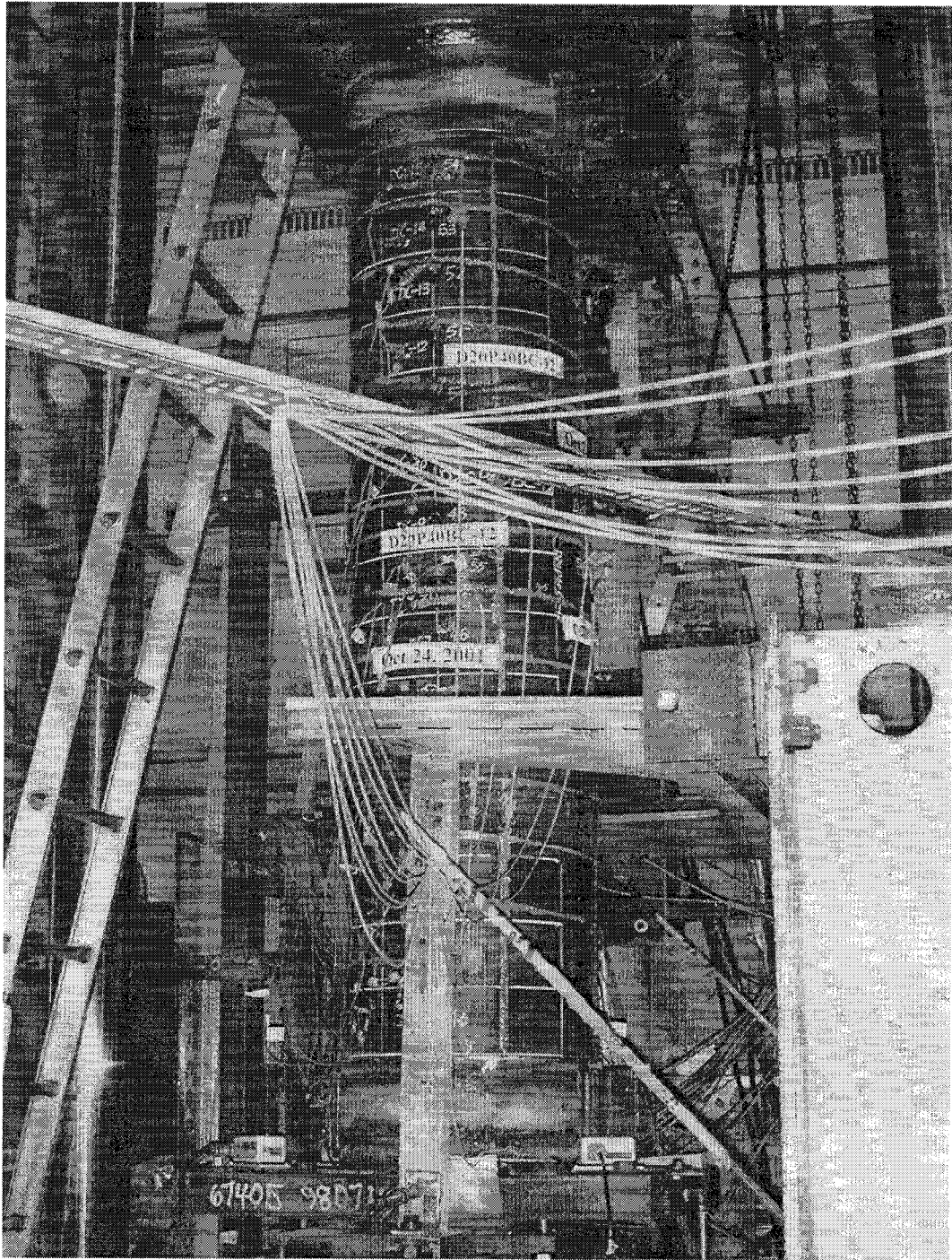


Figure 3.88 Buckle Position in D20P40BC-12

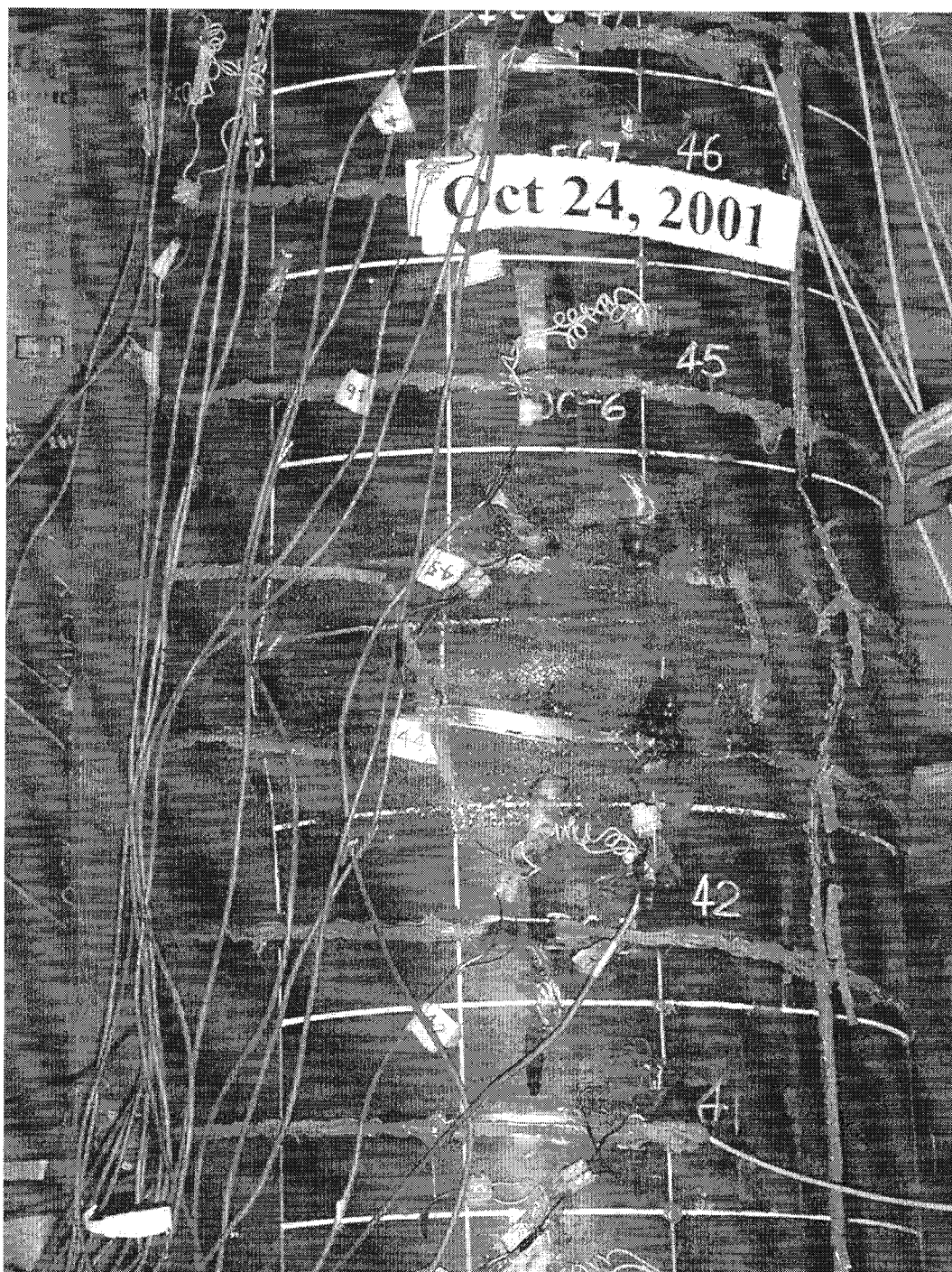


Figure 3.89 Buckle Position in D20P40BC-12

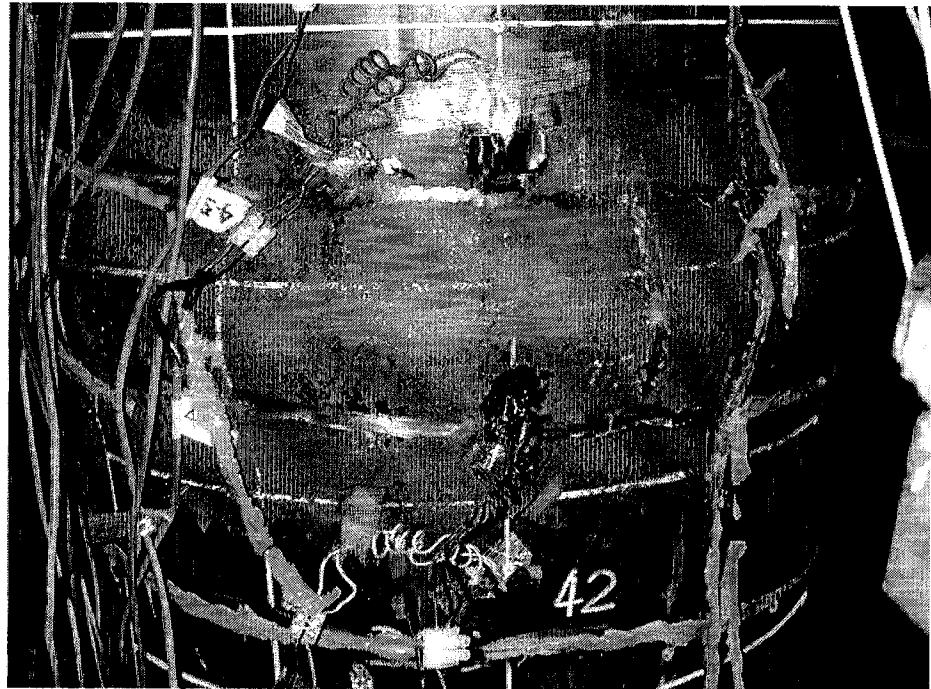


Figure 3.90 Buckle Shape of D20P40BC-12



Figure 3.91 Second Bulge Position in D20P40BC-12



Figure 3.92 The Family Picture of 20 inch Pipes after Tests

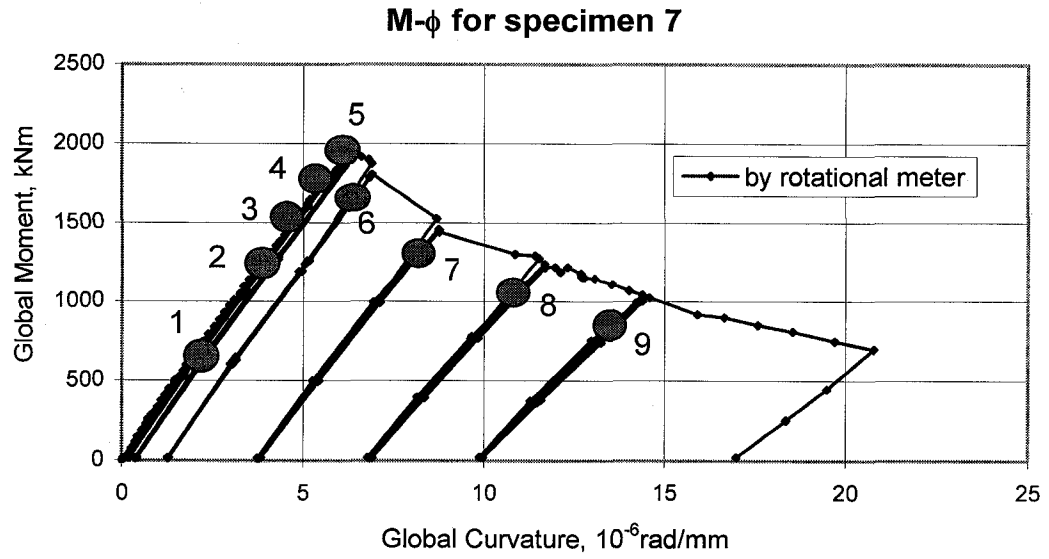


Figure 3.93 Global Moment vs. Global Curvature For D30P0BC-7

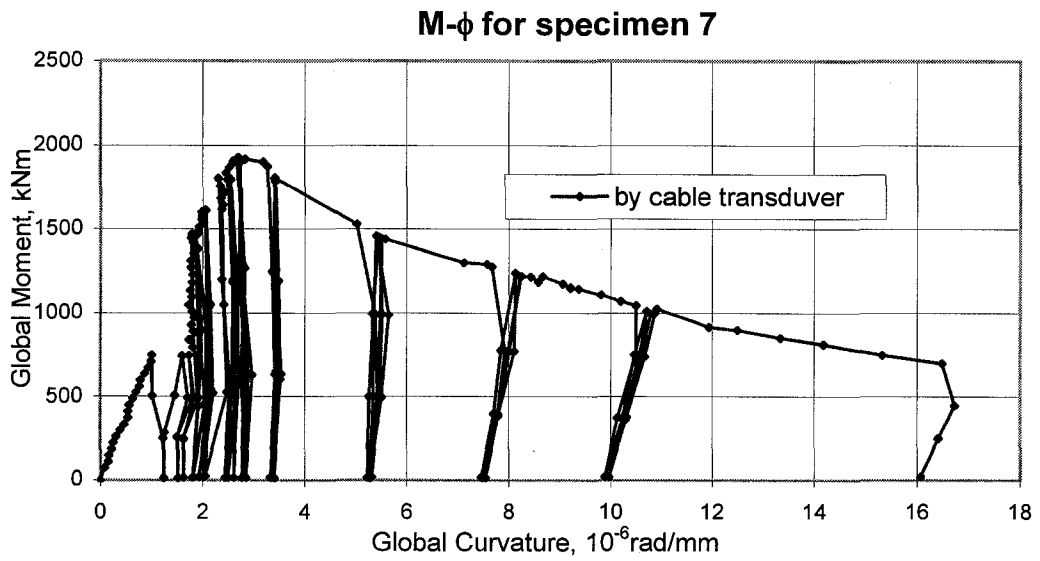


Figure 3.94 Global Moment vs. Global Curvature For D30P0BC-7

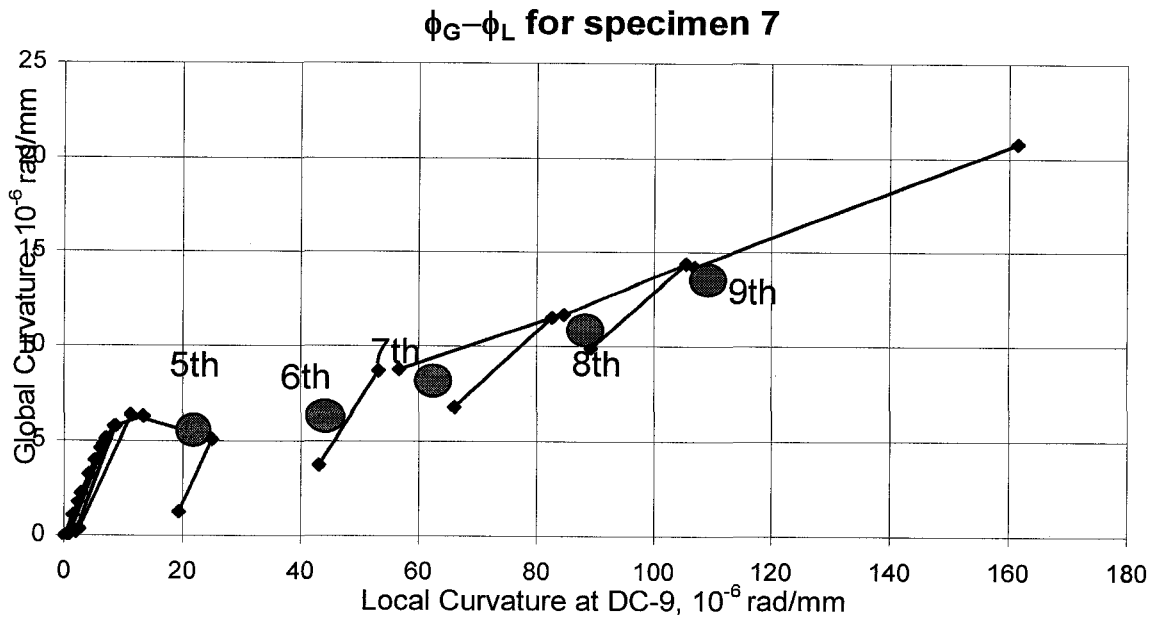


Figure 3.97 Global Curvature vs. Local Curvature at DC-9 For D30P0BC-7

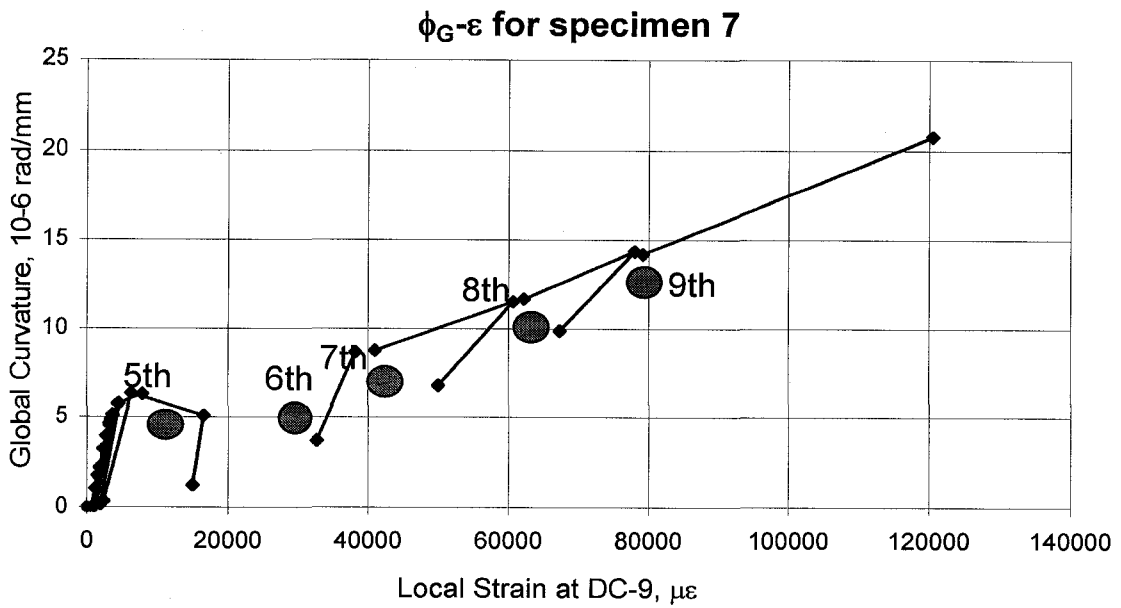


Figure 3.98 Global Curvature vs. Local Strain at DC-9 For D30P0BC-7

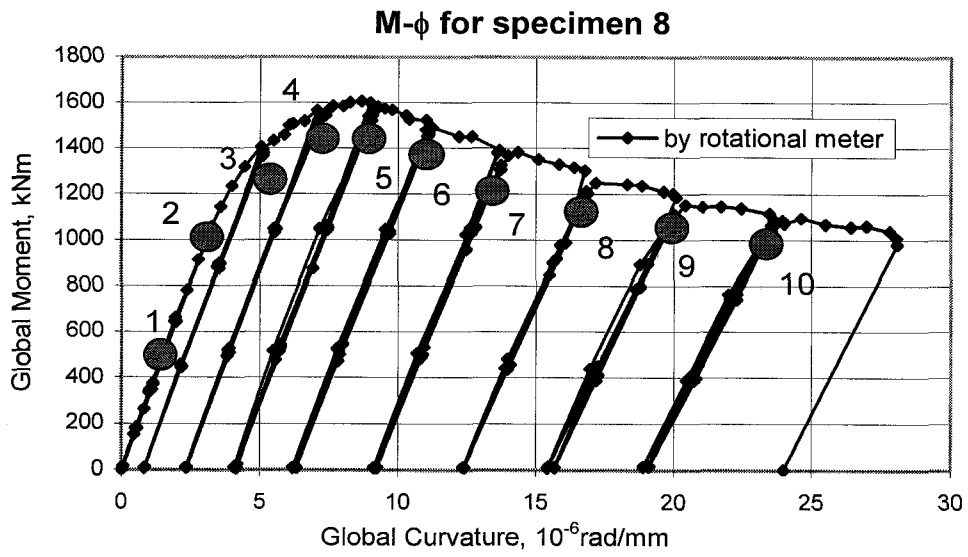


Figure 3.99 Global Moment vs. Global Curvature For D30P80BC-8

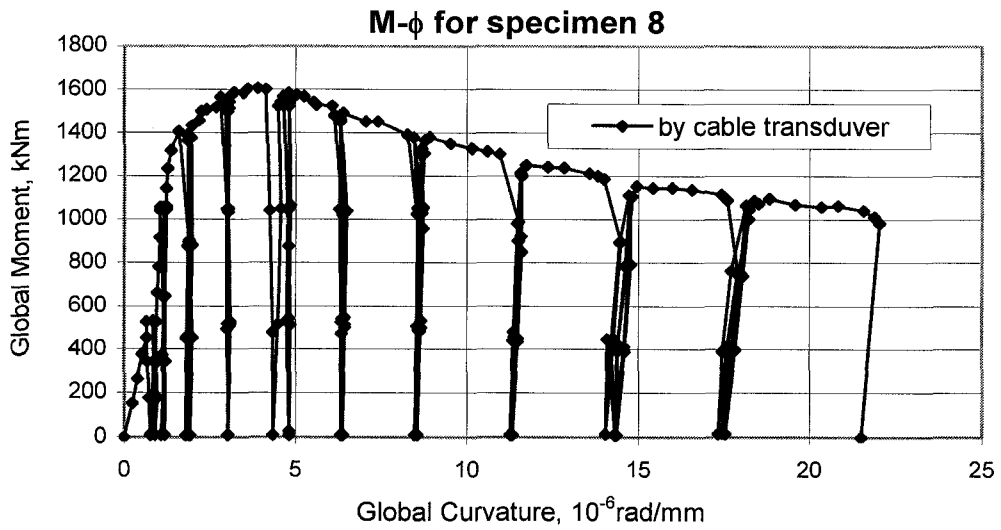


Figure 3.100 Global Moment vs. Global Curvature For D30P80BC-8

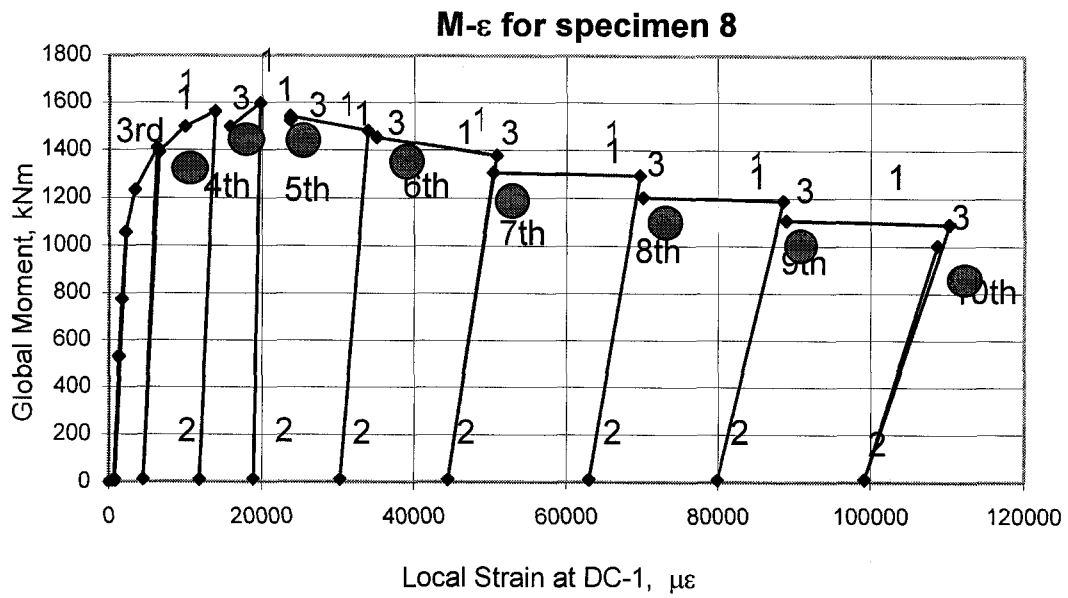


Figure 3.101 Global Moment vs. Local Strain At DC-1 For D30P80BC-8

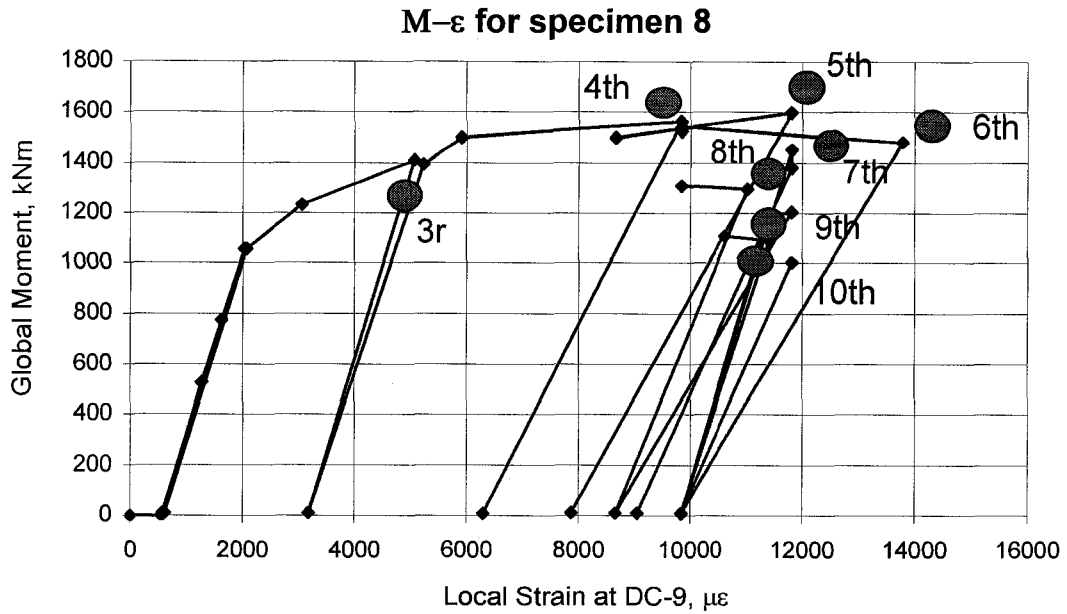


Figure 3.102 Global Moment vs. Local Strain At DC-9 For D30P80BC-8

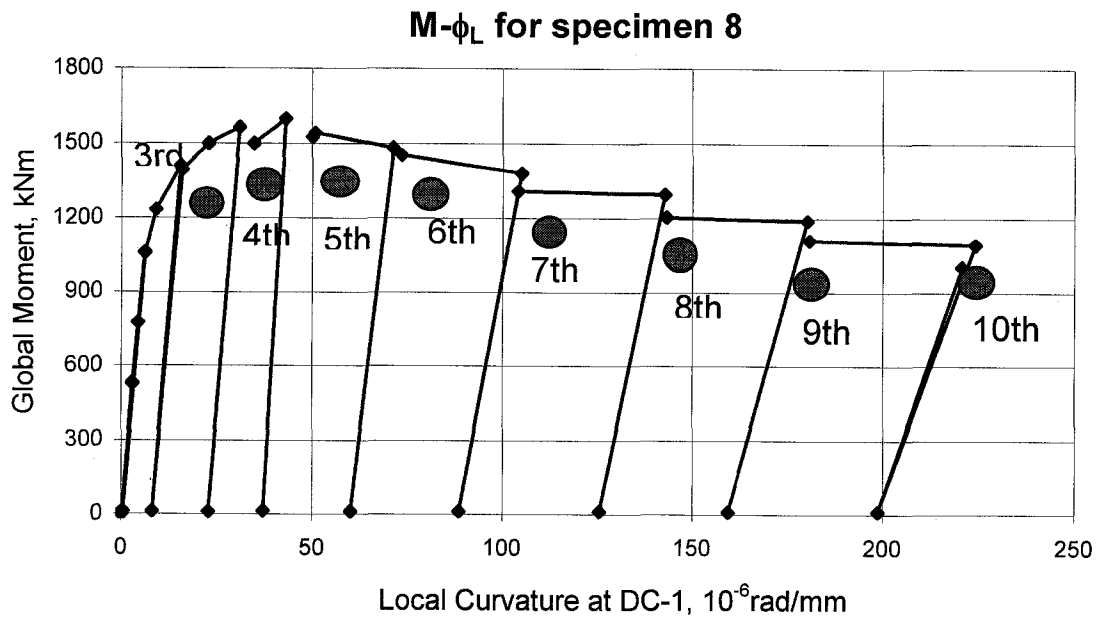


Figure 3.103 Global Moment vs. Local Curvature At DC-1 For D30P80BC-8

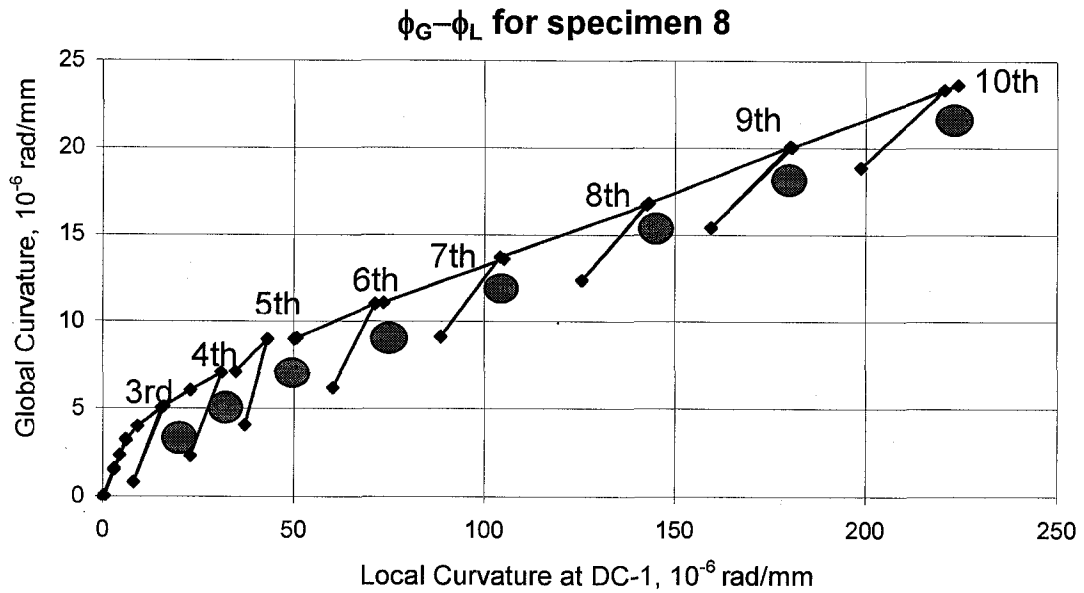


Figure 3.104 Global Curvature vs. Local Curvature At DC-1 For D30P80BC-8

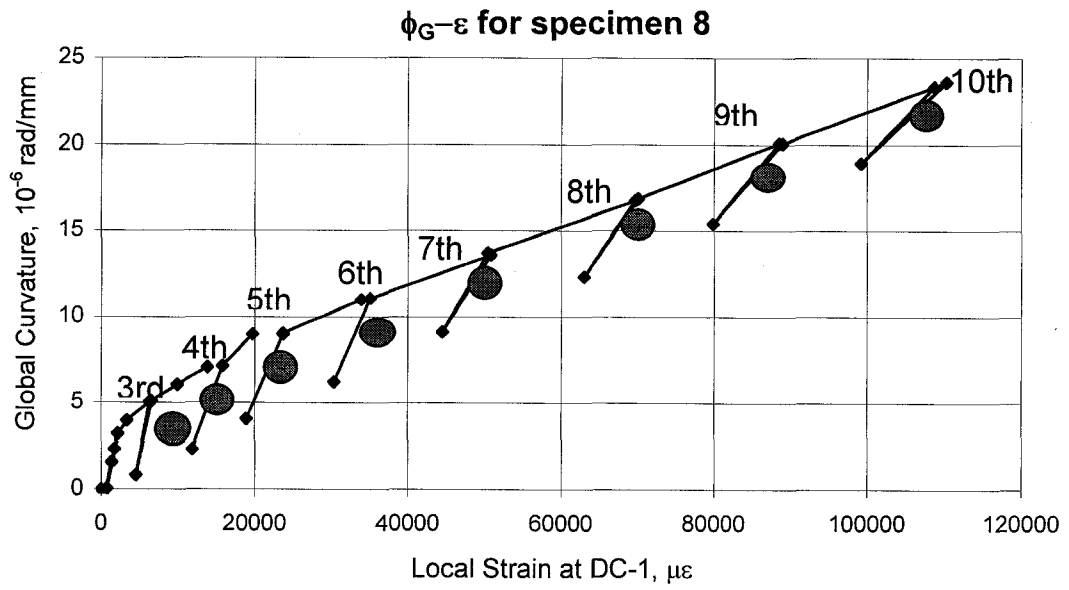


Figure 3.105 Global Curvature vs. Local Strain At DC-1 For D30P80BC-8

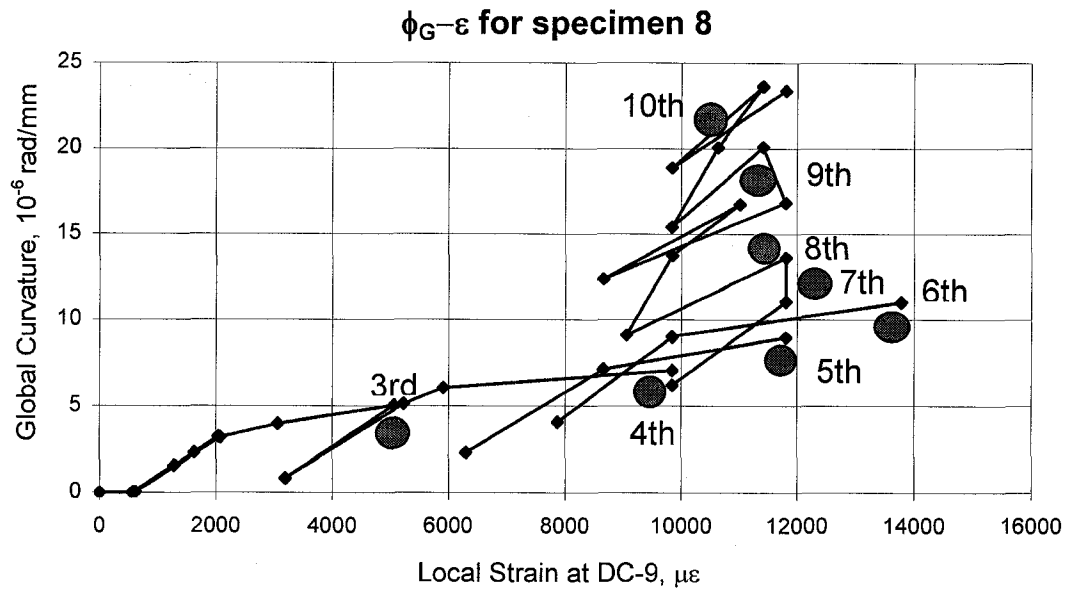


Figure 3.106 Global Curvature vs. Local Strain At DC-9 For D30P80BC-8

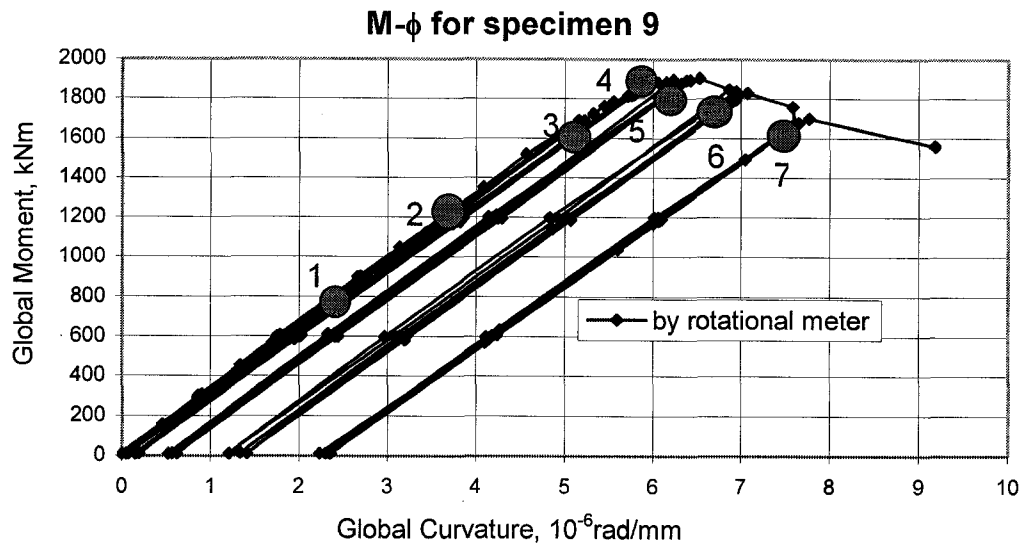


Figure 3.107 Global Moment vs. Global Curvature For D30P20BC-9

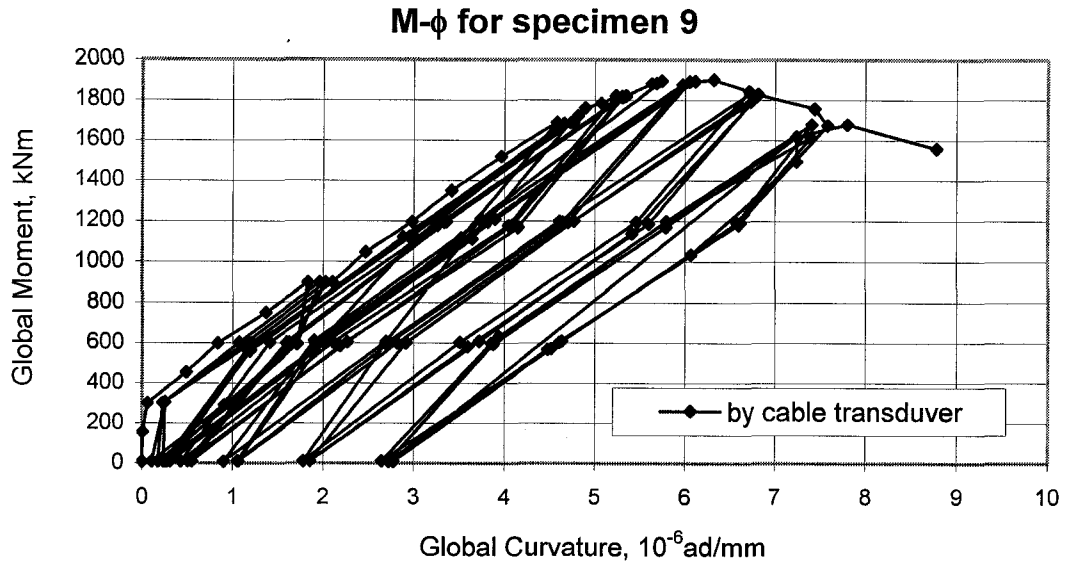


Figure 3.108 Global Moment vs. Global Curvature For D30P20BC-9

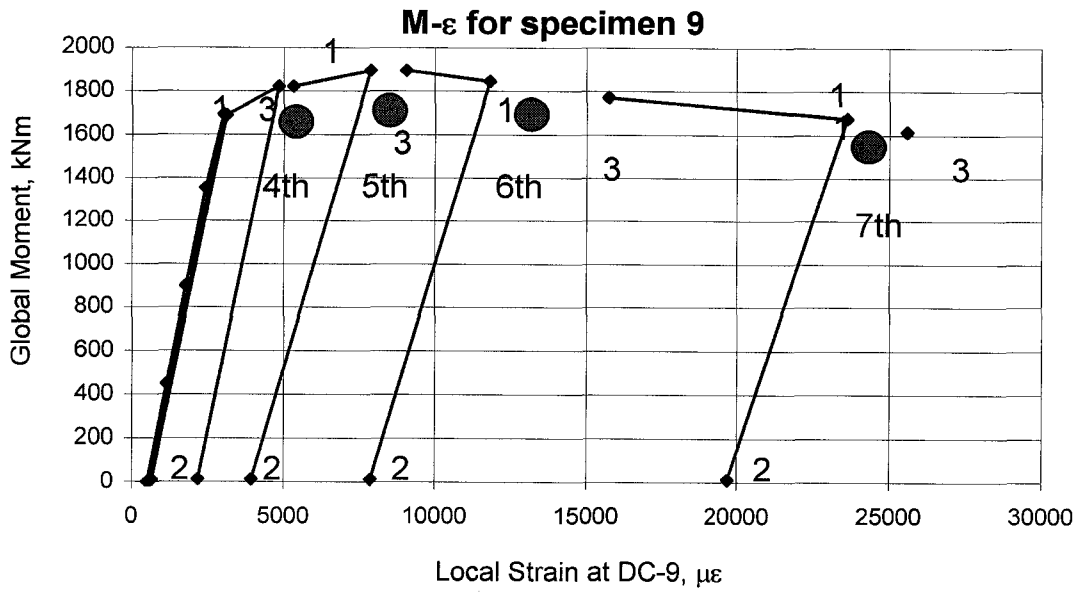


Figure 3.109 Global Moment vs. Local Strain At DC-9 For D30P20BC-9

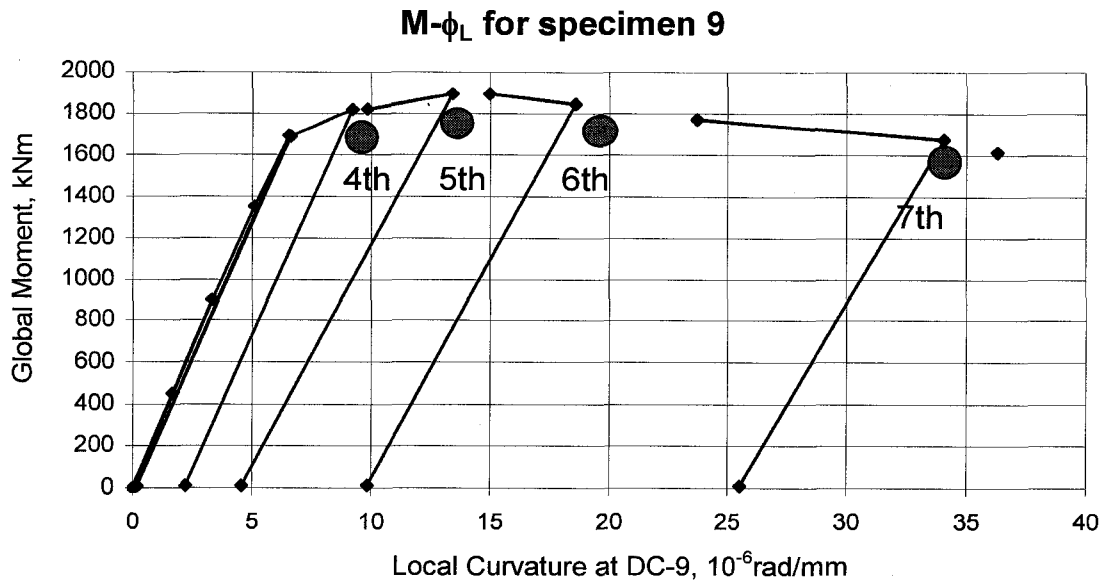


Figure 3.110 Global Moment vs. Local Curvature At DC-9 For D30P20BC-9

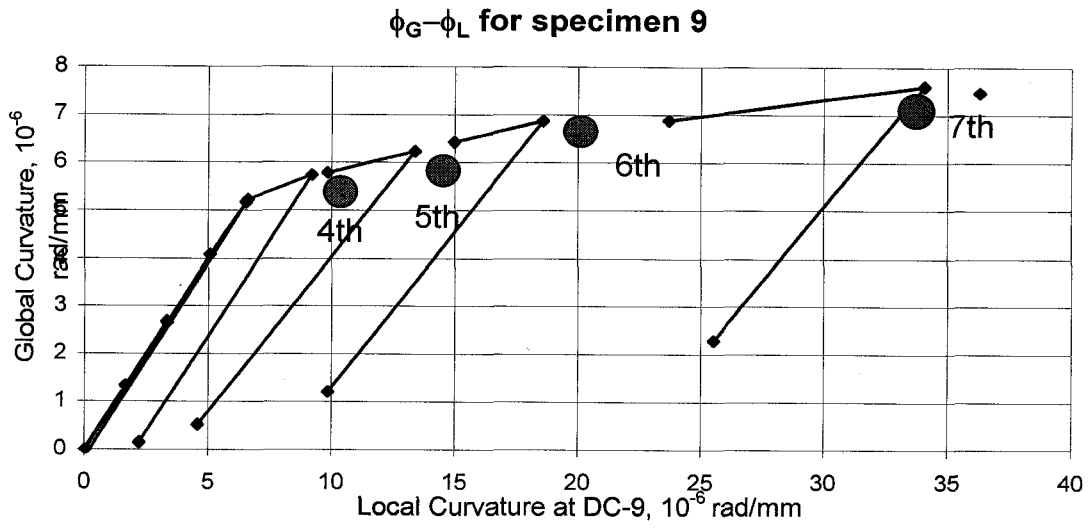


Figure 3.111 Global Curvature vs. Local Curvature At DC-9 For D30P20BC-9

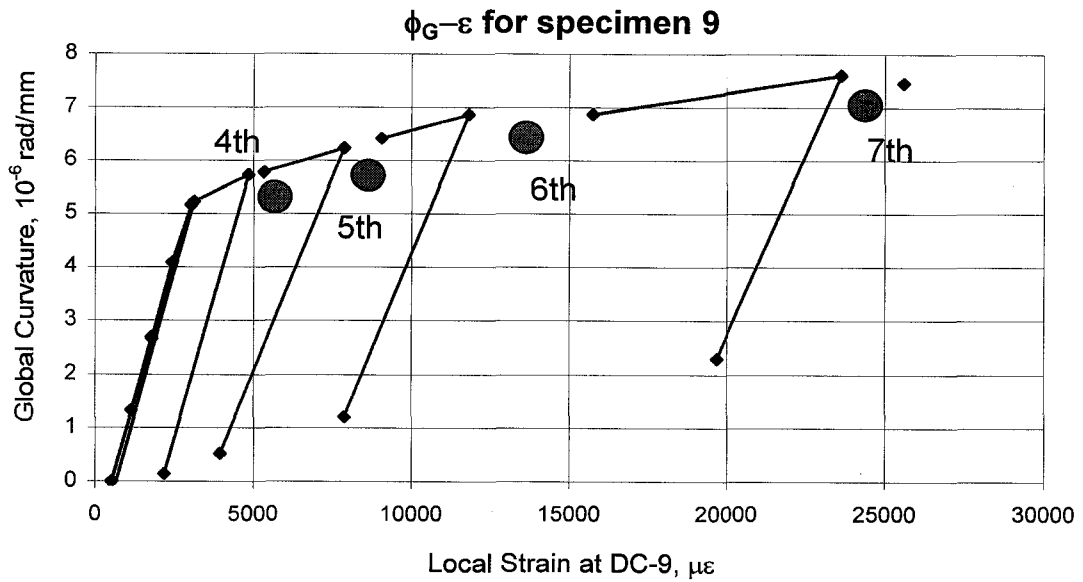


Figure 3.112 Global Curvature vs. Local Strain At DC-9 For D30P20BC-9

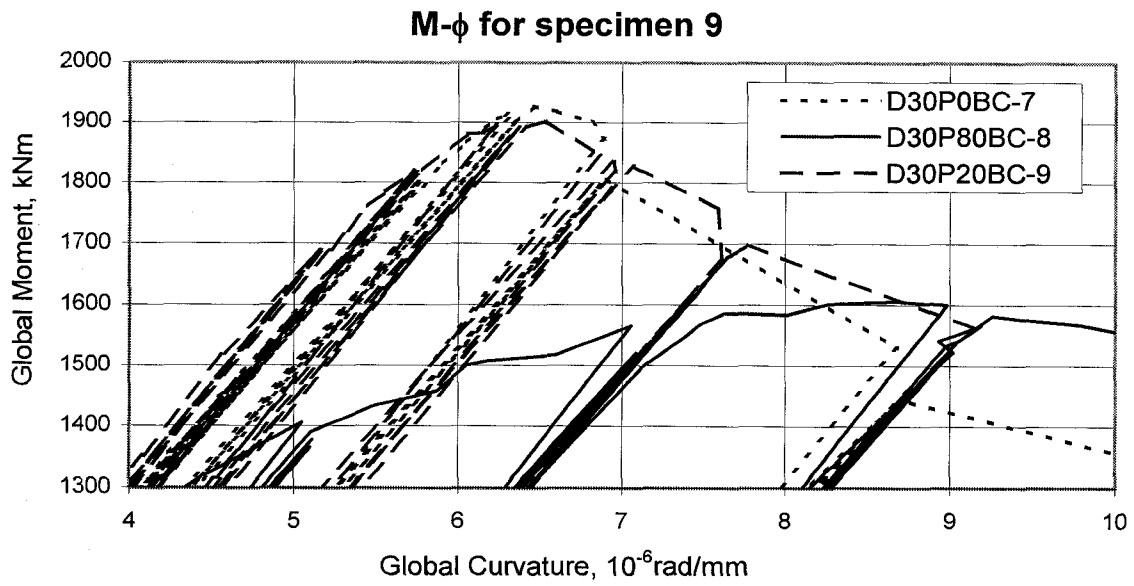


Figure 3.113 Global Moment vs. Global Curvature For 30' Pipes

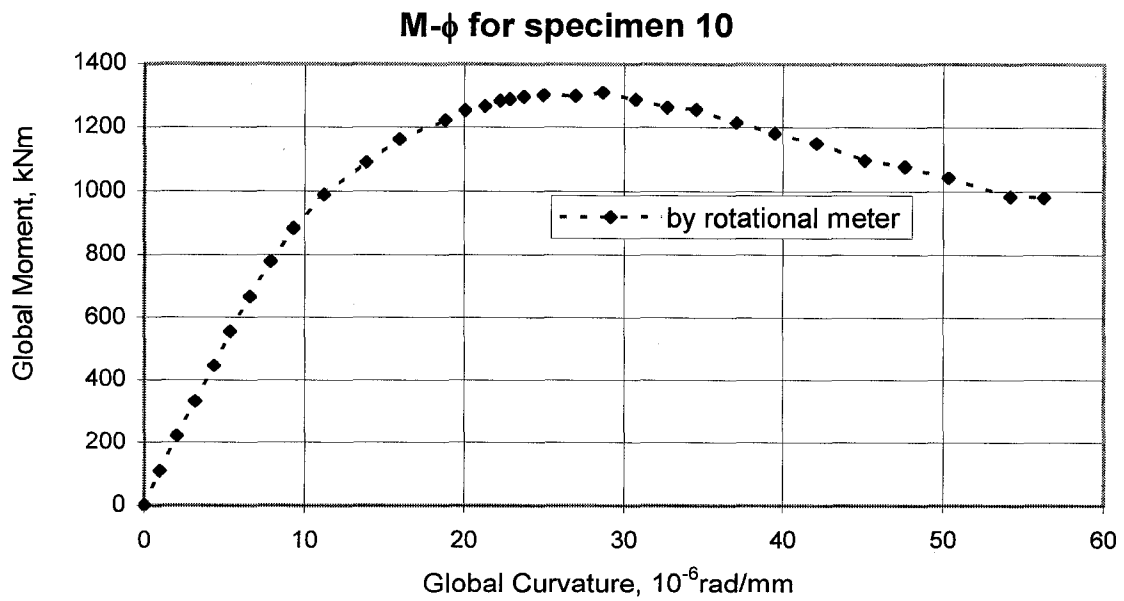


Figure 3.114 Global Moment vs. Global Curvature For D20P80BM-10

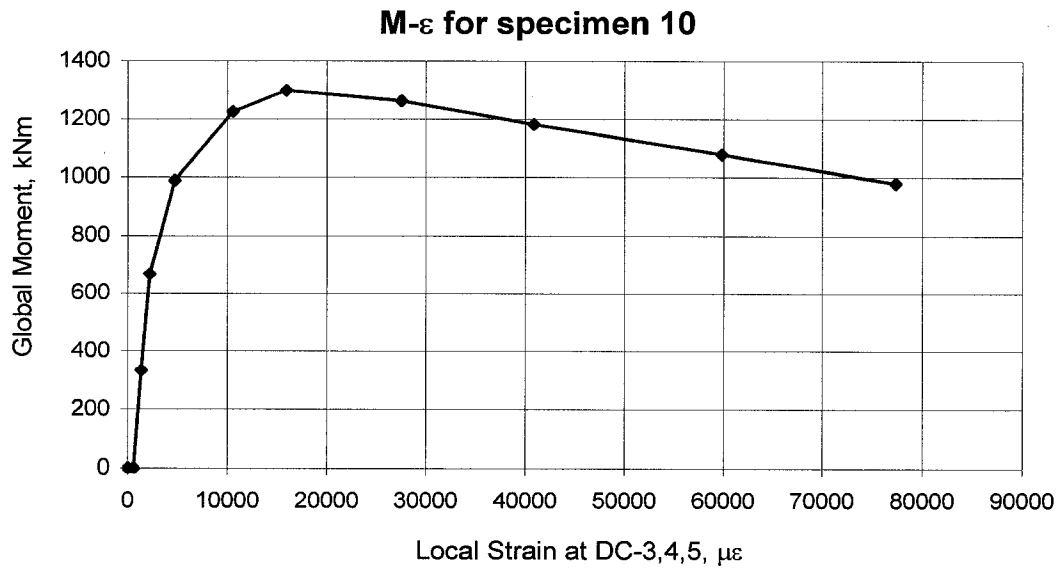


Figure 3.115 Global Moment vs. Local Strain At DC-3,4,5 For D20P80BM-10

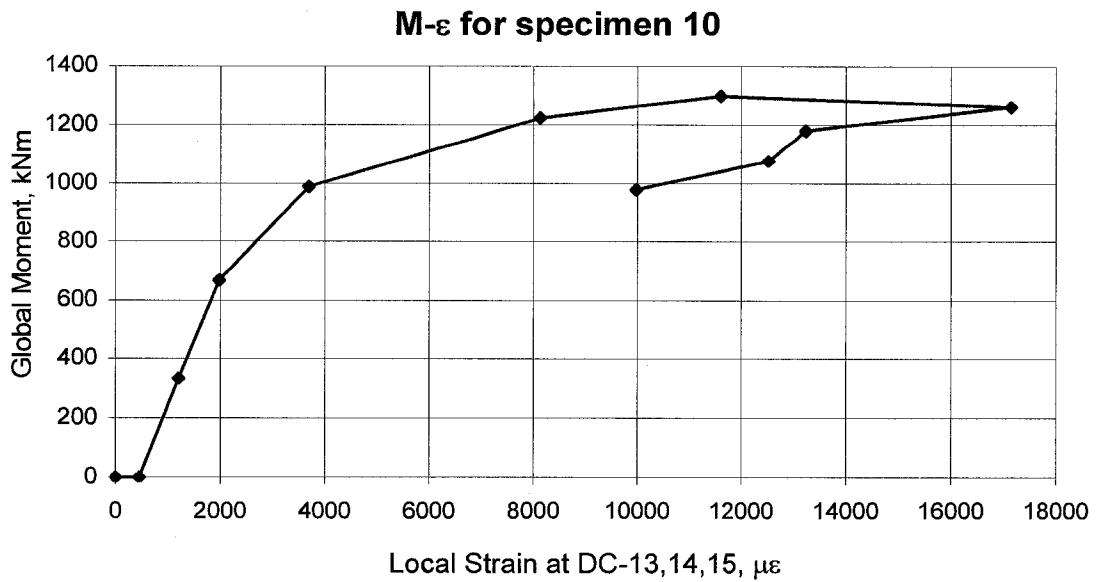


Figure 3.116 Global Moment vs. Local Strain At DC-13,14,15 For D20P80BM-10

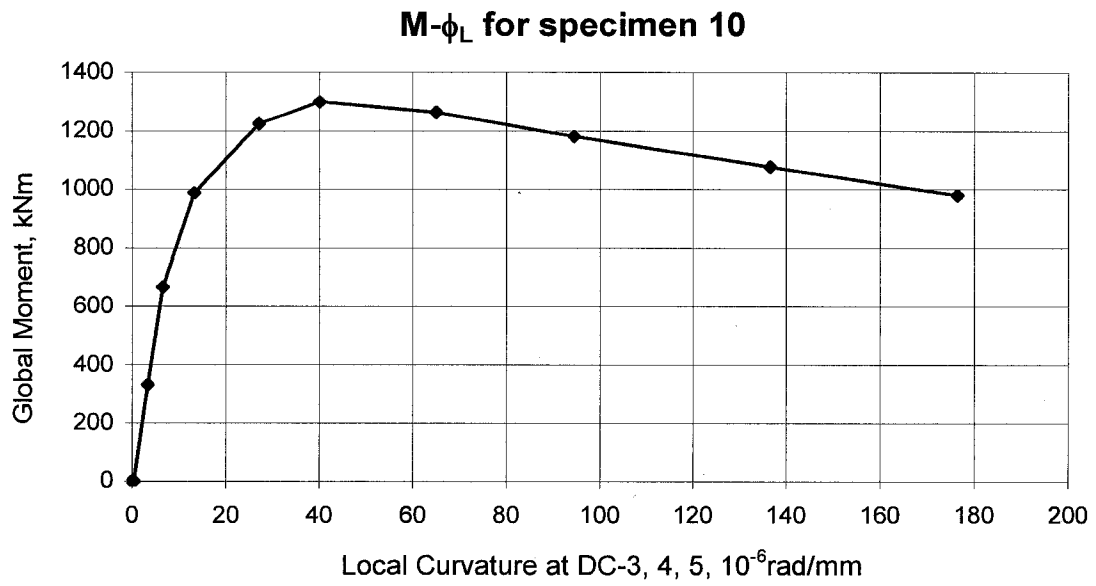


Figure 3.117 Global Moment vs. Local Curvature At DC-3,4,5 For D20P80BM-10

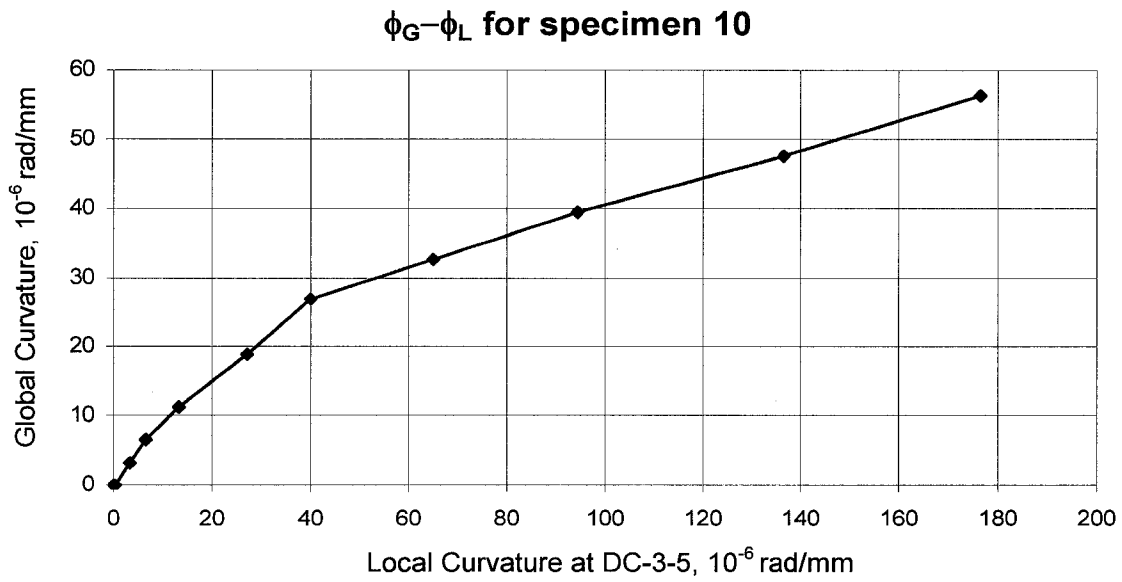


Figure 3.118 Global Curvature vs. Local Curvature At DC-3-5 For D20P80BM-10

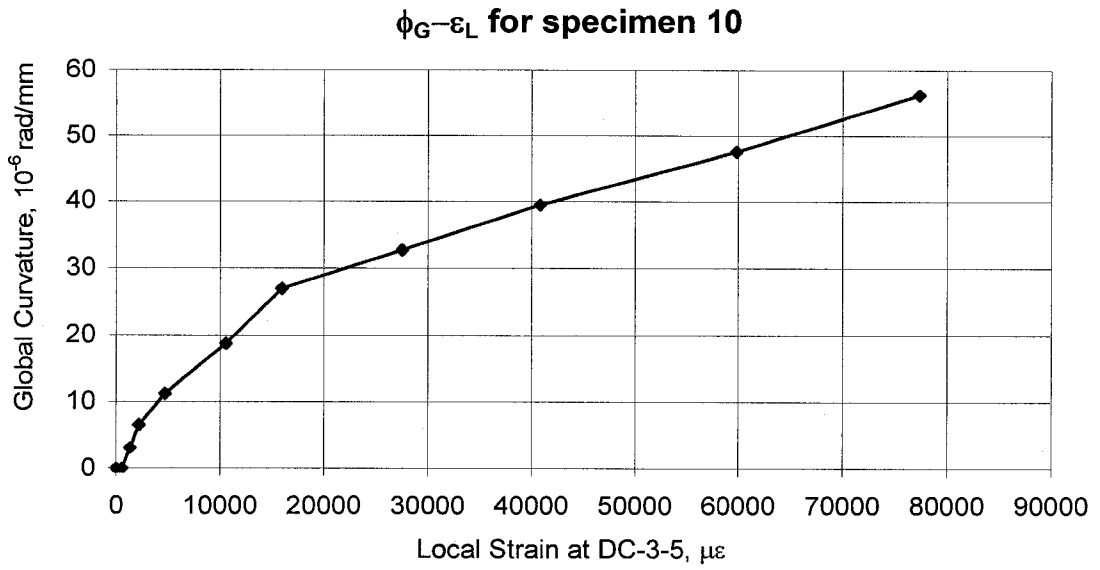


Figure 3.119 Global Curvature vs. Local Strain At DC-3-5 For D20P80BM-10

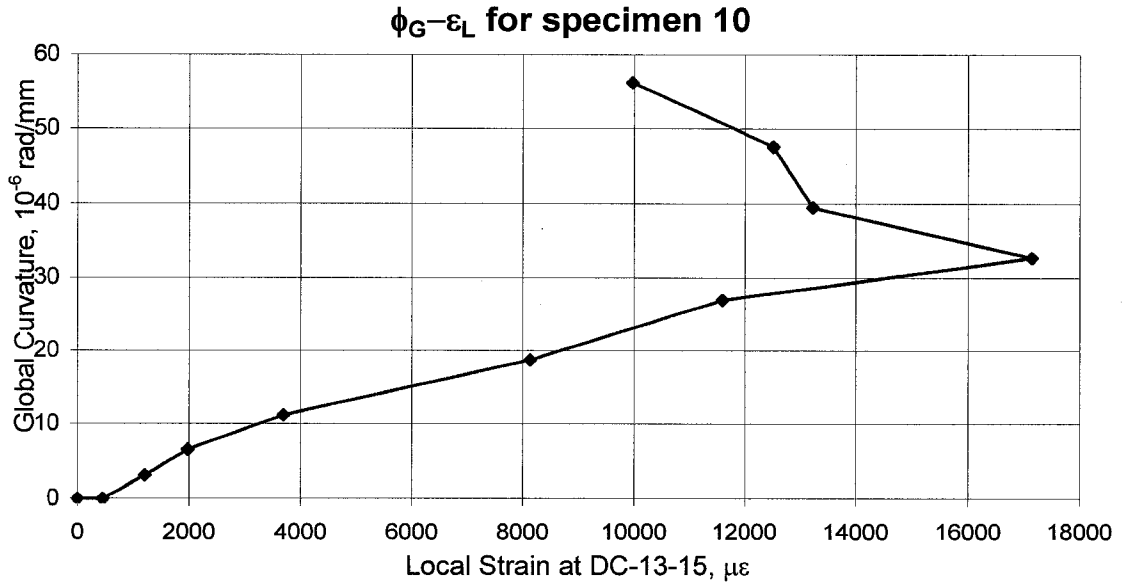


Figure 3.120 Global Curvature vs. Local Strain At DC-13-15 For D20P80BM-10

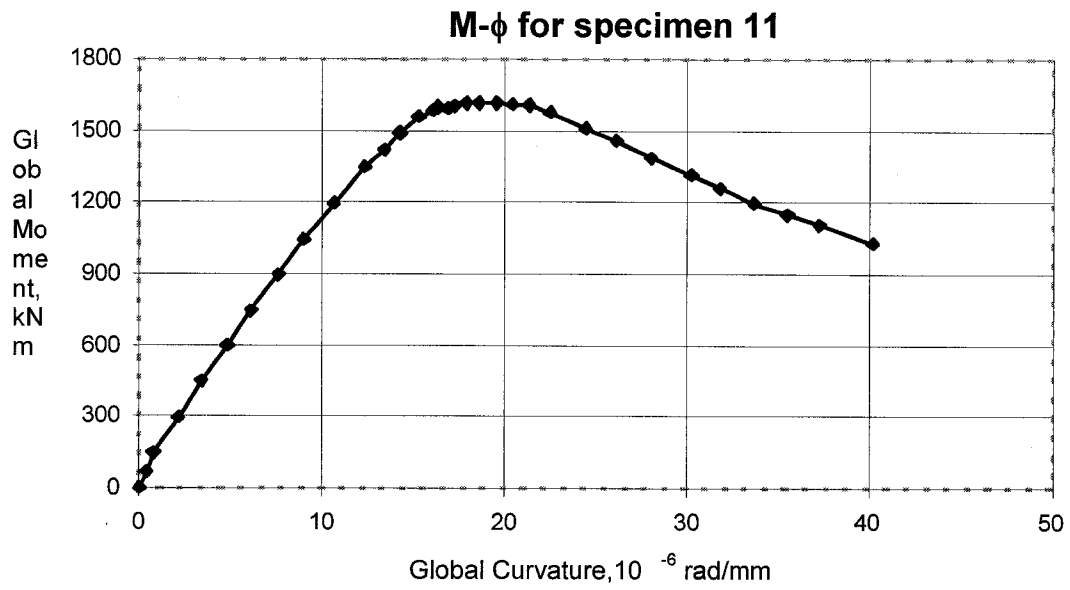


Figure 3.121 Global Moment vs. Global Curvature For D20P40BM-11

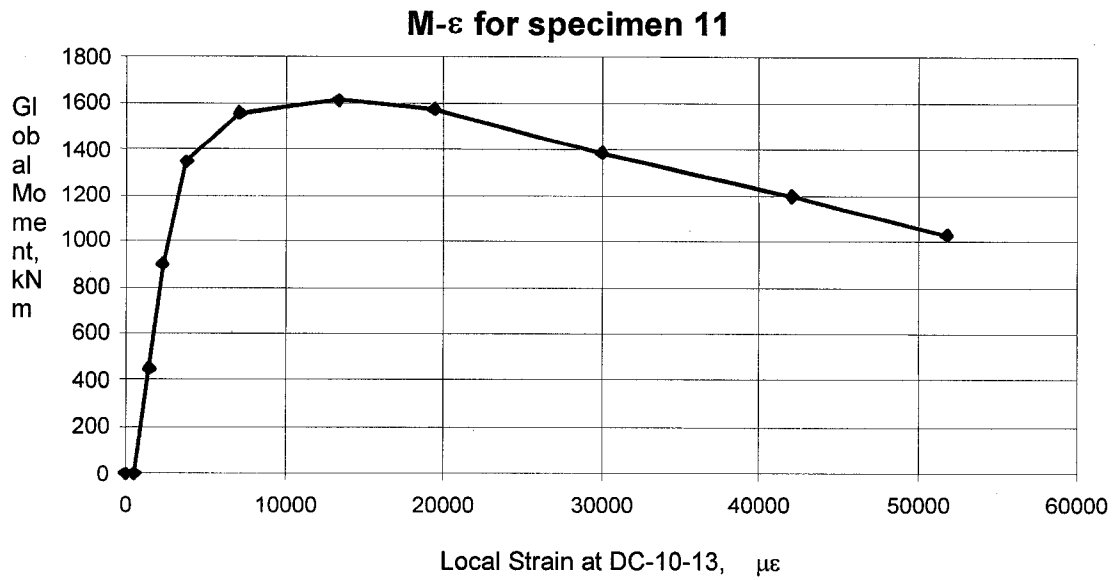


Figure 3.122 Global Moment vs. Local Strain At DC-10-13 For D20P40BM-11

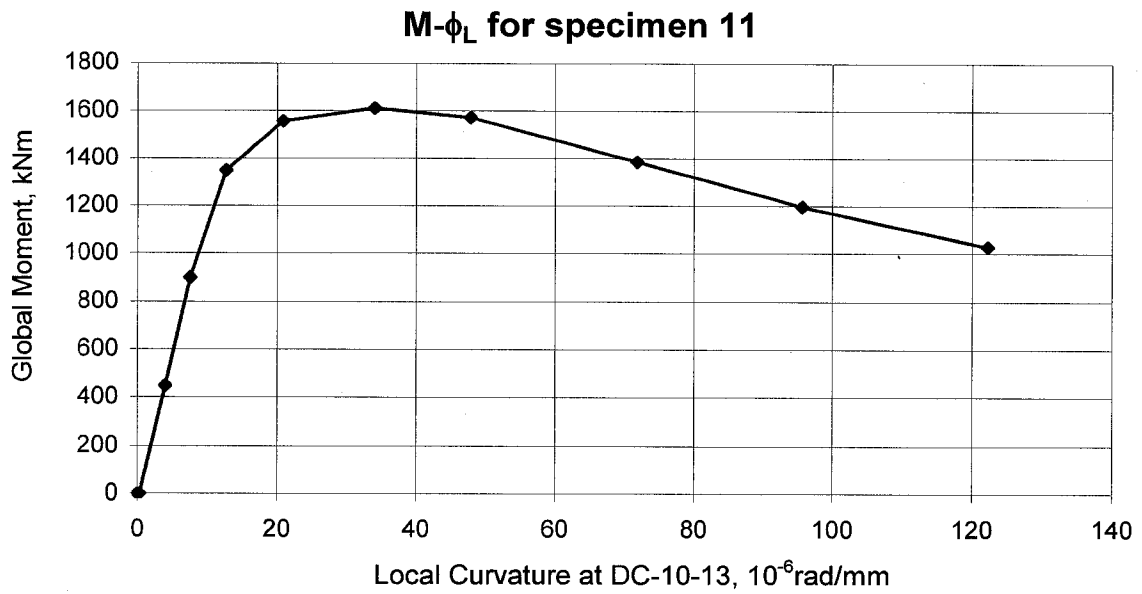


Figure 3.123 Global Moment vs. Local Curvature At DC-10-13 For D20P40BM-11

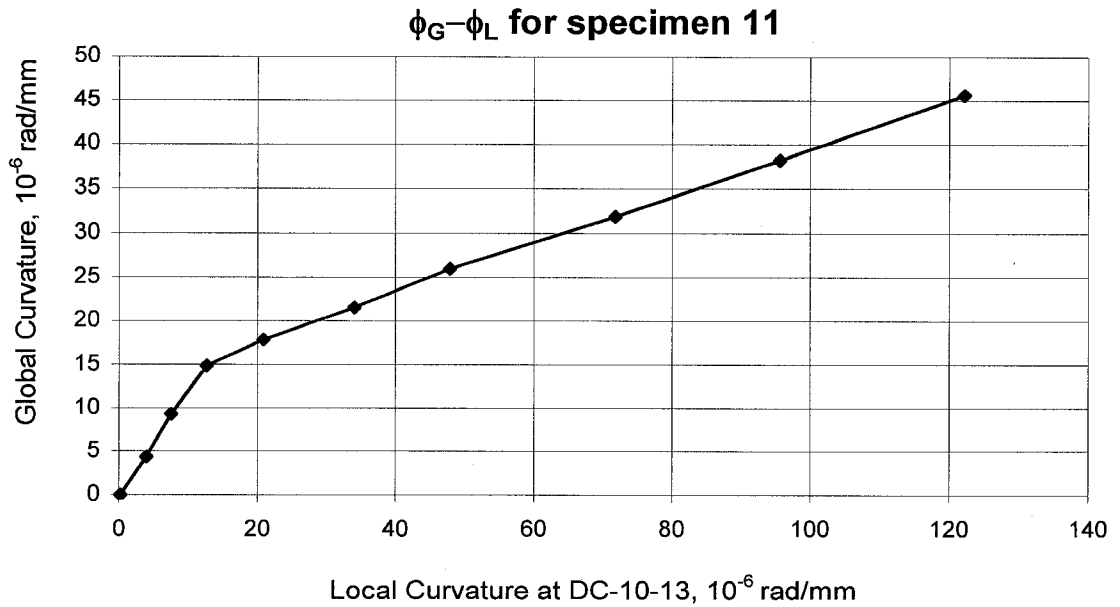


Figure 3.124 Global Curvature vs. Local Curvature At DC-10-13 For D20P40BM-11

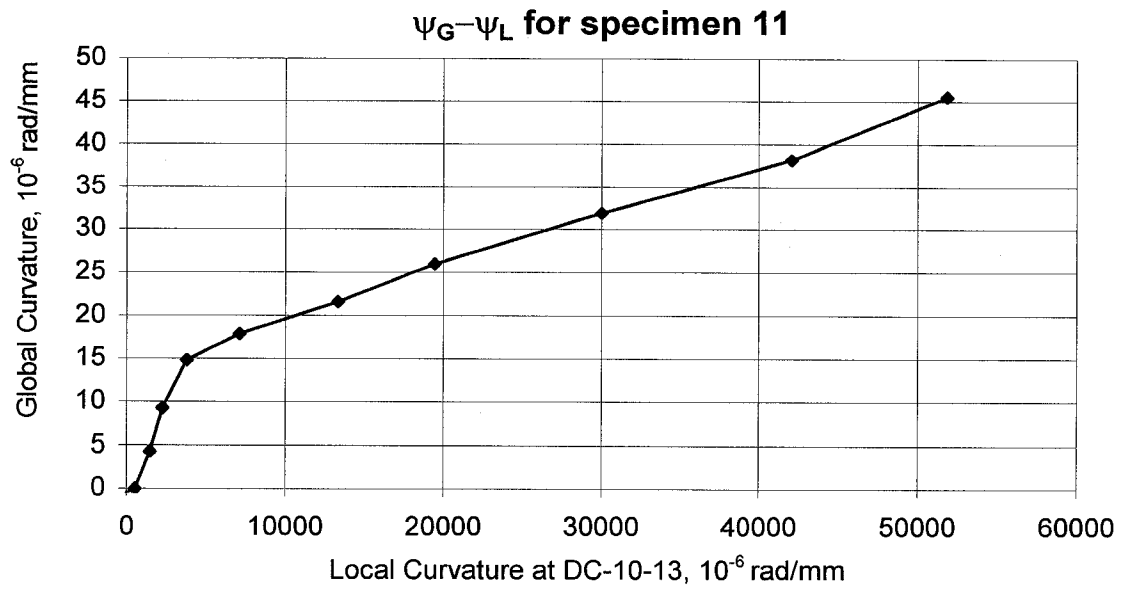


Figure 3.125 Global Curvature vs. Local Strain At DC-10-13 For D20P40BM-11

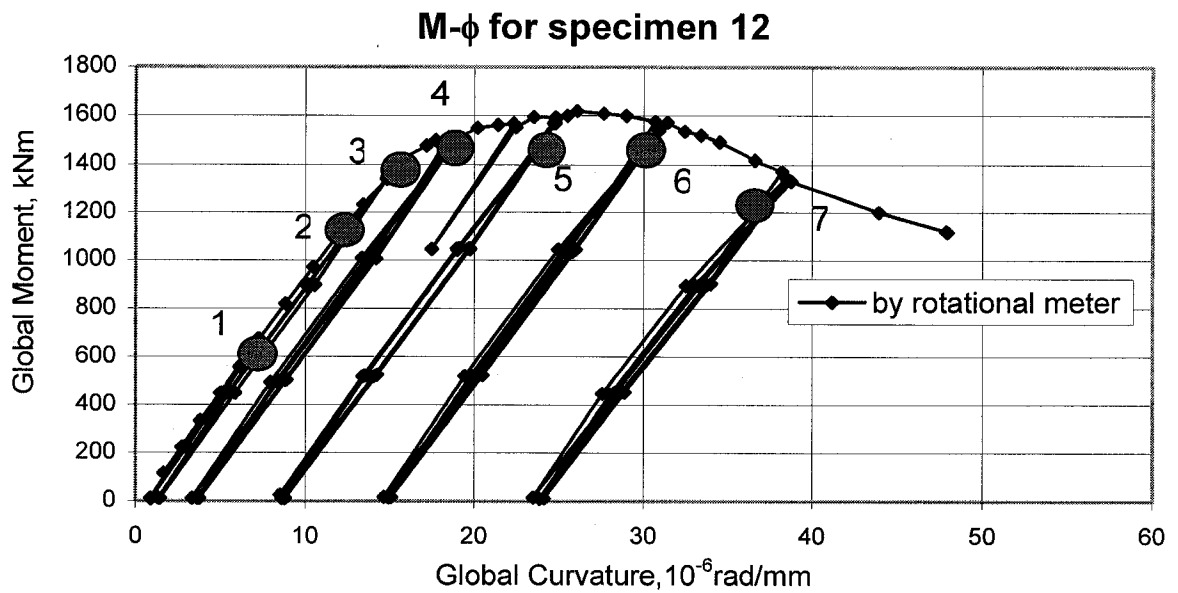


Figure 3.126 Global Moment vs. Global Curvature For D20P40BC-12

Global Moment, kNm

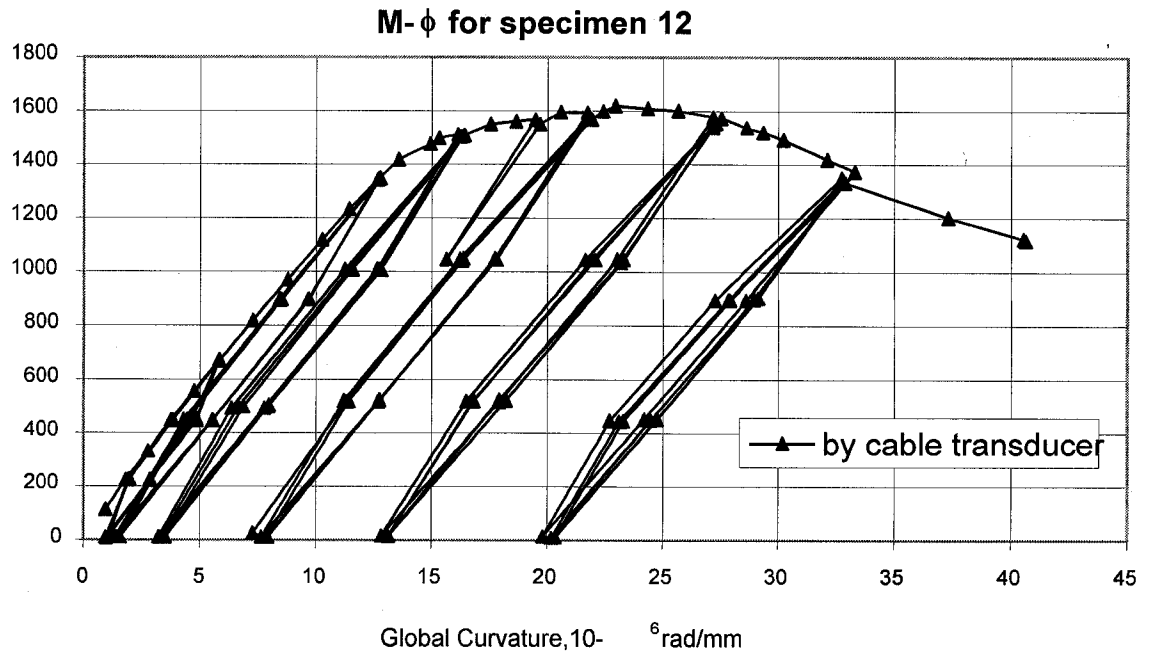


Figure 3.127 Global Moment vs. Global Curvature For D20P40BC-12

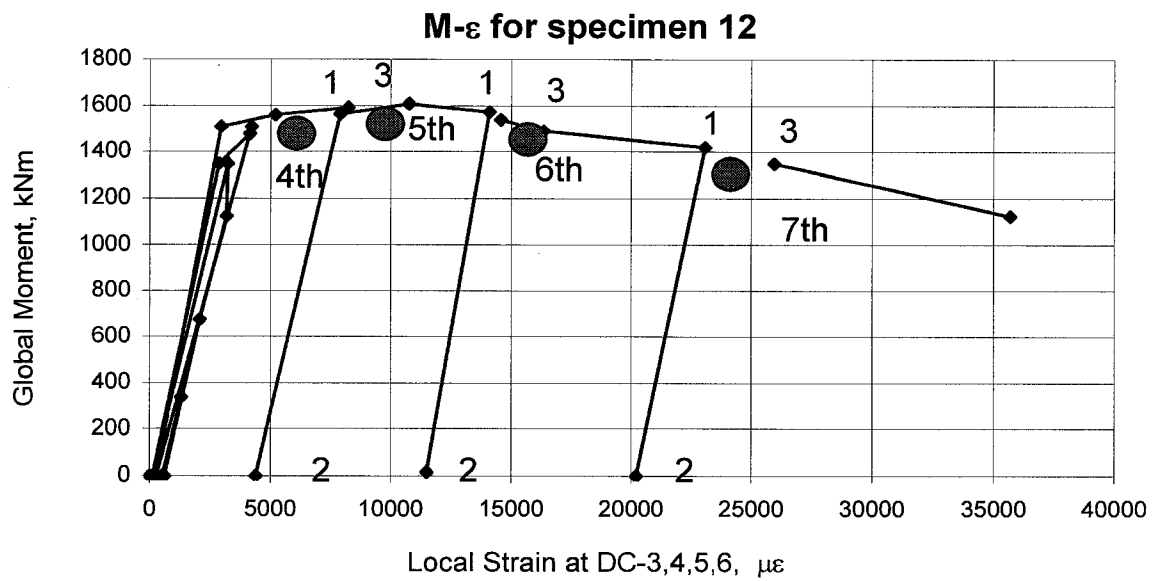


Figure 3.128 Global Moment vs. Local Strain At DC-3,4,5,6 For D20P40BC-12

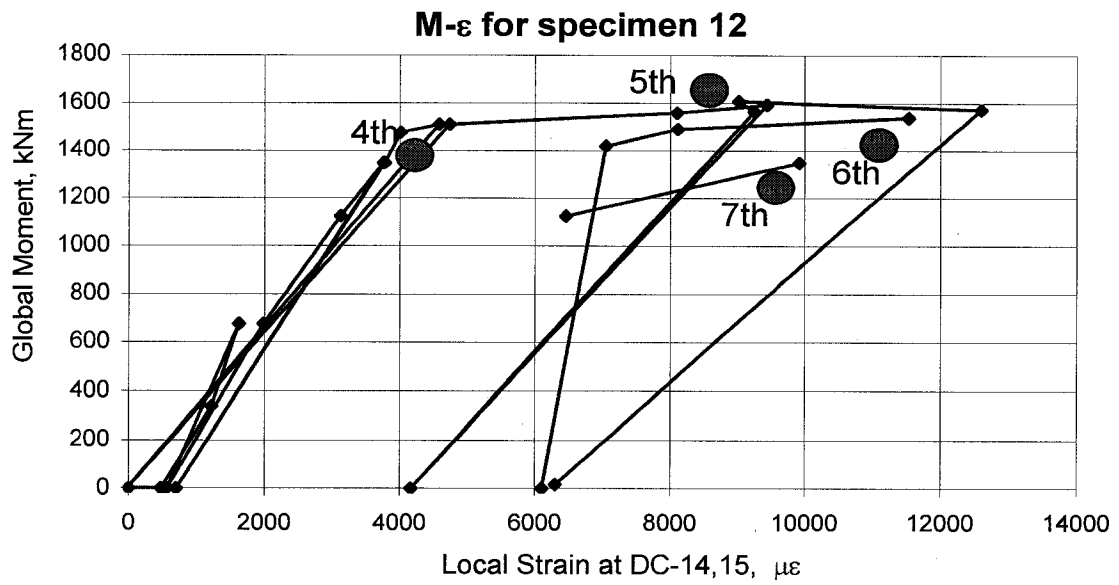


Figure 3.129 Global Moment vs. Local strain At DC-14,15 For D20P40BC-12

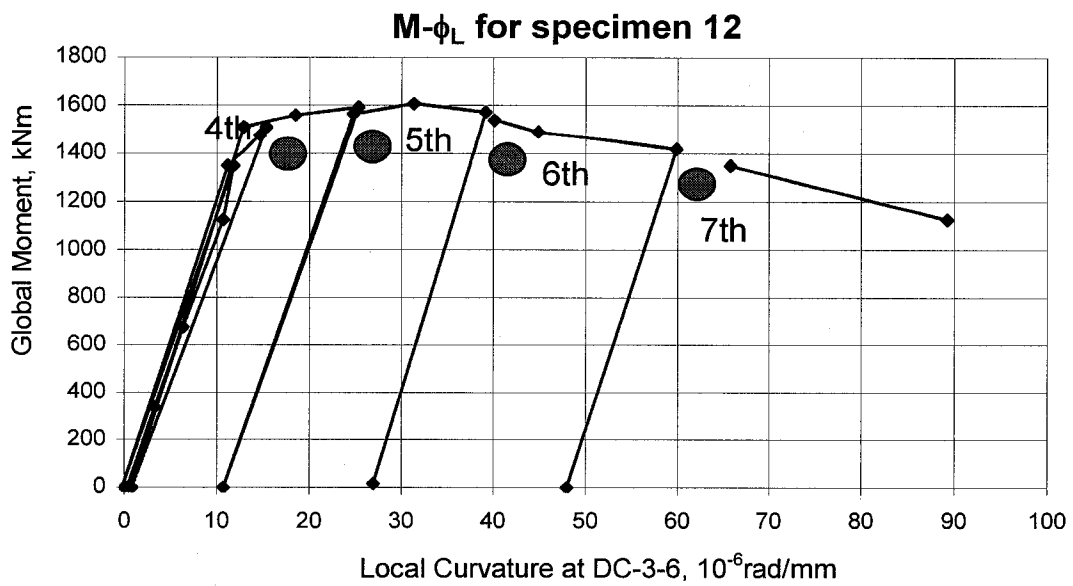


Figure 3.130 Global Moment vs. Local Curvature At DC-3-6 For D20P40BC-12

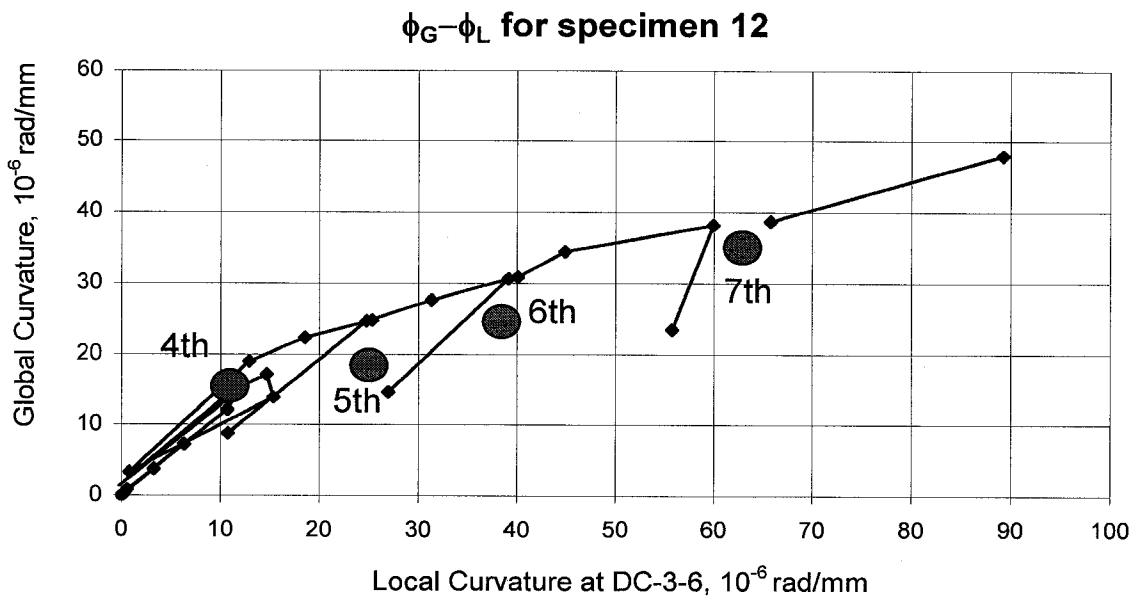


Figure 3.131 Global Curvature vs. Local Curvature At DC-3-6 For D20P40BC-12

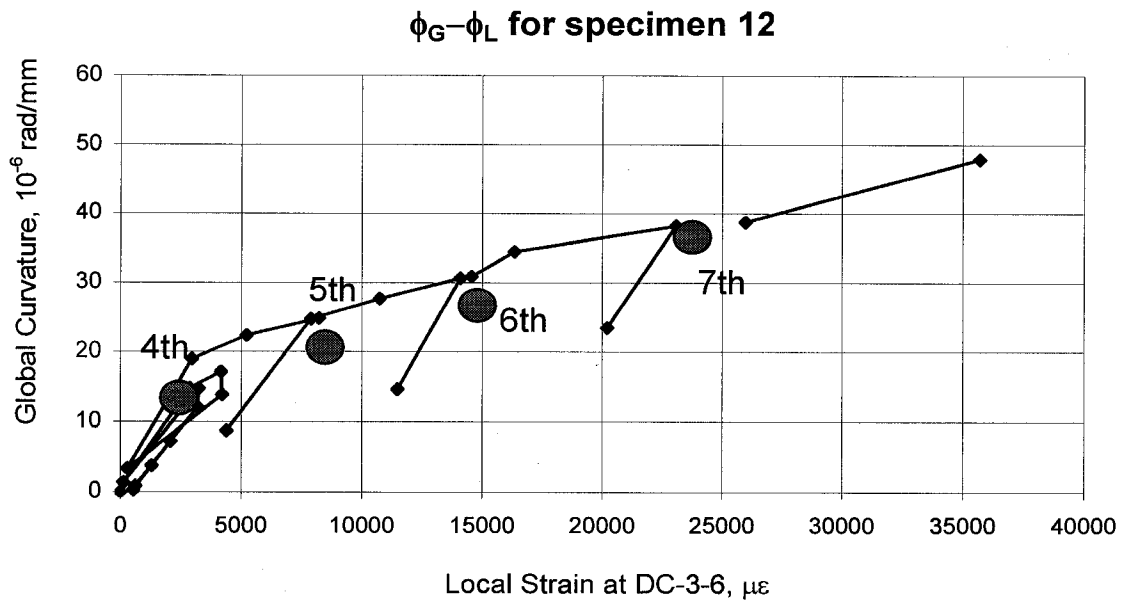


Figure 3.132 Global Curvature vs. Local Strain At DC-3-6 For D20P40BC-12

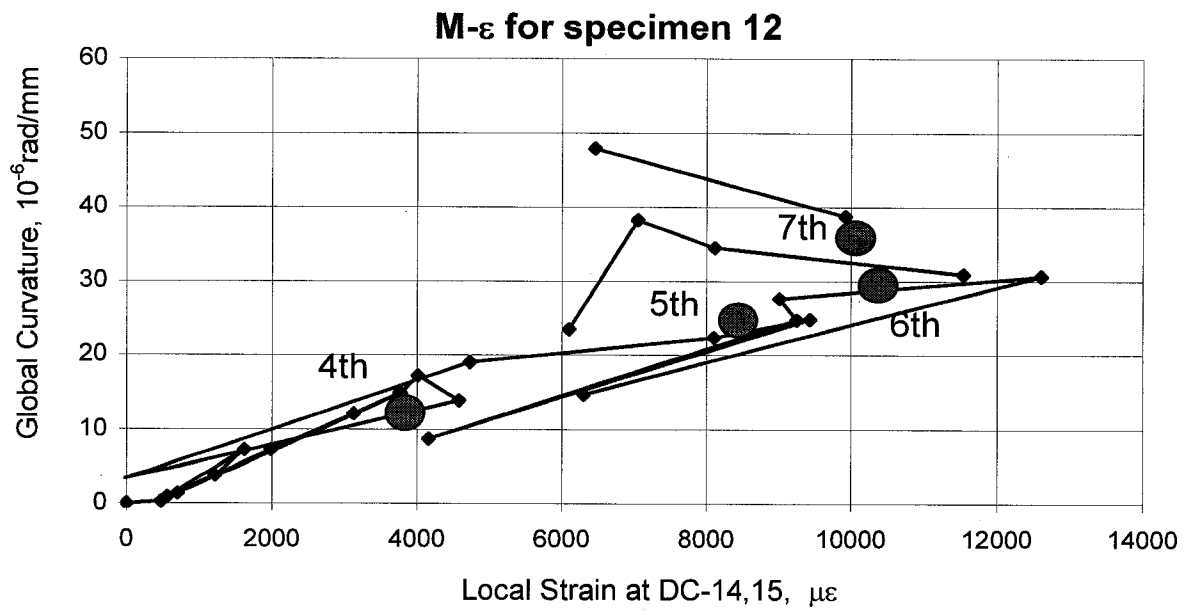


Figure 3.133 Global Curvature vs. Local Strain At DC-14,15 For D20P40BC-12

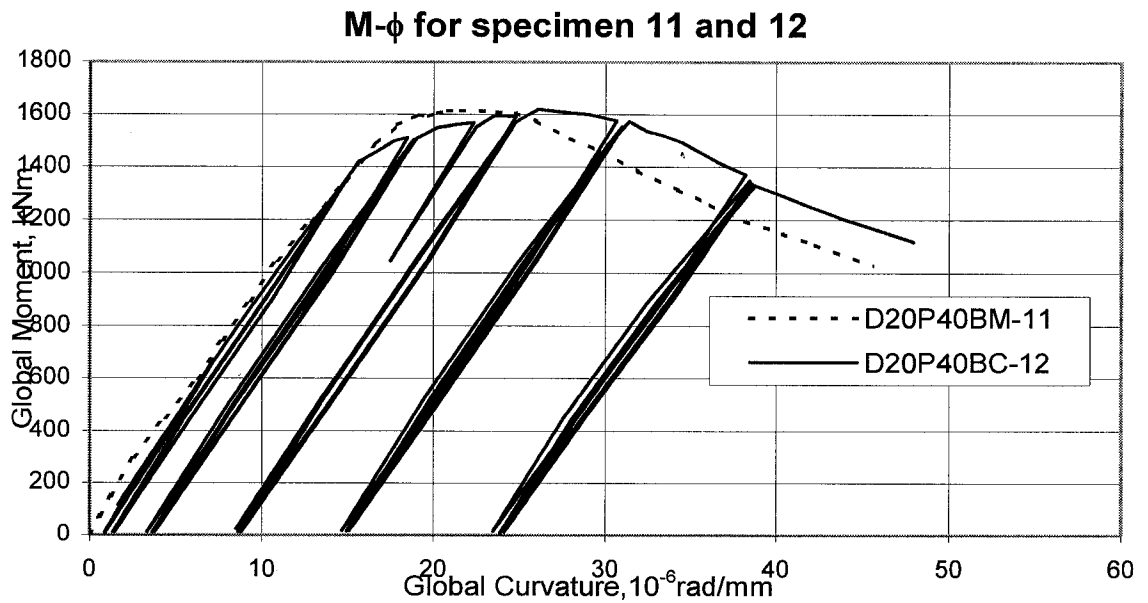


Figure 3.134 Global Moment vs. Global Curvature For D20P40BM-11, D20P40BC-12

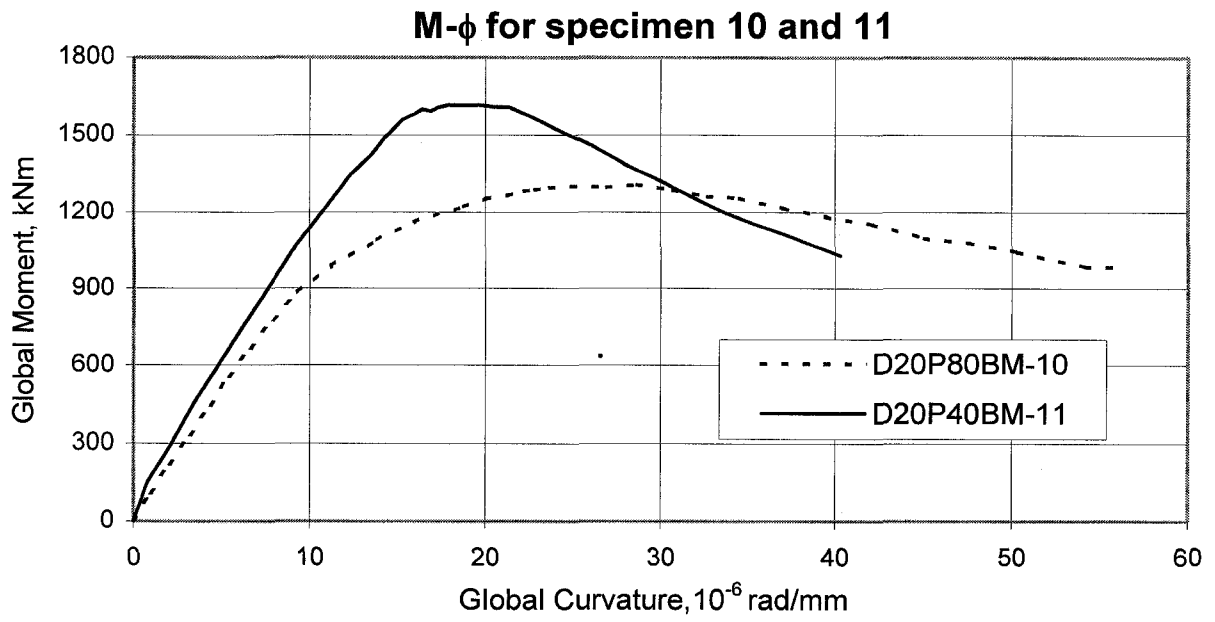


Figure 3.135 Global Moment vs. Global Curvature For D20P80BM-10, D20P40BM-11

CHAPTER 4 FINITE ELEMENT ANALYSIS OF THE STRESS RELIEF TEST RESULTS AND DISCUSSION

4.1 Introduction

Numerical analyses were carried out using ABAQUS (2006). The purpose of the analysis is to verify the test results in Chapter 3. FEA model in this study was based on the model developed by Dorey et al. (2001). The pipe is modelled with S4R, a four-node reduced integration finite strain shell element. Steel is assumed to be isotropic and behaving according to incremental plasticity with isotropic hardening.

The global strain is defined in section 3.3. The segment of the pipe is modelled with collar twice the thickness of pipe wall. Thus, the effective length for calculating the global strain of the finite element results is taken as the overall pipe length minus half the total collar length.

$$(4.1) \quad L_e = L - L_{\text{collar}}$$

where, L_e is the effective length of the pipe specimen;

L is the overall length of the pipe specimen;

L_{collar} is the length of one collar.

The following Sections present the analysis and comparison with compression and bending test results.

4.2 Numerical Analysis of Compression Tests

4.2.1 General

In the modelling, the re-measured pipe thickness of 8.84 mm is used for 30 inch pipes rather than the initial measurement of 8.64 mm. Preliminary analytical results with a thickness of 8.84 mm were found to give a better agreement with the test data. Numerical analyses were carried out with the measured material properties shown in Tables 3.4 to 3.6, with an assumed Poisson's ratio of 0.3. For a number of analyses, modified values of these properties are used. In order to initiate the buckling away from

the collar, a quarter pipe diameter long segment of the pipe is modelled with 99.5% of wall thickness. The segment is located at the mid-length of the specimen. The differences between the finite element models are listed below.

- 80M1 - model for D30P80AM-1 test with the measured yield strength 567 MPa.
- 80M2 - model for D30P80AM-1 test with a yield strength of 578 MPa, a 2% increase above the measured yield strength.
- 80C2 - model for D30P80AC-2 test with a yield strength of 578 MPa, a 2% increase above the measured yield strength.
- 20M1 - model for D30P20AC-3 test with the measured yield strength 567 MPa, but for monotonic loading.
- 20C1 - model for D30P20AC-3 test with the measured yield strength 567 MPa.

Dibattista et al. (2000) have reported that yield strength in the hoop direction of a pipe may be higher than the axial direction. But no material test was carried out in the hoop direction of the pipe. For 80M2 and 80C2, the numerical analyses were carried out with a yield strength that was 2% higher than the measured yield strength. This is an attempt to account for the effect of higher yield strength in the hoop direction. At 80% internal pressure, the dominant stress component at buckling is in the hoop direction. However, for 20% internal pressure, the dominant stress component is in the axial direction. For this reason, numerical analyses for 20M1 and 20C1 were carried out without any increase in the yield strength. In addition, two additional analyses were conducted for D20P80AM-4 using increased yield strength, 1.03 and 1.05 yield stress, to study the hoop strength effects.

4.2.2 Discussion

30 Inch Specimens

The results of the numerical analyses for 30 inch specimens are shown in Figures 4.1 to 4.9 and Table 4.1. The predicted results closely match the test results. Figure 4.1 for D30P80AM-1 clearly shows that 80M2 gives a better prediction than 80M1. This indicates that the yield strength in the hoop direction may indeed be higher than in the

axial direction. The numerical solutions also give a good prediction of the test, even for the cyclic tests, D30P80AC-2 and D30P20AC-3. In Figures 4.3 and 4.5, the numerical analysis is able to retrace the path of the load cycling and the upper envelope of the load-deformation curve.

The load versus local D compressive strain for both the test and the numerical analysis are shown in Figures 4.2 and 4.6. In Figure 4.2, the predicted curve closely matches the test results for D30P80AM-1. For D30P20AC-3; there is no post peak test D local strain data to compare to. But looking only at the initial segment of the curve in Figure 4.6, the predicted curve is only slightly steeper than the test data. The analytical solution also clearly shows there is hardly any non-linear deformation before the peak load is reached. Table 4.1 shows the predicted D local buckling strain. The predicted D local buckling strain is very close to the measured buckling strain.

In general, the post peak load-global strain response is gentler for a P80 test. This means that the post buckling deformation is not as localised for a P80 test as compared to a P20 test. This can be seen in Figures 4.8 and 4.9 where wavelength of the buckle for the P80 test is longer than the P20 specimen. Note that the wrinkle for the P80 test extends outside the refined mesh region where as the wrinkle for the P20 test is within the region.

The predicted load-global strain curves for the monotonic and the cyclic tests are shown in Figures 4.4 and 4.7. They clearly show that the range of cyclic loading applied in the test has no effect on the overall behaviour of the pipe. However, it should be noted that the material hardening model used in the numerical analysis is only applicable when there is no significant stress reversal, which happens to be the case for this series of test.

20 Inch Specimens

The results of the numerical analyses of 20 inch tests are shown in Figures 4.10 to 4.12. In Figure 4.10 for D20P80AM-4, the predicted curves are lower than the test curve. An additional analysis (shown in Figure 4.10) was done by removing the collar from the

model, however no difference in results was found. In Figure 4.11, an increased yield stress was used to study the hoop strength effects. The figure shows that by an increase of 5% yield strength the predicted results closely match the test results. This indicates that the yield strength in the hoop direction may be higher than in the longitudinal direction. In Figure 4.12, the numerical analysis is able to retrace the path of the load-deformation curve of specimen D20P40AM-5. Again, the figure shows that collar has little effect on the pipe behaviour. No numerical analysis is done on the specimen D20P40AC-6 since the tests show the identical path of the monotonic load-deformation curve and upper envelope of the cyclic load-deformation curve, shown in Figure 3.35. It implies that the load cycling has minimum effect on the response of the pipes.

4.3 Numerical Analysis of Bending Tests

Numerical analyses for both 30 inch and 20 inch pipes were done based on the material properties obtained from the Section 4.2. Only monotonic analysis was carried out for each specimen. Further numerical analysis based on the material test results obtained from this Section, more specifically for 20 inch specimens, are needed.

The results of the numerical analyses are compared with the test results and are shown in Figures 4.13 to 4.18. The predicted results closely match the test results for 30 inch pipes (specimens 7-9). Although only monotonic analysis was carried out, good agreement can be seen from Figures 4.13 to 4.15. The numerical analysis is able to retrace the upper envelope of the load-deformation curve of the load cycling. This indicates that the load cycling has little effect on the local buckling strength and the response of the specimens.

For 20 inch pipes (specimens 10-12), however, the numerical analysis overestimates the carrying capacity and critical compressive strain of the pipes when compared to the test results. The reason is because the material properties from Phase I pipes were used in the analysis. If the longitudinal coupon results are used, the yield strength and ultimate strength from Phase I are 641 MPa and 717 MPa, respectively, while 680 MPa and 767 MPa are obtained from Phase II pipes. Further analyses are

needed when the correct material properties are obtained. The moment curvature curves of three 20 inch pipe tests in Figure 4.18 show again that the load cycling has little effect on the local buckling strength and response of the specimens.

In general, the post peak load-global strain response is gentler for a P80 test. This means that the post buckling deformation is not as localized for a P80 test as compared to a P0 or P20 test. This can be seen in Figure 3.21 where wavelength of the buckle for the P80 test is longer than the P20 specimen and P0 pipe exhibits diamond mode buckling.

4.4 Summary and Conclusions

A comparison of the test results on the twelve specimens to the FEA using the model was presented in this Chapter. The model performed remarkably when simulation the initial stiffness and post-buckling region of the load-deformation responses both globally and at the buckle location. Also, the model was able to replicate the bulge shaped buckle that occurred for the pressurized test specimens, as well as the diamond shaped buckle that formed during the un-pressurized specimen tests.

The percent differences between the test and model on peak load-deformation is less than 10 %, demonstrating a reasonable predictive capability for the load-deformation relationships of the test specimens.

The following summary and conclusions can be derived from this study for the compressive test.

- 1) For the load range applied in the test, the load cycling has minimal effect on the response of the pipes.
- 2) The load-deformation response of the pipes during the load cycling is essentially linear and elastic. There is hardly any hysteresis loop during the load cycling.
- 3) From the tension coupon test, it was found that the pipe has a large yield plateau. As a result, local buckling of the pipe occurred with little prior inelastic deformation.
- 4) The numerical analyses are able to verify the test results. The predicted values match the measured data.

The following summary and conclusions can be derived from this study for the bending test.

- 1) For the load range applied in the test, the load cycling has a minimum effect on the global response of the pipes.
- 2) Before the pipe buckles, load cycling does not yield any accumulated local strain in the pipe. However, after the peak moment, local behaviour of the pipe is influenced by the pipe geometry and loads applied. Accumulated strain was observed at the wrinkle locations after each load cycling.
- 3) The post buckling behaviour is influenced by the internal pressure. With higher internal pressure, the post peak load - global strain response is gentler and load cycling effects on local behaviour is less.
- 4) The moment-curvature response of the pipe during the load cycling is essentially linear and elastic. There is a little hysteresis loop during the load cycling, especially when internal pressure is high.
- 5) Significant differences are found for the X80 material properties between longitudinal and transverse (hoop) coupons. Flattened transverse coupons give inconsistent test results.
- 6) The numerical analyses are able to verify the pipe behaviour and test results.

Table 4.1 Test and predicted compressive D local buckling strain

Specimen	D local compressive buckling strain, microstrain	
	Test	Finite element analysis
D30P80AM-1	2000	2130
D30P80AC-2	2150	2130
D30P20AC-3	2760	2750

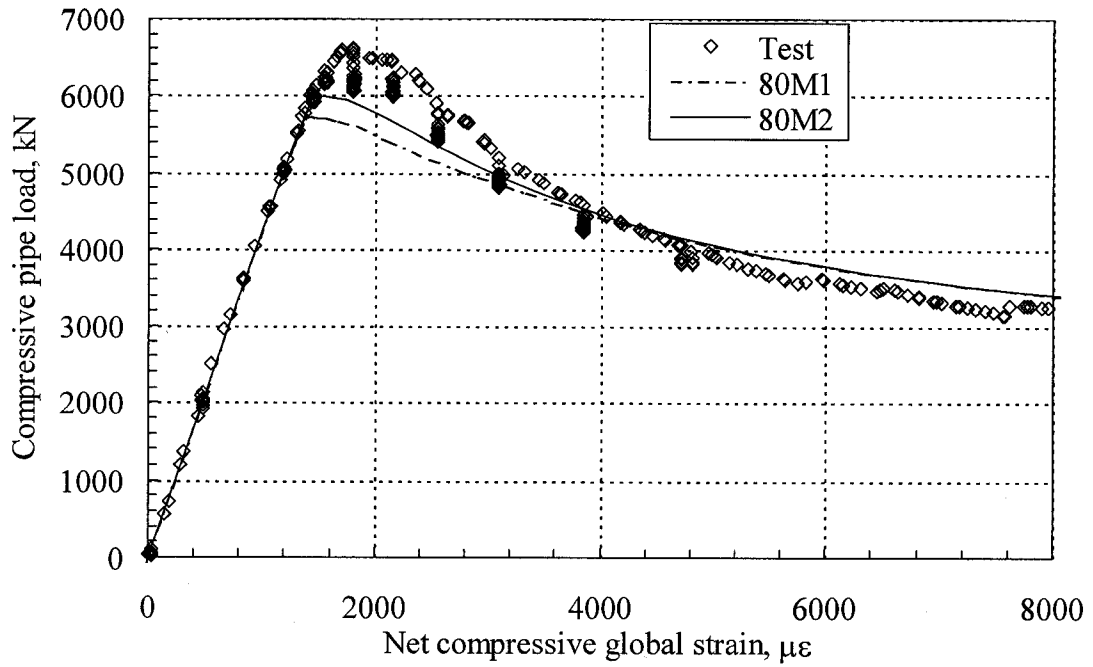


Figure 4.1 Test and predicted load vs. net compressive global strain for D30P80AM-1

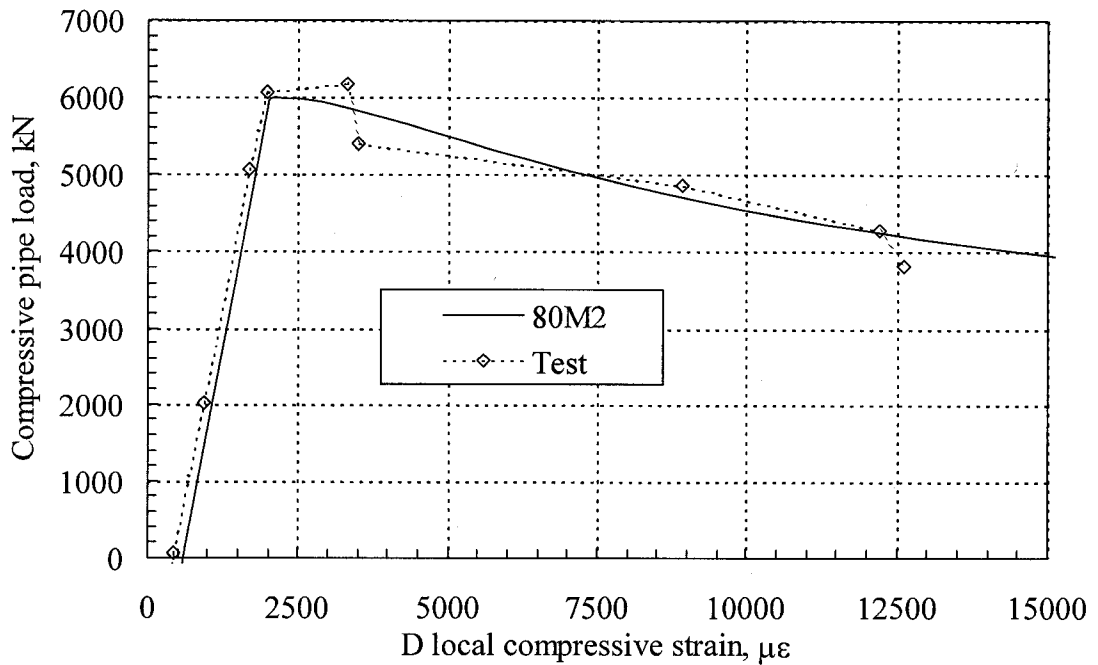


Figure 4.2 Test and predicted load vs. D local compressive strain for D30P80AM-1

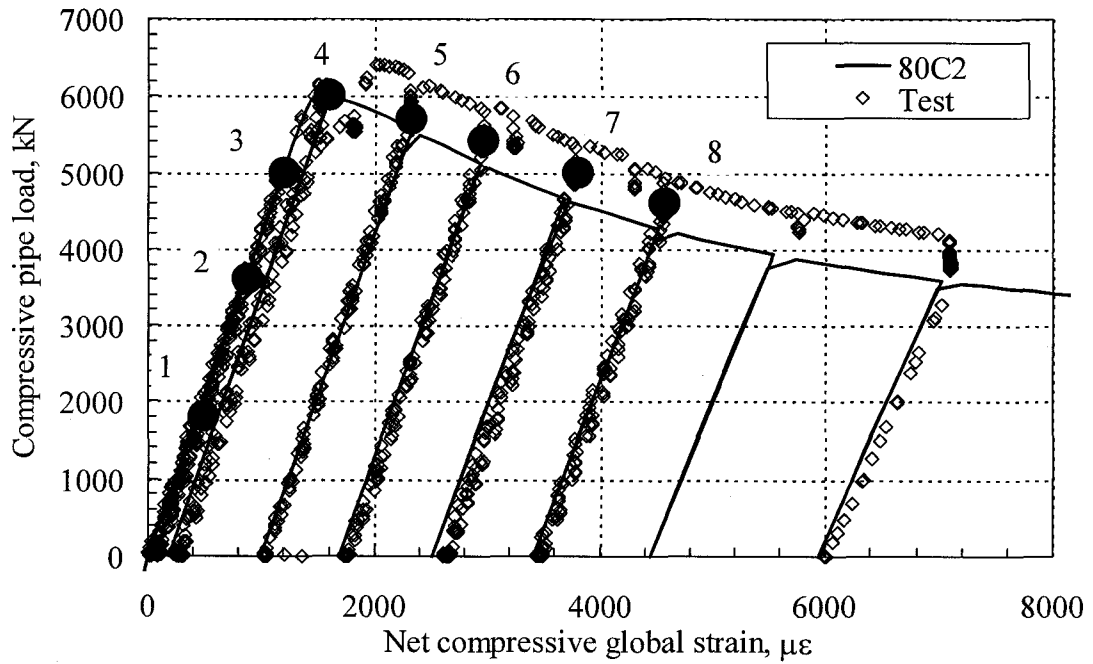


Figure 4.3 Test and predicted load vs. net compressive global strain for D30P80AC-2

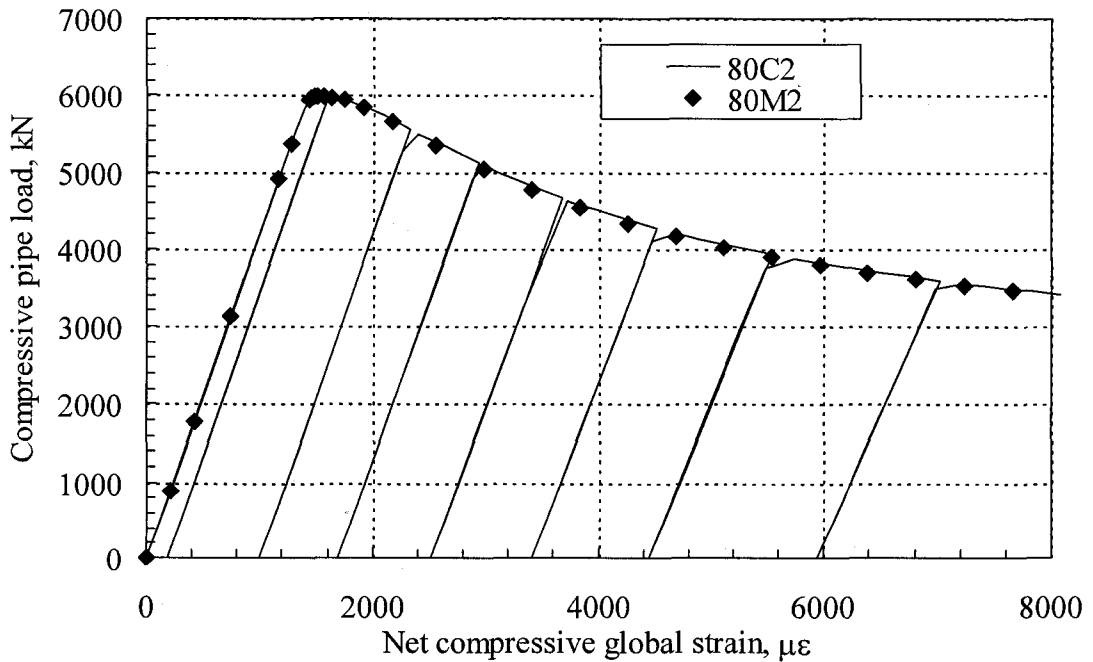


Figure 4.4 Analytical load vs. net compressive global strain for P80 tests

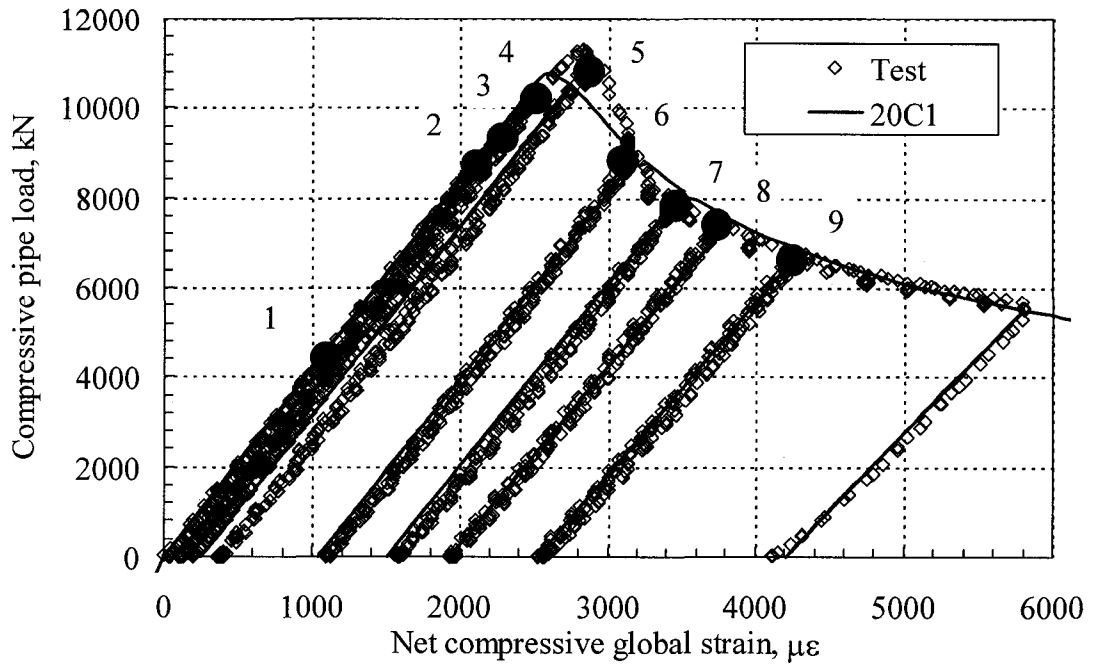


Figure 4.5 Test and predicted load vs. net compressive global strain for D30P20AC-3

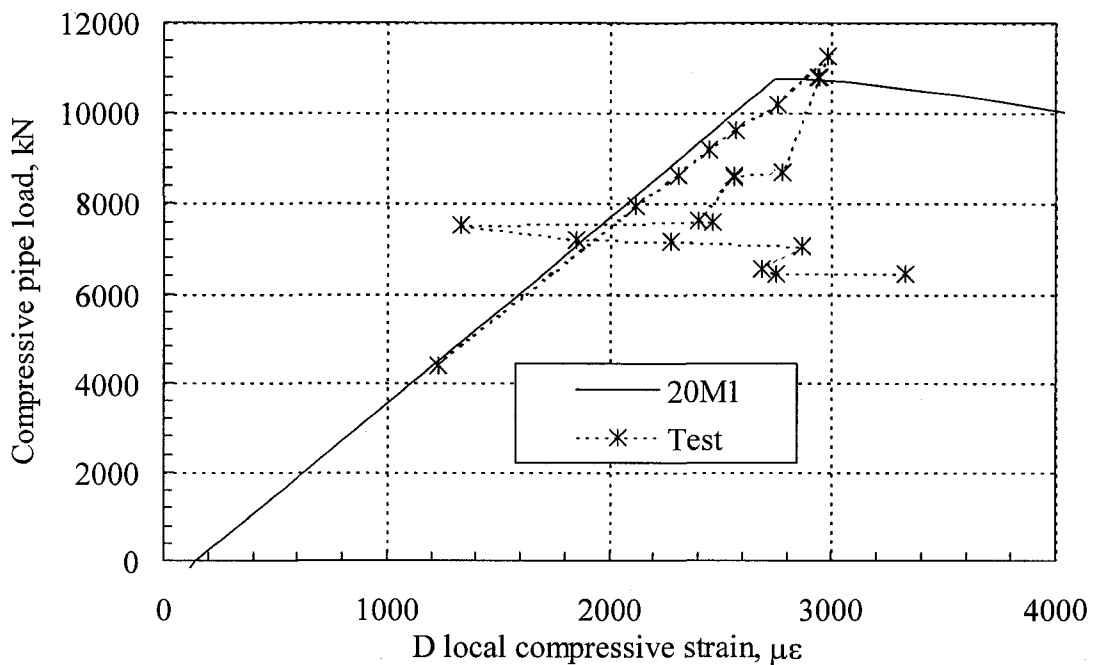


Figure 4.6 Test and predicted load vs. D local compressive strain for D30P20AC-3

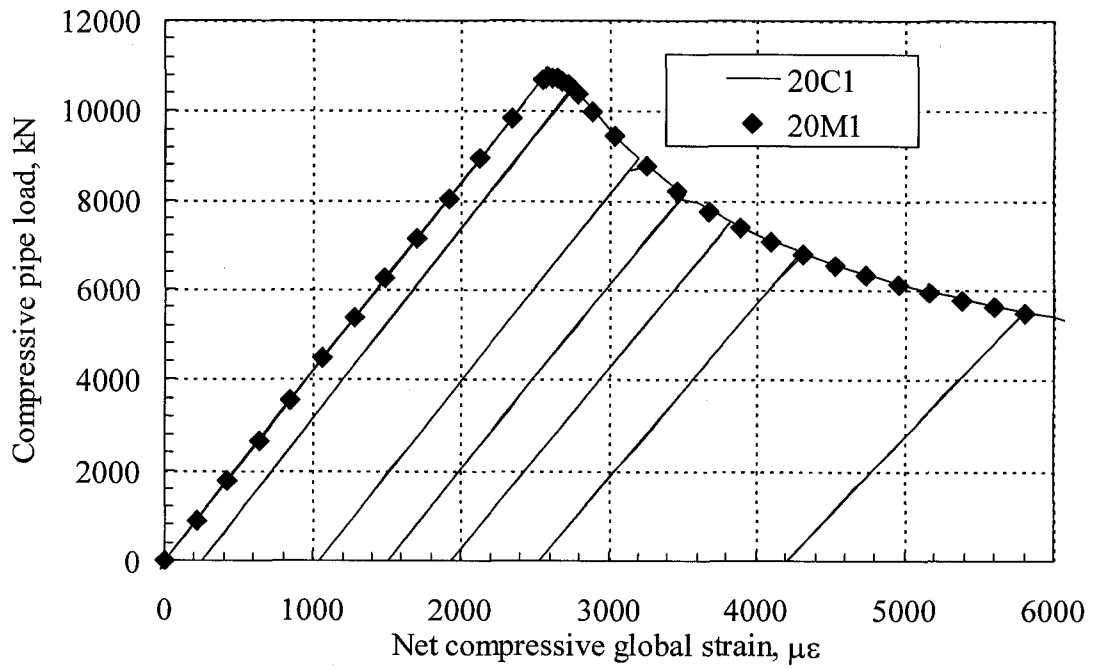


Figure 4.7 Analytical load vs. net compressive global strain for P20 tests

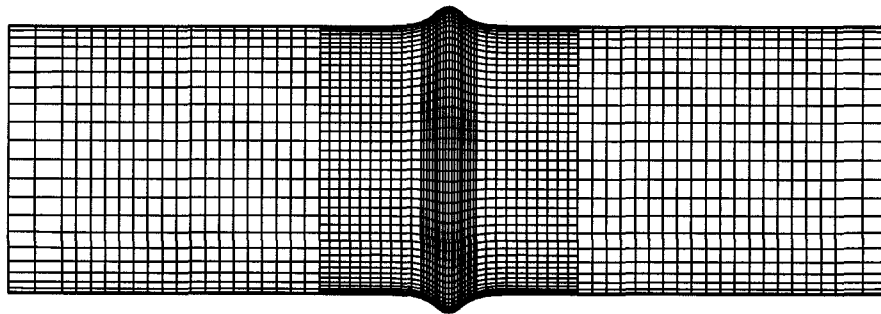


Figure 4.8 Predicted deformed shape for P80 test

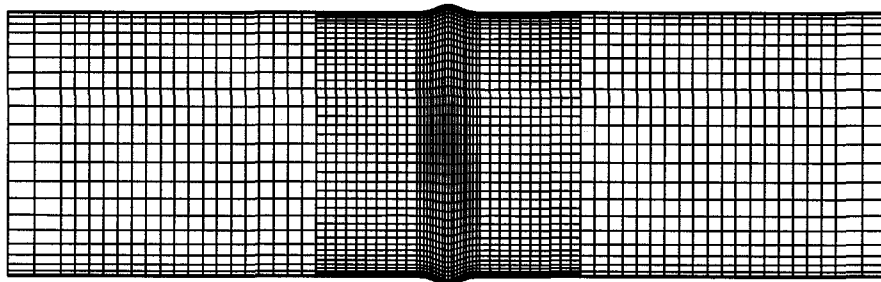


Figure 4.9 Predicted deformed shape for P20 test

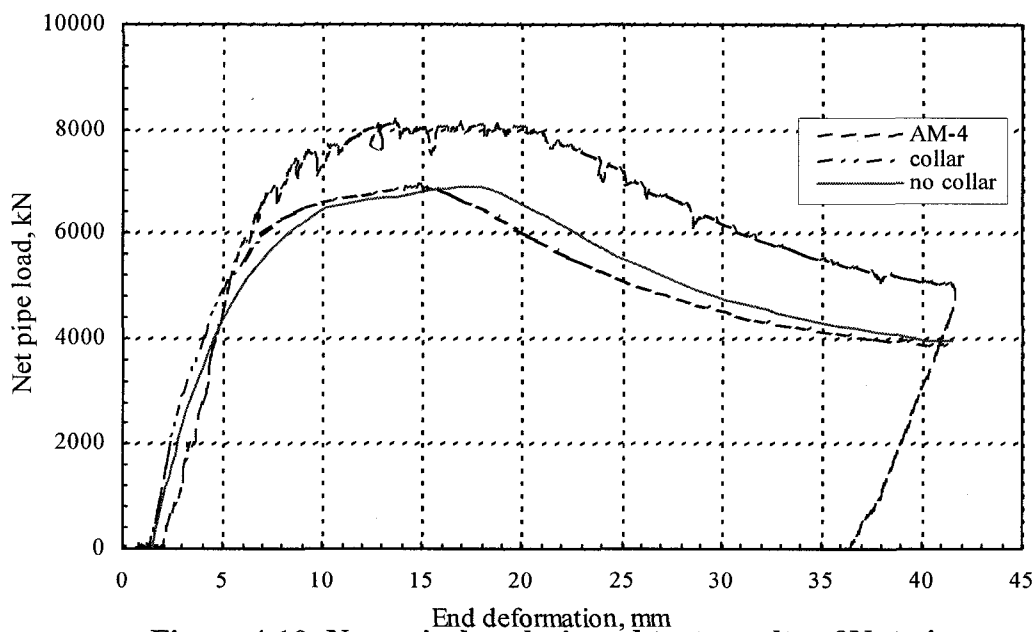


Figure 4.10 Numerical analysis and test results of Net pipe load vs. End deformation for D20P80AM-4

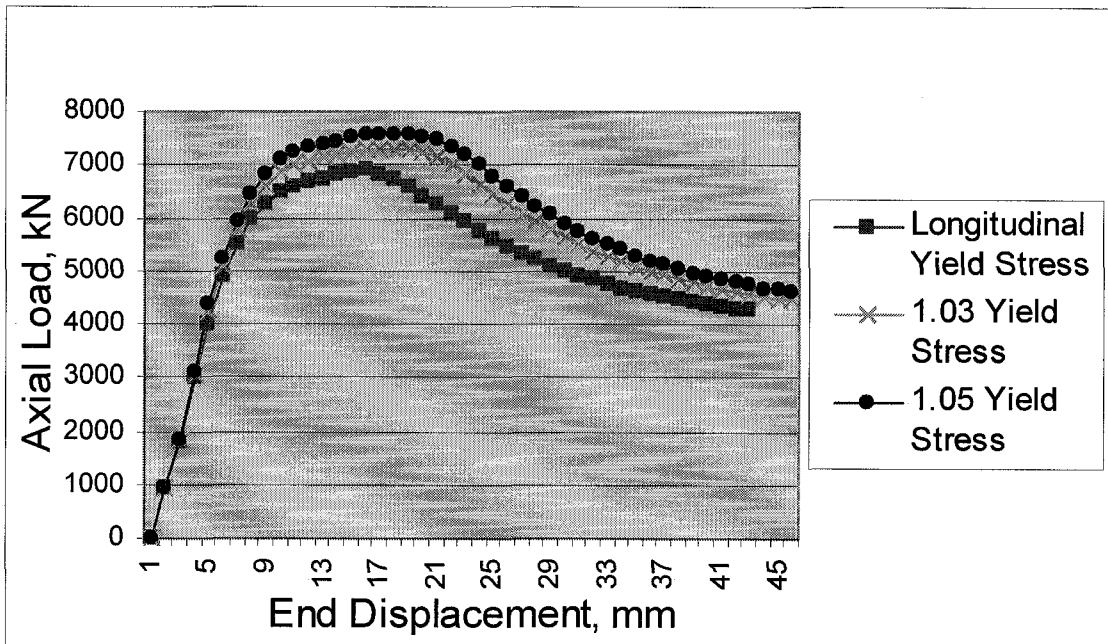


Figure 4.11 Effect of hoop yield stress on the buckling behaviour of D20P80AM-4

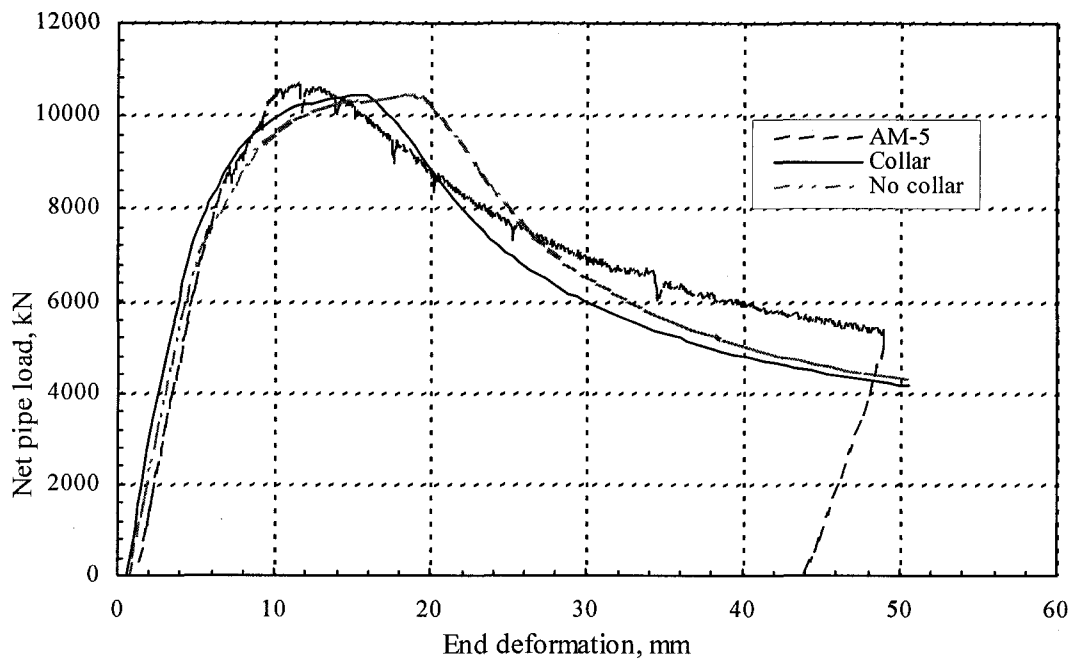


Figure 4.12 Numerical analysis and test results of net pipe load vs. end deformation for AM-5

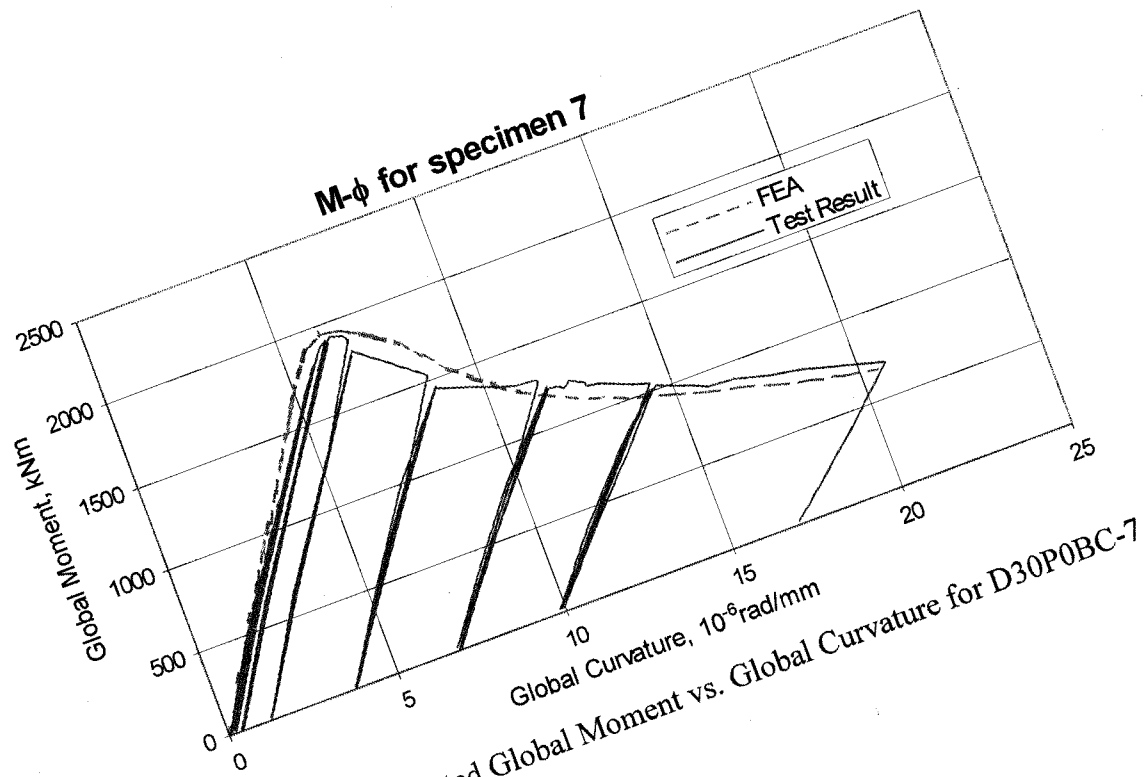


Figure 4.13 Test and Predicted Global Moment vs. Global Curvature for D30P0BC-7

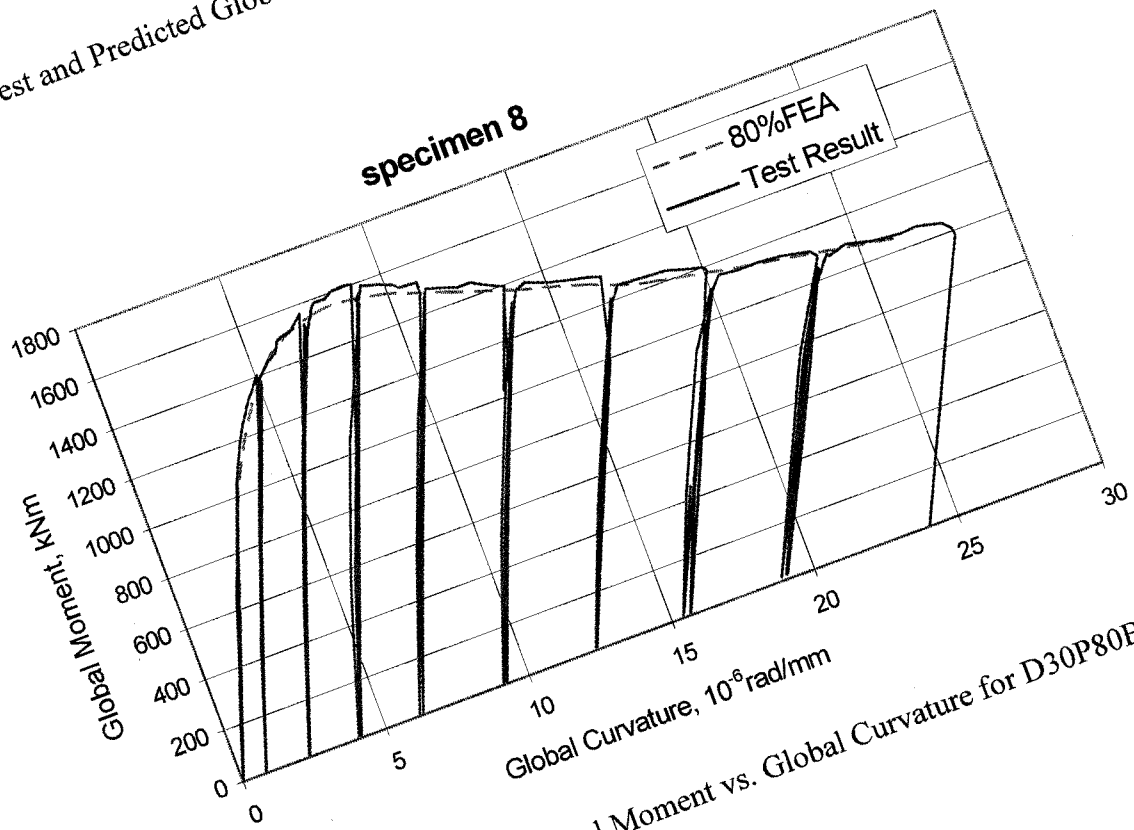


Figure 4.14 Test and Predicted Global Moment vs. Global Curvature for D30P80BC-8

for specimen 9

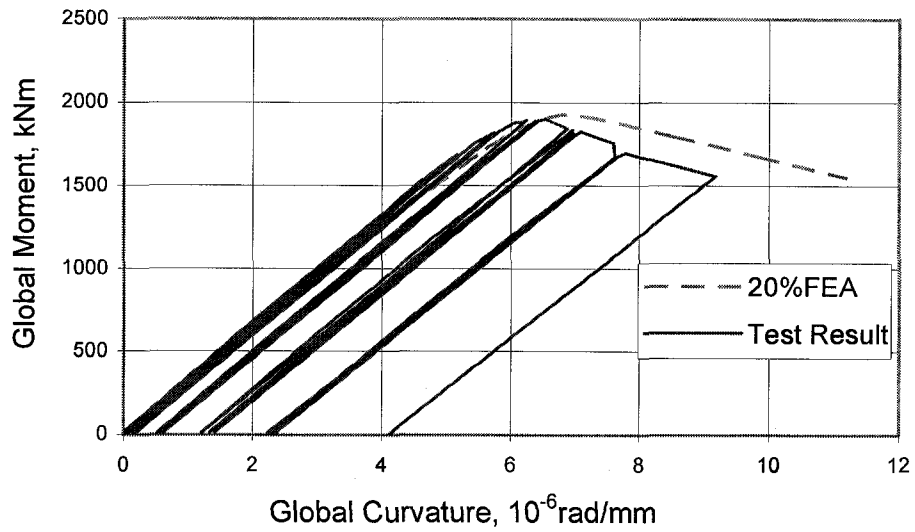


Figure 4.15 Test and Predicted Global Moment vs. Global Curvature for D30P20BC-9

specimen 10

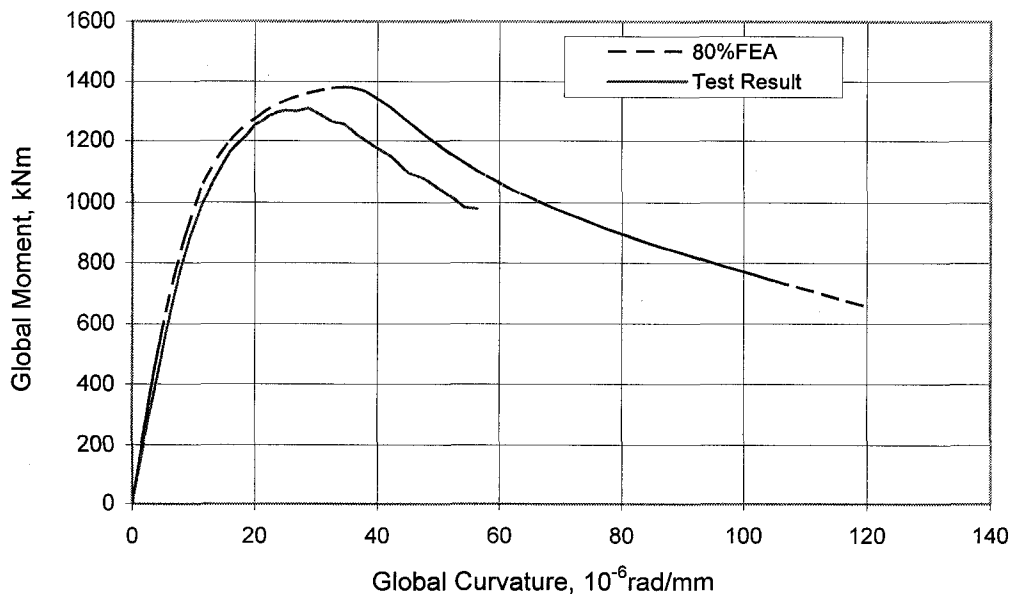


Figure 4.16 Test and Predicted Global Moment vs. Global Curvature for D20P80BM-10

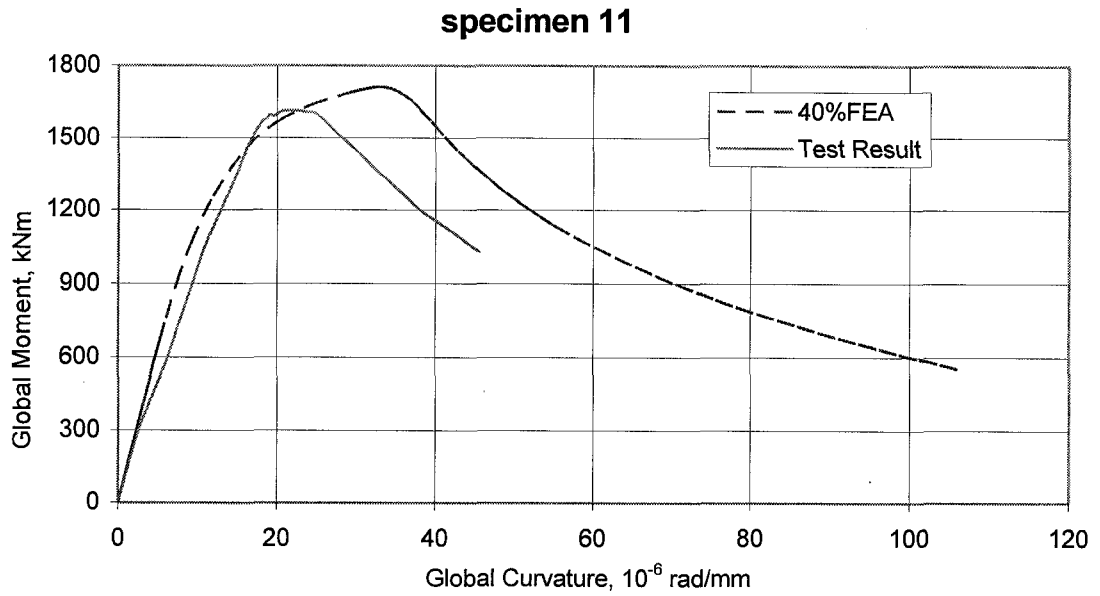


Figure 4.17 Test and Predicted Global Moment vs. Global Curvature for D20P40BM-11

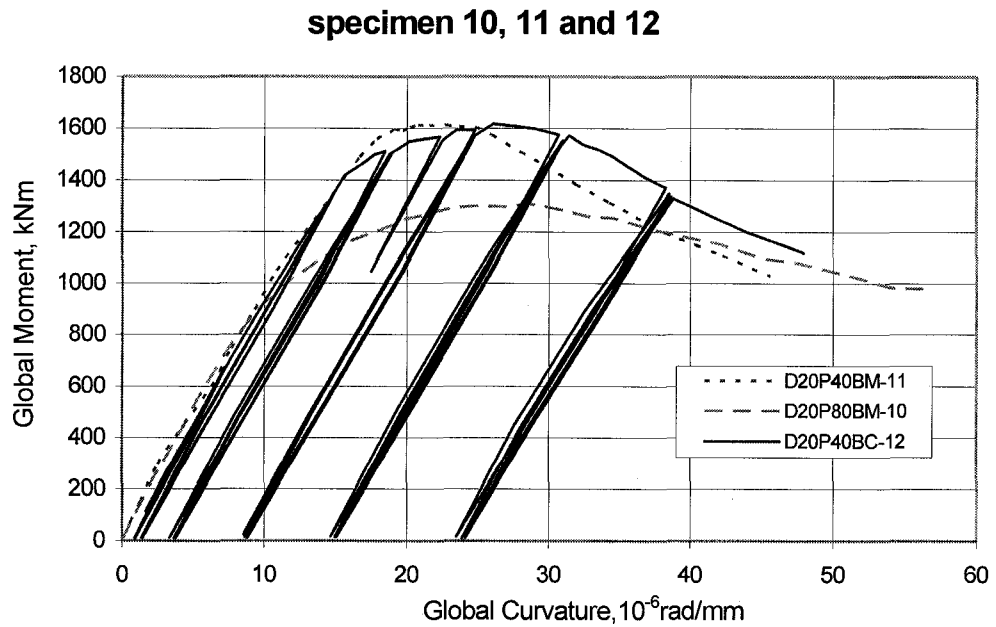


Figure 4.18 Global Moment vs. Global Curvature for Specimens 10, 11, and 12

CHAPTER 5 PEMBINA RIVER CROSSING MONITORING PROGRAM

A number of natural gas and petroleum product pipelines have been constructed across active landslides in Alberta. In managing the various geotechnical hazards occurring throughout the pipeline system, the Pipeline Engineering Geotechnical Team at TCPL uses various programs to obtain information necessary for the analysis, assessment, and possible mitigation of geotechnical hazards. Within the Alberta System, more than 20 site locations are part of a condition monitoring program that are inspected to provide the necessary data. Pembina River Crossing and Simonette River Crossing are two pipeline sites located at active slopes. Simonette River Crossing is stated in Chapter 6.

5.1 Description of the Pembina River Crossing

5.1.1 Location

Pembina Pipeline is part of the NPS30 (outside diameter 762 mm) Western Alberta System Mainline. The site is located approximately 6 km south and 3 km east of the town of Lodgepole, Alberta, in NE ¼-8-47-9-W5M. See Figure 5.1 Geographic Location and Figure 5.2 Location Plan of Pembina River Crossing. Table 5.1 shows the Latitude and Longitude of Lodgepole and Edmonton.

5.1.2 The Natural Ground

The general characteristics of the existing ground conditions are described below. The original surface of the ground is sloped towards an unnamed creek. East slope of the creek is from 1.28° to 17.74°. West slope of the creek is from 8.3° to 18.9°.

At this site, the pipeline crosses an unnamed creek, which drains into the North Saskatchewan River, at a relatively straight and narrow east/west aligned section of the creek. Figure 5.3 and Figure 5.4 show pipeline plan and profile. The elevation profile and plan view of the pipeline and slope geometry is shown in Figure 5.5. The longitudinal

station for the start of the slope is 71380 m with the ending at 71687 m. The cover depth of the pipeline varies between 1.0 m and 4.4 m with the average being 1.67 m. The shear plane in the slope is about 11 m below the creek bed. The pipe wall thickness is 15.9 mm, steel grade is X60 (413 MPa) and the maximum internal pressure is 6.18 MPa.

5.1.3 Site History

There was a rupture experienced on the original line in 1986 due to geotechnical movement. The Pembina River Crossing is re-route, constructed in the same year. The original line is 0.5 km due east of the present crossing, and ran somewhat crosswise up the south hillside of the same creek. Before the rupture, that hillside was observed having slope movements, and was subsequently instrumented to monitor the rates of movement. After spring rain in 1986, the slope failed and the resulting soil movement contributed to rupturing the pipeline. Since the reroute was installed, the crossing has been continually monitored, with analysis leading to twice stress relief in 1992 and 2000 respectively. Extensive geotechnical information has been collected on the creek valley slopes since 1986, including the monitoring surface and deep-seated slope movements, groundwater conditions, and visual observations.

5.2 Field Monitoring Program

The current operating philosophy in examining pipeline integrity involves monitoring the soil movement and periodically excavating the line to relieve stresses. In order to monitor the soil movement, several boreholes were conducted, 3 in 1987, 2 in 1988, 7 in 1992 and 3 in 1997. These boreholes were logged and slope indicators (SI) and piezometers were installed to obtain representative sampling of geology, soil movement, and groundwater pressure.

Starting 2000 this site has only 4 slope indicators left monitoring the hillside, SI3, SI8, SI9 and SI13, after having slope movement shearing off SI5, SI10A, and SI12A in 1999. It was decided in 1999 to replace these SIs to maintain the monitoring coverage of the hill. SI12B was installed before excavation at the toe of the hill, this replaced SI12A. SI12B was critical to the monitoring of the site before and during the stress relief

excavation. During the stress relief the 3 additional SIs installed on the hill are SI5A, SI10B and SI12B. SI9 was destroyed during the stress relief, with no possibility of repair. But SI5A was sufficiently close to give results for that area of the slope. SI13 was also damaged during the relief but was repaired after the activity stopped and was back in service. There are 12 slope indicators data available, SI5, SI5A, SI6, SI7, SI8, SI10A, SI10B, SI11A, SI11B, SI12, SI12A and SI12B.

Part of the field monitoring program was the installation of a series of on-pipe strain gauge pods. These pods were placed to measure pipe stress levels induced by the various slope movements. Critical points, such as pipe bend locations, were particularly instrumented. Each pod of gauge is coupled to a datalogger (Data Dolphin), and loaded with a software package (Data Dolphin Software) to collect and store the field strain measurements.

The latest stress relief for the pipeline located on the southern slope of the crossing was in late March 2000. A total length of 236 m of the pipeline was de-coupled from the soil to allow the south slope of the crossing to rebound.

5.3 Location of Instrumentation

Strain gauge pods were mounted on the pipe longitudinally at four different stations to monitor pipe stress response before, during, and after the relief. The horizontal coordinates of the four sections are 71434.5 m, 71509.5 m, 71585.8 m, and 71606.6 m. The distance between the four strain gauge stations is 75 m, 76.3 m and 20.8 m. Figure 5.3 and Figure 5.4 show plan and profile of the pipeline with strain gauge sections. At each pipe section, there are four strain gauges (see Figure 5.6). One strain gauge is on the top, one on the bottom, the other two were mounted 90° clockwise from the top strain gauge and bottom strain gauge respectively. A data collection telemetry system was also installed to facilitate remote monitoring in the future.

The 15 in-place working slope inclinometers covering the hill, from the crest to near the lower bench at the south slope monitor the soil motion. During the stress relief in

2000 two were damaged. The pipeline and slope profile are given in Figure 5.5 and Figure 5.7 (geometry of FEA model in Chapter 7), in which the locations of slope indicator and strain gauges are shown.

5.4 Geologic Background

The geology of the creek valley consists of silty clay and clay till overlying bedrock, which consists of claystone and sandstone. The stratigraphy is consistent on the north and south sides of the creek, and because the south slope has shown more slope movement there are more boreholes advanced on the south slope. The surficial geology is characterized by a stiff, medium plastic, silty clay, overlying a stiff to firm, low to medium plastic, silty clay till.

Bedrock was encountered in 5 boreholes on the south side of the creek, consisting of claystone in boreholes 8 and 9, and sandstone in boreholes 7, 10, and 11. Here the borehole number is the same as SI number. The thickness of silty clay from ground surface varies from 0 to 4m, in boreholes 12 and 3, respectively. Till thickness are not fully known because bedrock was not encountered in each borehole, but vary between 32 m to 59 m, in boreholes 9 and 14, respectively. The clay till also contains lenses/layers of siltstone and clayshale (borehole 8), laminated sand and coal seams (borehole 5 and 12), clay lenses (boreholes 4, 7, 10 and 11), and sandstone layers (boreholes 4, 5, and 14). It should be mentioned that boreholes 1 and 2 were drilled on the original route and will not be discussed here.

5.5 Hydrogeology

Groundwater conditions have been monitored since 1988. Four pneumatic piezometers have been installed and monitored on the south slope, 3 in the lower portion of the slope and 1 in the upper slope. Five standpipe piezometers have also been installed and monitored, 1 on the north slope and 4 covering the majority of the south slope. The piezometers have been installed in various geological units, including claytill, clay, lenses/layers of silt, sand, and gravel, and one pneumatic piezometer was installed at the elevation of the shear plane in borehole SI-5

Three pneumatic piezometers were installed in boreholes SI-4 at various depths and geology, including sand, silty sand, and clay till. The two piezometers above the clay till piezometer have been reading Opsi pressure since 1997, suggesting that these units are not connected to an aquifer system. The third piezometer measures water pressure very close to the shear plane elevation within 0.5m and has increased significantly in 1999. Standpipe piezometer SI-4-SP, which is measuring water pressure at a higher elevation within the silty clay, shows a much higher water pressure. This suggests that water is locally recharging downslope, possibly feeding the shear plane. A pneumatic piezometer was also installed in SI-5, which measures the piezometer water pressure slightly above the intersected shear plane. This pressure is much higher than measured in any of the other geological units. It appears that there is significant water pressure building along this shear plane reducing the stability of the slope. This is a concern because of the increased piezometer readings in 1999 and the observed increased slope movement which could suggest that the slope is beginning to move at a faster rate, likely due to a raised water table. The standpipe piezometer results indicate that the water pressures within the clay and clay till units are allowing the standpipe levels to be close to ground surface and for two of the piezometers a perched condition exists. The results show an increased standpipe water level in borehole 5 and 7, and increases in pneumatic levels in 4 and 5. These increases have occurred in the first half of 1999 and explain observed increases in slope movement.

5.6 Available Field Data

So far we have got two sets of data. Twelve slope inclinometer data are available at different periods of time from January 1988 to September 2001. Four sections strain gauge data is available from July to November 2000 and December 2000 to May 2002.

5.6.1 Slope Indicator

The general idea behind slope indicator is to provide a cost-effective way of monitoring lateral movements which may occur some distance below the ground surface. The available SI data is presented with the X direction giving down slope movement and

the Y direction yielding cross movement. Figure 5.7 presents profile of pipeline and slope at Pembina River Crossing with instrumentation of slope indicator (SI). There are fifteen SI installed along slope, from the upslope to down slope, they are SI8, SI5, SI5A, SI10, SI10A, SI10B, SI7, SI4, SI11, SI11A, SI11B, SI6, SI12, SI12A and SI12B, 6-15m away from the centerline of the pipe. “W” represents west, “E” represents east, eg. SI8-W7.25m means SI8 is to the west of pipeline center 7.25m away. Apart from SI4, SI10 and SI11, twelve SI data is available.

Figure 5.8 to Figure 5.54 show the soil movements in X and Y directions at these twelve SI locations. Table 5.2 presents maximum of X , Y and the ratio Y of to X. From Table 5.2, Y to X ratio is from 0.013 to 0.4 except SI8, the ratio becomes smaller as SI location is down slope. SI8 has 12.93mm in Y direction, and 8.16mm in X direction in 9.5 years, which is very small compared with other SI data. From Figure 5.8 to Figure 5.54, it can be seen the soil movement in general goes larger at the lower part of the slope than the upper part. The slope indicators installed have clearly identified the shear plane and the magnitude of experienced slope movement.

5.6.2 Strain Gauge

Vibrating wire strain gauges have been used to monitor longitudinal pipeline strain changes to help mitigate the risks associated with maintaining pipelines in active landslides. Strain monitoring provides sensitive measurement of changes in pipeline strains caused by the landslide deformations. This enables timely stress relief execution.

Figure 5.7 presents the profile of pipeline and slope at Pembina River Crossing with instrumentation of strain gauge (SG) Stations. There are four SG Stations installed along the pipeline, from the upslope to down slope, they are SG Station 1, SG Station 2, SG Station 3 and SG Station 4.

Figure 5.55 to Figure 5.86 show the strain reading at these four strain gauge locations. Review of the strain monitoring data in 2000 indicated that high strains had accumulated in the pipeline at the location of the creek area. Most strain gauge readings

in 2001 to 2002, could not be analyzed due to huge jump of the data. It is noticeable that in summer of 2000, strain gauge reading is decreasing larger than the fall and winter. The relatively uniform rates of increase in strain indicated that ground movements and precipitation had caused the strain changes, occurring at a uniform rate during the monitoring period. The strain gauge at the up slope has tensile trend, at the down hill compressive.

The above SI data, SG data and observations play an important role in the finite element modeling in Chapter 7, and they will be used to calibrate the model. Details will be introduced in Chapter 7.

Table 5.1 Latitude and Longitude of Lodgepole and Edmonton

	North Latitude	West Longitude
Edmonton	53°33'	113°28'
Lodgepole	53°06'	115°19'

Table 5.2 The latest X and Y and Ratio of Y to X near ground at Twelve SI locations

	X,mm	Y,mm	Y/X	Depth, m
SI5	203	-30	-0.147	-2.5
SI5A	28	8	0.4	-4.0
SI6	86	-15	-0.17	-2.0
SI7	44	-13	-0.29	-2.0
SI8	8.16	-12.93	-1.58	-2.5
SI10A	72.56	-22	-0.3	-2.0
SI10B	60.64	-0.78	-0.013	-1.5
SI11A	13.2	-4	-0.3	-1.6
SI11B	43.23	4.6	0.1	-0.8
SI12	148	-14	-0.09	-0.8
SI12A	70	-4	-0.057	-2.0
SI12B	45	2.6	0.057	-2.0

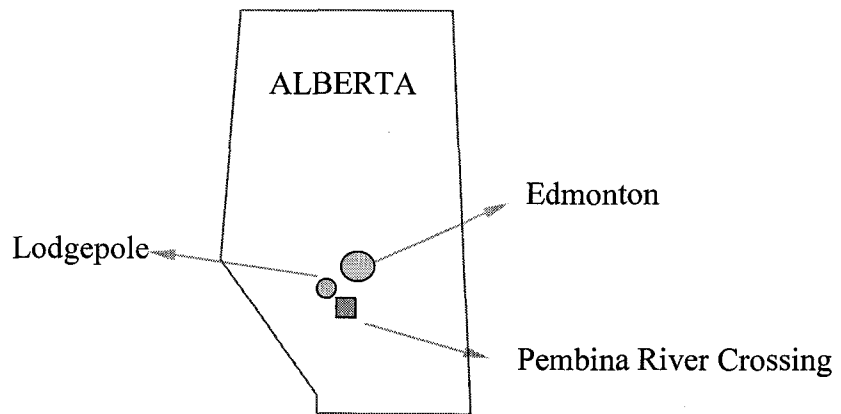


Figure 5.1 Geographic Location of Pembina River Crossing

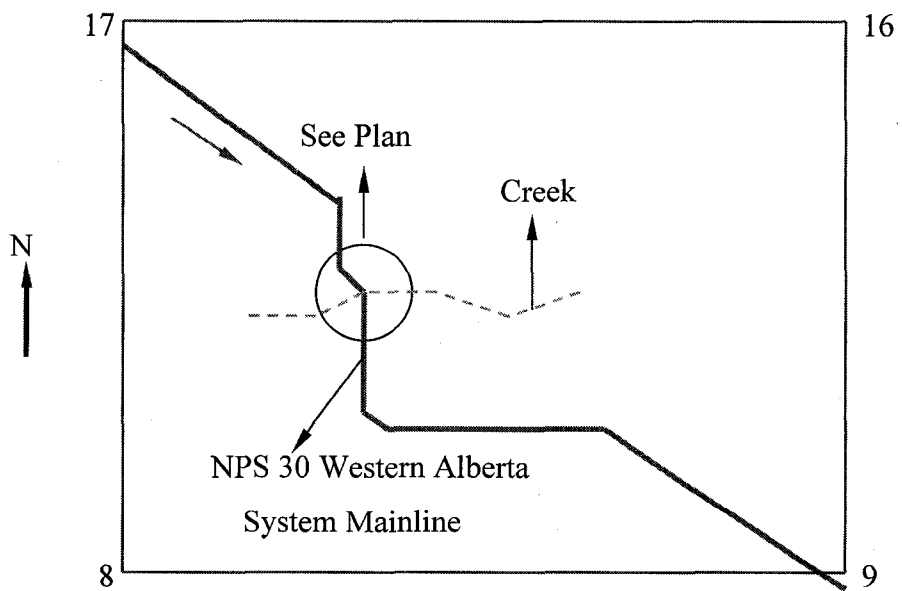


Figure 5.2 Location Plan of Pembina River Crossing
N.E. ¼ SEC. 8 TWP. 47 RGE. 9 W5M

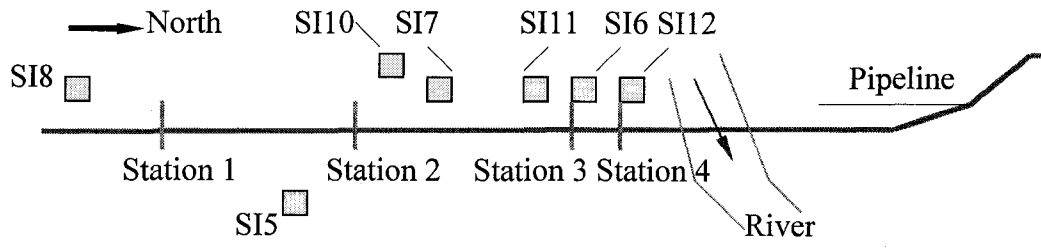


Figure 5.3 Plan of Pipeline with Strain Gauge Sections

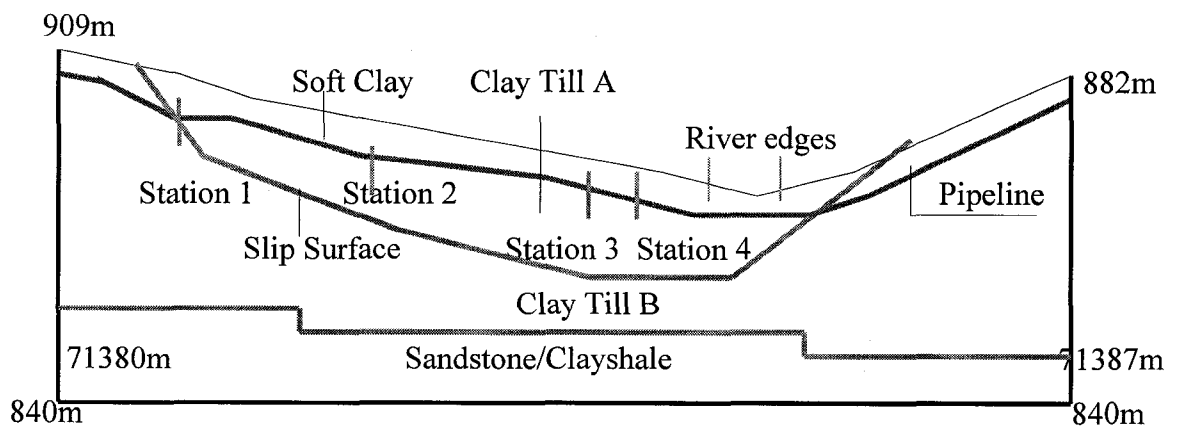


Figure 5.4 Profile of Pipeline with Strain Gauge Sections

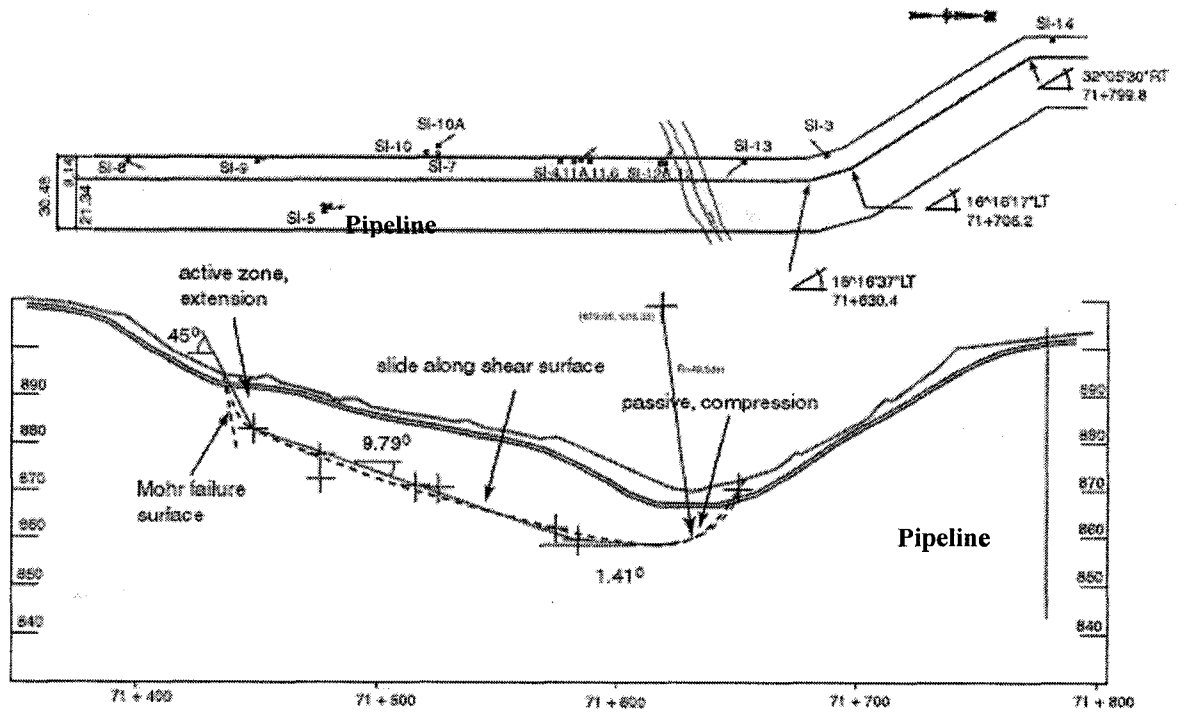


Figure 5.5 Pembina River Crossing Plan and Profile

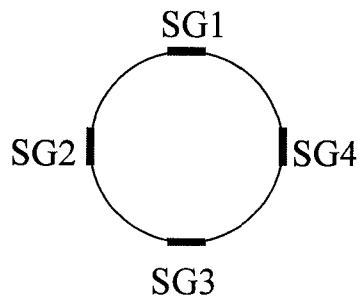


Figure 5.6 Locations of Strain Gauges on Pipe Section

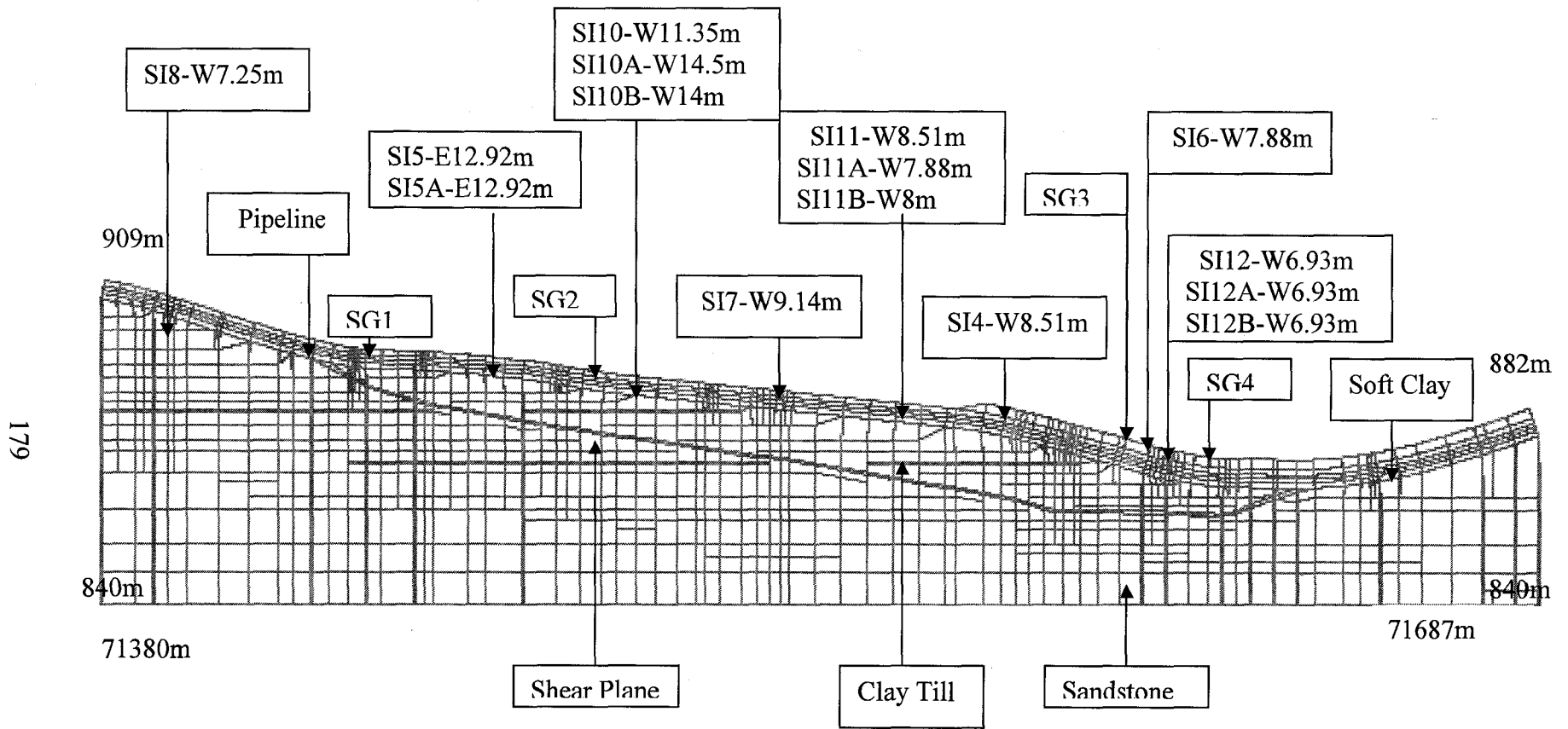


Figure 5.7 Profile of Pipeline and Slope at Pembina River Crossing with Instrumentation SIs and SGs

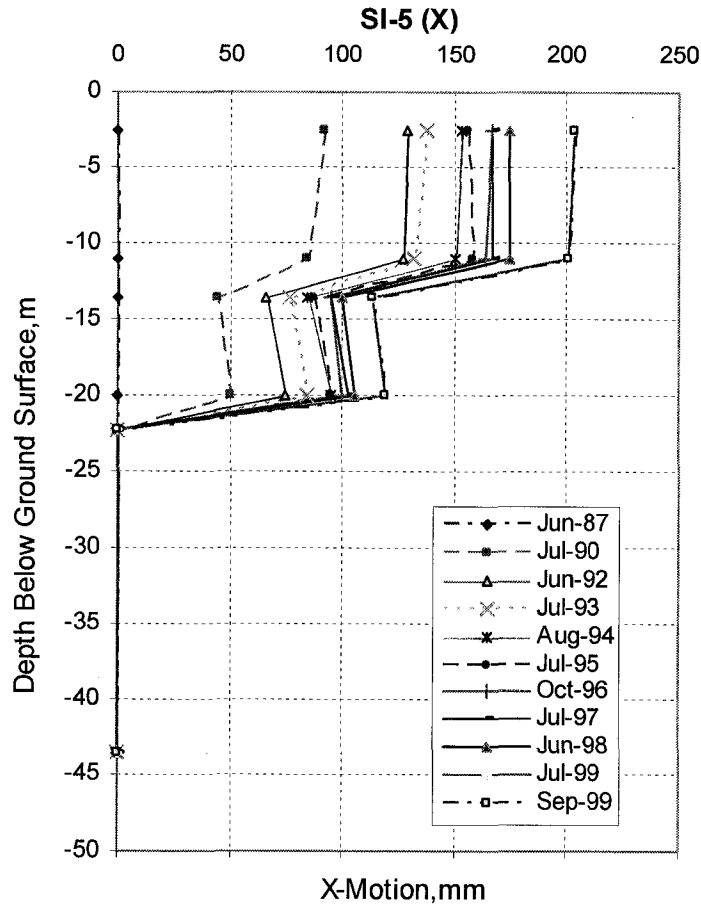


Figure 5.8 Soil Movement in X direction at SI5 at Different Period of Time

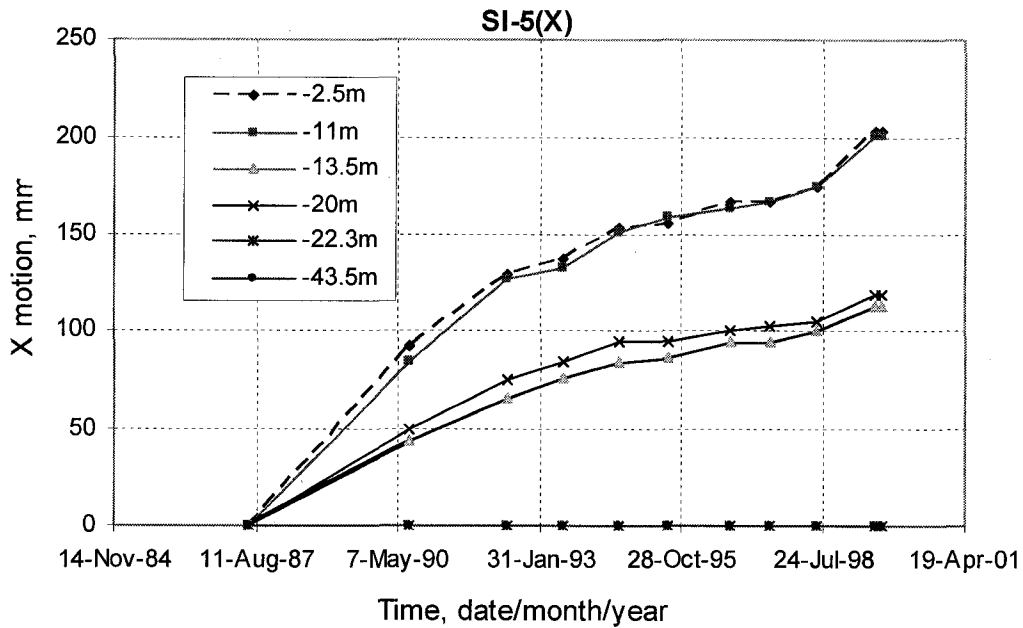


Figure 5.9 Soil Movement in X direction at SI5 at Different Depths

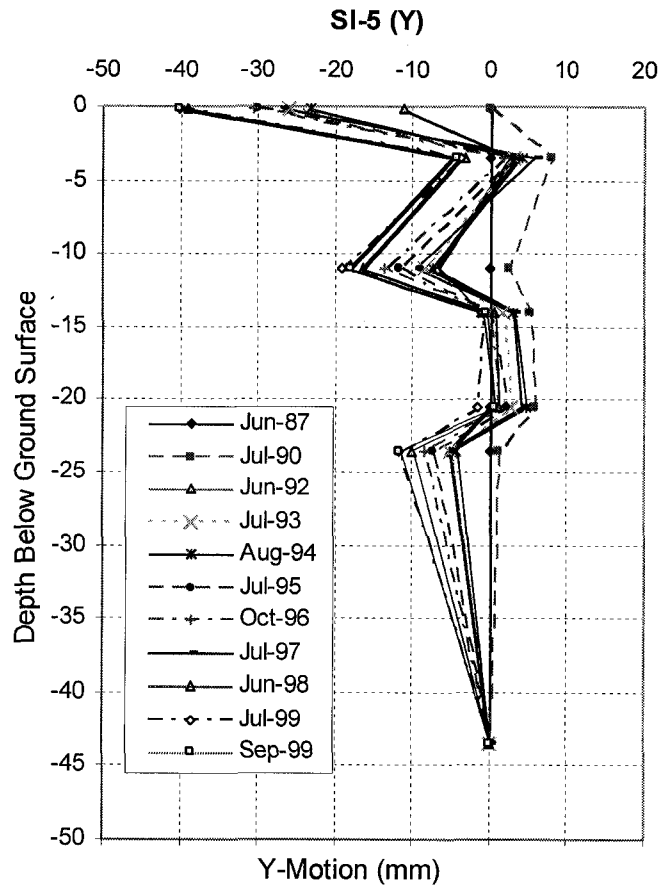


Figure 5.10 Soil Movement in Y direction at SI5 at Different Period of Time

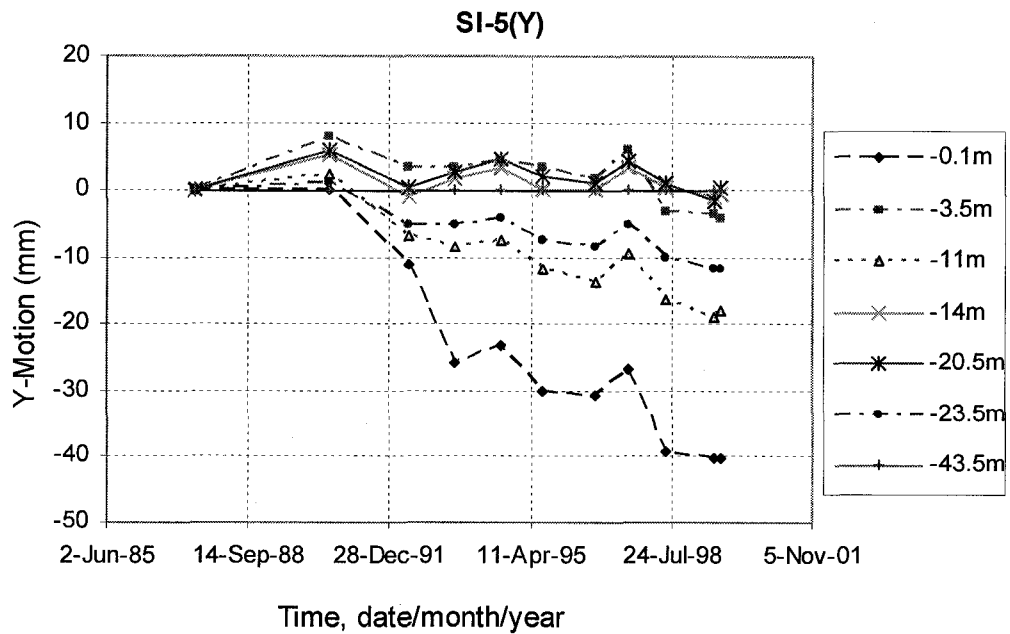


Figure 5.11 Soil Movement in Y direction at SI5 at Different Depths

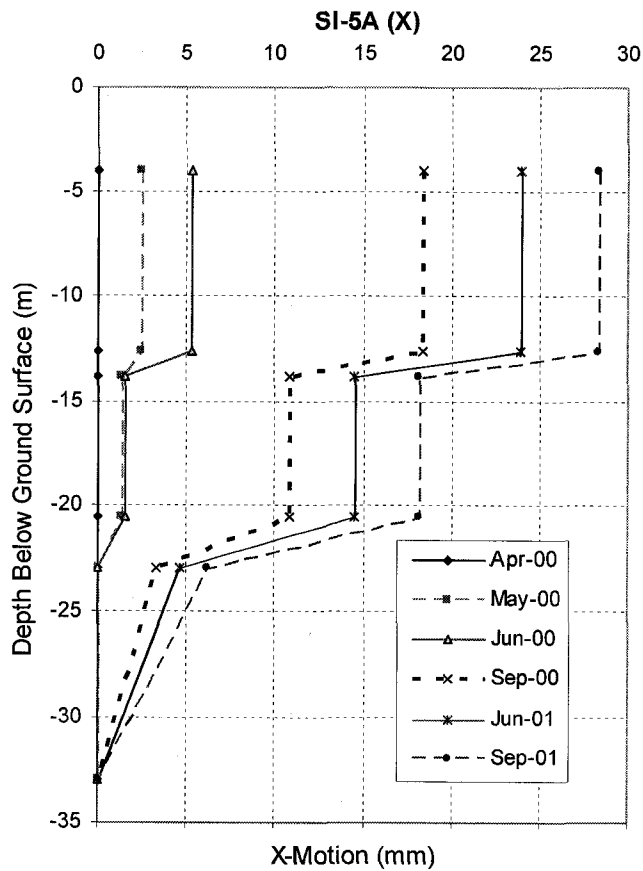


Figure 5.12 Soil Movement in X direction at SI5A at Different Period of Time

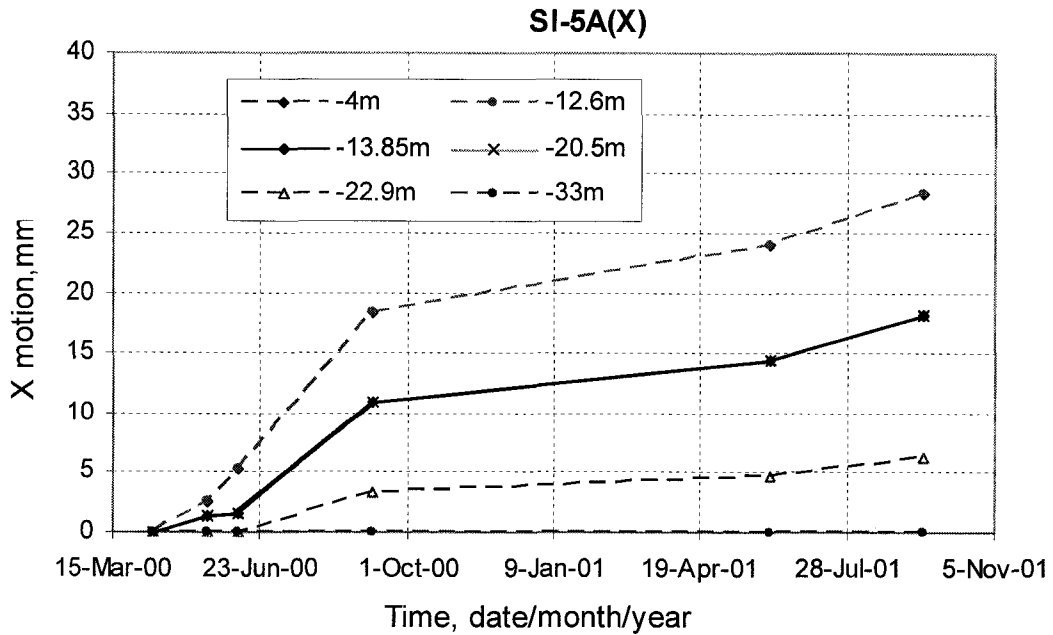


Figure 5.13 Soil Movement in X direction at SI5A at Different Depths

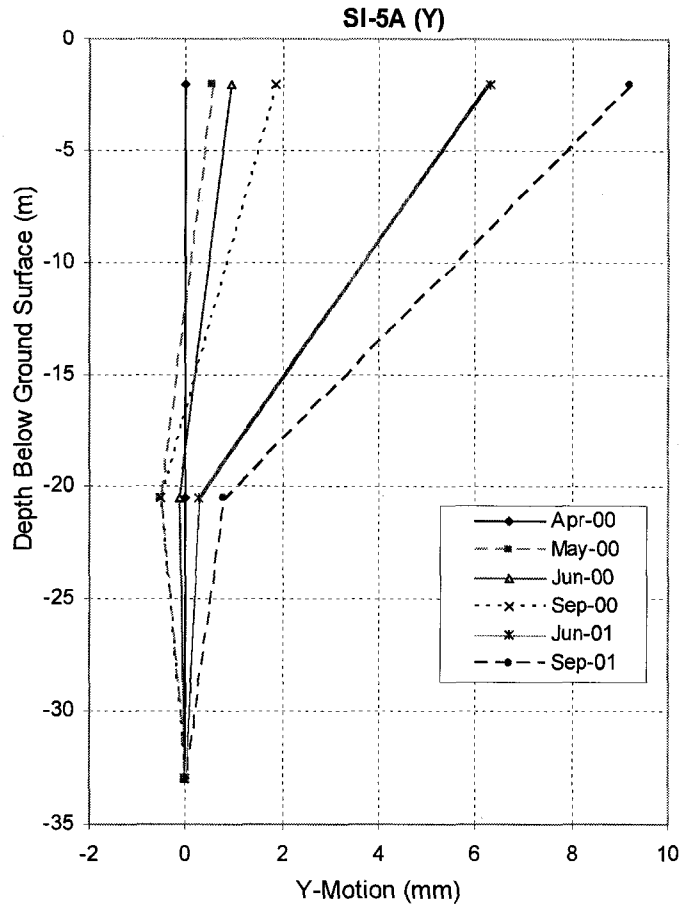


Figure 5.14 Soil Movement in Y direction at SI5A at Different Period of Time

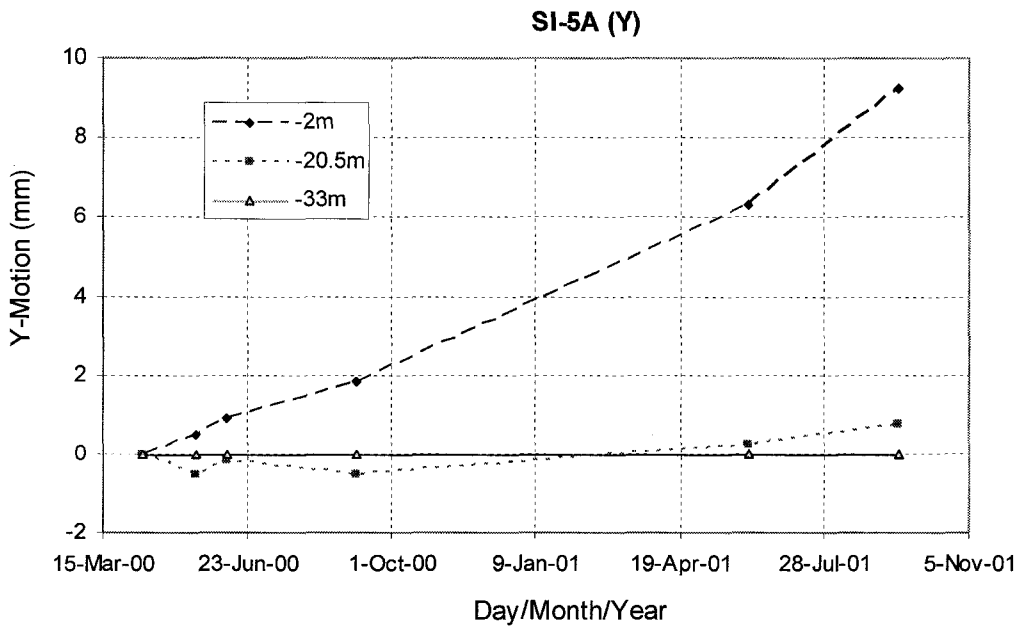


Figure 5.15 Soil Movement in Y direction at SI5A at Different Depths

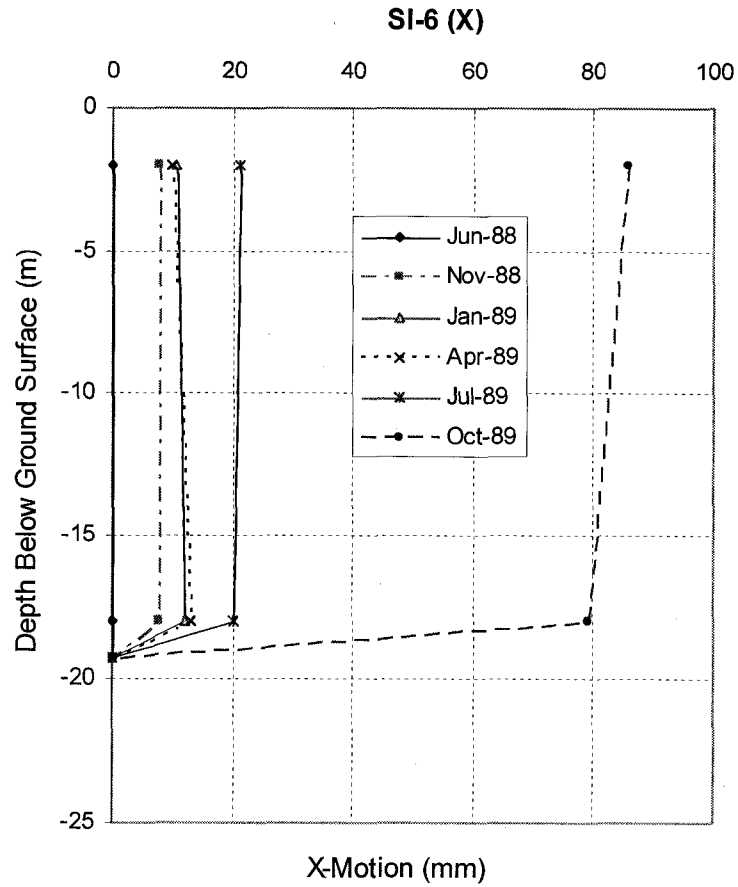


Figure 5.16 Soil Movement in X direction at SI6 at Different Period of Time

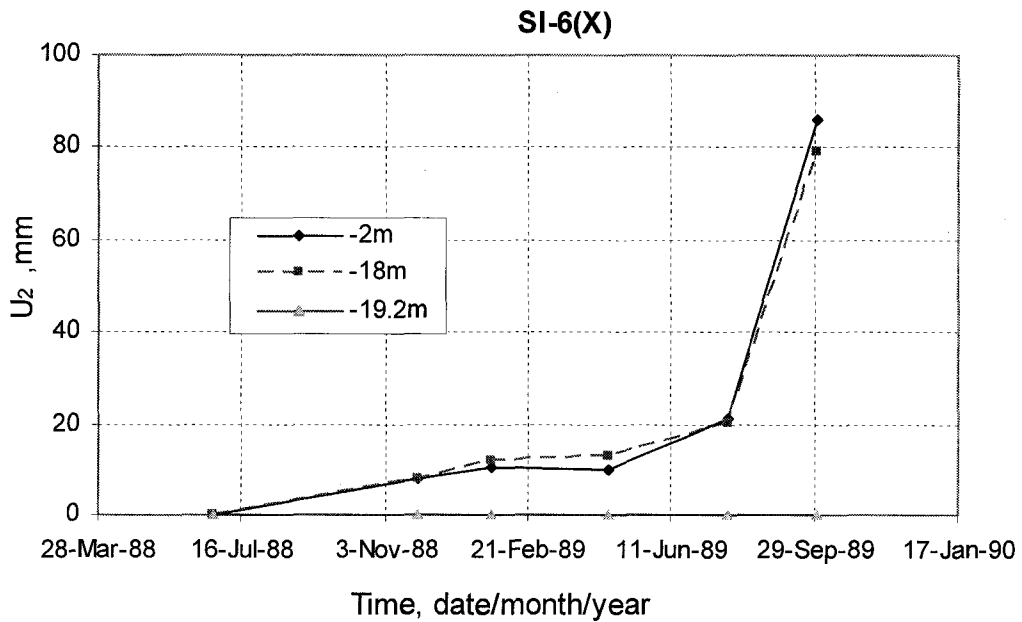


Figure 5.17 Soil Movement in X direction at SI6 at Different Depths

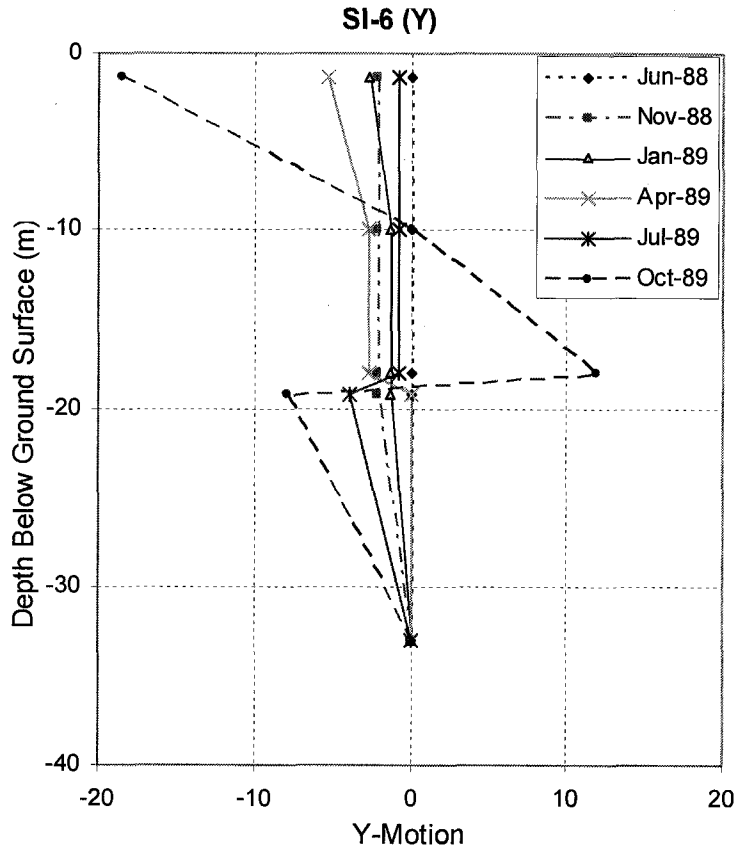


Figure 5.18 Soil Movement in Y direction at SI6 at Different Period of Time

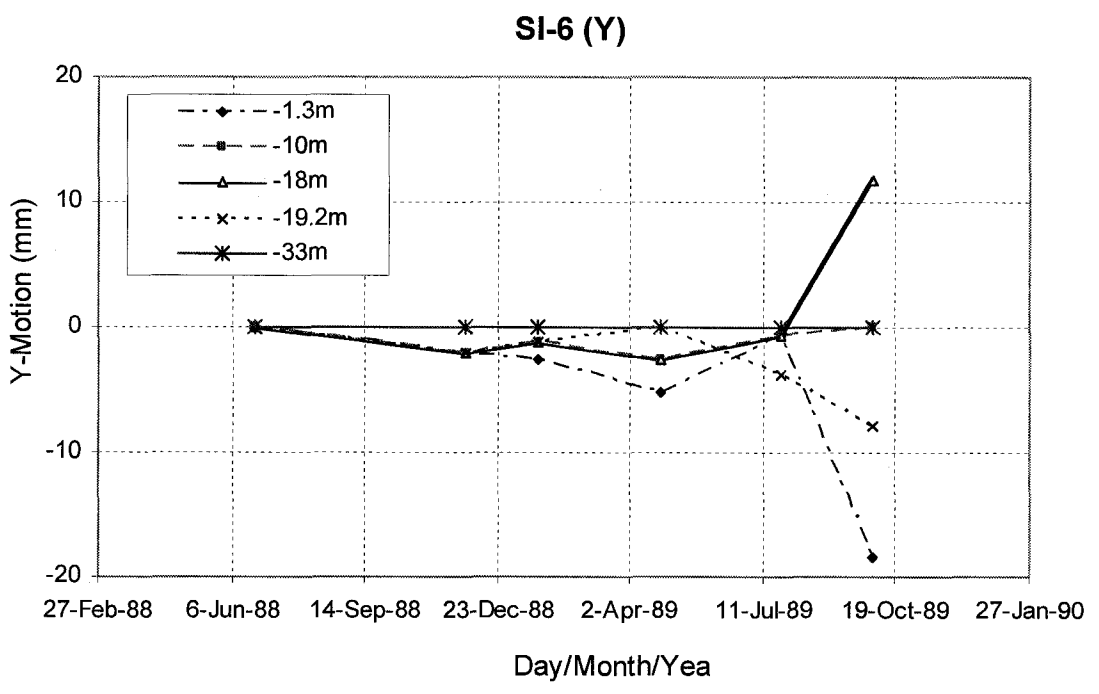


Figure 5.19 Soil Movement in Y direction at SI6 at Different Depths

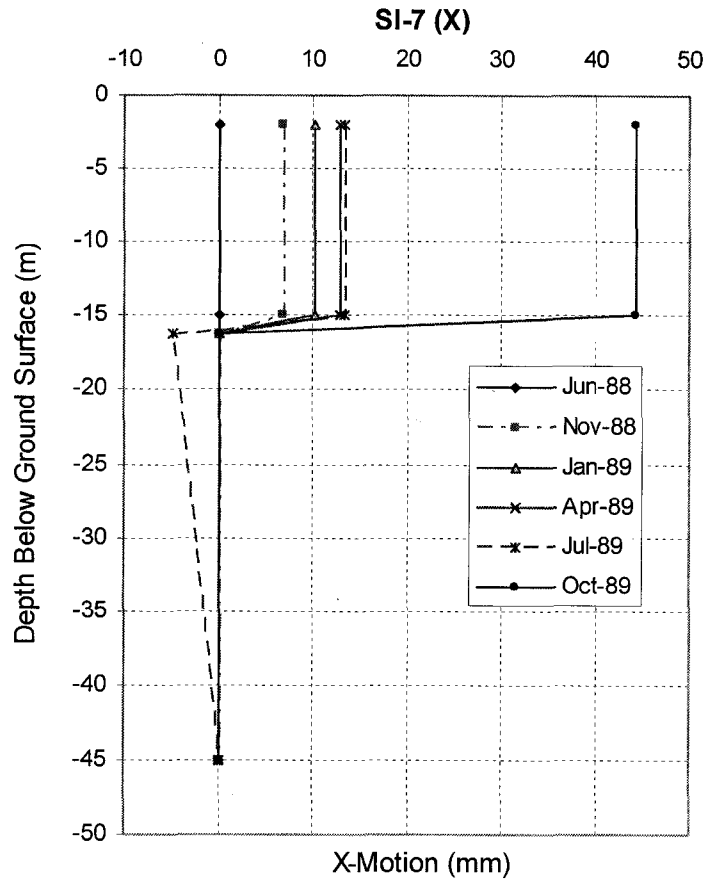


Figure 5.20 Soil Movement in X direction at SI7 at Different Period of Time

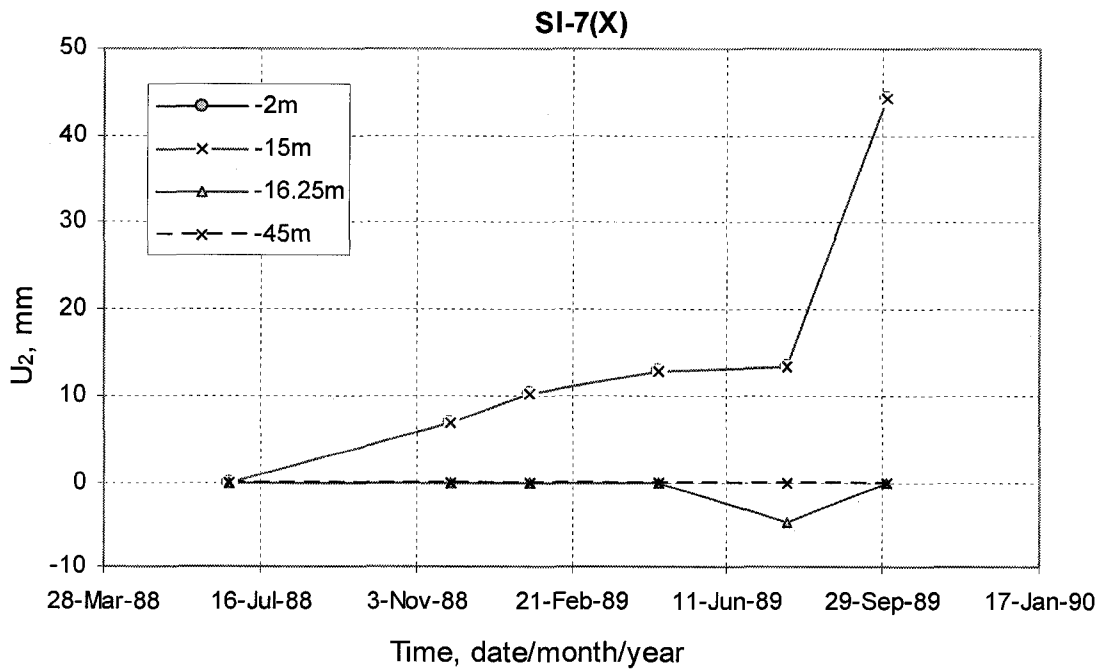


Figure 5.21 Soil Movement in X direction at SI7 at Different Depths

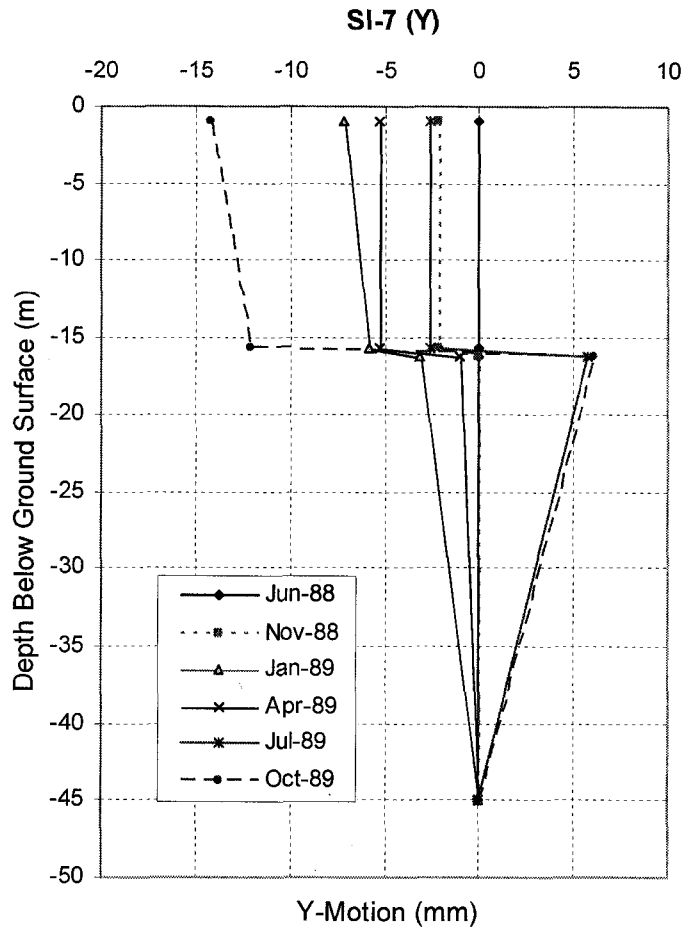


Figure 5.22 Soil Movement in Y direction at SI7 at Different Period of Time

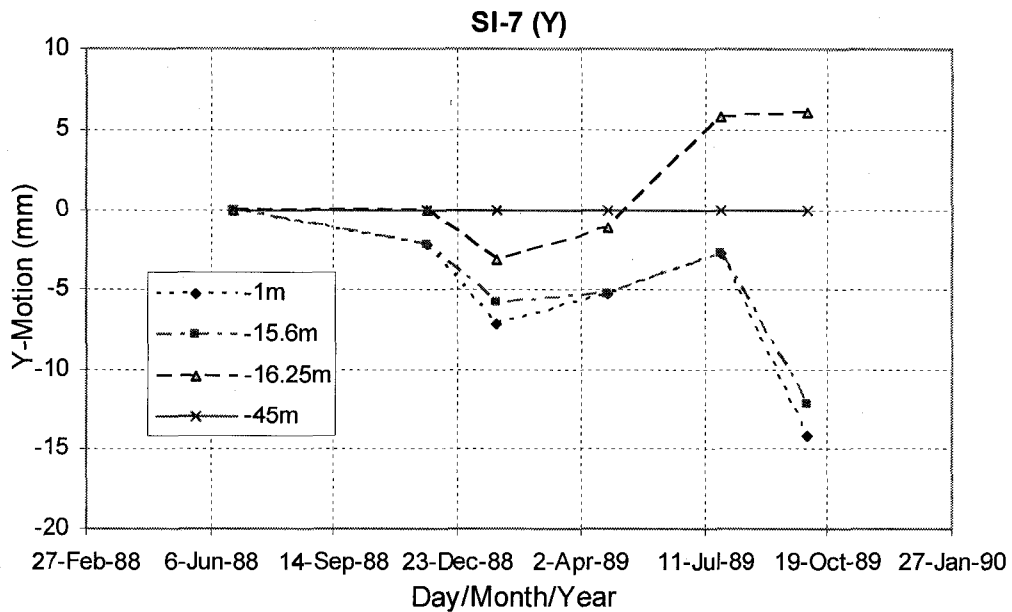


Figure 5.23 Soil Movement in Y direction at SI7 at Different Depths

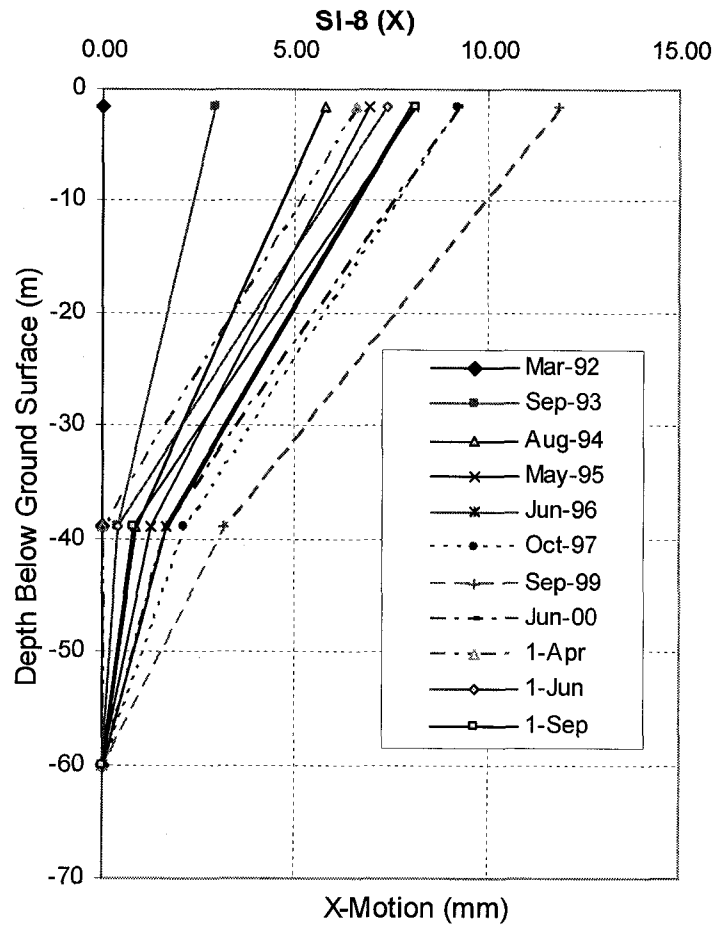


Figure 5.24 Soil Movement in X direction at SI8 at Different Period of Time

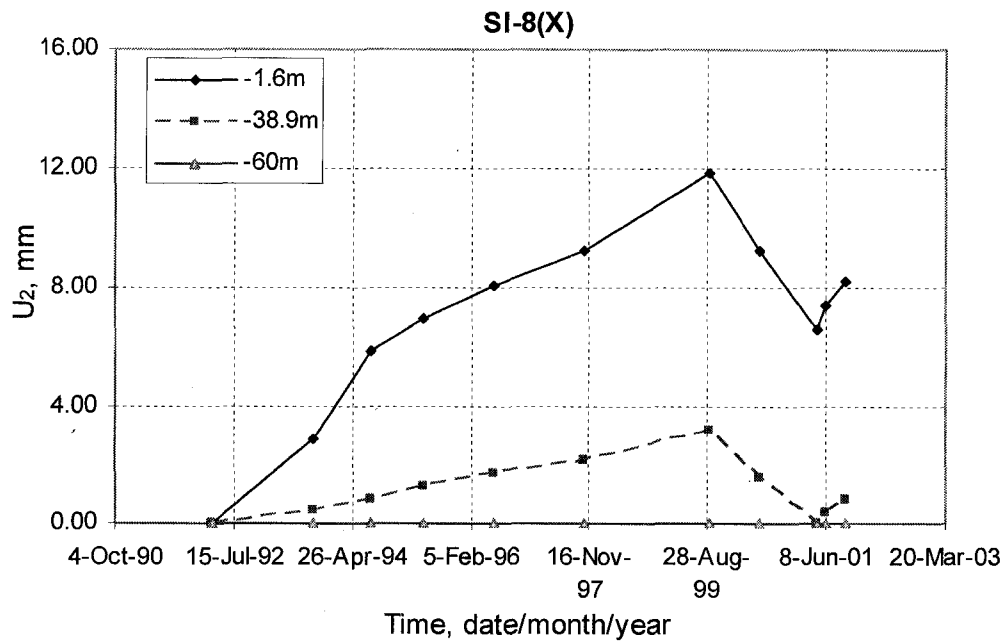


Figure 5.25 Soil Movement in X direction at SI8 at Different Depths

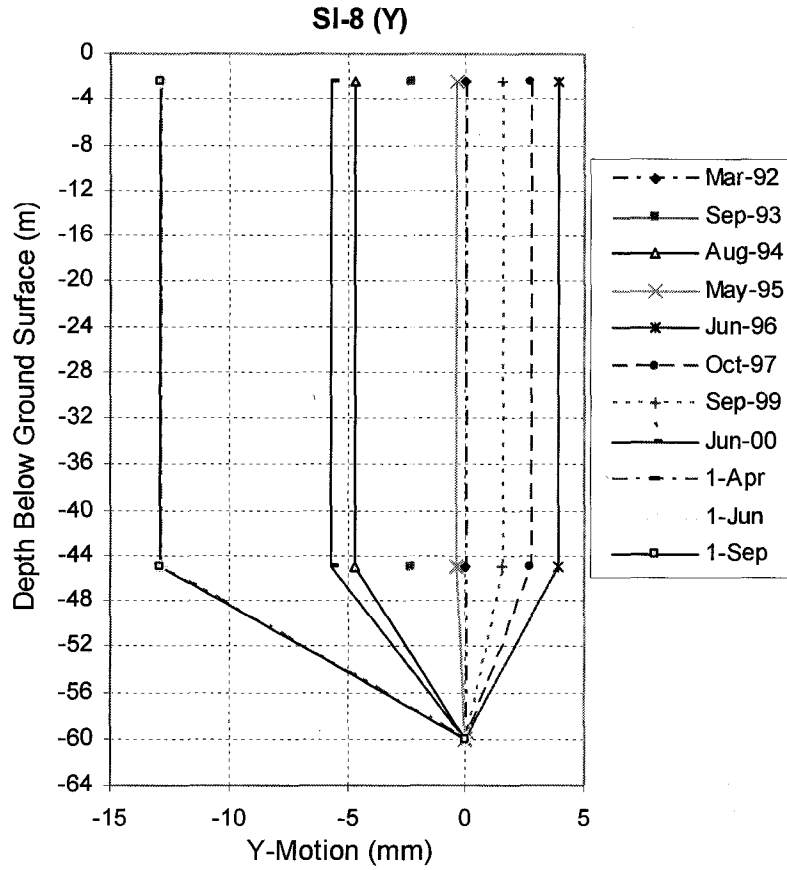


Figure 5.26 Soil Movement in Y direction at SI8 at Different Period of Time

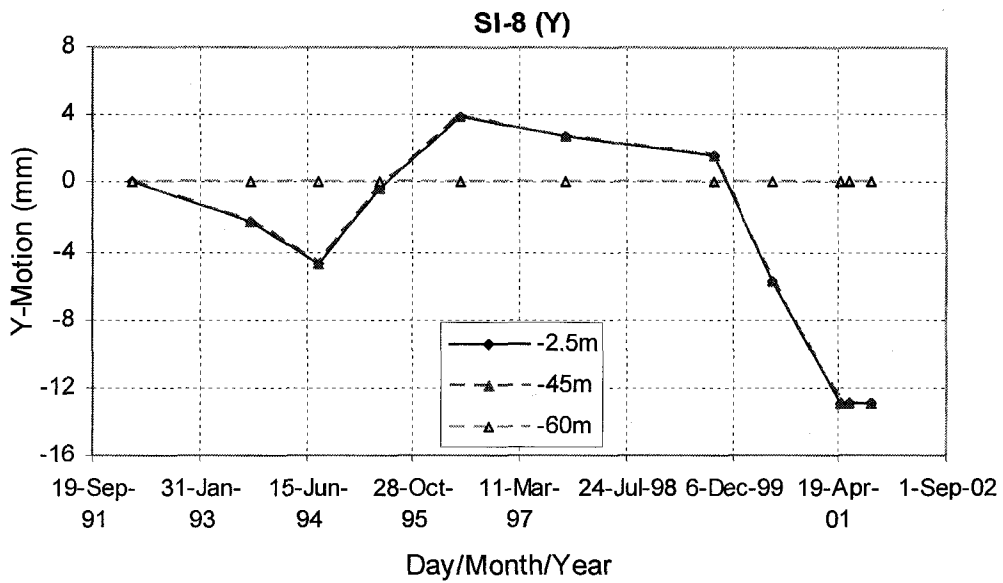


Figure 5.27 Soil Movement in Y direction at SI8 at Different Depths

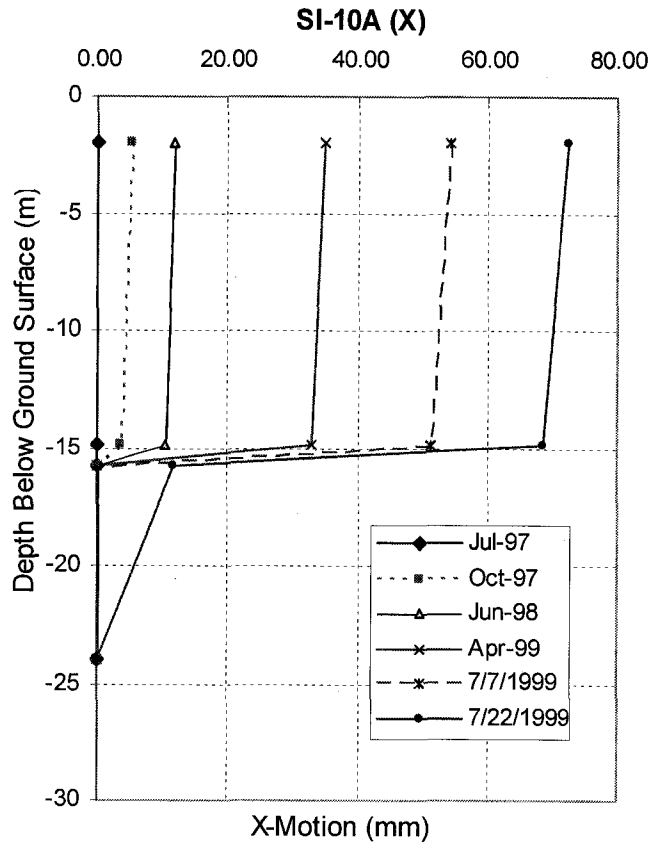


Figure 5.28 Soil Movement in X direction at SI10A at Different Period of Time

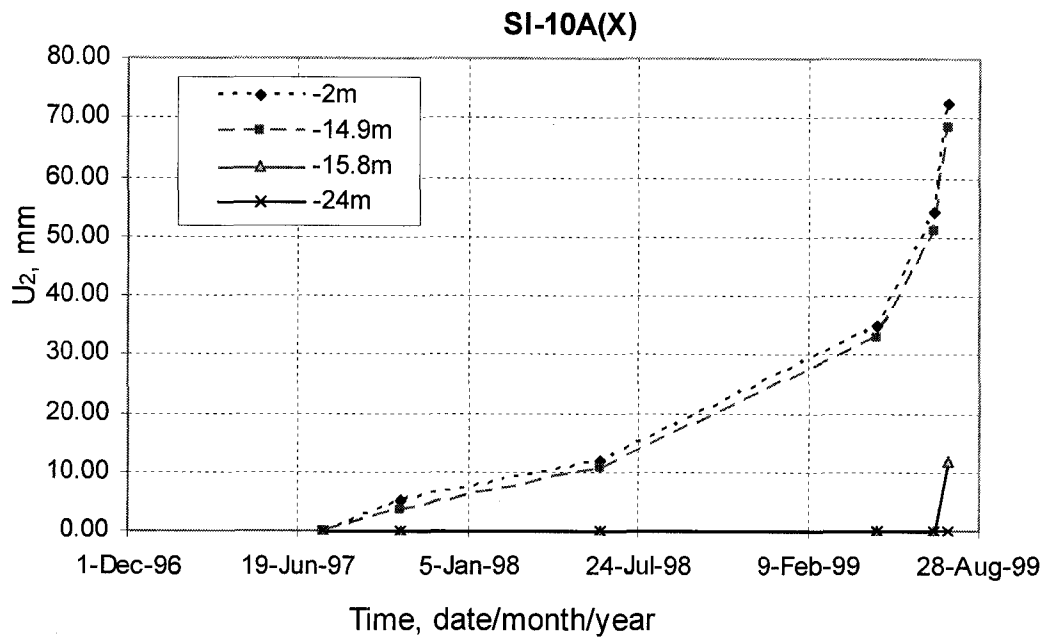


Figure 5.29 Soil Movement in X direction at SI10A at Different Depths

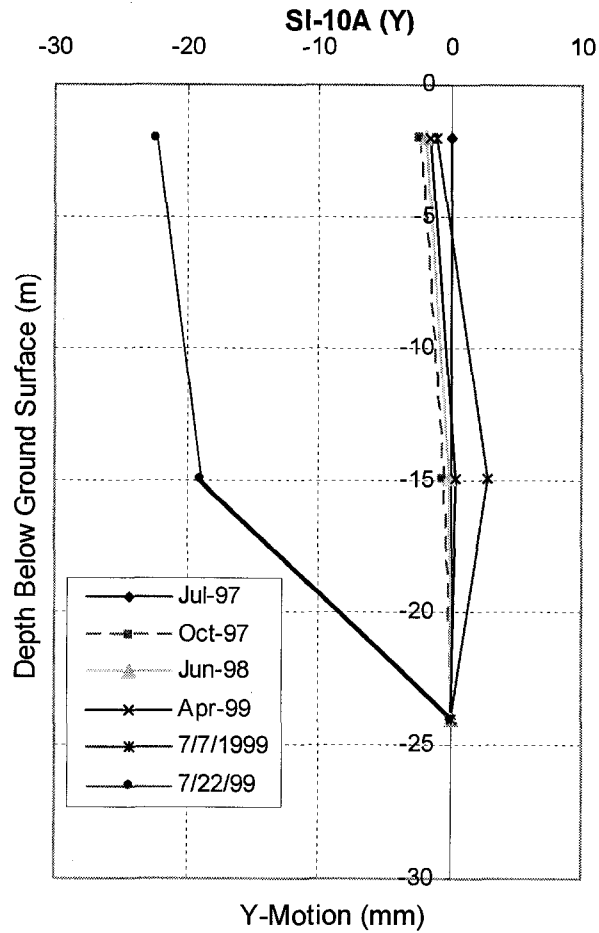


Figure 5.30 Soil Movement in Y direction at SI10A at Different Period of Time

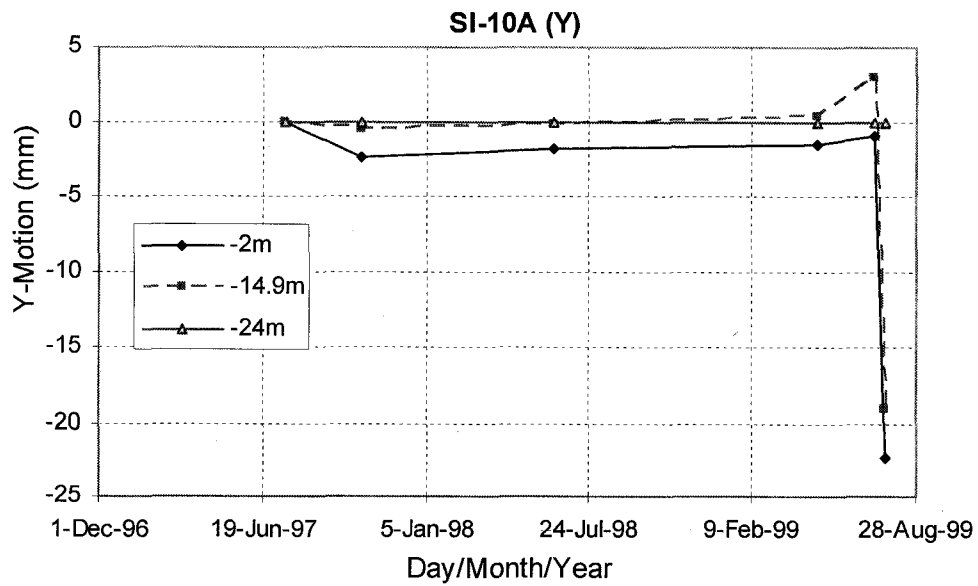


Figure 5.31 Soil Movement in Y direction at SI10A at Different Depths

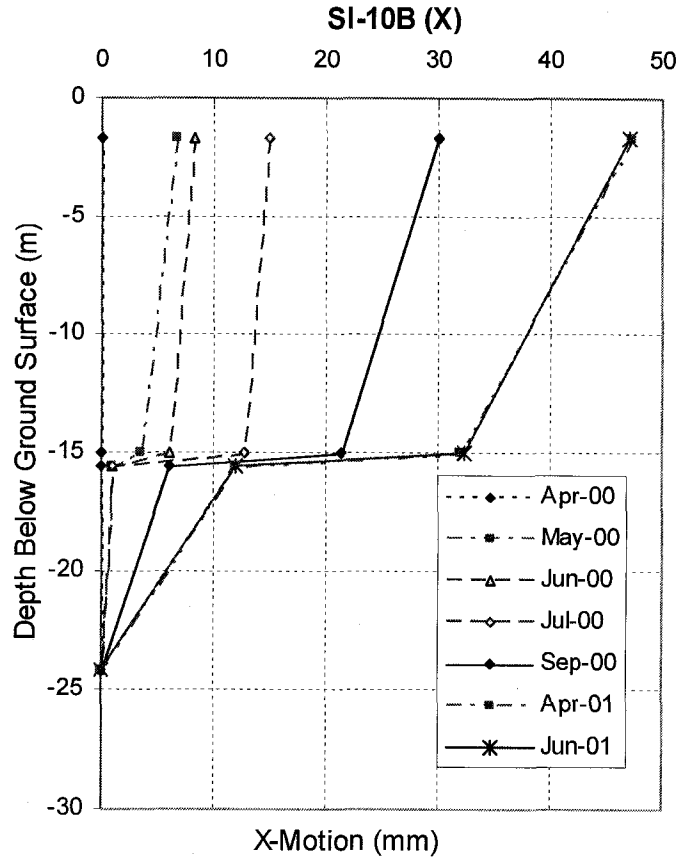


Figure 5.32 Soil Movement in X direction at SI10B at Different Period of Time

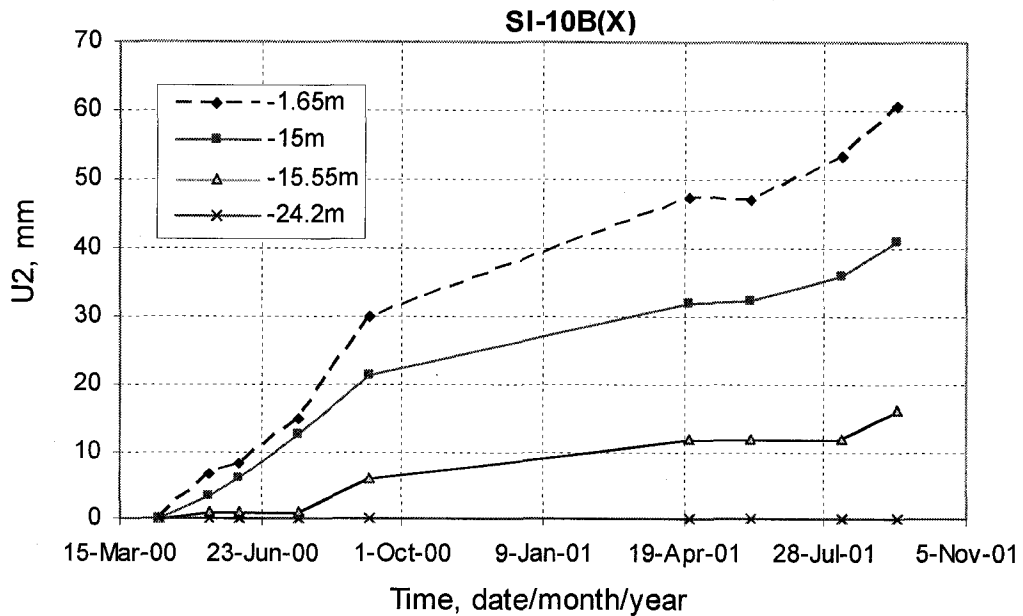


Figure 5.33 Soil Movement in X direction at SI10B at Different Depths

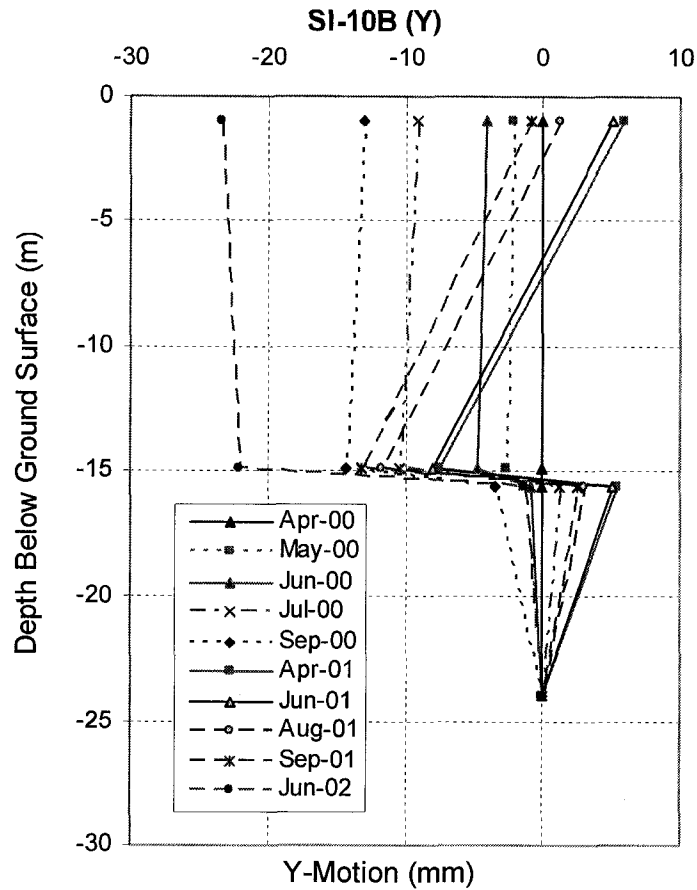


Figure 5.34 Soil Movement in Y direction at SI10B at Different Period of Time

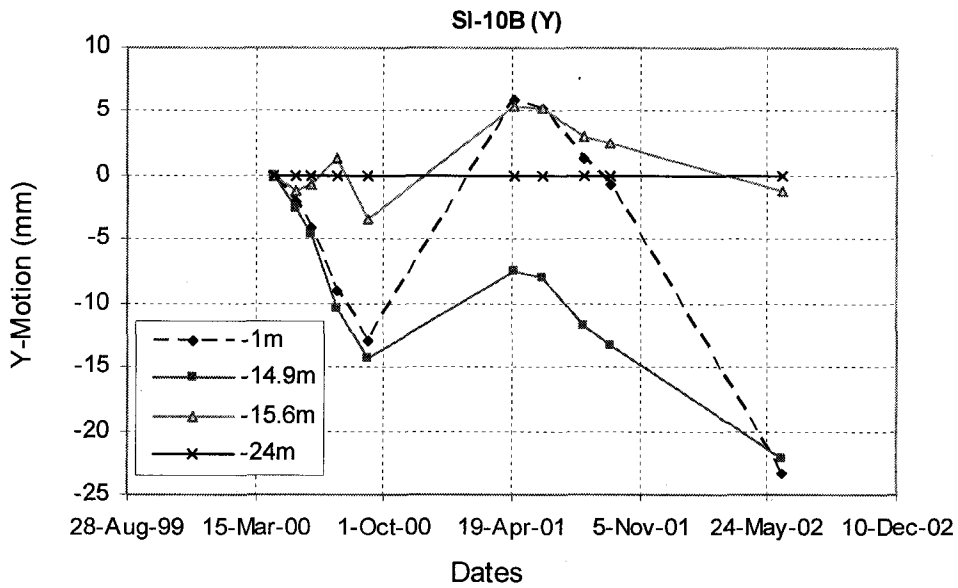


Figure 5.35 Soil Movement in Y direction at SI10B at Different Depths

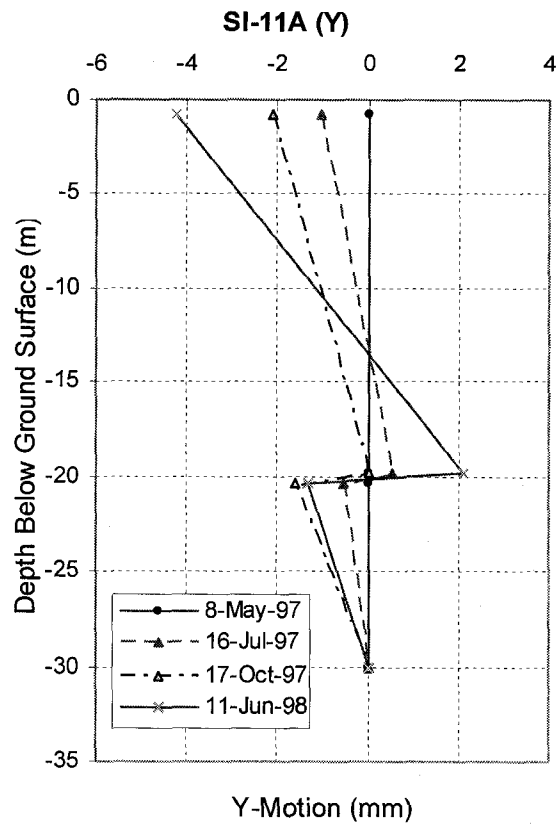


Figure 5.38 Soil Movement in Y direction at SI11A at Different Period of Time

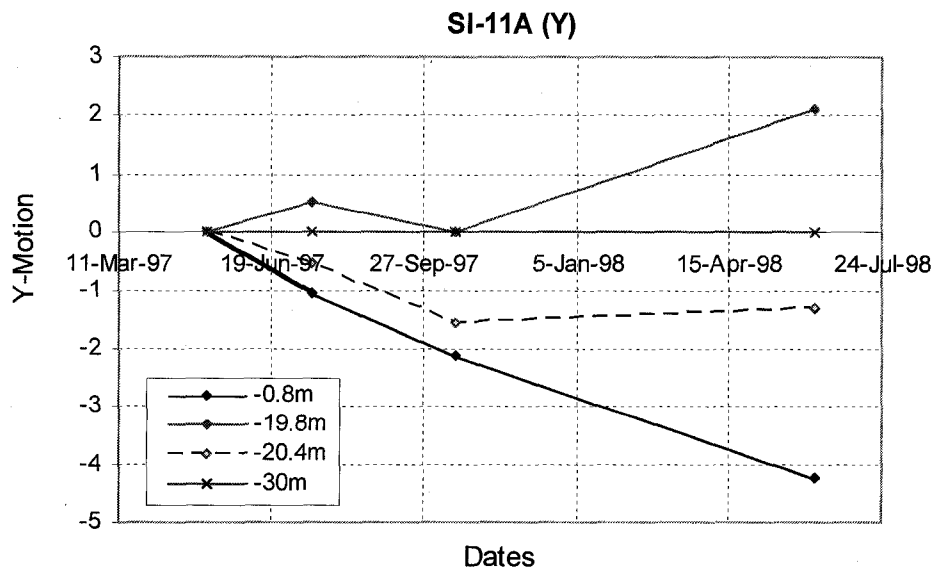


Figure 5.39 Soil Movement in Y direction at SI11A at Different Depths

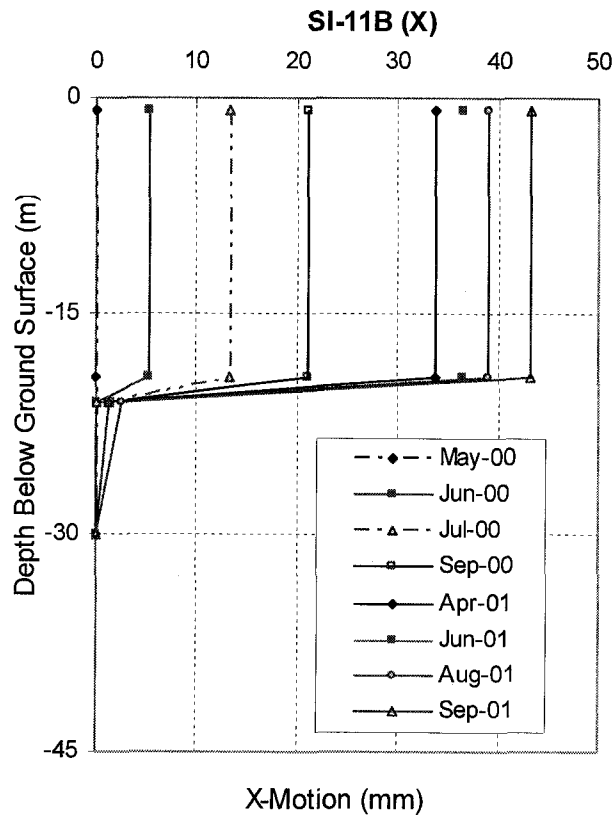


Figure 5.40 Soil Movement in X direction at SI11B at Different Period of Time

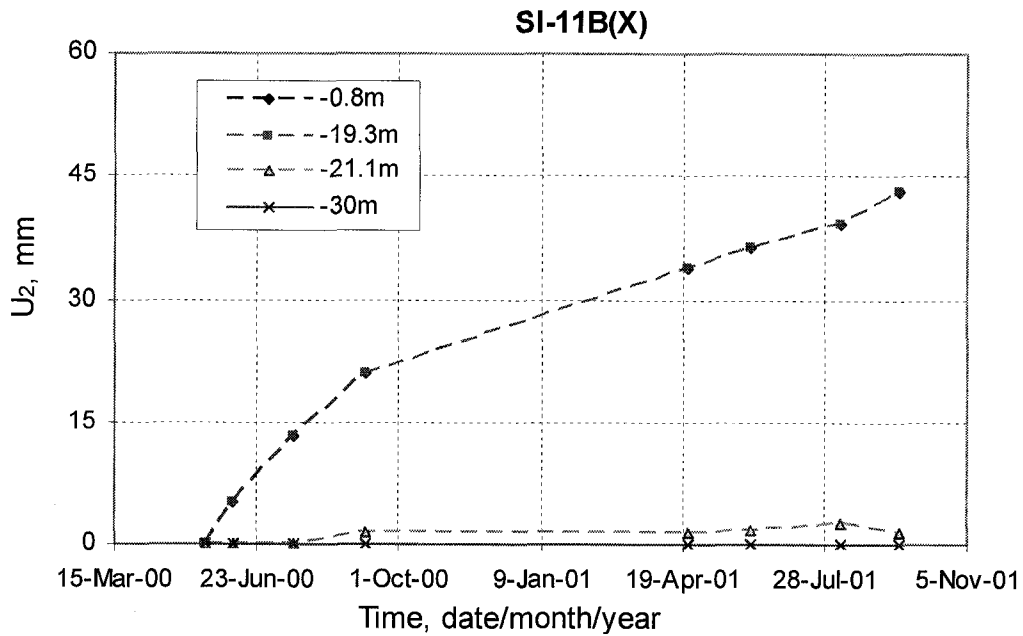


Figure 5.41 Soil Movement in X direction at SI11B at Different Depths

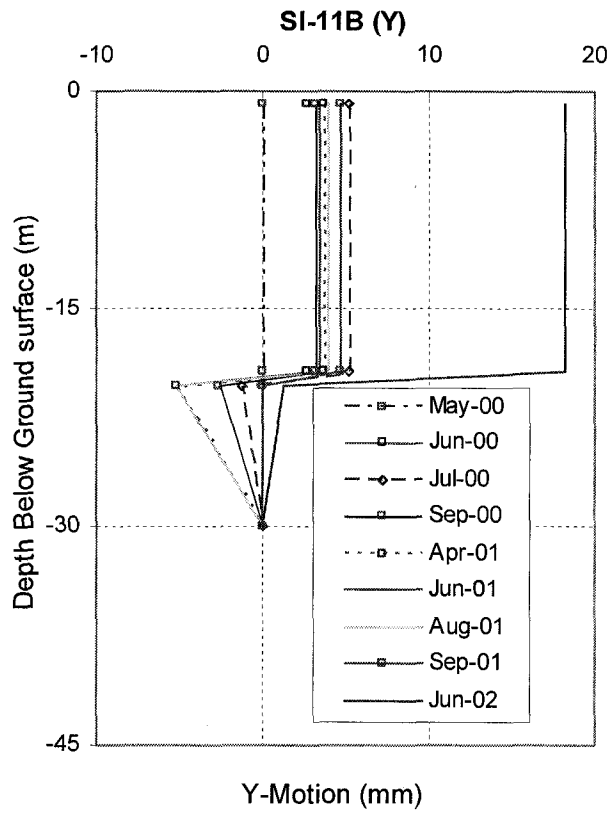


Figure 5.42 Soil Movement in Y direction at SI11B at Different Period of Time

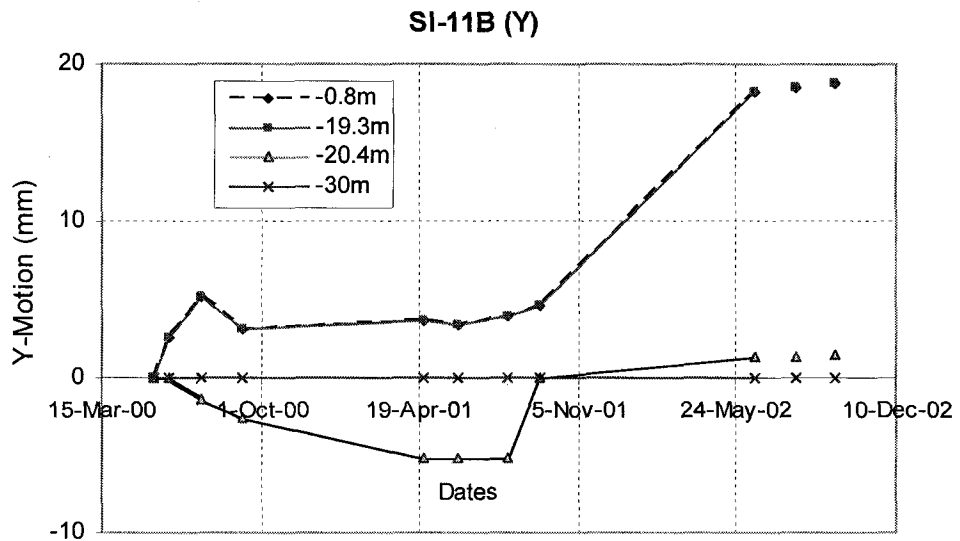


Figure 5.43 Soil Movement in Y direction at SI11B at Different Depths

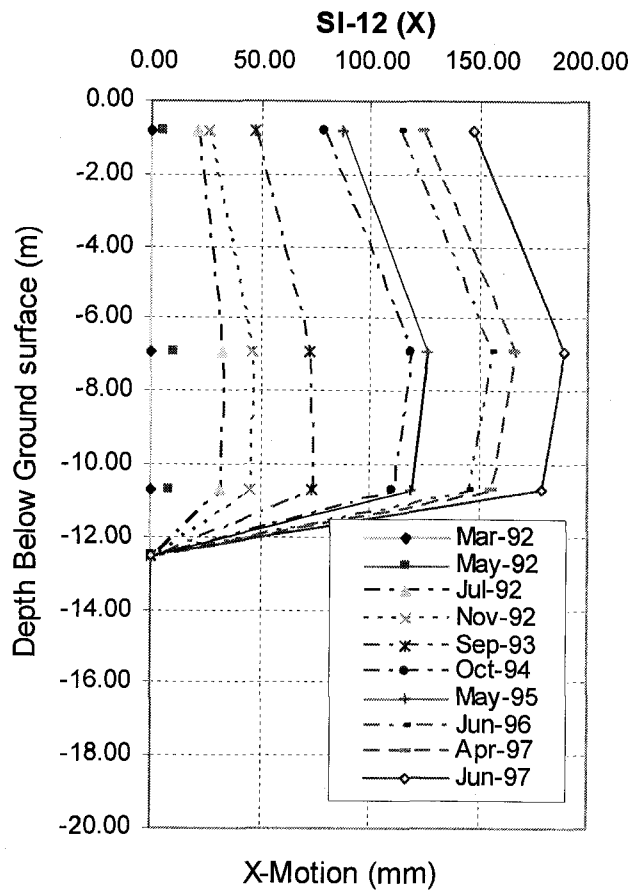


Figure 5.44 Soil Movement in X direction at SI12 at Different Period of Time

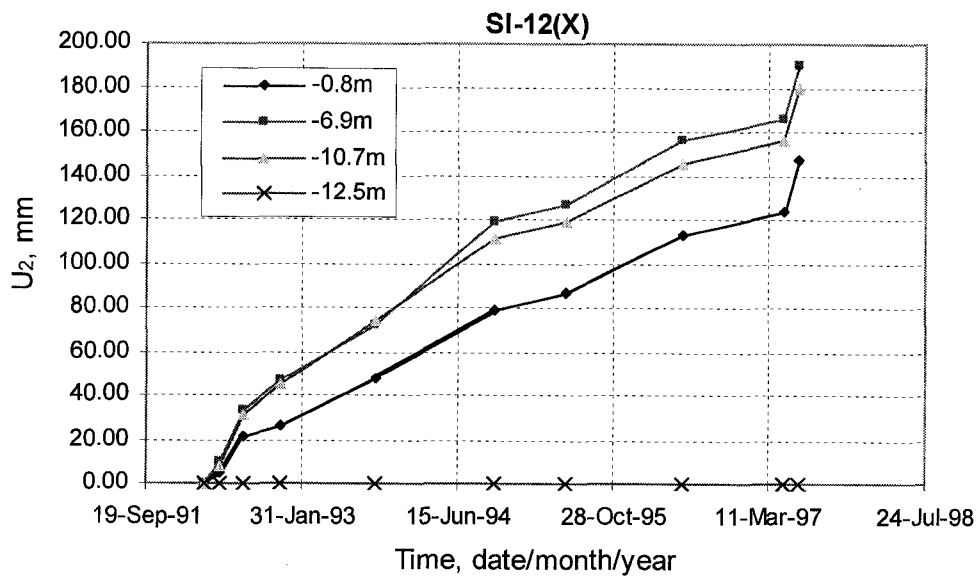


Figure 5.45 Soil Movement in X direction at SI12 at Different Depths

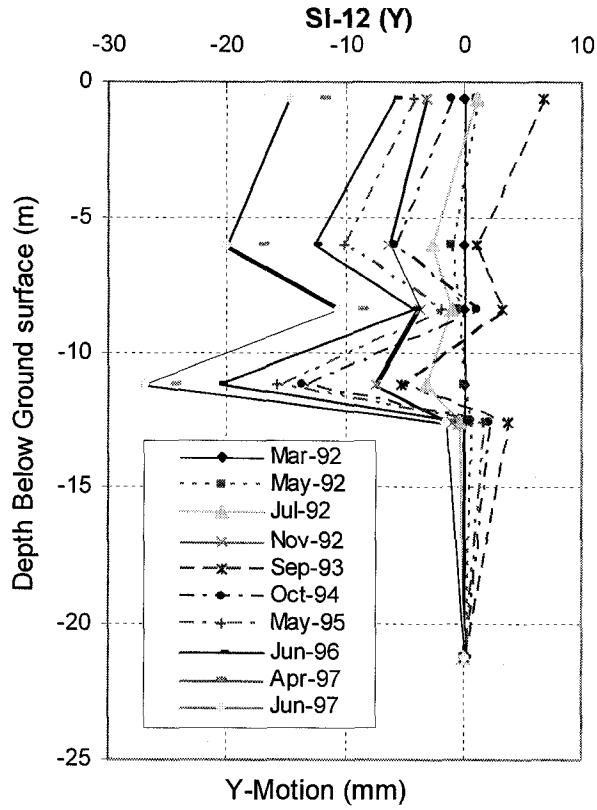


Figure 5.46 Soil Movement in Y direction at SI12 at Different Period of Time

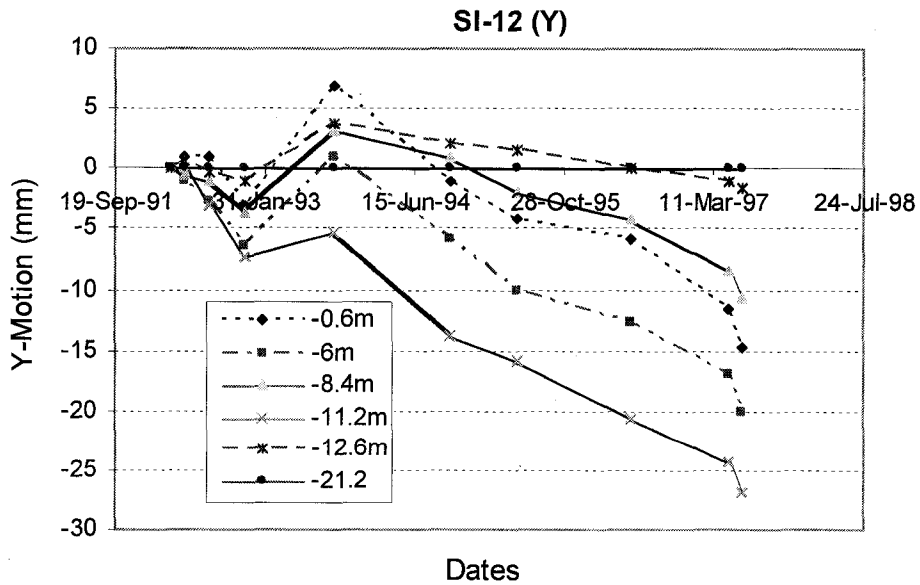


Figure 5.47 Soil Movement in Y direction at SI12 at Different Depths

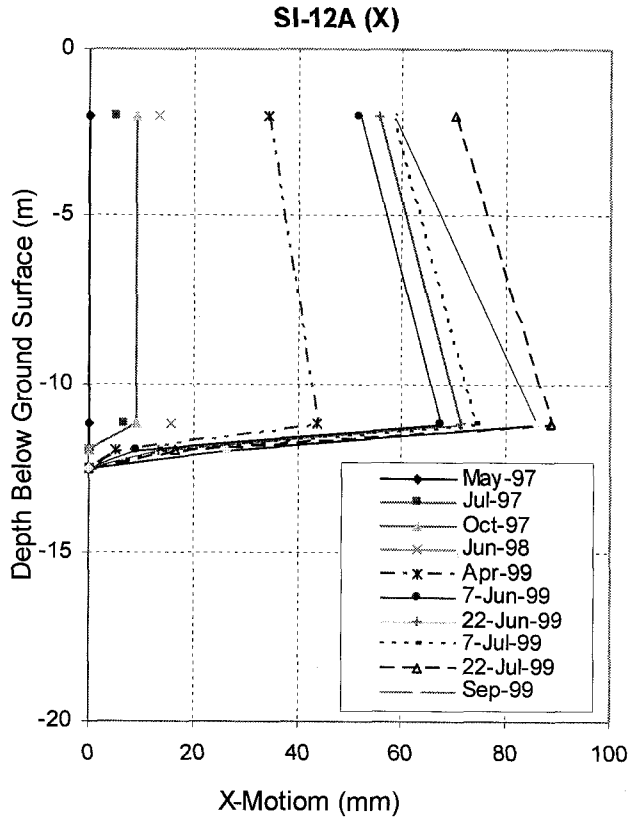


Figure 5.48 Soil Movement in X direction at SI12A at Different Period of Time

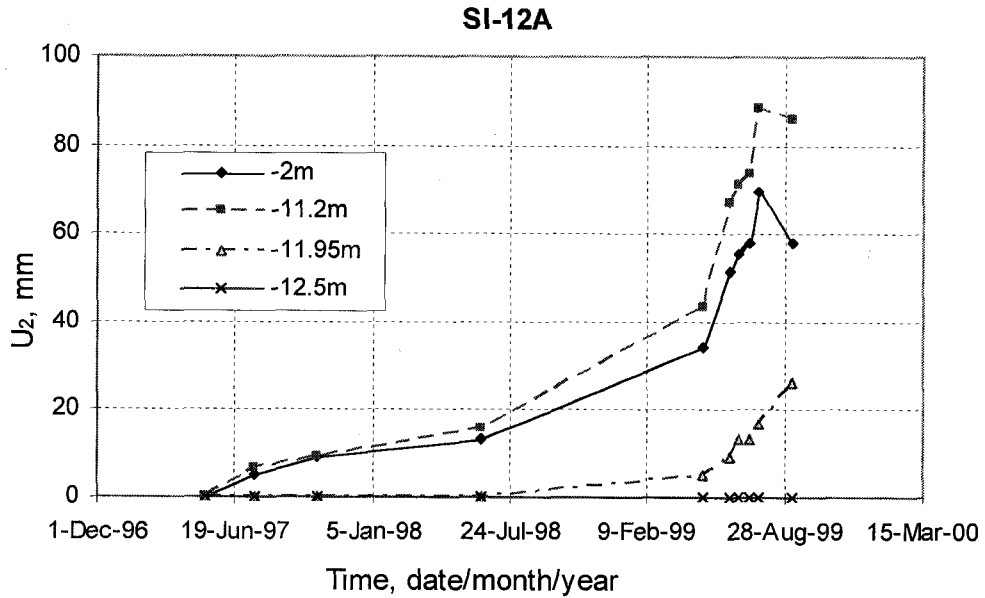


Figure 5.49 Soil Movement in X direction at SI12A at Different Depths

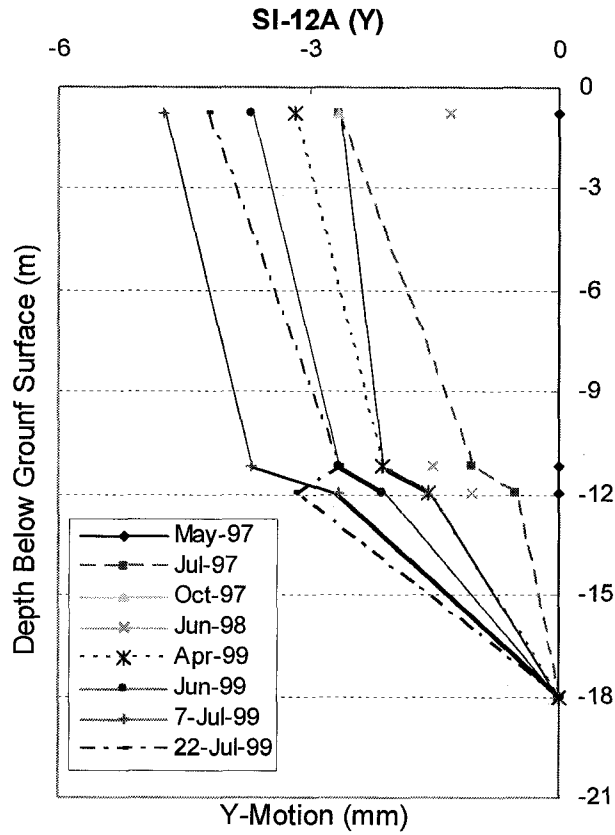


Figure 5.50 Soil Movement in Y direction at SI12A at Different Period of Time

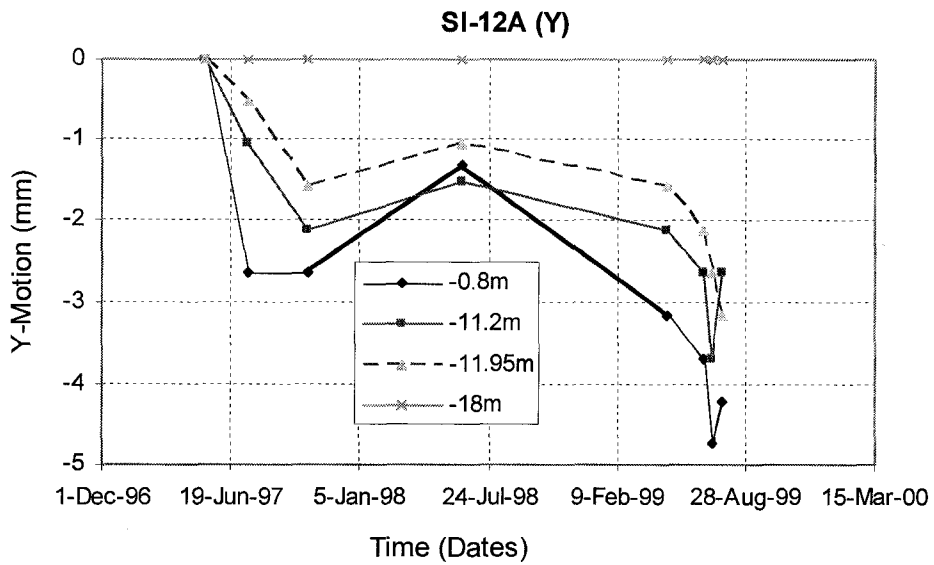


Figure 5.51 Soil Movement in Y direction at SI12A at Different Depths

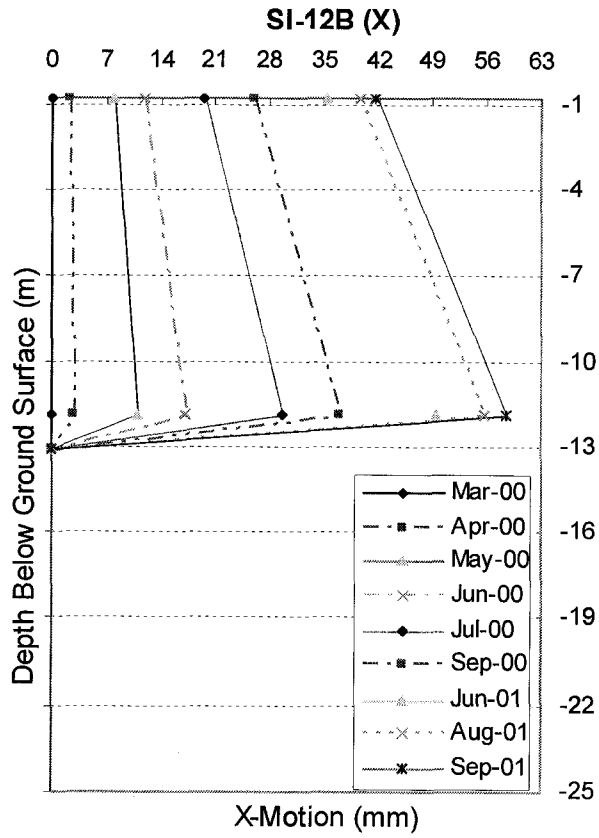


Figure 5.52 Soil Movement in X direction at SI12B at Different Period of Time

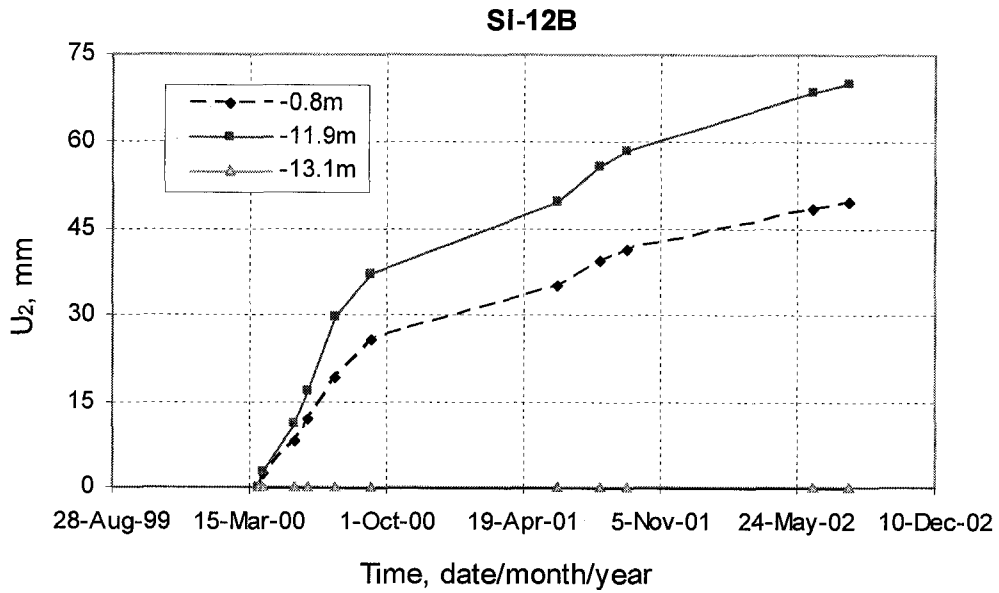


Figure 5.53 Soil Movement in X direction at SI12B at Different Depths

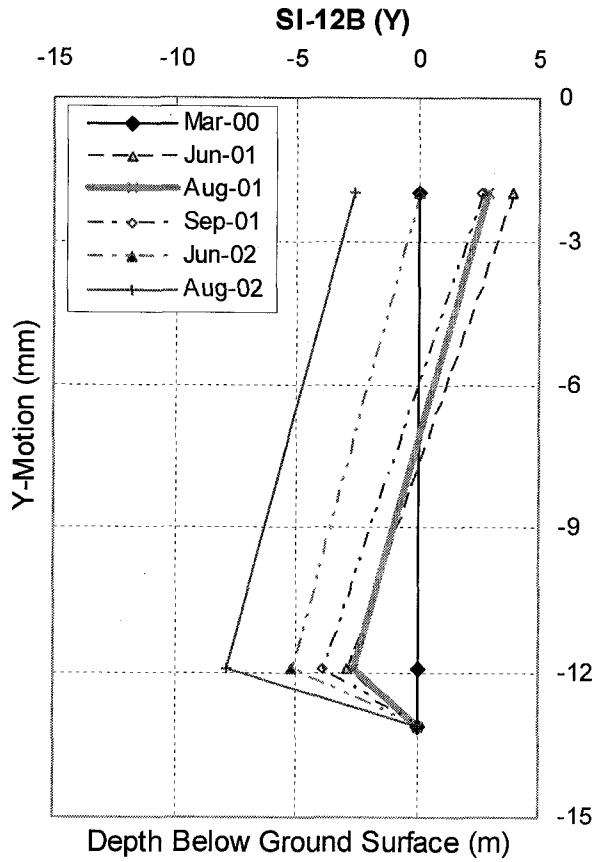


Figure 5.53 Soil Movement in Y direction at SI12B at Different Period of Time

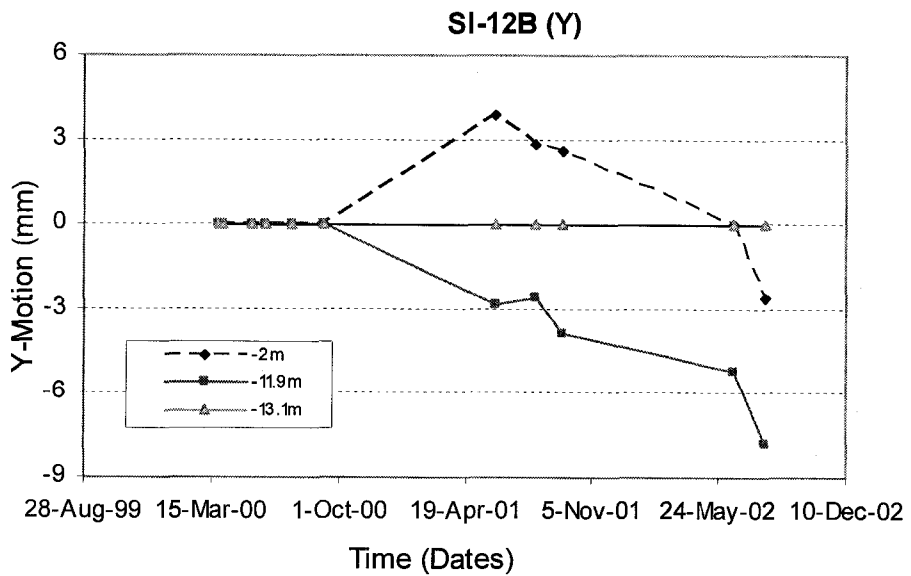


Figure 5.54 Soil Movement in Y direction at SI12B at Different Depths

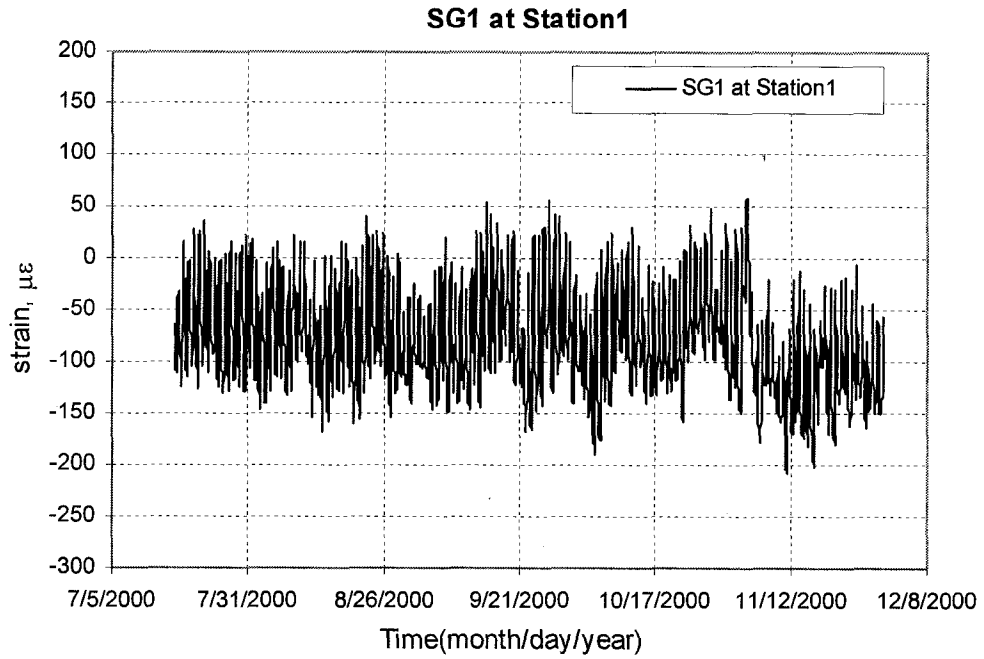


Figure 5.55 Strain Gauge 1 vs. time at Station 1

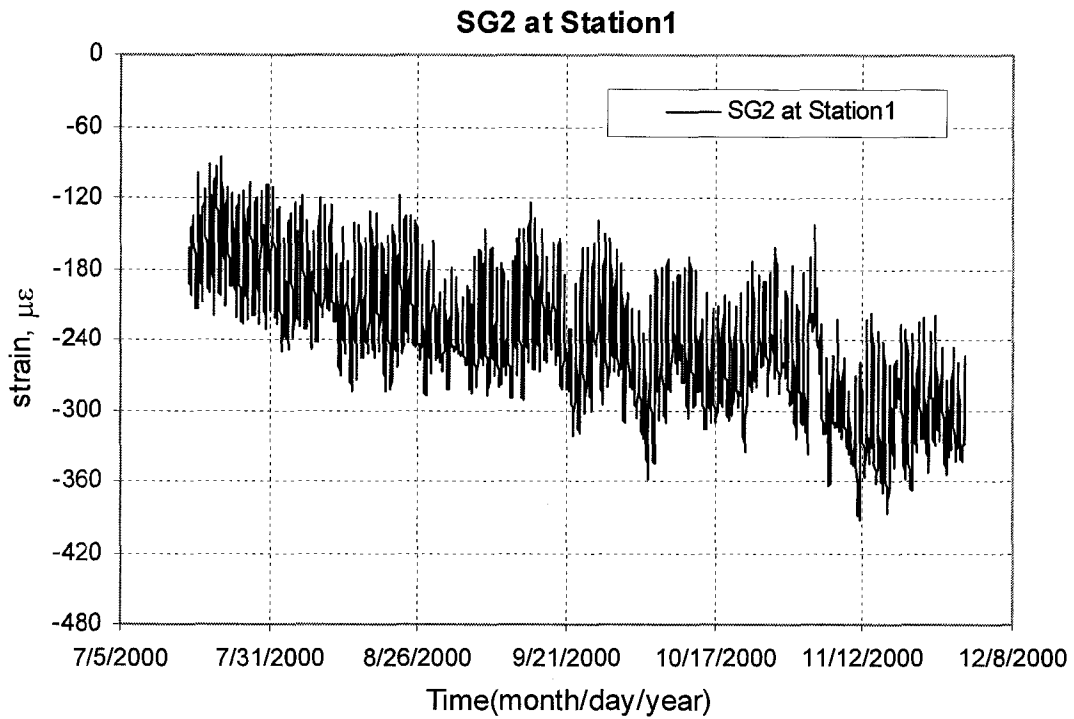


Figure 5.56 Strain Gauge 2 vs. time at Station 1

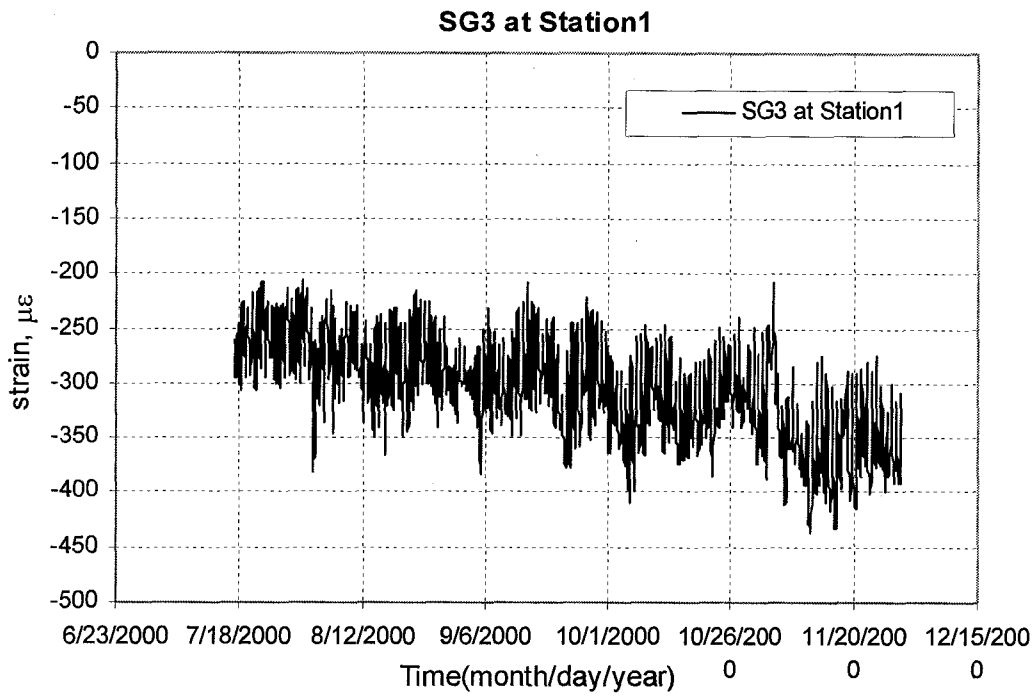


Figure 5.57 Strain Gauge 3 vs. time at Station 1

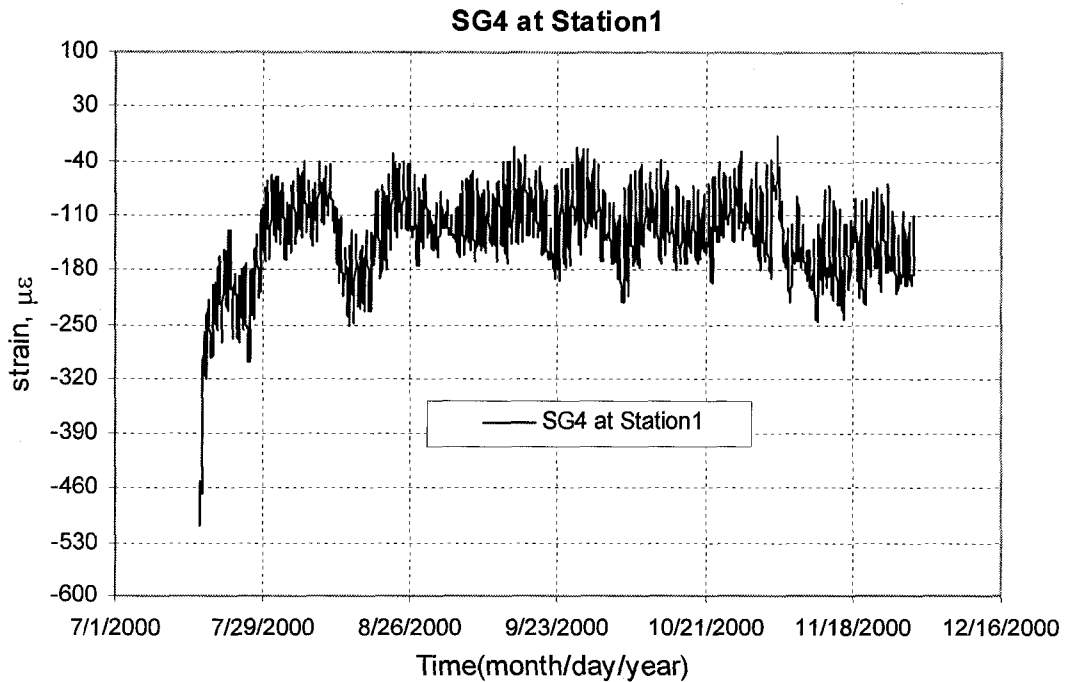


Figure 5.58 Strain Gauge 4 vs. time at Station 1

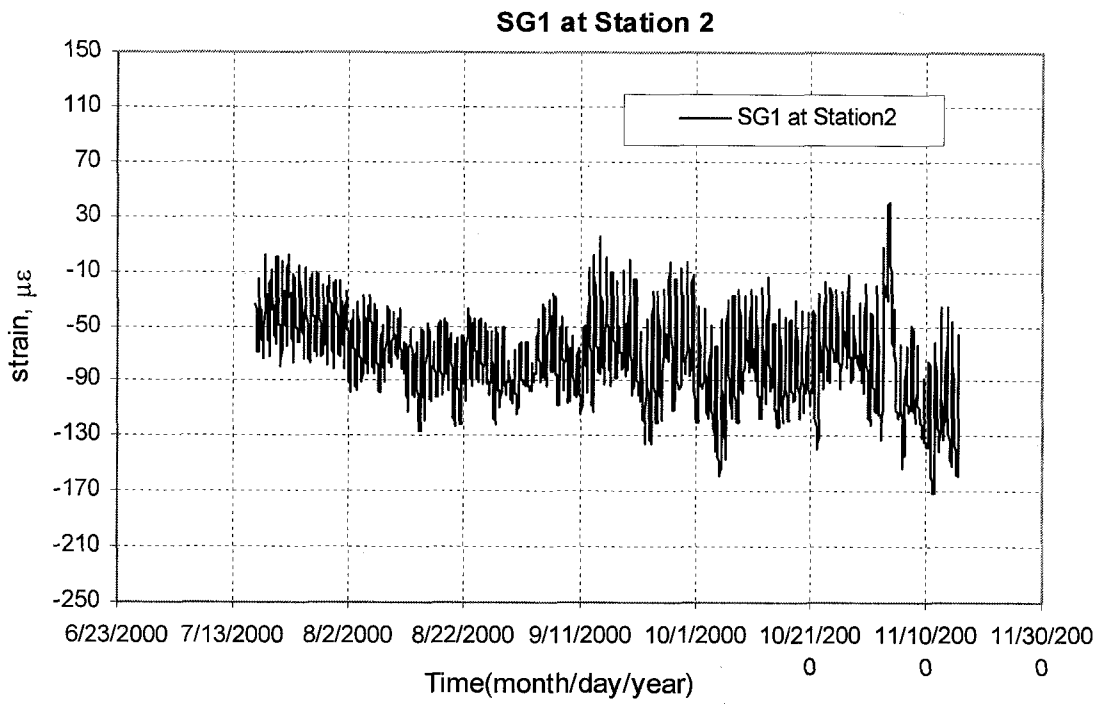


Figure 5.59 Strain Gauge 1 vs. time at Station 2

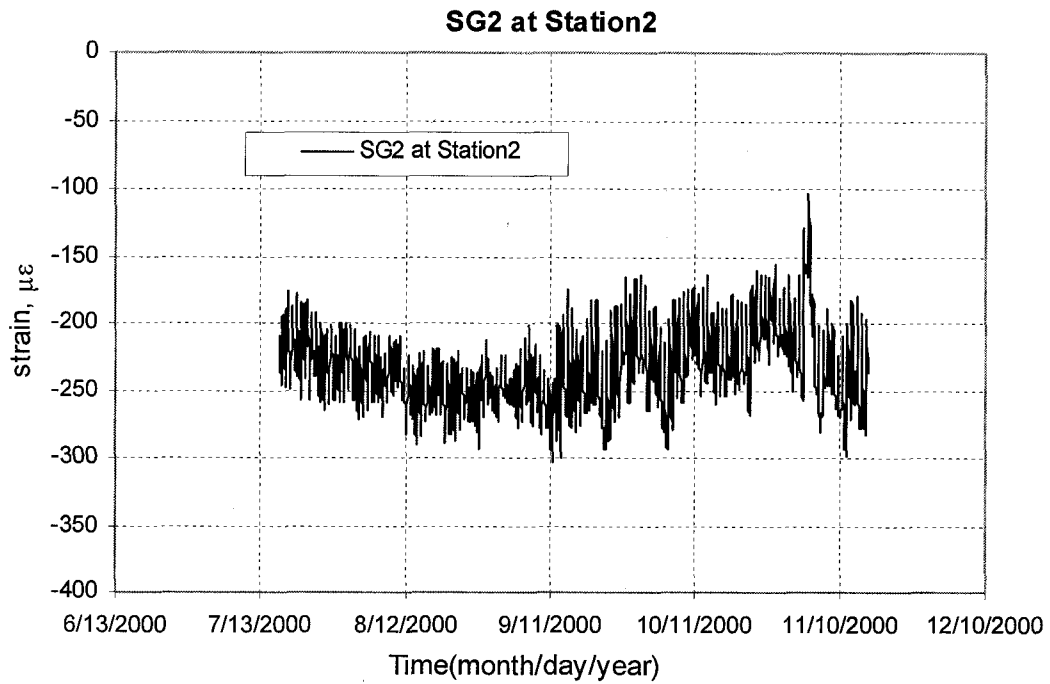


Figure 5.60 Strain Gauge 2 vs. time at Station 2

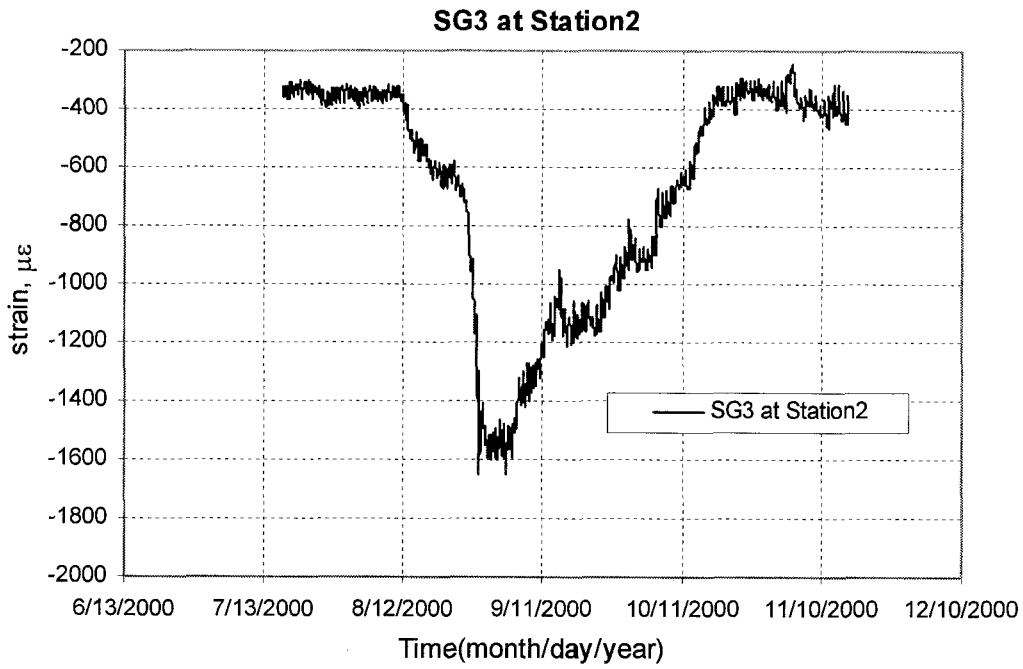


Figure 5.61 Strain Gauge 3 vs. time at Station 2

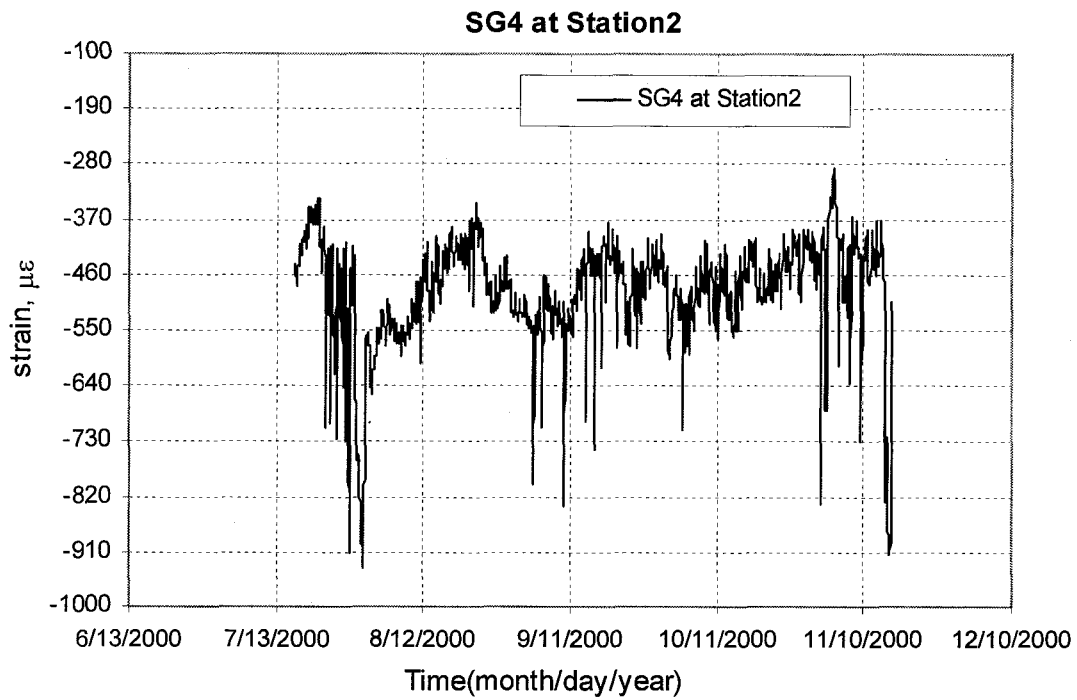


Figure 5.62 Strain Gauge 4 vs. time at Station 2

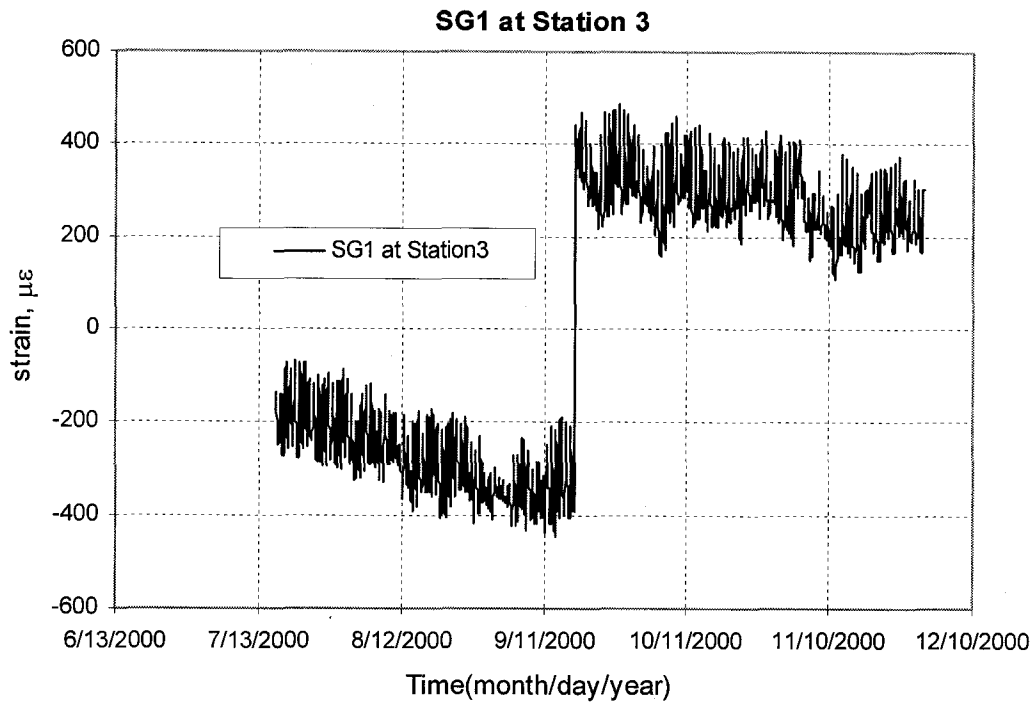


Figure 5.63 Strain Gauge 1 vs. time at Station 3

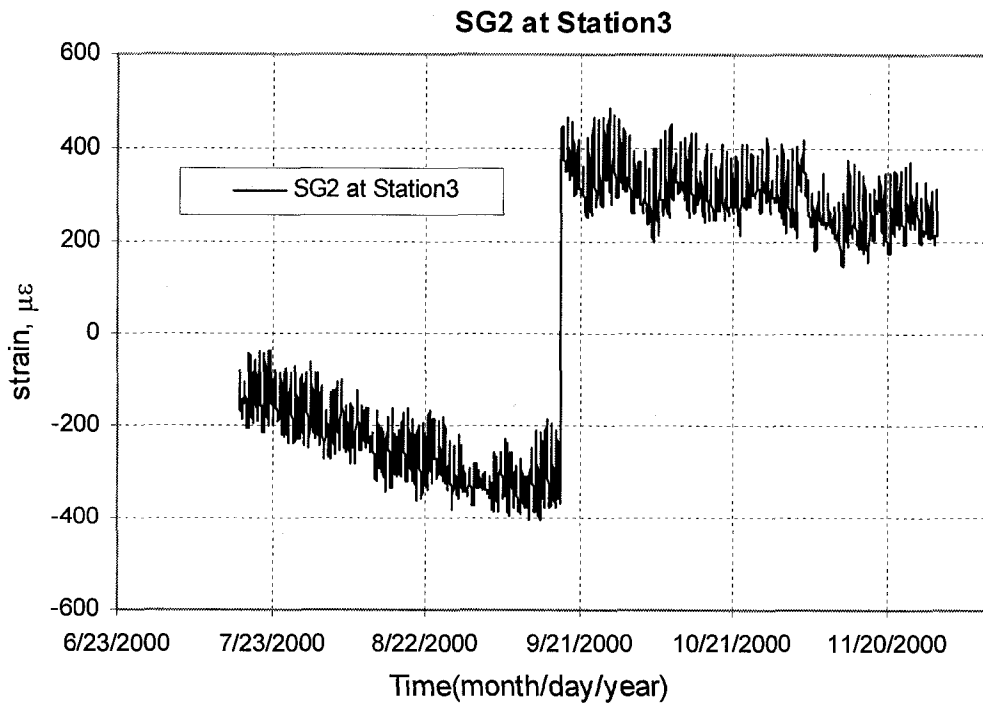


Figure 5.64 Strain Gauge 2 vs. time at Station 3

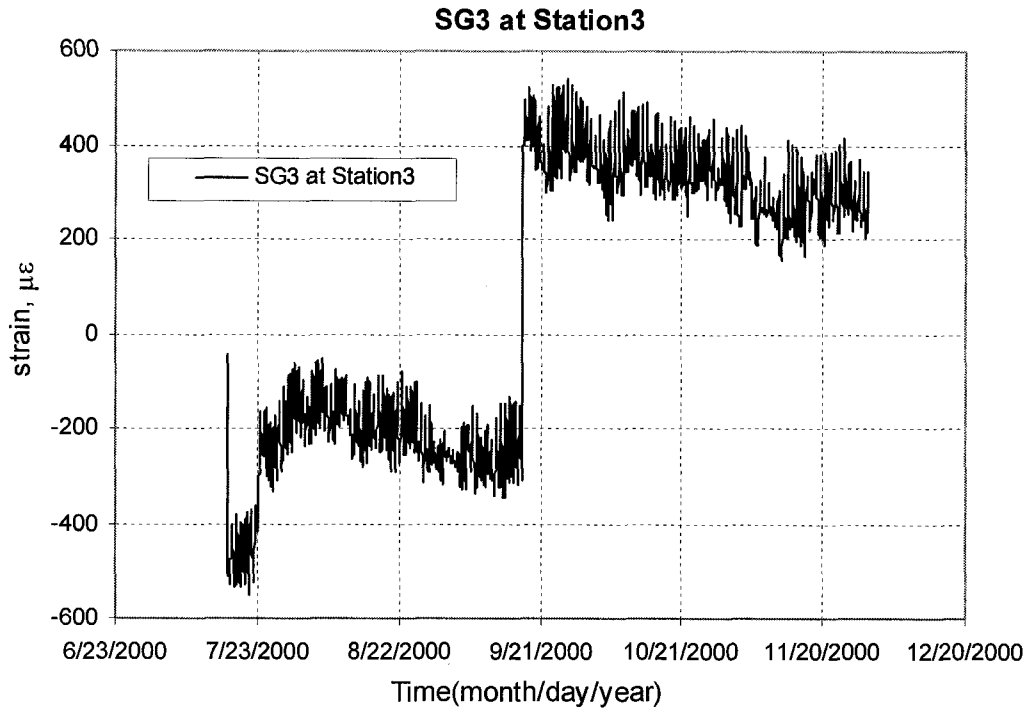


Figure 5.65 Strain Gauge 3 vs. time at Station 3

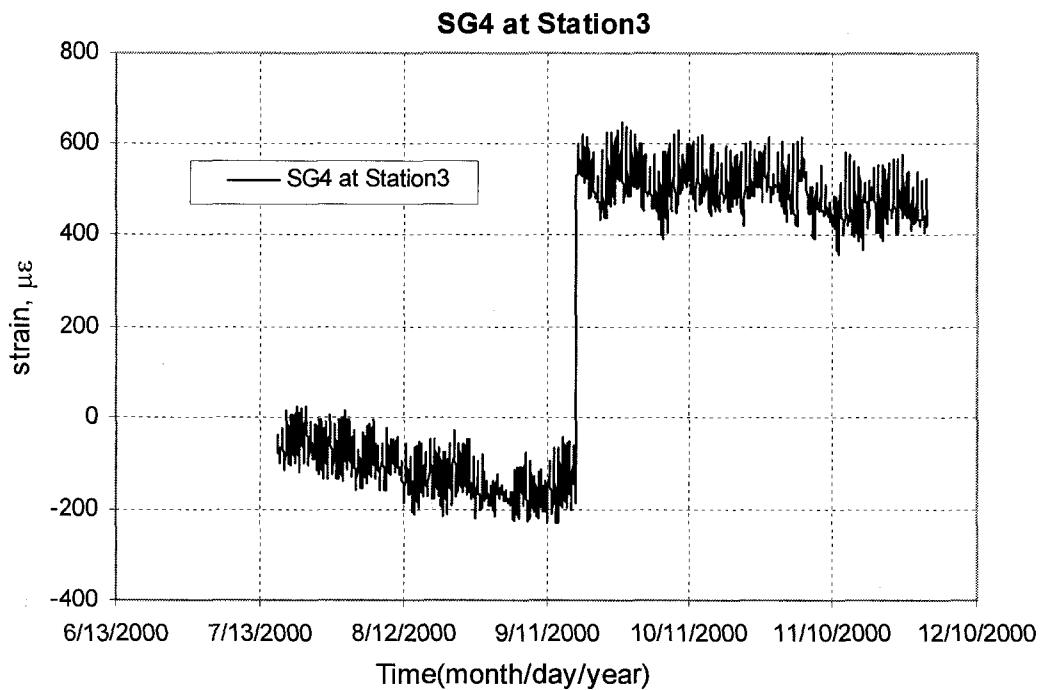


Figure 5.66 Strain Gauge 4 vs. time at Station 3

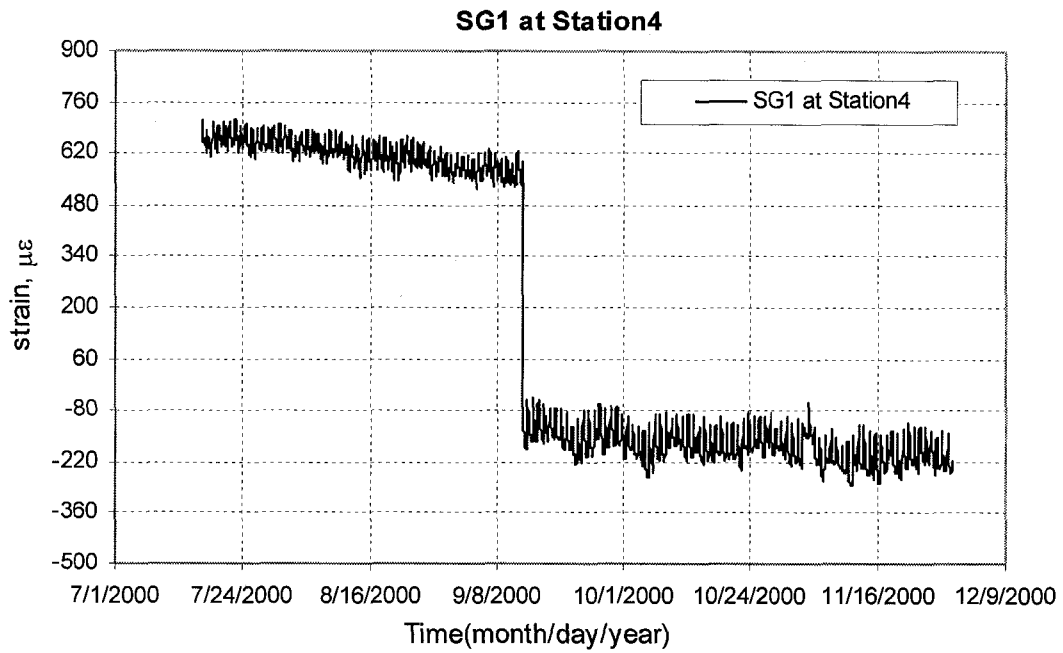


Figure 5.67 Strain Gauge 1 vs. time at Station 4

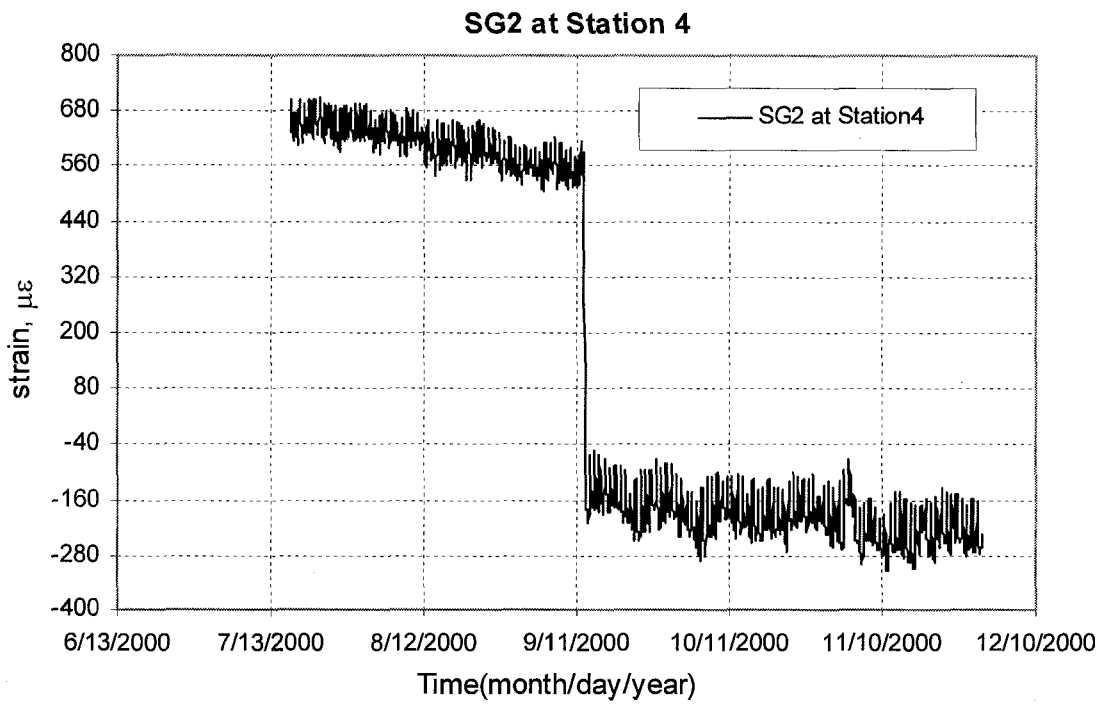


Figure 5.68 Strain Gauge 2 vs. time at Station 4

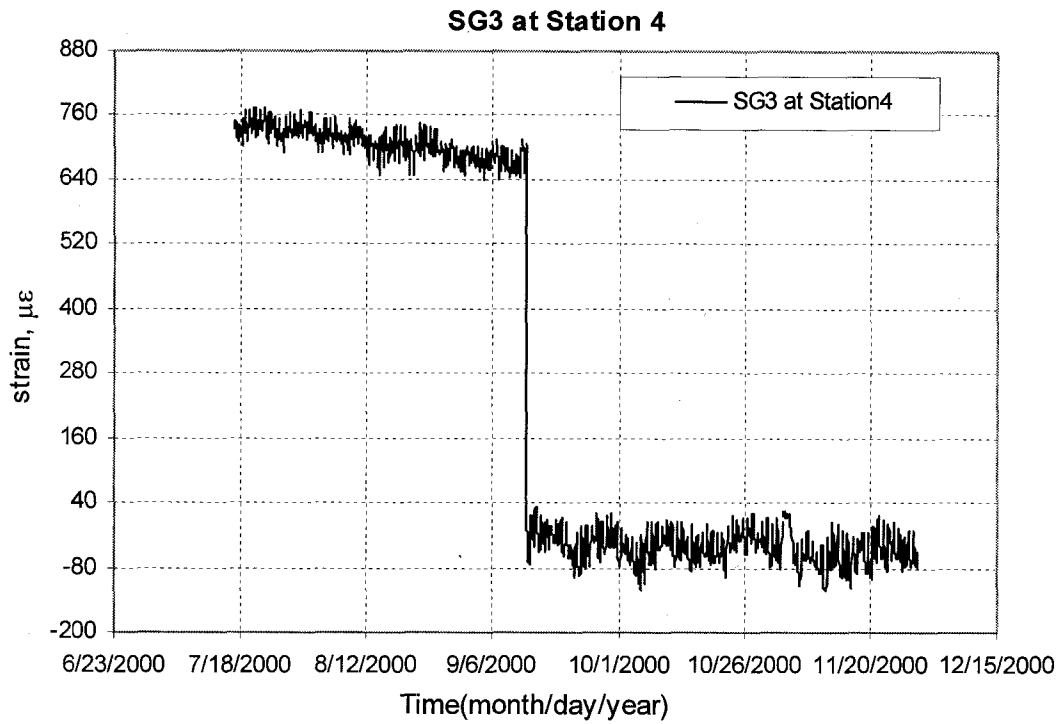


Figure 5.69 Strain Gauge 3 vs. time at Station 4

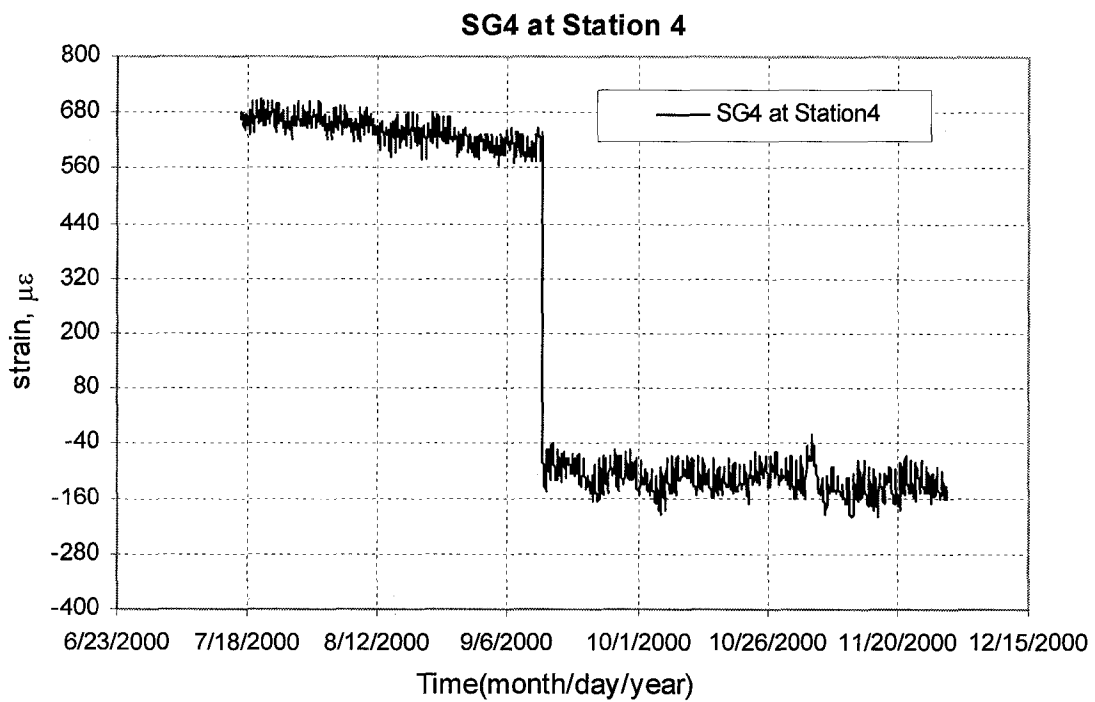


Figure 5.70 Strain Gauge 4 vs. time at Station 4

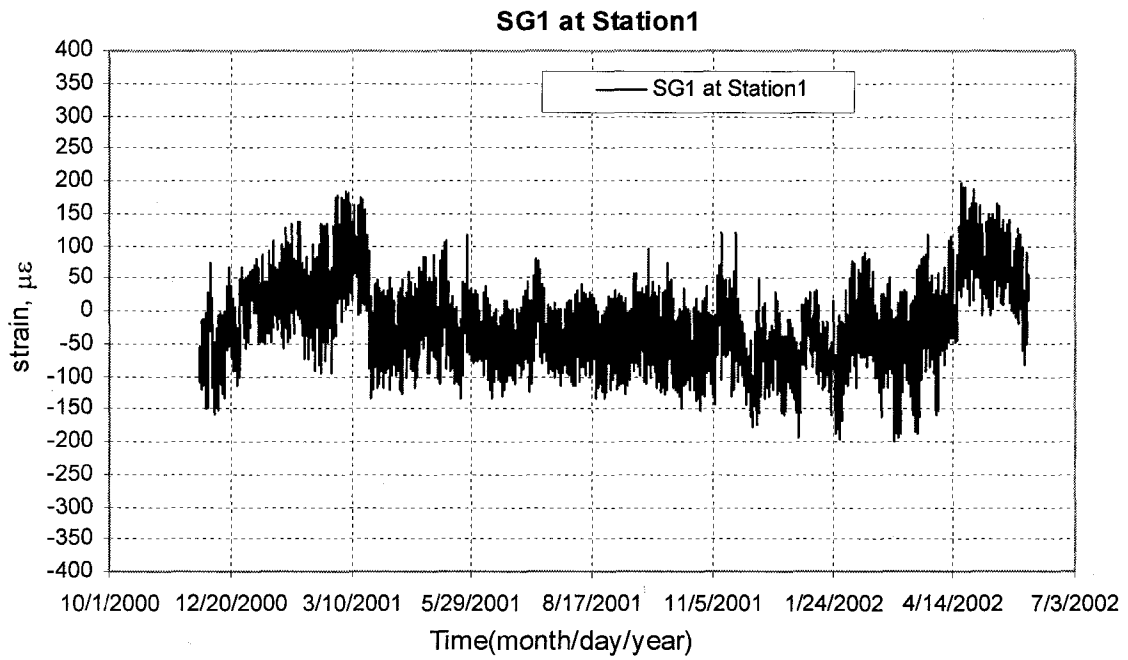


Figure 5.71 Strain Gauge 1 vs. time at Station 1

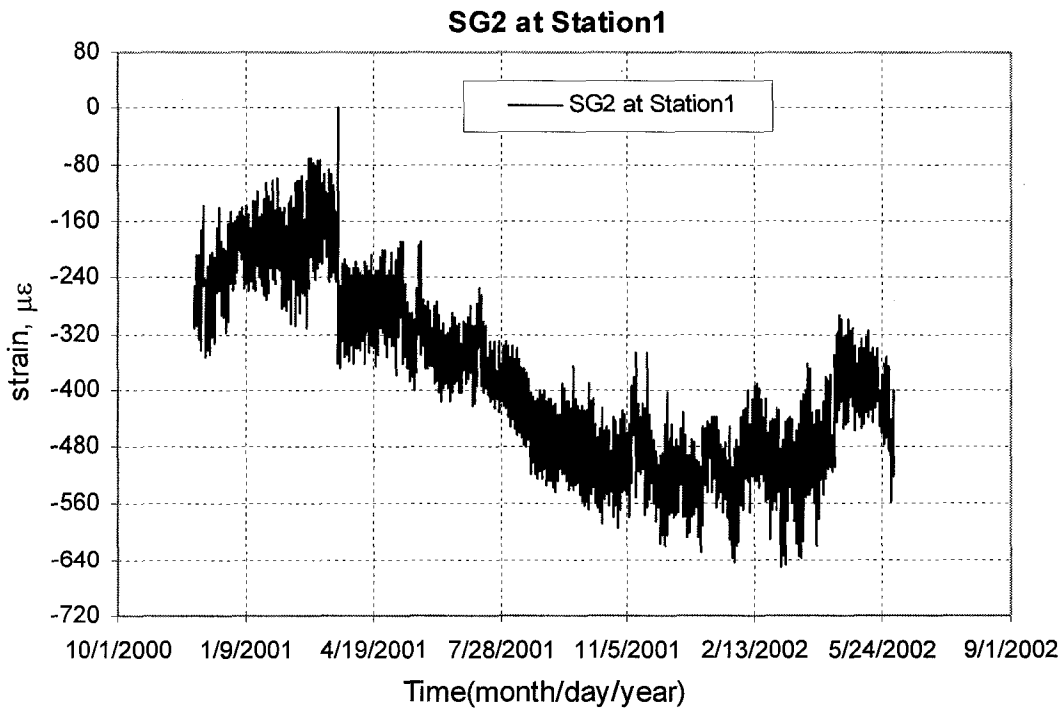


Figure 5.72 Strain Gauge 2 vs. time at Station 1

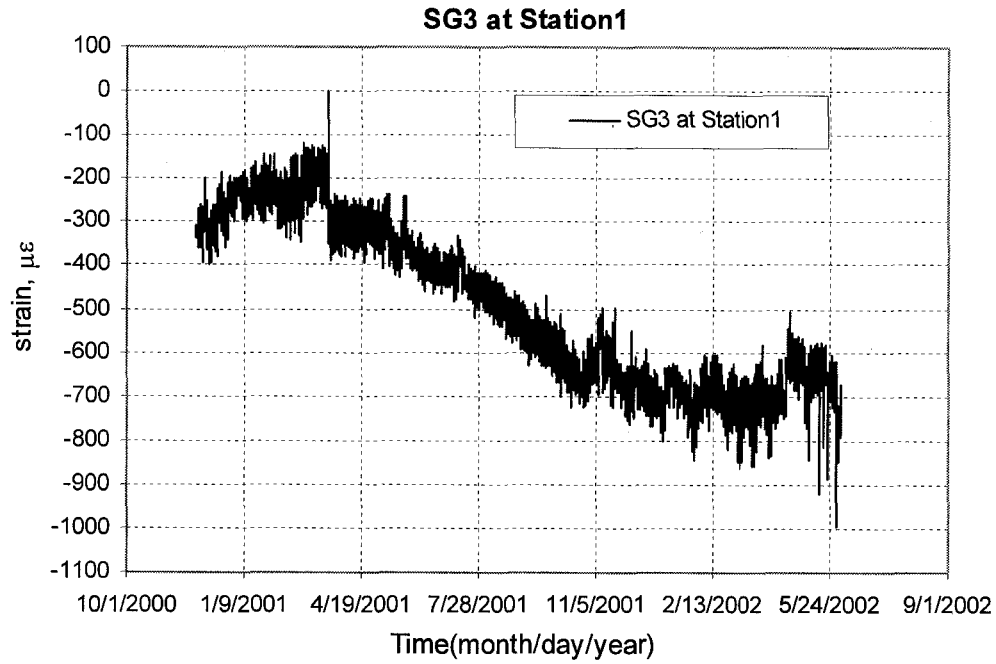


Figure 5.73 Strain Gauge 3 vs. time at Station 1

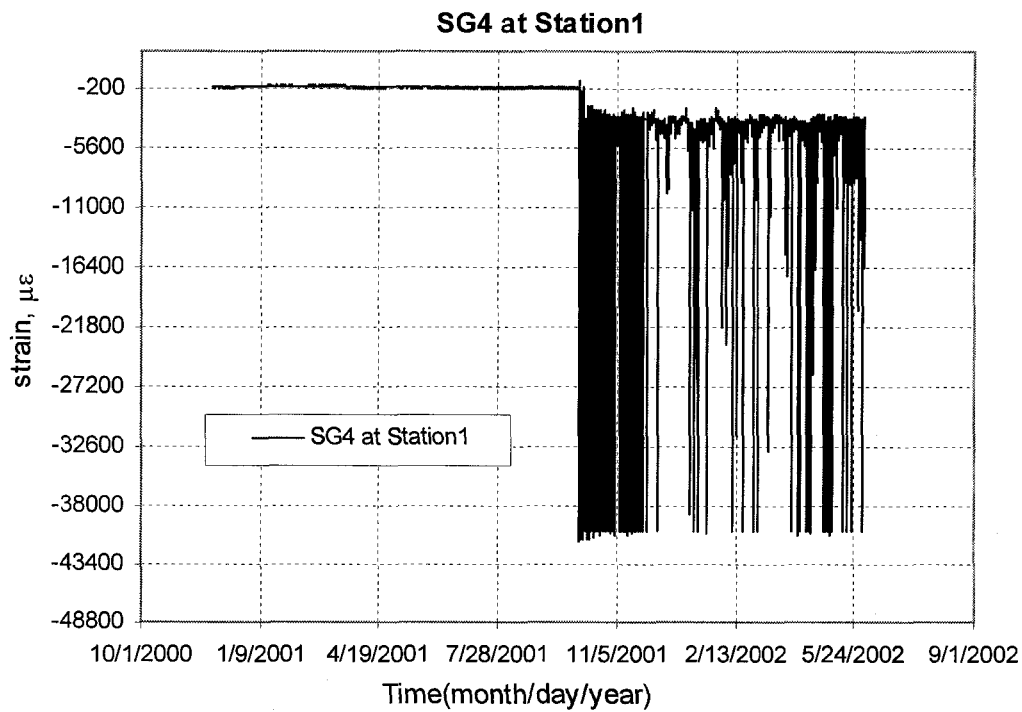


Figure 5.74 Strain Gauge 4 vs. time at Station 1

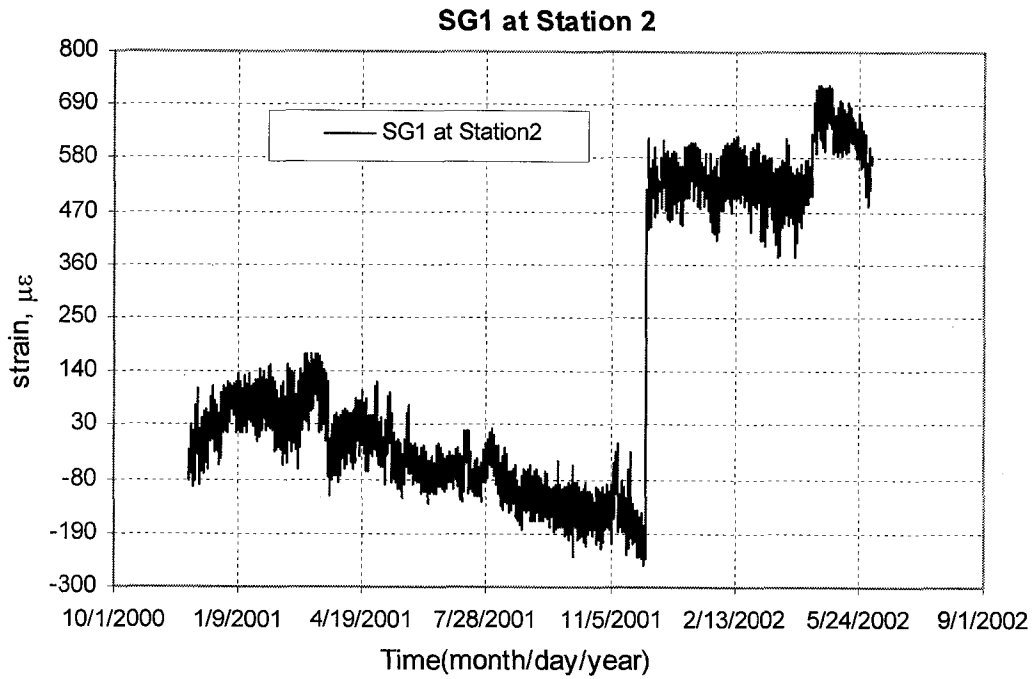


Figure 5.75 Strain Gauge 1 vs. time at Station 2

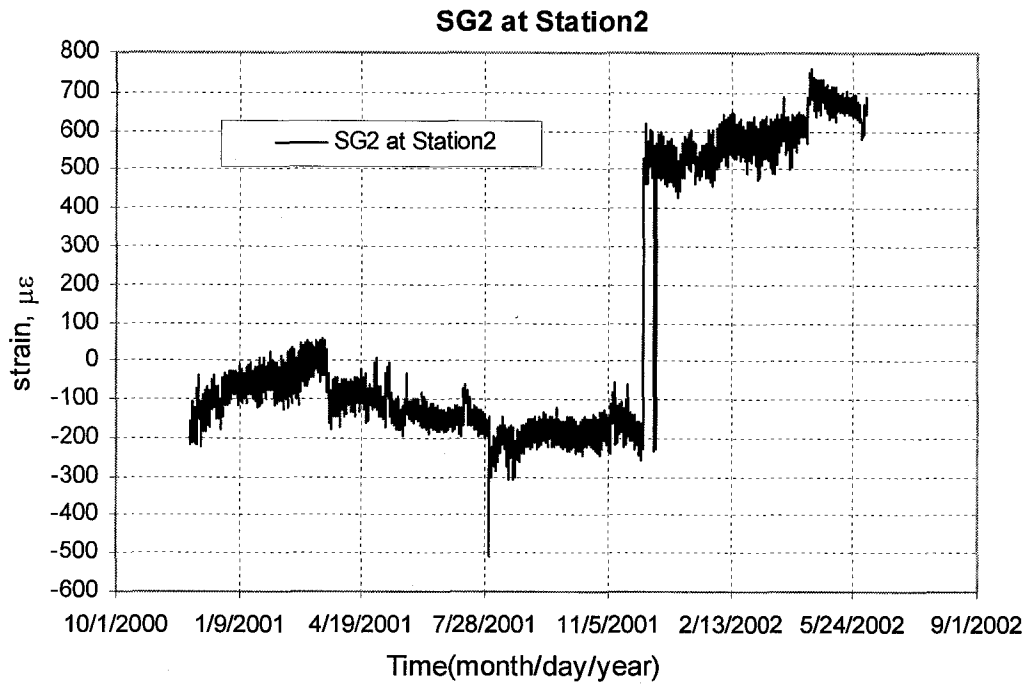


Figure 5.76 Strain Gauge 2 vs. time at Station 2

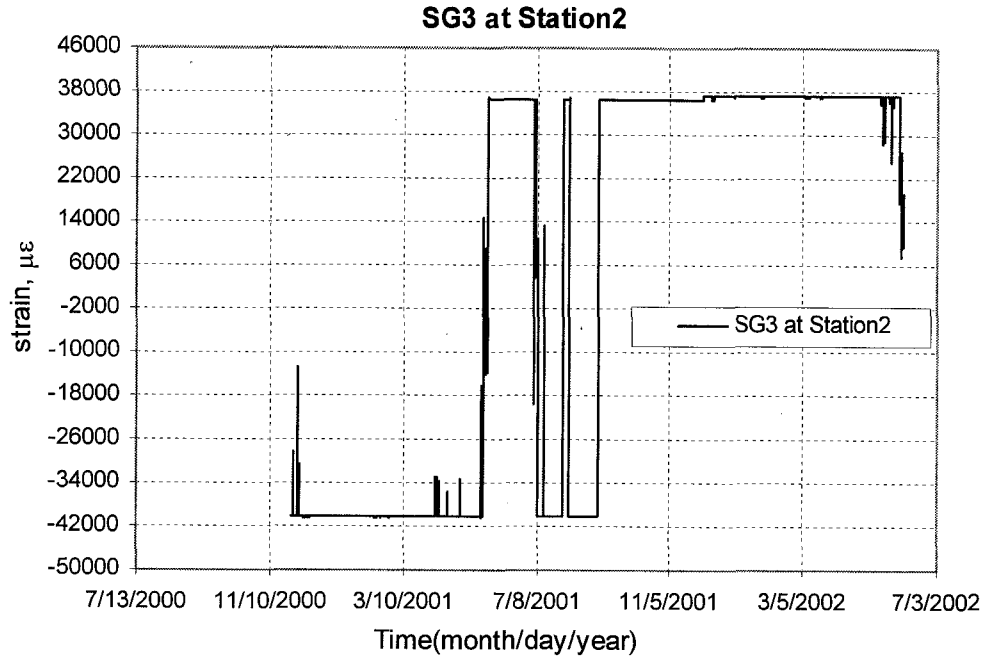


Figure 5.77 Strain Gauge 3 vs. time at Station 2

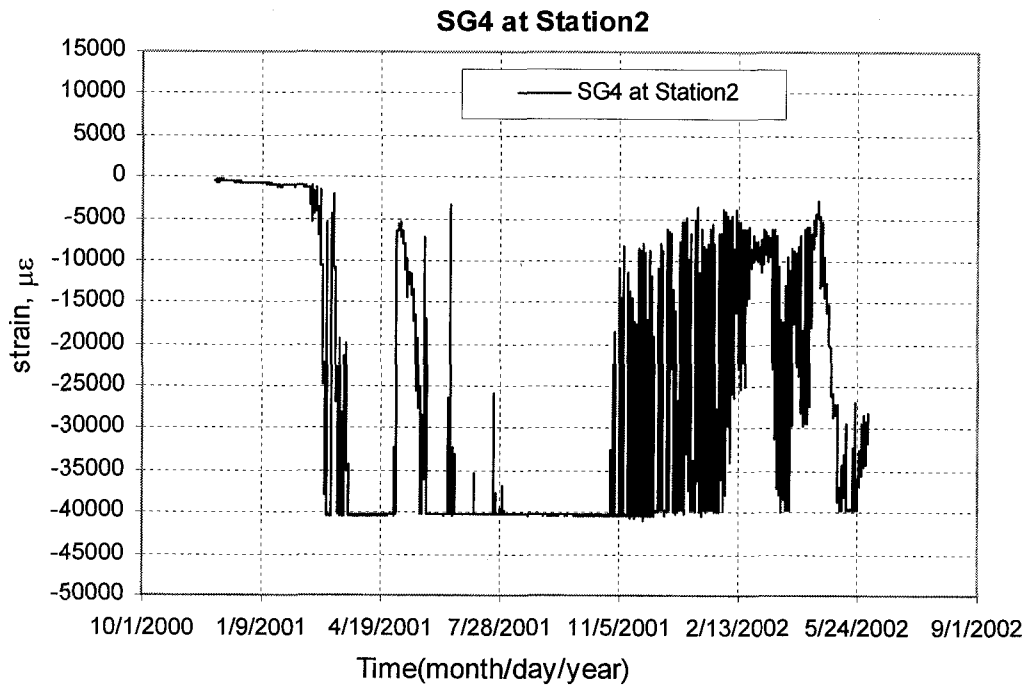


Figure 5.78 Strain Gauge 4 vs. time at Station 2

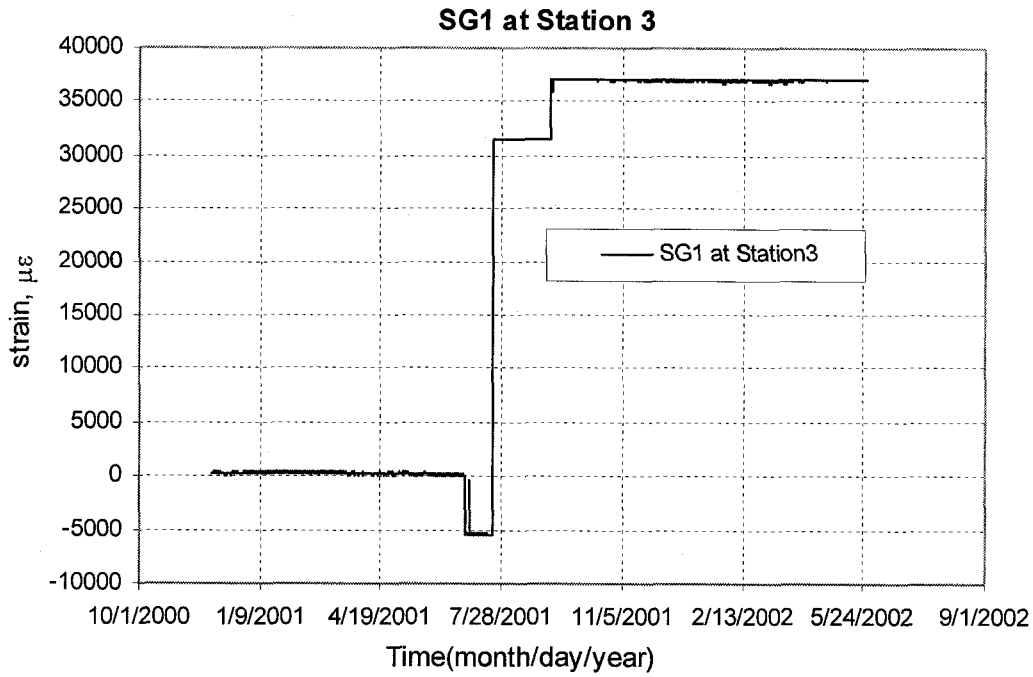


Figure 5.79 Strain Gauge 1 vs. time at Station 3

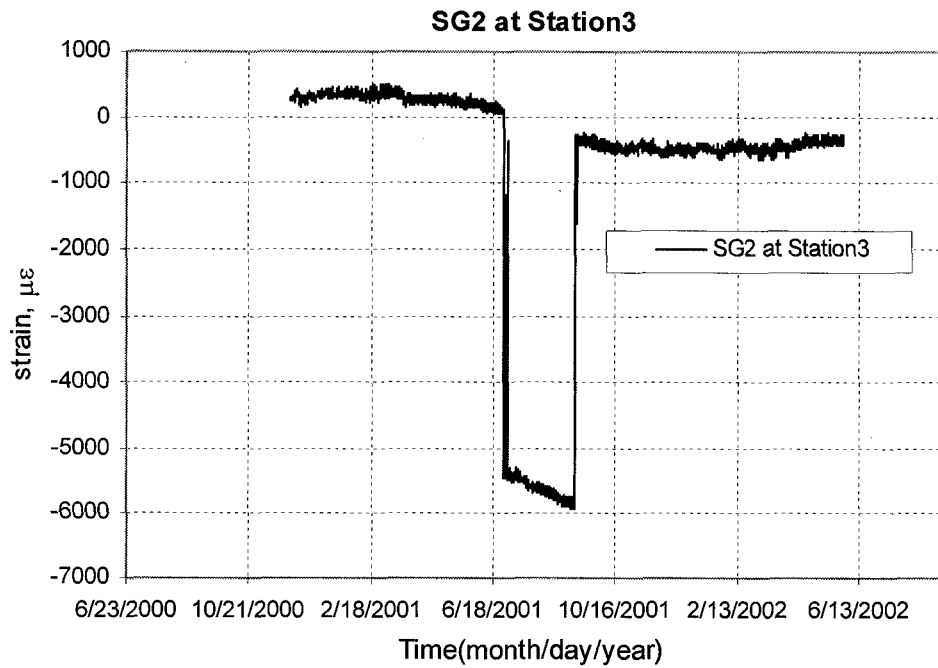


Figure 5.80 Strain Gauge 2 vs. time at Station 3

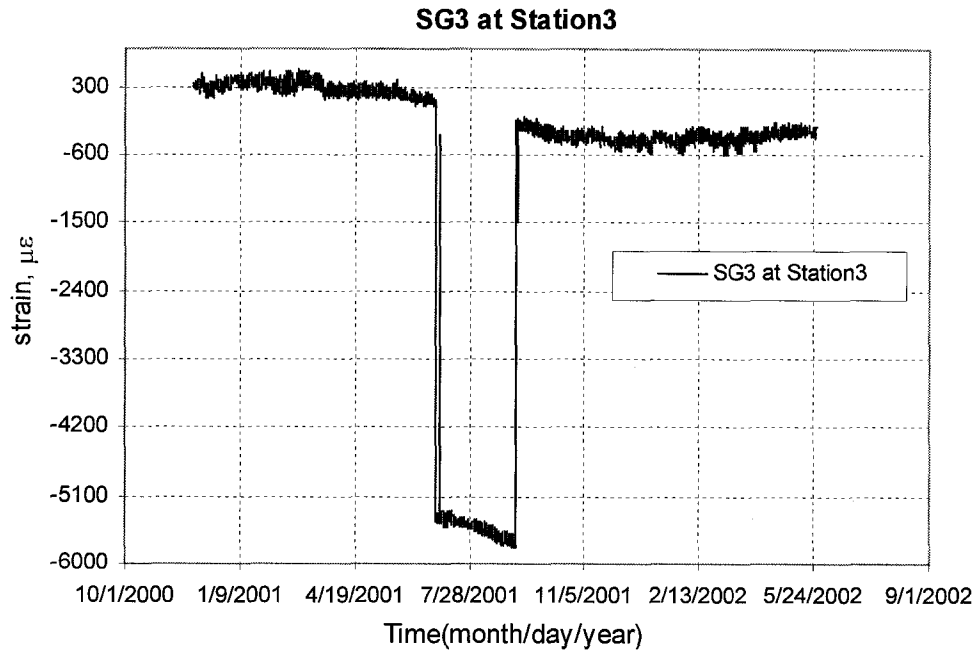


Figure 5.81 Strain Gauge 3 vs. time at Station 3

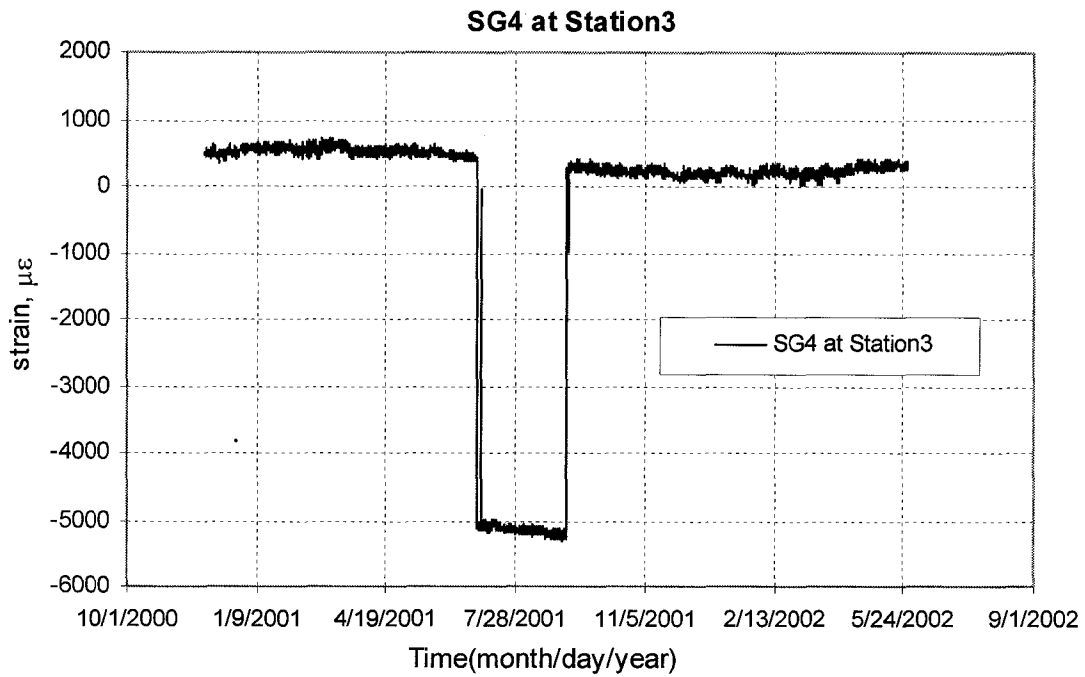


Figure 5.82 Strain Gauge 4 vs. time at Station 3

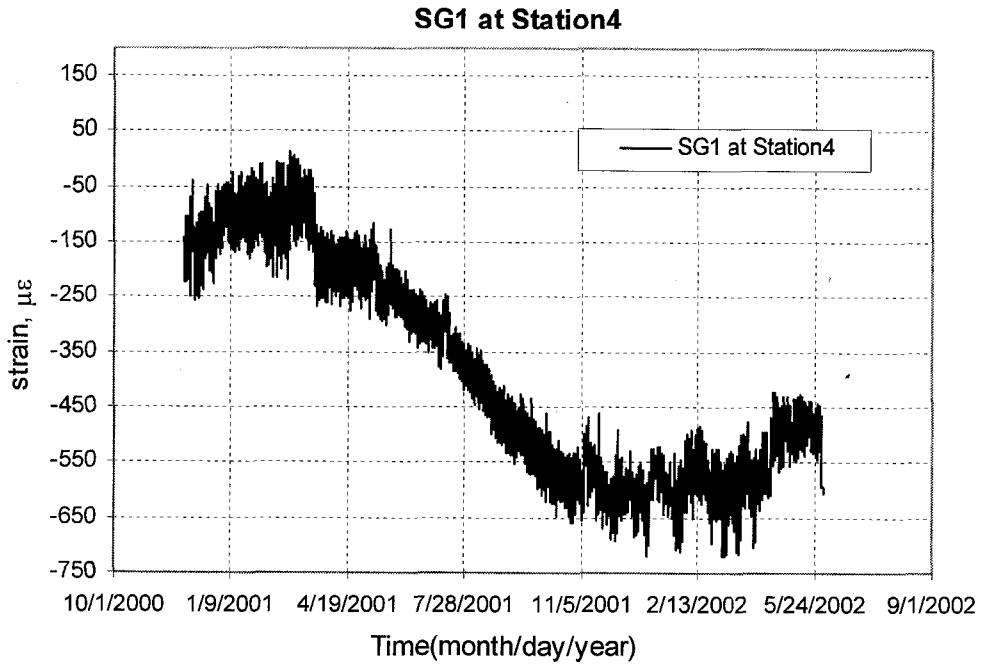


Figure 5.83 Strain Gauge 1 vs. time at Station 4

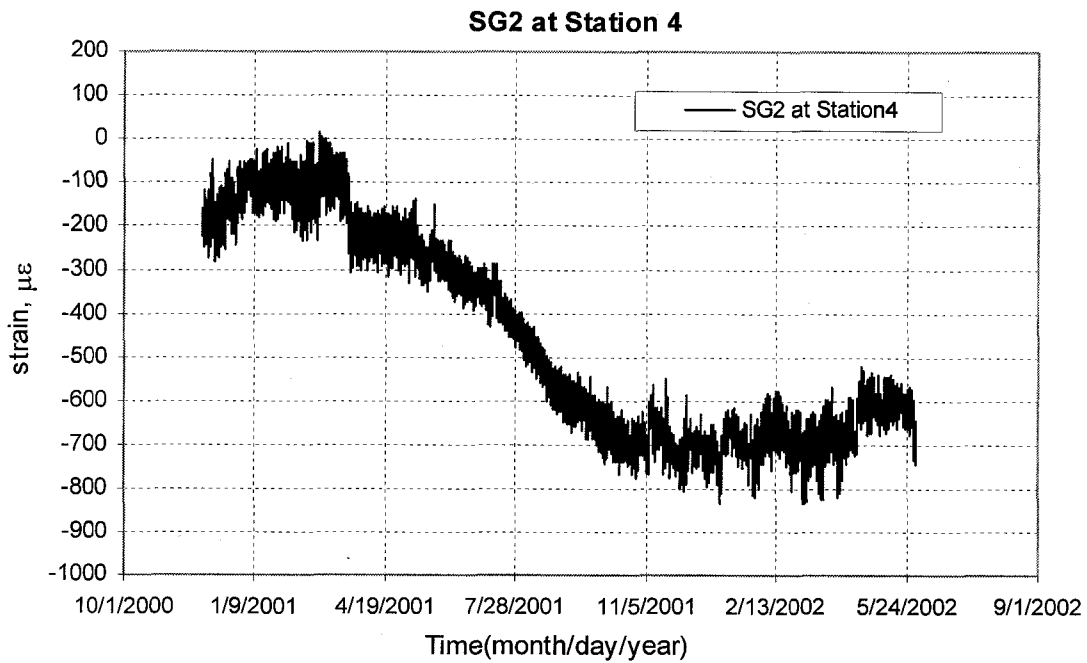


Figure 5.84 Strain Gauge 2 vs. time at Station 4

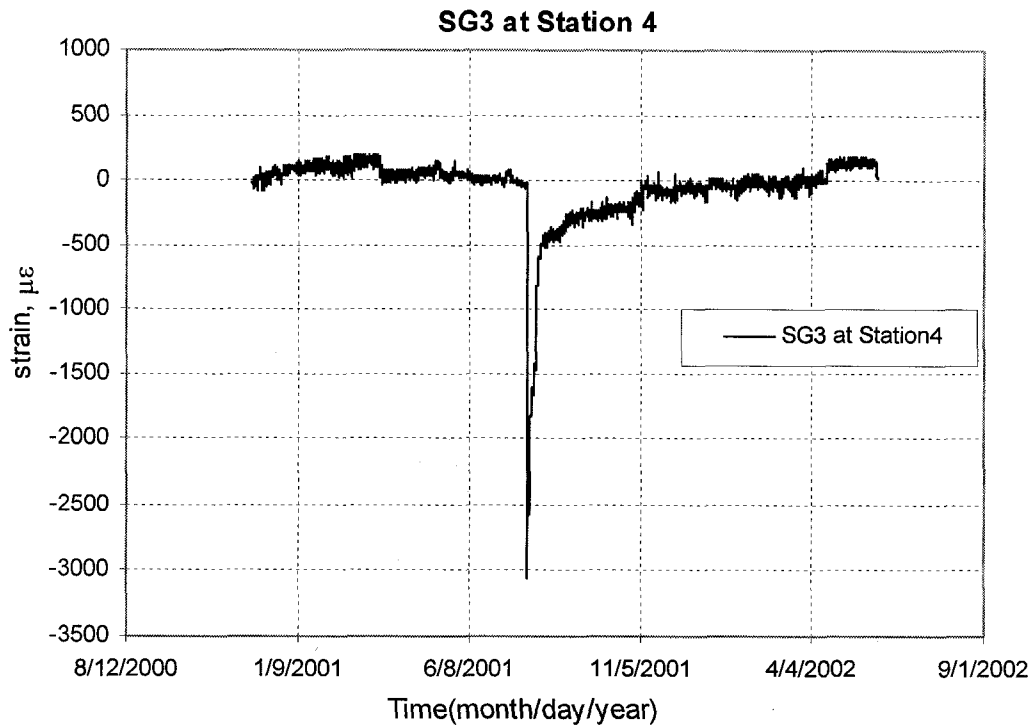


Figure 5.85 Strain Gauge 3 vs. time at Station 4

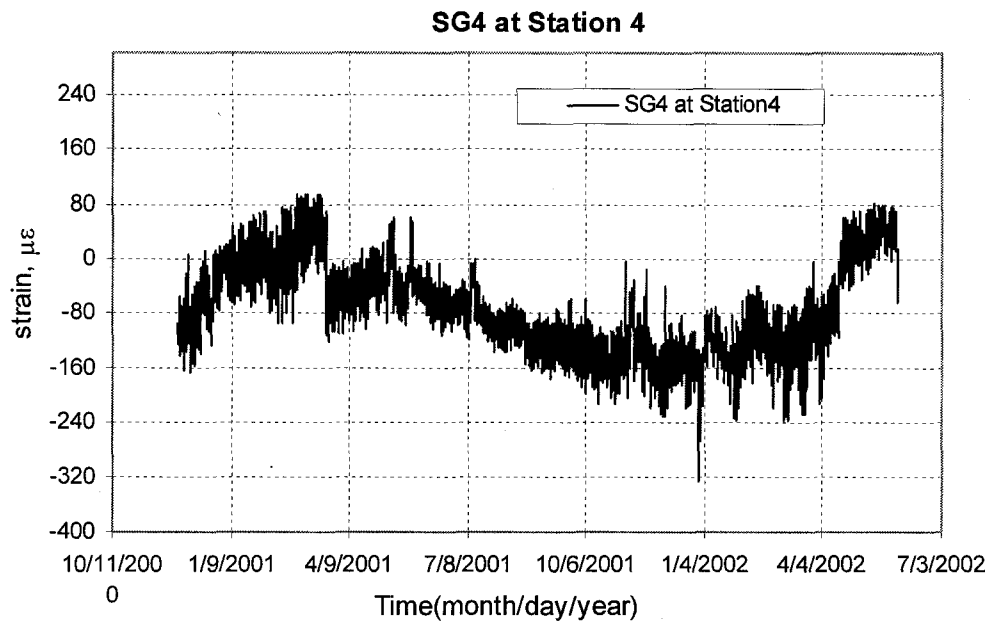


Figure 5.86 Strain Gauge 4 vs. time at Station 4

CHAPTER 6 SIMONETTE RIVER CROSSING MONITORING PROGRAM

An extensive instrumentation plan was designed and implemented in Simonette River Crossing in Alberta to monitor the development of stresses in buried pipe and soil movement.

6.1 Description of the Simonette River Crossing

6.1.1 Location of the Site

Simonette river crossing site is located approximately 70 km south east of the city of Grande Prairie, Alberta, see Figure 6.1 for the geographic location of Simonette River Crossing. It is part of the NPS36 (outside diameter 914 mm) foothills mainline extension that crosses the Simonette River at a relatively straight and narrow east/west aligned section of the river, see Figure 6.2 and Figure 6.3 for the Simonette River Crossing pipeline plan, profile and locations of strain gauge Stations.

6.1.2 History of the Pipeline

The pipeline, constructed and put onto operation in 1976, experienced a rupture on the north valley slope in 1978 due to ground movement. Since then there has been seven stress reliefs performed on the pipeline. This was accomplished by excavating the soil surrounding the pipeline, allowing the pipe to rebound to close to its original position, and reburying the pipe. The pipe has a wall thickness of 8.18 mm, with steel grade is X70 (482 MPa) and the maximum internal pressure that has been applied to the pipe is 6.90 MPa. Extensive geotechnical information has been collected on the north valley slope since 1979, which includes the monitoring of surficial and deep-seated slope movement, ground conditions, and visual observations. The latest stress relief for the pipeline located on the northern slope of the crossing was carried out in late February/early March 2000. A total length of 1101.7 m of the pipeline was excavated.

6.2 Geology

There are several sources of information that have been used to understand the

geology and geotechnical characteristics of the Simonette site: air photos, borehole logs, and site reconnaissance. Air photos were taken in 1990 and 1993. A rigorous air photo interpretation has not been carried out and concluded that landslide features are dominant within the river valley. Erosion of the north river bank is visible when comparing aerial photographs from year to year. The majority of the aerial photograph work is associated with re-route investigations and erosion concerns. A 1989 internal report, which discusses stabilization measures, notes the apparent rotational and translational failure features visible on the air photos. The rotational failures are characterized in the upper part of the slope by crescent-shaped scarps. The translational failures are seen in the lower portion of the slope as continuous parallel linear ridges. A large number of boreholes have been advanced along the north slope. The local geology will be summarized in the following section.

Site reconnaissance and mapping were undertaken on several occasions, the earliest being in 1976. The observations made during these visits have been incorporated into this section. Bedrock exposure is minimal, but in 1987 bentonite seams interbedded with lignite and sandstone were visible after a major flood.

6.2.1 Regional Geology

The valley is cut by the Simonette River, which through erosion and down-cutting, created the present valley formations. The lower portion of the valley contains floodplain deposits of sand and gravel. The valley slope contains glacial till and lacustrine deposits overlying bedrock of Cretaceous age. Within the valley itself this stratigraphy is altered because of the affects of previous instability within both the overburden and bedrock materials. The tills are derived from the Wapiti bedrock group and are typically dark grey, clay and silt dominant, with trace amounts of rounded gravel. The clays are stiff to very stiff, low plastic and increasing in plasticity with depth. Within the valley itself colluvium overlies the bedrock. This colluvium material is comprised of a mixture of till, clay, and bedrock, as a result of previous failure. The bedrock dips slightly to the southwest and is characterized by interbedded sandstone, siltstone, claystone and/or shale with interspersed beds of bentonite and coal. They are non-marine,

and “poorly indurated”, meaning that they have not been hardened by pressures associated with deeper deposits, and therefore not well cemented.

For the majority of the Peace River basin, the present day river channels coincide with preglacial valleys. The effect of glaciation has been to overconsolidate the glacial till material resulting in failures within the valley at slopes as flat as 3 to 10°. It was conceived in a 1989 internal report that bedrock instability may partially be caused by a mechanism called valley floor rebound. This mechanism was originally proposed as follows: Rapid erosion of post-glacial channels into the sedimentary bedrock removed considerable load from the strata underlying the valley floor. Load removal was accompanied by a rebound that gave rise to a gentle anticlinal structure beneath the valley bottom and a gentle unwarping of the strata comprising the valley walls. This upward flexing gave rise to interbed slip, which provided enough deformation to reduce the angle of shearing resistance from peak to some lesser value (residual). This weakened zone exerts an obvious influence on valley stability.

6.2.2 Local Geology

A total of 44 boreholes have been advanced on the north river slope between 1979 and 1998, primarily for the purposes of collecting geological information. Some of the boreholes have been advanced adjacent to a previous borehole to replace damaged instrumentation, and therefore have not been formally logged. Representative boreholes are located in Figure 6.4. Two boreholes, 7 and 8, were advanced to the east of the pipeline as a result of re-route investigations. It was concluded in 1985, after reviewing the slope inclinometer results, that the area of possible instability is extensive and stabilization or re-route in the general vicinity was not a viable alternative.

The geology of the north river slope is typical of deposits within the Peace River Valley. Overburden depths vary from approximately 6 m to over 45 m, consisting of predominantly clay, with varying amounts of silts, sand and gravel. There is an increase in content of sand and gravel closer to the Simonette River. Clay till is present from the valley slope crest, to within approximately 250 m of the north river edge, where flood

plain deposits dominate. Bedrock deposits consist of interbedded claystone, siltstone, and sandstone, which contain slip planes characterized by the presence of bentonite and/or coal.

For some of the boreholes, soils were sampled and index testing was performed, including moisture content, density, Atterberg limits, grain size distribution, and direct shear testing. For most of the boreholes the test results have been incorporated into the borehole logs, but some testing reports have been included with the logs. The bedrock was sampled and logged through rock coring. It appears that standard rock core logging practices were followed.

The stratigraphy of 13 boreholes has been placed on the drawing in Figure 6.4, the rest of the boreholes were not considered to provide any further stratigraphical or structural information, or were considered too far off the right-of-way. The following discussion details the boreholes on the profile drawing and then discusses what is known of the failure of the north slope at Simonette.

Boreholes SI-16 and SI-16A were drilled in 1990 and 1996, respectively. They are closest to the north river bank, currently 20-30 m within the rivers edge. Borehole 16A was installed to replace slope inclinometer 16, which was sheared in 1994, and has subsequently been destroyed in 1998. The overburden consists of predominantly sand and gravel, with minor amounts of silt and clay. The bedrock contact is located at 14.6 m. The bedrock consists mainly of claystone containing bentonitic sandstone inclusions. The failure plane is between 28.7 m and 29.3 m depth within the claystone unit, at elevation 596.8m.

Boreholes 10 and 10A were drilled in 1988 and 1998, respectively. They were located approximately 150 m horizontally upslope from boreholes 16 and 16A. Again, 10A was installed to replace a sheared slope inclinometer, and is still being read. It shows yearly movement of 13.5 mm of movement in 1999 and only 6 mm in 1998. There are approximately 7 m of overburden consisting of sand and silt. The bedrock consists of

sandstone, siltstone, and claystone. The shear failure plane exists between 36 m and 36.3 m depth within a claystone containing bentonite and lignite seams, at elevation 594.0 m, very close to the elevation of the shear failure delineated in boreholes 16/16A. SI number 10A shows a surficial failure at 2.5 m depth.

Borehole 14A, which was placed in 1992, is approximately 100 m upslope from boreholes 10/10A. This borehole also contains an SI, which was sheared in 1997. The movements continued to increase from 9 mm in 1992 to over 46 mm in 1997. The overburden deposit is approximately 7.9 m thick and mainly consists of clay till. From this point on the slope and up to the crest of the slope clay till is the predominant overburden deposit. This is also one of the shallowest overburden depths delineated by drilling. The bedrock consists mainly of sandstone and claystone interbedded with siltstone. The shear failure is at approximately 52 m depth with elevation 593 m and consists of bentonite and coal seams within the claystone/siltstone/sandstone interbedding. The deep failure plane within the bedrock along bentonite and lignitic seams is consistent between boreholes and nearly horizontal. Borehole 14, which is approximately 190 m off the right-of-way to the west, shows a drastically different stratigraphy, but a shear failure plane marginally higher than the previously discussed holes at 598.7 m elevation. The overburden exists down to approximately 32 m and consists of a mixture of clay, silt, sand, gravel and clay till. The bedrock is similar to what is seen in borehole 14A with the failure plane occurring close to the contact between bentonitic clay, and siltstone containing bentonitic inclusions.

Borehole 13A, located approximately 70 m upslope of 14A, was advanced in 1990 and was sheared in 1995. Movement prior to 1995 was roughly 10 mm per year, and the estimated movement required to shear the SI in 1995 was over 60 mm. Overburden is approximately 14 m thick and consists of clay till, gravel and sand. The bedrock is predominantly claystone, with the exception of the interval 51.8 m to 54.9 m depth, which is bentonitic sandstone. The failure plane is at approximately 53 m depth, at 593.9 m elevation, consistent with a deep-seated horizontal failure plane within the bedrock.

Borehole 13, located approximately 65-70 m upslope of 13A, was advanced in 1988 and was sheared in 1990. The overburden can be characterized as colluvium, containing a mixture of clay and silt till, sandstone, clay, silt, and sand. Bedrock is encountered at approximately 41.5 m depth, and consists of interbedded siltstone and sandstone. Two failure planes are seen from the SI readings: one at 50 m depth, and another at 29 m depth. The deeper failure plane is consistent with previous deep bedrock failure and occurs within bentonitic siltstone. The upper failure occurs within sand, and there are no indications of bentonite or coal within the borehole logs.

Boreholes 4A/4B were advanced approximately 140 m horizontally upslope from borehole 13 at mid slope in 1990 and 1996 respectively. SI 4A was sheared in 1995, and 4B was last read in 1997 because of only 1 mm movement in 1996 and 4 mm the previous year. The overburden consists of predominantly clay till, with local layers of sand and gravel. The bedrock contact is at 46 m depth and consists of interbedded claystone and sandstone. There are 3 failure planes recognized at 29 m, 38 m, and 55.1 m depths. The deep failure plane is typical of the main failure plane and exists within a coal seam at the contact between claystone and sandstone. The intermediate failure plane occurs at a coal seam within a highly plastic clay unit. The shallow failure occurs at a sand and gravel layer within the clay till. Movements along the shallow and intermediate failure planes have been minimal. Movements have increased from 8 mm to 38 mm for the deep failure plane from 1992 to 1994, and estimated to be of the same magnitude to shear the SI in 1995.

Boreholes 9B/9C were drilled approximately 120 m upslope horizontally from borehole 4A/4B, in 1990 and 1992, respectively, and were sheared in 1993 and 1996. Movements were 16 mm to 22 mm yearly prior to the year when they were sheared, which estimates the movement to be above 40 mm. The overburden exists to 8.6 m depth and consists of clay till over sand, silt, and clay. The bedrock consists of claystone and siltstone with interbedded sandstone, and occasional interbedded coal. There are two failure planes recognized at 650.5 m and 613.7 m elevation. The upper failure occurs

within bedrock and very close to a bentonitic sandstone layer. The lower failure appears to represent the rise in the deep failure plane and occurs within bedrock at the approximate location of a 0.5 m coal seam.

Boreholes 12A/B/C/D were drilled approximately 60m upslope horizontally from boreholes 9B/9C, between 1990 and 1998. SI 12A sheared in 1993, and SIs 12B/C sheared in 1996. SI12A showed a marked decrease in movement between 1992 and 1994 before subsequent shearing in 1995. SI12B showed similar movements prior to its failure, and SI12C failed in the year it was installed suggesting over 100 mm of movement in 1996. Overburden depths vary between 7 m and 9 m and consist of clay till over sand. Bedrock consists primarily of claystone with sandstone and coal interbedding. The failure plane has been observed between 8 m and 10 m depth within the upper 1-2 m of bedrock within claystone containing coal interbedding. The deep failure planes observed downslope are no longer present and therefore the failure plane seen in SI12 have been interpreted to be the culmination of the deep and surficial failure surfaces.

Boreholes 1D/E/F/G were drilled approximately 50 m upslope horizontally from boreholes 12A/B/C/D, between 1990 and 1998. The movements associated with these SI readings are very similar to the movements recorded for SI12B through 12D. This is expected because both intersected a surficial failure plane that has been interpreted to be part of the same failure mechanism. The stratigraphy is clay till to 6.1 m depth over bentonitic claystone bedrock. The failure plane is at approximately 8.5 m depth within bedrock, likely at a bentonitic parting.

Boreholes 2B was drilled approximately 125 m upslope horizontally from the previous boreholes in 1991. The stratigraphy is clay till over sand over coal. The bedrock is claystone with interbedded coal seams. The failure plane is at 16.7 m depth at a coal seam within claystone. The total recorded movement since 1991 is 88 m, but has decreased from 28 mm in 1997 to 1 mm in 1999.

Borehole 3B is approximately 10 m further upslope than 2B and shows essentially the same stratigraphy. It was drilled in 1987 and sheared in 1996. The failure plane is at 22 m depth at the location of a coal seam within claystone. For boreholes 2B and 3B the failure plane is at the overburden/bedrock contact.

The final borehole to be discussed is SI2C, which is at or back from the crest of the slope. The overburden consists of clay till, clay, and sand to 19.8 m depth. The bedrock consists primarily of claystone with bentonitic seams. The SI installed has shown very minimal movement since its installation in 1998 (total movement of 2.8 m). It has been interpreted that this borehole is north of any distinct failure planes that are affecting the stability of the north slope.

6.3 Hydrogeology

Minimal information exists regarding the regional groundwater regime. There are two main conclusions that have been drawn:

The contours of the near-surface groundwater regime generally replicate the topographic contours, and, aquifers are found in either the bentonitic sandstones, or in fractured coal seams. The sandstone aquifers are noted to be lenticular and of limited lateral extent.

Groundwater conditions have been monitored since 1988 using both standpipe and pneumatic piezometers. The pneumatic piezometric levels have not fluctuated significantly since 1988. For the past 4 years the readings have either decreased or have remained unchanged. Only one piezometer has shown a noticeable increase prior to being severed, measuring water pressures within a claystone unit. The standpipe piezometer water level readings have also remained steady since 1988. There are currently only 3 piezometers still being read, and only one of them has shown a significant increase since 1995. Only one piezometer that is installed within a clay unit, showed a minor increase prior to slope movement severing the standpipe.

Within the lower slope area the water table appears to exist at the top of bedrock contact. In the midslope area, at the location of borehole 13, the top of bedrock elevation decreases by 30 m from the downslope, but the water table only drops by 10-15 m. At the top of the slope the water table approaches the top of bedrock contact again, and is at the top of bedrock and upper shear plane contact at the top of the slope.

6.4 Available Field Data

So far we have got two sets of data. Four slope inclinometer data is available from June 1998 to September 2002. Fifteen Stations of strain gauge data are available from January 2000 to November 2000 except for Station 2 and Station 15 without effective reading from February to July 2000, Station 4 from March to July 2000 and Stations 12, 13, 14 from August 2000 to November 2000.

6.4.1 Slope Indicator

The general idea behind the slope indicator is to provide a cost-effective way of monitoring lateral movements which may occur some distance below the ground surface. The available SI data is presented with the X direction giving down slope movement and the Y direction yielding cross movement.

Figure 6.3 presents profile of the pipeline and slope at Simonette River Crossing with instrumentation of strain gauge stations. There are fifteen strain gauge stations installed along the slope, from the upslope to down slope, they are Station 1 to Station 15.

Figure 6.4 presents plan of the pipeline and slope at Simonette River Crossing with instrumentation of slope indicators. There are twenty-two slope indicators shown long the slope.

6.4.2 Strain Gauge

Strain gauges pods were mounted on the pipe longitudinally at 15 different Stations to monitor pipe stress response before, during, and after the stress relief. The average distance between the strain gauge Stations is 53 m, see the Figure 6.2 and Figure

6.3. At each pipe station there are four strain gauges on the surface of pipe longitudinally, see Figure 6.5. The five in-place working slope inclinometers covering the hill, from the crest to near the lower bench at the northern slope would be monitored during the relief, and subsequently once a month from March till September in 2000 to provide data. A data collection telemetry system was also installed to facilitate remote monitoring in the future.

Vibrating wire strain gauges have been used to monitor the longitudinal pipeline strain changes to help mitigate the risks associated with maintaining pipelines in active landslides. Strain monitoring provides sensitive measurement of changes in pipeline strains caused by the landslide deformations. This enables timely stress relief execution. Figure 6.3 presents profile of pipeline and slope at Simonette River Crossing with instrumentation of strain gauge (SG) stations. Figure 6.6 to Figure 6.30 show the strain reading at these fifteen strain gauge locations. The latest stress relief for the pipeline located on the northern slope of the crossing was carried out in late February/early March 2000. From these Figures, strain relief can be seen. For example, Station 2 has about $500\mu\epsilon$ relieved, Station 3 about $240\mu\epsilon$, Station 5 about $320\mu\epsilon$, Station 6 about $400\mu\epsilon$, Station 10 about $200\mu\epsilon$, Station 12 about $300\mu\epsilon$, were removed. This provides the magnitude of strain relieved.

6.5 Slope Stability

The development of slope instability is a result of the steep valley slopes, the relatively low shearing resistance of the slope-forming materials, and the unfavorably high groundwater conditions in the slope created by groundwater recharge from poorly drained adjacent uplands. Clay till and the underlying clayey bedrock typically exhibit long-term shearing resistance. The high shear strains, which are associated with the landslides, cause further reduction in the shearing resistance of these strata so that, in the long run, reactivation of old landslides can be caused by relatively small increases in groundwater levels, or by local changes in the slope geometry due to creek-related erosion.

The slope inclinometers have delineated the major shear planes that control slope movement of the north Simonette valley slope. Within the lower valley area a distinct, near horizontal shear plane exists within the bedrock. This failure plane is nearly 30 m below the ground surface near the toe of the slope, at 596.8 m elevation. It is approximately 65 m deep at the point where it starts to rise to ground surface, at roughly the 595 m elevation. There are two shear planes that break off from the deep-seated failure, one located at borehole 13, and another between boreholes 4A/4B and 9B/9C. Deep-seated failure is not intersected by any boreholes north of 9B/9C. These observations further substantiate the notion that the bedrock beneath the upper slope is probably not at residual strength. In contrast, the bedrock beneath the lower portion of the slope is probably at residual strength, and as a result continues to move. The other failure mechanism involves movement along the overburden/bedrock contact within the upper portion of the slope. It dips slightly into the valley. At the crest it is at elevation 669.1 m, while at the toe it is at 668.69 m. A scarp marks the extent of upslope failure, located some distance back of the slope crest. This shear plane follows the relatively flat top of bedrock and daylight between boreholes 12A/B/C and 9B/C. The two shear planes appear to intersect in a specific area and therefore it is believable that the deep-seated bedrock movement has initiated the upper surficial movement, also aided by a high groundwater level.

Slope stability analysis was carried out in 1989 and 1996 by TransCanada Pipeline Limited (TCPL). It was assumed that the factor of safety of the north slope is at or slightly below unity. It was found that the results were highly sensitive to the bedrock residual strength values. The shallow failure mechanism was largely understood, but the deep failure mechanism was less defined, and therefore conclusive results were not reached.

6.6 Summary

The Simonette River Crossing has been active since 1976. A large amount of geotechnical data has been collected and an understanding of the processes affecting the integrity of the pipeline has been developed. The method of slope movement monitoring

has progressed from monitoring surficial pin movement to installing slope inclinometers which allow observation of slope movements with depth. The stresses that slope movements impose upon the pipeline are determined on a yearly basis, and these results determine when action is required. Action taken has historically been stress relieved on the pipeline by excavation, but other options such as rerouting, toe berm construction, pile placement, above ground pipe installation, and directional drilling, have been studied in the past.

The Simonette north valley slope is an active landslide area. This was known before the pipeline installation, and rupture in 1978 prompted the start of a lengthy geotechnical investigation. The information collected has been summarized in this chapter, and effectively outlines the complicated geology and failure mechanisms controlling slope movements. The groundwater pressures have been monitored within several geological units, and it is certain that increased groundwater pressures reduce stability, but how water flows and intercepts the shear planes are not understood. In terms of slope stabilization it is imperative that a thorough understanding of the aquifers, water pressures, and pathway of groundwater are determined. It is clear that slope movement increases with precipitation, but a correlation between piezometric increases and slope movement is not apparent.

There are two primary failure mechanisms that have been delineated from slope inclinometer data. The first is a surficial failure located in the upper slope area. This failure initiates back from the valley crest and terminates in the mid slope area. It occurs at the near horizontal bedrock contact and is likely controlled by groundwater pressures acting on this plane. The second failure mechanism is a deep-seated failure occurring in the lower slope area. The shear plane exists within bentonite and coal seams in bedrock, and is also near horizontal. The failure appears to initiate in the area where the first failure plane terminates. The termination of the second failure plane is not clear, but likely occurs in an area beneath the Simonette River. The way the two failure mechanisms interact is not understood. It is likely that the deep-seated failure has initiated the surficial failure in the upper slope. Obviously, this surficial failure is aided

and controlled by groundwater pressures. Total movements since 1981 show that the toe of the upper slope failure has moved approximately 80 cm, roughly 4 times the movement that has been recorded near the toe of the deep-seated failure. In terms of pipeline integrity, the upper slope failure is consequently more important.

A complete understanding of the geology, shear plane mechanism and geometry, groundwater conditions, and soil and bedrock strength parameters is essential to perform slope stability analysis. Slope stability analysis was carried out in 1989. The purpose of this analysis was to determine the effect of stabilization. In doing so, the subsurface conditions, namely the strength parameters and groundwater conditions, were determined to achieve a factor of safety of unity. The shear plane geometry was not entirely understood at the time, however, and as a result these results may not coincide with further analysis. Slope movements are expected to continue. The movement in 1999 was lower than previous years, but yearly toe movements are still significant, up to 25 mm on the upper and 14 mm along the lower shear plane.

Table 6.1 Latitude and Longitude of Grande Prairie and Edmonton

	North Latitude	West Longitude
Edmonton	53°33'	113°28'
Grande Prairie	55°27'	118°45'

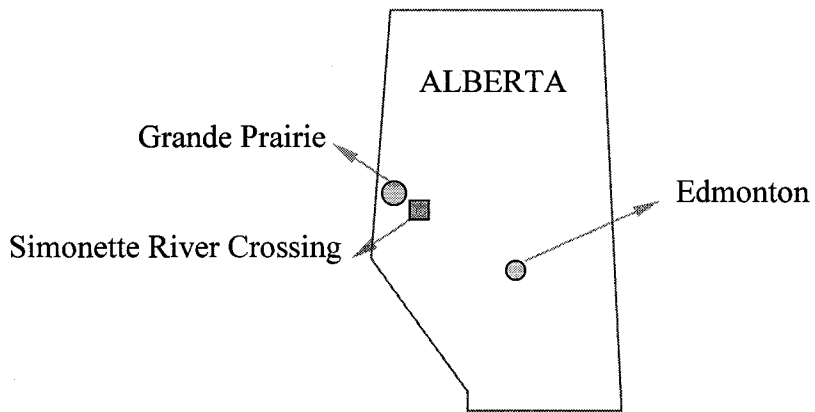


Figure 6.1 Geographic Location of Simonette River Crossing

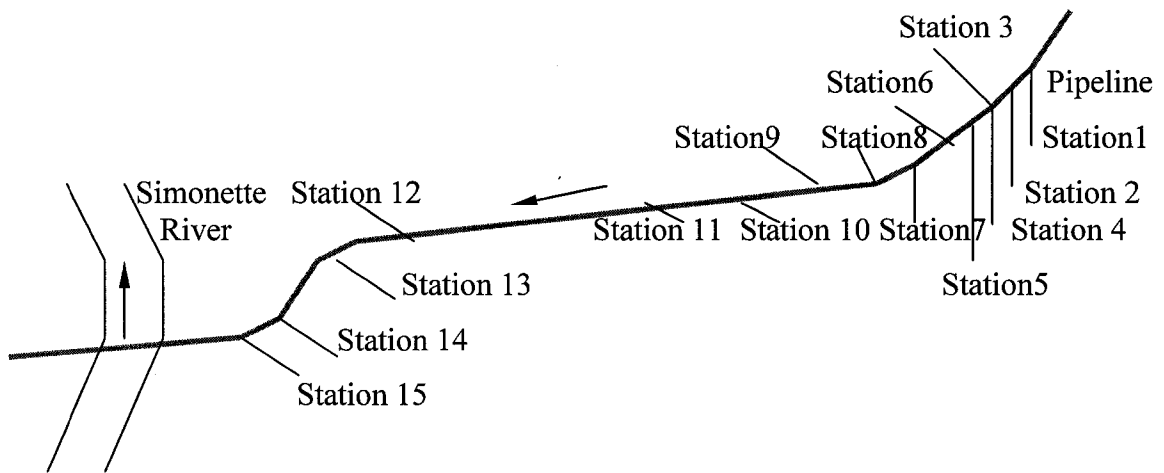


Figure 6.2 Simonette River Crossing Pipeline Plan View and Strain Gauge Sections

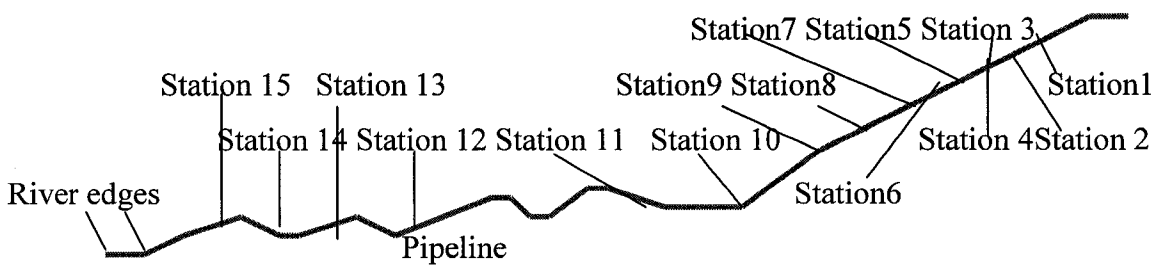


Figure 6.3 Simonette River Crossing Pipeline Profile and Strain Gauge Sections

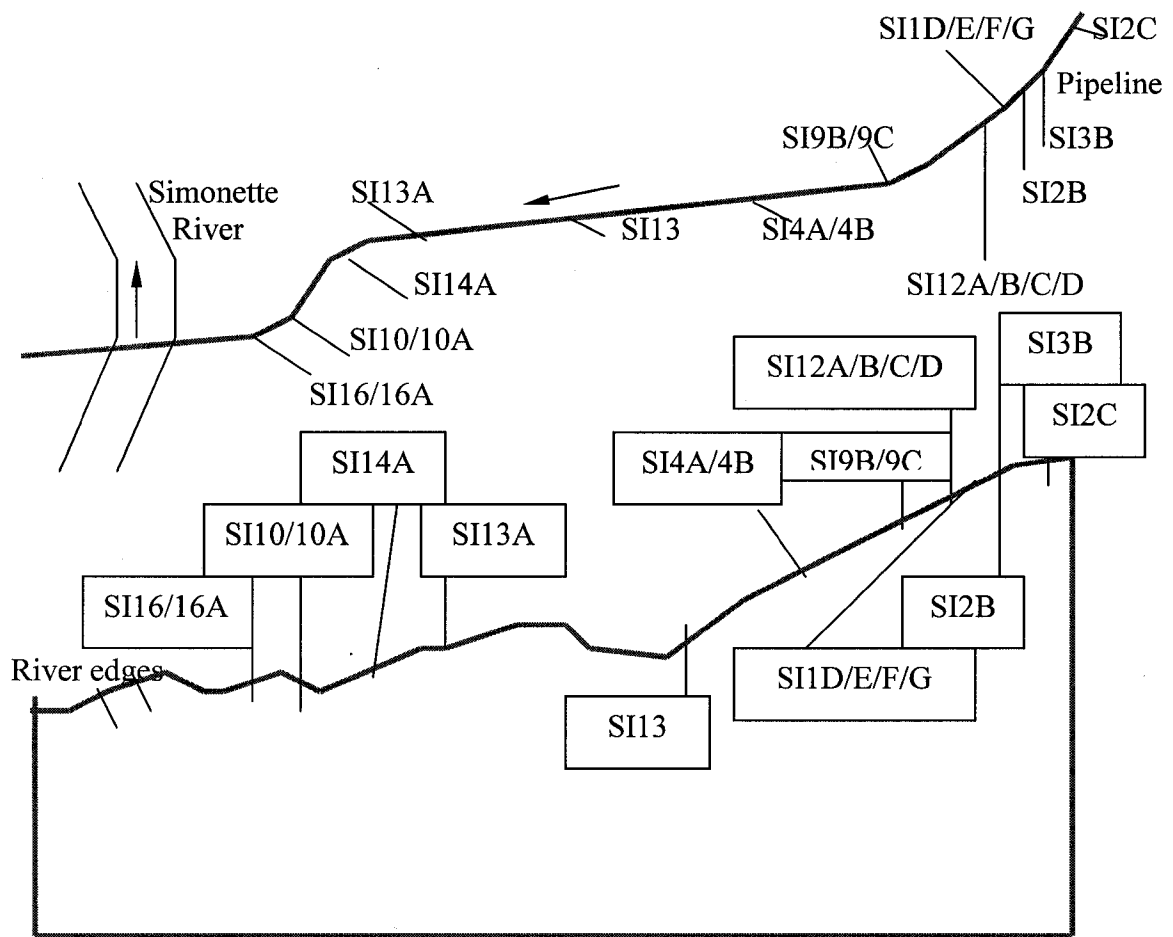


Figure 6.4 Simonette River Crossing Plan (top figure) and Profile (bottom figure) Views of Slope Indicator Locations

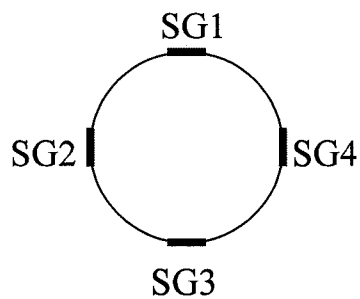


Figure 6.5 Locations of Strain Gauges on Pipe Station

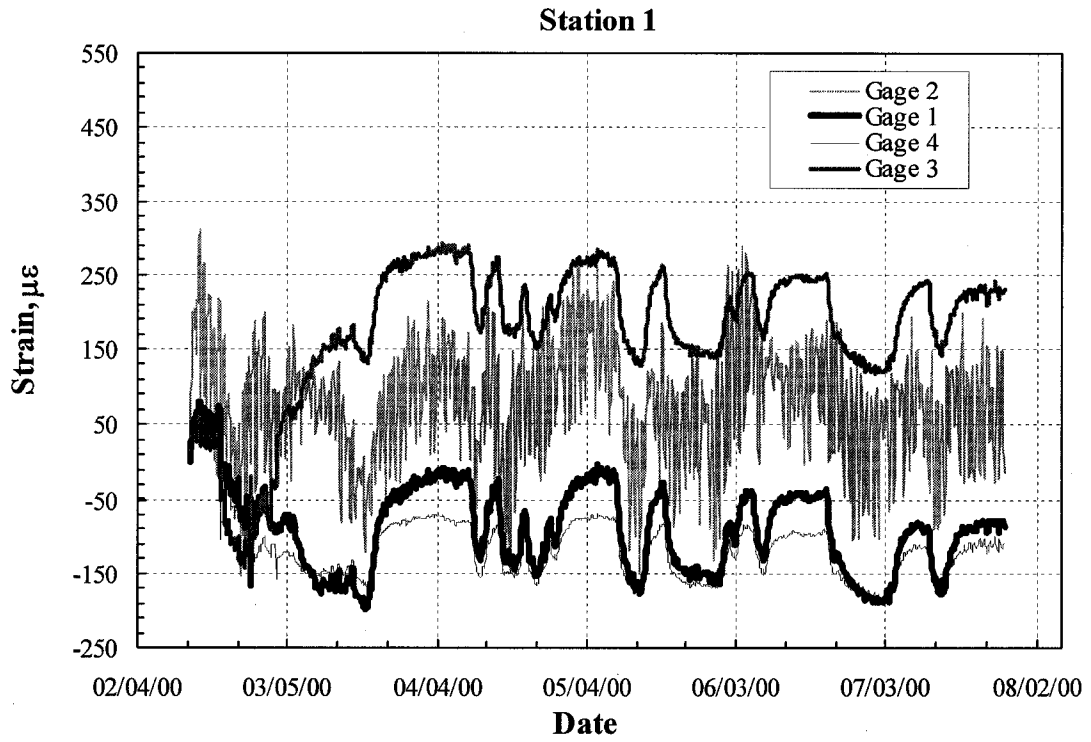


Figure 6.6 Zeroed Strain vs. Time at Station 1

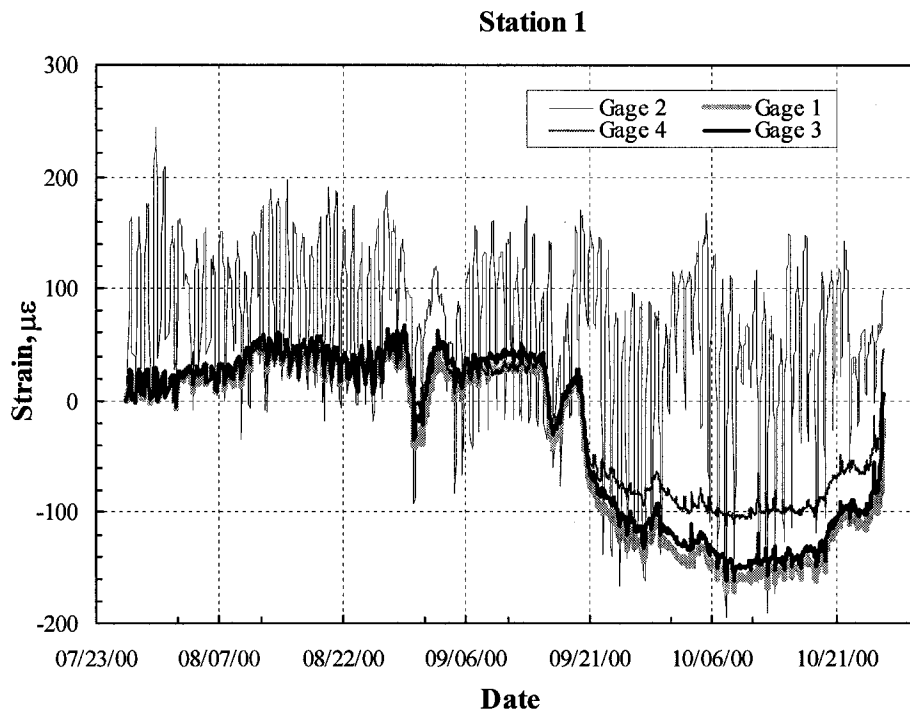


Figure 6.7 Zeroed Strain vs. Time at Station 1

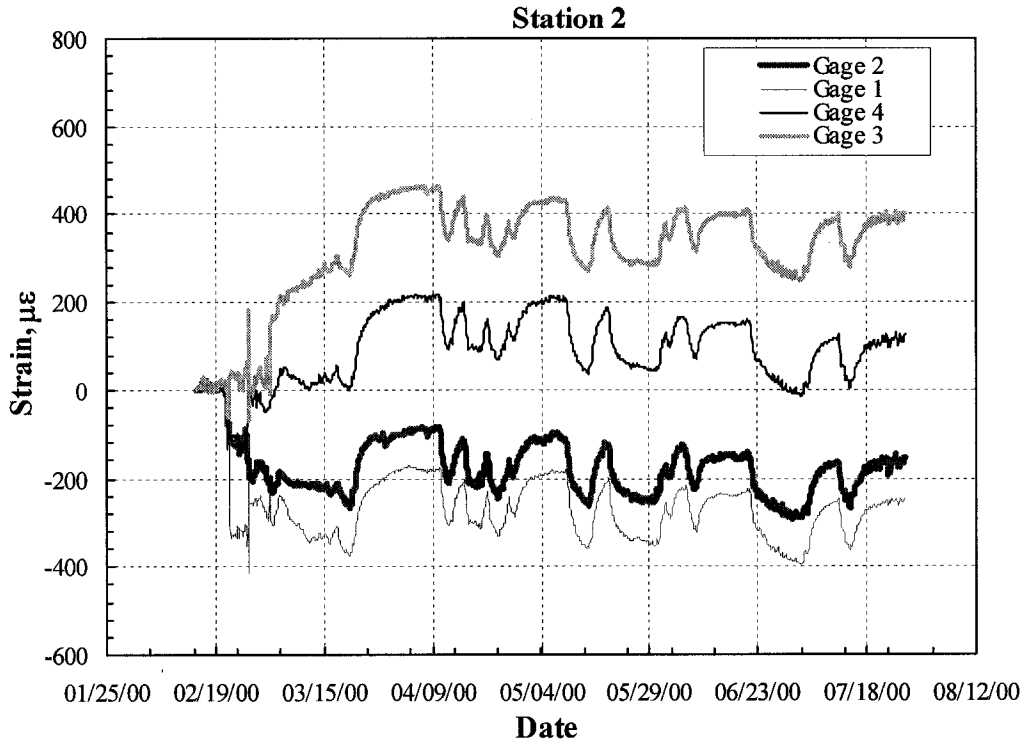


Figure 6.8 Zeroed Strain vs. Time at Station 2

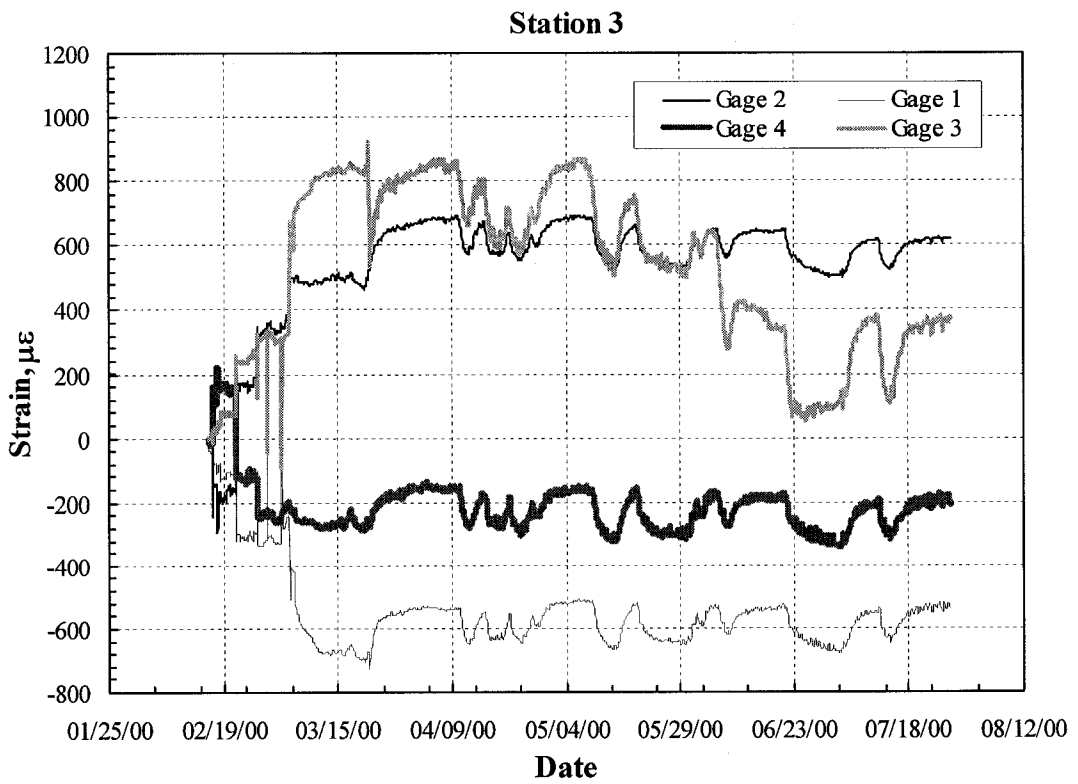


Figure 6.9 Zeroed Strain vs. Time at Station 3

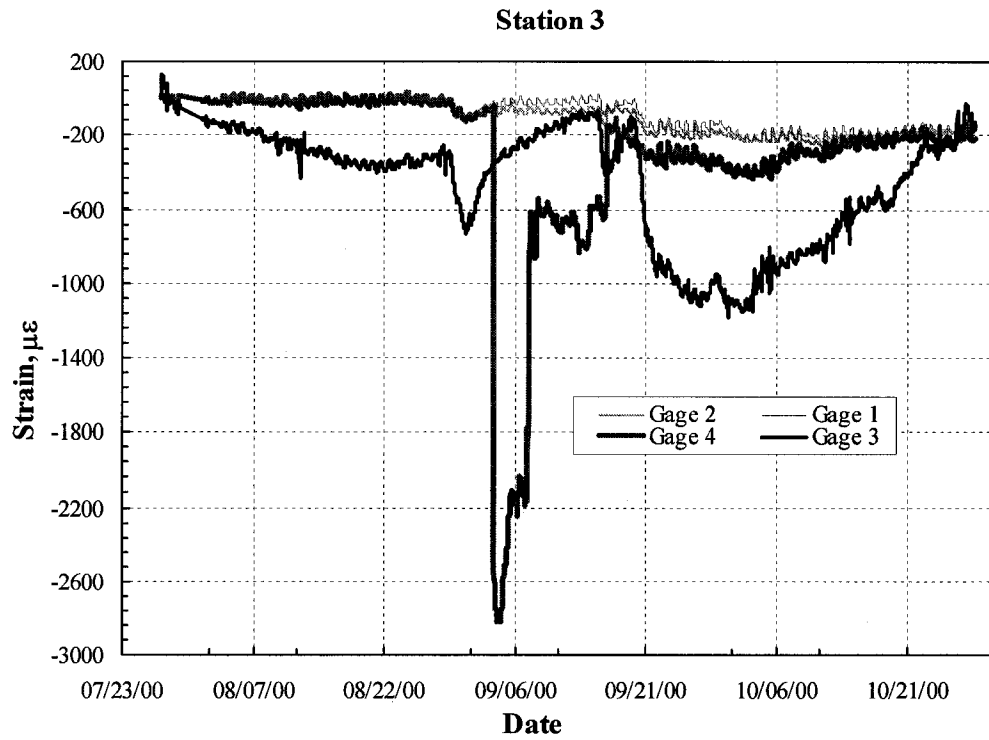


Figure 6.10 Zeroed Strain vs. Time at Station 3

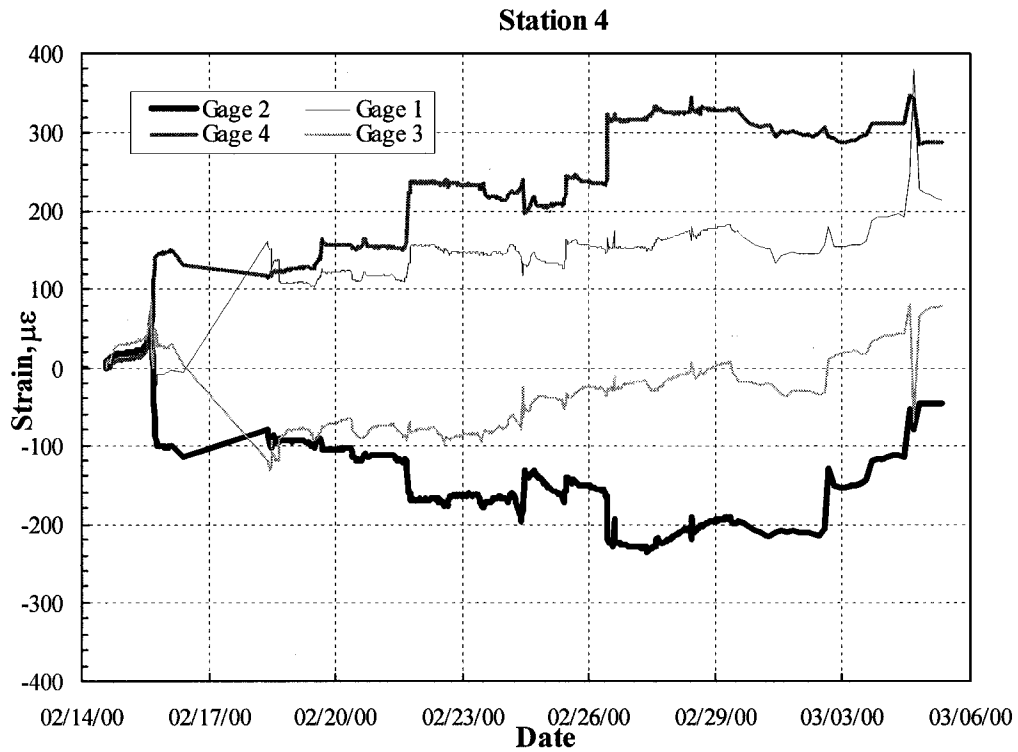


Figure 6.11 Zeroed Strain vs. Time at Station 4

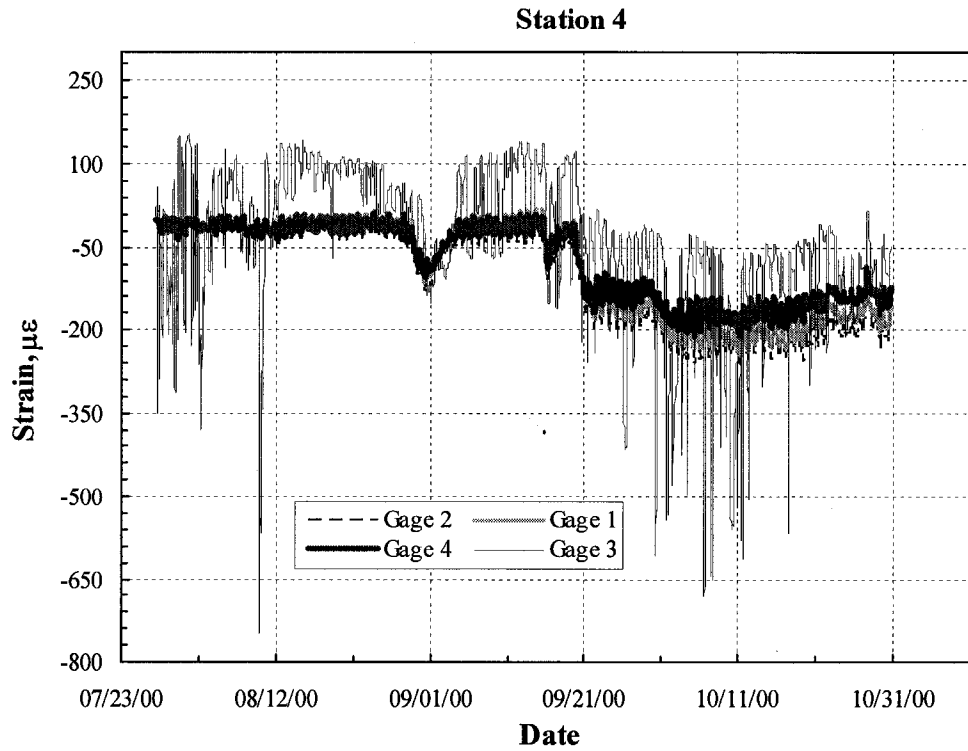


Figure 6.12 Zeroed Strain vs. Time at Station 4

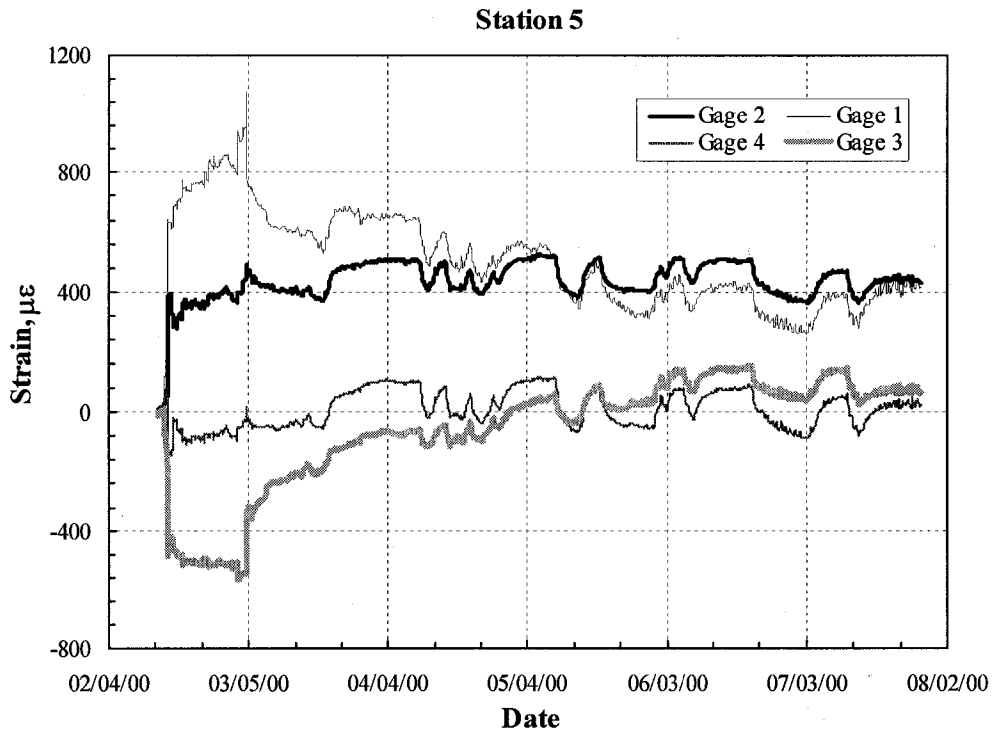


Figure 6.13 Zeroed Strain vs. Time at Station 5

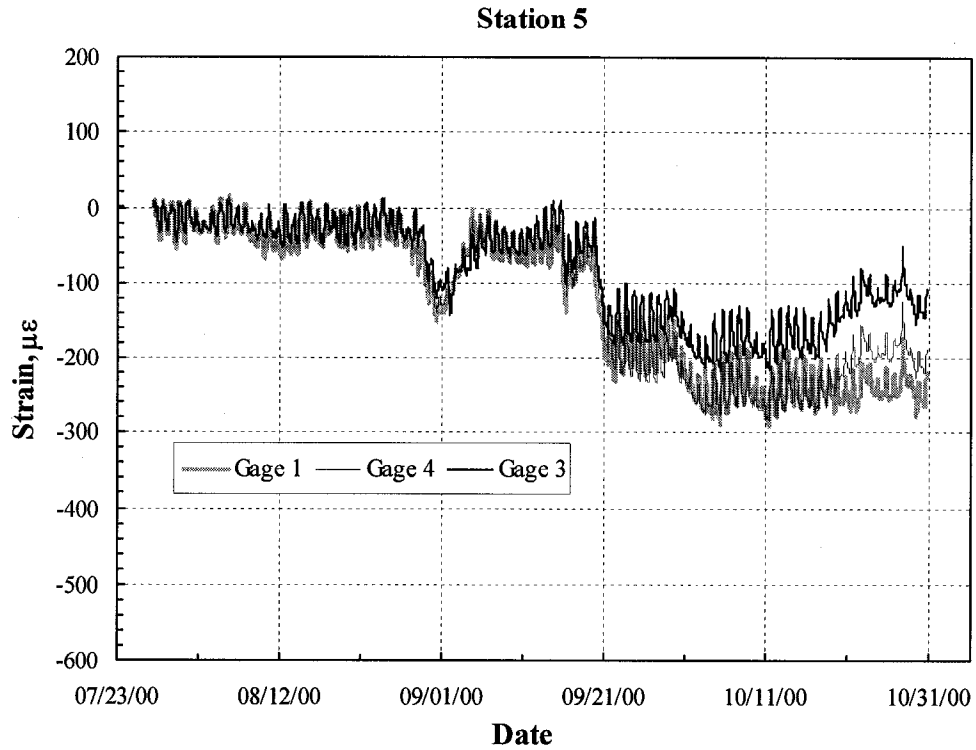


Figure 6.14 Zeroed Strain vs. Time at Station 5

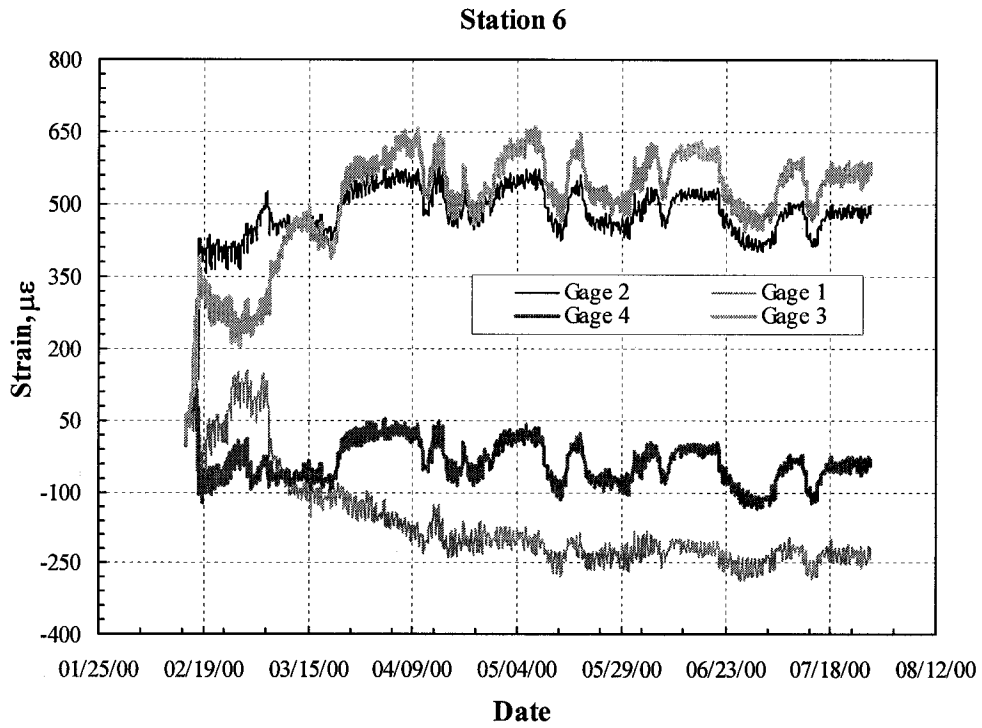


Figure 6.15 Zeroed Strain vs. Time at Station 6

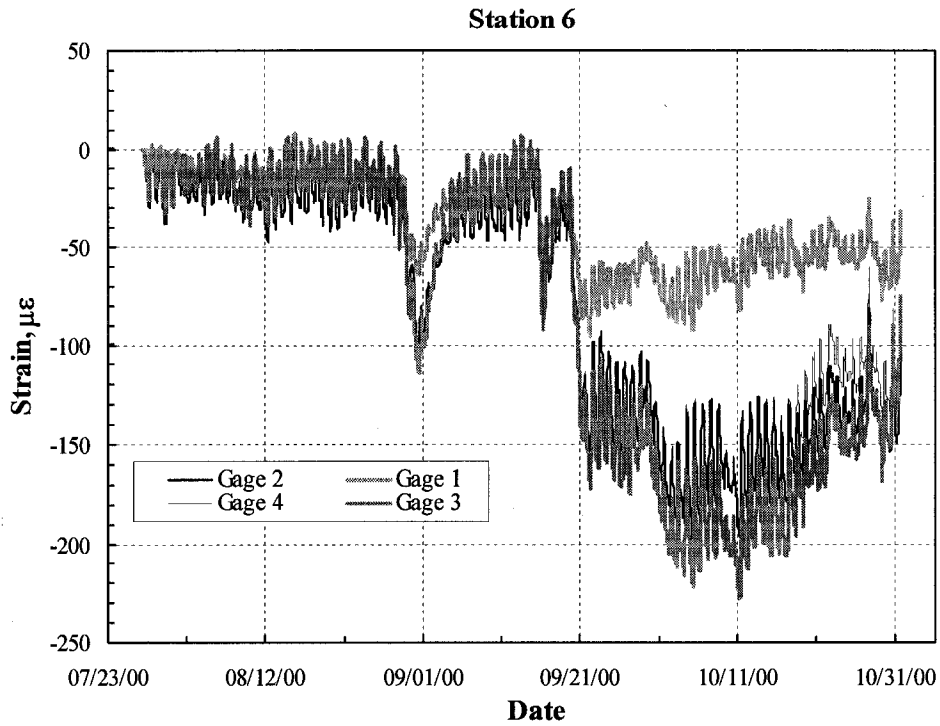


Figure 6.16 Zeroed Strain vs. Time at Station 6

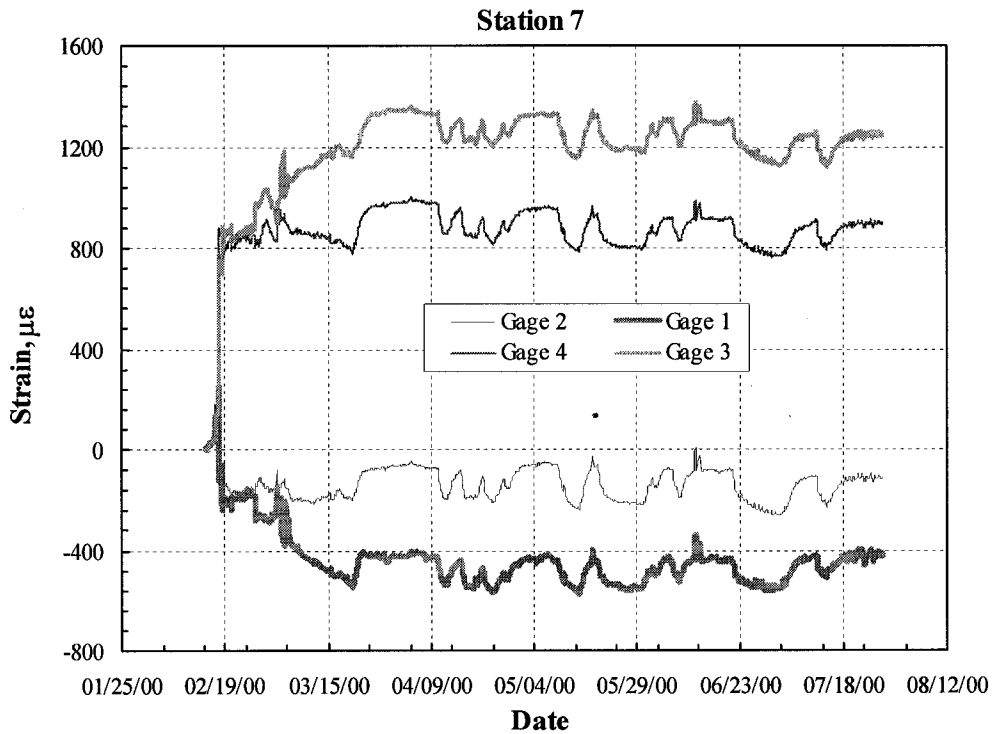


Figure 6.17 Zeroed Strain vs. Time at Station 7

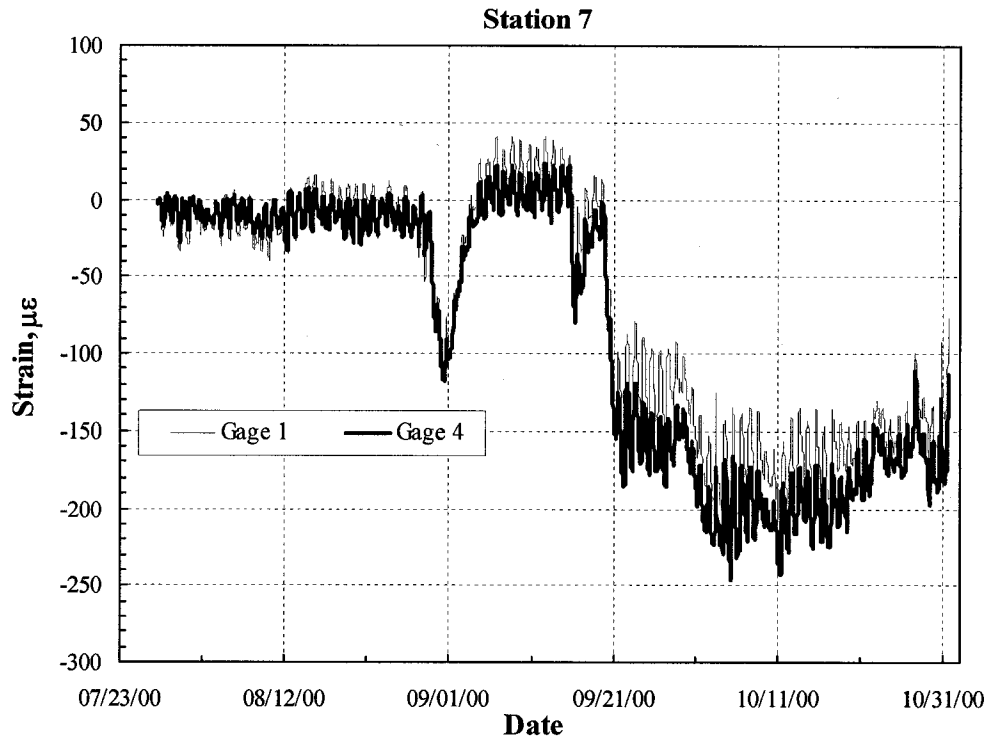


Figure 6.18 Zeroed Strain vs. Time at Station 7

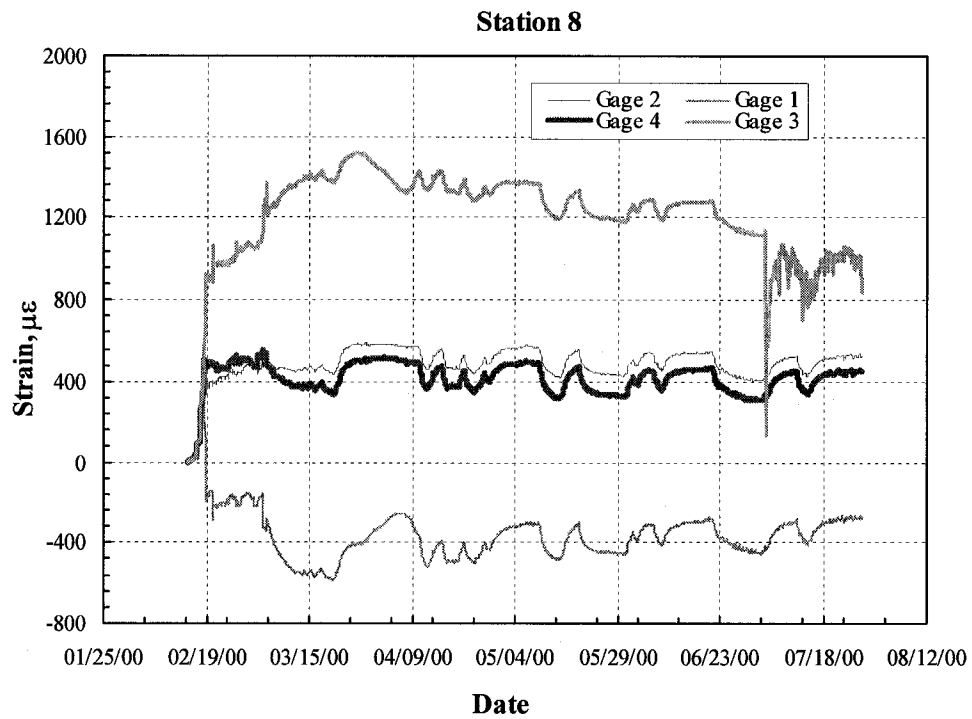


Figure 6.19 Zeroed Strain vs. Time at Station 8

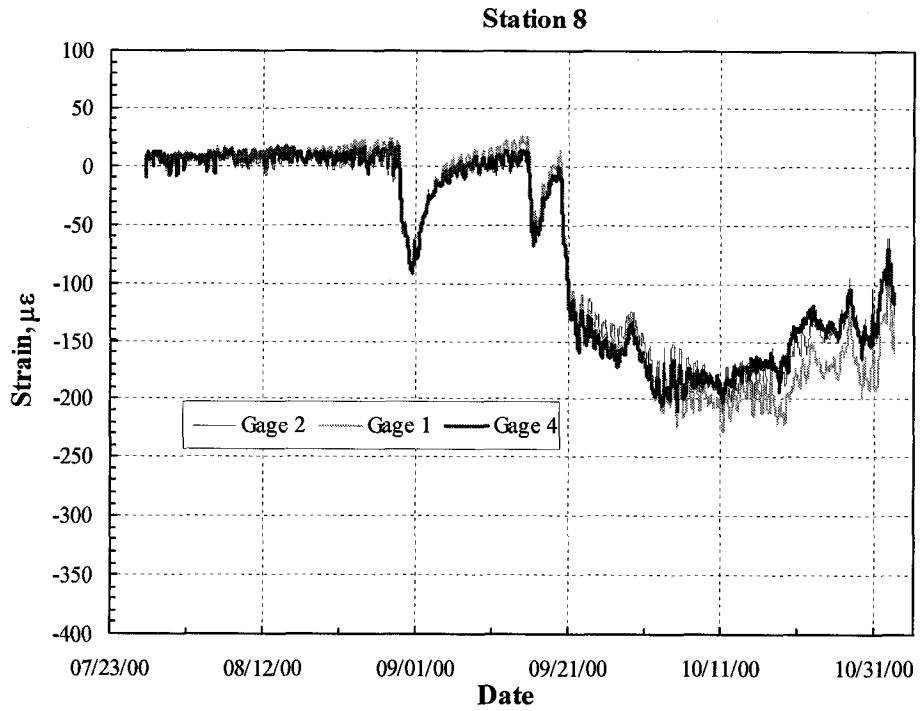


Figure 6.20 Zeroed Strain vs. Time at Station 8

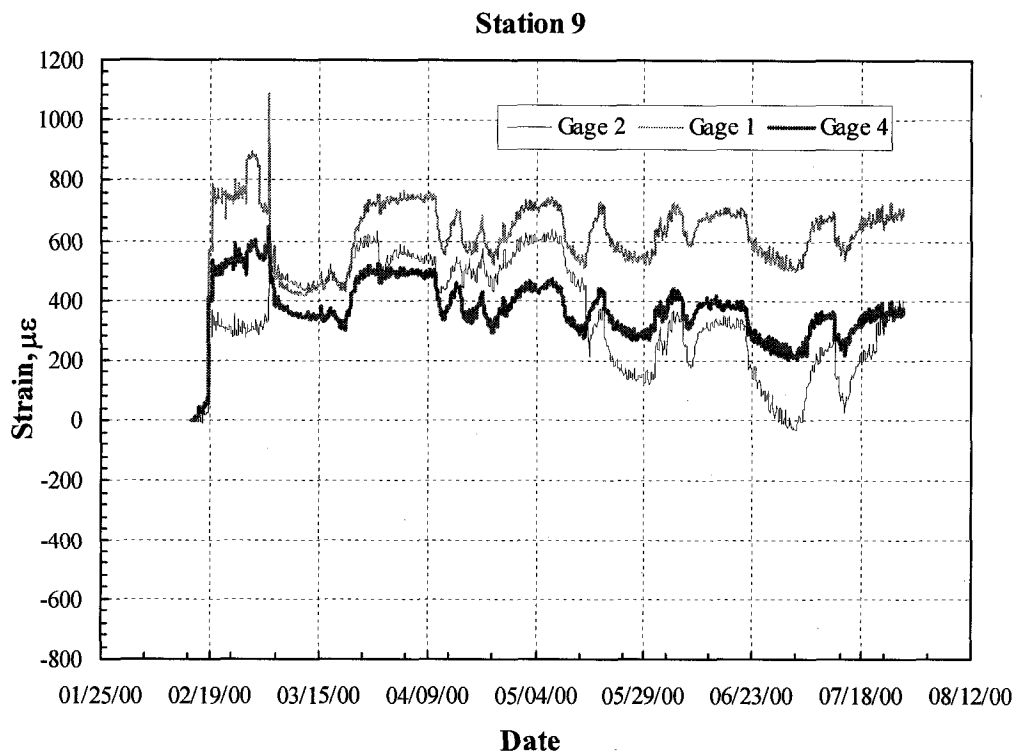


Figure 6.21 Zeroed Strain vs. Time at Station 9

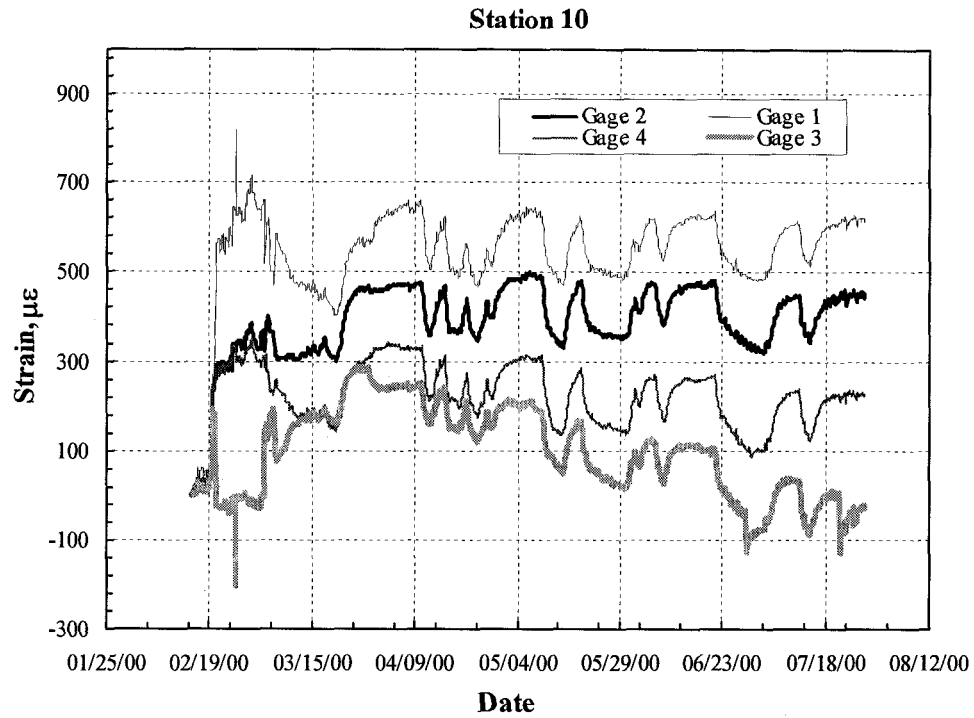


Figure 6.22 Zeroed Strain vs. Time at Station 10

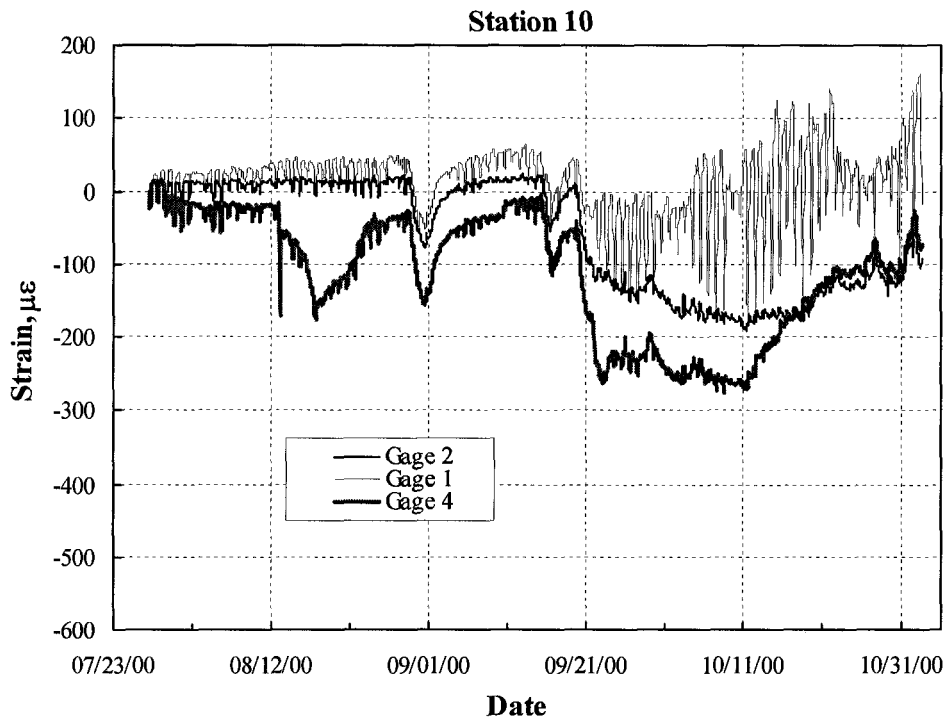


Figure 6.23 Zeroed Strain vs. Time at Station 10

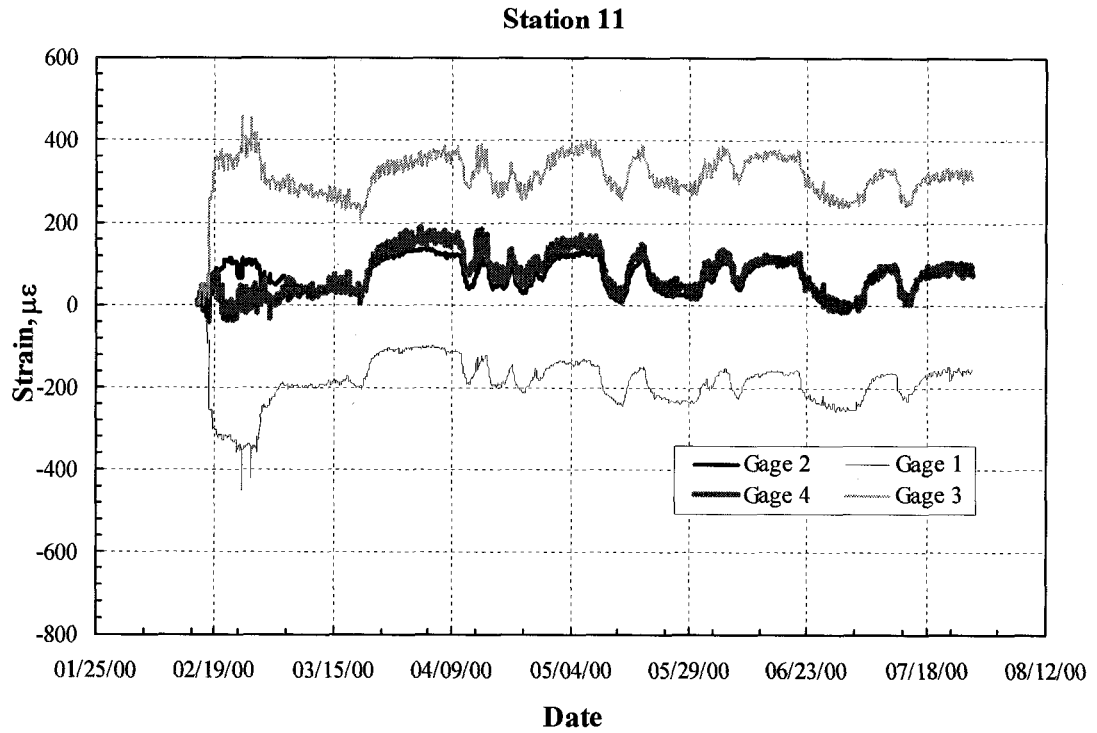


Figure 6.24 Zeroed Strain vs. Time at Station 11

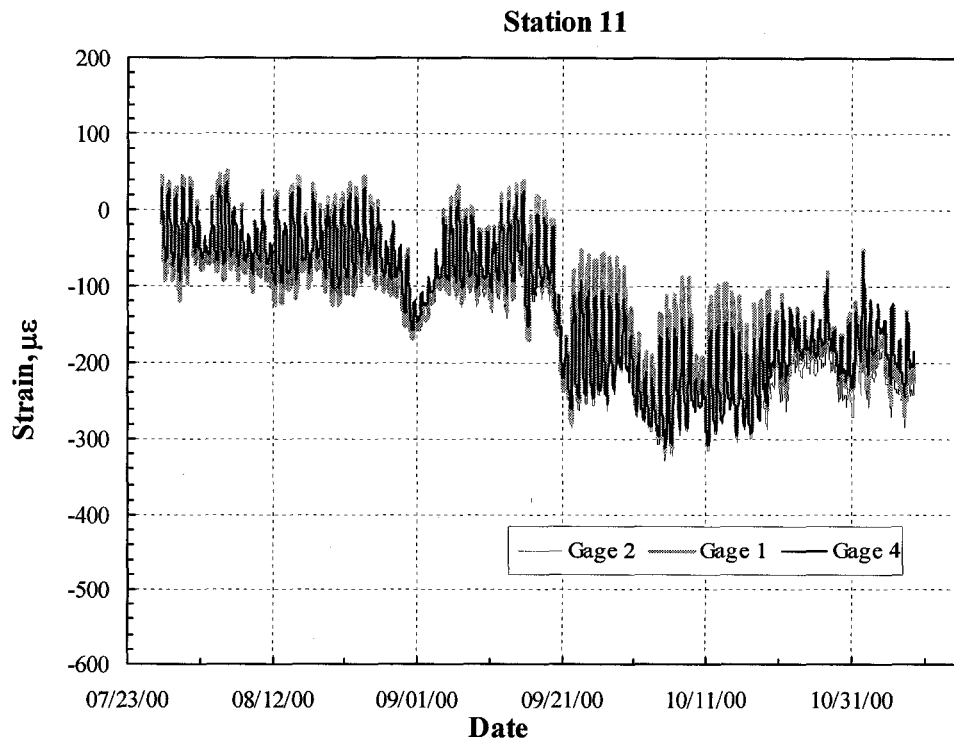


Figure 6.25 Zeroed Strain vs. Time at Station 11

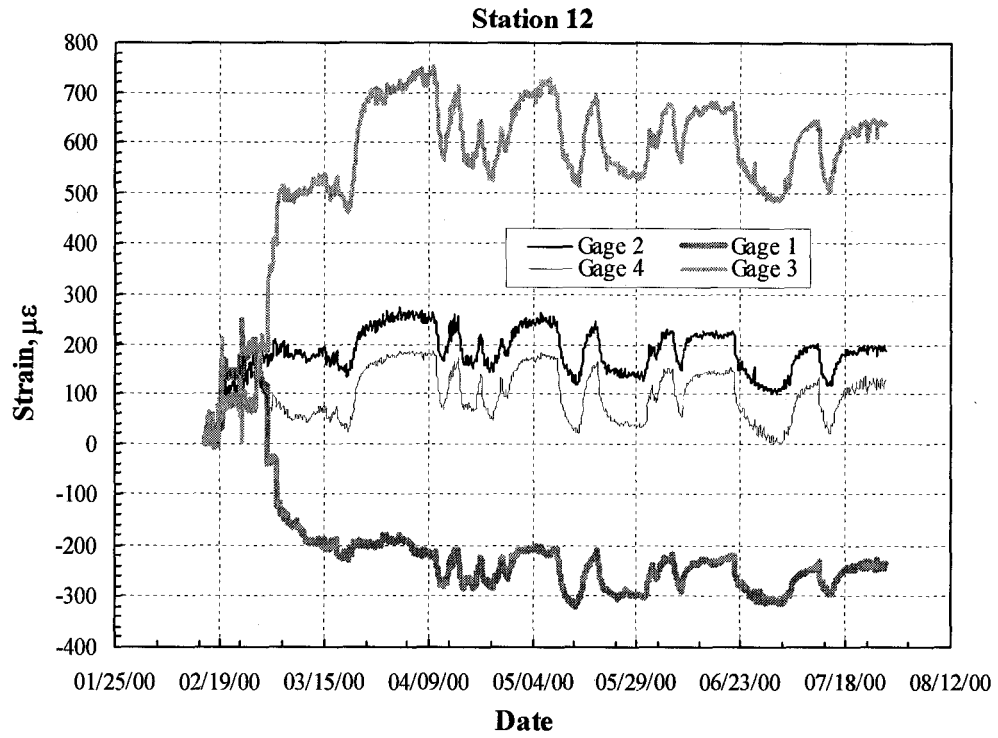


Figure 6.26 Zeroed Strain vs. Time at Station 12

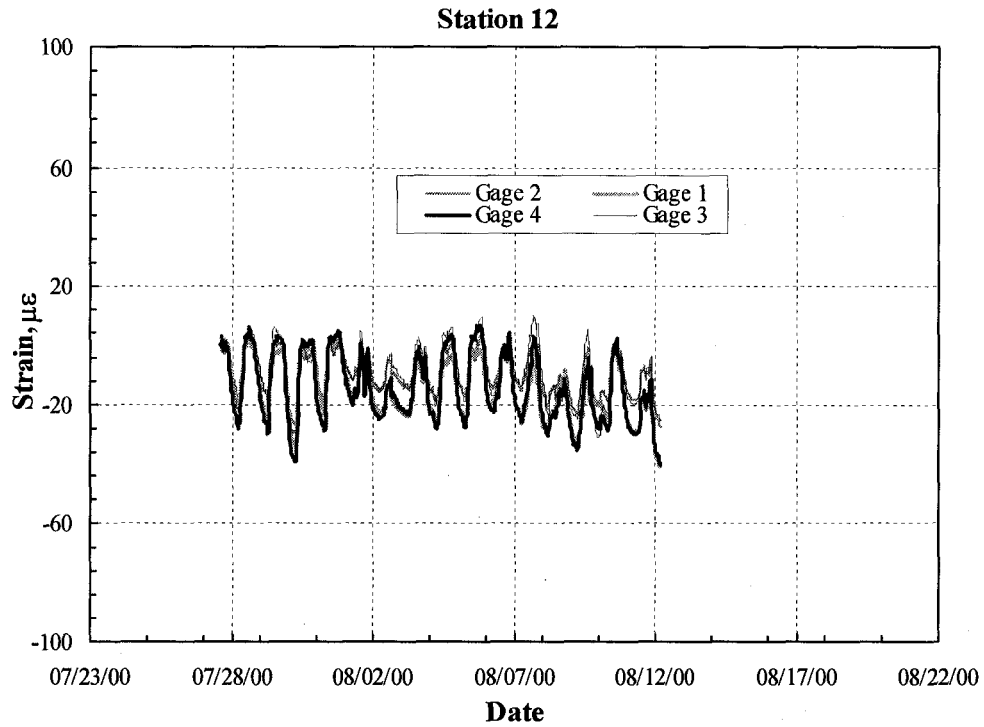


Figure 6.27 Zeroed Strain vs. Time at Station 12

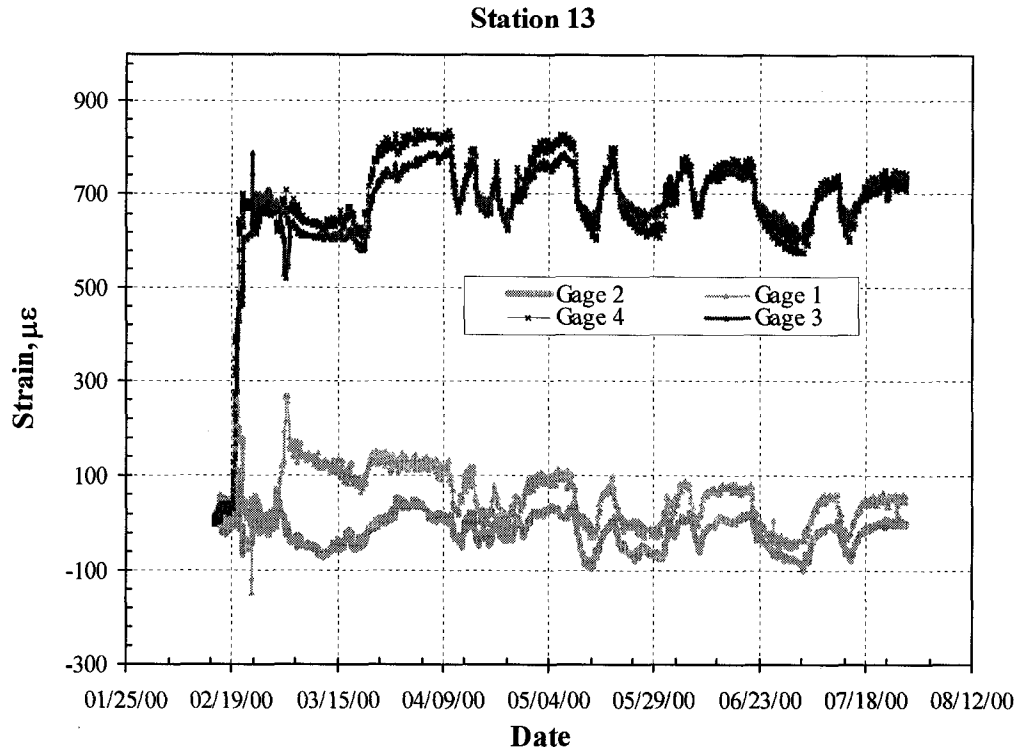


Figure 6.28 Zeroed Strain vs. Time at Station 13

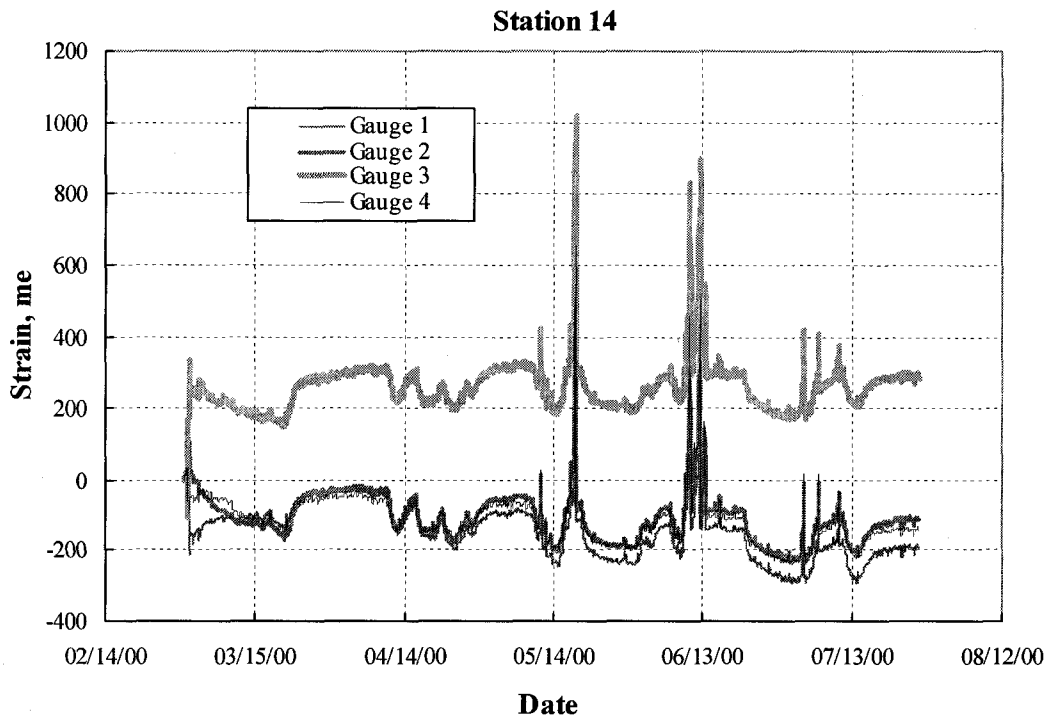


Figure 6.29 Zeroed Strain vs. Time at Station 14

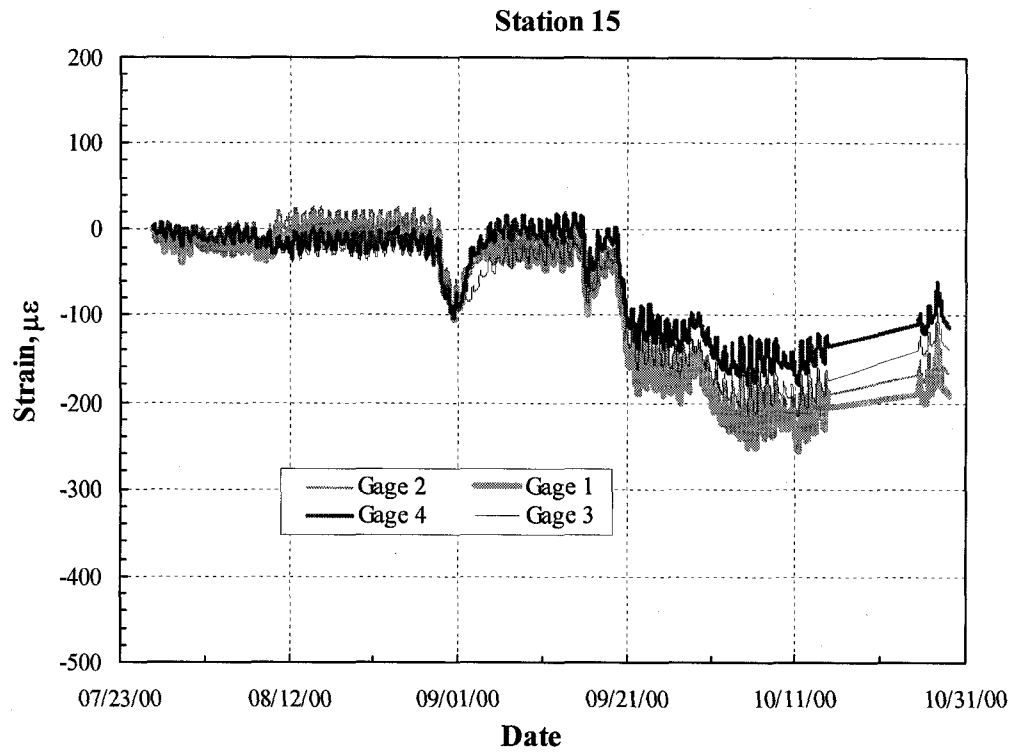


Figure 6.30 Zeroed Strain vs. Time at Station 15

CHAPTER 7 DEVELOPMENT OF THE NUMERICAL MODEL

This Chapter describes the finite element modeling (FEM) of long term slope movement, pipe soil interaction and pipeline behaviour; as well as the stress relief procedures of the pipeline at Pembina River Crossing in LodgePole, Alberta. The technique and development of the model are described in this Chapter. Model verification and application of the model will be presented in Chapter 8 based on the field data from slope indicators and strain gauges. Further investigations of the stress relieve procedure using a parametric study of the finite element model will be presented in Chapter 9.

7.1 Introduction

In order to investigate the strain accumulation of pipeline over time, find out the critical location of the pipeline and determine the effectiveness of the stress relief procedures, a finite element model of the pipeline and slope was developed. The FEM incorporates nonlinear material models, soil creep, changes of water table, pipe-soil interaction and replacing soil with special springs for stress relief. The commercial finite element program ABAQUS STANDARD 6.4 (Hibbitt et al. 2004) was used in this study.

To capture global and local behaviour of the pipeline shell elements were adopted for pipe and solid elements for soil. The correlation between precipitation, soil movement and pipe deformation was also investigated. This Chapter starts with preliminary assessment of the problem, the mechanism of slope movement, followed by a discussion of the finite element modeling procedures. It should be noted that site description, monitoring program and available field data at Pembina River Crossing have already been discussed in Chapter 5.

7.2 Preliminary Thoughts and Concerns

Before modeling the pipeline at Pembina River Crossing, a few preliminary assessments of the main issues are listed below. The main problem is how to model the

soil as well as the pipe-soil interaction, and eventually, how to model the stress relief procedure.

7.2.1 Scope of the Model

It has been expounded in Chapter 5 that there are instrumentation installed in the slope and the pipeline. The numerical model has to accommodate instrumentations for the calibration of the model. In addition, soil movement in the south slope is more than the north slope based on careful examination of the slope movement data. Therefore modeling will focus on the south slope. The pipeline is to be taken long enough to avoid the effects of the boundary. In modeling the soil, there is a slip surface located beneath the pipeline where considerable movements have occurred. Therefore a slip surface needs to be considered in the model. The width of the model is governed by the ground movement in the transverse direction.

From Chapter 5, the centerline of the pipe is two dimensional line south of the creek. It has been examined in Table 5.2 that the ratio of soil movement downslope to that in transverse direction varies from 0.2 to 0.013 for top $\frac{3}{4}$ part of the slope. When it is close to the lower part of the slope, the ratio is almost zero. The ratio is bigger towards the top of the slope with a maximum value of 1.58 at SI-8, but the magnitude of soil movement is small, 1.58 mm/year. Therefore the transverse soil movement can be neglected. Detailed information is provided in the following Sections for modeling.

There is no bedrock shown in the subsurface profile of Pembina River Crossing. The bottom boundary of the finite element model is located where the displacement is zero. According to the slope indicator data, there are a couple of shear planes (a subsurface failure plane) in this slope, which will be captured in the model. Shear plane is modeled as a weak layer in the soil.

The rate of soil movement is large at some locations. Creep is an important factor to be considered in analyzing the stability of the slope. An analysis of slope motion will include the possibility of deep-seated movement depending on the geometry of the slope

and the geotechnical material properties. Also the soil pipe interaction has to be considered. The extent of the finite element model has to be deeper than the depth of boreholes in order to consider the entire domain of down hill soil movement. To satisfy all of the above criteria, the dimensions of the finite element model were 31 m – 70 m in height, 308 m in length and 12 m in width. Lateral pressure from the adjacent soil was applied to the model.

7.2.2 Soil Properties

The analysis procedure accounts for the nonlinear and creep model for the soil. Based on the geotechnical report at Pembina River Crossing, clay is the major geological unit of the site. Chapter 5 presented the observed soil movement as a function of time, and creep is cogitated in the soil model while soil plasticity is required.

Four geotechnical material models are available in ABAQUS Standard. They are Extended Drucker-Prager Model, Modified Drucker-Prager/Cap Model, Mohr-Coulomb Model and Critical State (clay) Plasticity Model. The four material models are investigated. The Extended Drucker-Prager model is used to model frictional materials, which are typically granular-like soils and rock which exhibit pressure-dependent yielding (the material becomes stronger as the pressure increases); The modified Drucker-Prager/Cap plasticity/creep model is intended to model cohesive geological materials that exhibit pressure-dependent yield, such as hard soils and rocks; Mohr-Coulomb Model and Critical State (clay) Plasticity Model are not associated with creep behaviour. Since clay is the main soil type constituting the slope, the Modified Drucker-Prager/Cap Model is chosen to model the clay behaviour. The parameters for the Modified Drucker-Prager/Cap Model will be determined and calibrated based on the direct shear test results on the clay.

7.2.3 The Choice of Finite Elements

To ascertain the section of maximum strain accumulation in the longitudinal direction along the pipeline and to estimate the effectiveness of the stress relief

procedure, pipe has to be simulated by means of shell elements for obtaining local behaviour of the pipeline. Continuum elements are used for modeling soils.

For pipe soil interaction modeling, conventional beam/spring type of model has some significant shortcomings. For example, the springs describing the soil resistance to deformation are usually assumed to be independent of one another, that is no connection between adjacent soil zones is considered, which does not truly replicate the observed behaviour. Another approach proceeds from the discontinuous Winkler model and eliminates its discontinuous behaviour by providing mechanical interaction between individual spring elements. However the Winkler-type soil model is unable to describe the complicated soil behaviour, such as stress path dependencies, pore pressure diffusion and creep.

In this project, the numerical treatment of the soil-pipeline interaction is achieved via a non-linear finite element scheme which models the pipeline as a cylindrical shell (4 node doubly curved general-purpose shell element, reduced integration with hourglass control, finite membrane strains) and adjacent soil as continuum element (C3D8R, 8-node linear brick, reduced integration with hourglass control, hybrid with constant pressure; C3D6, 6-node cylinder continuum element). Soil pipe interaction will be simulated using a special layer of soil elements between the soil and the pipe. The soil properties of this layer will be adjusted to match the pipeline deformation measured by strain gauges.

7.2.4 Stress Relief Procedures

The constraint condition of the pipeline needs to be changed to apply the stress relief procedure to the pipeline. It will be modelled by nonlinear springs. The following Sections will provide details of the modeling procedures of stress relief.

7.2.5 Load History and Expected Results

Based on slope indicator measurements, rate of ground movement can be determined (in mm/yr). From March 2000, strain gauges were installed on the pipeline in

the longitudinal direction. Soil movement occurring at the same time is imposed to pipe, as well as other loads, such as internal pressure, creep of soil, alteration of water levels, etc.

Calibration of the model can be conducted by contrasting the corresponding variables with the slope indicator data from the slope and strain gauge data from the pipe. Stress relief will be simulated and the scope of soil excavation can be investigated. The effect of stress relief effect will be evaluated.

Stress relieves were carried out in the field in 1992 and 2000. The model should be able to estimate the amount of strains after the stress relief procedure was carried out in 1992 and 2000. Moreover, the model should be able to provide the time to effectuate a new stress relief procedure in the future.

In a parametric study, the model is used to obtain insights on pipelines for other sites by varying the parameters in the model.

7.3 Mechanism of Slope Movement

According to Environment Canada's precipitation record, pipeline monitoring data, long term slope motion data, and field observation, the slope movement is mainly caused by precipitation, shear plane slipping and long term creeping of the clay. The monitoring program has been described in Chapter 5.

7.3.1 Slope Indicator Data

To find out the cause of the soil movement, 12 SI data in the downhill horizontal direction (X direction) and local precipitation during the same time period were correlated. Increment of soil movement, U_2 , was also calculated, based on the available SI data in terms of frequent measurement, SI5A, SI6, SI7, SI8, SI10B, SI11B, SI12A, SI12B were chosen for this comparison. U_2 is horizontal down-slope soil movement.

Total precipitation (including rain, snow, drizzle, etc.) over a period of time from Environment Canada's database of historical climate data in nearby weather stations was obtained. This data corresponds to three basic sampling frequencies of climate data collection: Hourly, daily and monthly data are provided for each hour of the day, each day of the month and each month of the year respectively. Data collection, processing, quality control checks and procedures have evolved and changed over the years. For the sake of comparison, characteristic features in the relationship between SI and precipitation data are investigated.

It should be noted that there is no climate station in LodgePole, however, a few climate stations near LodgePole give reference precipitations with time. Table 7.1 shows the locations of these stations compared with LodgePole and the time period of available precipitation record from Environmental Canada. Not all the data are complete at these stations. Precipitation data is taken from the stations closest to Lodgepole.

SI data is shown in Chapter 5. It has been concluded that the slope slides along a weak layer in the clay till. The rates of slope movement in the X direction with respect to time at the ground surface at twelve slope indicators are averaged from 1.58-40.35mm/yr as shown in Table 7.2. SI data in the summer of 1989 is regarded as extreme, and is not taken into account on the average yearly soil movement in the X direction, since the total precipitation in 1989 was 872 mm, much higher than the total average yearly precipitation of 552 mm, and precipitation in the rainy season (May to September) in 1989 was 641 mm, much higher than the average precipitation of 375 mm of the same months. Precipitation history in 1986-2000 can be seen in Table 7.10 and Figure 7.7. The majority of the yearly precipitation occurs in May to September. This extreme case will be considered separately. It is noticeable in table 7.2 that during rain seasons (May to September) or snow melting periods (March to May) the slope moves downhill faster, especially at four periods of time, July-October 1989, May-July, 1997, April-July, 1999 and April-September, 2000.

Slope Indicator SI5

Figure 7.1 shows U_2 versus time at different depths for SI5 from June 1987 to September 1999. U_2 at the surface from June 1987 to June 1992 is 2.11 mm/month, from June 1992 to June 1998 is 0.6 mm/month, and from June 1998 to July 1999 is 2.2 mm/month. Table 7.3 shows the SI record for SI5.

The closest place to Lodgepole is Brazeau Lo, but data is only available from May to September between 1987 and 1999. Figure 7.2 reveals the monthly average precipitation for 1987-1996 from Wildwood Newbery and 1997-1999 from Entwistle. The average monthly precipitation of 1987-1991 in July and August is about 14% and 27% more than that of 1998-1999 and 1992-1997. The average monthly precipitation of 1998-1999 in May is about one time more than that of the other two periods. Table 7.4 displays the total precipitation in 1987-1991 at Wildwood Newbery. The average yearly precipitation is 596 mm. Table 7.5 shows the total precipitation in 1992-1997 at Wildwood Newbery and Entwistle. The average yearly precipitation is 512 mm. Table 7.6 shows the total precipitation in 1998-1999 at Entwistle. The average yearly precipitation is 561 mm. The comparison gives consistent trend between SI5 and precipitation at the different periods of time.

Slope Indicator SI5A

Figure 7.3 shows U_2 versus time at different depths for SI5A from April 2000 to September 2001. The surface movement from April to May in 2000 is 2.5 mm/month, from May to September in 2000 is 4.2 mm/month, from September 2000 to June 2001 is 0.6 mm/month, and from June to September 2001 is 1.5 mm/month. Soil movement rate is higher in summer time, and in year 2000 the ground has moved more than two times of that in 2001. Table 7.7 shows the SI record for SI5.

Figure 7.4 shows the precipitation at Entwistle in 2000 and Violet Grove in 2001. Total precipitation in August is the maximum over the year. Overall, precipitation in summer 2000 is higher than 2001. It can also be seen in Table 7.8 that the total precipitation in 2000 at Entwistle is 642.8 mm, about 1.5 times of the precipitation in 2001 at Violet Grove of 435.2 mm. Figure 7.5 shows the increment of U_2 versus time at

different depths for SI5A. From June to September 2000, soil movement on average increases by 4.4 mm/month, June to September 2001 it increases by 1.5 mm/month. Table 7.9 shows the magnitude of the increment of soil motion in the X direction. SI5A and precipitation have the same trend.

Slope Indicator SI6

Figure 7.6 is U_2 versus time at different depths for SI6 from June 1988 to September 1989. Surface movement from June 1988 to July 1989 is 0.13 mm/month, from July to September 1989 soil is 33 mm/month. According to the rainfall record in Table 7.10, the maximum precipitation in May to September for 1986-2000 is 641.1 mm, and January to December is 872.4 mm in 1989. Figure 7.7 gives the total precipitation in May to September, January to December in 1986-2000. Table 7.11 shows the magnitude of soil motion in the X direction.

Figure 7.8 shows the monthly increment of soil movement at different depths from June 1988 to September 1989. The increment of soil movement near the ground surface in August and September in 1989 is 30 mm/month, correspondingly, precipitation reaches 234.6 mm at the Wildwood Newbery station, with maximum value in August of 1986-2000. This again indicates the correlation between ground movement and precipitation.

Slope Indicator SI7

Figure 7.9 shows U_2 versus time at different depths for SI7, from June 1988 to September 1989. Ground surface movement from June 1988 to July 1989 is 1.0 mm/month, from July to September 1989 the soil movement at 2 m below ground is 30.8 mm in two and a half months, which is smaller than that of SI6. This is due to different slope angles. SI6 is located at the slope of 14.5° and SI7 of 5.7° . Table 7.12 shows the magnitude of soil motion in the X direction.

Figure 7.10 shows monthly the increment of U_2 versus time at these same depths for SI7 From July to September in 1989, soil movement near the ground surface at SI7 increases to 14 mm/month which corresponds to a high rainfall in the summer of 1989.

Slope Indicator SI8

Figure 7.11 shows U_2 versus time at different depths for SI8, from March 1992 to September 2001. U_2 at the surface from March 1992 to September 1999 is 0.13 mm/month, from September 1999 to September 2001 is -0.15 mm/month, the slope has moved uphill. This may be due to the transverse motion of the soil. At location SI8, the ground is not moving. Table 7.13 shows the magnitude of soil motion in the X direction.

Slope Indicator SI10A

Figure 7.12 shows U_2 versus time at different depths for SI10A, from July 1997 to July 1999. U_2 at the surface from July 1997 to June 1998 is 0.88 mm/month, from June 1998 to April 1999 is 1.72 mm/month and from May to July 1999 is 15.04 mm/month. There are only two measurements in June 1998 and April 1999, slope movement in summer of 1998 is unknown. Table 7.14 shows the magnitude of soil motion in the X direction. Figure 7.13 shows the monthly precipitation in 1997-1999 at Entwistle. Apart from July, precipitation from April to August, 1999 is higher than that in 1998. Table 7.10 shows that the total precipitations in 1997, 1998 and 1999 are 559mm, 549mm and 573mm respectively, and soil movement has the maximum rate in 1999. Figure 7.14 shows the precipitation at Brazeau Lo, in 1997-1999. It is found that the 1999 precipitation is higher than that in the summer of 1997, same as that in the SI10A record.

Slope Indicator SI10B

Figure 7.15 shows U_2 versus time at different depths for SI10B, from April 2000 to September 2001. U_2 at the surface soil motion, from April to September 2000, it moves 6mm/month. From September 2000 to June 2001, the rate of movement is 1.9 mm/month and from June to September 2001, it is 3.9 mm/month. The movement from June to September in 2000 and 2001 are higher, which means that the soil motion rate is higher at summer time. Table 7.15 shows the magnitude of soil motion in the X direction. Figure

7.4 and Figure 7.7 indicate that year 2000 has more rain than 2001. Figure 7.16 shows the precipitation at Brazeau Lo in 2000 and 2001 which gives the same trend. Table 7.8 shows the total precipitation in 2000 is 642 mm and 435 mm in 2001.

Figure 7.17 shows the monthly increment of U_2 versus time at the same depths for SI10B. From June to August 2000, soil movement keeps increasing at 9.5mm/month, which coincides with the precipitation rates as shown in Figure 7.16 measured at Brazeau Lo.

Slope Indicator SI11A

Figure 7.18 shows U_2 versus time at different depths for SI11A from May 1997 to June 1998. U_2 at 1.6 m below ground surface from May to July 1997 is 4.0 mm/month and from July 1997 to June 1998 is 0.48 mm/month. Table 7.16 shows the magnitude of soil motion in the X direction. Table 7.10 shows that in June 1997 the precipitation is 176 mm which is the maximum of the year, and in June 1998, it is 136 mm which is consistent with the slope movement at SI11A.

Slope Indicator SI11B

Figure 7.19 shows U_2 versus time at different depths for SI11B, from May 2000 to September 2002. U_2 at 0.8 m below ground surface from May to September 2000 is 5.7 mm/month, and from September 2000 to September 2001 it is 1.8 mm/month. Table 7.17 shows the magnitude of soil motion in the X direction for SI11B. Figure 7.4 and Figure 7.7 indicate that year 2000 has more rain than 2001. Figure 7.16 shows the precipitation at Brazeau Lo, in 2000, 2001, which has the same trend. Table 7.8 shows in 2000 the total precipitation is 643 mm, in 2001 it is 435 mm.

Figure 7.20 shows the monthly increment of U_2 versus time at the same depths for SI11B. In July 2000, the increment of soil movement is 11 mm/month, showing the same trend as the precipitation.

Slope Indicator SI12

Figure 7.21 shows U_2 versus time at different depths for SI12, from March 1992 to June 1997. U_2 at 0.8 m below ground surface from March to July 1992 is 7.9 mm/month, from July 1992 to October 1994 is 3.3 mm/month, from October 1994 to April 1997 is 2.6 mm/month and from April to June 1997 is 16 mm/month. (May-June, 220mm) Figure 7.22 shows the precipitation at Brazeau Lo between 1992 and 1997. In August 1995 and July 1997 precipitation reach 170 mm and 160 mm respectively which is consistent with the slope movement. Table 7.18 shows the magnitude of soil movement in the X direction for SI12.

Slope Indicator SI12A

Figure 7.23 shows U_2 versus time at different depths for SI12A, from May 1997 to September 1999. U_2 at 2 m below ground surface from May to October 1997 is 1.8 mm/month, from October 1997 to June 1998 it is 0.5 mm/month, from June 1998 to April 1999, it is 2.01mm/month and from April to July 1999 it is 11.873mm/month. From July to September 1999, the ground moved upslope at a rate of 118 mm/month, which is unusual.

Figure 7.24 shows the monthly increment of U_2 versus time at the same depths in 1999 for SI12A. In May and July 1999, soil movement at the surface kept increasing at a rate of 20 mm/month, which coincides with the precipitation changes measured at Entwistle, see Figure 7.16. Table 7.19 shows the magnitude of soil motion in the X direction for SI12A.

Slope Indicator SI12B

Figure 7.25 shows U_2 versus time at different depths for SI12B, from March 2000 to September 2001. U_2 at 0.8 m below ground surface, from March to September 2000 is 5.2 mm/month and from to September 2000 to September 2001 it is 1.3mm/month. Slope movement from June to September in year 2000 and 2001 are bigger. Table 7.20 shows the magnitude of soil motion in the X direction for SI12B.

Figure 7.26 shows the monthly increment of U_2 versus time at the same depths for SI12B. In June, July and August 2000, soil movement is increasing at a rate of 7mm, 9mm and 9mm/month, which coincides with the precipitation change measured at Brazeau Lo station, see Figure 7.16.

In summary, the above analysis indicates:

1. The rate of slope movement is higher in summer time due to rain than other months of the year.
2. The movement of slope is result of the rise of the ground water table.
3. Time-dependent soil creep is another reason of slope movement.
4. Slope movement is localized on a slip surface.

7.3.2 Pipeline Monitoring Data

As described in Chapter 5, strain gauges were mounted longitudinally along the pipeline at four stations. There are four strain gauges at each station. Figure 5.55 to Figure 5.58 show the measurements of Strain Gauge 1 (SG1), Strain Gauge 2 (SG2), Strain Gauge 3 (SG3) and Strain Gauge 4 (SG4) vs. time at Station 1 respectively from July 16 to November 29, 2000. The positions of SG1 to SG4 on the pipeline are shown in Figure 5.6. SG1 is located at a horizontal coordinate of 71434.5 m, at the upper part of the south slope. Table 7.21 shows the strain accretion of SG1~SG4 at Station 1, tension is positive and compression is negative. The average axial compressive strain is $53.9\mu\epsilon$ at Station 1. Figure 5.59 to Figure 5.62 shows SG1, SG2, SG3 and SG4 vs. time at Station 2 from July 16 to November 15, 2000. SG2 is located at a horizontal coordinate of 71509.5m, near the middle of the south slope. Table 7.21 gives the strain increment at SG1~SG4 at Station 1- Station 4, however at Station 2, SG3 and SG4 are unavailable due to malfunction of the strain gauges.

Figure 5.63 to Figure 5.66 show SG1, SG2, SG3 and SG4 vs. time at Station 3 from July 16 to November 29, 2000. SG3 is located at a horizontal coordinate of 71585.8m, at the lower part of the south slope. Table 7.21 shows the strain accretion at SG1~SG4 at Station 3. On September 16 all strain gauges have about $700\mu\epsilon$ abnormal

rise. Figure 5.67 to Figure 5.70 show SG1, SG2, SG3 and SG4 vs. time at Station 4 from July 16 to November 29, 2000. SG4 is located at a horizontal coordinate of 72606.6m, near the creek on the south slope. Table 7.21 gives the strain accretion at SG1~SG4 at Station 4. On September 12 all strain gauges have about 720 $\mu\epsilon$ abnormal drop.

In summary, pipeline strain data shows:

1. The strain accumulation is higher at summer time than other months of the year; consistent with SI and precipitation data.
2. Pipeline deformation is a function of time. It is dependent of the slope movement.

7.4 Mechanical Behaviour and Conditions of Geotechnical Materials

Chapter 5 has already discussed the general characteristics of the natural ground and the slope. Here, the mechanical and hydraulic behaviour of each of the material involved will be quantitatively described for conducting the numerical simulations. To differentiating among various parameters, those parameters that have a dominating influence will be noted in each part of the section. The soils being modeled consist of saturated and unsaturated materials. The material parameters are needed for the Modified Drucker Prager/Cap plasticity and creep model with hardening. These parameters are calibrated by simulating the direct shear test using ABAQUS. The material model is then implemented in three-dimensional finite element simulations for its validation and robustness.

As shown in Figure 7.28, the subsurface stratigraphy consists of, from the deepest layer to the surface, sandstone/clay shale bedrock, clay till A, clay till B, slip layer, soft clay and clay inside pipe (see Section *Load Sequence for the Pipeline*). Sandstone/clay shale bedrock, clay inside pipe before pipe installation, and clay till B are modeled using the elastic porous material model. High permeability is assumed for the sandstone while low permeability is assigned to the rest the soil layers. Soft clay, slip layer and clay till A are modeled using the modified Drucker-Prager Cap plasticity model. Both elastic and inelastic material properties are tabulated in Table 7.22.

The mechanical models employed to represent the behaviour of various materials correspond to the characteristics given in Chapter 5. Essentially all the models, in which the Modified Drucker Pager/Cap model are used, are elasto-plastic model with friction that have a shear strength related to the level of effective compression exerted on the shear surface (see Section *Constitutive Model*). The strength that can be developed remains unaffected by the amount of deformation.

Initially, all natural materials have been assumed to have an isotropic state of effective stresses. This means that, as a result of the precondition, the effective stresses in the two horizontal directions have been assumed to be 72% of the effective vertical stress; i.e. a coefficient of earth pressure at rest, k_0 of 0.72. As the slope deforms due to water table rises and soil creeps, the stresses at each point are allowed to change in response to the changing conditions. This is discussed later in the Section: *Load Sequence*.

The materials constituting the slope have been allowed from the beginning to develop their own states of stress, resulting from the geometry, rate of creep, density and mechanical behaviour of the various materials. This initial state of stress satisfies the condition of equilibrium and the boundary conditions.

7.4.1 Soft Clay

Soft clay deposit at Pembina River Crossing is found to be silty, moist, medium plastic and brown. The layer of soft clay has some trace of coarse grained sand and coal. It is wet, firm and grey near the river area. The depth of the soft clay layer is one to three meters from the ground surface. Figure 7.28 displays the slope and pipeline at Pembina River Crossing. Soft clay is located above line AB in Figure 7.27. The circular layer surrounding the pipe is made up of pipe-soil interaction elements of the clay material. This will be addressed at interface modeling section presented later in this Chapter.

The stress strain response of the soft clay is assumed to be elasto-plastic governed by Modified Drucker-Prager/Cap plasticity/creep material criterion. The material's elastic response is assumed to be linear and isotropic, with Young's modulus of 30 MPa,

Poisson's ratio of 0.42, and a density of 17.2 kN/m^3 . A friction angle of 21.5° is assumed, Cohesion is 30 kPa and permeability is 10^{-8} m/s with void ratio of 0.6.

7.4.2 Clay till

Clay till can be very heterogeneous and varying in composition and stiffness. At the same profile, there can be several layers of different origin and composition deposited on top of each other. Figure 7.28 displays a layer of clay till at Pembina River Crossing. There are three layers with different types of clay till: clay till A, slip surface and clay till B on top of clay shale/sandstone bedrock. The depth of the clay till varies from 16 to 37 meters from the bottom of soft clay layer.

The stress strain response of clay till A is assumed to be elasto-plastic governed by the Modified Drucker-Prager/Cap plasticity/creep material criterion. The material's elastic response is assumed to be linear and isotropic, with Young's modulus of 30MPa, Poisson's ratio of 0.42, and a density of 17.2 kN/m^3 . A friction angle of 21.5° is assumed, value of cohesion is 30kPa. Permeability is 10^{-9} m/s , and void ratio is taken as 0.6. Slip layer is stated in next Section. The stress strain response of clay till B is assumed to be elastic. The material's elastic response is assumed to be linear and isotropic, with Young's modulus of 100 MPa, Poisson's ratio of 0.42, and a density of 17.2 kN/m^3 . The permeability of the material is 10^{-9} m/s and void ratio is taken as 0.6.

7.4.3 Modelling the Slip Surface

Soil samples were taken from the slip layer, and direct shear test were conducted. Figure 7.28 shows the location of slip surface. The depth of slip surface is within 2 m in the clay layer, between clay till A and clay till B.

Based on the direct shear test, stress strain response of the slip layer is assumed to be elasto-plastic, governed by the Modified Drucker-Prager/Cap plasticity/creep material criterion. The material response is assumed to be linear elastic and isotropic, with Young's modulus of 10 MPa, Poisson's ratio of 0.42, and a density of 17.2 kN/m^3 . A friction angle of 19.5° is obtained from the laboratory test with effective cohesion of 5 kPa. The permeability of material is assumed to be 10^{-9} m/s with and void ratio of 0.6.

7.4.4 Sandstone

The sandstone and clay shale bedrock underlying the clay till are located too deep for their mechanical characteristics to have significant effects on the response of the pipeline. This layer has relatively high permeability and will be acting as a drainage boundary compared with the clay till. The depth of the sandstones/clay shale bedrock varies from 3 m to 28 m below the clay till B layer. Figure 7.28 displays the location and depth of the sandstone/clay shale bedrock.

The stress strain response of the sandstone is assumed to be elastic. The material is assumed to be linear elastic and isotropic, with a Young's modulus of 200MPa, Poisson's ratio of 0.35, and a density of 18 kN/m³. The permeability of the material is assumed to be 10⁻⁴ m/s and void ratio is taken as 0.6.

7.5 Finite Element Modeling Procedures

This section describes the manner in which the information already given in the previous chapters has been used in the numerical simulation of the problem. The FEA model in this study is a soil mechanics problem. The analysis is carried out assuming fully saturated flow through the soil domain since the soil is fully saturated with ground water. Movement is due to time-dependent consolidation of the soils as well as changes in the water table with time. Total pore pressure is assigned in the model, which is proportional to the depth below the ground water table.

Static stress/displacement analysis and coupled pore fluid diffusion/stress analysis are carried out using ABAQUS. A static stress analysis is carried out here because the inertia effect is negligible, while time-dependent material effects (creep, swelling, visco-elasticity) are ignored. Coupled pore fluid diffusion and stress analysis involving partially and/or fully saturated fluid flow is carried out. A coupled pore fluid diffusion/stress analysis is used to model single phase, partially or fully saturated fluid flow through porous media. It can be performed in terms of either total pore pressure or excess pore pressure by including or excluding the pore fluid weight. It can be linear or nonlinear.

The use of pore pressure elements is required with associated pore fluid flow properties defined.

7.5.1 Introduction – Purpose of Finite Element Analysis

Finite Element Analysis (FEA) is a discretization technique that provides approximate answers by simulating structures with only finite degrees of freedom in terms of a mathematical model, usually a system of partial differential equations (PDEs). The physical domain is discretized into a mesh of finite elements. FEA software calculates the response of the structure due to externally applied stress, or fluid flow. The finite element (FE) method is a numerical method suitable for modeling large problems with complex geometry and material behaviour.

The pipeline deformation under the slope movement involves complex structural and geotechnical issues. The slope at Pembina River Crossing is composed of different materials. To carry out the stability analysis of a slope is not an easy task. Evaluation of the variables, such as the soil stratification and its in-plane shear strength parameters, may prove to be a formidable task. Pipe soil interaction and seepage through the slope add to the complexity of the problem. This model simulates pipeline deformation due to creep and changes in water table. The commercial finite-element package, ABAQUS STANDARD, is employed in this study to solve problems involving fluid flow through saturated porous medium, inelastic material properties with time-dependent creep behaviour. Field SI data and strain gauges data are used to calibrate the FEA model.

7.5.2 Geometry of the Model

As described in Chapter 5, the pipeline at Pembina River Crossing was constructed in 1986. It is part of the NPS 30, located at about 8km south-east of Lodgepole, Alberta. The model consists of a pipeline buried at 1 m to 4 m below the ground surface with an overall size of the domain of 308 m×12 m×depth (42m to 69m) slope. The ground consists of five soil layers, including soft clay, clay till A, slip layer, clay till B and sandstone from elevation 840 m to 909 m, see Figure 7.28. The size of the

model is considered sufficiently large to analyze a 12 m wide slope in transverse direction.

Horizontally, the model has been extended sufficiently far upstream and downstream from the creek with a total length of 308 m to ensure that the boundary conditions will not affect the solution of the problem. The lower boundary of the finite element domain extends to a depth of 42 m – 69 m (elevation 840 m) which is the layer of sandstone, in order to minimize the effect on the lower boundary on the response of the pipeline.

The pipeline, with external diameter of 762 mm and wall thickness 15.88 mm, is composed of 53 straight segments joined at cold bend angle of $1.5^\circ/\text{diameter}$. The slope angles vary from 1.2° to 18.9° . The pipeline is buried at 1 m ~ 4 m below the ground surface.

The ratios of the horizontal downhill movement to the horizontal transverse movement from the SI data are shown in Table 5.2. It is clear that SI located in the lower part of the slope has smaller ratio compared to the upper part of the slope which implies that soil movement is mainly downhill along the pipeline. In order to catch the characteristic performance of the pipeline and to save time and memory space, the transverse movement can be ignored. This assumption enforces symmetry about the centerline of the pipeline.

In this study, it was assumed that pipeline and slope are symmetrical with respect to the vertical plane of centerline of the pipe. This simplifies the FEA model to half of the slope and pipeline, because:

1. Slope indicator shows that the transverse soil movements are smaller and movement is mainly downward;
2. The pipe is straight in the problem;
3. Model size is always a concern in numerical simulation in term of time and computer memory, especially with complex material properties.

7.5.3 Hydraulic Behaviour and Conditions of Soils

All materials where water flow is being modeled have been assumed to follow Darcy's law. This means that the velocity at which the water moves is proportional to the hydraulic gradient (the unbalanced change in hydraulic head per unit length). The constant of proportionality is the hydraulic conductivity, or coefficient of permeability. Fully saturated isotropic permeability is used in the analysis.

The values of the permeability, together with the compressibility of the material, influence the transient hydraulic flow in the soils. It is assumed that creep occurs when water table is in the vicinity of the slip surface. During rainy seasons, water table rises towards the ground surface. As a result soil creep and increase in pore water pressure have important effect on soil inelastic deformation and in the evaluation of the effectiveness of the stress relief procedure.

The initial water table is assumed to be located below the slip surface before the pipeline was installed. At the bottom of the sandstone on east end of the model, the maximum initial water pressure is taken to be 0.50 MPa. This linear distribution of water pressures is assumed to exist between the two water tables levels mentioned. This distribution is the one that necessarily develops over a uniform stratum after maintaining its boundary conditions (above and below) for a long time, that is, under steady-state conditions. During the process of pipeline construction, water pressures have been assumed to remain unaffected. After that the water table is raised to a level above the slip surface.

7.5.4 Finite Element Mesh and Boundary Conditions

A 3D finite element model (FEM) mesh was generated to represent the global domain of interest. Finer mesh is used at the locations of the instrumentations. The finite element model has a total 13,478 nodes and 11,215 elements. Typical element size is about 1.92 m. Due to the big size of the model, coarser mesh is used except that at the slope indicators and strain gauges locations, as well as along the slip surface. A finer mesh is

used to obtain better results for the soils and pipe at these locations for comparison with field measurements. There is a standard method in ABAQUS for mesh refinement of first-order element; see the left side of Figure 7.28 between the sandstone and clay till B for example, the mesh for the sandstone gets coarser. There are three nodes A, B and P, and node P is not connected to nodes in the element below. Each degree of freedom at node P is constrained to be interpolated linearly from the corresponding degrees of freedom at nodes A and B. The representative 3D FEA meshes are shown in Figure 7.27 and Figure 7.28. Soil layers and pipeline are labeled in these figures.

Majority of the soils are modeled by first-order eight-node continuum elements with pore pressure and reduced-integration C3D8RP; first-order six-node continuum elements C3D6 are used for the soil inside the pipe (see the section *Finite Element Procedures*), adjacent parts between different layers and a few locations where horizontal domain of soil joins the slanted, see Figure 7.27 and 7.28. Reduced integration is always recommended, because it usually gives more accurate results and is less expensive than full integration.

Four-node first-order shell element SR4 with reduced-integration is selected to represent the pipe. This doubly curved shell element with hourglass control is intended for both thick shell and thin shell applications that accounts for finite membrane strains and allows for transverse shear stress.

The nodes of pipe shells are bonded with the nodes of the surrounding soil elements, called pipe-soil interaction elements, as shown in Figure 7.27. The relative slip between pipe and soil is simulated by this special circular layer wrapping the pipe. The material properties of pipe-soil interaction elements are applied as special soil and are calibrated based on strain gauge data of the pipeline. It has been addressed in previous Sections.

The boundary conditions for the FEA model are as follows. The upper surface of the model has been assumed to remain free of any loads during the analysis. At the

bottom of the model, under the sandstones, all movements have been considered to remain negligible. As a consequence, the bottom boundary of the model is fixed at elevation 840m. The four vertical side boundaries of the model allow the materials to move freely in the direction parallel to the boundary, but impede the movement in a direction perpendicular to it. Rollers are set up at east, south, west and north boundary planes to constrain translational degree of freedom. The north and the south boundary planes are constrained from moving north-south directions. The east boundary plane is roller supported, prevented from moving east-west directions. The west boundary plane is a plane of symmetry in the FEA model. Figure 7.27 displays that the west boundary plane is a vertical plane which passes through the centerline of the pipe. The nodes of the pipeline at the west boundary plane are constrained with translational degree of freedom about the x axis and rotational degree of freedom about the y axis and the z axis, see Figure 7.27 and Figure 7.29.

Although all this information about the boundary conditions is given here for the sake of completeness, it is only partially relevant since the boundaries are thought to be far enough as not to have influence on the deformation of the slope as well as the pipeline.

7.5.5 Numerical Approach and Hypothesis

Before commencing the FE analysis, the objective of the analysis should be established. This may determine whether a linear analysis will be sufficient for the purpose or whether a full non-linear analysis (including material and geometric non-linearity) will be required. For the purpose of studying soil-pipe interaction and long term pipeline deformation, large displacement of the soil is expected. As such, a full non-linear analysis, including material and geometric non-linearity is required. Large-displacement theory should be used.

The essence of a numerical simulation of the type conducted here consists in decomposing a large, complex problem, untreatable by hand using analytical procedures, into a large number of simpler problems which need to be solved simultaneously.

Computers are very adapt to this task of conducting large number of repetitive calculations. Many variables of interest in the problem, such as displacement, deformations, stresses, pore pressures etc., will vary over the domain. The global domain is decomposed into finite elements and assumed a simple type of variation of the variable across the individual elements. If the number of elements is sufficiently large, the program will be able to reconstruct the actual distribution of the variables by combining the results obtained for each of the individual element. Each small element interacts with all the surrounding ones, which requires that all the equations of the governing mechanisms or the processes at all elements and the specific conditions of the problem must be satisfied simultaneously. The governing equations of pore fluid diffusion/deformation are equilibrium equation and pore fluid flow equation, which are coupled.

For a coupled diffusion/displacement analysis care should taken when choosing the units of the problem. The coupled equations may be numerically ill-conditioned if the choice of the units is such that the numbers generated by the equations of the two different fields differ by many orders of magnitude. The units chosen for this project are m, kg, and second.

There are two common approaches to solving these coupled equations. One approach is to solve one set of equations first and then use the results obtained to solve the second set of equations. These results in turn are fed back into the first set of equations to see what changes (if any) result in the solution. This process continues until succeeding iterations produce negligible changes in the solutions obtained. This is the so-called staggered approach to the solution of coupled systems of equations. The second approach is to solve the coupled systems directly. This direct approach is used in the analysis because of its rapid convergence even in highly nonlinear cases.

The slope in the model contains ground water. The soil is treated as a porous medium, which is modeled using a conventional approach that considers the medium as a multiphase material and adopts an effective stress principle to describe its behaviour. The

porous medium modeling provided in ABAQUS considers the presence of two fluids in the medium. One is the “wetting liquid,” which is assumed to be relatively (but not entirely) incompressible. The other is gas, which is relatively compressible.

The slope is divided into two parts; the domain above the water table is unsaturated and the domain below the water table is fully saturated in which the voids are completely filled with the wetting liquid. The elementary volume, dV , is made up of a volume of grains of solid material, dV_g ; a volume of voids, dV_v ; and a volume of wetting liquid, $dV_w \leq dV_v$, that is free to move through the medium if driven. The soil is modeled by attaching the finite element mesh to the solid phase; fluid can flow through this mesh. The mechanical part of the model is based on the effective stress principle. The total stress acting at a point, σ , is assumed to be made up of an average pressure stress in the wetting liquid, u_w , called the “wetting liquid pressure,” an average pressure stress in the other fluid, u_a , and an “effective stress,” $\bar{\sigma}^*$, $\sigma = \bar{\sigma}^* + u_a$. The model uses a continuity equation for the mass of wetting fluid in a unit volume of the medium. It is written with pore pressure (the average pressure in the wetting fluid at a point in the porous medium) as the basic variable. The conjugate flux variable is the volumetric flow rate at the node.

7.5.6 Constitutive Models

This project developed a computer model which simulates the behaviour of soil movement over time. The constitutive relationships describing the soil inelastic and creep behaviour are implemented into numerical codes consider important features such as creep effect. There are basically four layers of soil: soft clay, clay till, slip layer and sandstone/clay shale according to the geotechnical monitoring data. The modified Drucker-Prager/Cap Model was used for soft clay, clay till, slip surface, where soil movements developed. Ground movement was mainly caused by the soil inelastic and creep behaviour and relative motion from the slip layer. An elastic material model was applied to sandstone/clay shale, because this layer is located 40 m below pipeline, its creep performance has little effect on pipeline. Clay till B was assigned elastic material property. It is below the slip layer and has little influence on soil movement. Next

Chapter will show the comparison of FEA results with field data. This section discusses the Modified Drucker-Prager/Cap Model.

A material model, the modified Drucker-Prager/Cap plasticity/creep model, is used for three kinds of soils in the slope: soft clay, clay till A and slip layer, to simulate the deformation behaviour of soil subjected to gravity loading and varying saturation. This capped Drucker-Prager plasticity model with hardening is intended to model cohesive geological materials that exhibit pressure-dependent yield, such as soils and rocks. It is based on the addition of a cap yield surface to the Drucker-Prager plasticity model, which provides an inelastic hardening mechanism to account for plastic compaction and helps to control volume dilatancy when the material yields in shear. This model is used to simulate creep in materials exhibiting long-term inelastic deformation through a cohesion creep mechanism in the shear failure region and a consolidation creep mechanism in the cap region. It can be used in conjunction with the elastic material model. Cap model provides a reasonable response to large stress reversals in the cap region; however, in the failure surface region the response is reasonable only for essentially monotonic loading.

The modified Drucker-Prager/Cap plasticity model is defined by the yield surface parameters, the material's volumetric strain-driven hardening/softening behaviour and, and creep model is defined by time-dependent inelastic behaviour. The pipeline was assumed to be elastic perfectly plastic.

Yield Surface

The addition of the cap yield surface to the Drucker-Prager model serves two main purposes: it bounds the yield surface in hydrostatic compression, thus providing an inelastic hardening mechanism to represent plastic compaction; and it helps to control volume dilatancy when the material yields in shear by providing softening as a function of the inelastic volume increase created as the material yields on the Drucker-Prager shear failure surface. The yield surface has two principal segments: a pressure-dependent Drucker-Prager shear failure segment and a compression cap segment, as shown in

Figure 7.30. The Drucker-Prager failure segment is a perfectly plastic yield surface (no hardening). Plastic flow on this segment produces inelastic volume increase (dilation) that causes the cap to soften. On the cap surface plastic flow causes the material to compact. The Drucker-Prager failure surface is written as

$$(7.1) \quad Fs = t - p \tan \beta - d = 0$$

where $\beta(\theta, fi)$ and $d(\theta, fi)$ represent the angle of friction of the material and its cohesion, respectively, and can depend on temperature, θ , and other predefined fields $fi, i = 1, 2, 3, \dots$

The deviatoric stress measure t is defined as

$$(7.2) \quad t = \frac{1}{2}q \left[1 + \frac{1}{K} - \left(1 - \frac{1}{K}\right) \left(\frac{r}{q}\right)^3 \right]$$

where $p = -\frac{1}{3} \text{trace}(\sigma)$ is the equivalent pressure stress,

$q = \sqrt{\frac{3}{2} S : S}$ is the Mises equivalent stress,

$r = \left(\frac{9}{2} S : S : S\right)^{\frac{1}{3}}$ is the third stress invariant, and

$S = \sigma + p I$ is the deviatoric stress.

$K(\theta, fi)$ is a material parameter that controls the dependence of the yield surface on the value of the intermediate principal stress, as shown in Figure 7.31. The yield surface is defined so that K is the ratio of the yield stress in triaxial tension to the yield stress in triaxial compression. $K=1$ implies that the yield surface is the von Mises circle in the deviatoric principal stress plane (the Π -plane), so that the yield stresses in triaxial tension and compression are the same. To ensure that the yield surface remains convex requires $0.778 \leq K \leq 1.0$.

The cap yield surface has an elliptical shape with constant eccentricity in the meridional ($p-t$) plane, as shown in Figure 7.30 and also includes dependence on the third stress invariant in the deviatoric plane, as shown in Figure 7.31. The cap surface hardens

or softens as a function of the volumetric inelastic strain: volumetric plastic and/or creep compaction (when yielding on the cap and/or creeping according to the consolidation mechanism, as described later in this section) causes hardening, while volumetric plastic and/or creep dilation (when yielding on the shear failure surface and/or creeping according to the cohesion mechanism, as described later in this section) causes softening. The cap yield surface is

$$(7.3) \quad F_c = \sqrt{(p - p_a)^2 + \left[\frac{Rt}{(1 + \alpha - \alpha / \cos \beta)} \right]^2} - R(d + p_a \tan \beta) = 0$$

where $R(\theta, \beta)$ is a material parameter that controls the shape of the cap, $\alpha(\theta, \beta)$ is a small number that we discuss later, and $p_a(\varepsilon_{vol}^{pl} + \varepsilon_{vol}^{cr})$ is an evolution parameter that represents the volumetric inelastic strain driven hardening/softening. The hardening/softening law is a piecewise linear function relating the hydrostatic compression yield stress, p_b , and volumetric inelastic strain, as shown in Figure 7.32:

$$(7.4) \quad p_b = p_b(\varepsilon_{vol}^{in} |_0 + \varepsilon_{vol}^{pl} + \varepsilon_{vol}^{cr})$$

The volumetric inelastic strain axis in Figure 7.32 has an arbitrary origin:

$\varepsilon_{vol}^{in} |_0 = \varepsilon_{vol}^{pl} |_0 + \varepsilon_{vol}^{cr} |_0$ is the position on this axis corresponding to the initial state of the material when the analysis begins, thus defining the position of the cap (p_b) in Figure 7.30 at the start of the analysis. The evolution parameter p_a is given as

$$(7.5) \quad p_a = \frac{p_b - Rd}{(1 + R \tan \beta)}$$

The parameter α is a small number (typically 0.01 to 0.05) used to define a transition yield surface F_t ,

$$(7.6) \quad F_t = \sqrt{(p - p_a)^2 + \left[\left(t - \left(1 - \frac{\alpha}{\cos \beta} \right) (d + p_a \tan \beta) \right)^2 - \alpha (d + p_a \tan \beta) \right]} = 0$$

so that the model provides a smooth intersection between the cap and failure surfaces. The Modified Drucker-Prager/Cap model is associated in the deviatoric plane, associated

in the cap region in the meridional plane, and nonassociated in the failure surface in the meridional plane.

Creep Model

Classical “creep” behaviour of materials that exhibit plasticity according to the capped Drucker-Prager plasticity model is intimately tied to the plasticity behaviour (through the definitions of creep flow potentials and definitions of test data), so the plasticity options must be present as part of the material behaviour definition. If no rate-independent plastic behaviour is desired in the model, large values for the cohesion, d , as well as large values for the compression yield stress, P_b , should be provided in the plasticity definition: as a result the material follows the capped Drucker-Prager model while it creeps, without ever yielding. This capability is limited to cases in which there is no third stress invariant dependence of the yield surface ($K = 1$), that is, no intermediate principal stress effect is included; and to cases in which the yield surface has no transition region ($\alpha = 0$). Elasticity must be defined.

Creep behaviour defined by the modified Drucker-Prager/Cap option is active only during soils consolidation and transient quasi-static procedures. This model has two possible creep mechanisms that are active in different loading regions: one is a cohesion mechanism, which follows the type of plasticity active in the shear-failure plasticity region, and the other is a consolidation mechanism, which follows the type of plasticity active in the cap plasticity region.

Figure 7.33 shows the regions of applicability of the creep mechanisms in P - q space. In the model, we consider the consolidation creep mechanism. In this case we wish to make creep dependent on the hydrostatic pressure above a threshold value of P_a , with a smooth transition to the areas in which the mechanism is not active ($P < P_a$). Therefore, we define equivalent creep surfaces as constant hydrostatic pressure surfaces (vertical lines in the P - q plane). ABAQUS/Standard requires that consolidation creep properties be measured in a hydrostatic compression test. The effective creep pressure, $\bar{\sigma}^{cr}$, is then the point on the P -axis with a relative pressure of $\bar{\sigma}^{cr} = P - P_a$. This value is used in the

uniaxial creep law. The equivalent volumetric creep strain rate produced by this type of law is defined as positive for a positive equivalent pressure.

The internal tensor calculations in ABAQUS/Standard account for the fact that a positive pressure will produce negative (that is, compressive) volumetric creep components. The creep strain rate produced by the consolidation mechanism is assumed to follow a potential that is similar to that of the plastic strain rate in the cap yield surface (Figure 7.34)

$$(7.7) \quad G_c^{cr} = \sqrt{(p - p_a)^2 + (Rq)^2}$$

The consolidation creep potential is the von Mises circle in the deviatoric stress plane (the II-plane). The definition of the creep behaviour is completed by specifying the equivalent “uniaxial behaviour”—the creep “laws”, here “time hardening” form of the power law model was adopted

$$(7.8) \quad \dot{\epsilon}^{cr} = A(\bar{\sigma}^{cr})^n t^m$$

where $\dot{\epsilon}^{cr}$ is the equivalent creep strain rate;

$\bar{\sigma}^{cr}$ is the effective creep pressure;

t is the total time; and A, n, and m are creep material parameters defined as functions of temperature and field variables.

For the soil in the FEA model, the initial cap yield surface position, $\epsilon_{vol}^m |_0$, is set to 0.005. ABAQUS automatically adjusts the position of the cap yield surface if the stress lies outside the cap surface. Consolidation creep is modeled with a time-hardening power type creep model. The creep material data are set to constants.

7.5.7 Direct Shear Test

Direct shear tests had been carried out for some soil samples taken from the slope. Direct shear test results were used to set up the Modified Drucker-Prager/Cap mode employed in the slope. Soil material parameters for the modified Drucker-Prager/Cap

model with hardening are determined by simulating the direct shear test using ABAQUS. The material model is then applied in the three-dimensional finite element simulation of Pembina River Crossing. The test is conducted to estimate the angle of internal friction and cohesion of the soil with different normal loads. In soil mechanics, shear strength of the soil can be expressed by the Mohr Coulomb criterion as:

$$(7.9) \quad \tau_f = c + \sigma' \tan \phi$$

where τ_f = shear stress on the failure plane,

σ' = effective normal stress on the failure plane,

c = cohesion,

ϕ = angle of internal friction.

Direct shear apparatus consists primarily of a direct shear box, which is split into two halves, holding the soil specimen; a proving ring or load cell is used to measure the horizontal load applied to the specimen; one horizontal and one vertical dial gauges or LVDT is used to measure the deformation of the soil during the test, and a yoke by which a vertical load can be applied to the soil sample. Figure 7.35 shows a picture of the direct shear apparatus. A horizontal load is applied to the top half of the shear box by a motor and gear mechanism. In a strain-controlled unit, the rate of movement of the top half of the shear box can be controlled. Figure 7.36 to Figure 7.38 show the soil sample before, during and after the direct shear test.

Three tests were carried out under drained condition with overburden pressures 100 kPa, 400 kPa and 600 kPa. The results of the test are presented in terms of shear stress versus horizontal displacements, volume change versus horizontal displacement and shear stress versus normal stress at peak. The top half of the sample moves about 7 mm horizontally. A prescribed horizontal displacement of 0.18mm/min is applied to the upper half, similar to the quasi-static loading condition. Loads and displacements are measured so that simulation of results could be directly compared to the physical test results. For each test the vertical stress is held constant. With three pairs of vertical stresses and peak shear stresses, the failure envelope of the soil could be determined;

therefore, cohesion and internal friction angle can be measured. A baseline finite element model of the direct shear test based on the direct shear testing device is established in order to investigate the effects of various parameters associated with the soil model.

The direct shear box has been analyzed using the finite element method. The soil sample in the device is a cylinder with 50 mm diameter and 19.2 mm height of two equal halves. The mesh used is shown in Figure 7.39. The model consists of 342 solid elements, 270 8-node tri-linear displacement and pore pressure with reduced integration elements, and 72 6-node linear triangular prism elements. There are four layers in the upper half ABFE, four layers in the lower half CDHG. The middle layer BCGF represents the gap between the two halves of the shear box. The analysis is performed with the following boundary conditions.

1. The X, Y, Z displacements of nodes along the outside surface of the lower half cylinder CDHG are fixed.
2. Nodes along the outside surface of the upper half cylinder are given a prescribed displacement in the X direction. They are constrained to move in the Y direction.
3. The Z displacement of the nodes between A and B and between E and F are tied together, they are constrained to move by the same amount, the actual amount being a product of the analysis. This modeled the rigid behaviour of the upper part of the shear box.
4. The Z displacement of the nodes of the top is constrained to move the same magnitude. This models a solid top cap.

The duplicating conditions experienced shear box test are simulated by giving the upper half of the shear box a horizontal displacement 7 mm. The corresponding horizontal shear force is calculated by summing the horizontal nodal forces of the middle layer. The mean shear stress is obtained by dividing the total shear force by the initial area of the shear box. The material parameters for the soil sample are as the following.

Young's Modulus: 30,000kPa

Poisson Ratio: 0.42
Cohesion: 30 kPa
Friction Angle: 21.5°
Permeability: 1×10^{-8} m/s
Void ratio: 0.6
Density: 20.70 kN/m³

Yield Surface Parameters: cap eccentricity parameter is 0.3; initial cap yield surface position is 0.005; transition surface radius parameter is 0.0; the ratio of the flow stress in triaxial tension to the flow stress in triaxial compression is 1.0.

Creep Parameters: $A=2.546 \times 10^{-16}/(\text{Pa})^{0.3}/\text{s}$, $n=0.3$, $m=0$

Hardening Parameters: Hydrostatic pressure yield stress versus the absolute value of the corresponding volumetric inelastic strain are: 120×10^{-3} Pa, 0; 280×10^{-3} Pa, 0.005; 700×10^{-3} Pa, 0.007; 50×10^{-1} Pa, 0.012. These soil parameters are used in the finite element model for Pembina River Crossing. The direct shear test gives the conclusion that the soil at the slip surface has a small cohesion 5 kPa and friction angle as low as 19.5°. These values are used for the slip surface.

Comparison between the analysis and test results with the mean shear stress vs. horizontal displacement under three different vertical loads is shown in Figure 7.40, Figure 7.41 and Figure 7.42. The differences between the peak shear stress in the three cases are 0.9%, 1.4% and 19%. The comparison shows reasonably good agreement between the calculated and measured responses. Therefore these material parameters will be used in the simulation of the field cases.

7.5.8 Load Sequence

A basic concept in ABAQUS is the division of the problem history into steps. A step is any convenient phase of the history — a static analysis of a load development from one magnitude to another, soil creep with time, boundary condition alteration, etc.

Analysis procedure defines the type of analysis to be performed during each step. The simulation of the history of events, from the onset of the slope formation to construction of pipeline and its response after decades, has been carried out with ABAQUS.

The program is particularly well suited for non-linear and coupled problems, such as the one considered here, where a coupled diffusion/deformation solution is required for the equations governing the mechanical response and for those describing the flow of water in the materials. The procedure used by the program to carry out the time integration of various sets of equations is of the implicit kind. This type of procedure, where the integration can progress in large time increments at the cost of having to solve the complete system of equations at each integration step, is ideal for the problem where inertia forces are negligible and all variables involve with time at a reasonably slow pace.

The installation of pipeline usually evolves a complex sequence of construction steps. The construction details determine the appropriate approach to represent these steps accurately. Such details have been avoided here to simplify the modeling process. Based on this assumption, the history of pipeline loading will be modeled in nine phases. The results then are compared with field observations to verify the procedures and interpretation.

The buried pipeline is set up at the start of the model. The geometry of the pipeline and slope is set up with an initial stress field prescribed in the soil layers due to gravitational tectonic forces existing through the depth of the soil. It is assumed that this stress varies linearly with the depth and that the ratio between the horizontal and vertical stress components is 0.72. Since the slope had been formed over years, in finite element model, this was done by applying the soil gravity load at one step, while the pipeline was switched off temporarily.

An artificial soil was set up inside of the pipeline in order to maintain the entire stable slope domain for the analysis. This type of soil is the same as the real soft clay type except that it has an elastic modulus ten times as large as that of the soft clay. This does not influence the soil movement much, but keeps the pipe circular cross section when

pipeline is switched off, as the pipeline deformation is dependent on the soil movement. Water table was assumed near the slip surface when the pipeline was turned on. The pipeline was pressurized at 6178 kPa.

Time is a variable in the model, and water table is another variable which is changed in order to investigate the effect of precipitation. Water table is raised to cause soil movement by changing the magnitude of the pore pressure. Coupled pore fluid diffusion and stress analysis procedure was used in the history steps of creep and water table change. Initial time increment and time period as creep time are defined for the creep step. The creep law of the soils in FEM is "time hardening" form of the power law model, in which "total time" is assigned as "time period" in the step of creep.

Shell elements of line pipe were activated after the soil gravity load was applied to the slope and the water table was raised to the assumed level. The only mechanical loading imposed on the problem is the action of gravity on the masses of the various materials in terms of creep. Apart from the gravity load, the soil is subjected to water table change. With different precipitation each year, slope moves quicker or slower as water table changes with specified time as input data, this ongoing deformation loads the pipeline. The soil model is calibrated until the response matches with the SI data.

7.5.9 Stress Relief Simulation

The pipeline at Pembina River Crossing is buried parallel to the slope direction. The monitoring program has been discussed in Chapter 5. Stress relief procedure is carried out by removing the soil surrounding the pipe. In FEA model, stress relief is simulated by disconnecting the soil elements surrounding the pipe elements and assigning spring elements for connecting to the pipes.

Normally, the nodes of pipe shell elements are attached and constrained to the nodes of surrounding solid elements (pipe soil interaction elements) outside the pipe circle, thus shell elements are constrained in three translational directions. During stress relieve, the constraints in the longitudinal and transverse directions of the soil elements

are removed to relieve stress of the pipe. The soil elements are removed gradually over several steps to simulate the excavation process. In Figure 7.43, Part 1 with three elements, Part 2 with four elements and Part 3 with eight elements are removed sequentially in order to keep the analysis stable. This ongoing removal of soil unloads the stresses in the pipeline.

The soil elements at the bottom of the pipeline are replaced by a group of springs at the nodes of the shell elements. These spring elements relate a force with a relative displacement, used to model restraints to pipeline as the soil below the pipe are removed. They are defined to be perpendicular to the centerline of the pipe, act as ground support in reality to keep the pipeline at the position during the stress relief procedure. The technique can readily be used to assess the behaviour of pipeline after stress relief and the effectiveness of stress relief procedure. These springs take effects after the removal of the soil. The variables are the force and relative displacement in the spring. Spring element SPRING1 in ABAQUS/Standard is applied in the model. SPRING1 is between a node and ground, acting in a fixed direction. The spring behaviour is nonlinear in the model. The stiffness of the springs, shown in Table 3, is determined by adjusting the location of pipeline to be the same before installation of springs. The initial forces in the springs are specified to support the top soil. The force vs. corresponding displacement in the springs is -2×10^5 N, -1 m; -2×10^6 N, 0; 0, 1×10^{-5} m. The stiffness is nonlinear so that the springs act significant strong in compression and fragile in tension. This simulates the fact that the pipe rebounds freely while supported firmly by the soil below.

7.6 Summary

This Chapter describes the finite element model for the Pembina River Crossing. Technical issues, such as soil plasticity and creep, pipe soil interaction, slip layer and stress relief simulation have been discussed in detail. Pipeline behaviour is closely correlated to soil displacement and precipitation. Next Chapter will provide the validation of the FEM developed here. And further more, the FEM will be used to determine the optimum stress relief procedures using a parametric study.

Table 7.1 Locations of Climate Stations near LodgePole

Climate Stations	Longitude	Latitude	Elevation	Data available
LodgePole	West115°19'	North53°6'	NA	NA
Violet Grove	West115°7'	North53°9'	903m	2000-2005
Drayton Valley	West114°57'	North53°13'	883.1m	2000-2005
Brazeau Lo	West115°25'	North53°1'	1088.4m	1940-2005
Wildwood Newbery	West115°19'	North53°34'	853.4m	1980-1998
Entwistle	West114°58'	North53°36'	780.3m	1987-2005

Table 7.2 Soil Movement in X Direction near Ground Surface

SI	Data available	U2 vs. time	U2, mm/yr	U2, mm/yr	Note
SI5A	00-4-11 to 01-9-18	bilinear	00-4 to 00-9, 44.1mm/yr	19.88 mm/yr	
			00-9 to 01-9, 10mm/yr		
SI5	87-6-18 to 98-6-10	bilinear	87-6 to 92-6, 25.33mm/yr	16.58 mm/yr	1989 29.63 mm/yr
			92-6 to 98-6, 8mm/yr		
SI6	88-6-24 to 89-10-2	bilinear	88-6 to 89-7, 19.48 mm/yr	19.48 mm/yr	64.91mm Jul-Oct 1989
			89-7 to 89-10, 344 mm/yr		
SI7	88-6-24 to 89-10-2	bilinear	88-6 to 89-7, 12.42mm/yr	12.42 mm/yr	30.87mm Jul-Oct 1989
			89-7 to 89-9, 161mm/yr due to big rain		
SI8	92-3-17 to 01-9-18	linear	1.58mm/yr	1.58 mm/yr	
SI10A	97-7-17 to 99-7-22	bilinear	97-7 to 99-4, 19.44mm/yr	36.28 mm/yr	
			99-4 to 99-7, 158mm/yr		
SI10B	00-4-11 to 01-9-18	bilinear	00-4 to 00-9, 72mm/yr	40.35 mm/yr	
			00-9 to 01-9, 30.64mm/yr		
SI11A	97-5-8 to 98-6-11	bilinear	97-5 to 97-7, 47.4mm/yr	12.18 mm/yr	
			97-7 to 98-6, 5.8mm/yr		
SI11B	00-5-18 to 02-9-24	bilinear	00-5 to 00-9, 63.3mm/yr	32.42 mm/yr	
			00-9 to 01-9, 22.13mm/yr		
SI12	92-3-27 to 97-6-17	bilinear	92-3 to 97-4, 24.4mm/yr	28.29 mm/yr	
			97-4 to 97-6, 178.2mm/yr		
SI12A	97-5-8 to 99-9-9	bilinear	97-5 to 99-4, 22.23mm/yr	24.88 mm/yr	
			99-4 to 99-7, 179mm/yr		
SI12B	00-3-27 to 02-8-7	bilinear	00-3 to 00-9, 51.9mm/yr	20.88 mm/yr	
			00-9 to 02-8, 12.2mm/yr		

Table 7.3 Soil Motion at SI5 in X direction (mm)

Location(m)	18-Jun-87	30-Jul-90	11-Jun-92	12-Jul-93	8-Aug-94	19-Jul-95
-2.5	0	92.35	129.29	137.20	153.03	155.67
-11	0	84.43	126.65	131.93	150.40	158.31
-13.5	0	44.85	65.96	76.52	84.43	87.07
-20	0	50.13	74.93	84.43	94.99	94.99
-22.3	0	0	0	0	0	0
-43.5	0	0	0	0	0	0

Location	9-Oct-96	17-Jul-97	10-Jun-98	22-Jul-99	19-Sep-99
-2.5	166.23	166.23	174.14	203.17	203.17
-11	163.59	166.23	174.14	200.53	200.53
-13.5	94.99	94.99	100.26	113.46	113.46
-20	100.26	102.90	105.54	118.73	118.73
-22.3	0	0	0	0	0
-43.5	0	0	0	0	0

Table 7.4 Total precipitation (mm) in 1987-1991 at Wildwood Newbery

yyyy-mm	1987	1988	1989	1990	1991	Monthly average
Jan	10.1	10.8	78.8	33.8	8.5	28.4
Feb	10.5	37	24	24E	34.2	25.94
Mar	24.5	21.4	17	16.4E	27	21.26
Apr	6.6	15.2	30.8	41.2	64.1	31.58
May	76.8	28	63.8	40.4	85.9	58.98
Jun	62.6	133.5	168.1	152.9	64.6	116.3
Jul	118.6E	118.6	110.2	121.2E	109.5	115.6
Aug	52.8E	52.8E	234.6	52.8	40.8	86.76
Sep	27.8	63.6	64.4	34	23.6	42.68
Oct	5.2	9.4	22.4	21.1E	69.4	25.5
Nov	2.4	14.8	34.6	54E	8	22.76
Dec	8	17.5	23.7	32.4	19	20.12
Sum	405.9	522.6	872.4	624.2	554.6	
Average of Sum	595.94					

Note:

1. E = Estimated
2. * = The value displayed is based on incomplete data

Table 7.5 Total precipitation (mm) in 1992-1997

yyyy-mm	Wildwood Newbery					Entwistle	Monthly average
	1992	1993	1994	1995	1996	1997	
Jan	24.9	7	90.5	10	46	8	31.07
Feb	27	21.7	28	7.8	12	13.8	18.38
Mar	2.5	30.2	4	15.5	40.5	25.2	19.65
Apr	39.5E	12.7	0.9	24.9*	21E	19.E	19.67
May	54.4	44	73.2	39	48.9	64.2E	53.95
Jun	26.8	107.6E	112.4	112.8	87.9	176.3	104
Jul	64.6	146	120.6	71	63.2E	80	90.9
Aug	54.6E	75	34.8	138.8	74.1	55.4	72.12
Sep	32.8	28.3	29.2	17.6	49.1	50.8	34.63
Oct	3.6	19.5	16.2	16.1	6E	56.9E	19.72
Nov	22.6	24.3	17*	62.8	66.3E	3	32.67
Dec	25.6	24	6	22.9	6.5*	6.6	15.27
Sum	378.9	540.3	532.8	539.2	521.5	559.2	
Average of Sum	511.98						

Note: 1. E = Estimated
 2. * = The value displayed is based on incomplete data

Table 7.6 Total precipitation (mm) in 1998-1999 at Entwistle

yyyy-mm	1998	1999	Monthly average
Jan	38	86	62
Feb	0	14	7
Mar	15.0E	35.4	25.2
Apr	7.2	41	24.1
May	35.6*	80.6	58.1
Jun	130.6	73.4	102
Jul	64.8E	104.4	84.6
Aug	74.4E	95.2	84.8
Sep	54.2	11.8	33
Oct	55	17.6E	36.3
Nov	43.8	7E	25.4
Dec	30E	7	18.5
Sum	548.6	573.4	
Average of Sum	561		

Note: 1. E = Estimated
 2. * = The value displayed is based on incomplete data

Table 7.7 Soil Motion at SI5A in X direction (mm)

Location	11-Apr-00	18-May-00	8-Jun-00	7-Sep-00	6-Jun-01	18-Sep-01
-4m	0	2.46	5.30	18.36	23.92	28.32
-12.6m	0	2.46	5.30	18.36	23.92	28.32
-13.85m	0	1.29	1.55	10.86	14.48	18.10
-20.5m	0	1.29	1.55	10.86	14.48	18.10
-22.9m	0	0	0	3.36	4.66	6.21
-33m	0	0	0	0	0	0

Table 7.8 Total precipitation (mm) in 2000-2001

	Entwistle 2000	Violet Grove 2001
Jan	19.6	8.7
Feb	8	30.6E
Mar	36.4	13.5
Apr	23.4	10.0E
May	86	27.2E
Jun	123	67.2
Jul	177.1	192
Aug	56	33.0E
Sep	55.2	12
Oct	7.8E	12.9E
Nov	27	22.3E
Dec	23.3E	5.8E
Sum	642.8	435.2

E = Estimated

Table 7.9 Soil Motion Increment in X direction

Location(m)	11-Apr-00	18-May-00	8-Jun-00	7-Sep-00	6-Jun-01	18-Sep-01
-4	0	2.46	2.84	13.06	5.56	4.40
-12.6	0	2.46	2.84	13.06	5.56	4.40
-13.85	0	1.29	0.26	9.31	3.62	3.62
-20.5	0	1.29	0.26	9.31	3.62	3.62
-22.9	0	0	0	3.36	1.29	1.55
-33	0	0	0	0	0	0

Table 7.10 Monthly Precipitation, mm, for 1986-2000

	1986 WN	1987 WN	1988 WN	1989 WN	1990 WN	1991 WN	1992 WN	1993 WN
Jan	16.6	10.1	10.8	78.8	33.8	8.5	24.9	7
Feb	18.7	10.5	37	24	24E	34.2	27	21.7
Mar	41.4	24.5	21.4	17	16.4E	27	2.5	30.2
Apr	30E	6.6	15.2	30.8	41.2	64.1	39.5E	12.7
May	31	76.8	28	63.8	40.4	85.9	54.4	44
Jun	66.2	62.6	133.5	168.1	152.9	64.6	26.8	107.6E
Jul	252	98E	118.6	110.2	121.2E	109.5	64.6	146
Aug	24E	99E	124E	234.6	52.8	40.8	54.6E	75
Sep	114.5	27.8	63.6	64.4	34	23.6	32.8	28.3
Oct	12.8	5.2	9.4	22.4	21.1E	69.4	3.6	19.5
Nov	31.2	2.4	14.8	34.6	54E	8	22.6	24.3
Dec	9	8	17.5	23.7	32.4	19	25.6	24
May-Sep	487.7	364.2	467.7	641.1	401.3	324.4	233.2	400.9
Jan-Dec	647.4	431.5	593.8	872.4	624.2	554.6	378.9	540.3
Ratio-of- May-Sep. to whole year	75.3%	84%	78.8%	73%	64.3%	58.5%	61.5%	74.2%

	1994 WN	1995 WN	1996 WN	1997 EN	1998 EN	1999 EN	2000 EN	2001 VG
Jan	90.5	10	46	8	38	86	19.6	8.7
Feb	28	7.8	12	13.8	0	14	8	30.6
Mar	4	15.5	40.5	25.2	15E	35.4	36.4	13.5
Apr	0.9	24.9*	21E	19.2E	7.2	41	23.4	10
May	73.2	39	48.9	64.2E	35.6*	80.6	86	27.2
Jun	112.4	112.8	87.9	176.3	130.6	73.4	123	67.2
Jul	120.6	71	63.2E	80	64.8E	104.4	177.1	192
Aug	34.8	138.8	74.1	55.4	74.4E	95.2	56	33
Sep	29.2	17.6	49.1	50.8	54.2	11.8	55.2	12
Oct	16.2	16.1	6E	56.9	55	17.6E	7.8E	12.9
Nov	17*	62.8	66.3E	3	43.8	7E	27	22.3
Dec	6	22.9	6.5*	6.6	30E	7	23.3E	5.8
May-Sep	370.2	379.2	323.2	426.7	359.6	365.4	497.3	331
Jan-Dec	532.8	539.2	521.5	559.4	548.6	573.4	642.8	435
Ratio-of- May-Sep. to whole year	69%	70%	62%	76%	66%	64%	77%	76%

- Note: 1. E = Estimated
 2. * = The value displayed is based on incomplete data
 3. WN=Wildwood Newbery
 4.EN=Entwistle

Table 7.11 Soil Motion at SI6 in X direction (mm)

Location	24-Jun-88	28-Nov-88	23-Jan-89	24-Apr-89	24-Jul-89	2-Oct-89
-2m	0	7.92	10.55	9.76	21.11	86.02
-18m	0	7.92	11.87	12.93	20.05	79.16
-19.2m	0	0	0	0	0	0

Table 7.12 Soil Motion at SI7 in X direction (mm)

Location	23-Jan-89	24-Apr-89	24-Jul-89	2-Oct-89
-2m	10.13	12.98	13.46	44.33
-15m	10.13	12.98	13.46	44.33
-16.25m	0	0	-4.75	0
-45m	0	0	0	0

Table 7.13 Soil Motion at SI8 in X direction (mm)

Location	17-Mar-92	23-Sep-93	8-Aug-94	25-May-95	7-Jun-96	17-Oct-97	9-Sep-99	8-Jun-00	23-Apr-01	6-Jun-01	18-Sep-01
-1.6	0.00	2.89	5.79	6.93	8.07	9.21	11.8	9.21	6.58	7.37	8.16
-38.9	0.00	0.42	0.84	1.26	1.68	2.11	3.16	1.58	0.00	0.39	0.79
-60	0.00	0.00	0.00	0.00	0.00	0.00	0.00	0.00	0.00	0.00	0.00

Table 7.14 Soil Motion at SI10A in X direction (mm)

Location	17-Jul-97	17-Oct-97	10-Jun-98	30-Apr-99	7-Jul-99	22-Jul-99
-2	0.00	5.28	11.87	34.83	54.09	72.56
-14.9	0.00	3.43	10.55	32.98	51.19	68.60
-15.8	0.00	0.00	0.00	0.00	0.00	11.87
-24	0.00	0.00	0.00	0.00	0.00	0.00

Table 7.15 Soil Motion at SI10B in X direction (mm)

11-Apr-2000	18-May-2000	8-Jun-2000	19-Jul-2000	7-Sep-2000	23-Apr-2001
0	6.65	8.24	14.89	30.05	47.34
0	3.46	6.12	12.77	21.28	31.91
0	1.06	1.06	1.06	6.12	11.97
0	0	0	0	0	0

Table 7.16 Soil Motion at SI11A in X direction (mm)

Location	8-May-97	16-Jul-97	17-Oct-97	11-Jun-98
-1.6	0	7.92	10.55	13.19
-19.8	0	6.60	9.71	16.09
-20.4	0	1.58	1.58	-1.00
-30	0	0	0	0

Table 7.17 Soil Motion at SI11B in X direction (mm)

Location	18-May-00	7-Jun-00	19-Jul-00	7-Sep-00	23-Apr-01	6-Jun-01	9-Aug-01	18-Sep-01
-0.8	0	5.21	13.28	21.09	33.85	36.46	39.06	43.23
-19.3	0	5.21	13.28	21.09	33.85	36.46	39.06	43.23
-21.1	0	0	0	1.30	1.30	1.56	2.60	1.30
-30	0	0	0	0	0	0	0	0

Table 7.18 Soil Motion at SI12 in X direction (mm)

Location	27-Mar-92	11-May-92	29-Jul-92	26-Nov-92	23-Sep-93	11-Oct-94	25-May-95	7-Jun-96	29-Apr-97	17-Jun-97
-0.80	0.00	5.28	21.11	26.39	47.49	79.16	87.07	113.46	124.01	147.76
-6.90	0.00	10.03	32.72	46.44	72.30	118.73	126.65	155.67	166.23	189.97
-10.70	0.00	7.92	31.66	44.85	73.88	110.82	118.73	145.12	155.67	179.42
-12.50	0.00	0.00	0.00	0.00	0.00	0.00	0.00	0.00	0.00	0.00

Table 7.19 Soil Motion at SI12A in X direction (mm)

Location	29-Apr-99	7-Jun-99	22-Jun-99	7-Jul-99	22-Jul-99	9-Sep-99
-2m	34.30	51.45	55.41	58.05	69.92	58.05
-11.2m	43.54	67.28	71.24	73.88	88.39	85.75
-11.95m	5.28	9.23	13.19	13.19	16.62	26.39
-12.5m	0	0	0	0	0	0

Table 7.20 Soil Motion at SI12B in X direction (mm)

Location	27-Mar-00	03-Apr-00	18-May-00	07-Jun-00	19-Jul-00	07-Sep-00
-0.8	0	2.34	8.045	11.94	19.46	25.95
-11.9	0	2.85	11.16	17.13	29.58	37.11
-13.1	0	0	0	0	0	0

Table 7.21 SG1 SG2 SG3 SG4 at Station 1-4

Stations	Strain Accumulated	SG1	SG2	SG3	SG4	Average
Station 1	Jul.~Nov.2000	-63.18 $\mu\epsilon$	-152.37 $\mu\epsilon$	-92.66 $\mu\epsilon$	92.75 $\mu\epsilon$	-53.9 $\mu\epsilon$
Station 2	Sep.~Nov.2000	-72.89 $\mu\epsilon$	-28.93 $\mu\epsilon$	NA	NA	NA
Station 3	Jul.-Sep.2000	-143.1 $\mu\epsilon$	-171.81 $\mu\epsilon$	216.97 $\mu\epsilon$	-77.17 $\mu\epsilon$	-43.78 $\mu\epsilon$
Station 4	Jul.-Sep.2000	-91.87	-106.54 $\mu\epsilon$	-62.88 $\mu\epsilon$	-60.93 $\mu\epsilon$	-80.56 $\mu\epsilon$

Table 7.22 Soil Properties

	Parameter	Symbol	Magnitude
Pipe	Temperature Differential	ΔT	0°C
	Material Grade		API 5L X60
	Elastic Modulus	E	205GPa
	Poisson's Ratio	ν	0.3
	Yield strength	Fy	413MPa
Soil in Pipe	Elastic Modulus	E1	300MPa
	Unit Weight	γ	17.2kN/m ³
	Poisson Ratio	μ	0.42
	Void Ratio	e	0.6
	Permeability	Ks	1E-8m/s
Soft Clay	Elastic Modulus	E1	30MPa
	Unit Weight	γ	17.2kN/m ³
	Poisson Ratio	μ	0.42
	Void Ratio	e	0.6
	Permeability	Ks	1E-8m/s
	Friction angle	ϕ	21.5°
	Cohesion	c	30kPa
Pipe Soil Interaction Layer	Elastic Modulus	E1	25MPa
	Unit Weight	γ	17.2kN/m ³
	Poisson Ratio	μ	0.42
	Void Ratio	e	0.6
	Permeability	Ks	1E-8m/s
	Friction angle	ϕ	21.5°
	Cohesion	c	30kPa

1).Clay Till A 2).Soil Sample	Elastic Modulus	E1	30MPa
	Unit Weight	γ	17.2kN/m ³
	Poisson Ratio	μ	0.42
	Void Ratio	e	0.6
	Permeability	Ks	1E-9m/s
	Friction angle	ϕ	21.5°
	Cohesion	c	30kPa
1).Clay Till B	Elastic Modulus	E1	100MPa
	Unit Weight	γ	17.2kN/m ³
	Poisson Ratio	μ	0.42
	Void Ratio	e	0.6
	Permeability	Ks	1E-9m/s
Slip Layer	Elastic Modulus	E1	10MPa
	Unit Weight	γ	17.2kN/m ³
	Poisson Ratio	μ	0.42
	Void Ratio	e	0.6
	Permeability	Ks	1E-9m/s
	Friction angle	ϕ	19.5°
	Cohesion	c	5kPa
Sand- stone	Elastic Modulus	E1	200MPa
	Unit Weight	γ	18kN/m ³
	Poisson Ratio	μ	0.35
	Void Ratio	e	0.6
	Permeability	Ks	1E-4m/s
Clay Till A is above slip surface, Clay till B is below slip surface.			

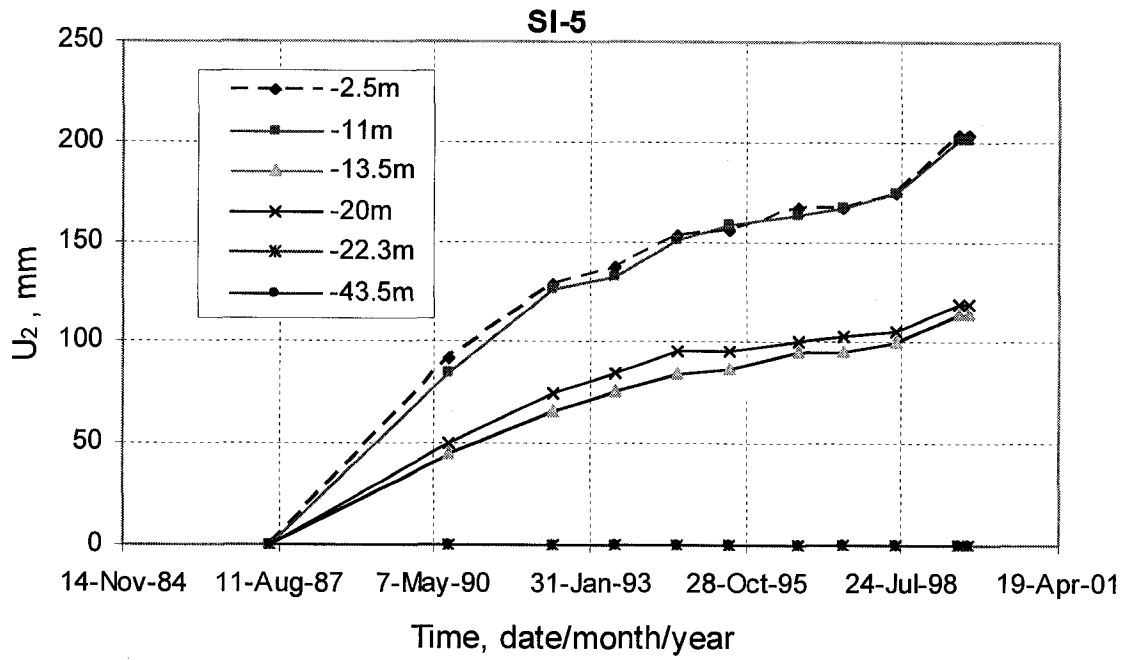


Figure 7.1 Soil Movement in X direction at Different Depths, U₂, at SI5

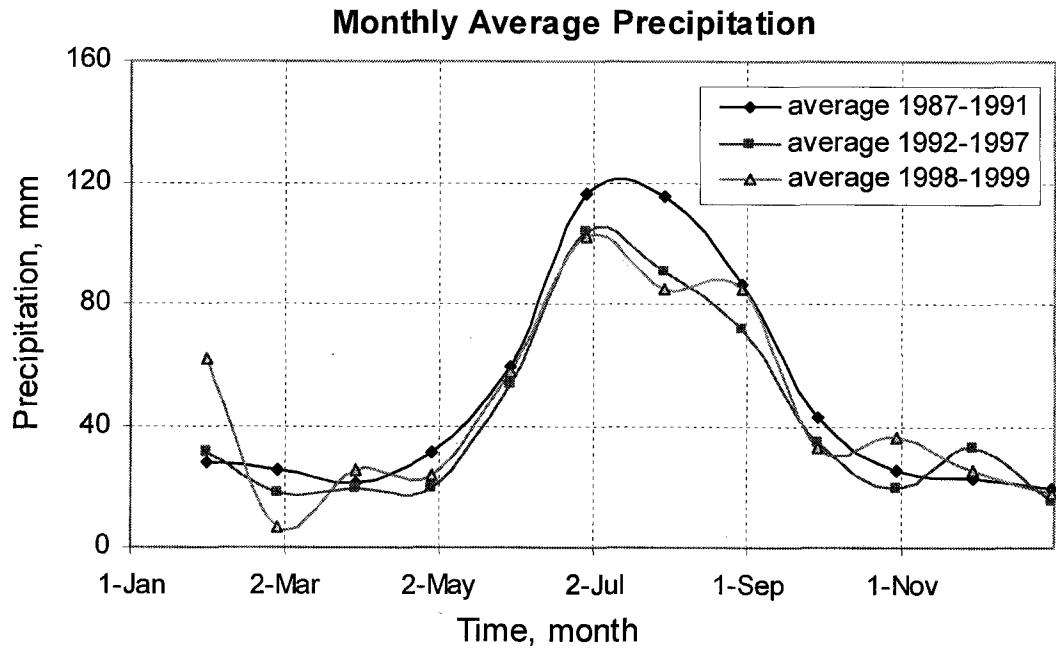


Figure 7.2 Monthly Average Precipitation 1987-1999

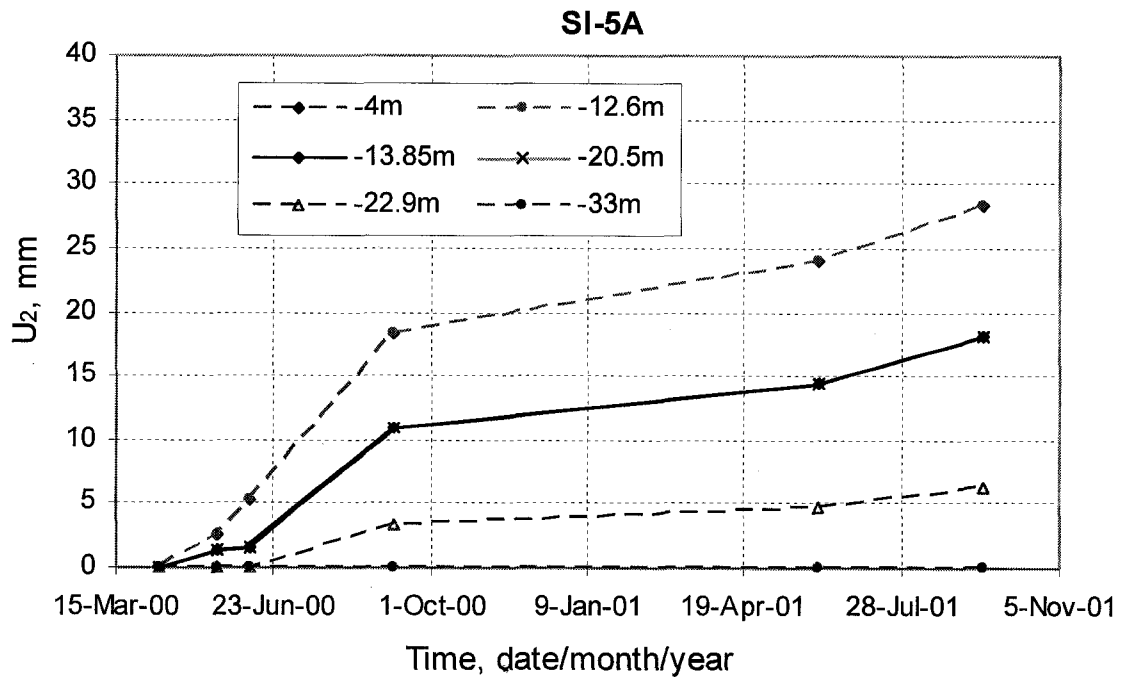


Figure 7.3 Soil Movement in X direction at Different Depths, U_2 , at SI5A

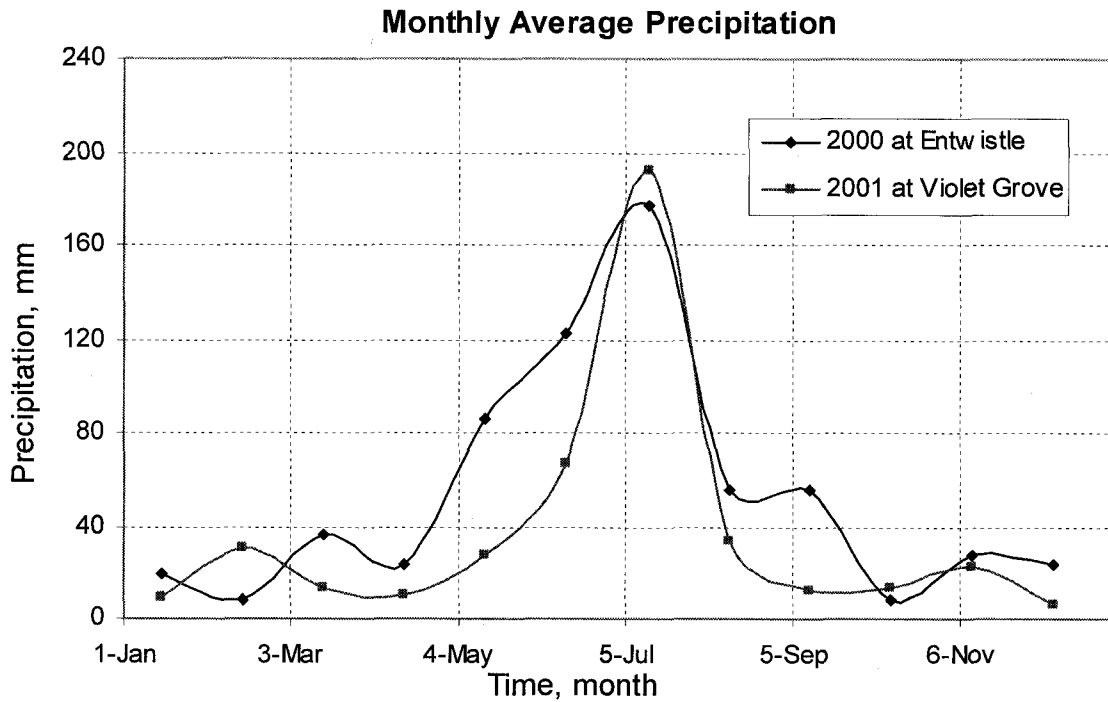


Figure 7.4 Total Precipitation in 2000-2001

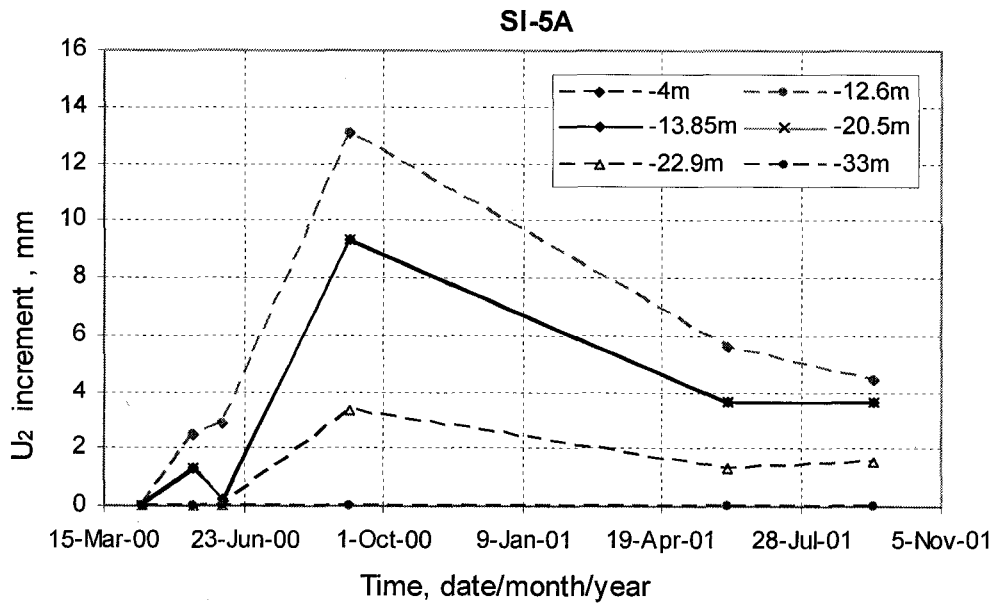


Figure 7.5 Soil Movement Increment in X direction at SI5A

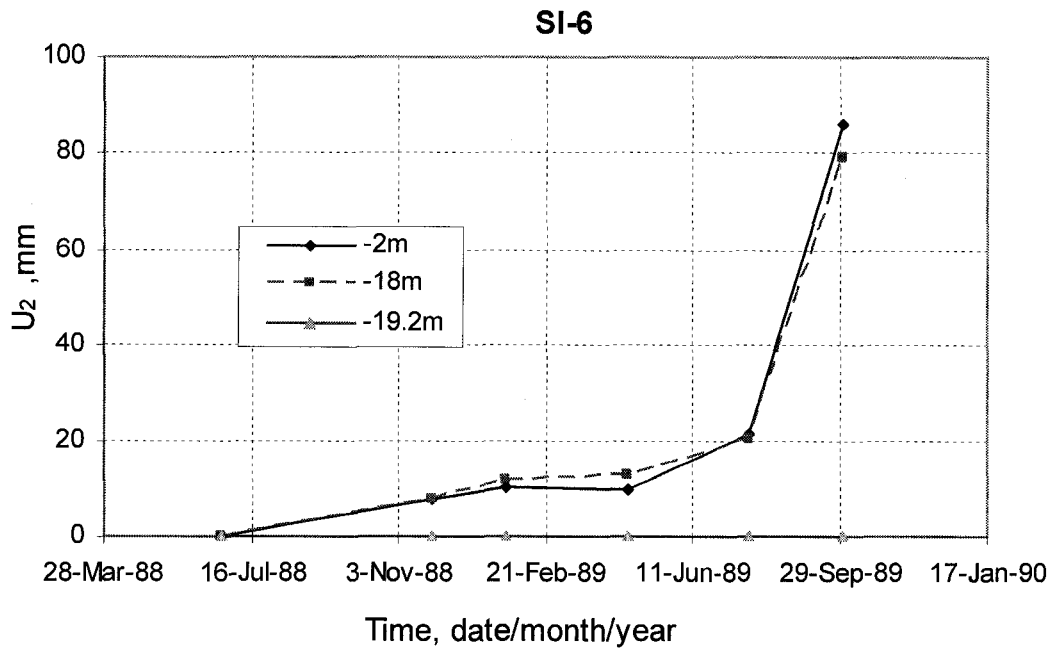


Figure 7.6 Soil Movement in X direction at Different Depths, U_2 , at SI-6

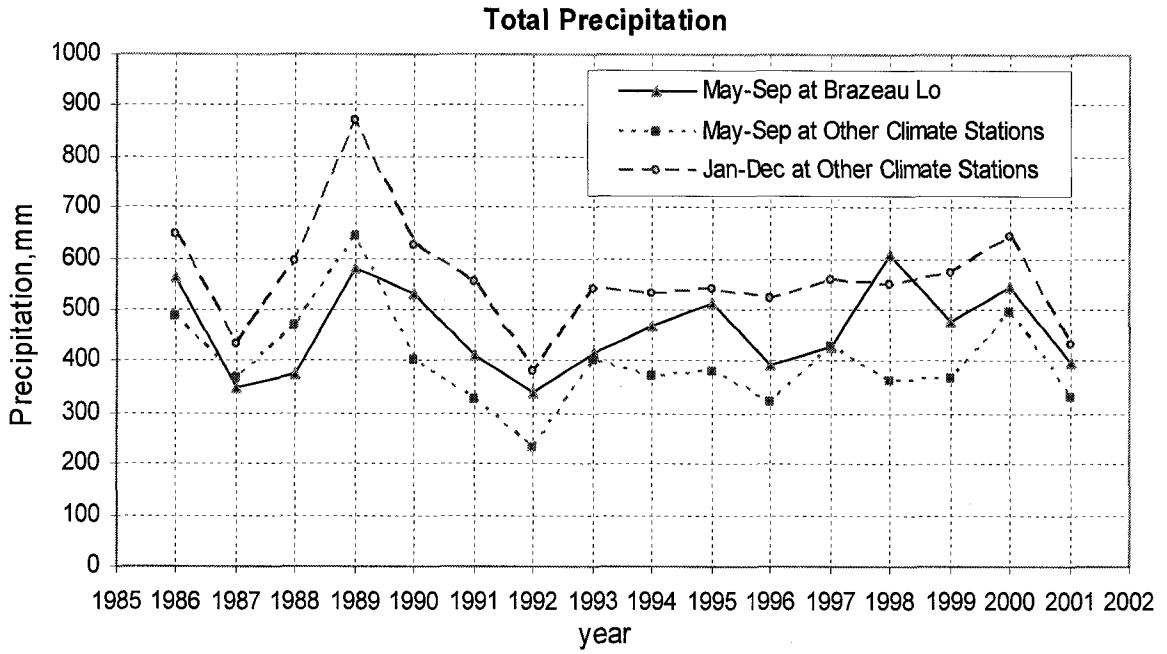


Figure 7.7 Yearly and May-Sep Precipitation for Years 1986-2001

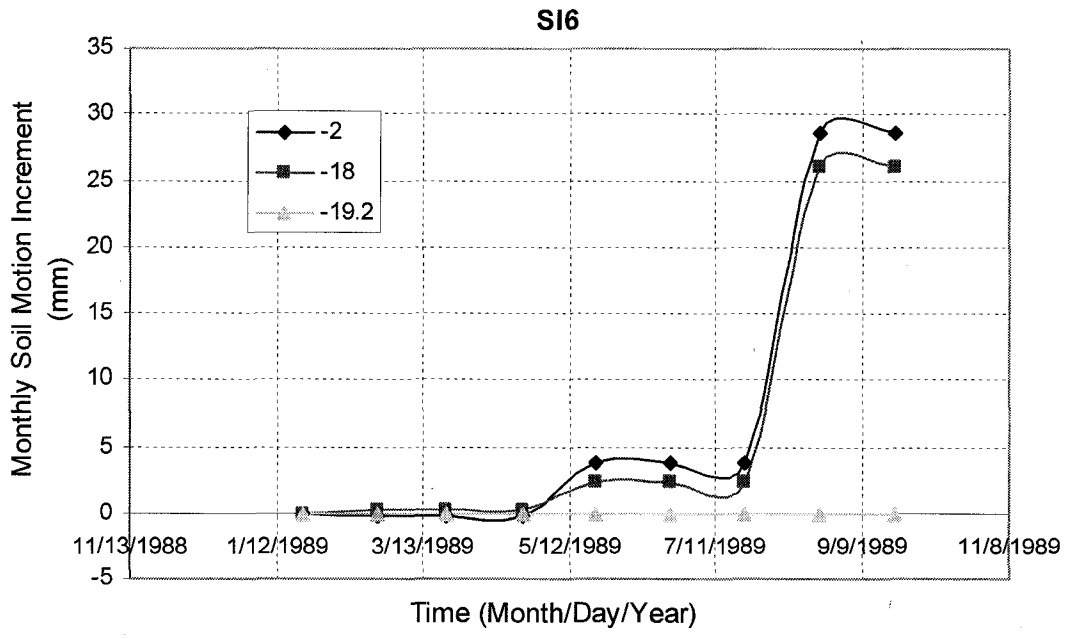


Figure 7.8 Monthly Soil Movement increment in X direction at SI6

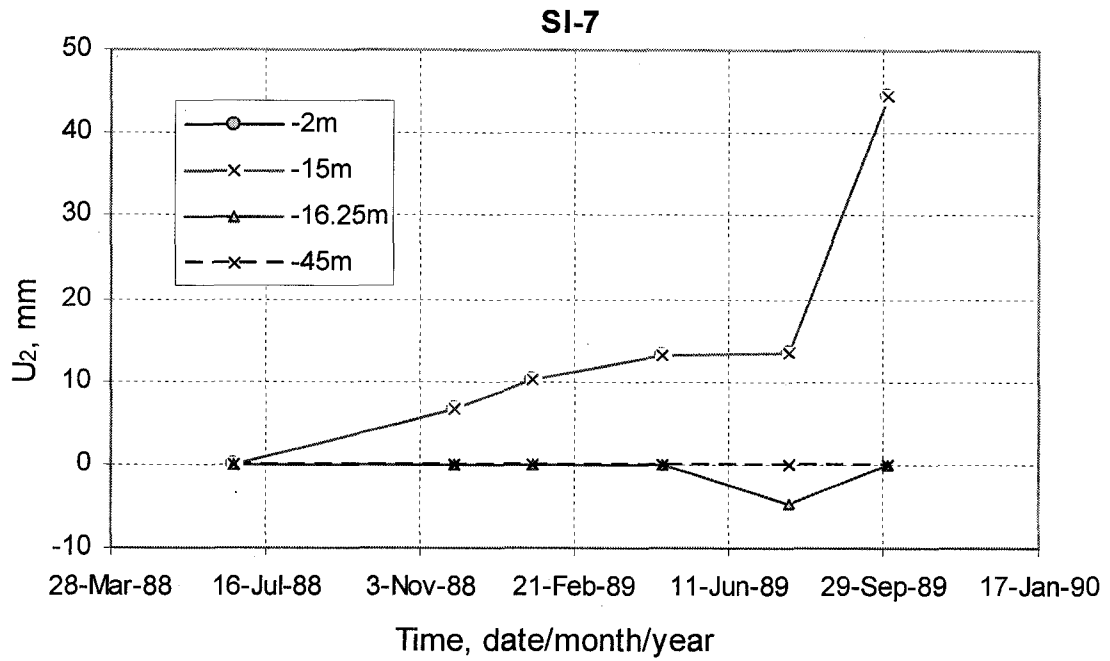


Figure 7.9 Soil Movement in X direction at Different Depths, U₂, at SI7

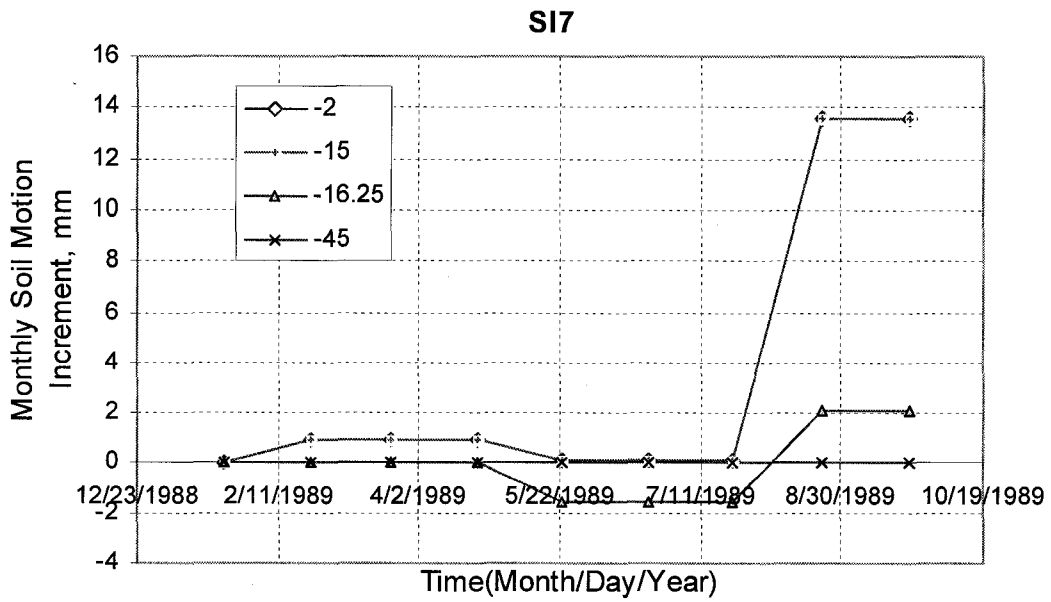


Figure 7.10 Monthly Soil Movement increment in X direction at SI7

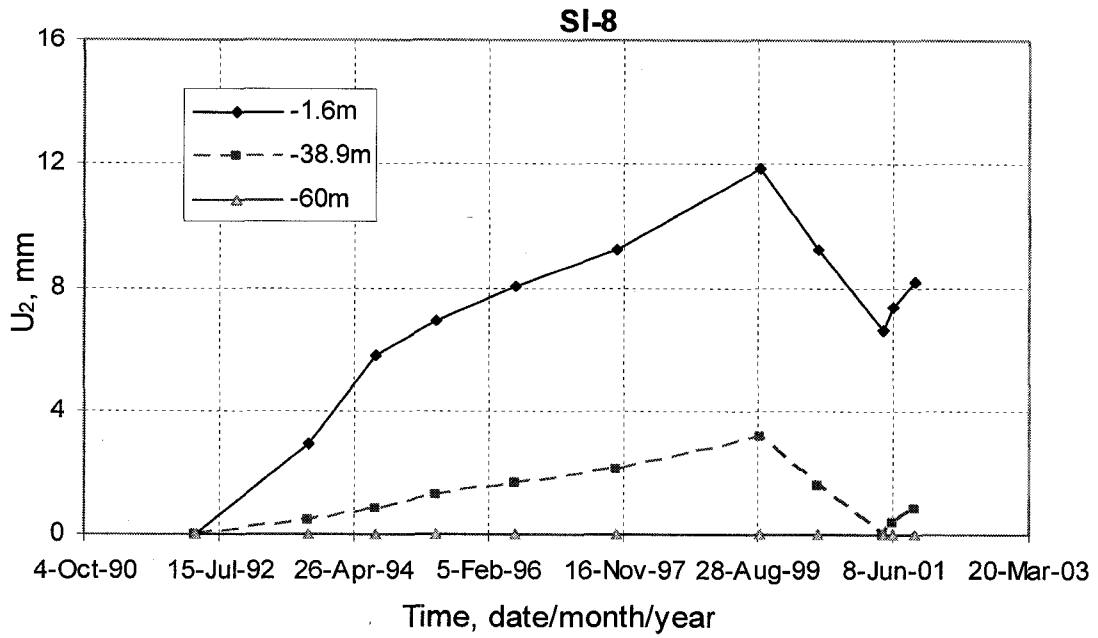


Figure 7.11 Soil Movement in X direction at Different Depths, U_2 , at SI8

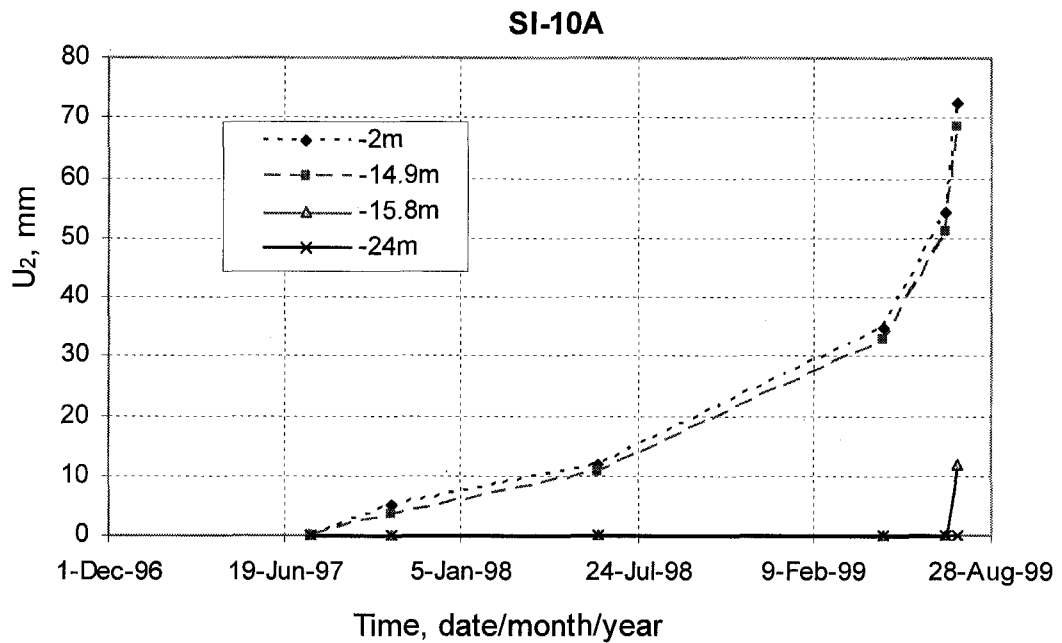


Figure 7.12 Soil Movement in X direction at Different Depths, U_2 , at SI10A

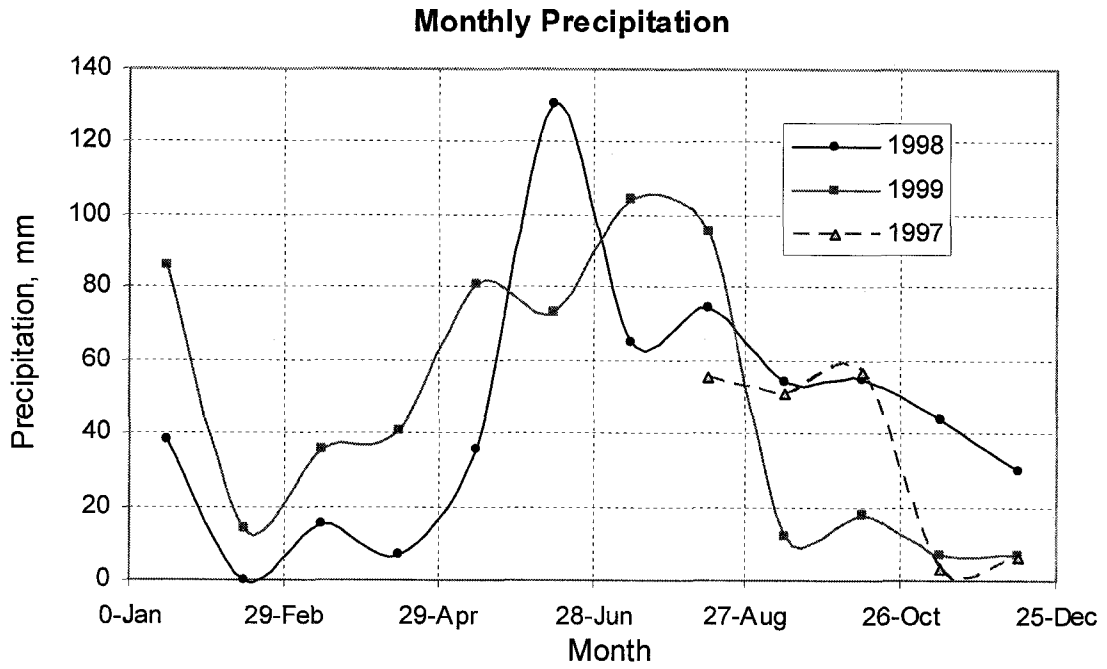


Figure 7.13 Monthly Precipitation in 1997-1999 at Entwistle

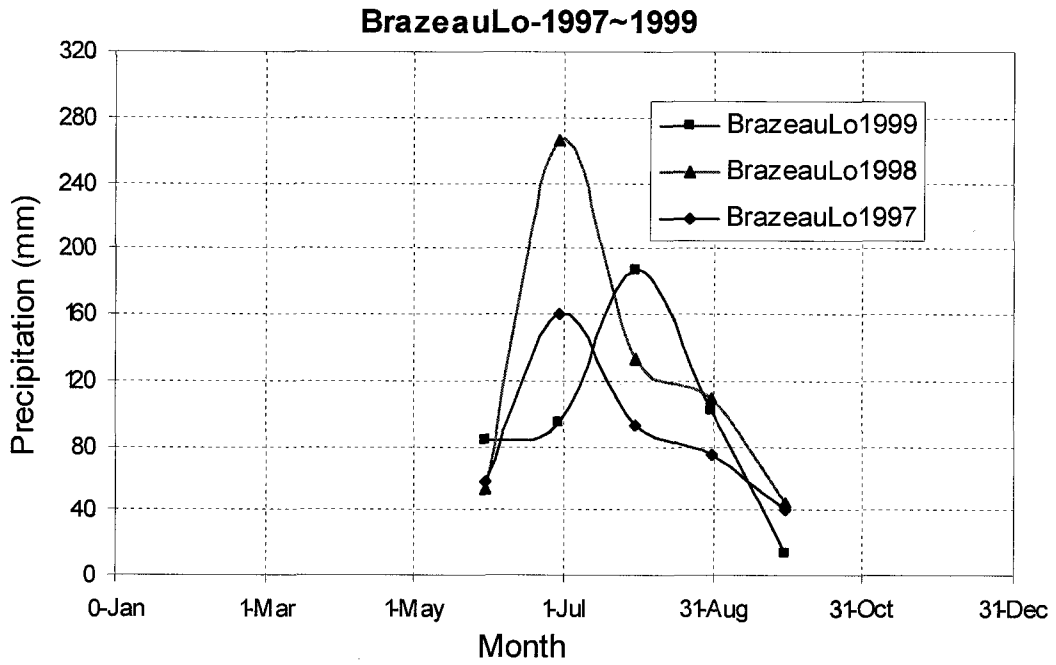


Figure 7.14 Precipitation at Brazeau Lo 1997-1999

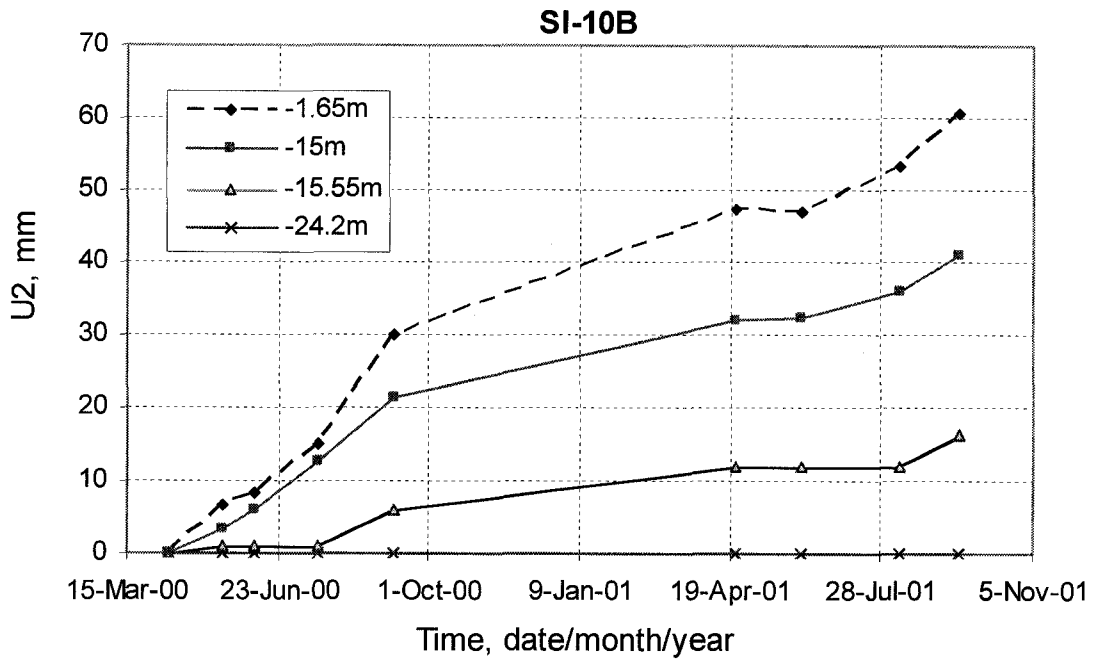


Figure 7.15 Soil Movement in X direction at Different Depths, U₂, at SI10B

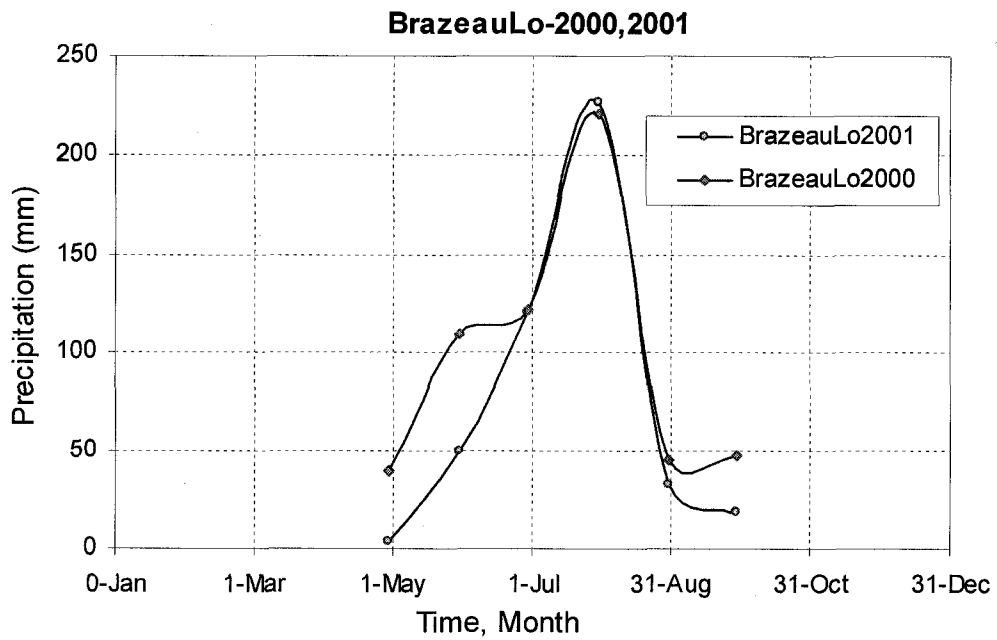


Figure 7.16 Precipitation at Brazeau Lo, in 2000, 2001

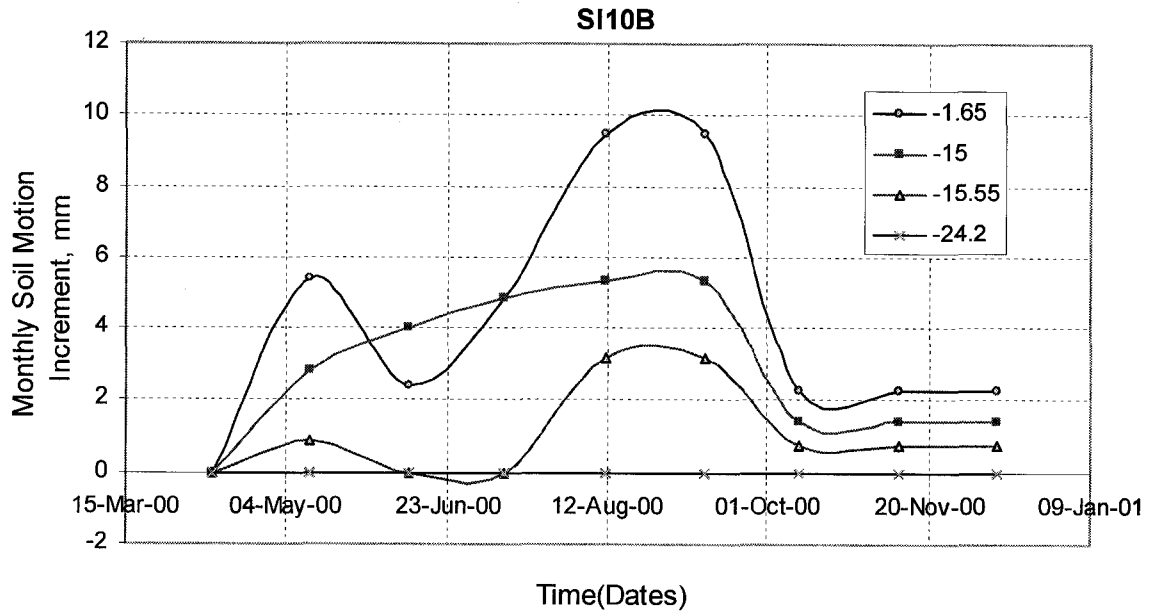


Figure 7.17 Monthly increment of U_2 versus time at different depths for SI10B.

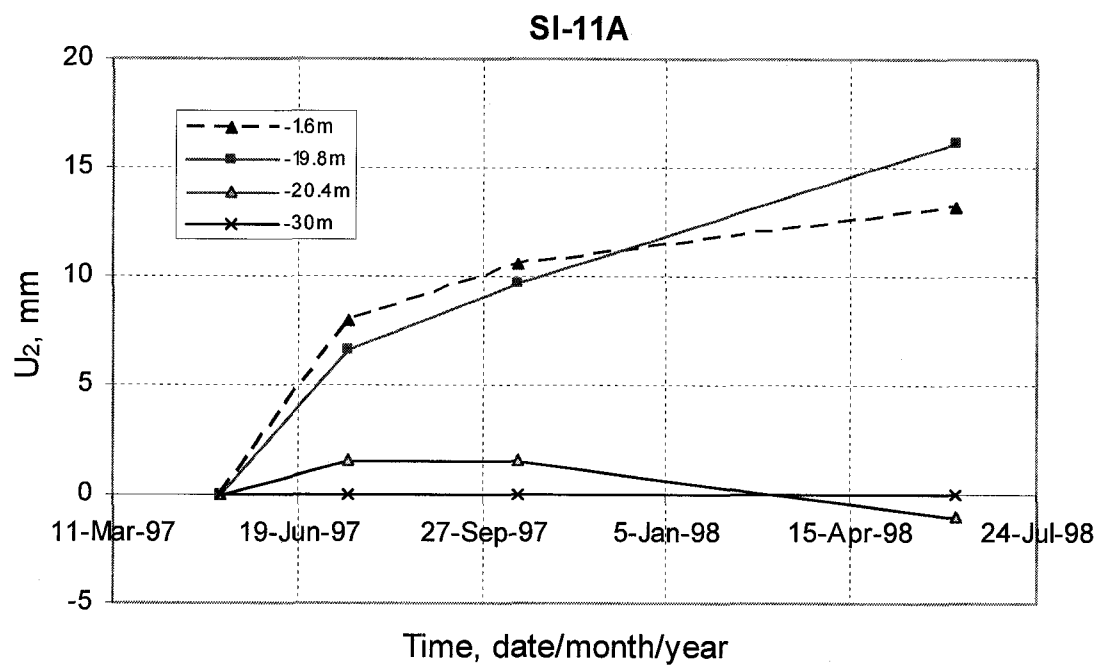


Figure 7.18 Soil Movement in X direction at Different Depths, U_2 , at SI11A

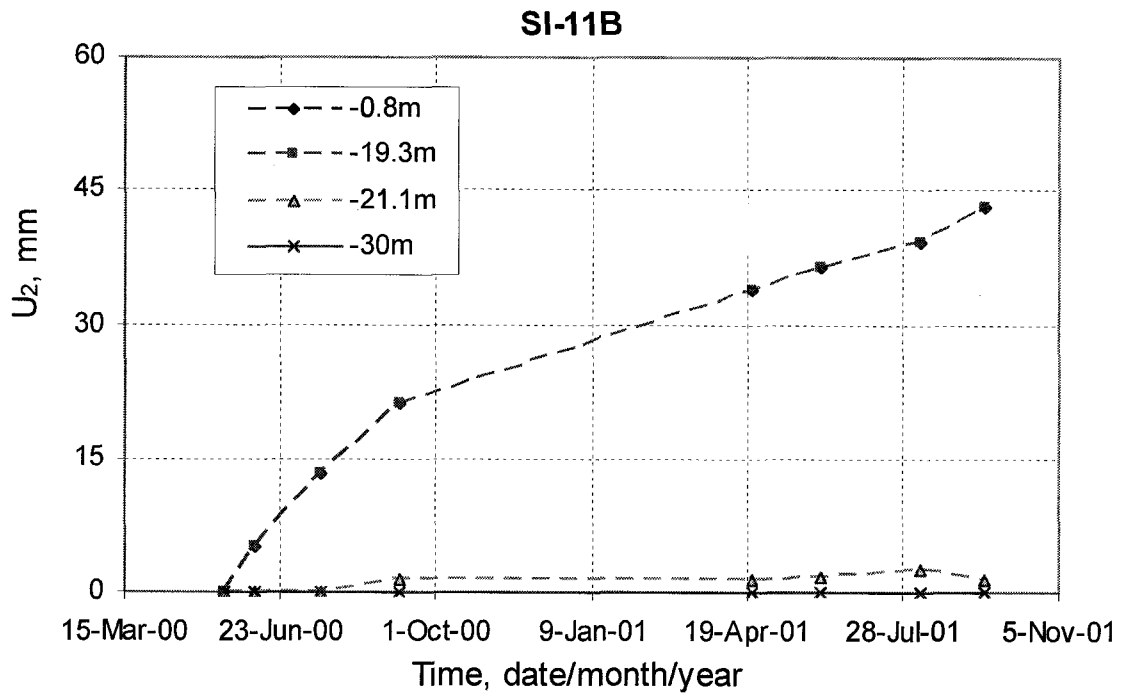


Figure 7.19 Soil Movement in X direction at Different Depths, U_2 , at SI11B

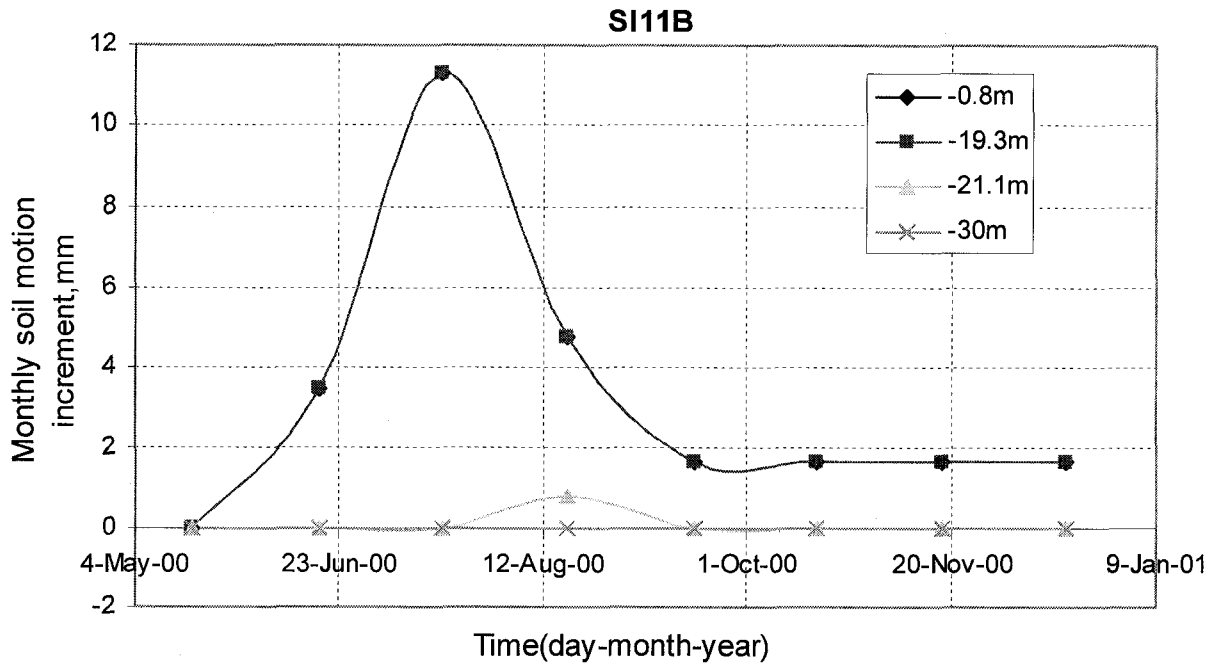


Figure 7.20 Monthly increment of U_2 versus time at these same depths for SI11B

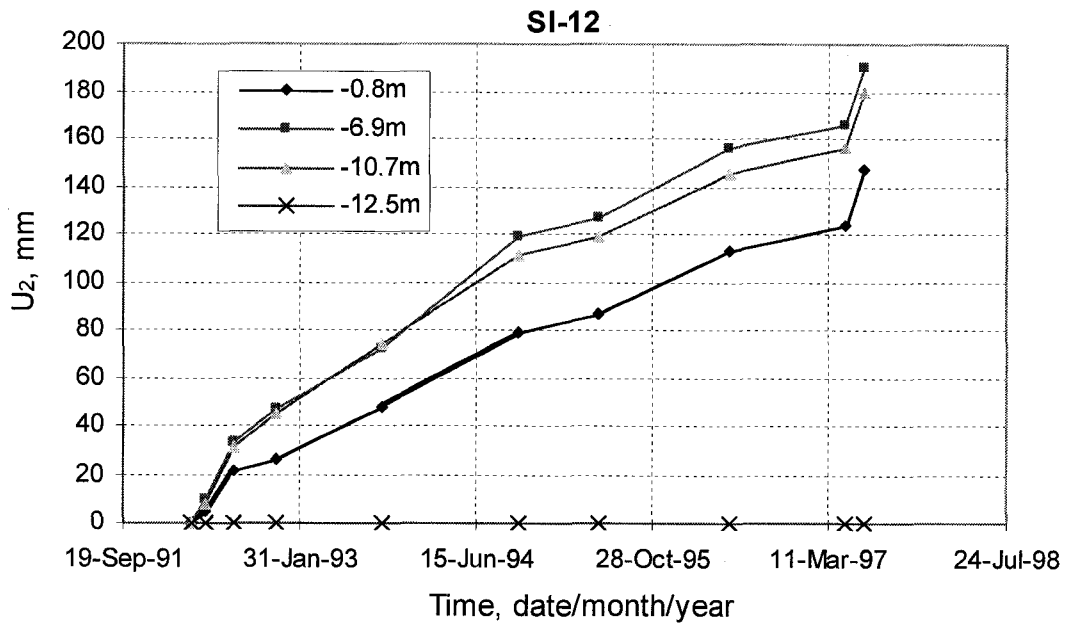


Figure 7.21 Soil Movement in X direction at Different Depths, U_2 , at SI12

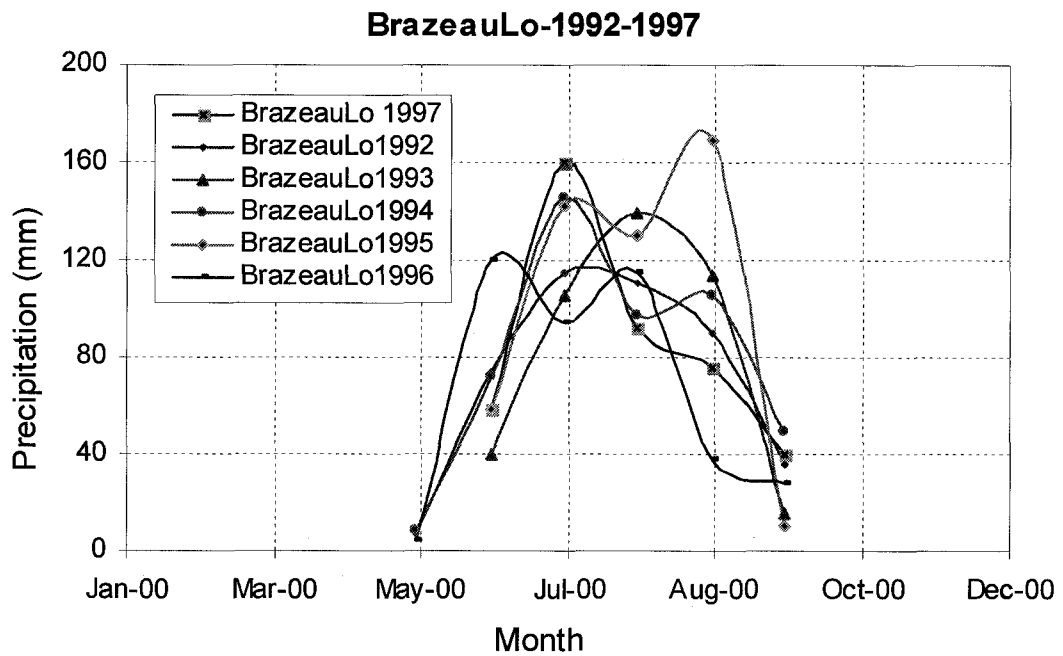


Figure 7.22 Precipitation at Brazeau Lo 1992-1997

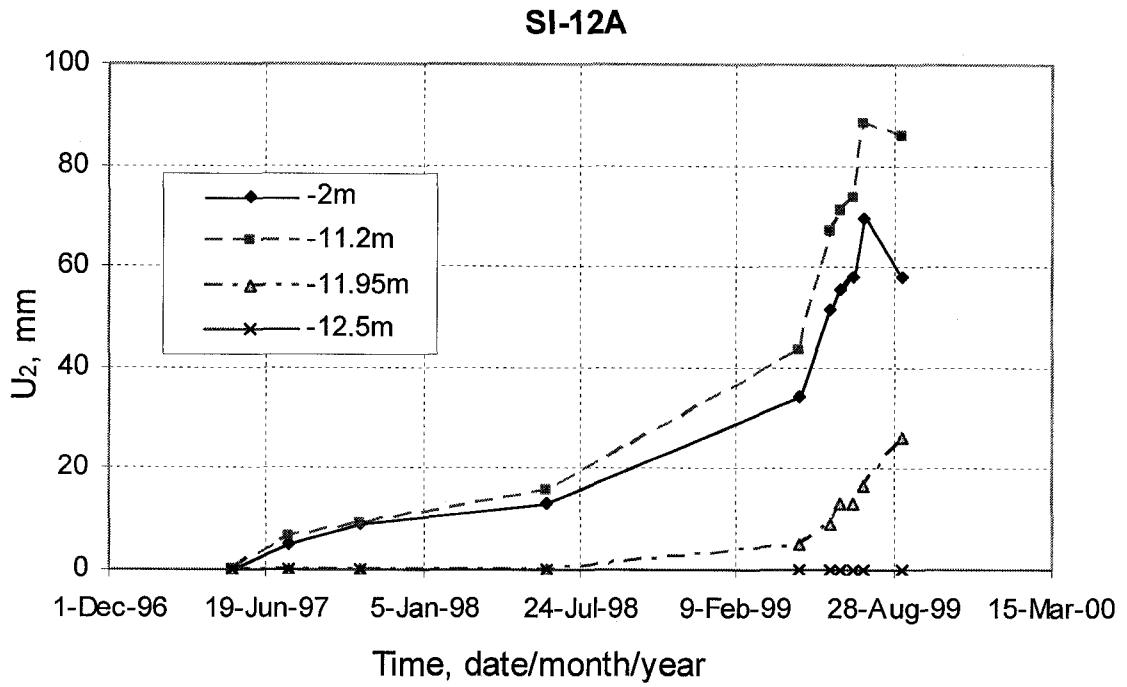


Figure 7.23 Soil Movement in X direction at Different Depths, U_2 , at SI12A

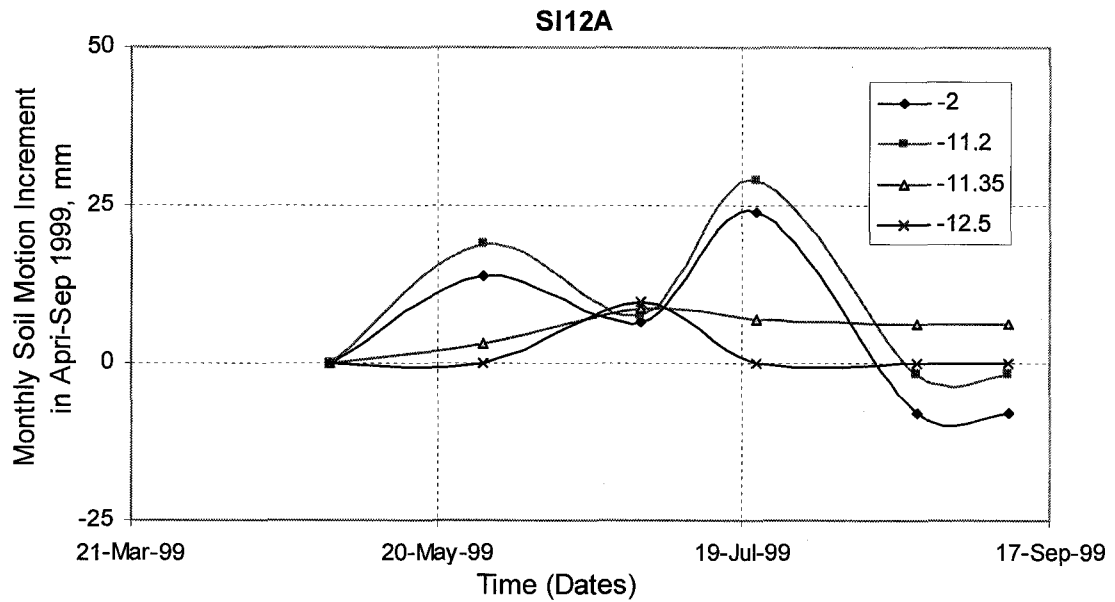


Figure 7.24 Monthly increment of U_2 versus time at these same depths for SI12A in 1999

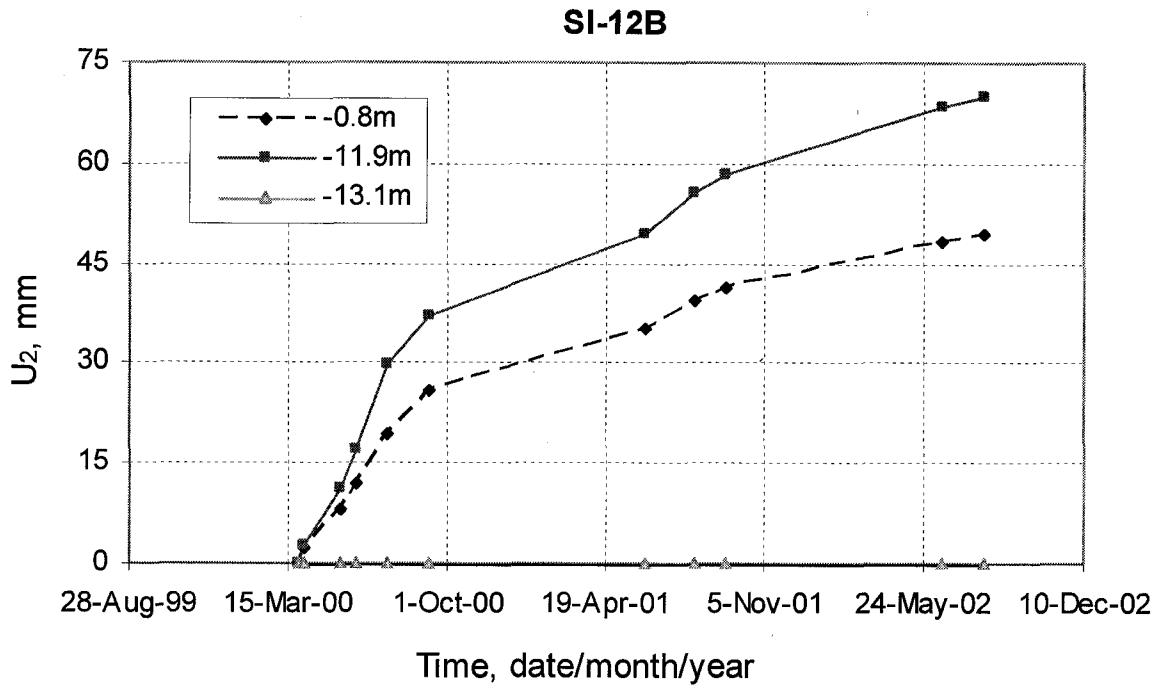


Figure 7.25 Soil Movement in X direction at Different Depths, U₂, at SI12B

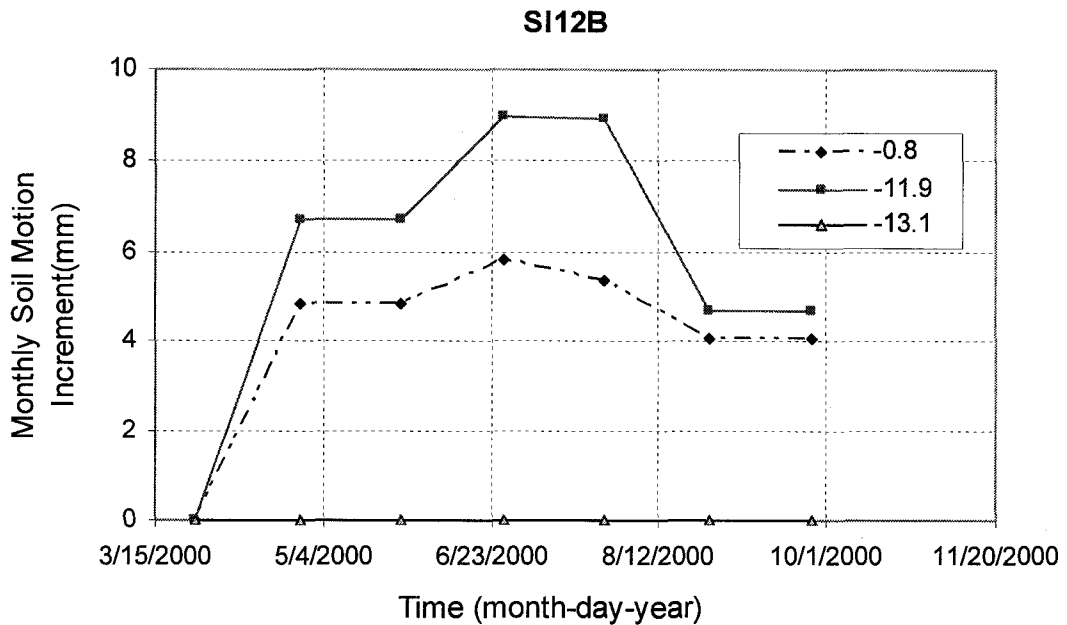


Figure 7.26 Monthly increment of U₂ versus time at these same depths for SI12B

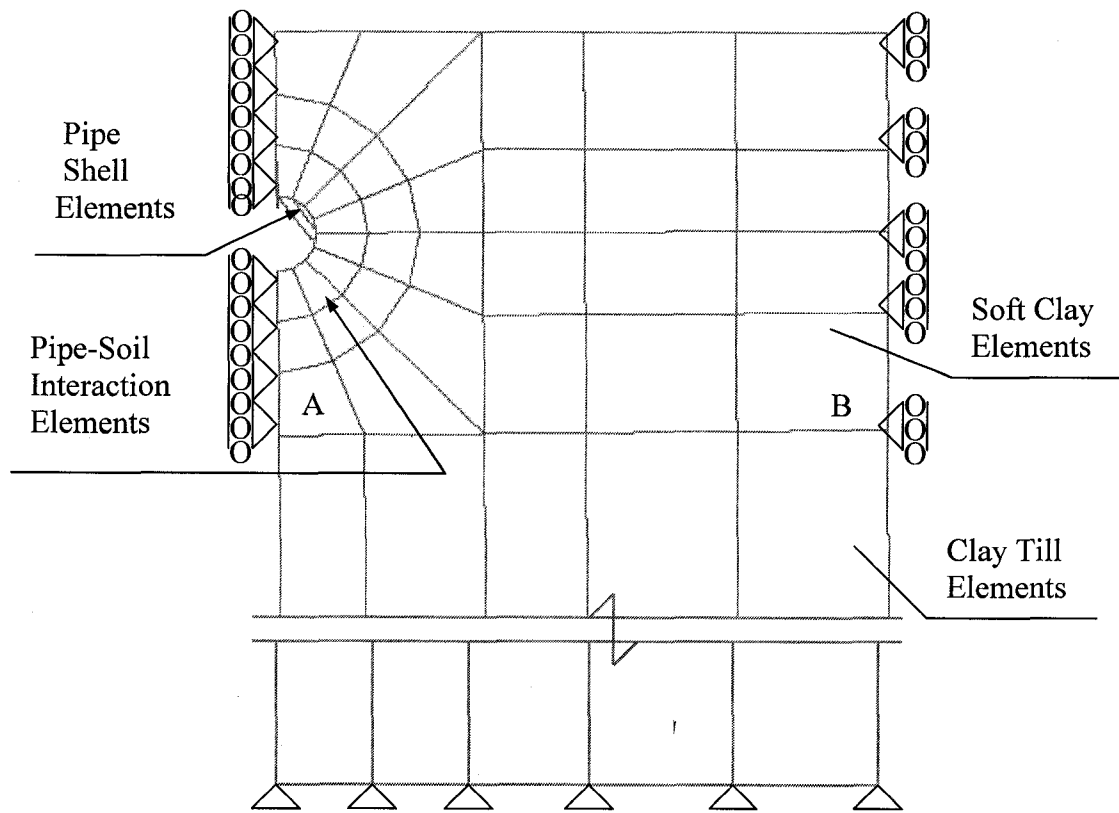


Figure 7.27 Pipe Cross Section and Slope Section

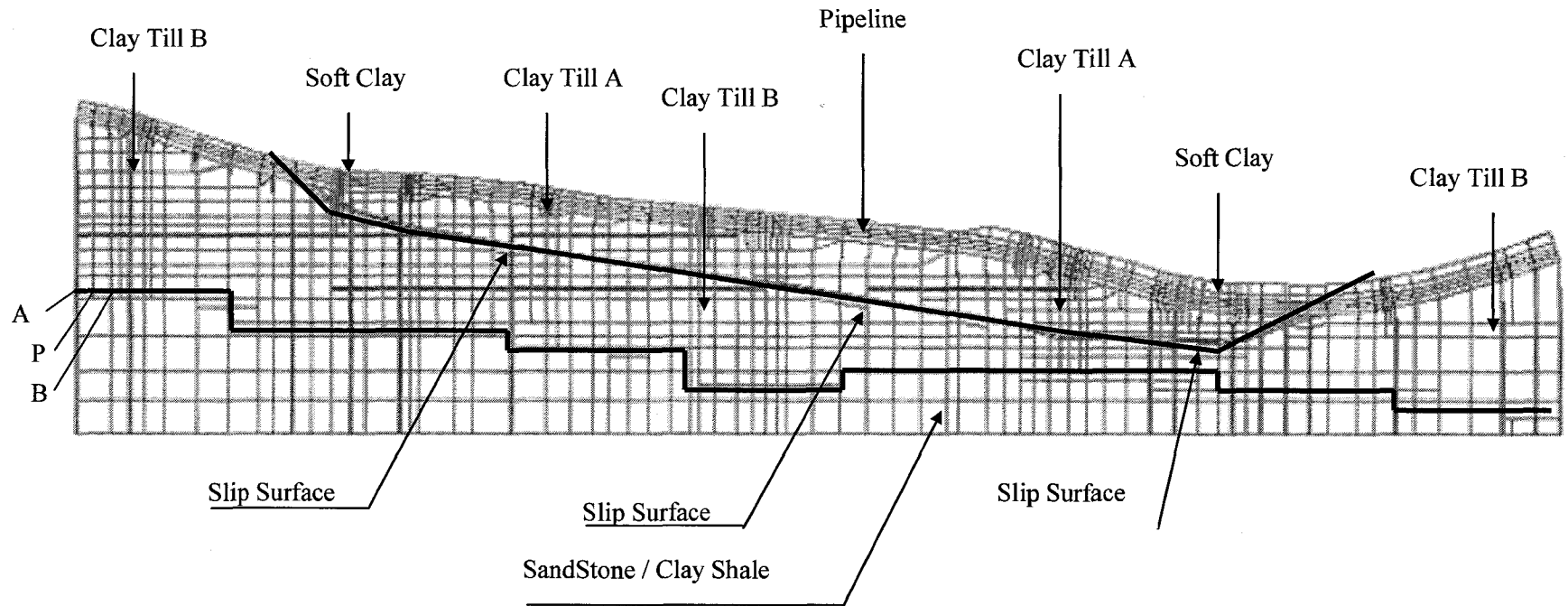


Figure 7.28 Soil Layers at Pembina River Crossing

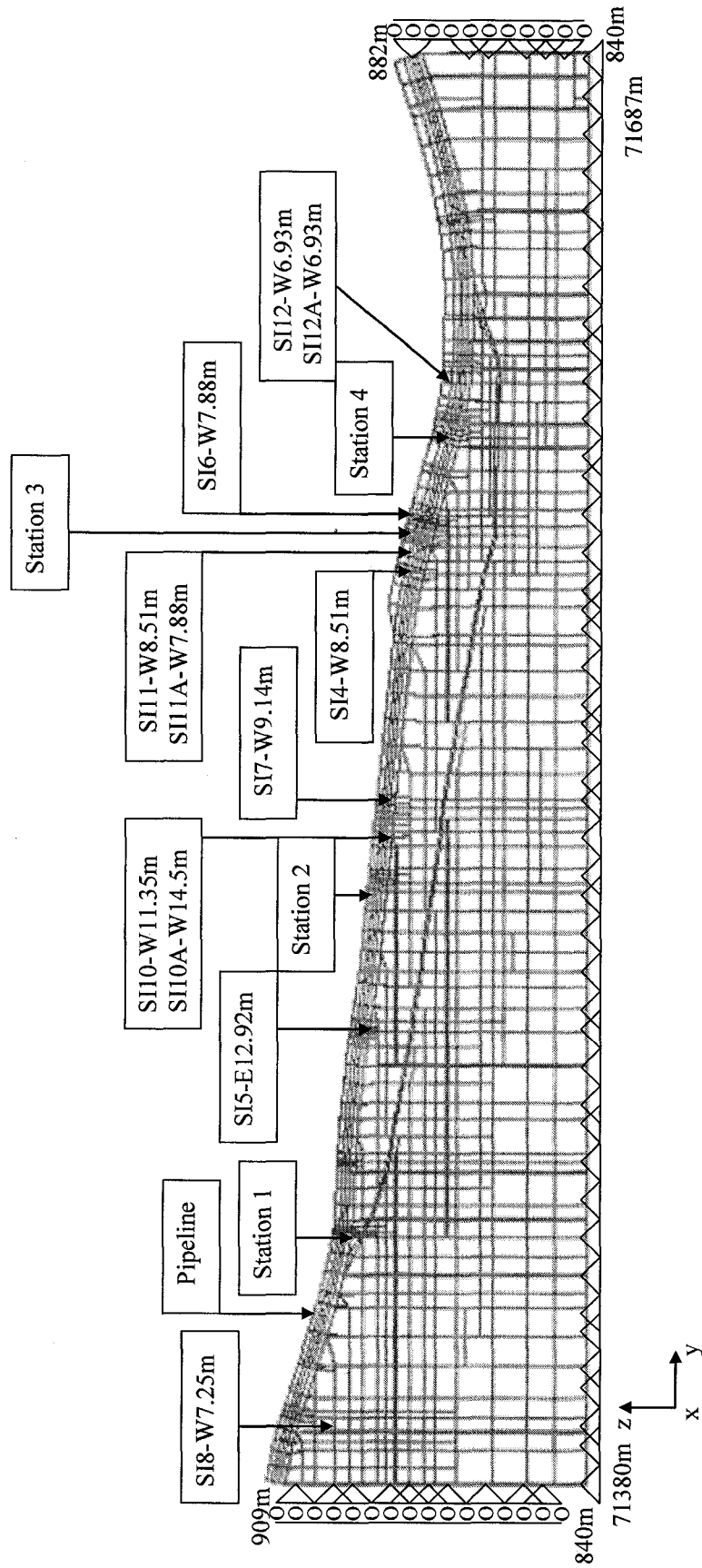


Figure 7.29 Boundary Conditions for FEA Model

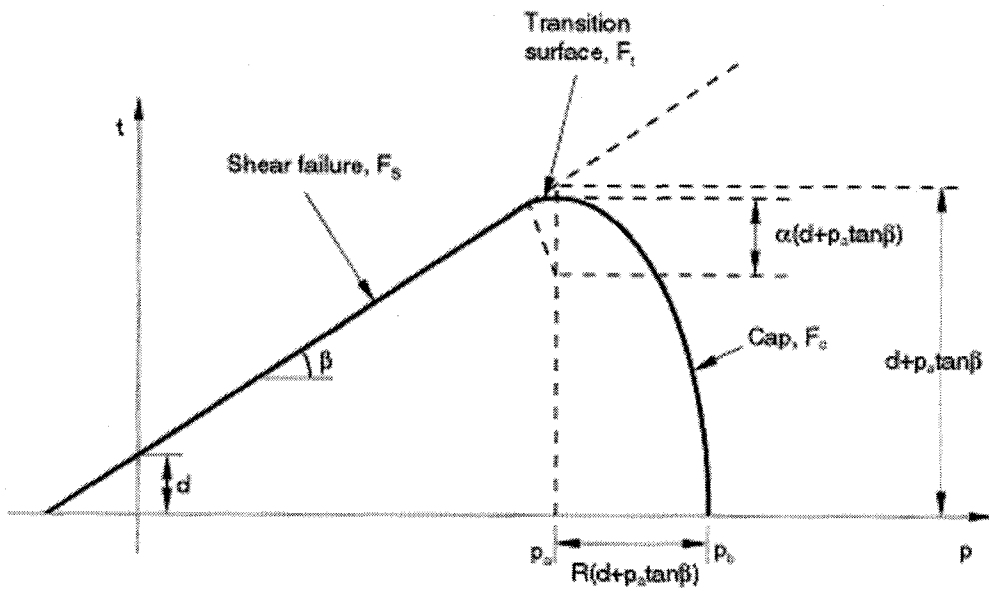


Figure 7.30 The Modified Drucker-Prager/Cap Model: Yield Surfaces in the p - t Plane

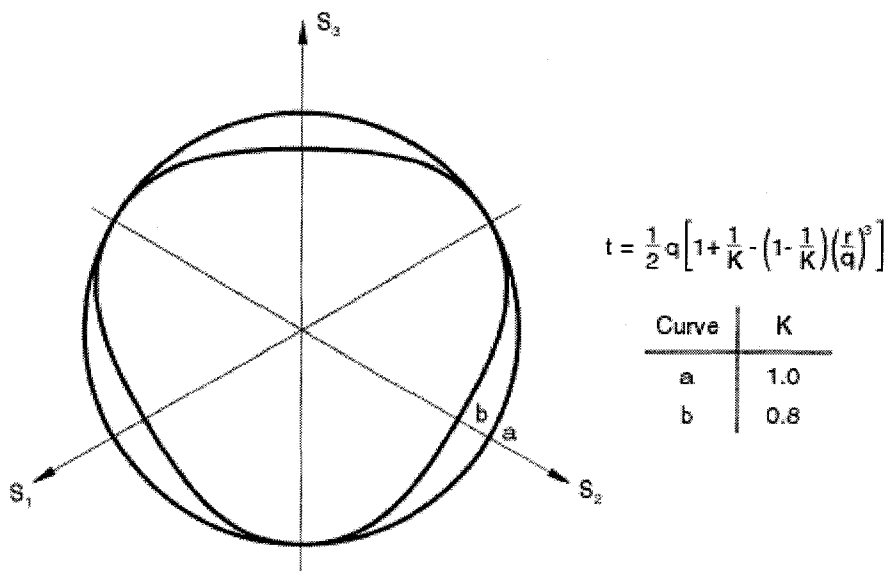


Figure 7.31 Typical Yield/Flow Surfaces in the Deviatoric Plane

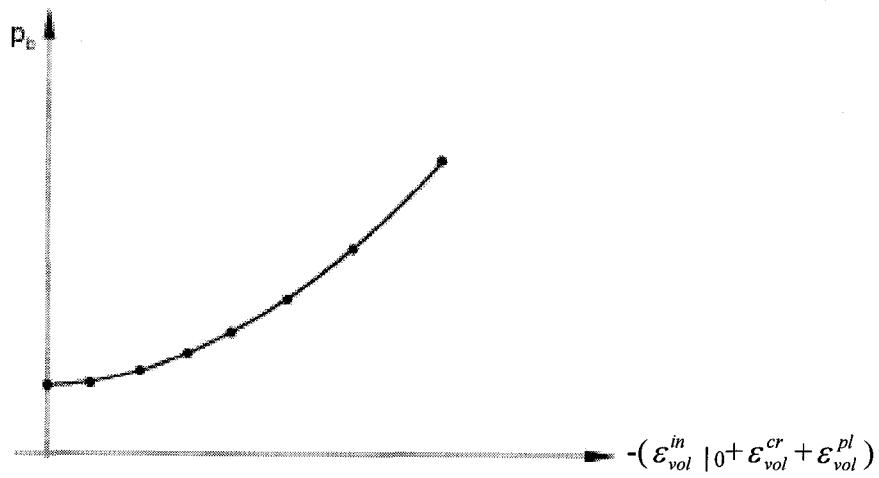


Figure 7.32 Typical Cap Hardening

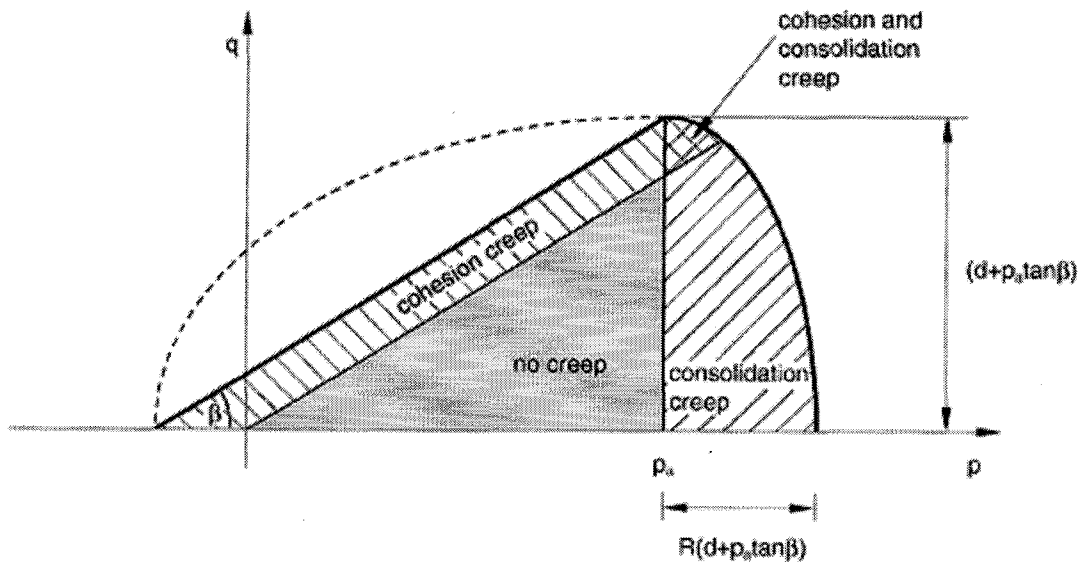


Figure 7.33 Regions of Activity of Creep Mechanisms

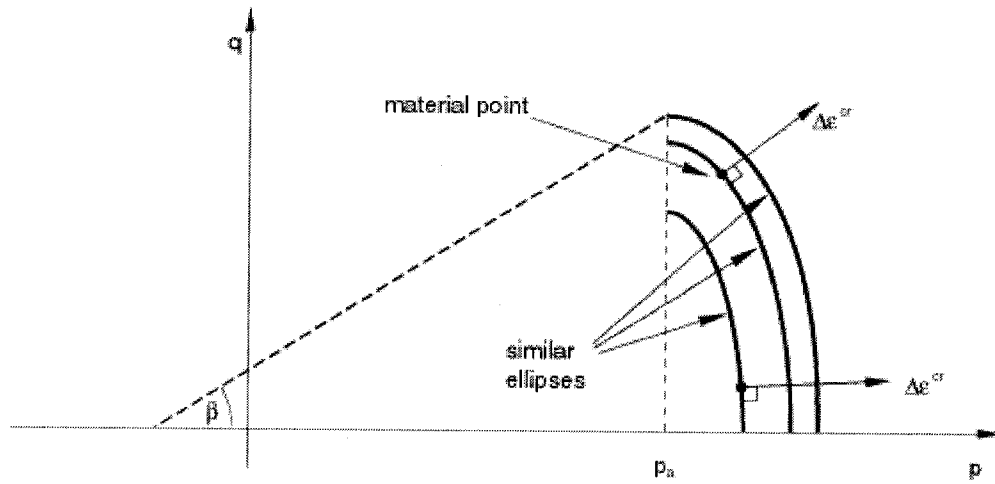


Figure 7.34 Consolidation Creep Potentials in the p - q Plane

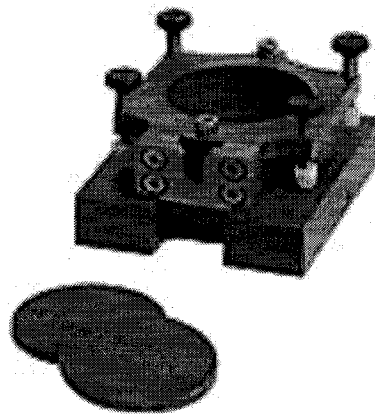


Figure 7.35 Direct Shear Box

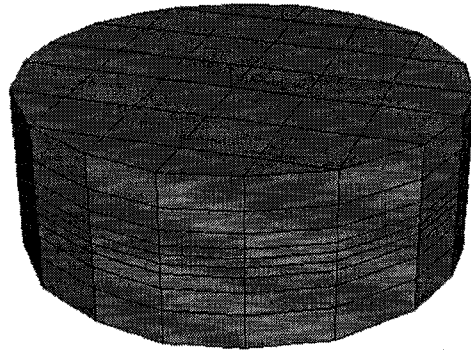


Figure 7.36 Soil Sample before Direct Shear Test

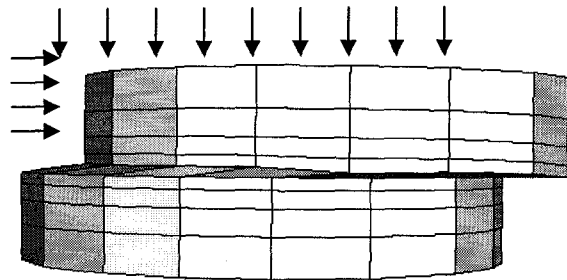


Figure 7.37 Soil Sample during Direct Shear Test

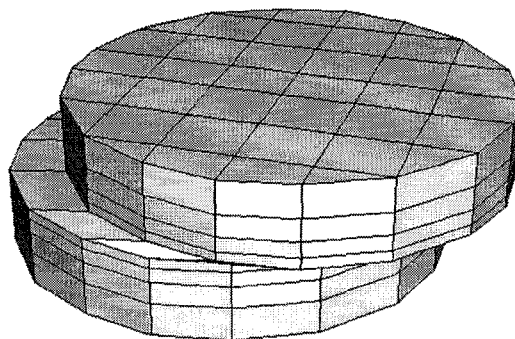


Figure 7.38 Soil Sample after Direct Shear Test

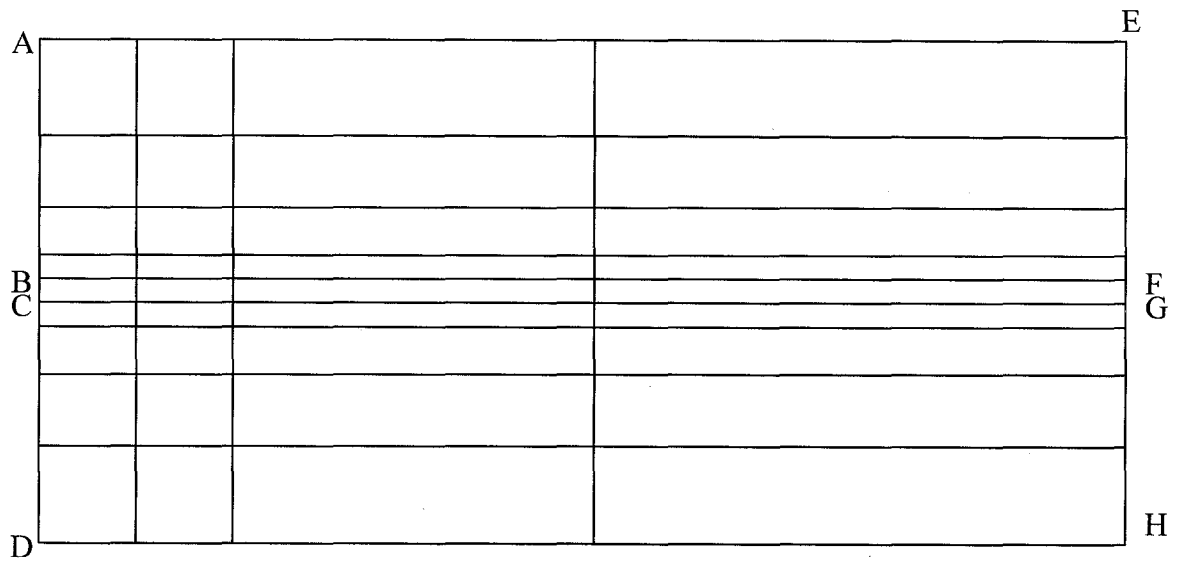
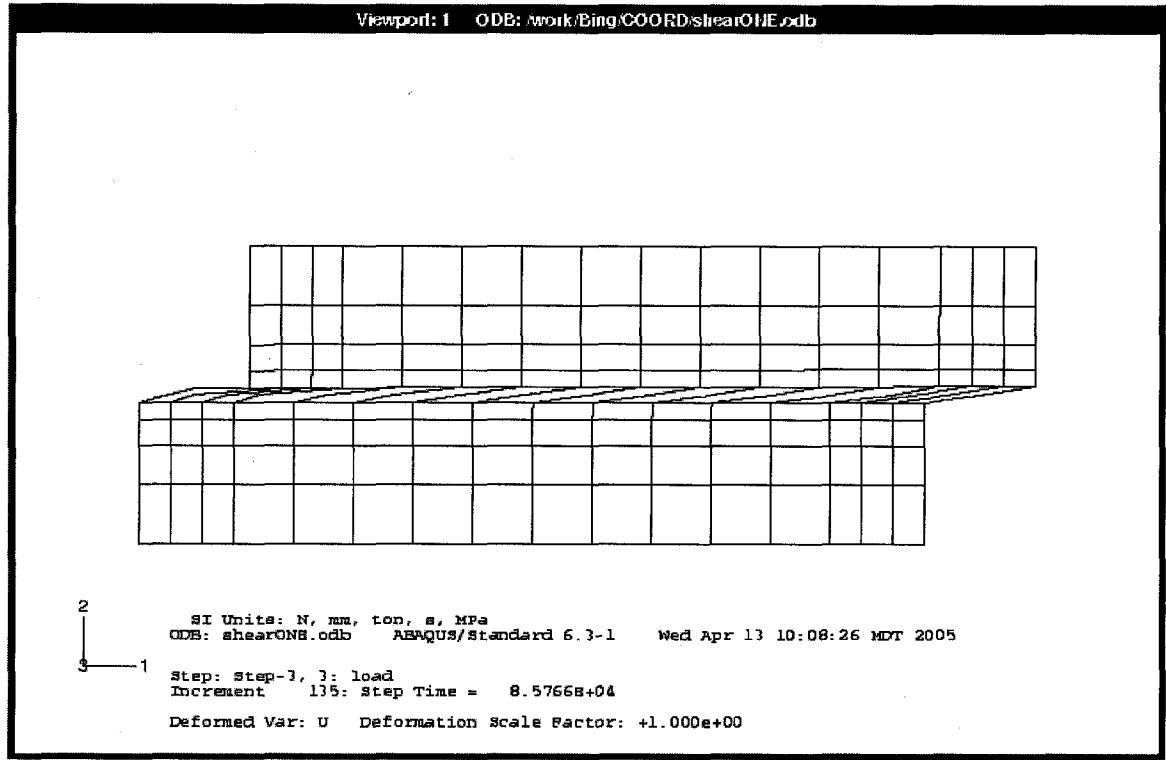
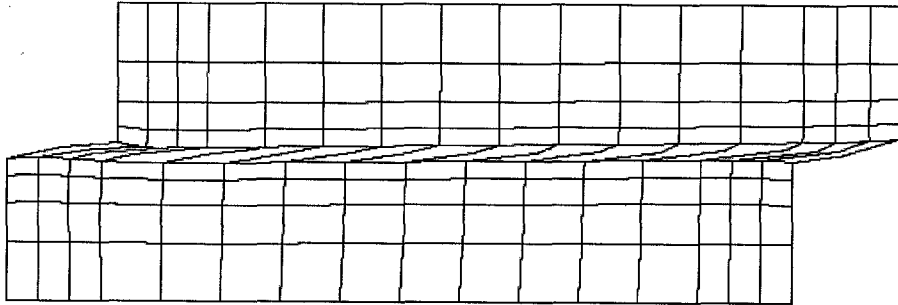


Figure 7.39 Profile of Soil Sample

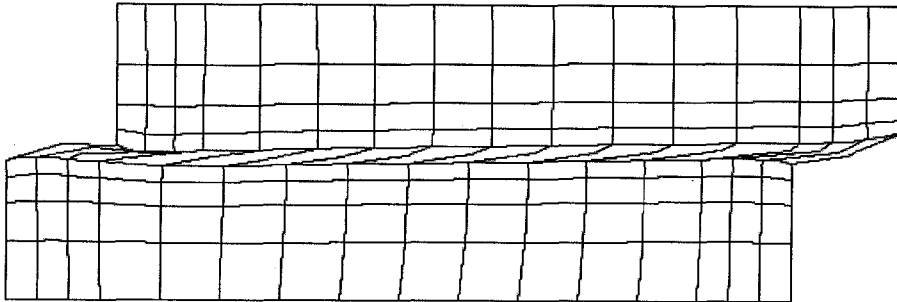


Viewport: 1 ODB: work/Eing/COORD/shearTWO.odb



SI Units: N, mm, ton, s, MPa
ODB: shearTWO.odb ABAQUS/Standard 6.3-1 Wed Apr 13 10:06:24 MDT 2005
Step: Step-3, 3: load
Increment 64: Step Time = 8.57668+04
Deformed Var: U Deformation Scale Factor: +1.000e+00

Viewport: 1 ODB: work/Eing/COORD/shear.odb



SI Units: N, mm, ton, s, MPa
ODB: shear.odb ABAQUS/Standard 6.3-1 Wed Apr 13 02:42:12 MDT 2005
Step: Step-3, 3: load
Increment 72: Step Time = 8.57668+04
Deformed Var: U Deformation Scale Factor: +1.000e+00

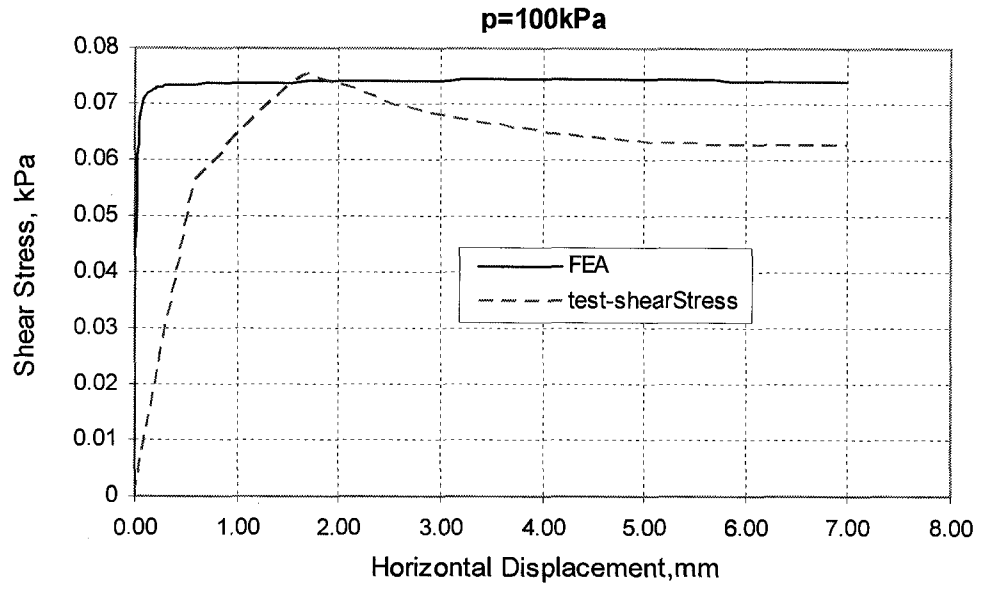


Figure 7.40 Comparison of FEA with Direct Shear Test Results

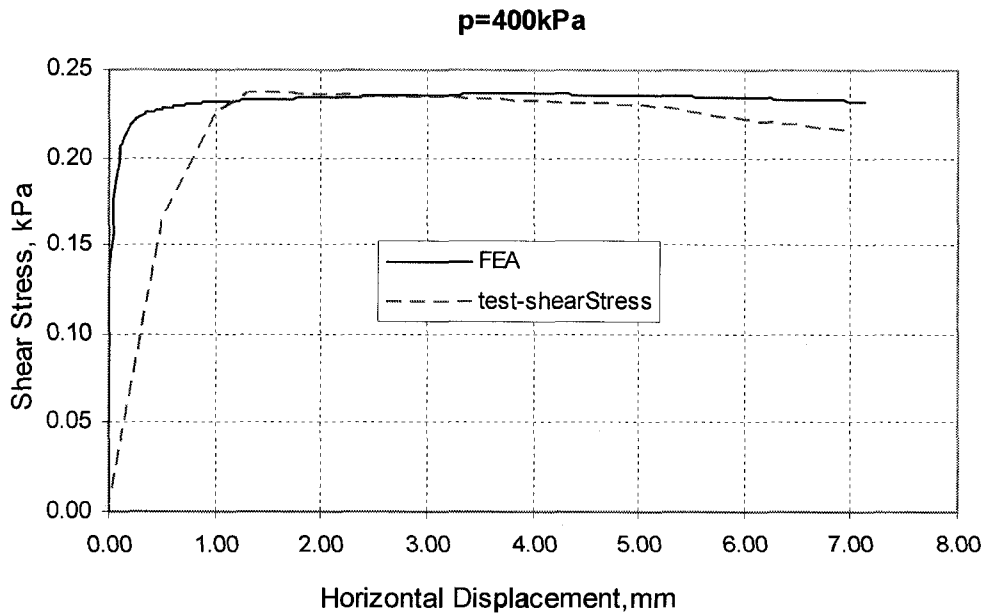


Figure 7.41 Comparison of FEA with Direct Shear Test Results

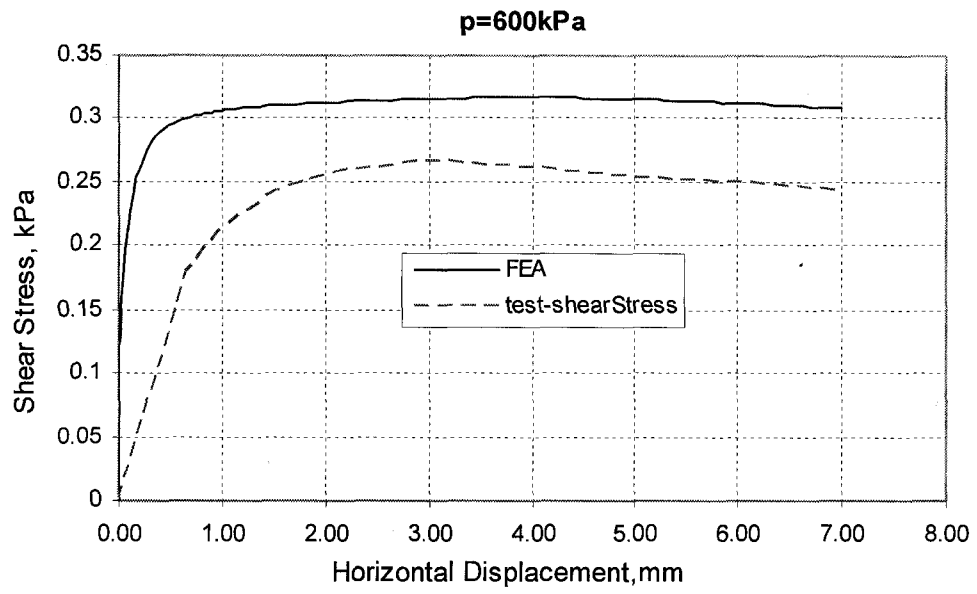


Figure 7.42 Comparison of FEA with Direct Shear Test Results

CHAPTER 8 FINITE ELEMENT RESULTS AND DISCUSSIONS

Chapter 8 is about the application of the finite element model (FEM) in Pembina River Crossing. This chapter has four sections: Section 8.1 provides the validation of the FEM; Section 8.2 and 8.3 discuss the simulation of pipeline performance at some typical years and the optimum stress relief procedures. The final section is the discussion.

The first part of this chapter will contain a discussion on the results obtained from the finite element analysis. The soil movement and the deformation of the pipe will be compared with the results from the field measurements in order to verify the predictive capability of the finite element model.

The second part of this chapter will present the simulation of pipeline response at some typical years when precipitation is at its maximum, minimum, median of the record during the sixteen years of precipitation monitoring. The results are compared with SI data and the critical locations of the pipeline for a given soil movements in these years are determined. Maximum axial stress/strain accumulation on the pipeline with respect to precipitation will be obtained from the analysis.

The third part of this chapter will provide the optimum stress relief procedures including stress relief operating schedule, prediction of the next stress relief procedure and effective scope of stress relief of the pipeline under the condition of average yearly precipitation. The final section of this chapter will provide discussions of the FEA results followed by an evaluation of the effectiveness of and providing guidelines for the stress relief procedure for the pipeline at Pembina River Crossing.

8.1 Validation of the Finite Element Model

8.1.1 Slope Stress and Displacement

The effect and evolution of the spatial and temporal development of the ground displacement field create a path dependency that affects the localization and development

of the pipe strains. This soil environmental load condition to the pipeline in FEM has to be authentic. Preliminary examination for the slope stress and displacement was conducted.

The FEA results of soil continuum elements are obtained in global coordinate system, as shown in Figure 8.1. The Cartesian coordinate system in 1, 2 and 3 directions is shown. The load sequence for the model has been described in Chapter 7, in which the gravity of slope is applied at the first step. Water table is located near the slip surface when pipeline is installed and subsequently pressurized. Increase in water level and creep are carried out sequentially to simulate slope and pipeline deformation in different precipitation years.

Contours of soil stresses and displacements of the layer A in the slope (which is perpendicular to the ground shown in Figure 8.2) in 1, 2 and 3 directions after the slope gravity load applied are shown in Figure 8.3 to Figure 8.8. Soil stresses are S_{11} , S_{22} and S_{33} , soil displacements are represented as U_1 , U_2 and U_3 in 1, 2 and 3 directions respectively. It can be seen from Figure 8.3 to Figure 8.5 that the ratio between S_{11}/S_{22} to S_{33} is about 0.7. It is close to the initial ratio, 0.72, of the horizontal and vertical stress components. Vertical stress S_{33} is proportional to the depth of slope. It shows that the slope gravity field is reasonable. Figure 8.6 to Figure 8.8 are the soil displacement at Layer A. Figure 8.6 indicates that U_1 is less than 1 mm, except at the boundary it is 4 mm. From Figure 8.7, soil moves in the 2-direction due to gravity. When the displacements U_2 results are compared with SI data, the initial soil displacements are set to zero since these displacement have occurred before any activities on the slope and they are not of practical interest. The ground moves faster near the creek on the lower part of the slope.

Contours of pore pressure of Layer A at different water tables are displayed in Figure 8.9 to Figure 8.12. It is clear that as the water level rises, pore pressures become higher. Figure 8.13 shows the contour of U_2 of layer A after certain time of creep, the ground surface and the soil near the creek on the south slope move faster. Contour of

axial stress S_{22} at the critical location of pipeline is compared at pipe-switch-on and after soil creep in Figure 8.14 and Figure 8.15, respectively. S_{22} stands for local axial stress in the pipe. Stress accumulation in this case is about 66 MPa.

Precipitation is closely related to ground movement, consequently influences the deformation of the pipe. Figure 8.16 shows the precipitation vs. specific number of year. Yearly precipitation or seasonal precipitation is obtained from Environmental Canada's database. The correlation between precipitation and pipeline deformation will be investigated in the following.

8.1.2 Comparisons of Soil Movement Data

The result of the developed FEM in chapter 7 is compared with site observations. Validation of the model is subdivided into comparisons of soil movement with the slope indicator data and pipeline deformation with strain gauge data in the year 2000 based on available data. In the finite element model, the pipeline deformation analysis with the operating internal pressure of 6.178 MPa and the given soil movement in the year 2000 have been implemented. The material parameters are shown in Table 7.22.

In Figure 8.17, displacement in the down slope direction 2, U_2 , is compared with slope indicator readings. Five available slope indicator data SI5A, SI8, SI10B, SI11B and SI12B in 2000 are contrasted with U_2 from the FEM.

The soil movement monitoring program at Pembina River Crossing has been discussed in Chapter 5. In the FEM, yearly soil movement, U_2 , in the horizontal down slope direction 2 m away from centerline of the pipeline at different depths is compared with slope indicator data at the same location. Table 8.1 shows the comparison of U_2 near the ground surface at SI5A, SI8, SI10B, SI11B and SI12B in 2000. Test-to-Predicted Ratio ranges from 0.976 to 1.4, the comparison of U_2 generally demonstrated reasonable agreement. The FEA results at SI5A, SI8 and SI11B have about 3% difference from the slope indicator data, while SI10B and SI12B, the FEA result is about 40% less than the

field data. Figure 8.17 to Figure 8.19 plot the comparison of soil movement U_2 of SI5A, SI8, SI10B, SI11B and SI12B at different depths in the year 2000 respectively.

8.1.3 Comparisons of Strain Gauge Data

Stresses of the pipe shell elements are given at the integration point in the hoop and axial directions at the local coordinate system. Directions of the hoop stress S_{11} and axial stress S_{22} are shown in Figure 8.24. In this large-displacement problem, the local directions defined in the reference configuration are rotated into the current configuration by the average material rotation.

There are four strain gauge stations at the pipeline. Each station has four strain gauges, measuring the pipe deformation in the longitudinal direction at every 90° along the circumference, as displayed in Figure 5.6. The strain gauges have recorded localized change of the pipe because of soil movement. Due to huge size of the model and the characteristics of the problem, the FEM is simplified to model half of the slope and pipeline as described in Chapter 7. It is reasonable to compare the average axial strain or stress accumulation at these strain gauge stations.

From Table 8.2 the monitored average axial accumulated compressive strain at station 1 in five months is $\epsilon_a = 33\mu\epsilon$, at Station 3 in three months is $\epsilon_a = -44\mu\epsilon$, and at Station 4 in three months is $\epsilon_a = -81\mu\epsilon$. At Station 2, strain gauges 3 and 4 are invalid, the average axial accumulated strain is not available. The monitored valid strain gauge data at Station 1 is from July to November, Station 3 and Station 4 are from July to September, including the rainy season of the year. Since yearly strain accumulation is of the main interest, the average axial strain increment in 2000 at these stations can be conservatively calculated, as well as average axial accumulated stress with elastic modulus E taken as 205 GPa, as the following:

$$\text{Station 1, } \epsilon_a = 33\mu\epsilon/5 \times 12 = 79\mu\epsilon,$$

$$\sigma_a = 79\mu\epsilon \times 205\text{GPa} = 16.2\text{MPa}$$

$$\text{Station 3, } \epsilon_a = -44\mu\epsilon/3 \times 12 = -176\mu\epsilon,$$

$$\sigma_a = -176\mu\epsilon \times 205\text{GPa} = -36.1\text{MPa}, \text{ and}$$

$$\text{Station 4, } \epsilon_a = -81\mu\epsilon/3 \times 12 = -324\mu\epsilon,$$

$$\sigma_a = -324\mu\epsilon \times 205\text{GPa} = -66.4\text{MPa}$$

where ϵ_a – average axial accumulated strain

σ_a – average axial accumulated stress

Table 8.3 and Table 8.4 give the comparison of average axial accumulated strain ϵ_a and average axial accumulated stress σ_a respectively at Station 1, Station 3 and Station 4 in the year 2000. The Test-to-Predicted Ratios from the Tables are 0.66, 0.98 and 0.87 at Station 1, Station 3 and Station 4, showing good agreement. The above results verify the predictive capability of the finite element model.

8.2 Simulation of Pipeline Response at Some Typical Years

The following Sections are about applications of the Finite Element Model. Base on sixteen years of precipitation monitoring data, the FEM is used to simulate pipeline deformation due to soil movement at four typical years: 1989 with maximum precipitation, 1992 with minimum precipitation, 1995 with median precipitation and 2000 with relatively large precipitation (which has been carried out in section 8.1 to verify FEM with available strain gauge data in 2000).

It has been elaborated in Chapter 5 and Chapter 7 that slope displacements have been closely correlated with changes in water table, shear plane slipping and soil creep. Precipitation, directly related to soil movement, plays an important role in the pipeline deformation; it causes changes in the ground water level that contributes to changes in the effective stresses in the soil. It is the effective stresses that primarily control the local soil pipe interaction. As precipitation increases, soil movement increases, so does the pipeline deformation, and vice versa.

Figure 8.16 shows yearly and May-September precipitation for years 1986-2001 at climate station Brazeau Lo and other stations. Table 7.1 gives the exact locations of

these climate stations near LodgePole, where the Pembina River Crossing is located with no climate data available.

Brazeau Lo is the closest to Pembina River Crossing. In general, precipitation at Brazeau Lo is higher than other stations. It only has data from May to September every year, which shows three largest movements: 563mm in 1986, 580mm in 1989 and 607mm in 1998. This coincides with the two facts: the pipeline had a rupture in 1986, resulting in rerouting the pipeline; slope indicators show that soil movement in 1989 and 1998 is more than other years.

The precipitation data is consistent at different climate locations mostly, however there is exception, for example, data in May-Sep 1998 at Brazeau Lo gives 607 mm, while data in 1998 at other climate stations gives 549 mm, yet yearly precipitation at other stations provides important information. For example, 1989 data gives 872.4mm of precipitation, a maximum, and 1992 has 379 mm, a minimum over sixteen years.

From Figure 8.16 relatively average yearly precipitation occurs in 1993-1998, range from 522 mm to 560 mm, the median of which is 529mm in 1995; nine out of sixteen years have yearly precipitation between 500mm and 600mm, which is defined in this thesis as the normal or average yearly precipitation. Year 1995 is representative of the normal precipitation year. From data at other stations, May-Sep precipitation is about 62%-84% of the yearly precipitation.

By changing the water table, simulation of pipeline stress accumulation in 1989, 1992 and 1995 and 2000 is conducted separately. Slope indicator (SI) is taken as the criteria to determine the corresponding water table levels, in other words, the water table is varied to match the movements that are measured in the slope indicators. In other years with inconsistent precipitation, the ground moves at diverse rates. The water table is then varied to match the movements in different years.

Tables 8.5, 8.6 and 8.7 show the comparison of U_2 at three available SIs near the ground surface in 1995, 1992 and at two available SIs near the ground surface in 1989. Good agreement is obtained between the FEM and SI data, except in the year 1992, calculated movement in SI12 is 60% of the measurement. This may be mainly due to the lack of slope indicator between SI12 and SI13. This fact consequently results in the assuming slip surface which may not be the real case.

Figure 8.19 to Figure 8.20 give the comparison of soil movement U_2 at SI5, SI8 and SI12 at different depths in 1995. Figure 8.21 to Figure 8.22 give the comparison of soil movement U_2 at SI5, SI8 and SI12 at different depths in 1992. Figure 8.22 and Figure 8.23 give the comparison of soil movement U_2 at SI6 and SI7 at different depths in 1989. In general the FEM results render good agreement with the SI data.

Figure 8.25 to Figure 8.40 lay out the top and bottom axial stress and strain accumulation of the cross section along the whole pipeline in 2000, 1995, 1992 and 1989. It can be seen that as the precipitation increases, axial stress/strain accumulation also increases. The maximum accumulated compressive stress/strain and their locations in 1989, 1992, 1995, and 2000 are presented in Table 8.8, the critical location is 16m south of the center of the creek. The maximum accumulated strain can reach as much as $1075\mu\epsilon$ if precipitation reaches 872mm/yr (year 1989). Figure 8.25 to Figure 8.40 shows that the pipeline is subjected bending moment.

The yearly maximum axial stress/strain accumulations at these four years 2000, 1995, 1992 and 1989 vs. the May-Sep precipitation at Brazeau Lo (closest to Pembina River Crossing) are shown in Figure 8.41 and Figure 8.42. There is a reasonable correlation between axial strain and precipitation because as rain aggrandizes, slope movement is more significant, causing quicker built up of pipeline deformation. Precipitation in May-Sep represents the trend of the yearly precipitation, as shown in Table 7.10, constituting 75% of the whole year precipitation. It can be seen that when the precipitation exceeds 500 mm, axial stress/strain accumulation increases much quicker. The maximum axial compressive strain occurred at 16 m away from the south bank of the

creek. From Figure 8.41, yearly maximum axial stress/strain accumulation can be assessed at any given precipitation in May-September by interpolation or extrapolation.

Table 8.9 gives the computed yearly maximum axial stress/strain accumulation in 1986-2005 based on linear interpolation. Figure 8.43 and Figure 8.44 display yearly maximum axial accumulated stress/strain vs. yearly precipitation of other climate stations. Since these stations are farther away from Pembina River Crossing, if yearly precipitation is collected, the accumulated strain can be used as reference to the one obtained from Table 8.9.

8.3 Optimum Stress Relief Procedures

Last Section presents the relationship between pipe deformation and the amount of precipitation. Apart from Table 8.9, strain gauge provides spot check.

8.3.1 Stress Relief Operating Schedule

The testing program of 12 pipe segments in chapter 3 and chapter 4 conducted under repetitive axial and bending load has concluded that before material yielding occurs, the repetitive axial and bending load style has little effect on the pipe behaviour. However plastic strain accumulates once the yield strength of the material has been exceeded under cyclic bending loads. This conclusion is applied to the pipeline at Pembina River Crossing in that the stress relief procedure should be applied before the pipe reaches its yield strength. In Table 8.9, the median precipitation in May-September at Brazeau Lo from 1986 to 2005 is 428mm, correspondingly the maximum strain is $-338 \mu\epsilon$. If this yield strain is taken as a criterion, stress relief is needed in every six years.

8.3.2 Prediction of Next Stress Relief Procedure

The latest stress relief for the pipeline was carried out in late March 2000. It is predicted that stress relief should be carried out in 2007 if precipitation since 2005 is approximately median level 420mm in May-September at Brazeau Lo. The results from this research give a conservative estimation of the pipeline deformation, since the available strain gauge data, taken as caliber for adjustment of pipe soil interaction in

modeling the pipeline performance in Section 8.1, was conservatively extrapolated into yearly response of pipe. In addition, by observing the limited source of strain gauge data in 2001 and 2002 from Chapter 5, the yearly cross sectional average strain accumulation is less than the standard magnitude set up in Section 8.1.

8.3.3 Effective Scope of Stress Relief

The pipeline orientation mostly coincides with the direction of the landslide movement. The strains in the lower part of the landslide are compressive. Optimal stress relief may be difficult to obtain by excavation of strain relief trenches randomly. It is necessary to determine the critical location of the pipeline where the maximum compressive strain occurs (this was included in Section 8.2) and the scope of soil removal to get the best stress relief effect.

Pembina River Crossing pipeline was constructed in 1986 and it has been continually monitored. There were two stress relieves since 1992. In March 2000, a long strain relief trench was excavated in the southern slope of the crossing. A total length of about 240 m of the pipeline was detached from the soil and allowed to rebound. The pipeline with about 10 m long concrete coating around the pipe surface is set on the bed of the creek.

Due to the existence of the slip surface, soils at the south slope move faster than the north slope. With the concrete coating around the pipe in the creek and the critical location being very close to the creek, the maximum length of stress relief at the south slope can be as much as 240 m long from the south bank of the creek to the left boundary of the slope. Stress relief procedure simulation has been illustrated in chapter 7. Large-displacement theory is used. To study the pattern and effective scope of stress relief procedure, maximum accumulated stress levels -82MPa, -143MPa and -250MPa at the critical portion of the pipe, correspondingly about one year, two years and four years of strain accumulation at average yearly precipitation, are relieved by digging the soil in different range of the pipe. Partial and full stress relieves are examined. Stress relief is assumed to be carried out at the south slope from trench length of 20m to 180m.

Figure 8.45 displays the relieved stress vs. distance from south bank of creek. It illustrates that if the initial stress level before stress relief is higher, the demanded trench scope is longer, and the effect of the stress relief procedure is more significant. The trench needs to be at least 180 m from south bank of creek for a complete stress relief.

The above FEA results show that as the soil is excavated, it results in a partial or full strain decrease in the pipeline at the south slope, but the stress in the pipeline at the north side of the creek is fairly high. This can be seen from Figure 8.46 to Figure 8.53. The pipeline with a maximum accumulated stress level of -250MPa was stress relieved at the south slope with trench lengths of 60m, 75m, 89m, 115m and 178m. Although the maximum stress of the pipeline was reduced, the compressive stress of the pipeline at the north slope is still high. Figure 8.46 and Figure 8.47 show that the top and bottom stresses of pipe cross section does not change after digging 60m trench on the south slope.

Figure 8.48 and Figure 8.49 show that the maximum compressive top and bottom stresses of the pipe cross section varying from 250MPa to 100MPa and 245MPa to 80MPa after stress relief with 89m long trench on the south slope, while leaving the compressive stress as high as 220MPa and 223MPa on the north slope. Figure 8.50 and Figure 8.51 shows the maximum top and bottom compressive stresses of the pipe cross section varying from 250MPa to 75MPa and 245MPa to 65MPa after digging 115m trench on south slope, while leaving the compressive stress as high as 210MPa and 215MPa on the north slope.

Figure 8.52 and Figure 8.53 show that the maximum top and bottom compressive stresses of pipe cross section varying from 250MPa to 1MPa and 245MPa to 0.5MPa after digging 178 m trench on south slope, while leaving the compressive stress as high as 200MPa and 201MPa on the north slope.

The analysis thus shows that excavating the pipeline only on the south slope is not enough, stress relief procedure has to be consummated on the north slope as well to reduce the high compressive stress in the pipe at the north slope. The same procedures as that done for the south slope are fulfilled. The results are seen from Figure 8.46 to Figure 8.53 that with the additional excavation of the pipeline on the north slope, the maximum top and bottom compressive stresses after stress relief in the pipe are 100MPa and 100MPa for an 89m south trench, 100MPa and 85MPa for a 115m south trench and 80MPa and 60MPa for a 178m south trench.

8.4 Discussion of the Finite Element Analysis

This Chapter has been aimed to apply the numerical procedure for the buried pipeline in Pembina River Crossing. The validity of the model is verified using the field data. Moreover the stress relief procedure has been investigated. The finite element model is used to develop the optimum stress relief procedure and operating schedule based on the precipitation data.

FEA results demonstrate that the stress relief procedure of the pipeline at Pembina River Crossing is necessary to reduce the compressive stress level in the pipe. In general if precipitation in May-September is about 400mm, or yearly precipitation is about 550mm, this procedure is needed every six years. The effectiveness of stress relief is related to the length of the stress relieve section. Pipeline excavation should be implemented at the south slope and north slope for a complete stress relief.

Though this model was developed from the specific site, it may be employed to carry out parametric study on pipeline behaviour with different variables, which will provide valuable guidelines for pipelines at other sites. This will be presented in the Chapter 9.

Table 8.1 Comparison of Soil Movement U_2 , mm/yr near Ground Surface at 5SIs in 2000

SI	SI5A	SI8	SI10B	SI11B	SI12B
Field data	19.9 mm/yr	1.6 mm/yr	40.4 mm/yr	32.4 mm/yr	20.9 mm/yr
FEM	20.4 mm/yr	1.5 mm/yr	28.7 mm/yr	31.4 mm/yr	14.7 mm/yr
Test-to-Predicted Ratio	0.98	1.07	1.41	1.03	1.42

Table 8.2 SG1 SG2 SG3 SG4 at Strain Gauge Stations 1-4

Stations	Strain Accumulated	SG1	SG2	SG3	SG4	Average
Station 1	Jul.-Nov.2000	-44 $\mu\epsilon$	-118 $\mu\epsilon$	-79 $\mu\epsilon$	371 $\mu\epsilon$	33 $\mu\epsilon$
Station 2	Sep.-Nov.2000	-73 $\mu\epsilon$	-29 $\mu\epsilon$	NA	NA	NA
Station 3	Jul.-Sep.2000	-143 $\mu\epsilon$	-172 $\mu\epsilon$	217 $\mu\epsilon$	-77 $\mu\epsilon$	-44 $\mu\epsilon$
Station 4	Jul.-Sep.2000	-92 $\mu\epsilon$	-107 $\mu\epsilon$	-63 $\mu\epsilon$	-61 $\mu\epsilon$	-81 $\mu\epsilon$

Table 8.3 Comparison of Average Axial Accumulated Strain ϵ_a at Station 1, Station 3 and Station 4 in the Year 2000

	Station 1	Station 3	Station 4
Field data	79 $\mu\epsilon$	-176 $\mu\epsilon$	-324 $\mu\epsilon$
FEM	119 $\mu\epsilon$	-180 $\mu\epsilon$	-372 $\mu\epsilon$
Test-to-Predicted Ratio	0.66	0.98	0.87

Table 8.4 Comparison of Average Axial Accumulated Stress σ_a at Station 1, Station 3 and Station 4 in the Year 2000

	Station 1	Station 3	Station 4
From Field data	16.2 MPa	-36.1 MPa	-66.4 MPa
FEM	24.5 MPa	-36.8 MPa	-76.2 MPa
Test-to-Predicted Ratio	0.66	0.98	0.87

Table 8.5 Comparison of Soil Movement U_2 , mm/yr near Ground Surface in 1995

SI	SI5	SI8	SI12
Field data	9.4 mm/yr	1.6 mm/yr	12.7 mm/yr
FEM	13.6 mm/yr	2.2 mm/yr	11.8 mm/yr
Test-to-Predicted Ratio	0.69	0.71	1.08

Table 8.6 Comparison of Soil Movement U_2 , mm/yr near Ground Surface in 1992

SI	SI5	SI8	SI12
Field data	7.3 mm/yr	1.6 mm/yr	15.8 mm/yr
FEM	9.8 mm/yr	1.6 mm/yr	13.6 mm/yr
Test-to-Predicted Ratio	0.75	1.00	1.16

Table 8.7 Comparison of Soil Movement U_2 , mm/yr near Ground Surface in 1989

SI	SI6	SI7
4Months Field data	64.9mm/4month	30.9mm/4month
Yearly Field data	81.4mm/yr	46.0 mm/yr
FEM	80.4mm/yr	55.0mm/yr
Test-to-Predicted Ratio	1.01	0.84

Table 8.8 Maximum Accumulated Compressive Stress/Strain and Theirs Locations in 1989, 1992, 1995, and 2000

	1989	1992	1995	2000
ϵ_{\max} , $\mu\epsilon$	-1074.6	-292.7	-380.5	-544.4
σ_{\max} , MPa	-220.3	-60.0	-78.0	-111.6
Horizontal Coordinate,m	71614.5 Top	71614.5 Top	71614.5 Top	71614.5 Top

Table 8.9 Estimation of Yearly Maximum Axial Stress/Strain Accumulation in 1986-2005

Year	May-Sep Precipitation at BrazeauLo mm	Yearly Maximum Axial Stress, MPa	Yearly Maximum Axial Stain, $\mu\epsilon$
1986	563.30	-166.0	-810
1987	348.20	-61.0	-298
1988	376.90	-64.0	-312
1989	579.50	-220.3	-1075
1990	532.90	-94.8	-462
1991	408.90	-67.3	-328
1992	338.60	-60.0	-293
1993	413.60	-67.8	-331
1994	470.60	-73.8	-360
1995	511.30	-78.0	-380
1996	394.00	-65.8	-321
1997	426.60	-69.2	-337
1998	607.00	-307.2	-1499
1999	478.90	-74.6	-364
2000	545.10	-111.6	-544
2001	397.80	-66.2	-323
2002	329.10	-59.0	-288
2003	293	-55.2	-269
2004	430.1	-69.5	-339
2005	486.8	-75.4	-368

Table 8. Soil Movement U_2 mm in three years near Ground Surface with normal precipitation

SI	SI5	SI8	SI12
Field data	28.3 mm	4.7 mm/yr	38.0 mm/yr
FEM	34.0 mm	3.6	34.3
Test-to-Predicted Ratio	0.83	1.31	1.11

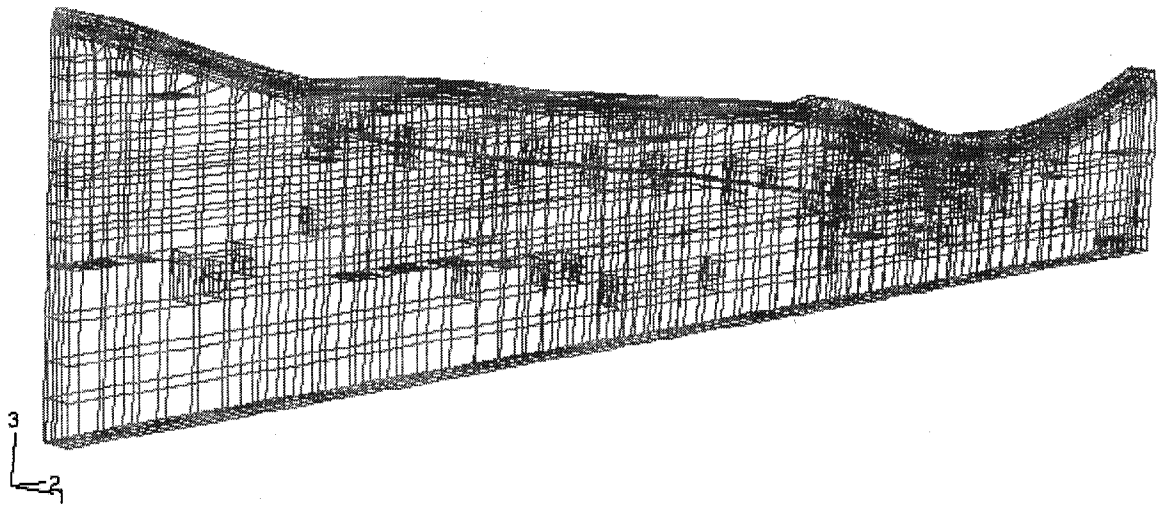


Figure 8.1 3D View of the Finite Element Model of the Pipeline and Slope

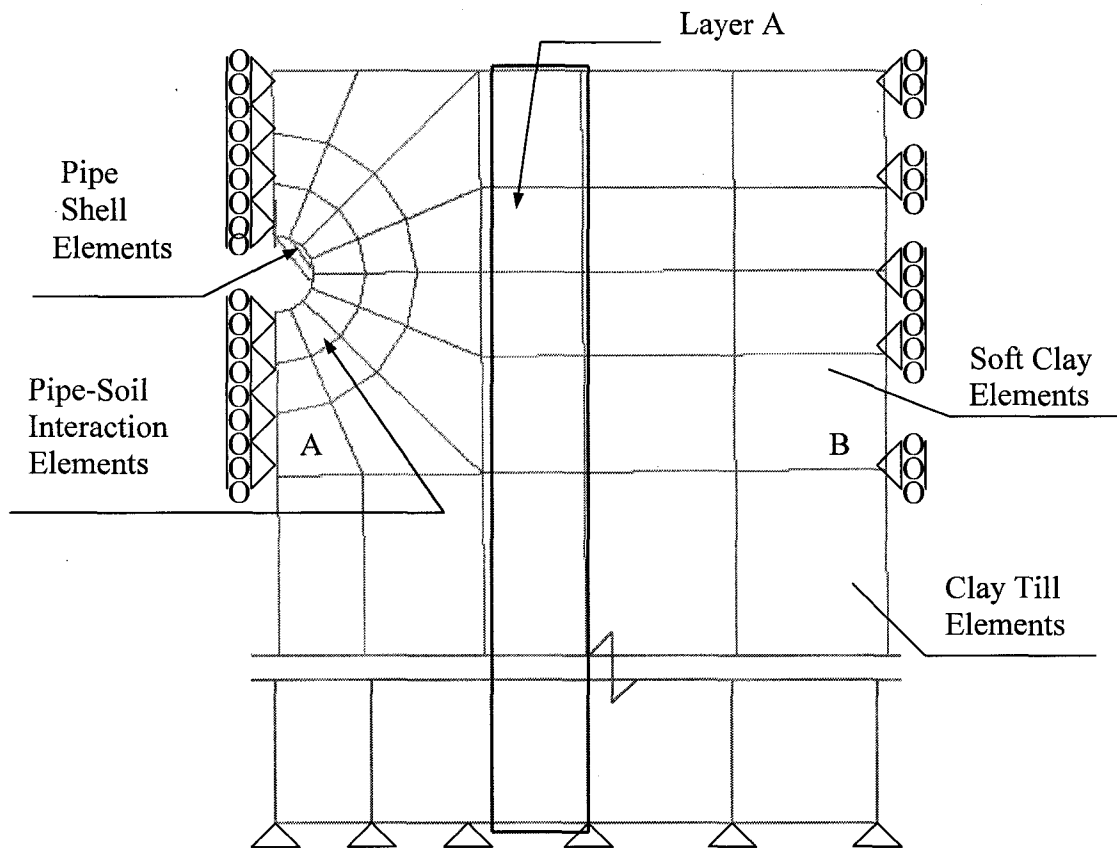


Figure 8.2 Soil Layer

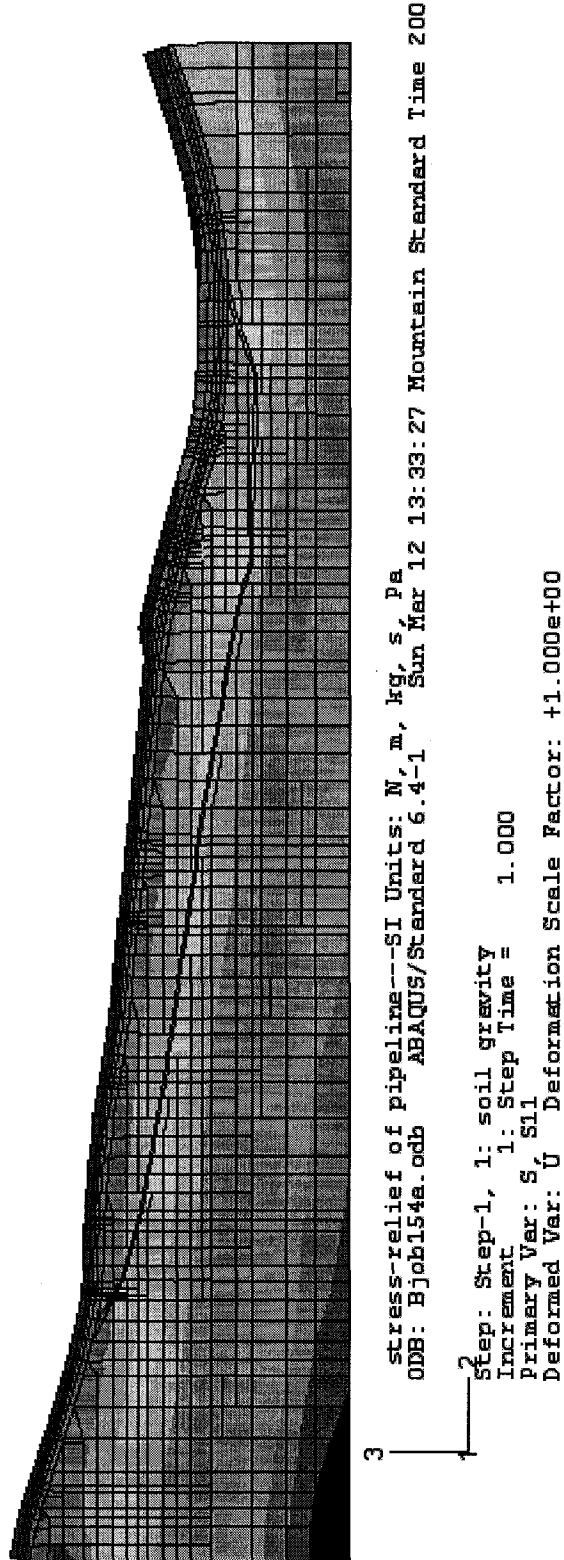
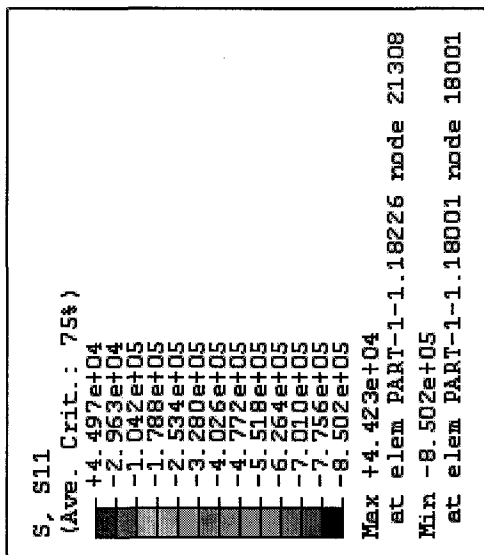
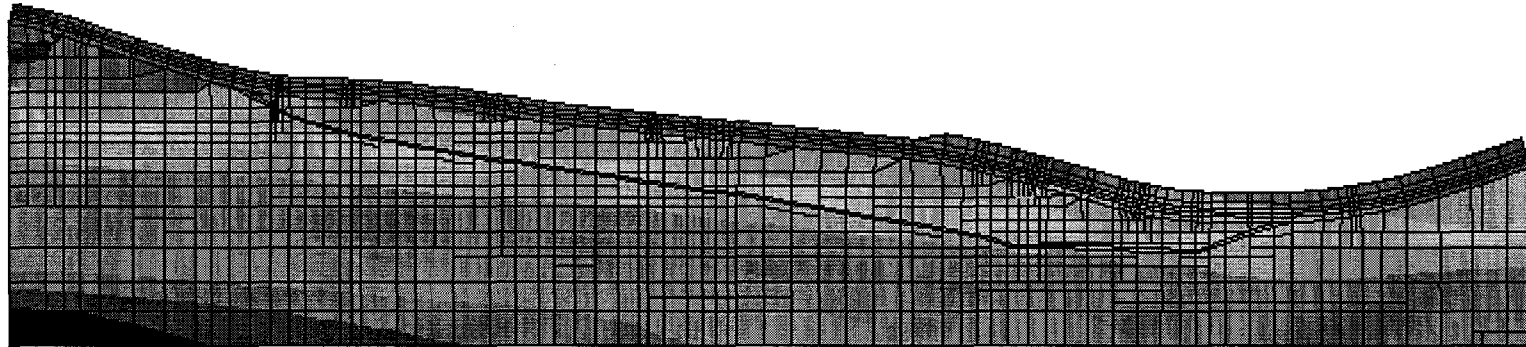
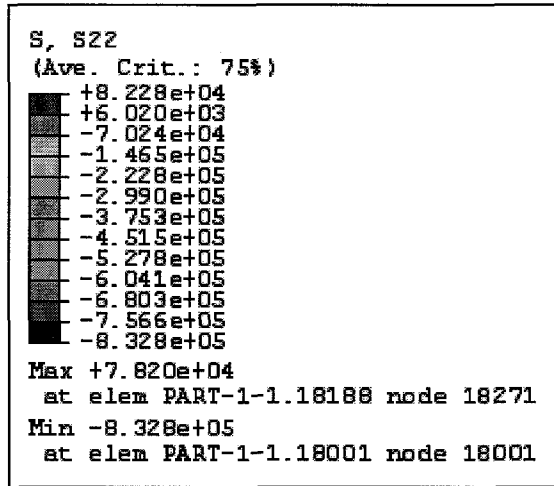


Figure 8.3 Contour of Stress S11 at Soil Layer A after Gravity Load

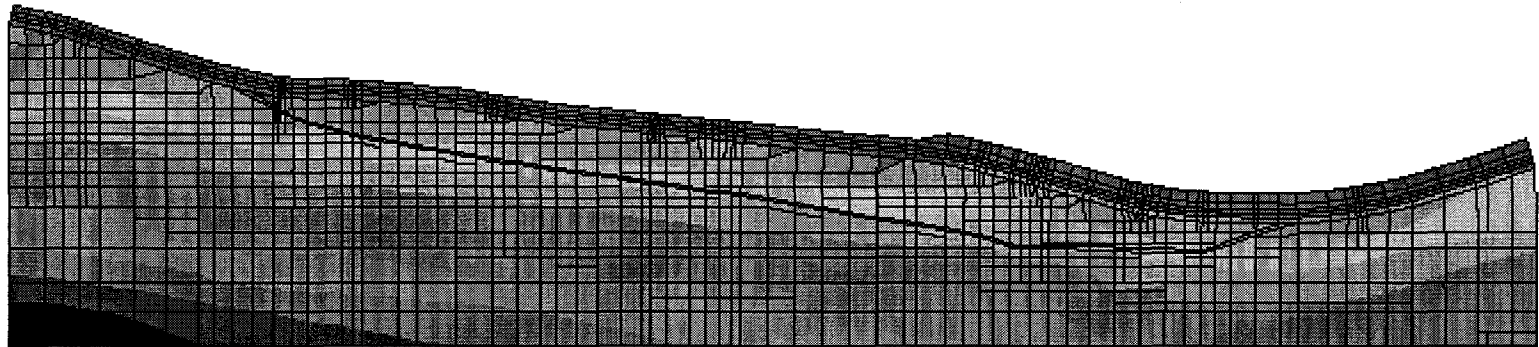
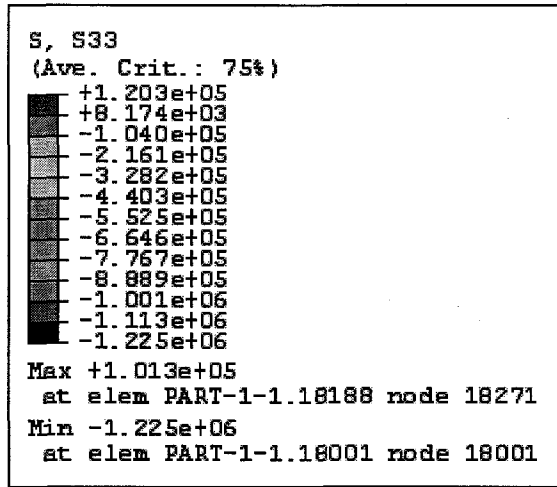


3
stress-relief of pipeline---SI Units: N, m, kg, s, Pa
ODB: Bjob154a.odb ABAQUS/Standard 6.4-1 Sun Mar 12 13:33:27 Mountain Standard Time 200

2
Step: Step-1, 1: soil gravity
Increment 1: Step Time = 1.000
Primary Var: S, S22
Deformed Var: U Deformation Scale Factor: +1.000e+00

1

Figure 8.4 Slope Stress S22 Contour at Soil Layer A after Gravity Load

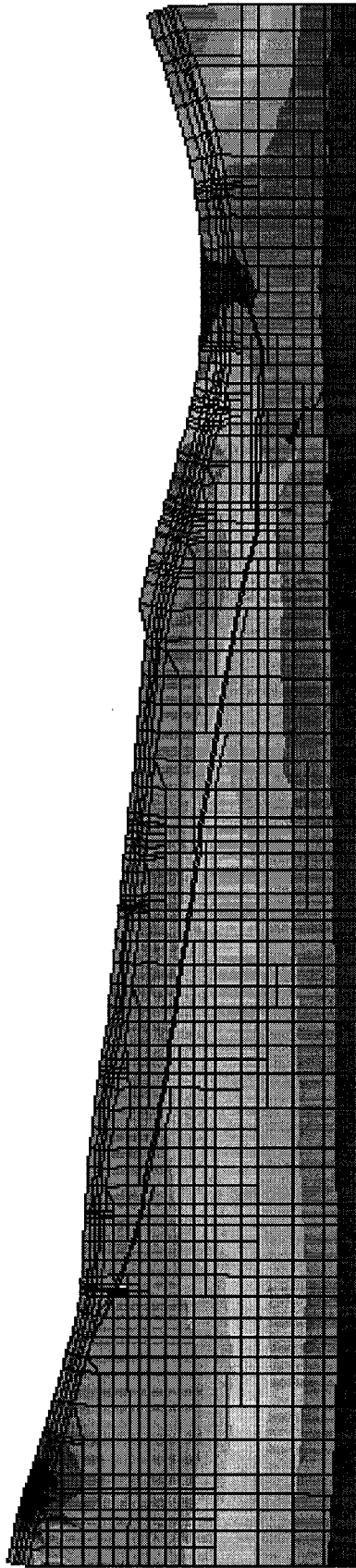
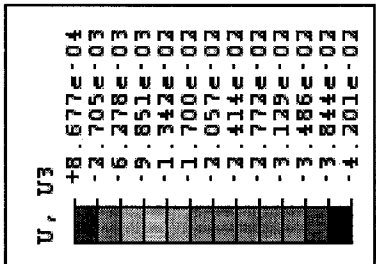


3
stress-relief of pipeline---SI Units: N, m, kg, s, Pa
ODB: Bjob154a.odb ABAQUS/Standard 6.4-1 Sun Mar 12 13:33:27 Mountain Standard Time 200

2
Step: Step-1, 1: soil gravity
Increment 1: Step Time = 1.000
Primary Var: S, S33
Deformed Var: U Deformation Scale Factor: +1.000e+00

1

Figure 8.5 Slope Stress S33 Contour at Soil Layer A after Gravity Load



3

stress: relief of pipeline... SI Units: N, m, kg, s, Pa
 CDB: 154eD15.cdb ABAQUS/standard 6.4-1 Wed Apr 19 19:44:06 PDT 2006

2

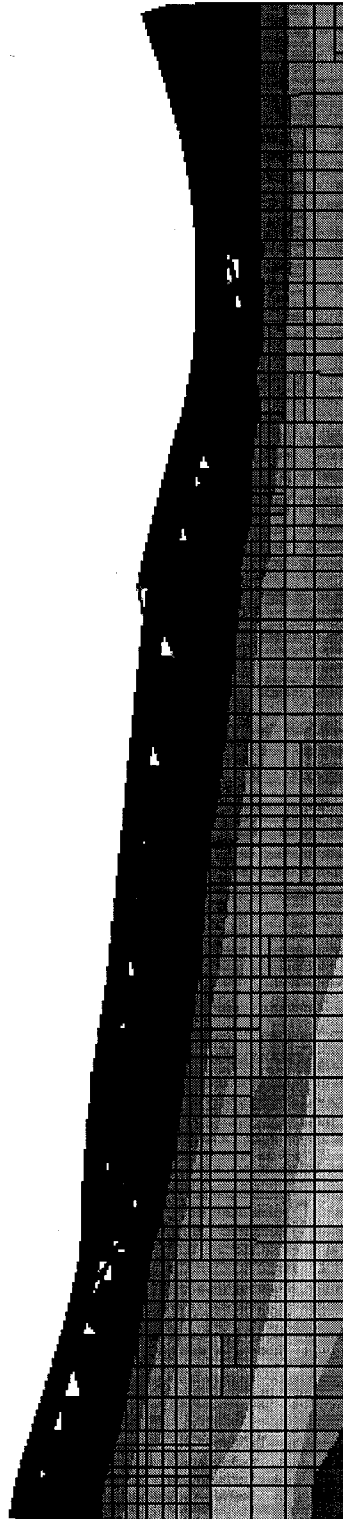
Step: Step-1, 1: soil gravity
 Increment 1: Step Time = 1.000
 Primary Var: U, U3
 Deformed Var: U Deformation Scale Factor: +1.000e+00

Figure 8.8 Contour of Soil Movement U_3 of Layer A after Gravity Load

```

POIR
(Ave. Crit.: 75%)
+4.964e+05
+4.551e+05
+4.137e+05
+3.723e+05
+3.309e+05
+2.896e+05
+2.482e+05
+2.068e+05
+1.655e+05
+1.241e+05
+8.274e+04
+4.137e+04
-8.419e-39
Max +4.964e+05
  at elem PART-1-1.18001 node 18001
Min +0.000e+00
  at elem PART-1-1.6333 node 6343

```



3

SI Units: N, m, kg, s, Pa-4m W-rise
 ODB: Bjob33.odb ABAQUS/Standard 6.4-1 Wed Nov 30 00:29:43 Mountain Standard Time 2005

2

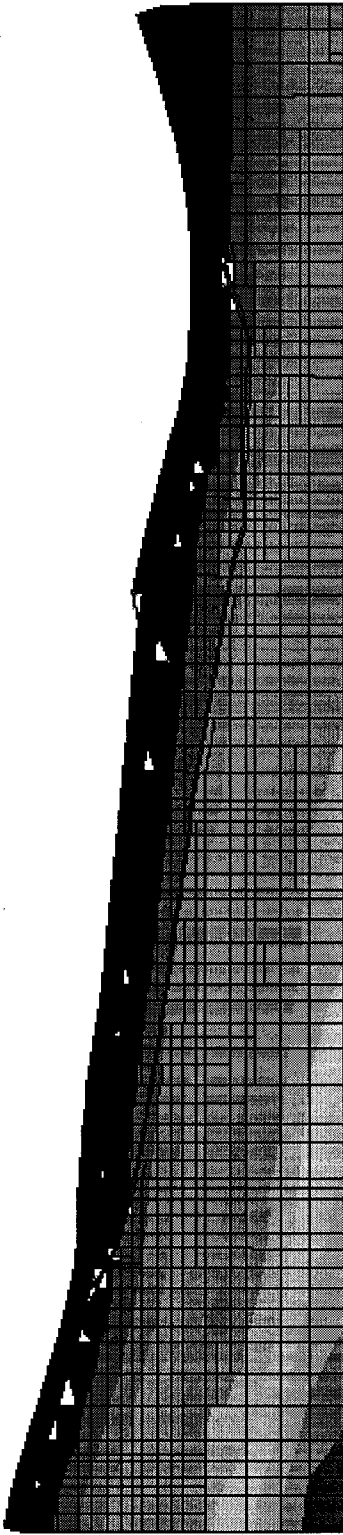
Step: Step-14, 14: water14
 Increment 18: Step Time = 2.5920E+06
 Primary Var: POR
 Deformed Var: U Deformation Scale Factor: +1.000e+00

Figure 8.9 Pore Pressure Contour at Soil Layer A at Water Table 14

POR
 (Ave. Crit.: 75%)

+	5.856e+05
+	5.368e+05
+	4.880e+05
+	4.392e+05
+	3.904e+05
+	3.416e+05
+	2.928e+05
+	2.440e+05
+	1.952e+05
+	1.464e+05
+	9.759e+04
+	4.880e+04
-	1.306e-38

Max +5.856e+05
 at elem PART-1-1.18001 node 18001
 Min +0.000e+00
 at elem PART-1-1.4633 node 4643

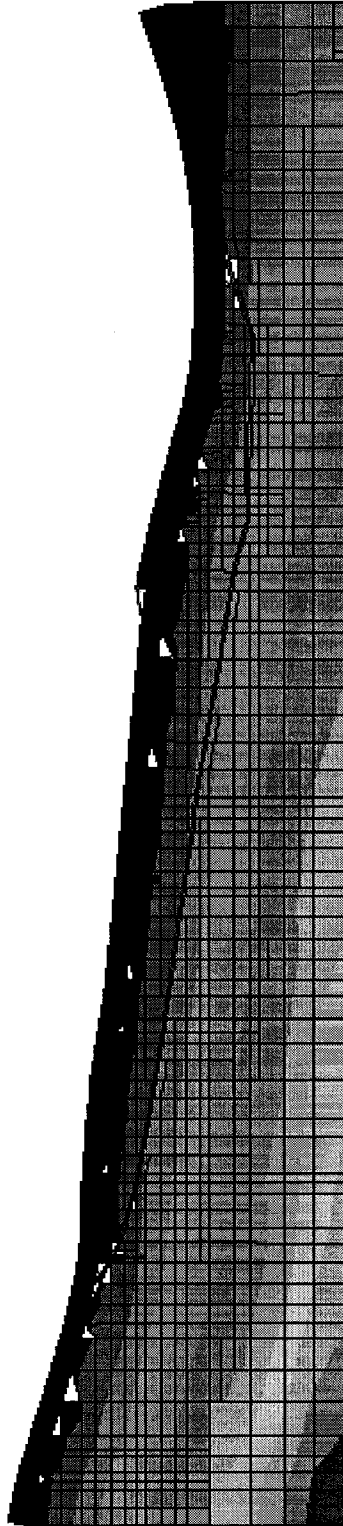
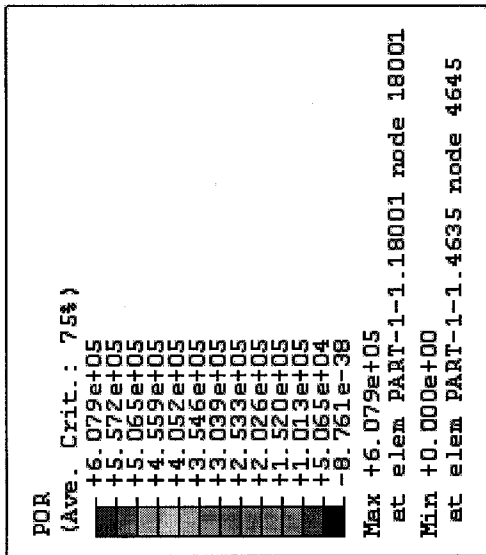


3
 2
 1

SI Units: N, m, kg, s, Pa--4m W-rise
 ODB: Bjob33.odb ABAQUS/Standard 6.4-1 Wed Nov 30 00:29:43 Mountain Standard Time 2005

Step: Step-16, 16: water16
 Increment 20: Step Time = 2.5920E+06
 Primary Var: POR
 Deformed Var: U Deformation Scale Factor: +1.000e+00

Figure 8.10 Pore Pressure Contour at Soil Layer A at Water Table 16



SI Units: N, m, kg, s, Pa--4m W-rise
 ODB: Bjob33.odb ABAQUS/Standard 6.4-1 Wed Nov 30 00:29:43 Mountain Standard Time 2005

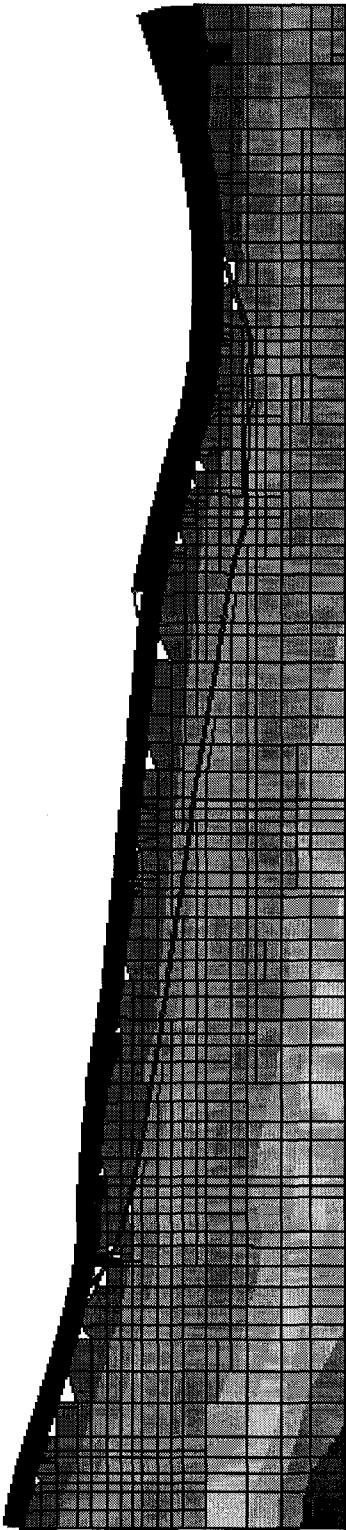
Step: Step-17, 17: water20
 Increment
 Primary Var: POR
 Deformed Var: U Deformation Scale Factor: +1.000e+00

Figure 8.11 Pore Pressure Contour at Soil Layer A at Water Table 20

POR
 (Ave. Crit.: 75%)

+	6.301e+05
+	5.775e+05
+	5.251e+05
+	4.726e+05
+	4.201e+05
+	3.676e+05
+	3.151e+05
+	2.626e+05
+	2.100e+05
+	1.575e+05
+	1.050e+05
+	5.251e+04
-	2.009e-38

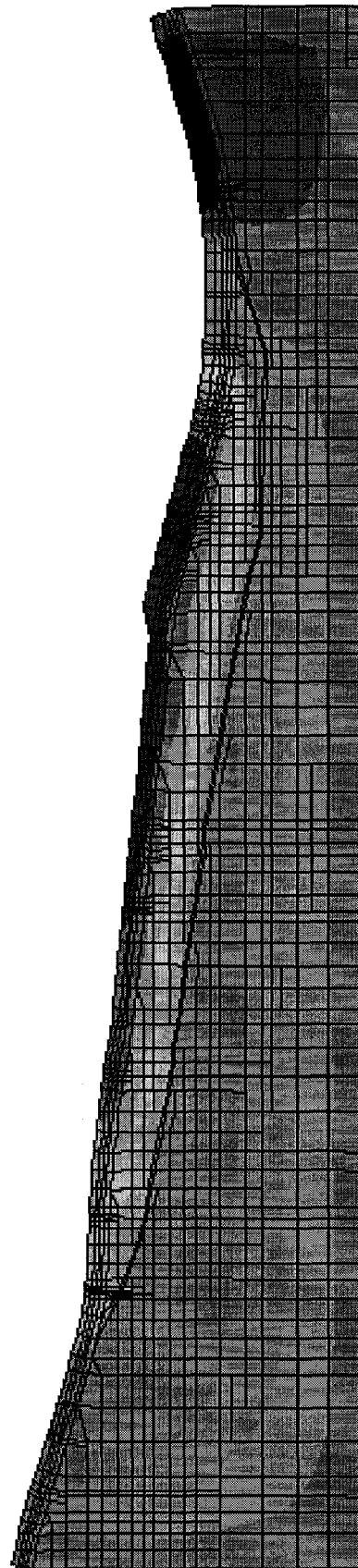
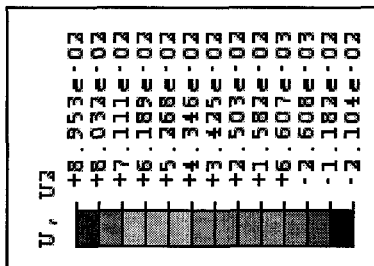
Max +6.301e+05
 at elem PART-1-1.18001 node 18001
 Min +0.000e+00
 at elem PART-1-1.11333 node 11343



SI Units: N, m, kg, s Pa--4m W-rise
 ODB: Bjob33.odb ABAQUS/Standard 6.4-1 Wed Nov 30 00:29:43 Mountain Standard Time 2005

Step: Step-18, 18: water704
 Increment 18: Step Time = 2.59208e+06
 Primary Var: POR
 Deformed Var: U Deformation Scale Factor: +1.000e+00

Figure 8.12 Pore Pressure Contour of Soil Layer A at Water Table 704



3

stress relief of pipeline...SI Units: N, m, kg, s, Pa
 CDB: 154aD15.cdb ABRQUS/Standard 6.4.1 Wed Apr 19 19:44:06 PDT 2006

2

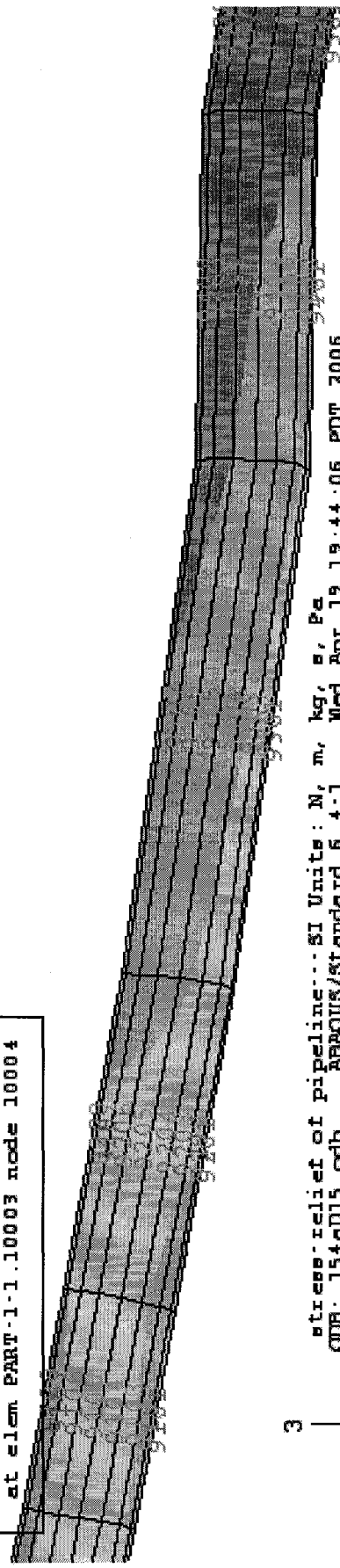
Step: Step-14, 14: creep
 Increment SI: Step Time = 1.6000E+07
 Primary Var: U, U2
 Deformed Var: U Deformation Scale Factor: +1.000e+00

Figure 8.13 Contour of Soil Movement U₂ of Layer A after Creep

```

S, S22
SMXS, (fraction = -1.0)
(Ave. Crit.: 75%)
-1.706e+02
-2.160e+02
-2.615e+02
-3.069e+02
-3.523e+02
-3.977e+02
-4.432e+02
-4.886e+02
-5.340e+02
-5.795e+02
-6.249e+02
-6.703e+02
-7.158e+02
Max -1.754e+02
at elem PART-1-1.7408 node 7409
Min -6.377e+02
at elem PART-1-1.10003 node 10004

```



3

stress relief of pipeline...SI Units: N, m, kg, s, Pa
ODB: 154d15.odb ABAQUS/Standard 6.4-1 Wed Apr 19 19:44:06 PDT 2006

Step: Step-9, 9: add pipe
Increment 2: Step Time = 1.000
Primary Var: S, S22
Deformed Var: U Deformation Scale Factor: +1.000e+00

Figure 8.14 Contour of Axial Stress S22 at the Critical Location of Pipeline Before Load

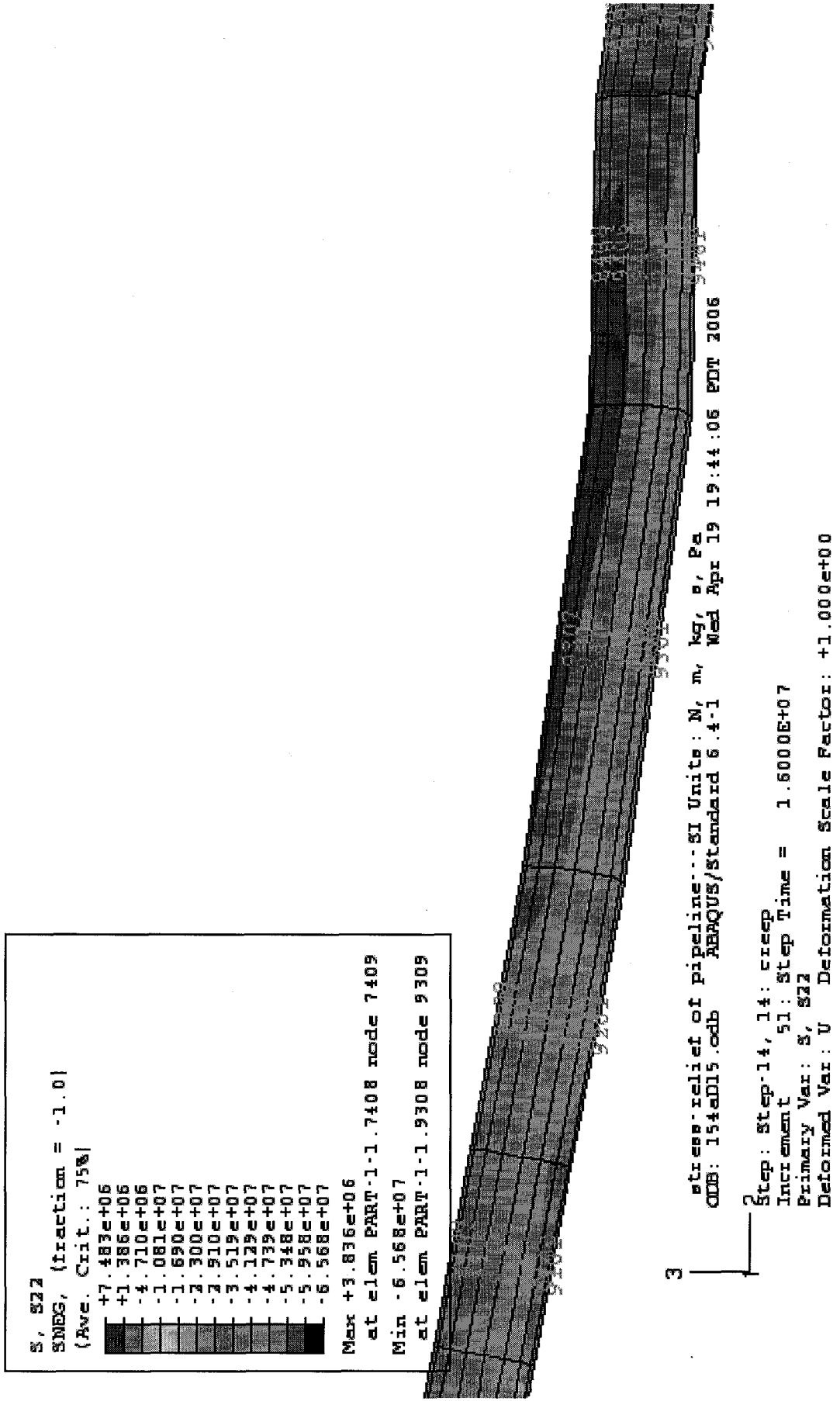


Figure 8.15 Contour of Axial Stress S22 at the Critical Location of Pipeline After Creep

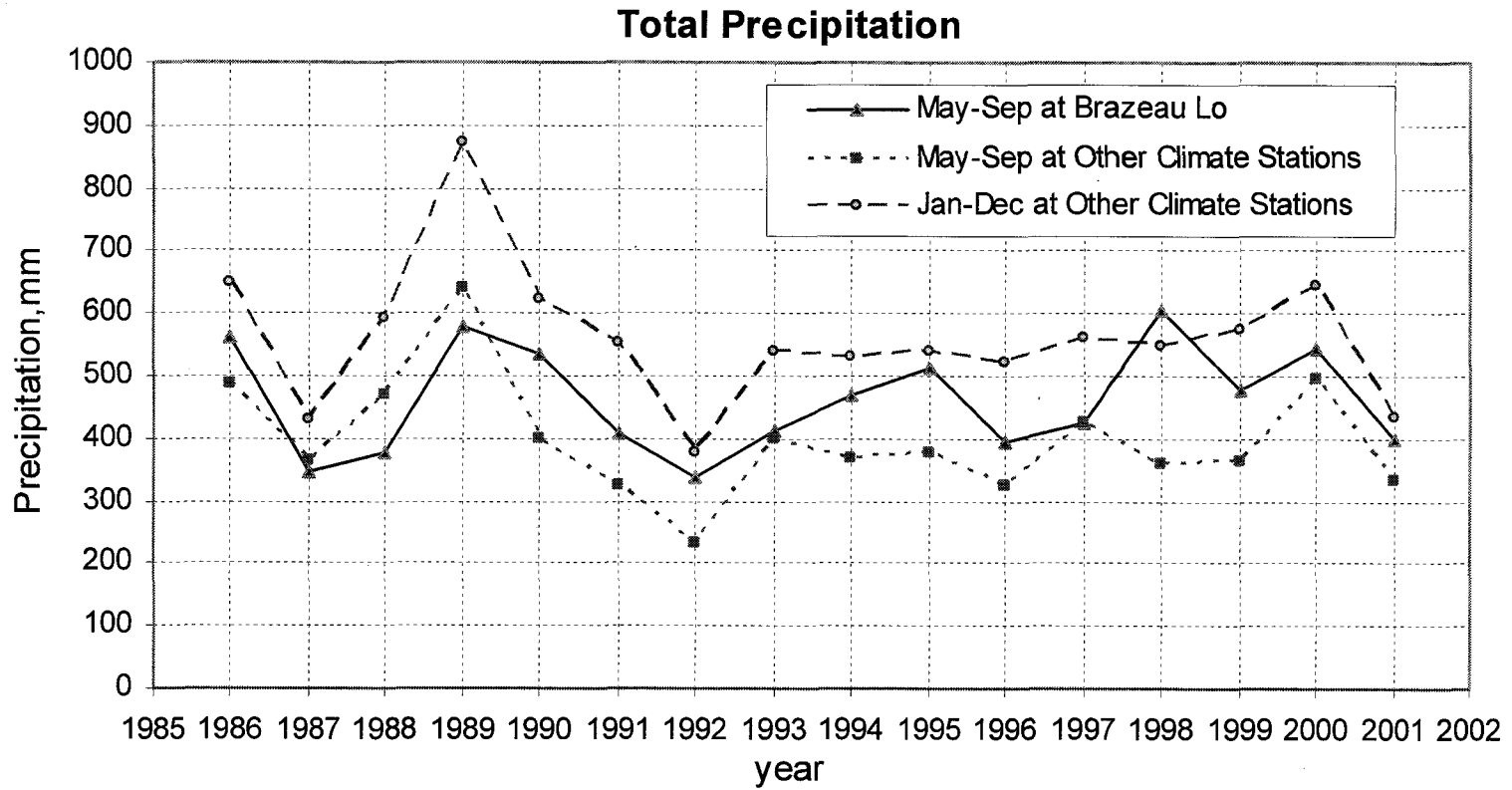


Figure 8.16 Yearly and May-September Precipitation for Years 1986-2001

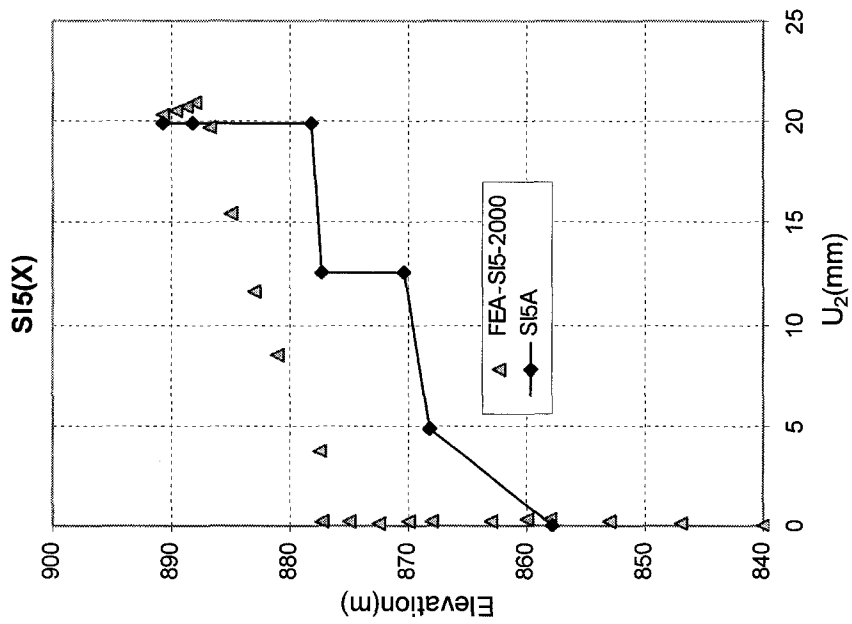
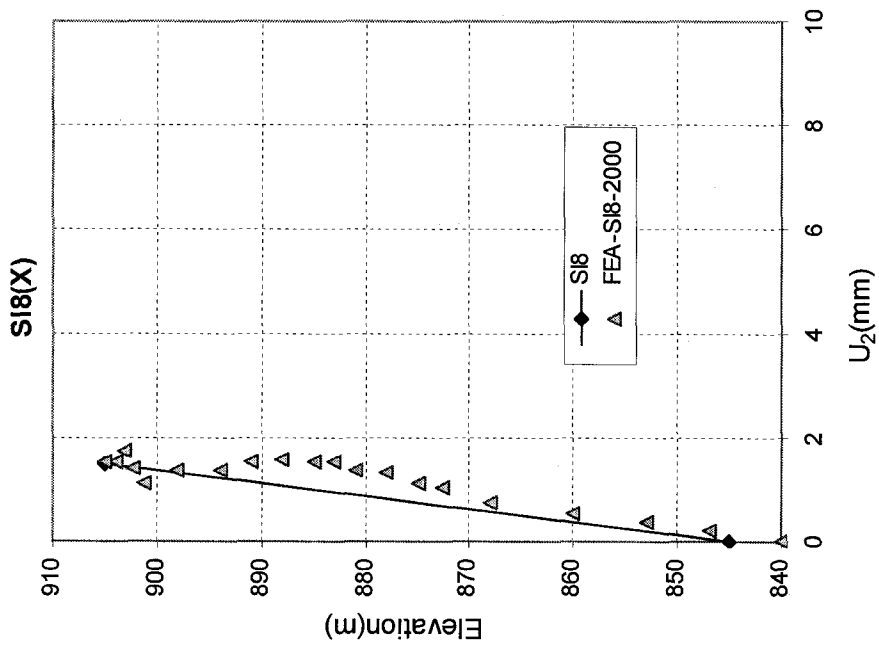


Figure 8.17 Comparison of Soil Movement U₂ at Different Depths for SI5 and SI8 in the Year 2000

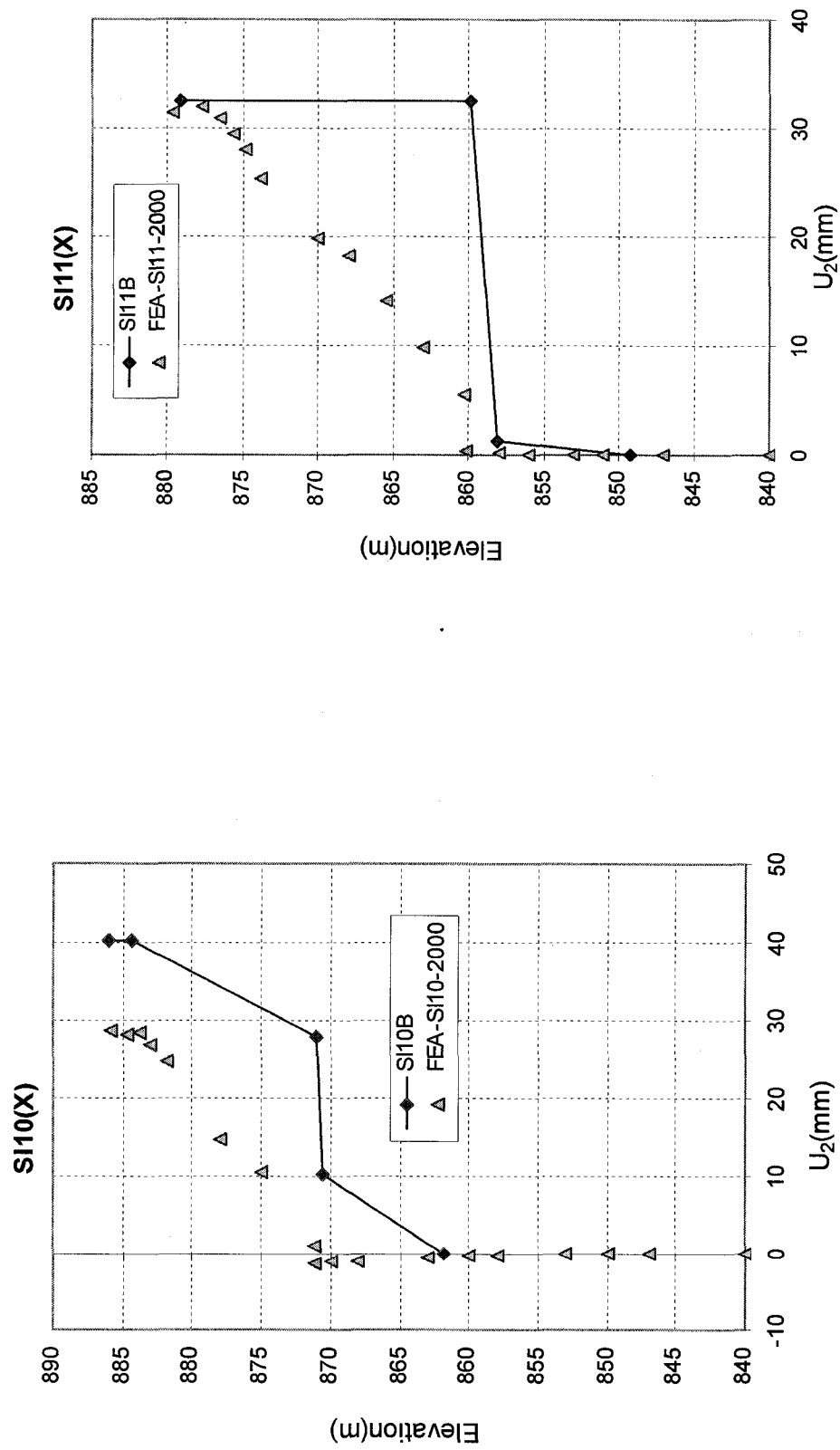


Figure 8.18 Comparison of Soil Movement U_2 at Different Depths for SI10B and SI11B in Year 2000

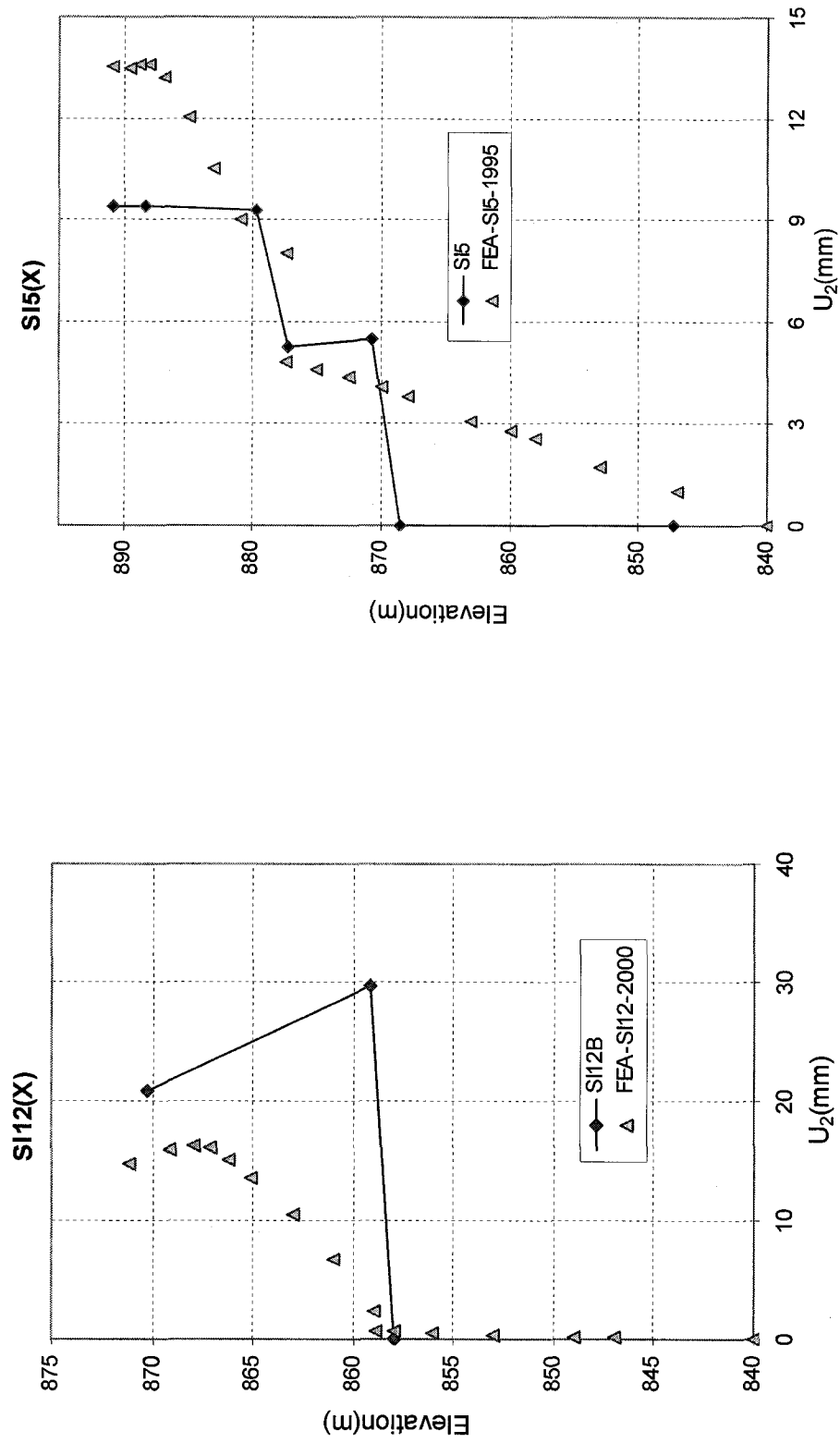


Figure 8.19 Comparison of Soil Movement U₂ at Different Depths for SI12B in 2000 and SI5 in 1995

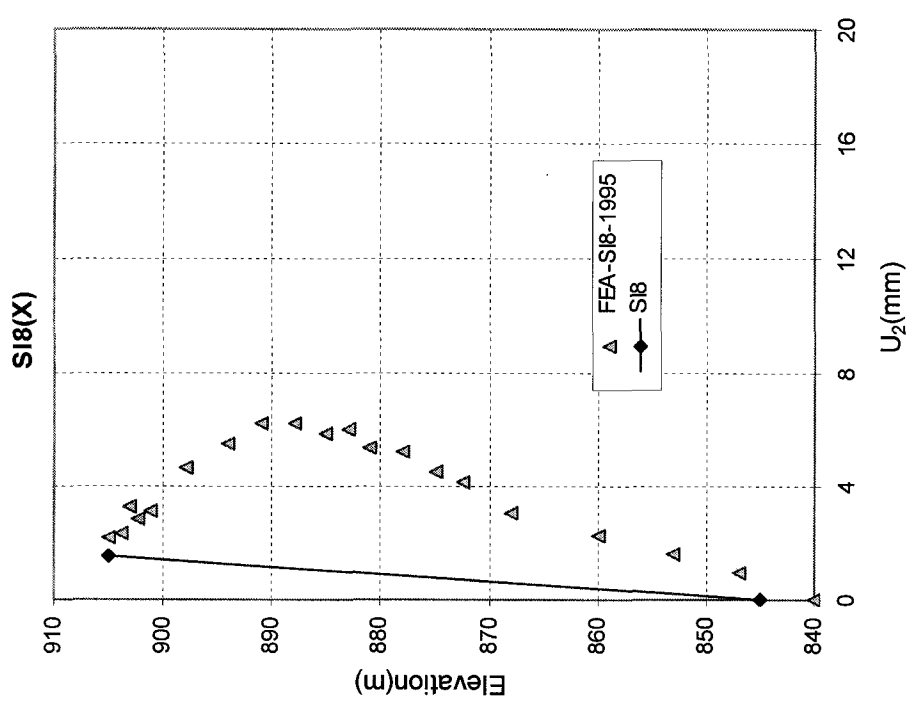
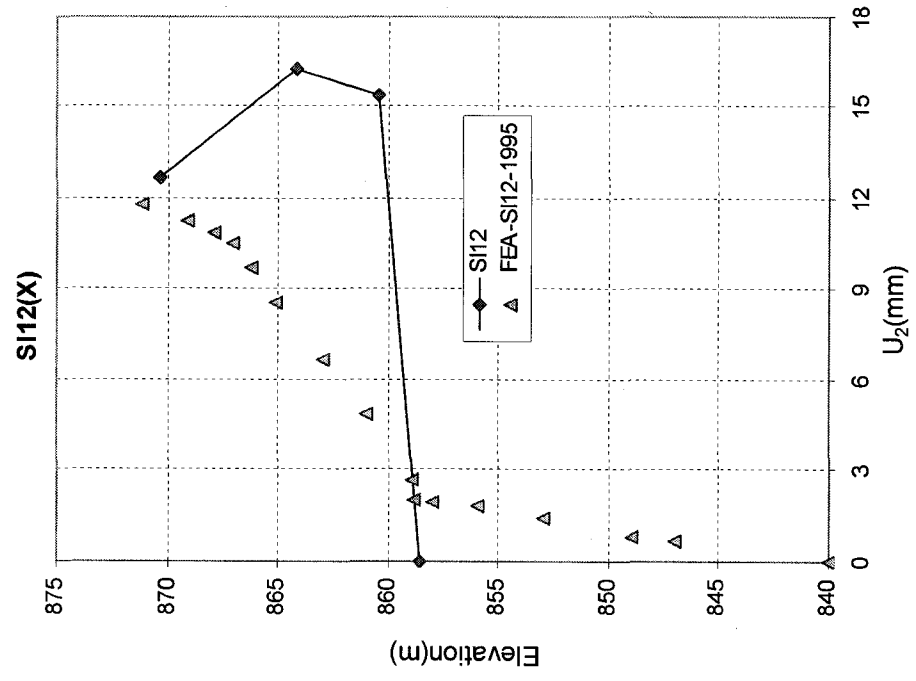


Figure 8.20 Comparison of Soil Movement U_2 at Different Depths for SI8 and SI12 in 1995

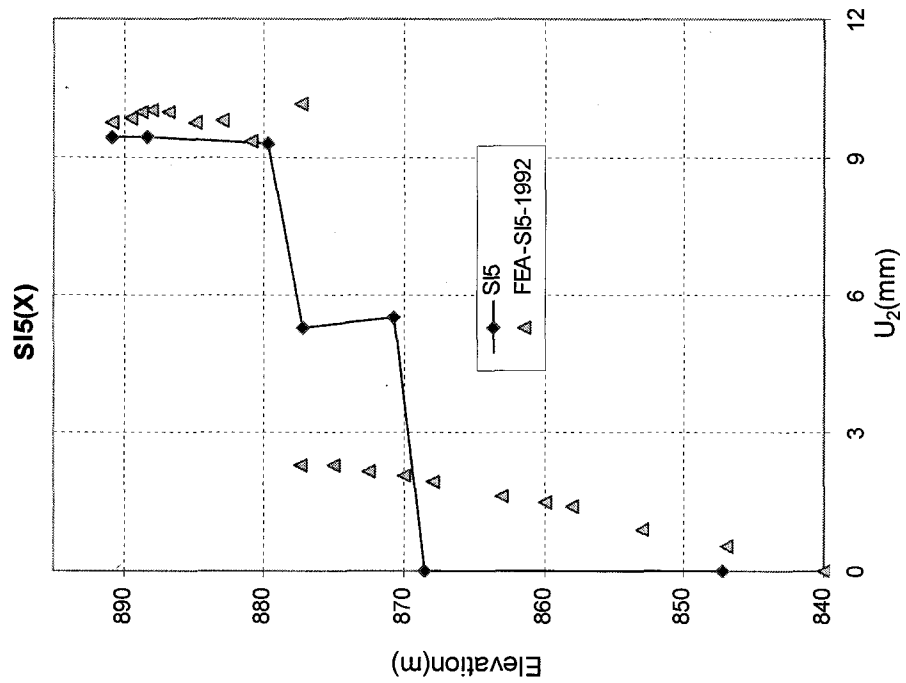
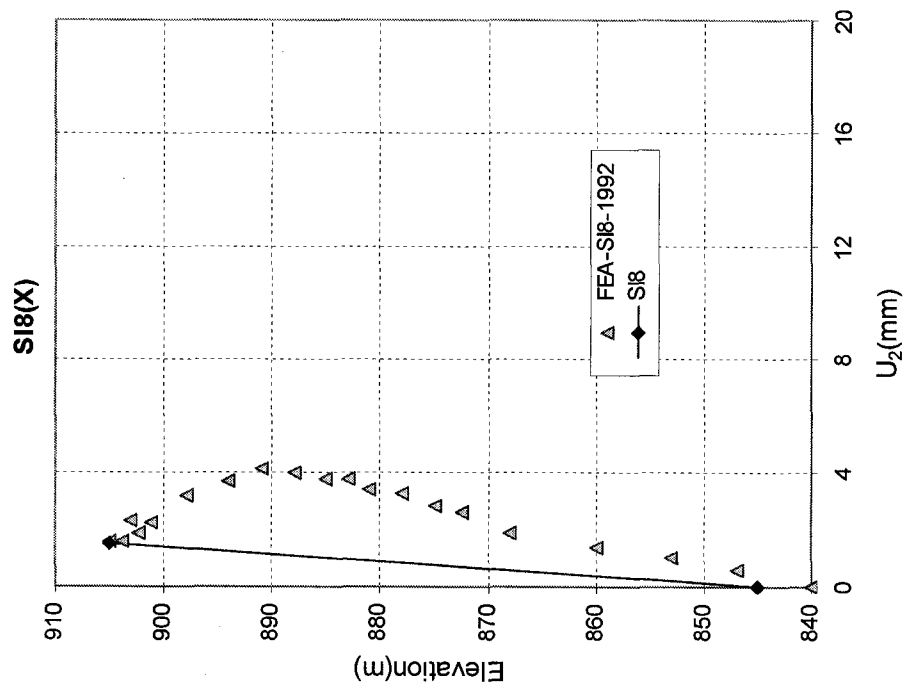


Figure 8.21 Comparison of Soil Movement U_2 at Different Depths for SI5 and SI8 in 1992

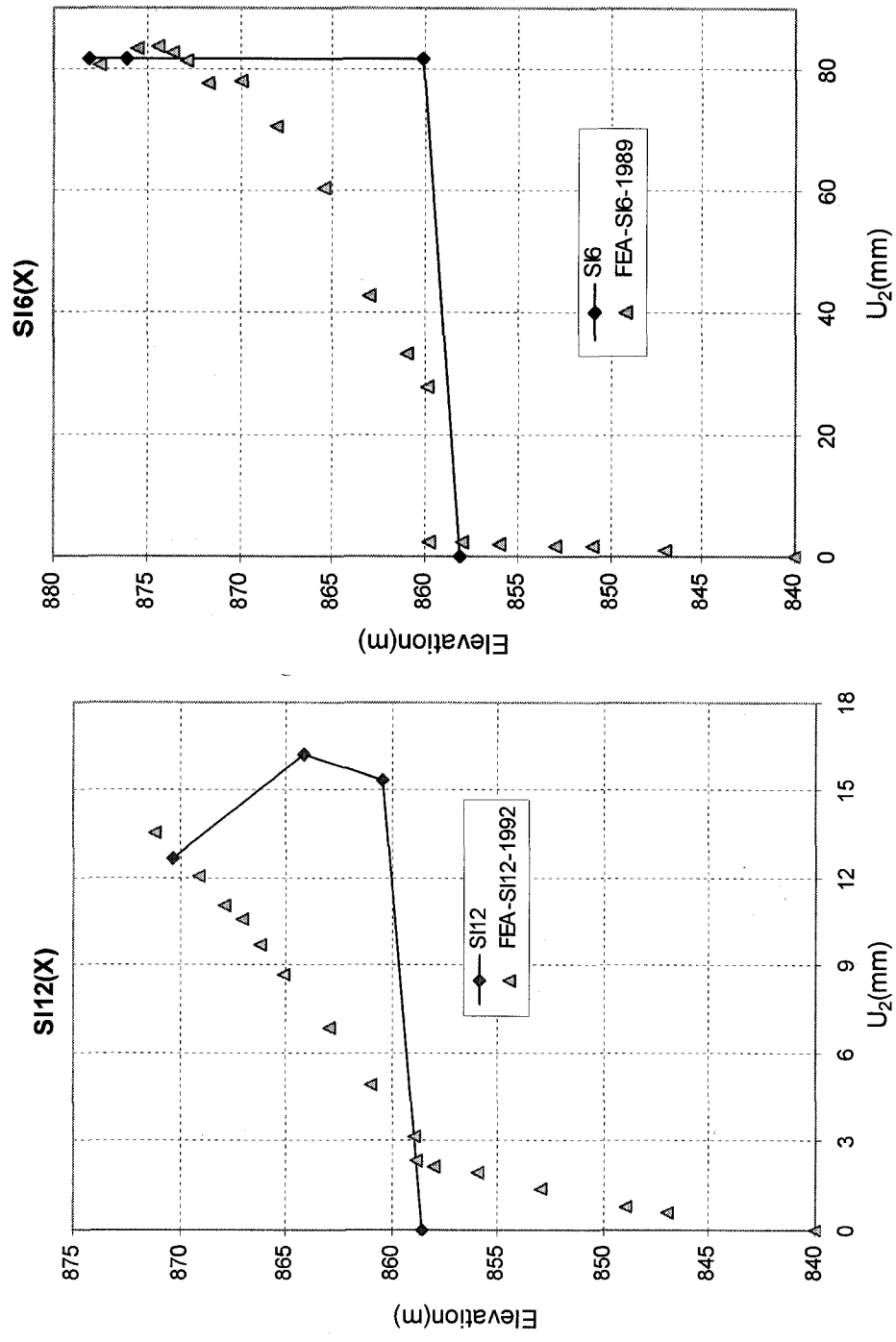


Figure 8.22 Comparison of Soil Movement U_2 at Different Depths for SI12 in 1992 and SI6 in 1989 .

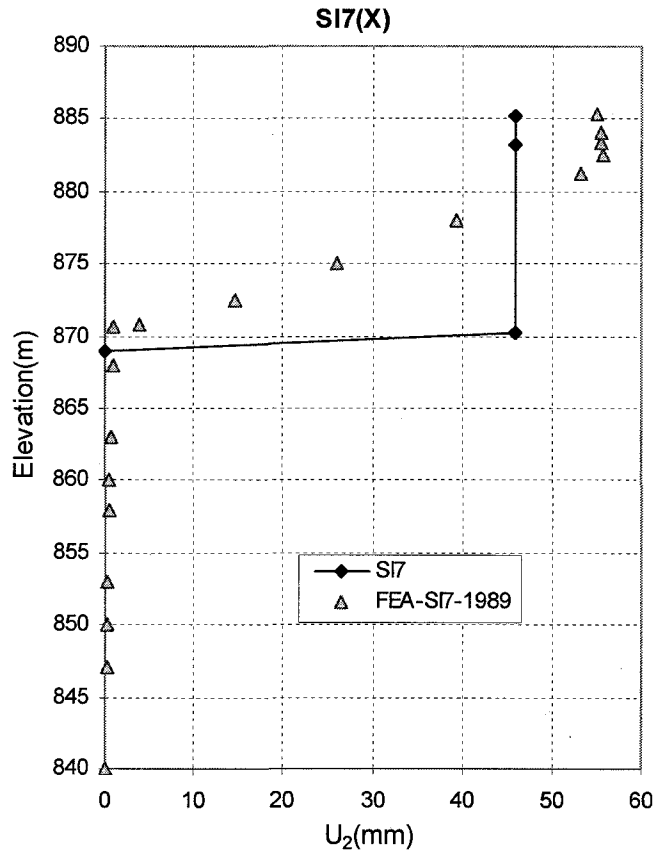


Figure 8.23 Comparison of Soil Movement U_2 at Different Depths for SI7 in 1989

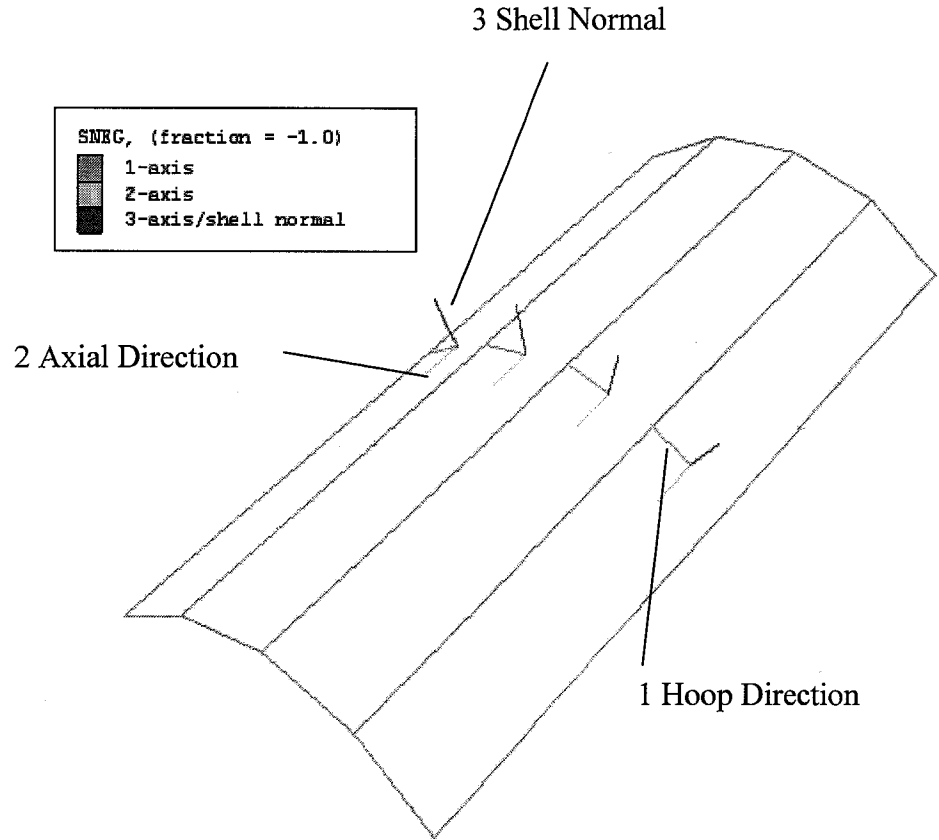


Figure 8.24 Local Coordinate System of Shell Element

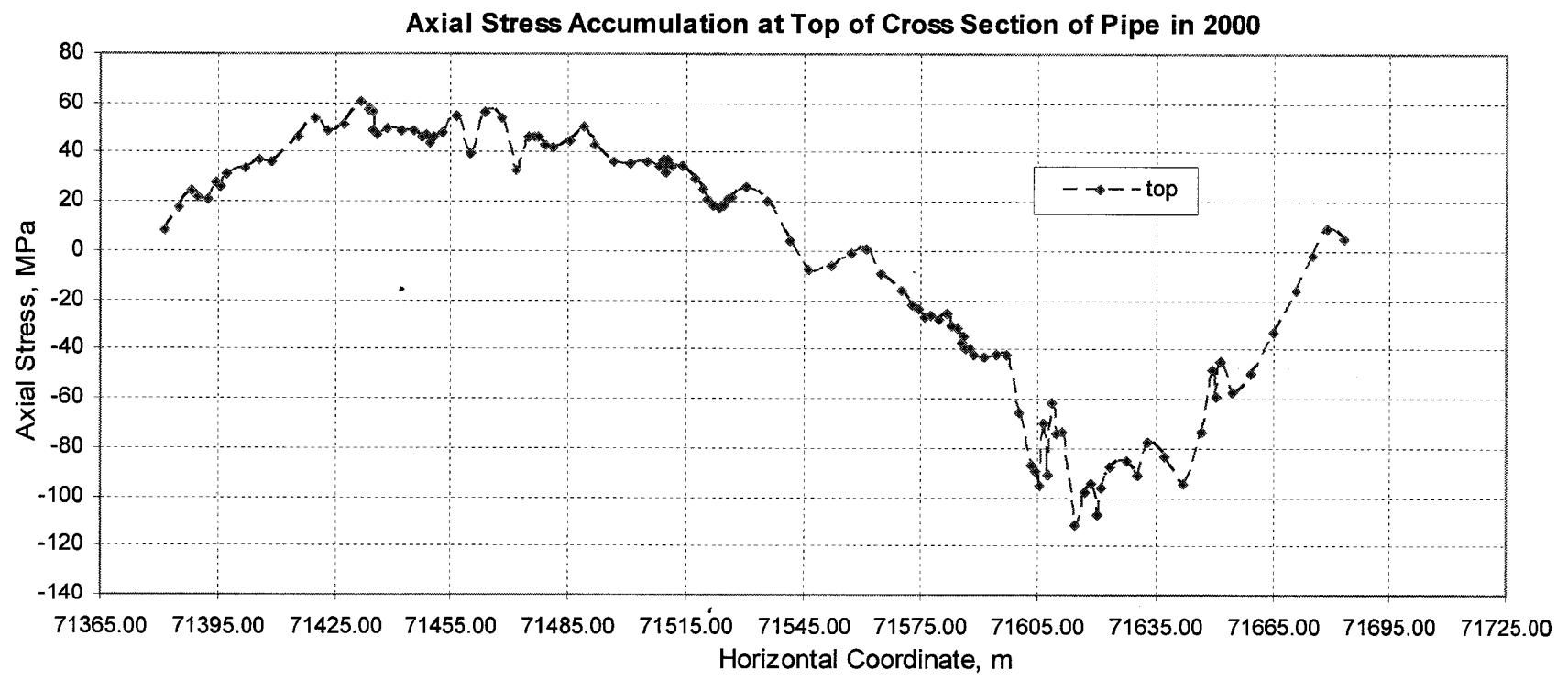


Figure 8.25 Top Axial Stress Accumulation of the Cross Section along the Pipeline in 2000

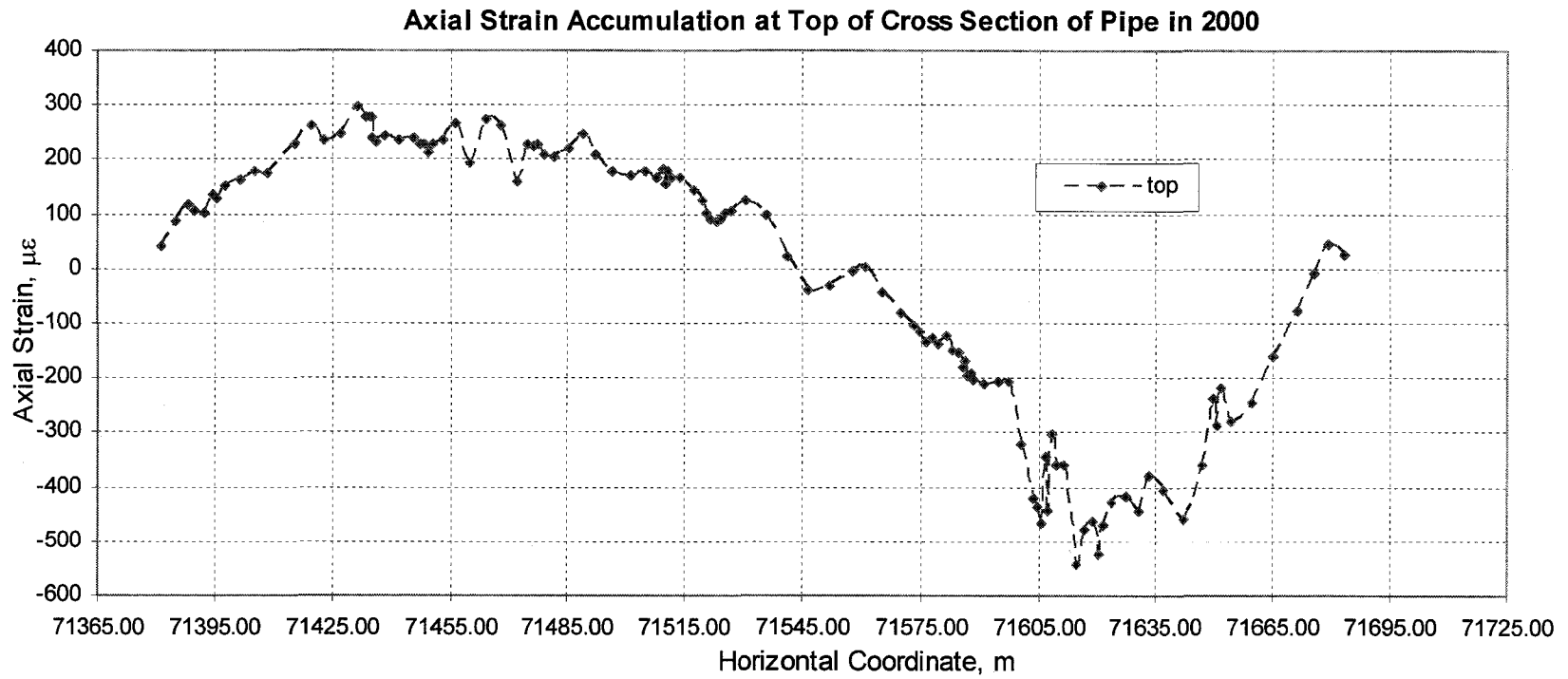


Figure 8.26 Top Axial Strain Accumulation of the Cross Section along the Pipeline in 2000

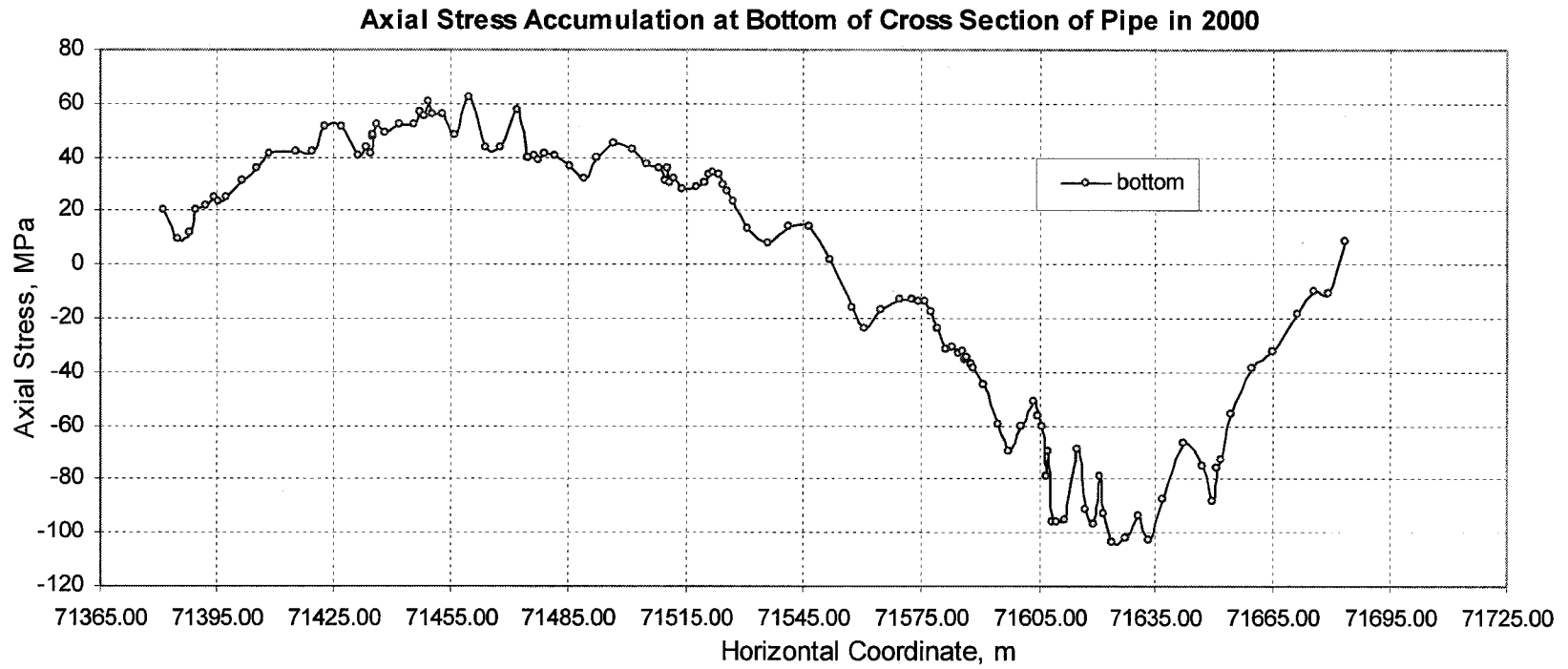


Figure 8.27 Bottom Axial Stress Accumulation of the Cross Section along the Pipeline in 2000

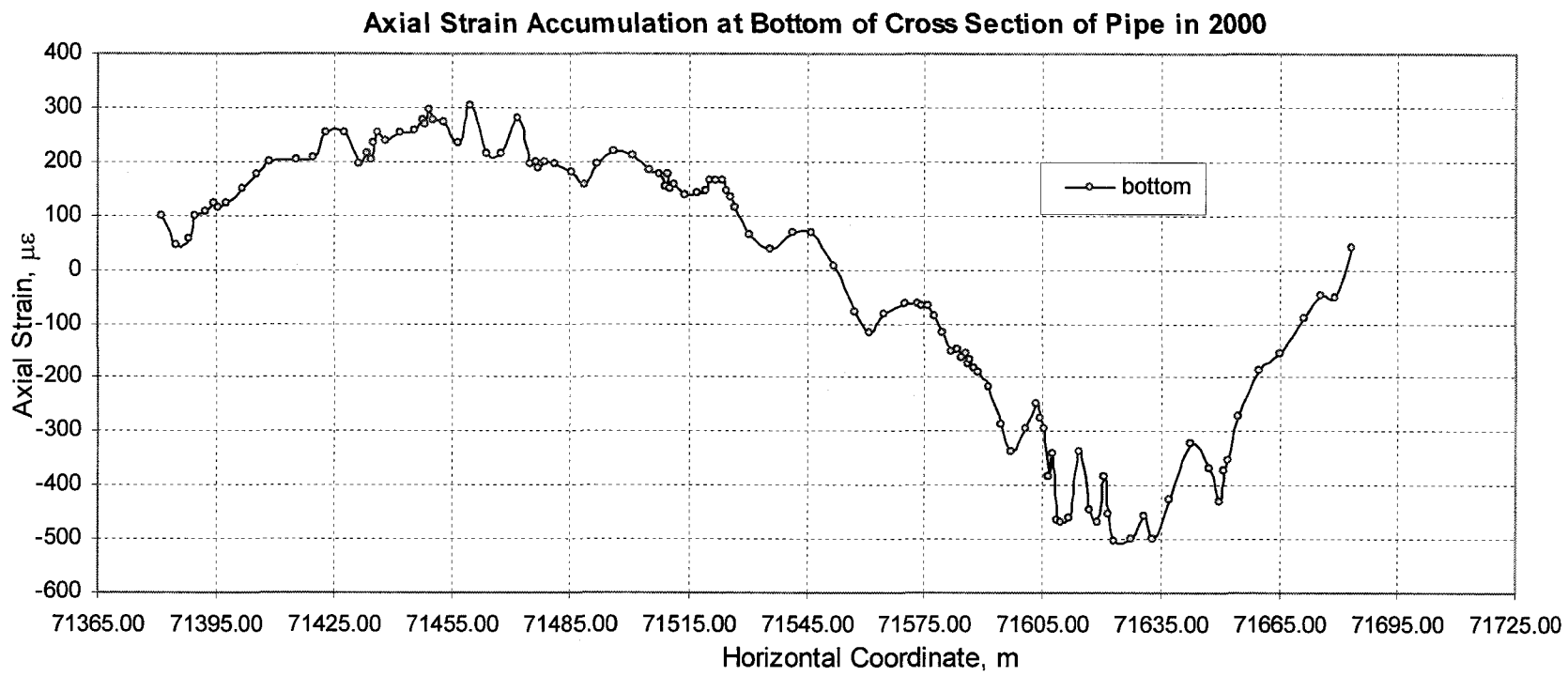


Figure 8.28 Bottom Axial Strain Accumulation of the Cross Section along the Pipeline in 2000

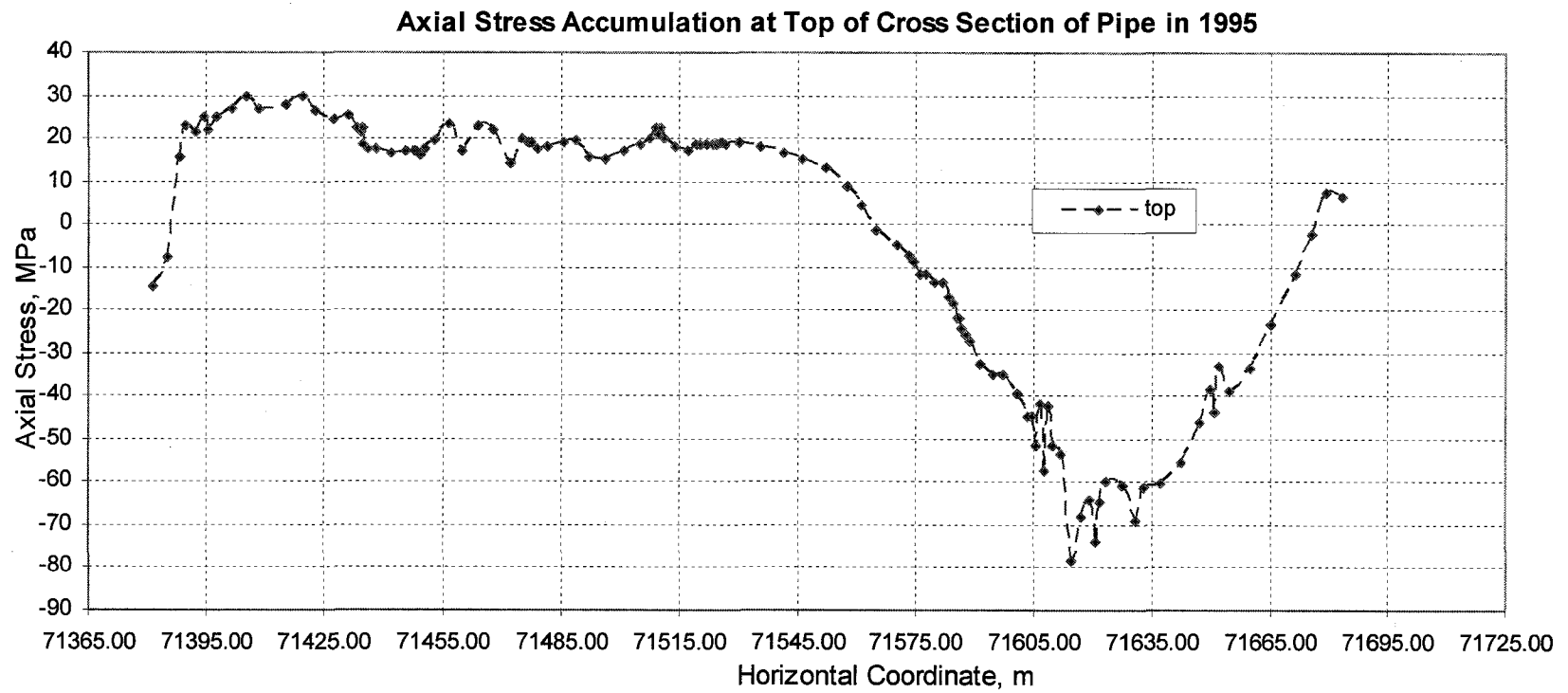


Figure 8.29 Top Axial Stress Accumulation of the Cross Section along the Pipeline in 1995

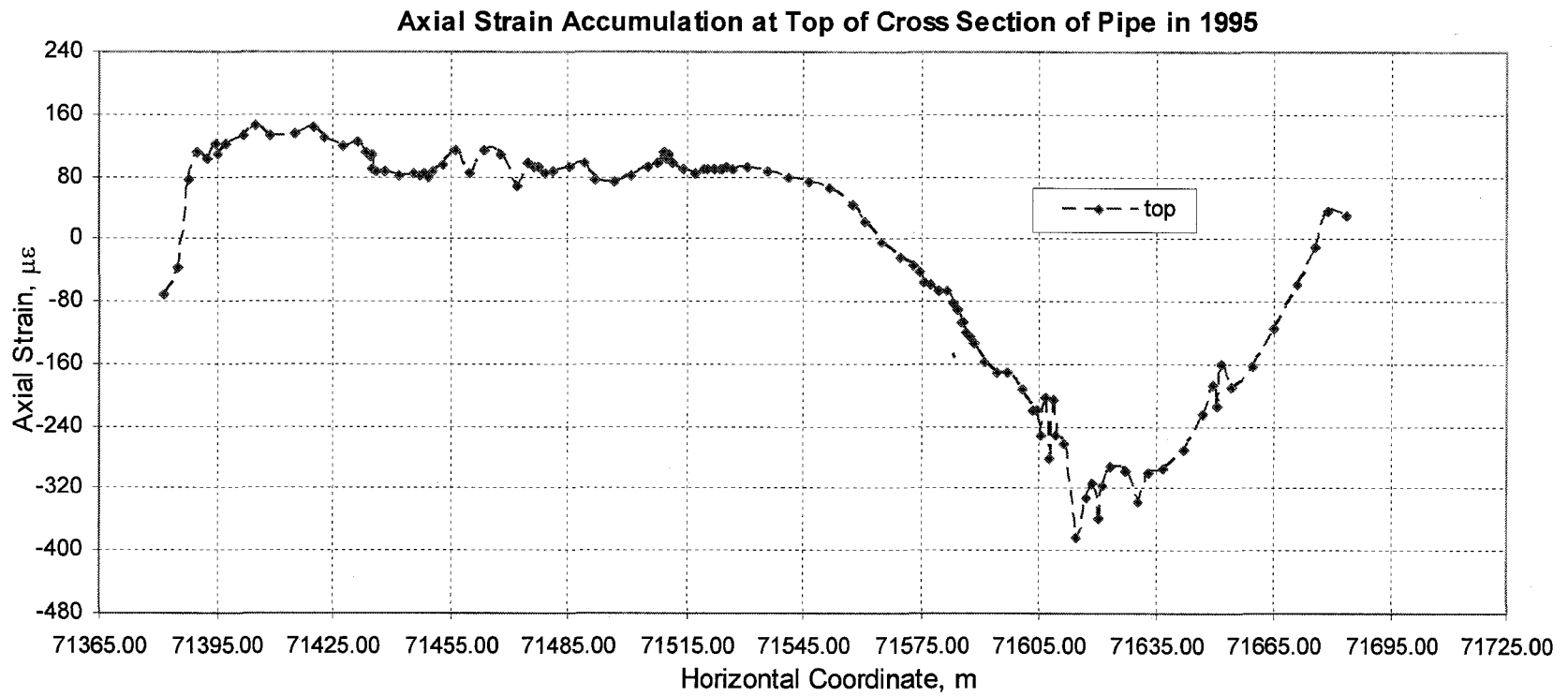


Figure 8.30 Top Axial Strain Accumulation of the Cross Section along the Pipeline in 1995

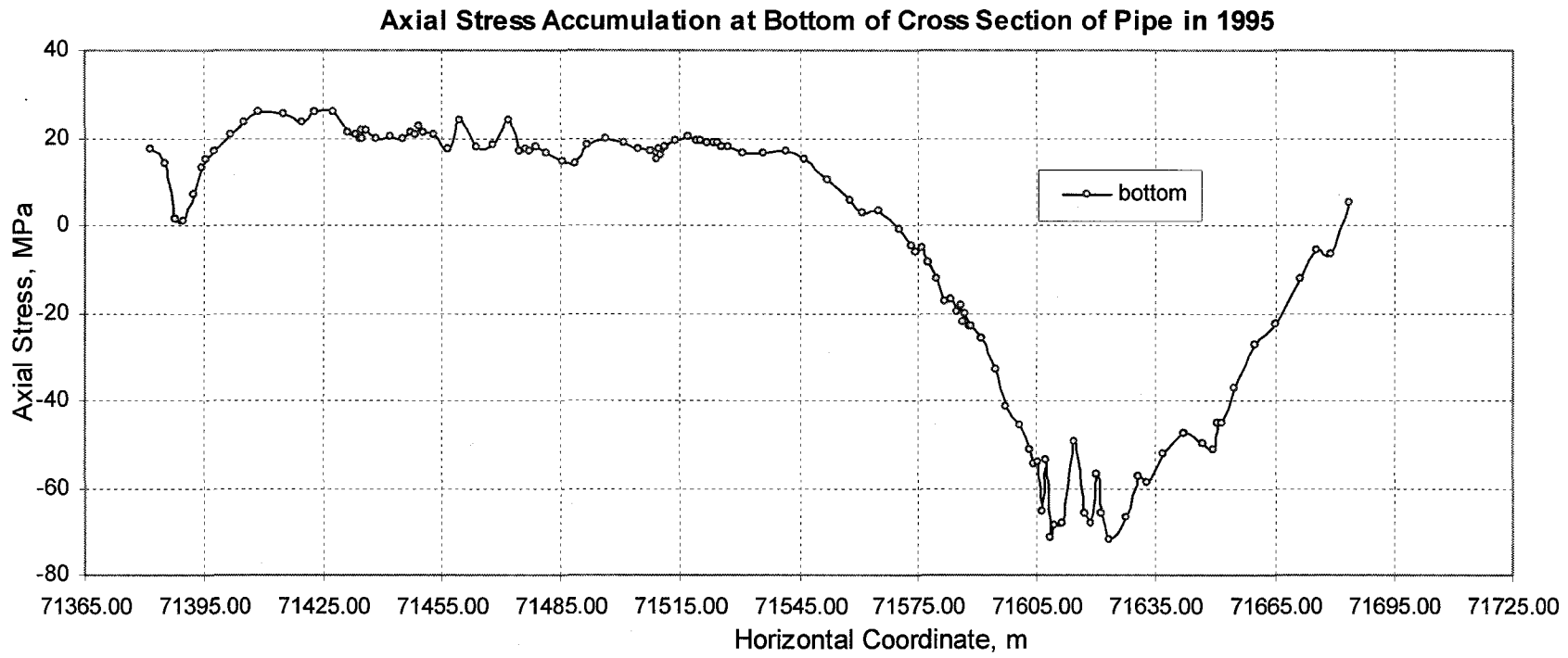


Figure 8.31 Bottom Axial Stress Accumulation of the Cross Section along the Pipeline in 1995

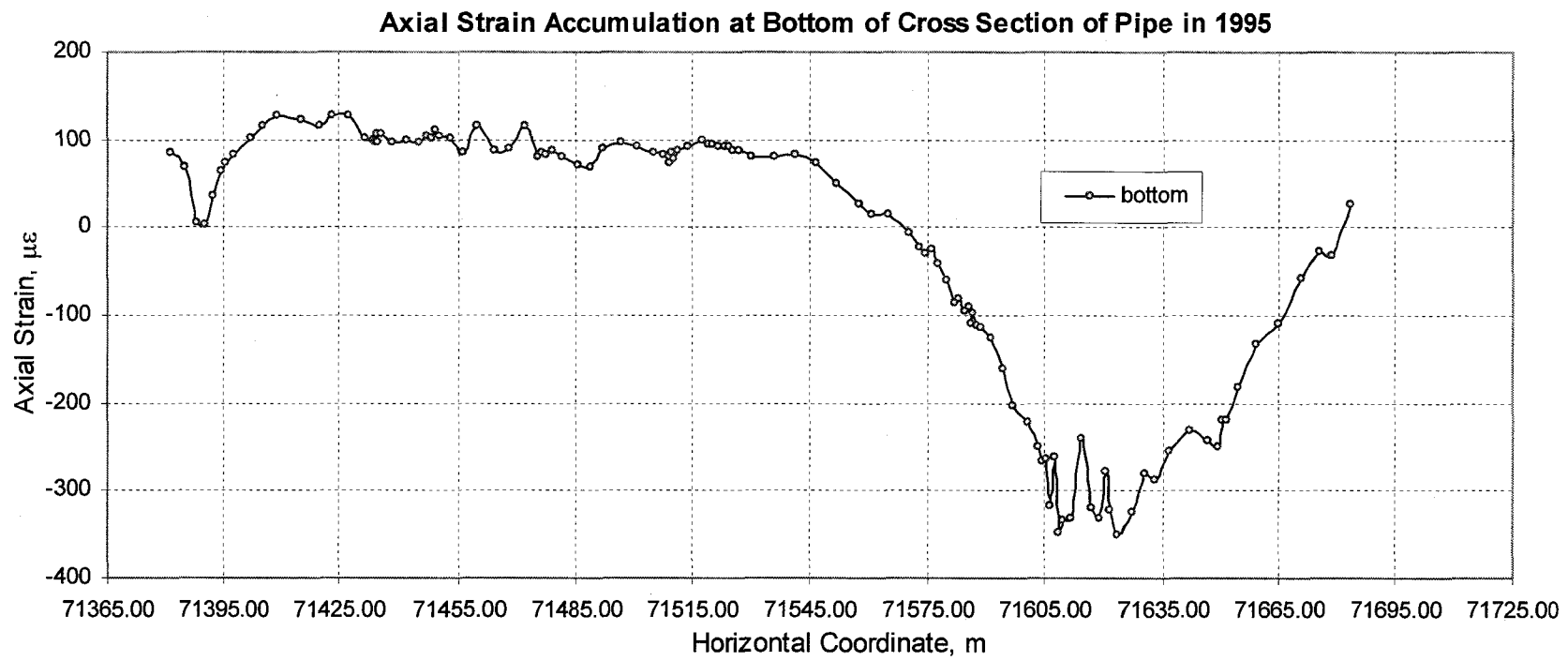


Figure 8.32 Bottom Axial Strain Accumulation of the Cross Section along the Pipeline in 1995

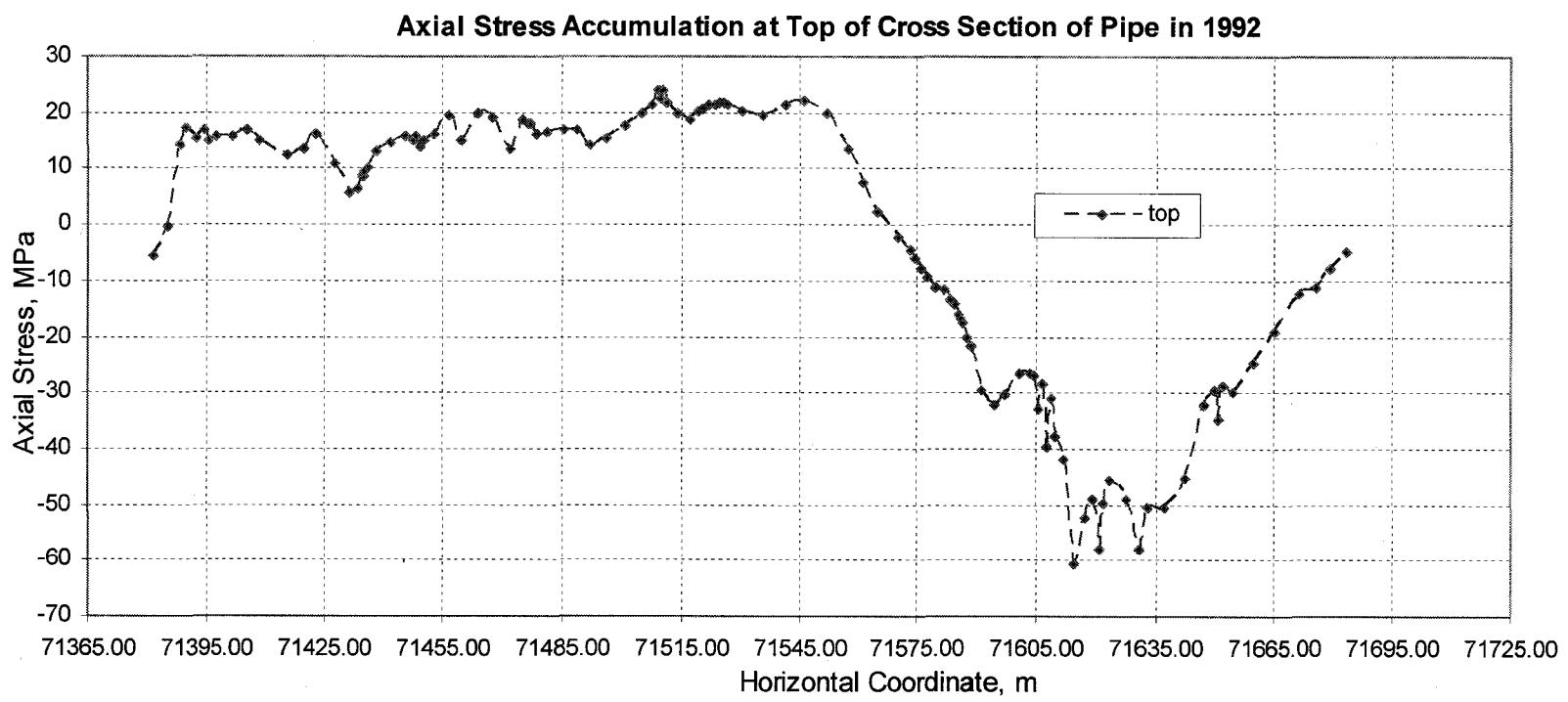


Figure 8.33 Top Axial Stress Accumulation of the Cross Section along the Pipeline in 1992

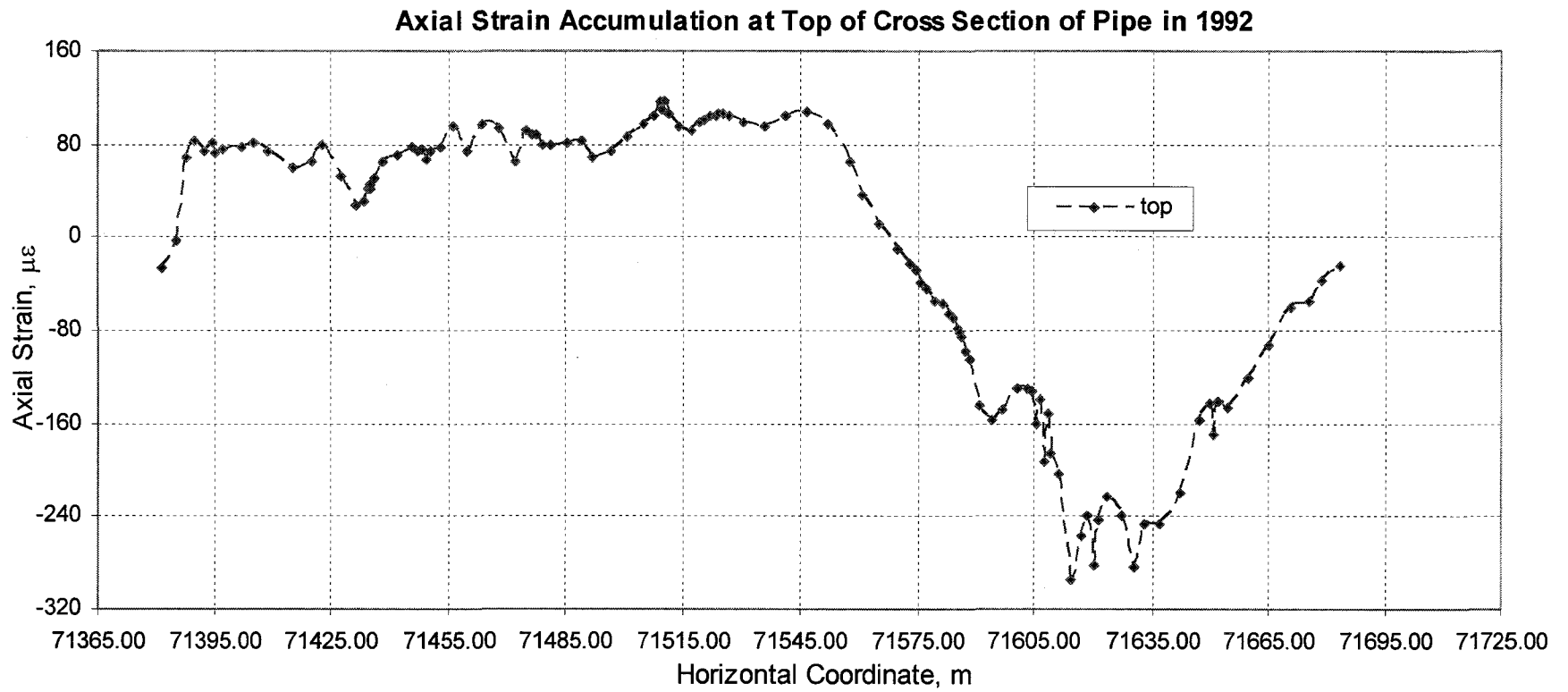


Figure 8.34 Top Axial Strain Accumulation of the Cross Section along the Pipeline in 1992

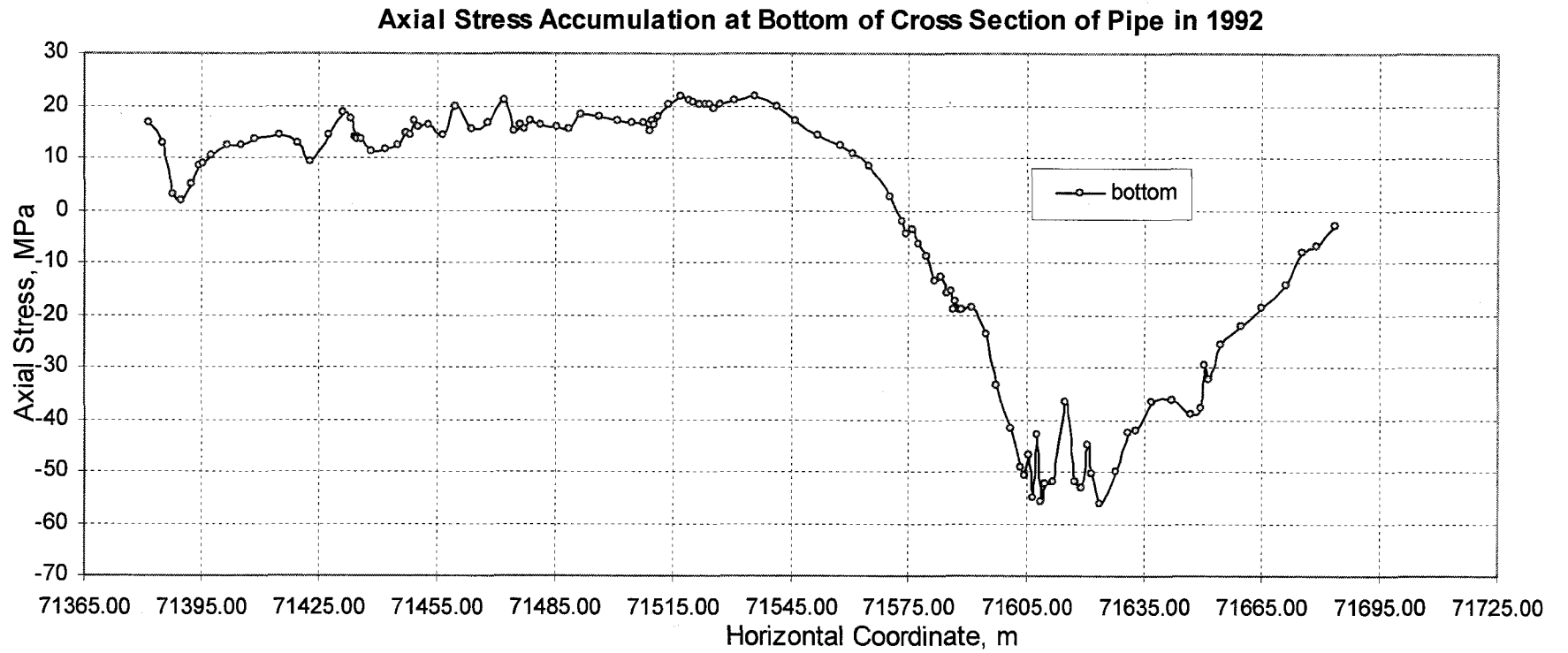


Figure 8.35 Bottom Axial Stress Accumulation of the Cross Section along the Pipeline in 1992

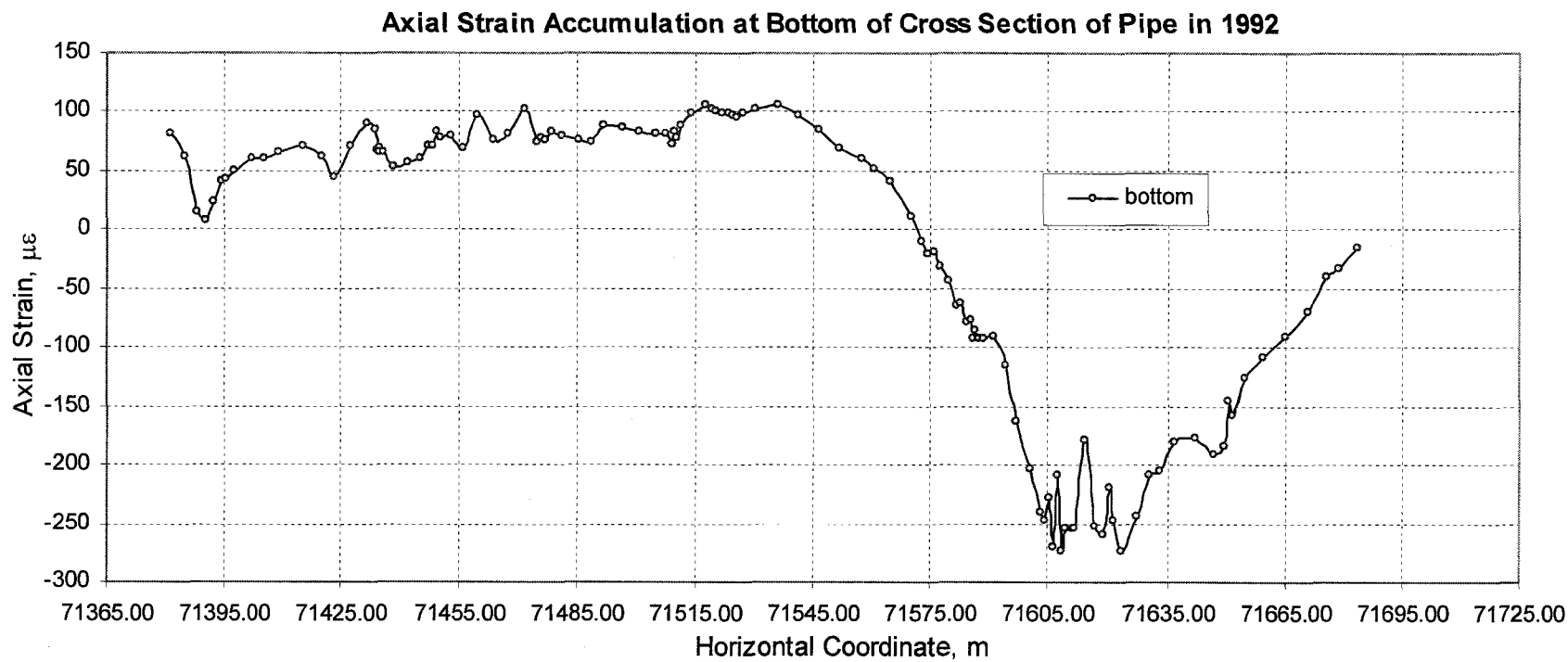


Figure 8.36 Bottom Axial Strain Accumulation of the Cross Section along the Pipeline in 1992

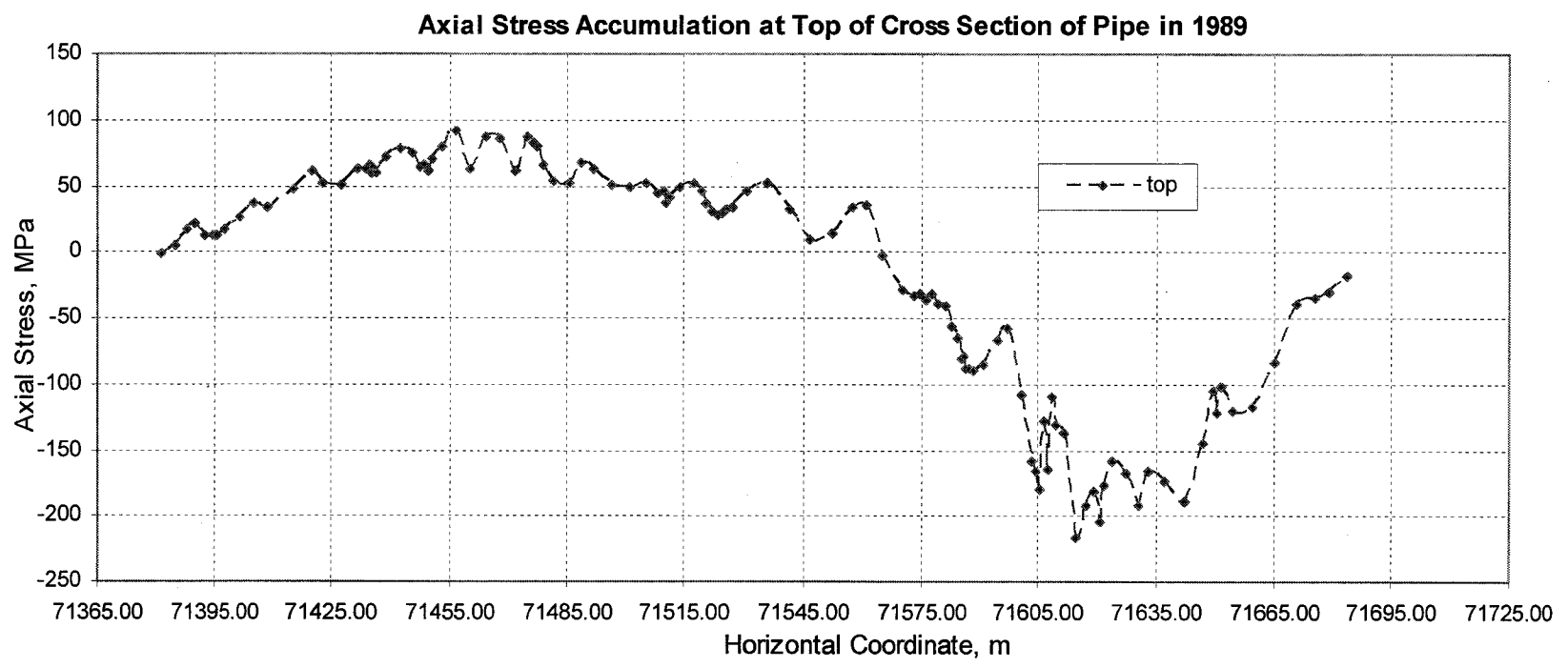


Figure 8.37 Top Axial Stress Accumulation of the Cross Section along the Pipeline in 1989

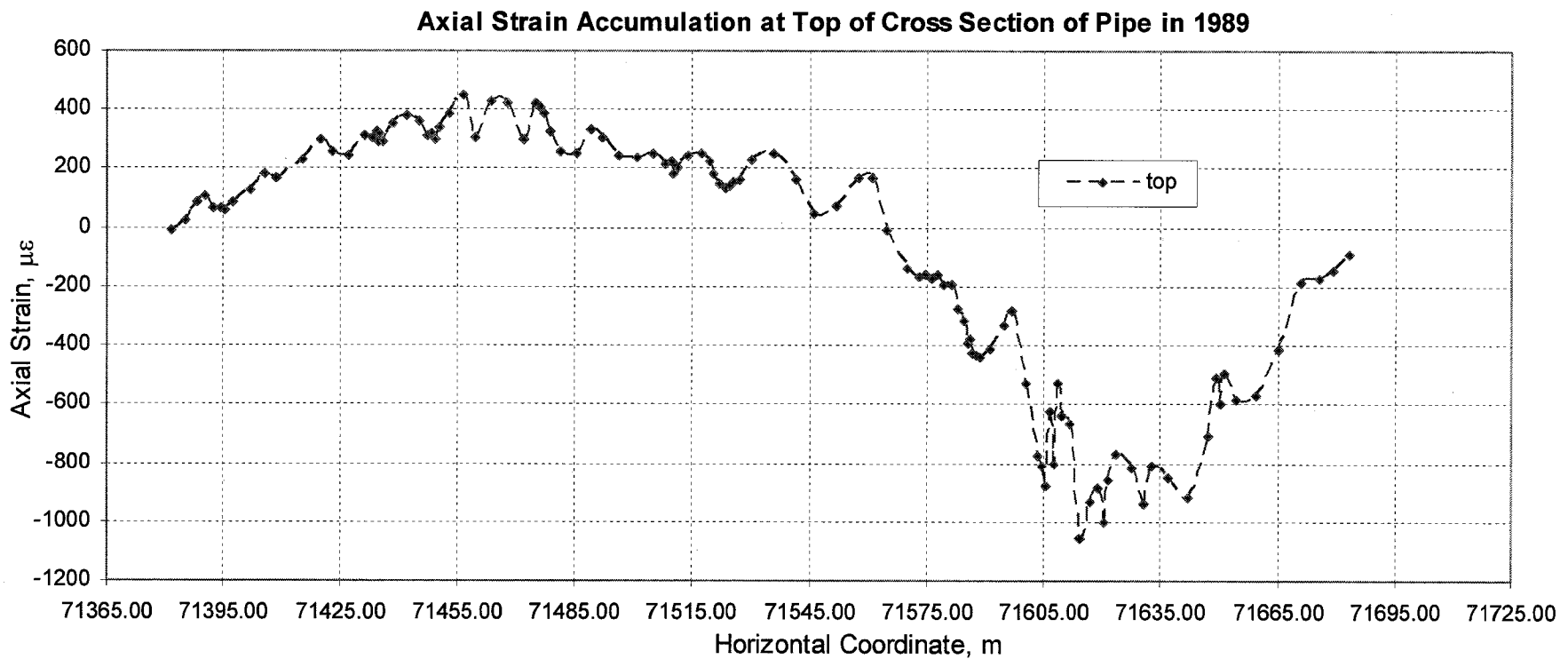


Figure 8.38 Top Axial Strain Accumulation of the Cross Section along the Pipeline in 1989

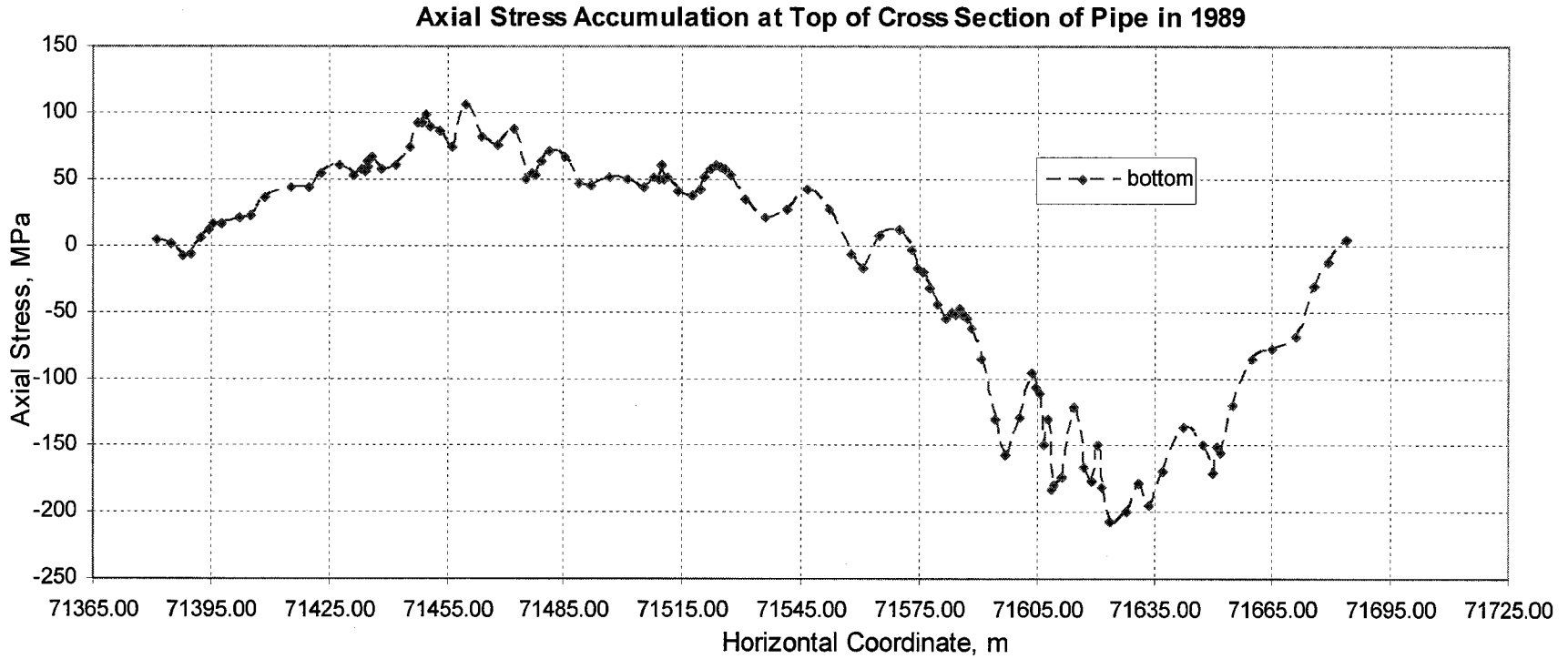


Figure 8.39 Bottom Axial Stress Accumulation of the Cross Section along the Pipeline in 1989

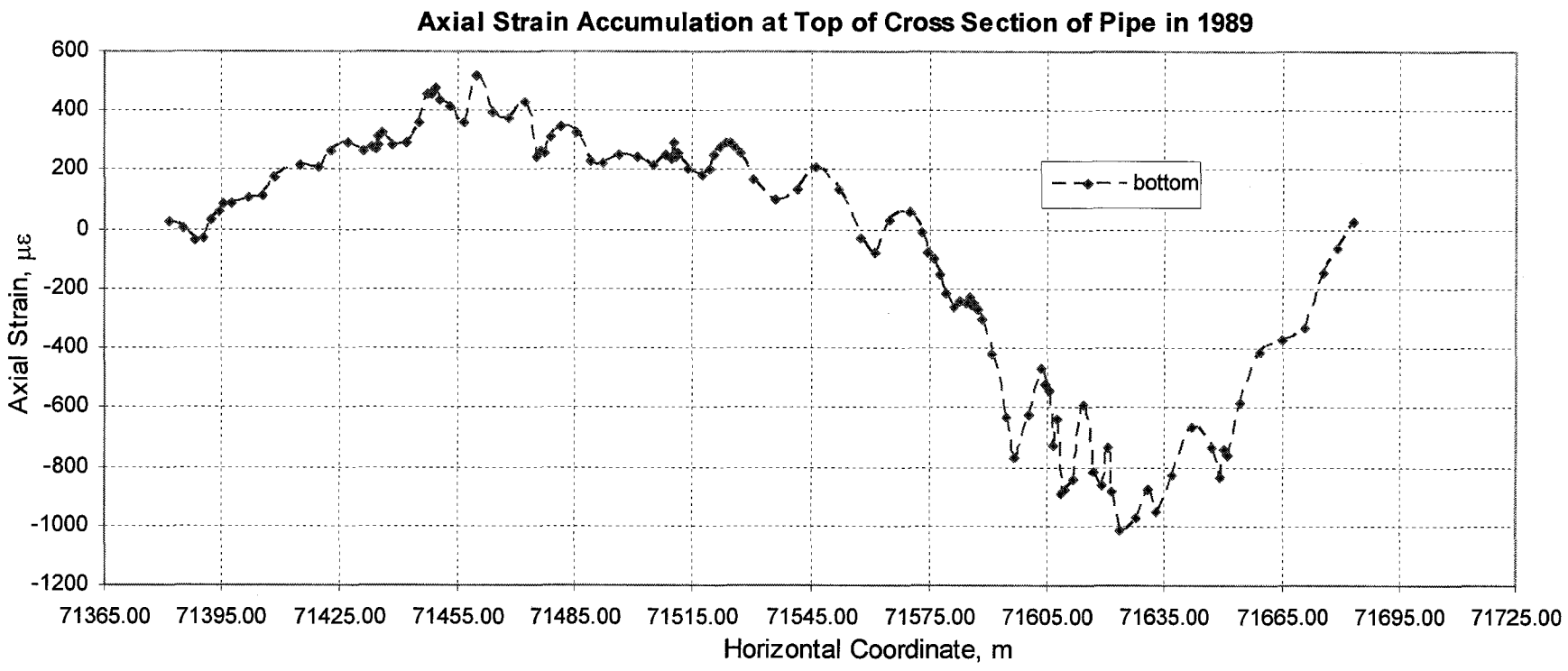


Figure 8.40 Bottom Axial Strain Accumulation of the Cross Section along the Pipeline in 1989

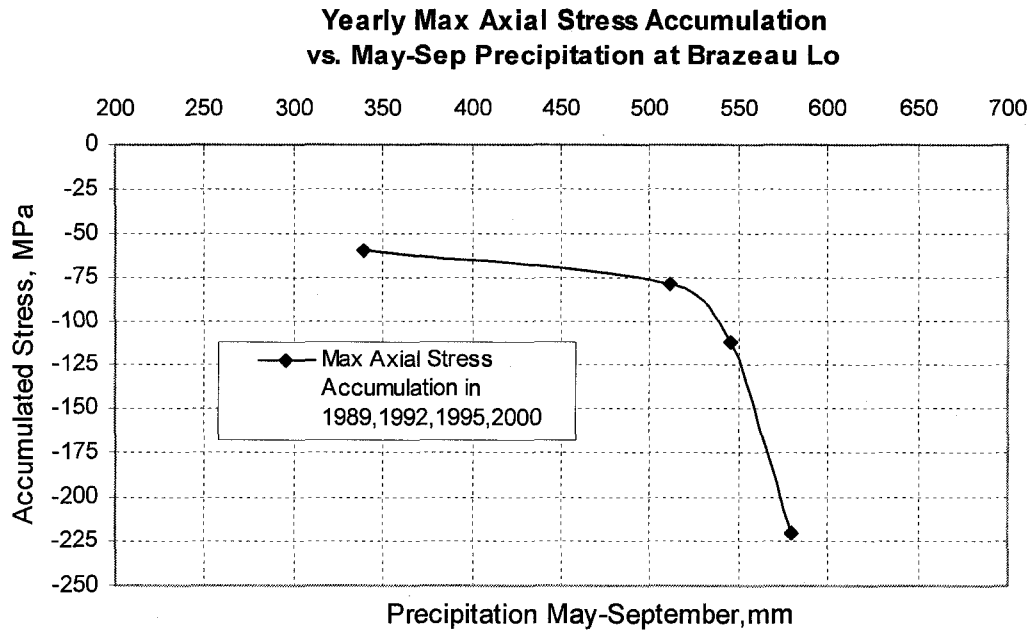


Figure 8.41 Yearly Max Axial Accumulated Stress vs. Precipitation for May-September at Brazeau Lo

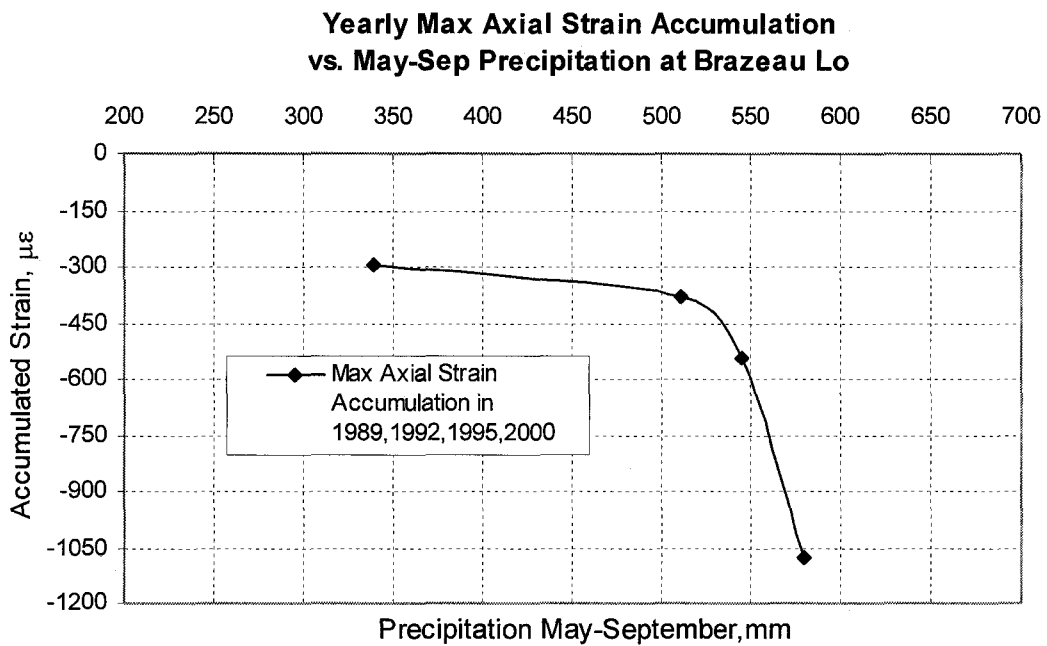


Figure 8.42 Yearly Max Axial Accumulated Strain vs. Precipitation for May-September at Brazeau Lo

**Yearly Max Axial Stress Accumulation
vs. Yearly Precipitation at Other Climate Stations**

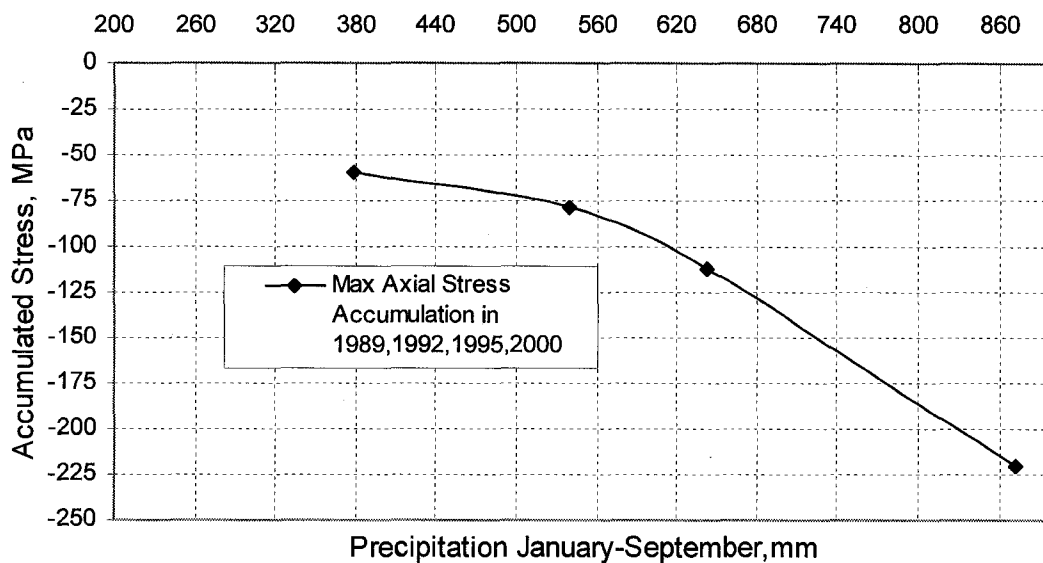


Figure 8.43 Yearly Max Axial Accumulated Stress vs. Precipitation for January-December at Other Climate Stations

**Yearly Max Axial Strain Accumulation
vs. Yearly Precipitation at Other Climate Stations**

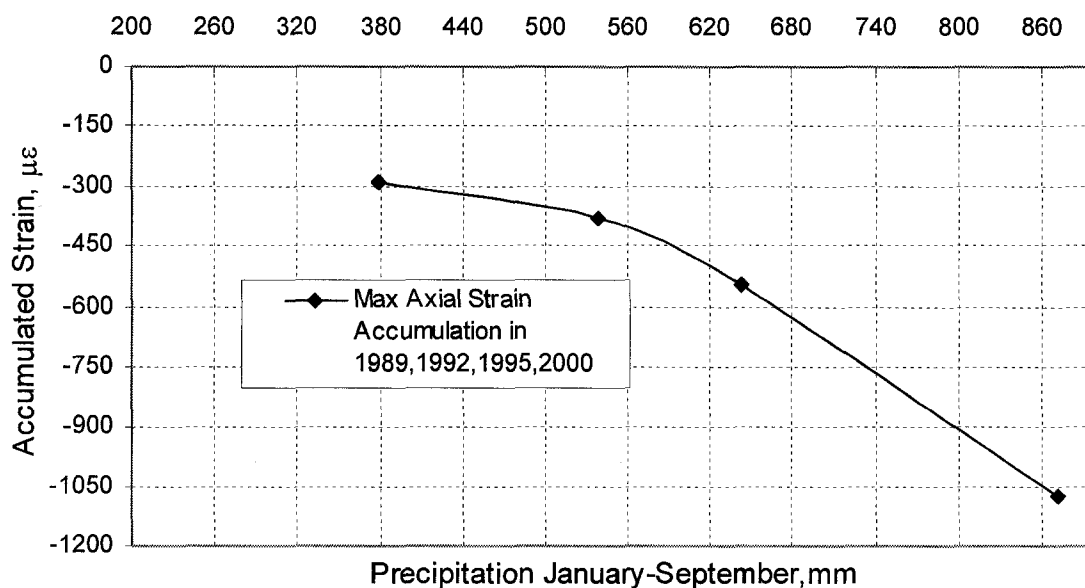


Figure 8.44 Yearly Max Axial Accumulated Strain vs. Precipitation for January-December at Other Climate Stations

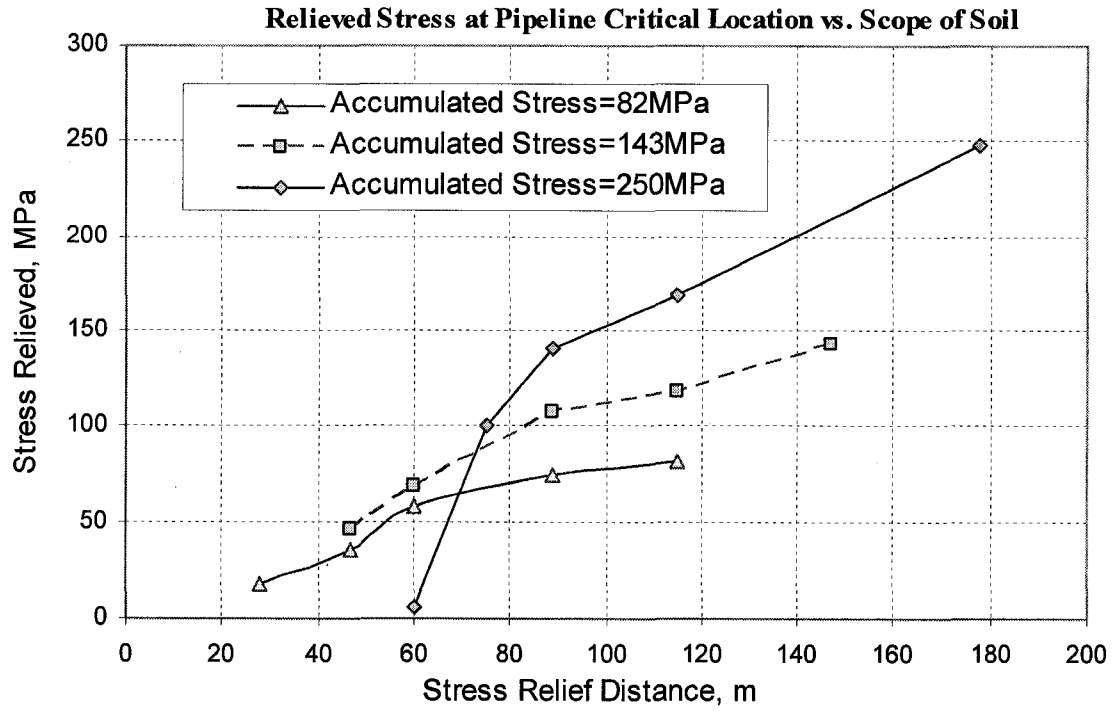


Figure 8.45 Relieved Stress at the Critical Location of Pipe vs. Distance from South Bank of Creek

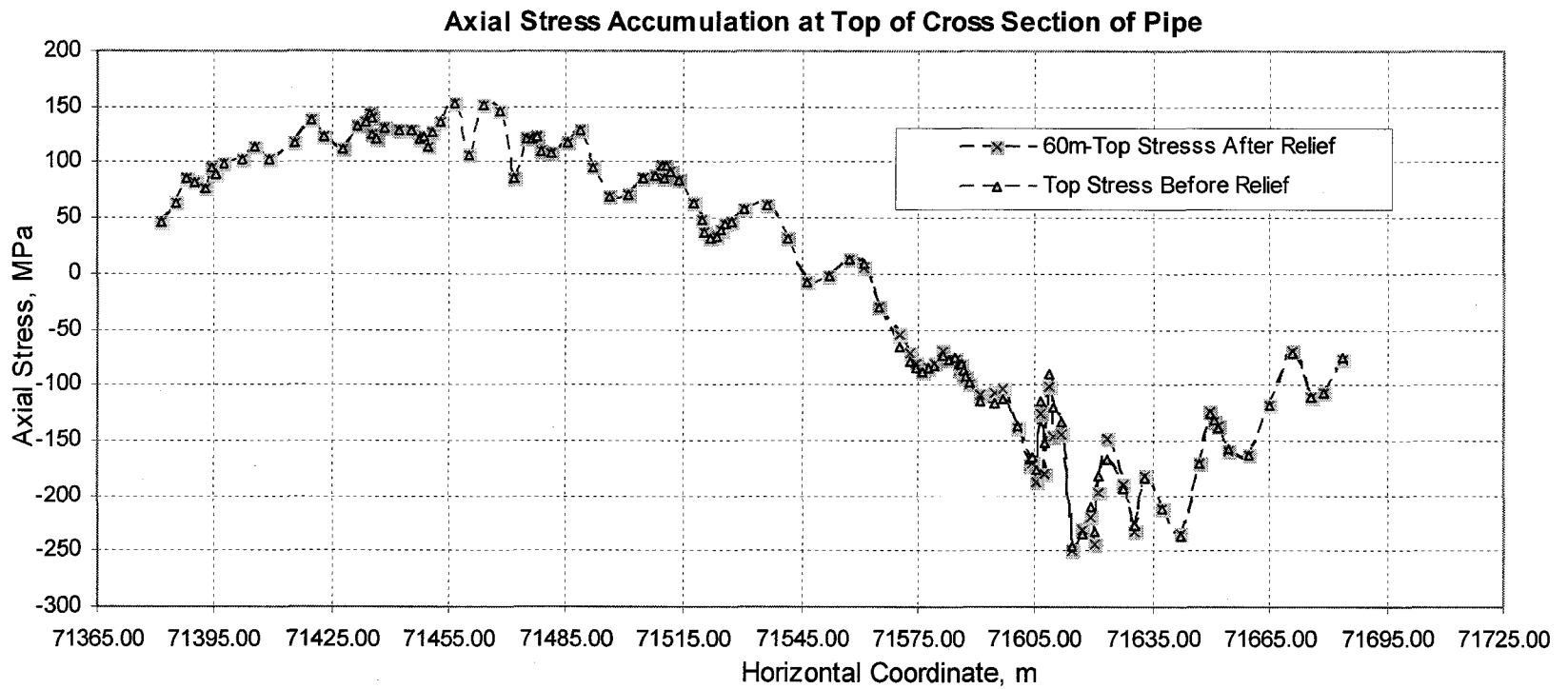


Figure 8.46 Axial Stress Accumulation at the Top of Cross Section of Pipe Before and After Digging 60m Soil on South Slope

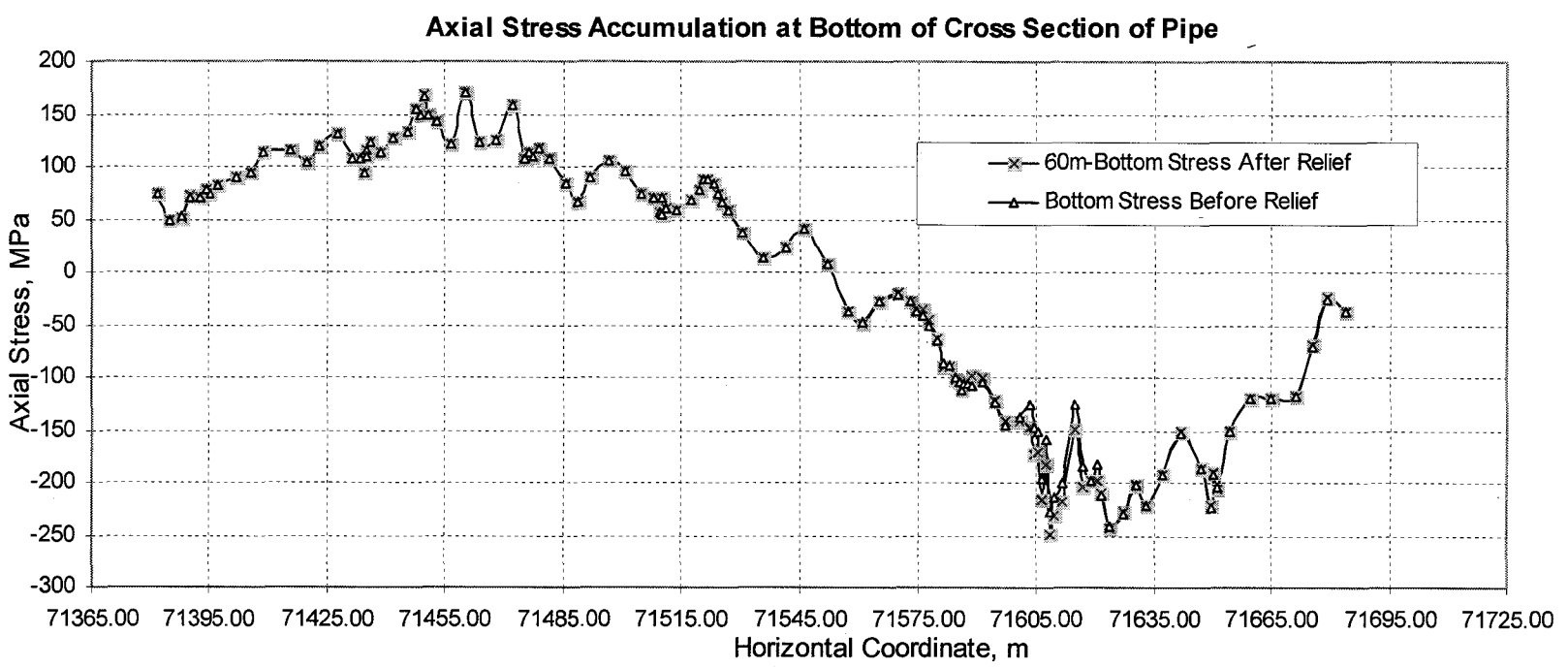


Figure 8.47 Axial Stress Accumulation at the Bottom of Cross Section of Pipe Before and After Digging 60m Soil on South Slope

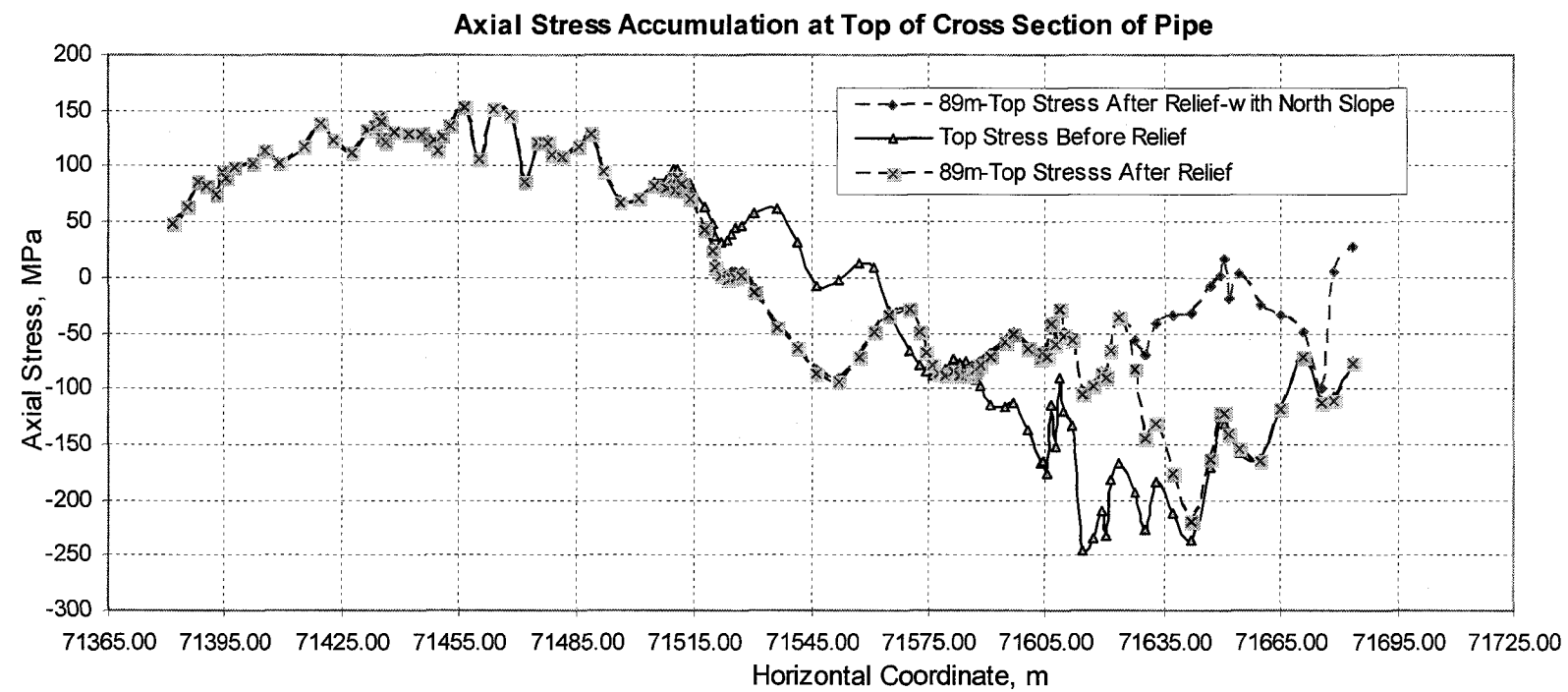


Figure 8.48 Axial Stress Accumulation at the Top of Cross Section of Pipe Before and After Digging 89m Soil on South Slope Only and Also Digging North Slope

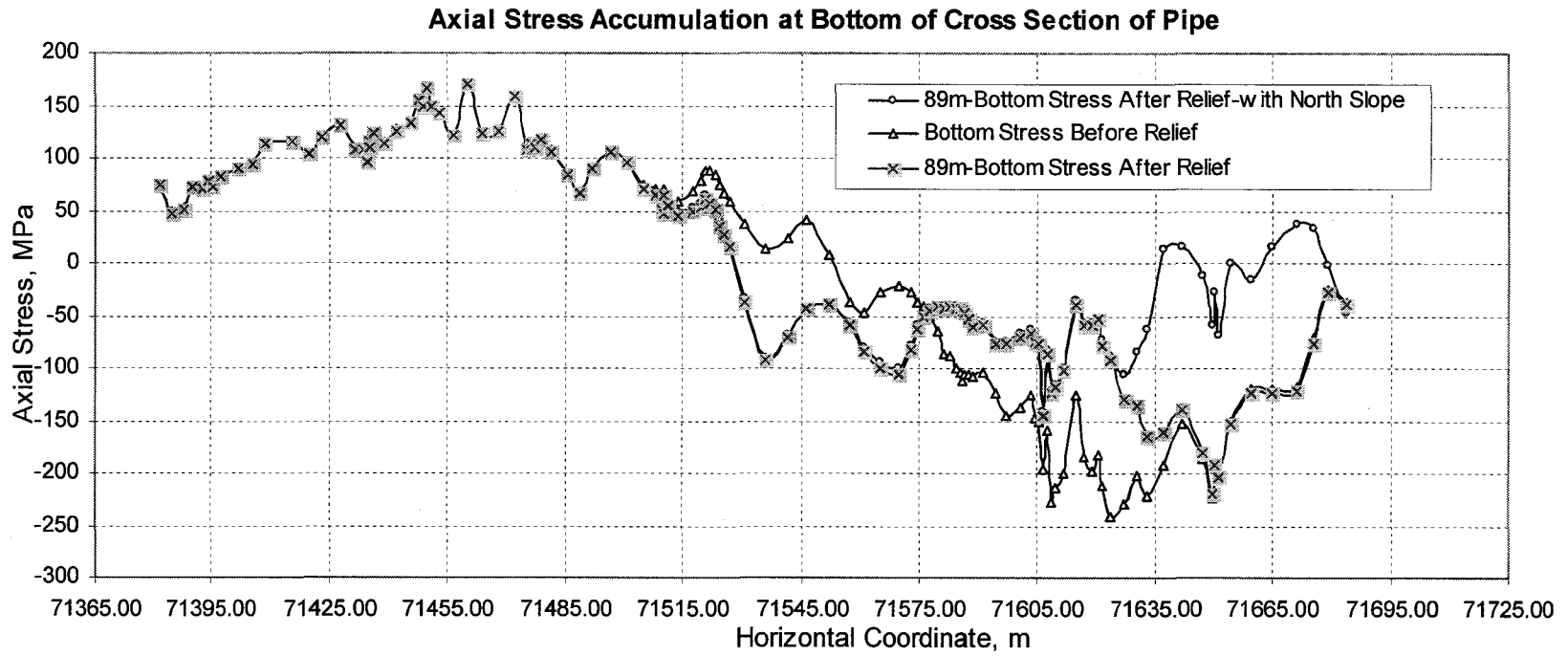


Figure 8.49 Axial Stress Accumulation at the Bottom of Cross Section of Pipe Before and After Digging 89m Soil on South Slope Only and Also Digging North Slope

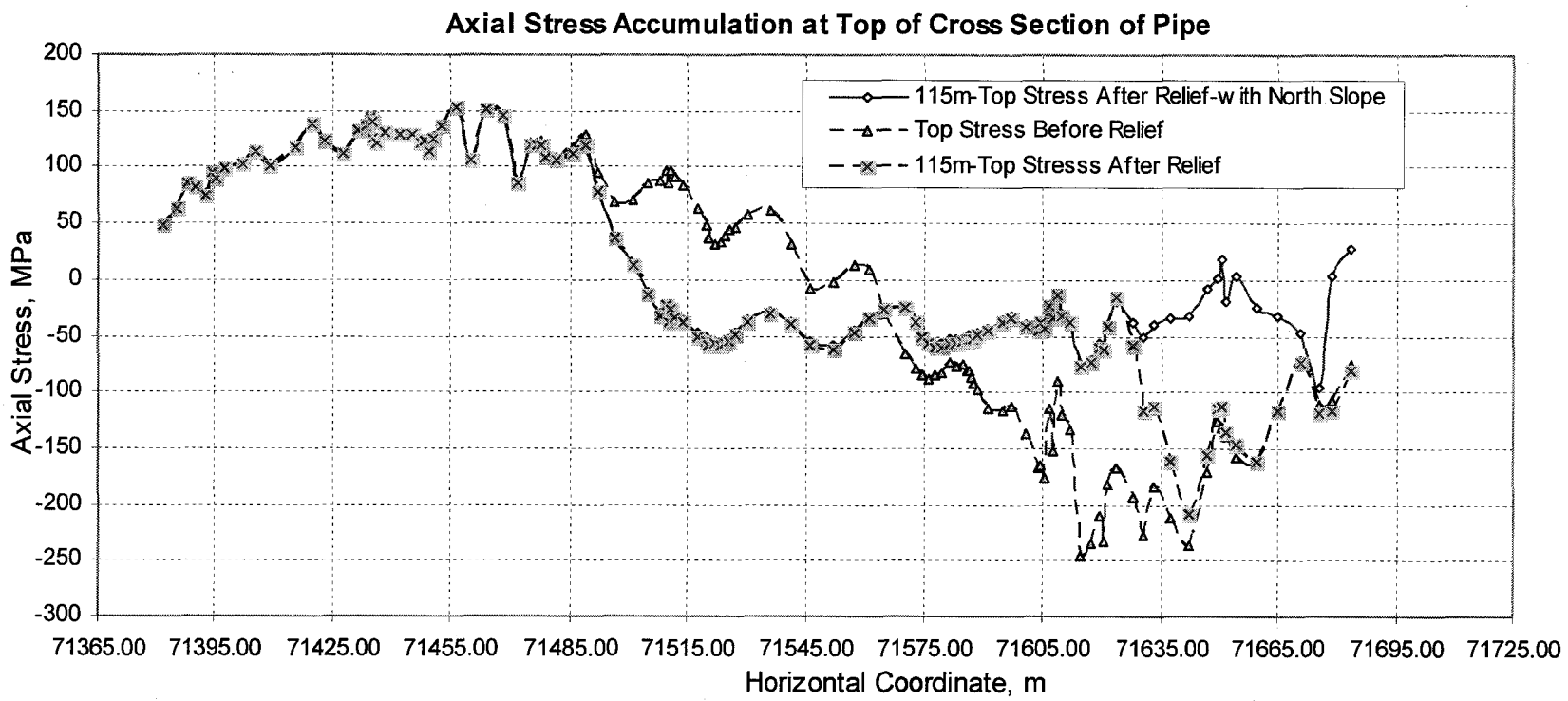


Figure 8.50 Axial Stress Accumulation at the Top of Cross Section of Pipe Before and After Digging 115m Soil on South Slope Only and Also Digging North Slope

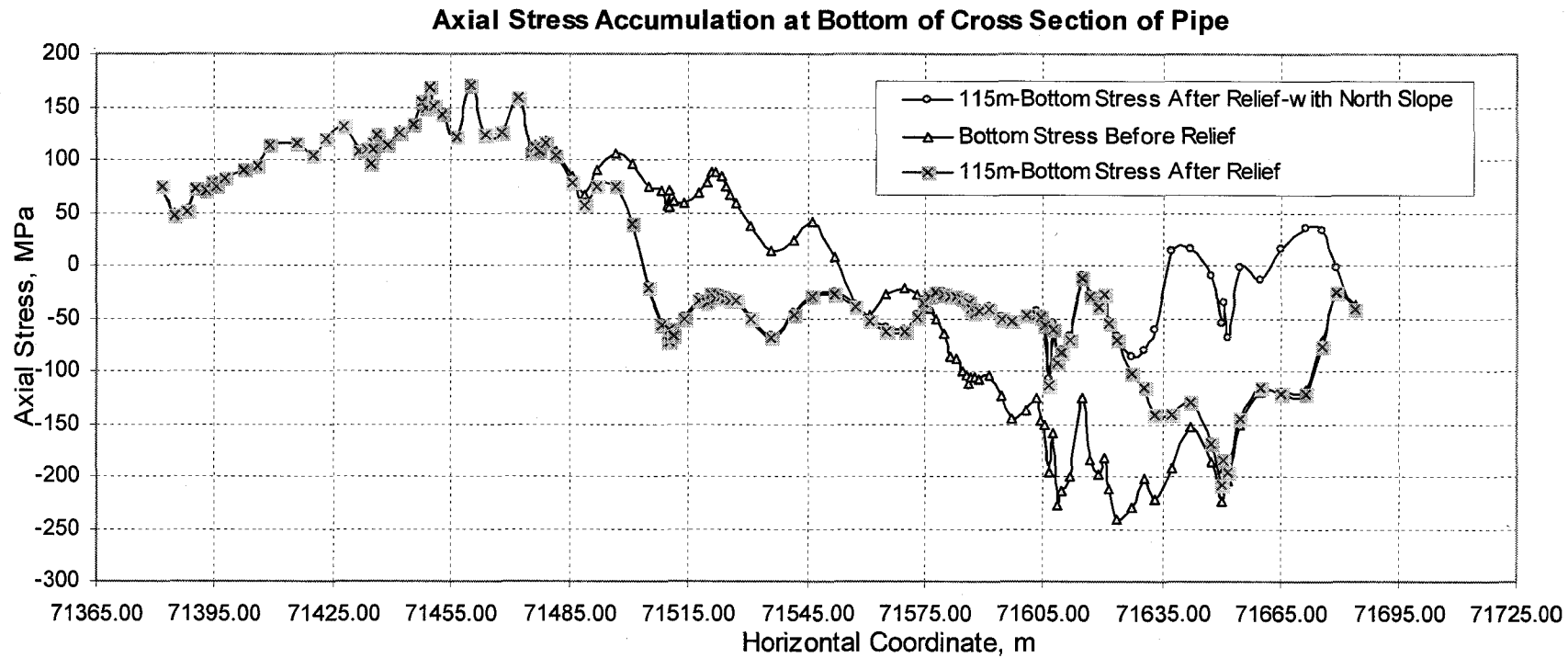


Figure 8.51 Axial Stress Accumulation at the Bottom of Cross Section of Pipe Before and After Digging 115m Soil on South Slope Only and Also Digging North Slope

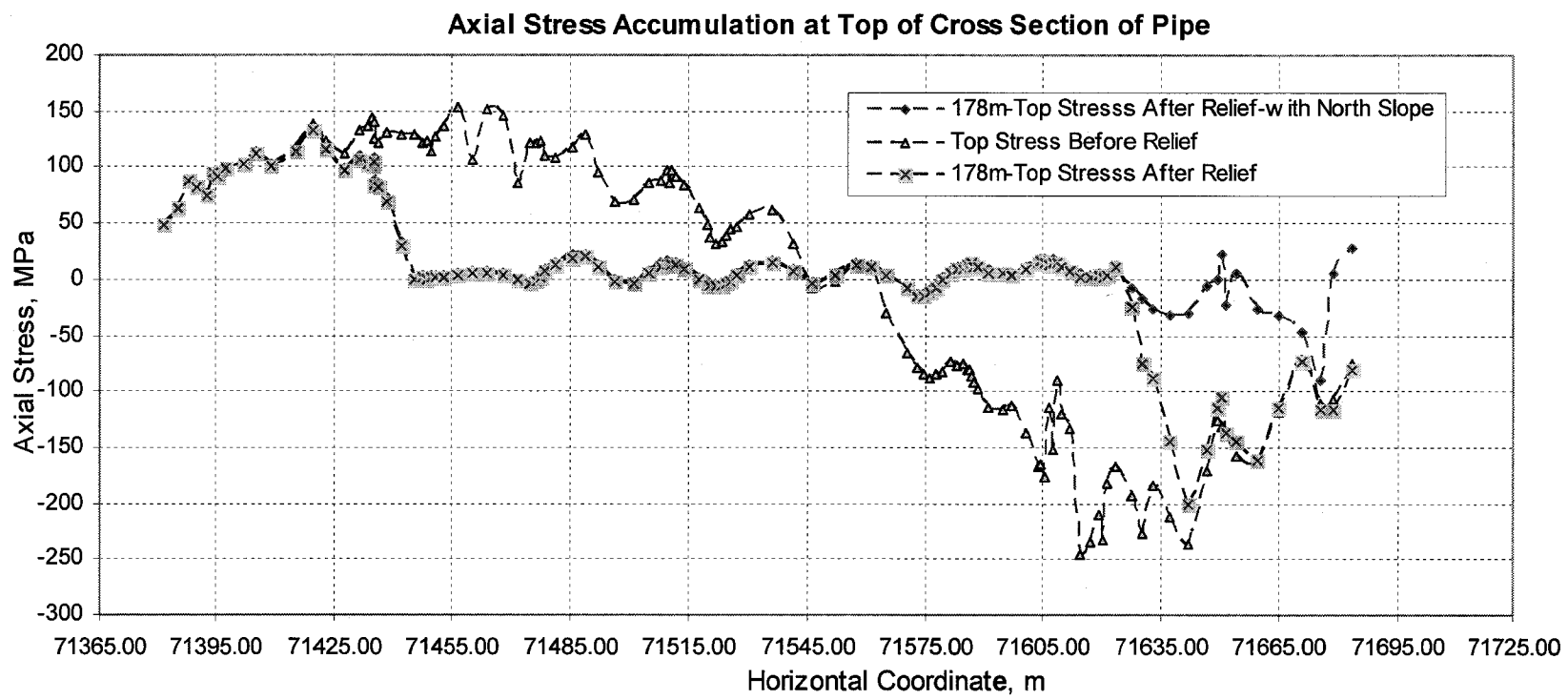


Figure 8.52 Axial Stress Accumulation at the Top of Cross Section of Pipe Before and After Digging 178m Soil on South Slope Only and Also Digging North Slope

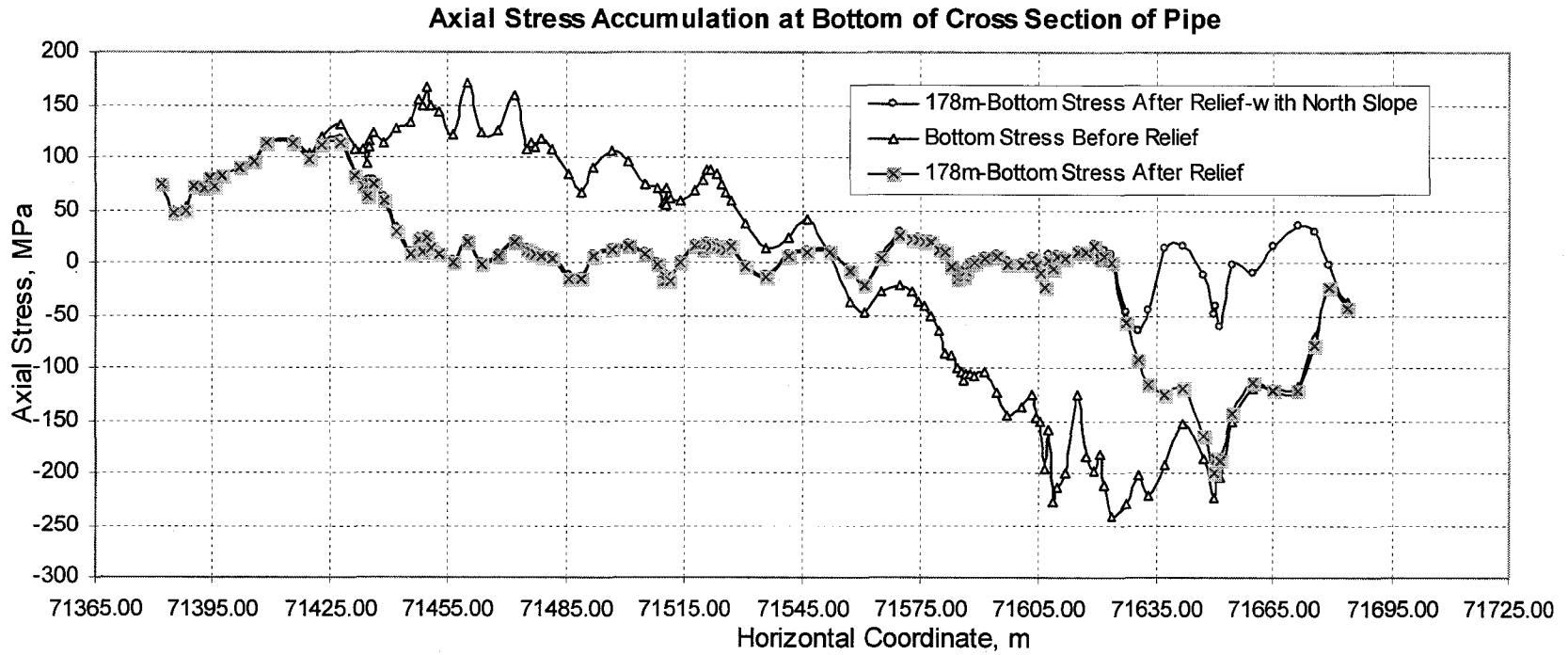


Figure 8.53 Axial Stress Accumulation at the Bottom of Cross Section of Pipe Before and After Digging 178m Soil on South Slope Only and Also Digging North Slope

CHAPTER 9 PARAMETRIC STUDY OF STRESS RELIEF PROGRAM

The FEA model (Figure 7.29), developed for Pembina River Crossing in Chapter 7, is employed to carry out a parametric study to examine the sensitivity of the deformational behaviour of pipeline to different variables. The results from the parametric study will provide valuable guidelines for pipelines at other sites.

9.1 Introduction

The established site-specific model in Figure 7.29 is confined to a limited range of variables. In fact, each variable may have different values which may affect the spatial (distribution and amplitude) and temporal characteristics of the displacement field, consequently, affecting the pipeline deformation. Using the finite element model in Chapter 7, an extensive parametric study is conducted to investigate the effects of various parameters on the behaviour of pipeline. The maximum compressive axial stress accumulations are plotted against the parameters studied. The investigation started with studying and selecting the potential variables and their ranges along with the analysis results.

There are a lot of variables that can influence the behaviour of a pipeline. These variables are: diameter and wall thickness of pipe, internal pressure, material grade of pipe steel, cold bend angle, water table, boundary condition, stress relief procedure and schedule, slip surface, pipe soil interaction, soil creep, layers of soils, soil strength, precipitation, temperature, and geometry of pipe, etc. In order to reduce the number of models in the study, some of the above variables were not considered in this study.

Since changing diameter of pipe and the geometry of pipe/slope is difficult, the geometry of the model used in the parametric study was kept constant. Precipitation and stress relief procedure were discussed in Chapter 8 and will not be discussed here. Effects of temperature and cold bend angle were not examined here. Hence the remaining variables that will be studied in the parametric study include: internal pressure, pipe wall

thickness, material grade, boundary condition, slip surface, pipe soil interaction, soil creep, soil strength, and strain accumulation time.

Matrix of parametric study is listed in Table 9.1. The values for different variables studied and the corresponding accumulated stresses and strains are summarized in Table 9.2.

9.2 Parametric Studies

To conduct a parametric study, the results from modifying each specific parameter will be assessed through direct comparison with the behaviour of standard slope pipe model. The standard model represents the median values of the variables selected for the parametric study. The parameters in the model under the same load sequences compared in the following Sections will be identical except for a single variable. This will allow for a direct study of the effect of each specific variable on the behaviour of the pipe. To quantify the influence of each variable on the pipeline, the peak axial compressive strain on the pipeline of each subsequent model will be compared to that of the standard model. The properties of the standard model are:

1. Diameter/Thickness Ratio = 48
2. Internal Pressure = 35.8% SMYS hoop stress
3. Material Grade = X60
4. Soil Parameters are the same as Pembina River Crossing in Chapter 8

9.2.1 Internal Pressure

The internal pressure of the models is varied in order to assess the effect on the pipeline. It is specified that the maximum operating internal pressure in the line pipe at Pembina River Crossing is 35.8% of the SMYS. In order to check the pipe performance at higher internal pressure, 54% of the SMYS serves as the upper bound of the internal pressure for the parametric study. During shutdowns the internal pressure in a pipeline may be reduced to zero, consequently the assessment of its compressive strains on the pipe wall is important. For this reason a zero pressure loading condition will serve as the

lower bound for the parametric study. The internal pressures of 10% and 20% SMYS are also tested.

Maximum compressive strain on the pipeline against percentage SMYS of the internal pressure is plotted in Figure 9.1. The maximum peak axial compressive strain of $517 \mu\epsilon$ occurs at zero internal pressure. The minimum peak axial compressive strain of $494 \mu\epsilon$ occurs at 10% SMYS. As the percentage of SMYS increases after 10%, the peak axial compressive strain reduces. It shows that the influence of the internal pressure on the strain accumulation in the pipe is not significant. The maximum pipe strain accumulation at zero internal pressure is 1.05 of the minimum at 10% SMYS. In conclusion, with zero internal pressure, there will be 1% to 5% increase in the maximum compressive strain compared with that in non-zero internal pressure.

9.2.2 D/t Ratio

Increasing the diameter to thickness ratio in line pipe is one of the foremost methods exercised to minimize material costs. In order to directly assess the sensitivity of the pipe to varying diameter to thickness ratio, diameter to thickness ratios of 24, 32 and 96 are incorporated for the models in the parametric study for comparison with the response of the standard model to the same combined loading.

As shown in Figure 9.2, the diameter to thickness ratio of the models demonstrates a significant effect on the deformational behaviour of pipeline. The peak compressive axial strain in the model increases approximately linearly as the diameter to thickness ratio increases. The rate of increase is $4.54 \mu\epsilon/\text{unit of } D/t$. When D/t ratio goes up by one unit, the compressive strain will be increased by $4.54 \mu\epsilon$. In this study, the D/t ratio varies from 24 to 96, the strain increases by about $350 \mu\epsilon$. It indicates that when the soil moves, with the same diameter, the thinner is the wall of pipe (or, with the same thickness, as the diameter gets larger), the larger is the strain accumulation for the same load steps. This is a typical structural response to the external load.

9.2.3 Material Grade

Increasing the grade of the steel in the pipe allows for increasing the allowable internal pressure with the same pipe geometry. Here the strain accumulation in the pipe with changing the grade of the steel is examined. The material grades of steel in this research program are commonly found in commercial pipes. Accordingly, the three grades being examined in this parametric study are Grades X60, X70 and X80. Nominal yield strength is used in the steel model. The modulus of elasticity is assumed to be the same for all grades, 205 GPa. The main parameters of the models are in Table 9.1.

Figure 9.3 gives the peak compressive axial strain vs. yield strength. The change of the material grade does not have any influence on the strain accumulation in the pipe. From the stress strain curves of the three steel materials it can be explained that before the materials reach the yield strain of X60, the pipe deforms elastically and all three responses are identical. It can be deduced that after the materials reach the yield strain of X60, the pipe of X60 will deform more than X70 and X80; and after the materials reach the yield strain of X70, the pipe of X70 will deform more than X80. Material grades in this case will have some influences.

9.2.4 Boundary Condition

The boundary conditions for the FEA model in Chapter 7 are constrained in the horizontal (2-direction in Figure 8.1) directions at the north and south ends, transverse directions (1-direction in Figure 8.1) at the east and west boundaries, while the bottom of the model is seated on the bedrock with displacement constraint to three global directions. The FEA model of the slope at Pembina River Crossing has a limited length of 308 m. Pipeline deformational performance needs to be examined when the south and north ends of the pipeline are constrained and not constrained in horizontal direction. The real boundary condition is in between these two cases.

Figure 9.4 gives the comparison results at four increasing water levels. The peak accumulated compressive strain without constraint is more than that with constraint about

2%-5%. It shows that the boundary condition does not affect the pipeline deformation very much. The scope of the model is big enough to simulate the pipeline behaviour.

9.2.5 Slip Surface

In general, soil movement at the slip surface in the FEA model in Chapter 7 is smaller than the SI data, though the soil movement near the ground surface agrees well with SI. The relative movement within the slip surface influences pipeline deformation. Here by changing the cohesion and friction angle, soil condition at the slip surface affects pipeline deformation demonstrated in three models. The first model has cohesion of 2 kPa and friction angle 18° , the second model has cohesion of 5 kPa and friction angle 19.5° , the third model has cohesion of 10 kPa, friction angle 25° . Figure 9.5 displays the peak compressive strain vs. cohesion (friction angle). It shows as the slip surface is weaker, the pipe deforms more significantly.

9.2.6 Pipe Soil Interaction

Pipe soil interaction was adjusted in the FEA model in Chapter 7. Pipeline deformation matched with the strain gauge reading with satisfactory agreement. Pipe shell elements share the same nodes as those of the soil continuum elements circumfluent the pipeline. The interaction is simulated by setting a special thin shell layer of soil with 0.5 m thickness surrounding the pipeline. Figure 9.6 shows the location of pipe soil interaction elements. The load transferred from the soil to the pipe is strongly affected by the calibration of this soil layer.

In circumstances of sites where slope is steeper or the soil is weaker, the pipeline deforms significantly with the soil motion, pipe soil interaction has to be modified to apply to this case. On the other hand, if the slope is flatter or soil is stiffer, relative movement between pipe and soil is much smaller.

The applicability of the pipe soil interaction is tested in the parametric study. The special layer is modeled by the Modified Drucker Parger/Cap model. Possible variables are cohesion, friction angle, soil hardening, elastic modulus and creep parameters, among

which cohesion is the main variable influencing the pipe soil interaction due to shear property of soil. Three models with respect of cohesion were conducted in the parametric study for comparison with the response of the standard model to combined loading.

Figure 9.7 shows the results of peak axial compressive strain vs. cohesion of the pipe soil interaction elements. As the cohesion increases from 2 kPa to 5 kPa, the peak axial compressive strain in the pipe increases at the approximate rate 25 $\mu\epsilon$ /kPa. The rate of peak axial compressive strain increment reduces as the cohesion exceeds 30 kPa. And when cohesion is the maximum 60 kPa in the models, 30 times of the minimum cohesion 2 kPa, the peak axial compressive strain in the pipe is 506 $\mu\epsilon$, increasing correspondingly 1.35 times of strain at the minimum cohesion. The model is flexible to match with the situ soil condition for pipe-soil interaction. Internal frictional angle of the pipe soil interaction elements can be another important parameter to affect the pipe soil interaction. Here it is not covered, but the results will be similar to that of the cohesion.

9.2.7 Soil Creep Parameters

In the FEA model, creep behaviour is specified as “time hardening” form of the power law model. The expression is as the following:

$$(9.1) \quad \dot{\epsilon}^{cr} = A(\bar{\sigma}^{cr})^n t^m$$

where $\dot{\epsilon}^{cr}$ is the equivalent creep strain rate,

$\bar{\sigma}^{cr}$ is the effective creep pressure,

t is the total time, and A, n, and m are creep material parameters.

For physically reasonable behaviour, A and n must be positive and $-1 < m \leq 0$. Different creep parameters A are adopted along the length of the slope calibrated by the SI data. In the parametric study, only creep parameters m and n are investigated.

Figure 9.8 and Figure 9.9 show the results of peak axial compressive strain vs. creep parameters m and n respectively. The change of creep parameters are applied to the plastic soil layers. In Figure 9.8, as the maximum creep parameter n increases 3 times of

the minimum n , the peak axial compressive strain in the pipe increases correspondingly as much as 1.95 with growing increment. As creep parameter n reaches 1.5, the peak compressive strain accumulation of pipe is $810 \mu\epsilon$ this model. The soil model can be adjusted for the given soil movement in term of changing creep parameter n .

Another creep parameter is m with the range $-1 < m \leq 0$. In Figure 9.9, as the creep parameter m increases from -0.5 to zero, the peak axial compressive strain in the pipe increases correspondingly as much as 1.22 with growing increment. As parameter m reaches the maximum allowable magnitude zero, the peak compressive strain accumulation of pipe is $502 \mu\epsilon$ for this model. The soil model can be adjusted for given soil movement by change of creep parameter m .

9.2.8 Strain Accumulation Time

Time is an important factor in slope creep analysis. The loading events can occur in various time periods. Four models are tested for the same loading sequences in 1.5, 3, 6 and 12 months separately. Figure 9.10 shows the results of peak axial compressive strain vs. time parameter. As time increases, the peak axial compressive strain in the pipe increases almost linearly at the rate $9 \mu\epsilon/\text{month}$. As time reaches 12 months, the peak compressive strain accumulation of pipe is $551 \mu\epsilon$ for this model. The soil model can be calibrated for given soil movement by change of time parameter in the load history.

9.2.9 Soil Strength

Soil layers are modeled by elastic material and the Modified Drucker Parger/Cap model. Possible variables are elastic modulus, cohesion, friction angle, and soil hardening behaviour. Cohesion has been examined partly in pipe-soil interaction at Section 9.9. Here only elastic modulus is chosen for the comparison due to the variety of soils and the huge size of the model. Different magnitudes of elastic modulus are adopted along the length of the slope calibrated by the SI data. Four models are conducted in the parametric study with the same combined loading.

Figure 9.11 shows the results of peak axial compressive strain vs. average elastic modulus of the four models. As the average elastic modulus increases twice of the minimum, the peak axial compressive strain in the pipe reduces correspondingly as much as 0.66 with reduced rate. As average elastic modulus exceeds 21 MPa, the influence on the pipe deformation drops quickly. At the minimum average elastic modulus 16 MPa, the peak compressive strain accumulation of pipe is 583 $\mu\epsilon$. The model can be applied to wide range of clay soils.

9.3 Summary of Parametric Study

The parametric study was conducted to evaluate the sensitivity of the behaviour of pipeline to the variables compared with the pipe in Pembina River Crossing. The variables investigated were the pipe internal pressure, D/t ratio, material grade, boundary condition, slip surface, pipe soil interaction, creep parameters, strain accumulation time and soil strength.

The results of the study demonstrated that the model is considerably more sensitive to some parameters than the others. It was established that increasing any of the following: D/t ratio, strength of soil surrounding the pipe, creep parameters m and n, time parameter, resulted in a substantial increment in the pipeline deformation. It was also revealed that increasing material grade or internal pressure of the pipe, demonstrated very little influence on the pipe deformation within the elastic range. It was found that increasing either slip surface strength or soil strength of all soil layers resulted in a significant reduction in the accumulated axial strain of the pipes. Boundary conditions of the two ends of pipeline have a little influence on the strain accumulation of the pipe. It can be predicted that the longer the pipeline, the less the influence.

Parametric study and FEA model setting up have proven that apart from pipe geometry condition, pipeline performance is largely depending on the soil properties within the 25 m depth of soil layers.

Table 9.1 Parametric Study Model Matrix

Models	D/t	Pressure % SMYS	Pipe Grade	Boundary Conditions	Slip Surface	P-S Interaction	Creep n	Creep m	Time (Month)
Standard	48	35.8%	X60	Pipe Constrained in Y at Ends	c=5kPa $\phi=19.5^\circ$	c=30kPa	1.0	0	6
P/P _y	48	0%	X60	Pipe Constrained in Y at Ends	c=5kPa $\phi=19.5^\circ$	c=30kPa	1.0	0	6
P/P _y	48	10%	X60	Pipe Constrained in Y at Ends	c=5kPa $\phi=19.5^\circ$	c=30kPa	1.0	0	6
P/P _y	48	20%	X60	Pipe Constrained in Y at Ends	c=5kPa $\phi=19.5^\circ$	c=30kPa	1.0	0	6
P/P _y	48	54%	X60	Pipe Constrained in Y at Ends	c=5kPa $\phi=19.5^\circ$	c=30kPa	1.0	0	6
D/t=96	96	35.8%	X60	Pipe Constrained in Y at Ends	c=5kPa $\phi=19.5^\circ$	c=30kPa	1.0	0	6
D/t=72	72	35.8%	X60	Pipe Constrained in Y at Ends	c=5kPa $\phi=19.5^\circ$	c=30kPa	1.0	0	6
D/t=24	24	35.8%	X60	Pipe Constrained in Y at Ends	c=5kPa $\phi=19.5^\circ$	c=30kPa	1.0	0	6
X70	48	35.8%	X70	Pipe Constrained in Y at Ends	c=5kPa $\phi=19.5^\circ$	c=30kPa	1.0	0	6
X80	48	35.8%	X80	Pipe Constrained in Y at Ends	c=5kPa $\phi=19.5^\circ$	c=30kPa	1.0	0	6
BC1	48	35.8%	X60	Pipe Constrained in Y at Ends Water level 1	c=5kPa $\phi=19.5^\circ$	c=30kPa	1.0	0	6
BC2	48	35.8%	X60	Pipe Free in Y at Ends Water level 1	c=5kPa $\phi=19.5^\circ$	c=30kPa	1.0	0	6

BC3	48	35.8%	X60	Pipe Constrained in Y at Ends Water level 2	c=5kPa $\phi=19.5^\circ$	c=30kPa	1.0	0	6
BC4	48	35.8%	X60	Pipe Free in Y at Ends Water level 2	c=5kPa $\phi=19.5^\circ$	c=30kPa	1.0	0	6
BC5	48	35.8%	X60	Pipe Constrained in Y at Ends Water level 3	c=5kPa $\phi=19.5^\circ$	c=30kPa	1.0	0	6
BC6	48	35.8%	X60	Pipe Free in Y at Ends Water level 3	c=5kPa $\phi=19.5^\circ$	c=30kPa	1.0	0	6
BC7	48	35.8%	X60	Pipe Constrained in Y at Ends Water level 4	c=5kPa $\phi=19.5^\circ$	c=30kPa	1.0	0	6
BC8	48	35.8%	X60	Pipe Free in Y at Ends Water level 4	c=5kPa $\phi=19.5^\circ$	c=30kPa	1.0	0	6
Slip Layer1	48	35.8%	X60	Pipe Constrained in Y at Ends	c=2kPa $\phi=18^\circ$	c=30kPa	1.0	0	6
Slip Layer2	48	35.8%	X60	Pipe Constrained in Y at Ends	c=3kPa $\phi=19.5^\circ$	c=30kPa	1.0	0	6
Slip Layer3	48	35.8%	X60	Pipe Constrained in Y at Ends	c=10kPa $\phi=25^\circ$	c=30kPa	1.0	0	6
P-S	48	35.8%	X60	Pipe Constrained in Y at Ends	c=5kPa $\phi=19.5^\circ$	c=60kPa	1.0	0	6
P-S	48	35.8%	X60	Pipe Constrained in Y at Ends	c=5kPa $\phi=19.5^\circ$	c=10kPa	1.0	0	6
P-S	48	35.8%	X60	Pipe Constrained in Y at Ends	c=5kPa $\phi=19.5^\circ$	c=5kPa	1.0	0	6
Creep n	48	35.8%	X60	Pipe Constrained in Y at Ends	c=5kPa $\phi=19.5^\circ$	c=30kPa	0.5	0	6

Creep n	48	35.8%	X60	Pipe Constrained in Y at Ends	c=5kPa $\phi=19.5^\circ$	c=30kPa	1.5	0	6
Creep m	48	35.8%	X60	Pipe Constrained in Y at Ends	c=5kPa $\phi=19.5^\circ$	c=30kPa	1.0	-0.2	6
Creep m	48	35.8%	X60	Pipe Constrained in Y at Ends	c=5kPa $\phi=19.5^\circ$	c=30kPa	1.0	-0.5	6
Time month	48	35.8%	X60	Pipe Constrained in Y at Ends	c=5kPa $\phi=19.5^\circ$	c=30kPa	1.0	0	1.5
Time month	48	35.8%	X60	Pipe Constrained in Y at Ends	c=5kPa $\phi=19.5^\circ$	c=30kPa	1.0	0	3
Time month	48	35.8%	X60	Pipe Constrained in Y at Ends	c=5kPa $\phi=19.5^\circ$	c=30kPa	1.0	0	12
Ave. E=16 MPa	48	35.8%	X60	Pipe Constrained in Y at Ends	c=5kPa $\phi=19.5^\circ$	c=30kPa	1.0	0	6
Ave. E=21 MPa	48	35.8%	X60	Pipe Constrained in Y at Ends	c=5kPa $\phi=19.5^\circ$	c=30kPa	1.0	0	6
Ave. E=25 MPa	48	35.8%	X60	Pipe Constrained in Y at Ends	c=5kPa $\phi=19.5^\circ$	c=30kPa	1.0	0	6
Ave. E=31 MPa	48	35.8%	X60	Pipe Constrained in Y at Ends	c=5kPa $\phi=19.5^\circ$	c=30kPa	1.0	0	6

Table 9.2 Maximum Axial Stress Results Matrix

Model	Before soil movement MPa	After soil movement MPa	Stress accumulation MPa	Strain accumulation $\mu\epsilon$	Location:Distance from creek center
P/P _y =0	-4	-110	-106	-517	11m
P/P _y =10	6	-95	-101	-494	18m
P/P _y =20	15	-88	-103	-503	18m
P/P _y =35.8	33	-72	-105	-512	18m
P/P _y =54	51	-54	-105	-514	18m
D/t=96	77	-67	-144	-702	18m
D/t=32	21	-66	-87	-424	18m
D/t=24	15	-59.8	-75	-366	18m
X70	33	-72	-105	-512	18m
X80	33	-72	-105	-512	18m
BC1	33	-18	-51	-249	18m
BC2	31	-22	-53	-259	18m
BC3	33	-39	-72	-351	18m
BC4	31	-43	-74	-361	18m
BC5	33	-51	-84	-410	18m
BC6	31	-55	-86	-420	18m
BC7	33	-70	-103	-502	18m
BC8	31	-76	-107	-523	18m
Slip-Layer1	33	-47	-80	-390	18m
Slip-Layer2	33	-40	-73	-356	18m
Slip-Layer3	33	-26	-59	-288	18m
P-S c=5kPa	33	-59	-92	-450	18m
P-S c=10kPa	33	-65	-98	-478	18m
P-S c=60kPa	33	-71	-104	-506	18m
Creep n=0.5	33	-52	-85	-415	18m

Creep n=1.5	33	-133	-166	-810	18m
Creep m=-0.2	33	-55	-88	-429	18m
Creep m=-0.5	33	-51	-84	-411	18m
Time 1.5months	33	-60	-93	-454	18m
Time 3months	33	-64	-97	-474	18m
Time 12months	33	-80	-113	-551	18m
Average E=16MPa	39	-81	-120	-583	22m
Average E=21MPa	32	-53	-85	-414	18m
Average E=25MPa	33	-47	-80	-390	18m
Average E=31MPa	34	-45	-79	-384	18m

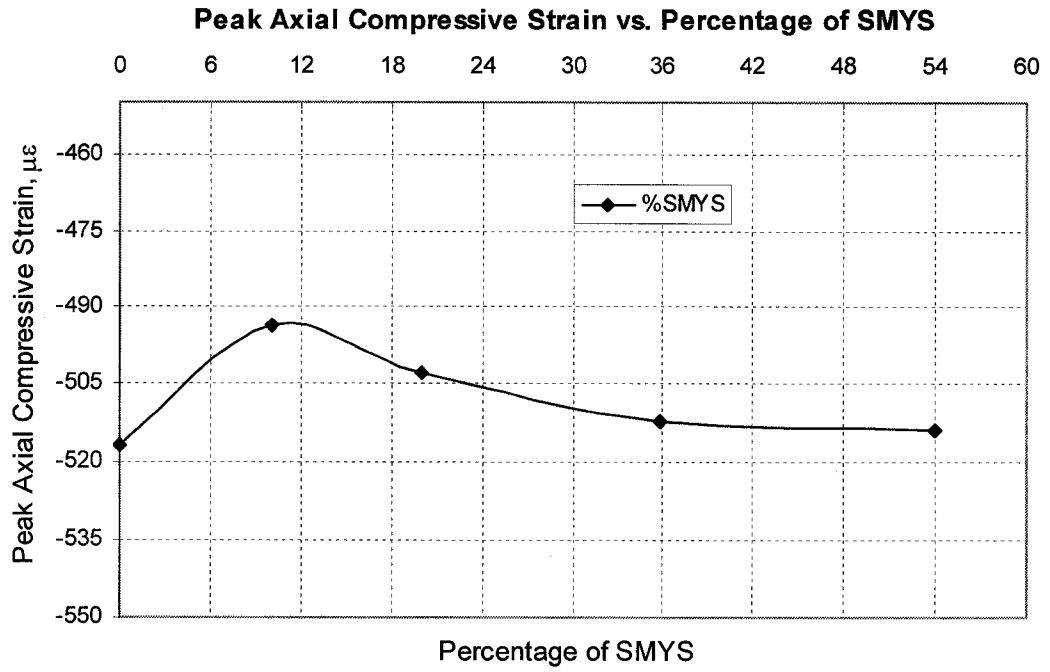


Figure 9.1 Peak Axial Compressive Strain vs. Percentage of SMYS

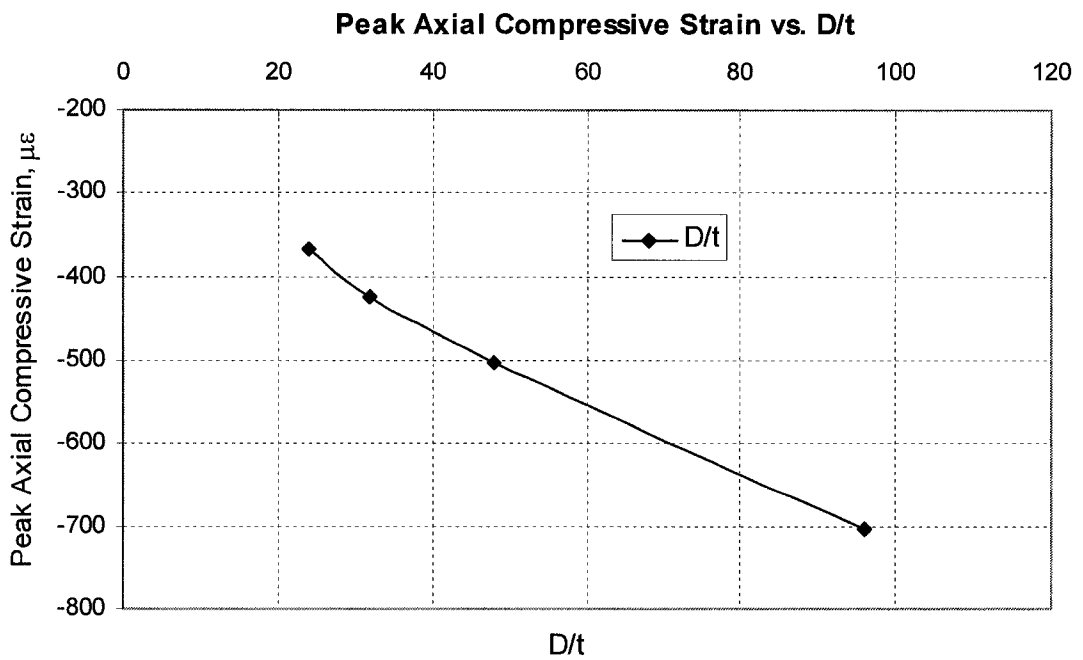


Figure 9.2 Peak Axial Compressive Strain vs. D/t Ratio

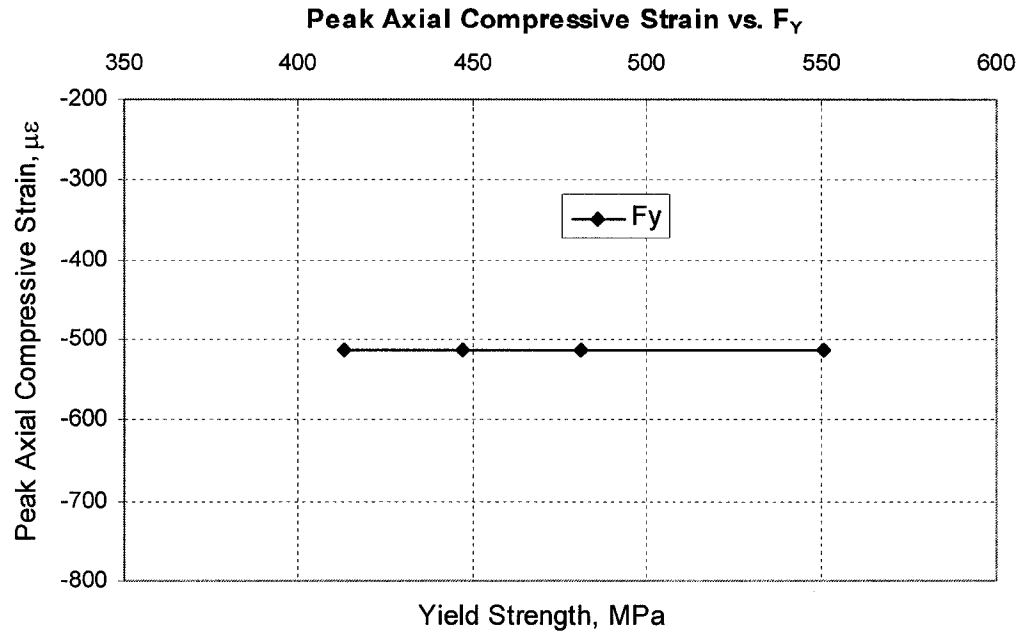


Figure 9.3 Peak Axial Compressive Strain vs. Pipe Yield Strength

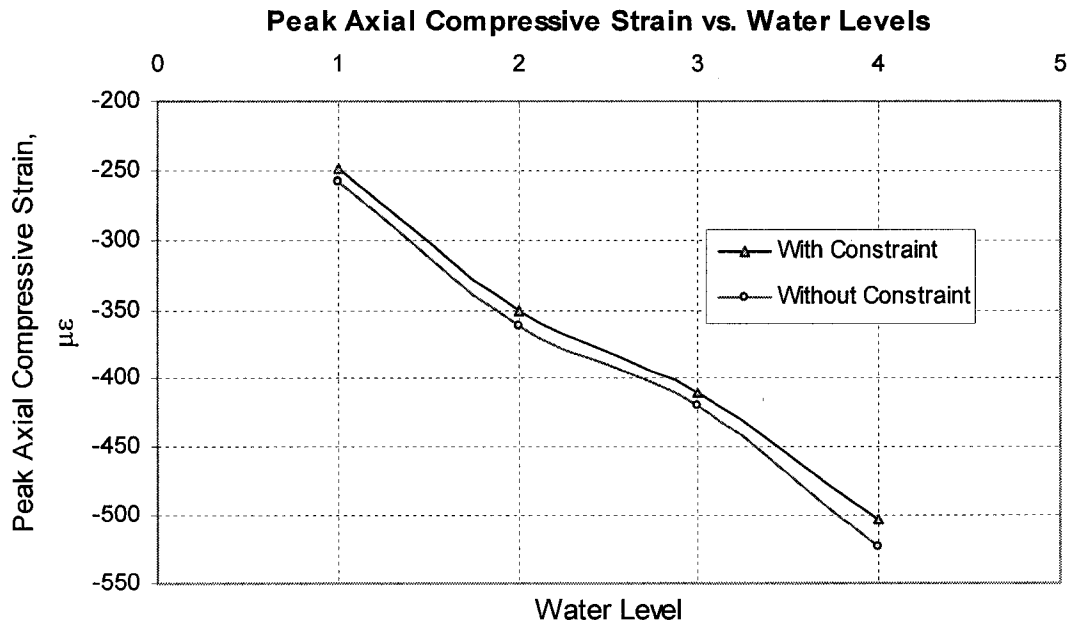


Figure 9.4 Peak Axial Compressive Strain vs. Boundary Condition

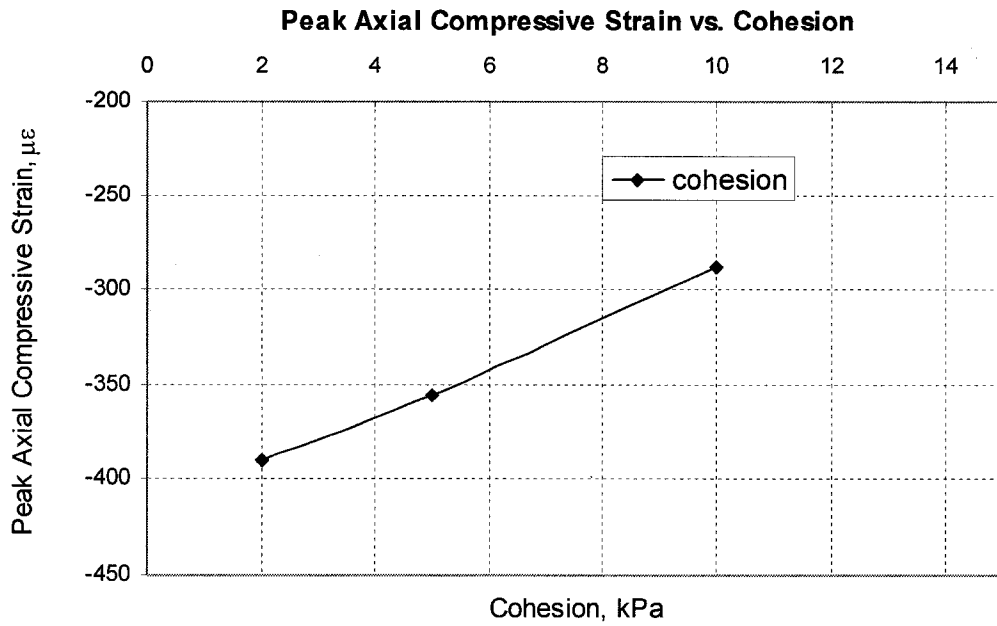


Figure 9.5 Peak Axial Compressive Strain vs. Slip Surface Condition

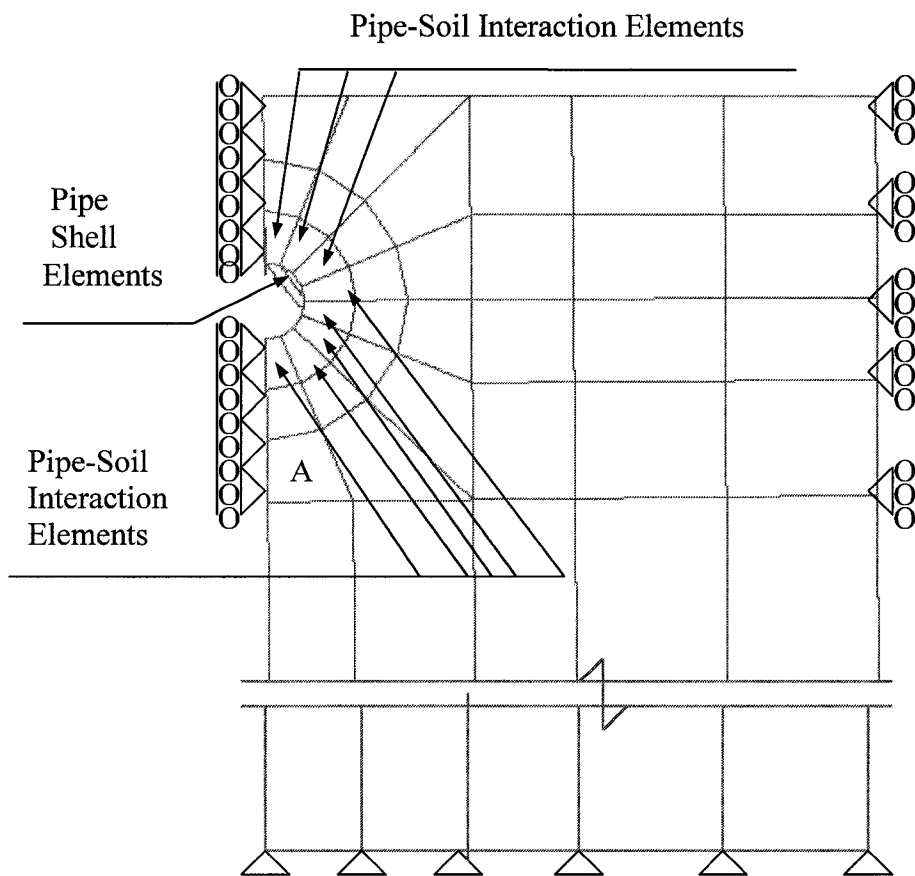


Figure 9.6 Pipe Soil Interaction Elements

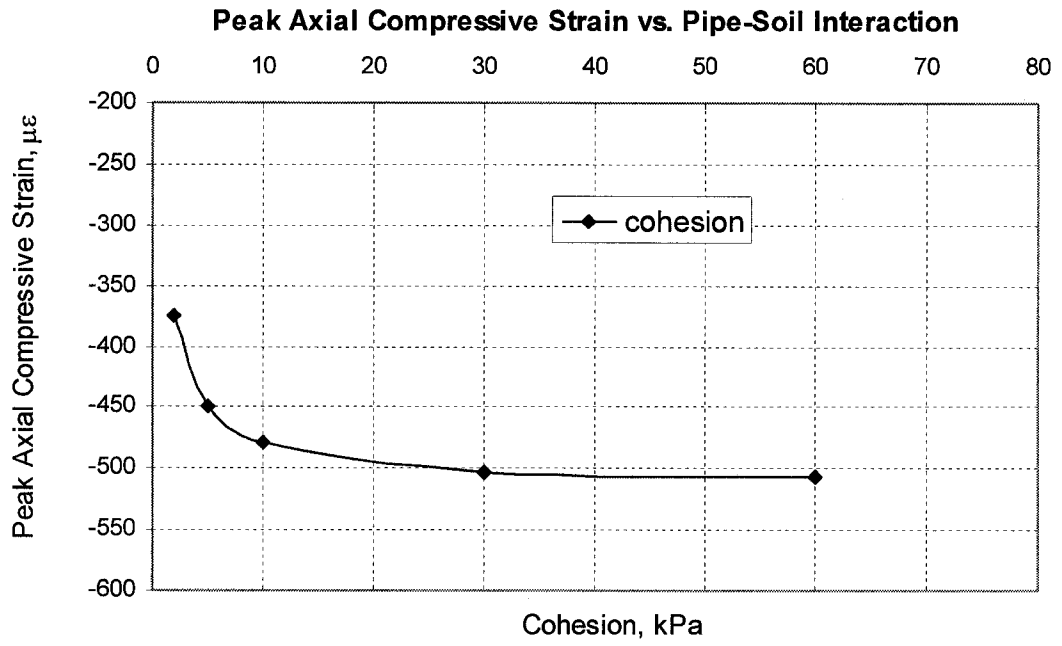


Figure 9.7 Peak Axial Compressive Strain vs. Pipe-Soil Interaction Condition

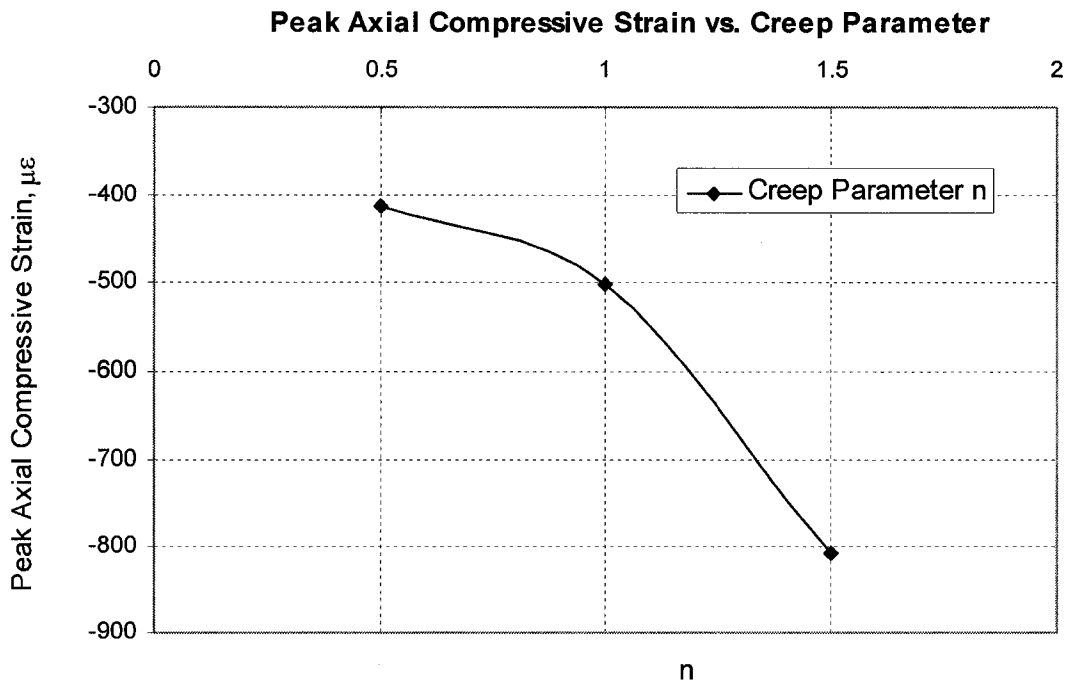


Figure 9.8 Peak Axial Compressive Strain vs. Creep Parameter n

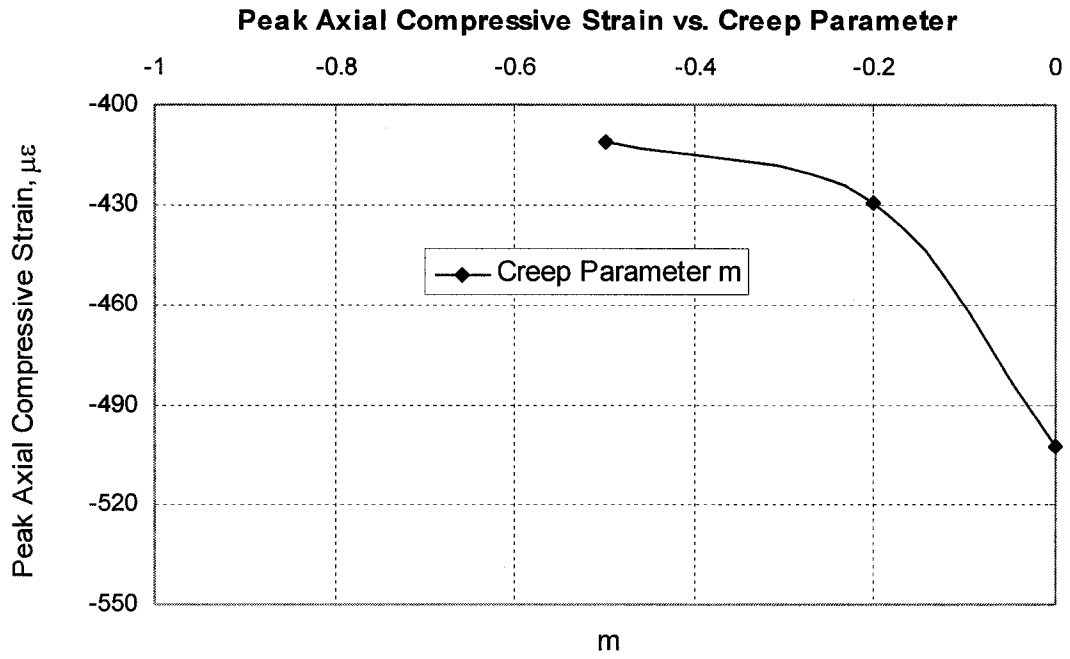


Figure 9.9 Peak Axial Compressive Strain vs. Creep Parameter m

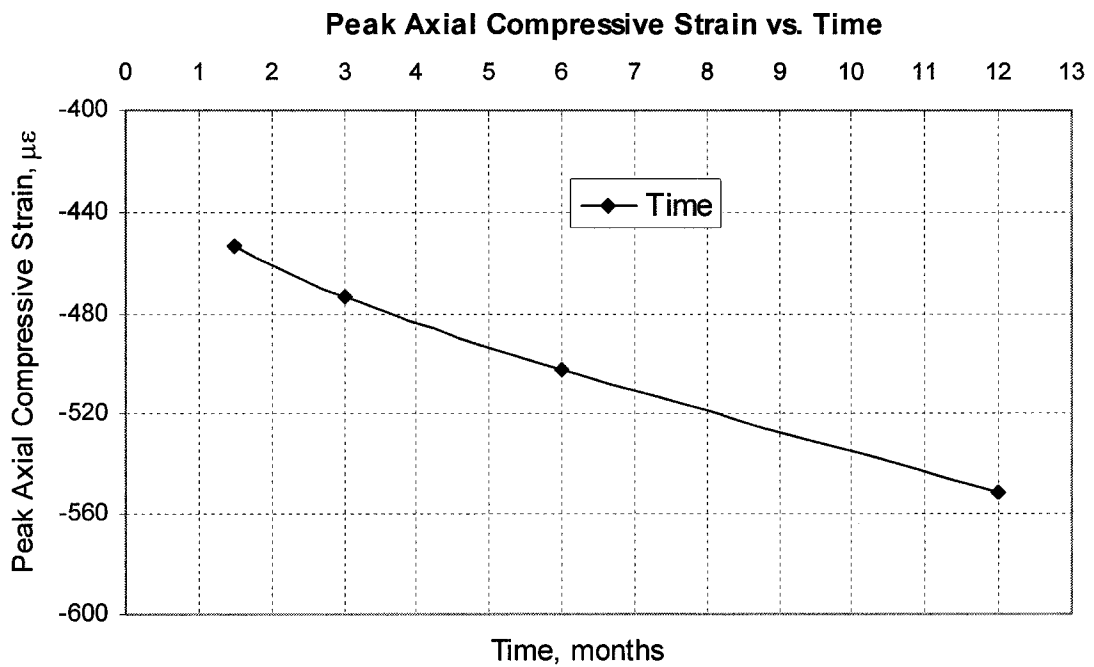


Figure 9.10 Peak Axial Compressive Strain vs. Time Parameter m

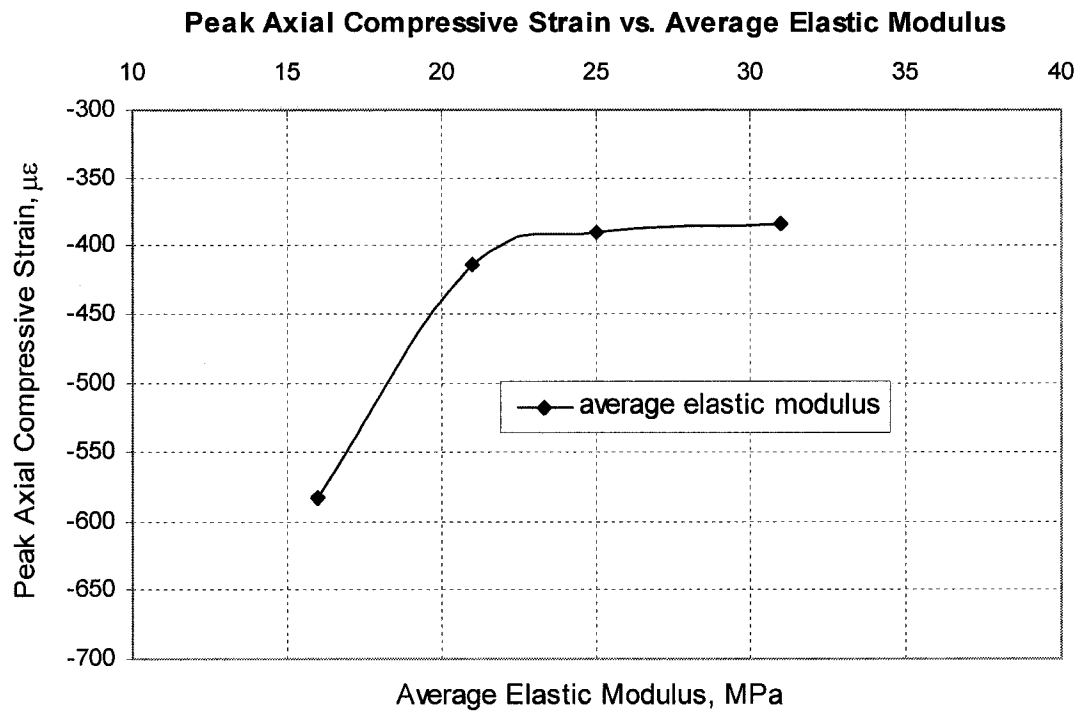


Figure 9.11 Peak Axial Compressive Strain vs. Average Elastic Modulus

CHAPTER 10 SUMMARY, CONCLUSIONS AND RECOMMENDATIONS

This Chapter summarizes the work and the main conclusions reported in the previous Chapters; recommendations for future research pertaining to pipe soil interaction and stress relief of pipelines are also presented here.

10.1 Summary

The stress relief procedure, one of the mitigation methods for buried pipelines, is based on the monitoring of pipeline strains and soil displacements in active or potentially active landslides. Such method requires periodic relief of the longitudinal strains and stresses of pipeline caused by the landslide deformations when accumulated strains approach predetermined levels.

The effectiveness of stress relief of the pipe depends largely on the orientation of the pipeline in the landslide. The two extreme cases are when the pipe is perpendicular to the direction of the landslide deformations, and when the pipe is parallel with the direction of the landslide deformations. Pipe orientations between these two cases should be considered case by case. The orientation of the pipeline in this research project is parallel with the direction of the landslide. As little is known about the strain accumulation rate in pipeline and the stress relief procedure, the main objective of this research program was to investigate the effectiveness of stress relief, and to develop a finite element model that can simulate strain accumulation of pipeline and provide the optimum schedule of stress relief.

To achieve the objective of the research twelve full-scale tests were conducted on twelve segments of pipe to study the effects of stress relief procedures on the local buckling behaviour of the pipes. These twelve specimens in the test program are six 762 mm (30 inch) and six 508 mm (20 inch) diameter pipes. The 762 mm pipe is grade X70 (SMYS = 483 MPa or 70 ksi), and the 508 mm pipe is grade X80 (SMYS = 552 MPa or 80 ksi). Three pipes of each size undergo axial deformation, and another three undergo

both axial and bending deformation. All tests are carried out with internal pressure to simulate the field condition.

Within the Alberta System, more than 20 sites are part of an condition monitoring program that are inspected to provide the necessary data from TCPL. Pembina River Crossing at LodgePole and Simonette River Crossing at Grande Prairie are the two pipeline sites locating at the active slopes. Field monitoring programs on these sites are elaborated carefully.

Finite element modeling of long term slope movement, pipe soil interaction and pipeline behaviour; as well as stress relief procedures of the pipeline at Pembina River Crossing was carried out. Technique and development of the model was stated in detail. Model verification based on the filed data and some application of the model, including simulation of pipeline performance at typical years and optimum stress relief procedure, were conducted. A further investigation on parametric study of the FEM with respect of internal pressure, wall thickness of pipe, material grade of pipe, boundary condition, slip surface, pipe soil interaction, soil creep, time and soil strength was presented.

10.2 Conclusions

A number of significant conclusions have been derived based on the experimental and numerical results:

- 1) For the load range applied in the compression and bending tests, the load cycling has minimal effect on the global response of the pipes.
- 2) In the compression tests, the load-deformation response of the pipes during the load cycling is essentially linear and elastic. There is hardly any hysteresis loop during the load cycling
- 3) In the compression tests, it was found from the tension coupon test that the pipe has a large yield plateau. As a result, local buckling of the pipe occurred with little prior inelastic deformation
- 4) In the bending tests, load cycling does not yield any accumulated local strain in the pipe before the pipe buckles. However, after the peak moment, local

- behaviour of the pipe is influenced by the pipe geometry and loads applied. Accumulated strain was observed at the wrinkle locations after each load cycling.
- 5) In the bending tests, the post buckling behaviour is influenced by the internal pressure. With higher internal pressure, the post peak load - global strain response is gentler and load cycling effects on local behaviour is less.
 - 6) In the bending tests, the moment-curvature response of the pipe during the load cycling is essentially linear and elastic. There is a little hysteresis loop during the load cycling, especially when internal pressure is high.
 - 7) Significant differences are found for the X80 material properties between longitudinal and transverse (hoop) coupons. Flattened transverse coupons give inconsistent test results.
 - 8) The numerical analyses for the experiments are able to verify the pipe behaviour and test results. The predicted values match the measured data
 - 9) Stress relief procedure of the pipeline at Pembina River Crossing is necessary to be conducted for reducing the axial compressive stress level in the pipe and elongating the service life of the pipeline.
 - 10) Without the stress relief operations, the pipeline would certainly buckle as the FEM analysis shows that pipe deformation continues with ongoing soil movement. Monitoring programs could be used to predict the potential failures in time for successful mitigation.
 - 11) The bigger the axial stress accumulated on the pipeline, the longer the scope of the soil to be excavated.
 - 12) The critical location of the pipeline at Pembina River Crossing is about 18m south to the centre of the creek. The location tends to be closer to the creek as the creep time increases and precipitation gets heavy.
 - 13) The frequency of stress relief procedure is based on the precipitation. In general precipitation (May-September is about 400 mm, yearly about 550 mm), stress relief procedure at Pembina River Crossing has to be carried out every six years.
 - 14) The effectiveness of stress relief is related to the scope of soil digging. Pipeline excavation at the Pembina River Crossing should be implemented at the south slope as well as north slope for efficient stress relief.

- 15) The model is considerably more sensitive to some parameters than the others. It was established that increasing any of the following: D/t ratio, strength of soil surrounding the pipe, creep parameters m and n, time parameter, resulted in a substantial increment in the pipeline deformation.
- 16) Increasing material grade or internal pressure of the pipe, demonstrated very little influence on the pipe deformation within the elastic range.
- 17) Increasing either slip surface strength or soil strength of all soil layers resulted in a significant reduction in the accumulated axial strain of the pipes.
- 18) Boundary conditions of the two ends of pipeline have a little influence on the strain accumulation of the pipe. It can be predicted that the longer the pipeline, the less the influence.
- 19) Parametric study and FEA model setting up have proven that apart from pipe geometry condition, pipeline performance is largely depending on the soil properties within the 25m depth of soil layers.

10.3 Recommendations

The results of this research provide a number of significant enhancements of the current state-of-art for estimating the effectiveness of stress relief procedure. Specifically, it has provided the assessment of the hazard level for the imposed combination of internal pressure, axial load and bending moment from the soil movement and has identified the important parameters that influence the stress accumulation of the buried pipeline. In addition to this, the finite element model can be used to develop the optimum stress relief procedure and operating schedule and to further understand the behaviour of pipe under repeated soil movement and stress relief procedures. Though this model was developed from the specific site, parametric study on pipeline behaviour with different variables was carried out to provide valuable guidelines for line pipes at other sites.

However, many areas were identified that require further investigation:

- 1) This FEA model is not sufficient enough to consider the soil movement in transverse direction. Future research needs to take this into account by modeling the wider range of slope in 20-30m width if transverse movement is significant.

- 2) For pipe soil interaction, the best approach is to set up connector elements between the nodes of shell elements and solid elements or to apply contact simulation algorithm between the surfaces of the shell elements and solid elements. This will allow more authentic simulation of the pipe soil interaction.
- 3) Numerical model for specimens in the experimental program under the cyclic load conditions needs to be developed to study the influence from the cyclic loading style and to expand the current experimental database.
- 4) Soil property for slip surface has to be modified for future prediction of the slope stability.
- 5) It is revealed from the FEA that the soil and concrete at the creek location constrain the pipe from complete stress relief. Further actions need to be studied.
- 6) Finally, it is possible to define a finite element mesh zones in which the discretization has to be revised and then to perform the rezoning transferring the solution from the original mesh to the new one to remedy the inefficiency and accuracy of the solution at the coarse mesh.

References

- ASCE (1984). "Guidelines for the Seismic Design of Oil and Gas Pipeline Systems. Committee on Gas and Liquid Fuel Lifelines", *Technical Council on Lifeline Earthquake Engineering*, ASCE, New York.
- Bathe, K-J., 1996. *Finite Element Procedures*. Prentice-Hall, Inc., Englewood Cliffs, NJ, USA.
- Boivin, R.P. and Cavanagh, P.C. 1992. "Remedial Action Required for Two Gas Pipelines Crossing an Unstable Slope". *Proceedings of 11th Offshore Mechanics and Arctic Engineering Symposium*, Volume V-B, pp.553-558.
- Bruschi, R., Spinazze, M., Tomassini, D., Cuscuna, S. and Venzi, S., 1995. "Failure Modes for Pipelines in Landslide Areas". *Proceedings of 14th Offshore Mechanics and Arctic Engineering*, OMAE, Houston, TX, USA, Volume 5, Pipeline Technology, pp.65-78.
- Bruschi, R., Monti, P., Bolzoni, G. and Tagliaferri, R. 1995. "Finite Element Method as Numerical Laboratory for Analysing Pipeline Response Under Internal Pressure, Axial Load, Bending Moment", *Proceedings of 14th Offshore Mechanics and Arctic Engineering*, OMAE, Houston, TX, USA, Volume 5, Pipeline Technology, pp.389-401.
- Bruschi, R., Glavina, S., Spinazze, M., Tomassini, D., Bonanni, S., Cuscuna, S. 1996. "Pipelines subject to Slow Landslide Movements: Structural Modelling vs Field Measurement", *Proceedings of 15th Offshore Mechanics and Arctic Engineering*, OMAE, Houston, TX, USA, Volume 5, Pipeline Technology, pp.343-353.
- Bowles, Joseph E. 1988, *Foundation Analysis and Design*. New York: McGraw-Hill.
- Bughi, S., Aleotti, P., Bruschi, R., Andrei, G., Milani, G., Scarpelli, G., Sakellariadi, E., 1996. "Slow Movements of Slopes Interfacing with Pipelines: Modelling and Monitoring", *Proceedings of 15th International Conference on Offshore and Arctic Engineering*, June 16-20, Florence, Italy, Volume 5, Pipeline Technology, pp.363-372.

Bukovansky, M., Greenwood, J.H., and Major, G. 1985. "Maintaining a Natural Gas Pipeline in Active Landslides". *Proceedings of Advances in Underground Pipeline Engineering*, J.K. Jeyapalan (ed.), ASCE, pp. 438-448.

Cappelletto, A., Tagliaferri, R., Giurlani, G., Andrei, G., Furlani, G., Scarpelli, G., 1998. "Field Full Scale Tests on Longitudinal Pipeline-Soil Interaction", *Proceedings of the International Pipeline Conference*, Fairfield, NJ, USA, Volume 2, ASME, pp.771-778.

Cavanagh, P.C. and Rizkalla, M. 1992. "The Development of an Alternative Approach for Pipeline Operation in Unstable Slopes: A Case History". *Proceedings of 11th Offshore Mechanics and Arctic Engineering Symposium*, Volume V-B, pp.543-551.

Chen, W-F., 1975. *Limit Analysis and Soil Plasticity*. Amsterdam, Elsevier.

Chen, W-F., 1985. *Soil Plasticity: Theory and Implementation*. Amsterdam, Oxford, Elsevier.

Cook, R.D., Malkus, D.S. and Plesha, M.E., 1989. *Concepts and Applications of Finite Element Analysis, Third Edition*. John Wiley & Sons, Inc., New York, NY, USA.

Cruden, D.M., and Varnes, D.J. 1996. "Landslide Types and Processes. Landslides: Investigation and Mitigation", *Special Report 247*, Transportation Research Board, National Research Council, pp.36-75. (ISBN 0-309-06151-2)

Czinkota, S., 1987. "Structural Analysis of Pipeline Stresses Created by Line lowering", *Canadian Journal of Civil Engineering*, Vol. 14 (6), December, pp. 719-727.

Das, B. M., 2002. *Soil Mechanics Laboratory Manual*. 6th Ed. Oxford University Press, New York.

Das, Braja M., 2005. *Fundamentals of Geotechnical Engineering*. 2nd Ed. Pacific Grove, California, Thomson.

Desai, C.S., Samtani, N.C., and Vulliet, L., 1995. "Constitutive Modeling and Analysis of Creeping Slopes." *Journal of Geotechnical Engineering*, ASCE, Volume 121, Number 1, pp.43-56.

Dorey, A.B., Cheng, J.J.R., and Murray, D.W., 2001. "Critical Buckling Strains for Energy Pipelines", *Structural Engineering Report No.237*, Department of Civil and Environmental Engineering, University of Alberta, April, 346 pages.

DiBattista, J.D., Cheng, J.J.R. and Murray, D.W., 2000. "Behaviour of Sleeper-Supported Line Pipe", *Structural Engineering Report No. 230*, Dept. of Civil and Environmental Engineering, University of Alberta, April, 220 pages.

EGIG. 1993, "*European Gas Pipeline Incident Data - 1993 Update*." European Gas Pipeline Incident Data Group Comprising: British Gas, Danisk Gasteknisk Center, Enagas, Gas de France, N.V. Nederlandse Gasunie, Ruhrgas AG, Distrigas, Snam.

Eslaamizaad, S. and Robertson, P.K. 1995. "Research on Soil-Pipeline Interaction Literature Review", *Report for NOVA Gas Transmission*, Calgary, AB, Canada, August, 124 pages.

Evgin, E. 1997. "Research Needs for Cost-Effective Design of Pipelines Buried in Creeping Slopes." *Report submitted to National Energy Board Engineering Branch*, Calgary, Alberta.

Galambos, T.V., 1988. *Guide to Stability Design Criteria for Metal Structures*. 5th Edition, John Wiley and Sons, Inc., New York.

Grivas, D.A., Schultz, B.C., O'Neil, G.D. and Simmonds, G.R. 1996. "Phenomenological Models to Predict Rainfall-induced Movements". *Proceedings of the International Conference on Offshore Mechanics and Arctic Engineering*, 15th, Vol. 5, Florence, Italy, 1996.

Hetnyi, M. 1946. *Beams on Elastic Foundations*. University of Michigan Press, Ann Arbor, Michigan.

Hibbitt, H.D., Karlsson, B.I., and Sorenson, E.P., 2006. "User's Manual: Volume 1, Volume 2 and Volume 3." *ABAQUS/Standard Version 6.4 Documentation*, Hibbitt, Karlsson & Sorenson Ltd., Providence, Rhode Island.

Hibbitt, H.D., Karlsson, B.I., and Sorenson, E.P., 2001. "Theory Manual." *ABAQUS Version 6.2 Documentation*, Hibbitt, Karlsson & Sorenson Ltd., Providence, Rhode Island.

Isenberg, J., Richardson, E., Kameda, H., O'Rourke, T. D., 1989. "Pipeline field experiment at Parkfield, California, Earthquake Behaviour of Buried Pipelines, Storage, Telecommunication, and Transportation Facilities", *ASME Pressure Vessels and Piping Conference*. July 23-27, Honolulu, HI, USA. Volume 162, pp.197-204.

Japan Gas Association, 1982. "*Specifications for Seismic Design of High Pressure Gas Pipelines*".

Kennedy, R.P., Chow, A.W., and Williamson, R.A. 1977. "Fault Movement Effects on Buried Oil Pipeline", *Journal of Transportation Engineering Division*, ASCE, Volume 103, Number TE5, pp.617-633.

Kenny, S., Phillips, R., McKenna, R.F. and Clark, J.I., 2000. "Response of Buried Arctic Marine Pipelines to Ice Gouge Events". *Proceedings of Offshore Mechanics and Arctic Engineering*, Paper OMAE00-5001, New Orleans, LA, USA.

Kim, H-S., Kim, W-S., Bang, I-W. and Oh, K.H.,1998. "Analysis of Stresses on Buried Natural Gas Pipeline Subjected to Ground Subsidence". *Proceedings of International Pipeline Conference*, Volume 2, Calgary, AB, Canada, pp.749-756.

Klever, F.J., van Helvoirt, L.C. and Sluyterman, A.C. 1990. "A Dedicated Finite-Element Model for Analyzing Upheaval Buckling Response of Submarine Pipelines." *Proceedings of 22nd Offshore Technology Conference*, Paper OTC 6333, Houston, TX, USA, pp.529-538.

Ladanyi, B. and Lemaire, G. 1984. "Behaviour of a Buried Pipeline Under Differential Frost Heave Conditions". *Proceedings of Cold Regions Engineering Specialty Conference*, CSCE, April 1984, pp.161-176.

Liu, X. and O'Rourke, M.J. 1997. "Behaviour of Continuous Pipeline Subject to Transverse PGD". *Journal of Earthquake Engineering and Structural Dynamics*. Volume 26, pp.989-1003.

McCavour, T. C., 1968. *Composite Design for Soil-Steel Structures*, Port Credit, Ontario, Corrugated Steel Pipe Institute.

McGrath, T. J., Selig, E. T., Webb, M. C., 1999. "Instrumentation for Monitoring Buried Pipe Behaviour During Backfilling", *ASTM Special Technical Publication*, Number 1358, pp.101-118

Miyajima, M. and Kitaura, M. 1989. "Effects of Liquefaction-Induced Ground Movement on Pipeline". *Proceedings of 2nd Japan-U.S. Workshop on Liquefaction, Large Ground Deformation, and their Effects on Lifelines*, Technical Report NCEER-89-0032, Multidisciplinary Center for Earthquake Engineering Research, Buffalo, NY, USA, pp.386-400.

Morsy, M. M., Chan, D. H., and Morgenstern, N. R., 1995. "An Effective Stress Model for Creep of Clay", *Canadian Geotechnical Journal*, Number 32, pp.819-834.

Morsy, M. M., Morgenstern, N. R. and Chan, D. H., 1995. "Simulation of Creep Deformation in the Foundation of Tar Island Dyke", *Canadian Geotechnical Journal*, Number 32, pp.1002-1023.

Newmark, N.M., and Hall, W.J. 1975. "Pipeline Design to Resist Large Fault Displacement". *Proceedings of U.S. National Conference on Earthquake Engineering*, Ann Arbor, MI, USA, Earthquake Engineering Research Institute, pp.416-425.

O'Rourke, M.J. and Liu, X., 1999. *Response of Buried Pipelines Subject to Earthquake Effects*. Multidisciplinary Center for Earthquake Engineering Research, Buffalo, NY, USA, 249p.

O'Rourke, M.J. 1989. "Approximate Analysis Procedures for Permanent Ground Deformation Effects on Buried Pipelines", *Proceedings of 2nd Japan-U.S. Workshop on Liquefaction, Large Ground Deformation, and their Effects on Lifelines*, Technical Report NCEER-89-0032, Multidisciplinary Center for Earthquake Engineering Research, Buffalo, NY, USA, pp.336-347.

Potts, D. M., 2001. *Finite Element Analysis in Geotechnical Engineering Application*. London, Thomas Telford.

Potts, D.M., Dounias, G.T. and Vaughan, P.R., 1987. "Finite Element Analysis of the Direct Shear Box Test", *Geotechnique* 37, Number 1, pp. 11-23

Rajani, B.B., Robertson, P.K. and Morgenstern, N.R. 1995. "Simplified Design Methods for Pipelines Subject to Transverse and Longitudinal Soil Movements". *Canadian Geotechnical Journal*, Volume 32, pp.309-323.

Reissner, E., 1958. "Deflection of plates on Viscoelastic Foundation", *Journal of Applied Mechanics*, ASME, Number 80, pp.144-145.

Rizkalla, M. and McIntyre, M.B., 1991. "A Special Pipeline Design for Unstable Slopes". *Proceedings of 14th Annual Energy-Sources Technology Conference and Exhibition of Pipeline Engineering*, ASME, Houston, TX, USA, PD-Volume 34, pp.69-74.

Rizkalla, M., Turner, R.D. and Colquhoun, I.R., 1993. "State of Development of a Fibre Optic Technology-based Pipeline Structural Integrity Monitoring System". *Proceedings of 12th Offshore Mechanics and Offshore Engineering Symposium*, Vol. V, pp. 295-302.

Scarpelli, G., Aleotti, P., Baldelli, P., Milani, G., Brambati, E., 1995. "Field Experience of Pipelines in Geologically Unstable Areas." *Proceedings, 14th Intl Conf on Offshore and Arctic Engineering*, Vol. 5, Pipeline Technology.

Schrock, B. J., 1990. "Technical Work on Flexible Pipe/Soil Interaction Overview", *Proceedings of the International Pipeline Design and Installation Conference*, New York, NY, USA, pp.351-362.

Selvadurai, A.P.S., 1979. "Elastic Analysis of Soil-Foundation Interaction". *Developments in Geotechnical Engineering*, Volume 17, Elsevier Scientific Publishing Company, Amsterdam, The Netherlands.

Shroff, A. V., 2003. *Soil Mechanics and Geotechnical Engineering*. Lisse, Exton PA, A.A. Balkema.

Simmonds, G., Zhou, Z.J. and Samchek, A.T., 1996. "A Rational Design and Operating Strategy for Pipelines Traversing Unstable Slopes". *Proceedings of International Pipeline Conference*, ASME, Volume 2, pp.1297-1306.

Song, B., Cheng, J.J.R. and Murray, D.W., 2003. "Effectiveness of Stress Relief Procedures on Buried Pipelines Phase II –Monotonic and Cyclic Bending Tests", *Pipeline Technology Report No. 2003-2*, Department of Civil and Environmental Engineering, University of Alberta, May, 115 pages.

Song, B., Cheng, J.J. Roger, Chan, Dave H. and Zhou, Joe Z.L., 2006. "Numerical Simulation of Stress Relief of Buried Pipeline at Pembina River Crossing", *Proceedings of International Pipeline Conference*, Calgary, Alberta, Canada, September 25-29.

Stepanov, I.V., Timofeyev, O.Y., Klepikov, A.V. and Malek, V.N., 1998. "An Approach to the Optimisation of the Burial Depth of Underwater Pipelines on the Arctic Offshore". *Proceedings of Ice Scour and Arctic Marine Pipelines Workshop, 13th International Symposium on Okhotsk Sea and Sea Ice*, Mombetsu, Hokkaido, Japan, pp.59-69.

Svan, G., Jostad, H.P. and Bjaerum, R.O., 1992. "Finite Element Response Analysis of a Law-Away Pipeline Expansion Curve on Soft Clay." *Proceedings of 24th Offshore Technology Conference*, Paper OTC 6878, Houston, TX, USA, pp.45-52.

Trigg, A. and Rizkalla, R., 1994. "Development and Application of a Closed Form Technique for the Preliminary Assessment of Pipeline Integrity in Unstable Slopes", *Proceedings of 13th International Conference on Offshore Mechanics and Arctic Engineering*, Halkidiki, Greece, June 12-17, pp.127-139.

TransCanada Pipelines Ltd. 2000, "Condition Monitoring Summary", *Western Alberta System Simonette River Crossing/Rupture Site*.

TransCanada Pipelines Ltd. 2000, "Condition Monitoring Summary", *Western Alberta System Pembina Reroute*.

TransCanada Pipelines Ltd. 2000, *Slope Indicators at Unnamed Creek STA.71+630.4 (Pembina)*

TransCanada Pipelines Ltd. 2000, *Pembina River South Slope Strain Relief (2000) Plan View and Profile*.

TransCanada Pipelines Ltd. 2000, *Simonette River North Slope Strain Relief (2000) Plan View*

TransCanada Pipelines Ltd. 2000, *Simonette River North Slope Strain Relief (2000) Profile*

Vlazov, V.Z. and Leontiev, U.N., 1966. *Beams, Plates and Shells on Elastic Foundations*. Israel Program for Scientific Translations, Jerusalem.

Webb, M. C., McGrath, T. J., Selig, E. T.. 1996. "Field tests of buried pipe installation procedures", *Transportation Research Record*. November, Number 1541, pp.97-106.

Wieczorek, G.F., 1996. "Landslide Triggering Mechanism. Landslides: Investigation and Mitigation." *Special Report 247*, Transportation Research Board, National Research Council, pp.76-90. (ISBN 0-309-06151-2)

Winterkorn, H.F. and Fang, H-Y., 1975. *Foundation Engineering Handbook*. Van Nostrand Reinhold Company, New York, 751 pages.

Wong, M.Y.T., 1992. *Geotechnical Investigation NPS 30 Western Alberta Mainline Crossing and Unnamed Creek NE 1/4 8-47-9-5*. NOVA Corporation of Alberta, August.

Yoosef-Ghodsi, N., Cheng, J.J.R, Murray, D.W., Doblanko, R. and Wilkie, S., 2000. "Analytical Simulation and Field Measurement for a Wrinkle on the Norman Wells

Pipeline”. *Proceedings of International Pipeline Conference*, Volume 2, ASME, Calgary, AB, Canada, pp.931-938. Paper IPC00 0009

Zhang, J. G., Stewart, D. P. and Randolph, M. F., 2002. “Modeling of Shallowly Embedded Offshore Pipelines in Calcareous Sand”, *Journal of Geotechnical and Geo-Environmental Engineering*, May, Volume 128, Issue 5, pp.363-371.